AFRL-RQ-ED-TR-2016-0023

Dynamics of High Pressure Reacting Shear Flows

AFOSR Final Laboratory Task Report

Dr. Doug Talley

Air Force Research Laboratory (AFMC)
Combustion Devices Branch
AFRL/RQRC
10 E. Saturn Blvd.
Edwards AFB, CA 93524

October 2016

In-House Report

AIR FORCE RESEARCH LABORATORY
AEROSPACE SYSTEMS DIRECTORATE

■ Air Force Materiel Command ■ United States Air Force ■ Edwards Air Force Base, CA 93524

- STINFO COPY -
NOTICE AND SIGNATURE PAGE

Using Government drawings, specifications, or other data included in this document for any purpose other than Government procurement does not in any way obligate the U.S. Government. The fact that the Government formulated or supplied the drawings, specifications, or other data does not license the holder or any other person or corporation; or convey any rights or permission to manufacture, use, or sell any patented invention that may relate to them.

This report was cleared for public release by the USAF 412 Test Wing (412 TW) Public Affairs Office (PAO) and is available to the general public, including foreign nationals.

AFRL-RQ-ED-TR-2016-0023 HAS BEEN REVIEWED AND IS APPROVED FOR PUBLICATION IN ACCORDANCE WITH ASSIGNED DISTRIBUTION STATEMENT.

FOR THE DIRECTOR:

//Signed//

DOUGLAS G. TALLEY, Ph.D.
Program Manager

//Signed//

INGRID J. WYSONG, Ph.D.
Chief, Combustion Devices Branch

//Signed//

Technical Advisor
Rocket Propulsion Division

This report is published in the interest of scientific and technical information exchange, and its publication does not constitute the Government's approval or disapproval of its ideas or findings.

REPORT DOCUMENTATION PAGE

Form Approved
OMB No. 0704-0188

1. REPORT DATE *(MM/DD/YYYY)*	**2. REPORT TYPE**	**3. DATES COVERED** *(From - To)*
10/26/2016	Technical Report	2014 - 2016

4. TITLE AND SUBTITLE
Dynamics of High Pressure Reacting Shear Flows
AFOSR Final Laboratory Task Report

5a. CONTRACT NUMBER

5b. GRANT NUMBER

5c. PROGRAM ELEMENT NUMBER

6. AUTHOR(S)
Dr. Doug Talley

5d. PROJECT NUMBER

5e. TASK NUMBER
LRIR#: 14RQ21COR

5f. WORK UNIT NUMBER
Q0YA

7. PERFORMING ORGANIZATION NAME(S) AND ADDRESS(ES)

AFRL/RQRC
Combustion Devices Branch
10 E. Saturn Blvd.
Edwards AFB, CA 93524

8. PERFORMING ORGANIZATION REPORT NO.

9. SPONSORING / MONITORING AGENCY NAME(S) AND ADDRESS(ES)

Air Force Research Laboratory (AFMC)
AFRL/RQR
5 Pollux Drive
Edwards AFB, CA 93524

10. SPONSOR/MONITOR'S ACRONYM(S)

11. SPONSOR/MONITOR'S REPORT NUMBER(S)
AFRL-RQ-ED-TR-2016-0023

12. DISTRIBUTION / AVAILABILITY STATEMENT
DISTRIBUTION STATEMENT A. Approved for public release; distribution unlimited.

13. SUPPLEMENTARY NOTES
Public Affairs Clearance No. 16494 Clearance Date: 21 October 2016
The U.S. Government is joint author of the work and has the right to use, modify, reproduce, release, perform, display or disclose the work.
Opinions, interpretations, conclusions, and recommendations are those of the author(s) and are not necessarily endorsed by the United States Air Force.

14. ABSTRACT
Hydrodynamic and combustion dynamics were investigated for reacting and non-reacting rocket injector flows. The experimental data was collected in a facility designed to directly visualize high pressure, acoustically driven flows. The facility was designed to establish traceability to extensive non-reacting data present in the literature, and to reproduce the challenging environment in liquid rocket engines, namely high (supercritical) pressures and cryogenic temperatures. The facility was upgraded to investigate both liquid hydrocarbons as well as hydrogen as fuels. Of special interest was how different rocket injector flow fields (shear coaxial, swirl coaxial, impinging etc.) coupled with acoustic perturbations. Acoustic-flame dynamics often rapidly amplify to reach the limit cycle of the thermo-acoustic instability cycle, passing through a series of intermediate states whose fundamentals are difficult to understand due to the rapidity with which the system passes through them. A unique "open loop" approach was taken to freeze these intermediate states for each injector by controlling both amplitude and frequency of the acoustic perturbations. Both sub and super-critical thermodynamic conditions were investigated to study the effect real gas effects have on atomization, mixing, and the combustion processes. High-speed diagnostics including pressure and image-based techniques were employed to investigate the dynamics. Optical diagnostics employed include back-lighting, shadowgraphy, and OH* chemiluminescence. Decomposition techniques like proper orthogonal decomposition (POD) and dynamic mode decomposition (DMD) were used to identify dominant modes and frequencies from the high speed images taken for each flow field.

15. SUBJECT TERMS

16. SECURITY CLASSIFICATION OF:			**17. LIMITATION OF ABSTRACT**	**18. NUMBER OF PAGES**	**19a. NAME OF RESPONSIBLE PERSON**
					Douglas G. Talley
a. REPORT	**b. ABSTRACT**	**c. THIS PAGE**			**19b. TELEPHONE NO** *(include area code)*
Unclassified	**Unclassified**	**Unclassified**	SAR	509	

Standard Form 298 (Rev. 8-98)
Prescribed by ANSI Std. 239.18

This Page Intentionally Left Blank

Final Laboratory Task Report

LRIR#: 14RQ21COR
Title: Dynamics of High Pressure Reacting Shear Flows
Reporting Period: 2014 – 2016
Laboratory Task Manager: Dr. Doug Talley, AFRL/RQRC
Commercial Phone: (661) 275-6174 **DSN: 5**25-6174 **Fax:** (661) 275-6245
Mailing Address: AFRL/RQRC, 10 E. Saturn Blvd. Edwards AFB, CA 93524
E-Mail Address: douglas.talley.1@us.af.mil
AFOSR Program Manager: Dr. Mitat Birkan

Research Objectives

Observe the dynamic response of the flame and flame holding region of a coaxial liquid oxygen gaseous hydrogen injector to open loop acoustic forcing. More generally, explore how the presence of chemical reactions alters the behavior of coaxial shear flows in the presence of acoustic waves.

Technical Summary

Hydrodynamic and combustion dynamics were investigated for reacting and non-reacting rocket injector flows. The experimental data was collected in a facility designed to directly visualize high pressure, acoustically driven flows. The facility was designed to establish traceability to extensive non-reacting data present in the literature, and to reproduce the challenging environment in liquid rocket engines, namely high (supercritical) pressures and cryogenic temperatures. The facility was upgraded to investigate both liquid hydrocarbons as well as hydrogen as fuels. Of special interest was how different rocket injector flow fields (shear coaxial, swirl coaxial, impinging etc.) coupled with acoustic perturbations. Acoustic-flame dynamics often rapidly amplify to reach the limit cycle of the thermo-acoustic instability cycle, passing through a series of intermediate states whose fundamentals are difficult to understand due to the rapidity with which the system passes through them. A unique "open loop" approach was taken to freeze these intermediate states for each injector by controlling both amplitude and frequency of the acoustic perturbations. Both sub and supercritical thermodynamic conditions were investigated to study the effect real gas effects have on atomization, mixing, and the combustion processes. High-speed diagnostics including pressure and image-based techniques were employed to investigate the dynamics. Optical diagnostics employed include back-lighting, shadowgraphy, and OH* chemiluminescence. Decomposition techniques like proper orthogonal decomposition (POD) and dynamic mode decomposition (DMD) were used to identify dominant modes and frequencies from the high speed images taken for each flow field.

Experimental Facility

The experiments were performed in the Combustion Stability Laboratory at the Air Force Research Laboratory (AFRL) Edwards Air Force Base, CA. The central concept was a chamber-within-a-chamber design. An outer chamber was used to contain pressure only and was exposed only to cold

gases. An inner chamber, not designed to contain large differential pressures, communicated the high pressure from the outer chamber and contained the hot gases and the acoustics. Thus the outer chamber seals needed to be designed to contain pressure only without being exposed to hot gases, and the inner chamber seals needed to be designed only to contain hot gases and acoustics but not to contain pressure. The inner chamber was designed to create a near ideal environment for one-dimensional acoustic wave propagation and acted as a wave guide from the piezo-sirens at each end. The piezo-sirens were specially designed to work in high-pressure environments (conventional sirens and speakers can't perturb the densified gas that exists at elevated pressures). High voltage amplifiers (Trek PZD 2000A) and a function generator (Fluke 292 Waveform Generator) drove the piezo-sirens. Multiple high frequency differential pressure transducers, strategically placed along the waveguide, were used to measure the standing wave created. Precise control of amplitude, frequency, and phase were achieved with real time analysis from the differential pressure transducers. Windows were placed in both the outer chamber and the central portion of the inner waveguide chamber to visualize the flow.

Heat exchangers were used to control the temperature of the different flows. The fuel and oxidant flows could be chilled down to 110 K. One of the heat exchangers was used to condense liquid nitrogen or liquid oxygen from their gaseous phases. All flow control and measurement was performed in the room temperature gaseous phase. Because of the proximity to the critical temperature at which it was required to control these cryogenic liquid oxygen and liquid nitrogen flows, this heat exchanger was designed to control temperature to within ± 1 K. The flowrates were controlled with Porter mass flow meters (122 and 123-DKASVDAA) to within ± 1%. The temperature of the flow exiting the injector was measured by physically submerging an E-Type thermocouple mounted on a linear transverse in the exiting flow. The thermocouple would then be moved out of the away after the injector exit conditions were measured in order to measure the undisturbed flow.

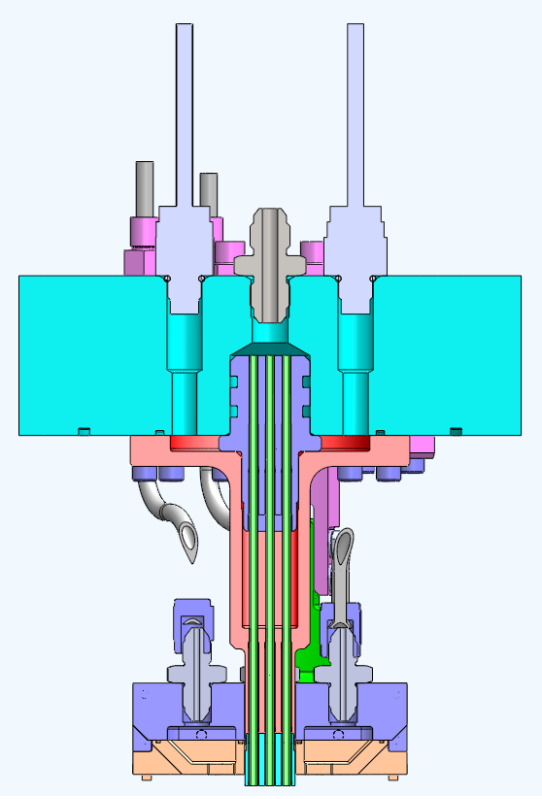

Figure 1. Multi-element injector.

Room temperature gaseous nitrogen (N2) was used to pressurize the outer windowed chamber. The pressurizing flow was much smaller than the injection flow rate; thus pressure came from the pressurizing flow and not the combustion flow. This allowed precise control over the conditions to which the injected flows were subjected. Photographs and further details about the facilities are contained in the source references below.

Multi-element injector

Full scale rocket engines have many injectors and are placed in strategic locations so as not to induce combustion instabilities. Although there are multiple single element studies, there are fewer multi-element studies with the intent of studying combustion instabilities. It is vital to capture the physics associated multiple injectors with acoustic perturbations. Equally important is to understand

how a single element behaves when influenced by a neighboring element.

To this end, a multi-element injector was designed to be used in the above facilities, but was not tested during this reporting period. Plans are to perform the research during the renewal effort. The final design is shown in Figure 1. The multi-element studies will be investigated with the same techniques used for single element studies. Using these high speed imaging techniques, the displacement of the flame fronts from individual injectors can be measured with respect to the acoustic perturbation. OH* or CH* chemiluminescence, depending on the fuel of choice, can be used to calculate Rayleigh indices for each injector. The flaming holding regions for each injector will be investigated, their interactions with each other, and the acoustic perturbations. The piezo-sirens will be used to set up a standing wave where the crests and troughs of the standing wave can be located at any one of the nozzle exits. Flame transfer functions and the combustion response between the single and multi-element configurations will be compared.

Results

The results summarized below are described in detail in the source references. Copies of the source references are provided in the appendices.

Dynamic-Mode Decomposition Based Analysis of Shear Coaxial Jets With and Without Transverse Acoustic Driving [1].

Modal decompositions of unperturbed and acoustically driven injector flows from shear coaxial jets were implemented using dynamic-mode decomposition (DMD). Dynamic mode decomposition is a continuous linear approximation to oscillator systems, linear or non-linear, and imposes a unique frequency for each mode in the decomposition. The model decomposition was applied to data previously collected at AFRL. Two geometries of shear-coaxial injectors using a center and outer flow of liquid and gaseous N2, respectively, were extensively studied. Proper orthogonal decomposition (POD) was used to reveal the most energetic pairs of coherent structures for these injector flows. One of the drawbacks of POD was that it was unable to extract and identify low-energy coherent structures associated with the injector flow among the noise and other irregular facets.

A DMD algorithm was introduced and used to differentiate among the low-energy coherent structures and the irregular flow and noise. The algorithm was applied to base line acoustically unforced conditions and pressure anti-node (PAN) and pressure node (PN) acoustically forced conditions. Using the DMD technique, the research group was able to identify different classes of robust dynamic modes present in the flow field of the shear coaxial injectors tested. The researchers define a ‘robust’ mode, as a mode that was persistent regardless of the sample size from the data that was used in the DMD analysis. They sub-divided these robust modes into: (1) background modes located outside the injector flow that decay rapidly, (2) injector modes – including those presented in POD studies – that have well defined spatial structure and exhibit high-frequency dynamics, (3) rotating modes present only for high momentum flux ratio (J) values, (4) linear response modes – modes responding linearly to the acoustic driving and, (5) persistent modes observed only in PAN forcing conditions, where the injector flows have a structure and period similar to unforced conditions.

Despite their apparent simplicity, shear coaxial jets exhibited highly complex dynamical behavior. The first robust mode contained a set of low-frequency excitations located outside the primary

injector flow that exhibited rapid decay. Reconstruction of the background modes showed that this flow constituent has no well-defined structure, hence can be identified as either noise or irregular facets. Identification of the background modes provided a systemic approach to differentiating noise from the actual flow structures, which could not be accomplished with the POD method. The second group of modes, referred as injector modes, are identified by their location near the primary injector flow. Unlike background modes, they have well-defined structures, they are high-frequency modes, they propagate along the direction of the injector flow, and they decay at a significantly slower rate. The third mode, the rotating mode, is only formed when $J \geq 5.2$. This mode is identified when an antiphase oscillatory behavior is present in the DMD spatial modes. For the fourth group of modes, acoustic driving generates additional small-wavelength modulations on the liquid nitrogen core and the injector. They are also identified as having an identical or higher harmonic frequency compared to the driving frequency. The last group of modes, the persistent modes, are a class of robust modes that retain the same structure and features of the unforced conditions even when subjected to acoustic perturbations.

Development of a Facility for Combustion Stability Experiments at Supercritical Pressure [2].

High-frequency instabilities, which are generally the most harmful in liquid rocket engines, can be driven by interactions between disturbances associated with transverse acoustic resonances and the combustion process. The combustion response to acoustic perturbation is a critical component of the instability mechanism, and is in general not well understood. A description of capabilities and development of the new experimental facility is given in this paper. The new facility was constructed at the Air Force Research Laboratory (AFRL) at Edwards Air Force Base to investigate the coupling between transverse acoustic resonances and single/multiple liquid rocket engine injector flames. Critical aspects of the facility that set it apart from other facilities include: the capability to operate at supercritical pressures that are relevant to high-performance liquid rocket engines, accurately controlled cryogenic propellants, optical access to facilitate the use of advanced diagnostics, and piezo-sirens capable of driving high pressure flows. A widely variable test matrix is achievable for non-reacting and reacting flows conditions by utilizing precise control of propellant temperatures and chamber pressure. Temperatures can be controlled with an accuracy of ±1 K in a range spanning from 100 K to room temperature for oxygen. The mean chamber pressure is controlled using an external pressurant, in most cases nitrogen. Externally pressurizing the chamber decouples the chamber pressure from the combustion process. The transverse acoustic resonance is induced through the use of carefully-controlled piezoelectric sirens, allowing monochromatic excitation across a range of amplitudes at a number of discrete frequencies. The location of the flame within the acoustic resonance mode shape can also be varied through relative phase control of the two acoustic sources.

Preliminary non-reacting and reacting data taken at 400 psi, demonstrates the quality of operation of this facility. The non-reacting back-lit imagery confirms the results from previous researchers. Physical flow features like the recirculation zone beneath the inner tube post is present, the coaxial flow field features the same 3 spatial zones as shown in Ko and Kwan (4). OH* chemiluminescence images of the reacting flow are also presented, confirming flame attaches at the injector exit.

Receptivity of a Cryogenic Coaxial Gas-Liquid Jet to Acoustic Disturbances [3,4].

An experimental study was conducted to explore the receptivity of cryogenic coaxial jet flows to transverse acoustic disturbances. The shear coaxial jet flow employed liquid nitrogen in the inner jet and cooled helium in the outer annular jet to represent the nominal fluid dynamical conditions of an oxygen/hydrogen liquid rocket engine injector. The injector flow was submerged in a chamber that experienced a monotonic transverse acoustic resonance characteristic of a rocket chamber in the presence of combustion instability. The coaxial jet was exposed to a variety of acoustic conditions including different frequencies, amplitudes, and locations within the resonant mode shape. High-speed back-lit images were captured to record the behavior of the natural (unforced) and forced coaxial jets. Proper orthogonal decomposition (POD) and spectral analysis were used to extract natural and forced modes. Convective modes were also extracted, and a new Strouhal number was developed to characterize the dominant natural convective mode. It was found that the convective mode is analogous to the preferred mode in free jets. The threshold of receptivity was found for a number of different injector flows and acoustic forcing conditions. The results indicate that the dimensionless frequency plays an important role, and there exists a finite forcing amplitude at which the threshold of receptivity occurs or when the injector flow responds to the acoustic perturbations. The receptivity threshold and post receptivity response provides useful insight on the suitability of a given injector design for specific rocket combustion chamber conditions.

It was found, over the range of conditions considered, that the shear flow structures along the inner jet convect at a speed well predicted by a previous model. The new Strouhal number put forth provided reasonable collapse of the frequency of convective modes as extracted from POD analysis. Several coaxial jets conditions, with different J values (momentum flux ratios), were chosen and forced at different frequencies and pressure amplitudes. Different forcing phases, including pressure antinode and pressure node conditions were investigated.

For both J values tested, the pressure antinode forcing generates pulsation in the outer jet flow rate that subsequently excites instabilities in the flow. The receptivity of the flow field to pressure antinode forcing occurs near the condition where $P' = \frac{1}{2}\rho U^2$ for the outer hydrogen jet, independent of the J value, with the exception of a condition exhibiting high natural frequencies present in the flow field. The pressure node forcing results in a strong coupling even at very low acoustic velocities. The relative magnitudes of the acoustic velocity to the characteristic velocities of the coaxial jet make it unlikely that the acoustics directly generate disturbances in the shear flow. A potential mechanism for this is that the coherent transverse velocity fluctuations of the acoustic field is exciting one or multiple helical modes in the outer jet. The receptivity trends for a pressure node were different depending on operating condition, suggesting subtle hydrodynamic effects in the receptivity mechanism. Interestingly, the lower J values conditions were less receptive at high frequency pressure antinode forcing while the higher J conditions were less receptive for the pressure node forcing.

Acoustically Forced Coaxial Hydrogen/Liquid Oxygen Jet Flames [5].

Combustion instabilities can pose serious problems in the development of liquid rocket engines. In order to understand and predict them, it is necessary to understand how representative liquid rocket injector flames react to acoustic waves. In this study, a representative coaxial gaseous hydrogen / liquid oxygen (LOX) jet flame in a high pressure environment were visualized for both reacting

and non-reacting cases and compared. The coaxial jet was visualized with high speed shadowgraph. A sensitively study of the non-reacting jet and the jet flame to increasing pressure forcing amplitudes was investigated. Two acoustic forcing configurations, pressure anti-node and pressure node, were studied.

For unforced flames, reactions are found to cause a significantly more expanded plume due to the vaporization and expansion of the LOX jet. Flame holding was established at the lip with a particularly dominant LOX recirculation zone. For the non-reacting jets, structures present on the LOX jet's surface propagate downstream at relatively constant velocity. For the reacting jets, structures on the LOX surface start at a slow speed and gradually accelerate with downstream distance. These structures never reach the velocity of the non-reacting structures. Pixels analysis along the shear layer of the LOX/GH2 shift the spectral content to lower frequencies for reacting jets, consistent with trends observed in the linear stability literature. For forced flames, acoustics do not appear to affect the flame holding. A critical finding since a detachment and reattachment of the flame can directly drive combustion instabilities.

Dynamic mode decomposition was used to detect jet response and sensitivity to the increasing pressure amplitudes. After a critical forcing pressure amplitude was reached, the DMD analysis detected not only the forcing frequency but higher harmonics as well. Reactions produce inconsistent trends in the harmonics: reactions promote harmonics at a pressure antinode while they damp harmonics at a pressure node. Another finding was that the non-reacting jets coupled with the acoustic forcing at lower pressure amplitudes compared to reacting conditions. It is believed that the flame present along the LOX/GH2 shear layer for the reacting conditions provides a shielding effect to the LOX jet, hence greater pressure amplitudes are needed to couple the injector flow field with the acoustic forcing.

Cryogenic Impinging Jets Subjected to High Frequency Transverse Acoustic Forcing in a High Pressure Environment [6]

Impinging jet injectors are one of the many injectors type used for liquid propellant atomization in rocket engines. Liquid rocket engines like the F-1 have successfully used like-on-like impinging jet injectors and are a preferred injector type for hypergolic and gelled-propellants. Extensive experimental and theoretical studies have been performed on understanding the spray characteristics of these injectors, but in the context of combustion instabilities, these injectors have not been extensively studied in an externally forced acoustic environment simulating combustion instabilities. To rectify this lacking of understanding, cryogenic nitrogen impinging jets were studied in a high pressure nitrogen environment and subjected to an acoustic perturbation. High speed backlit imaging was used to capture the physical response of the impact waves, a flow feature present on the impingement sheet formed from the impact of the two jets, to acoustic forcing. The study was split into two phases. For the first phase of the study, jet velocity and chamber pressure were varied until impact waves were visually prominent on the impingement sheet. Chamber pressures, up to 700 psi (well above the supercritical pressure of nitrogen of 500 psi), and jet velocity, 2 to 10 m/s, were investigated. It was observed that impact waves became visually prominent in a narrow range of chamber pressures and jet velocities, particularly when both jet velocity and chamber pressure are low. This contradicts observations that impact waves are present in all operating conditions, alluded to by past researchers. At supercritical pressure conditions, no droplets or ligaments were ever observed to form; instead, the flow field resembles a mist. At subcritical pressures both ligaments and

droplets were observed to be shed from the impingement sheet. At subcritical pressures there appears to be an influence of jet to chamber gas density ratio. It was observed for the same jet velocity but different chamber pressure, the two jets would fully atomize sooner at higher chamber pressures and no impingement sheet would form.

For the second phase, after the conditions that led to impact waves being visually prominent were identified, DMD was used to extract the natural frequencies of the impact waves and isolate the spatial structures for both the unforced and forced conditions. The chamber pressure (125 psi) and jet velocity (2 m/s) were kept constant for this phase of the study. For the forced conditions, the pressure amplitude was incrementally increased until the injector and the acoustic field fully coupled. The results indicate that the influence of impact waves appears to vanish once a certain pressure amplitude is reached. When subjected to pressure antinode forcing the impingement sheet size grows and decays and a large group of droplets are shed resulting in a downstream flow field with a 'christmas tree' appearance. For the pressure node forced conditions, in-plane flapping is generated and ligaments are stripped off the impingement sheet and result in a downstream zig-zag pattern of ligaments and droplets.

Nano-ignition Torch Applied to Cryogenic H2/O2 Coaxial Jet [7].

A high-pressure photoignition torch has been developed, with a patent application filed. The torch ignitor takes advantage of the photoignition properties of single wall carbon nanotubes (SWNT). The goal was to initiate combustion in a cryogenic O2-H2 coaxial injector at high pressure (up to 500 psi) at O2 temperature of about 130 K with SWNT-based "solid fuel mixtures". The investigation studied the effects of ignition at high chamber pressures, the presence of different solid oxidizers such as BKNO3 and KMnO4, and solid propellants on the functionality of the photoignition torch. The research group has shown that the ignition parameters such as burn temperature, burn time, and the ignition byproducts can be tailored to meet different ignition requirements.

Ignition of the SWNT is achieved by a short burst of light (achievable with a camera flash) which in turn ignites solid rocket propellant or other solid fuel mixtures. The reacting combination of SWNT and solid fuel propellant are then used to ignite the main injector flow. For the cryogenic O2/H2 shear coaxial injector studies mentioned earlier, this torch ignitor was used to ignite the main flow. This method has successfully proved that nano-particles can ignite liquid rocket engine type flows at elevated pressures where conventional spark plugs do not operate. It is anticipated that photoignition provides a suitable method for ignition of systems that require the start of combustion at high pressures. It is believed that this method of ignition system can operate up to 2000 psi chamber pressure. This ignition is well suited for liquid rocket engines since it is extremely small and lightweight. It is anticipated that this ignition method can be applied to other larger combustion chambers such as gas turbines, gas generators, and possibly multi grain solid rocket motors.

Conclusions

Hydrodynamic and combustion instabilities for several rocket injectors were systemically studied. Rich, complex behaviors were observed for each injector, either acoustically forced or unforced. Image decomposition techniques like POD and DMD were successfully applied to extract coherent, high frequency flow structures and natural frequencies of the flow field.

For shear coaxial injector studies, simulant gases were initially used to study the flow dynamics

for a large spread of conditions. The high speed images were processed using POD and DMD. Using the DMD technique, robust modes, independent of operating condition, were identified. These robust modes can then be used to simplify existing computation models, since shear coaxial flow can be reconstructed with a few robust modes. A new Strouhal number was proposed and collapsed the natural frequencies of the shear coaxial flow, independent of the operating condition, to a single value. For the sensitivities studies to acoustic pressure amplitudes, DMD was used to detect the coaxial flow response. It was discovered that a critical pressure amplitude is needed before the coaxial flow couples with the acoustic forcing. The critical pressure amplitude is on the order of the co-flow dynamic pressure.

For the impinging jet studies, contrary to past research, impact waves on the impingement sheet were only present in a narrow range of operating conditions. Once the conditions were identified where impact waves are present, the flow field was then subjected to acoustic perturbations. Impact waves appeared to vanish once a critical pressure amplitude was reached. In a pressure antinode forcing configuration, a large group of droplets were shed resulting in a downstream flow field with a 'christmas tree' appearance. For the pressure node forced conditions, in-plane flapping was generated and ligaments are stripped off the impingement sheet and result in a downstream zig-zag pattern of ligaments and droplets.

A nano-particle ignitor was developed. Single-wall carbon nanotubes were used to ignite a solid fuel mixture. The carbon nanotube and solid fuel mixture were then used to ignite cryogenic shear coaxial flow at elevated pressures. A patent application has been filed for this unique and novel ignitor.

Funding Summary by Cost Category

Funding Utilized ($k):	**FY14**	**FY15**	**FY16**
Non-Military Government Personnel Cost			
In-House Contractors Cost	365	435	348
Travel (Be Specific)			
Training (Be Specific)			
Supplies			
Other Expenses (Be Specific)			
Total Resource Requirements	365	435	348

Appendix A: In-House Activities

Personnel:

Name	Degree	Discipline	Involvement
Air Force Employees:			
Doug Talley	Ph.D.	Mechanical	1/5
Ivett Leyva	Ph.D.	Aerospace	1/5
On-Site Contractors:			
David Forliti	Ph.D.	Mechanical	1/2
Jeffrey Wegener	Ph.D.	Aerospace	1
Dr. Al Badakhshan	Ph.D.	Physics	1/2
Mario Roa	Ph.D.	Aerospace	1/2
Randy Harvey		Technician	3/4

Publications

Published in Peer Reviewed Journals, Books, etc:

[1] Hua, J.C., Gunaratne, G. H., Talley, D. G., Gord, J. R., and Roy, S., " Dynamic-mode decomposition based analysis of shear coaxial jets with and without transverse acoustic driving," Journal of Fluid Mechanics, 2016, Vol. 790 (Appendix C1)

Wegener, Jeffery, Multi-phase Combustion and Transport Processes Under the Influence of Acoutic Excitation, PhD Thesis, UCLA, 2014 (Appendix C8)

Published in Un-reviewed Literature (e.g., Technical Proceedings):

[2] Wegener, J. L., Leyva, I. A., Forliti, D. J., Talley, D. G., "Development of a Facility for Combustion Stability Experiments at Supercritical Pressures," 52nd Aerospace Science Meeting, 13-17 January 2014, National Harbor Maryland (Appendix C2)

[3] Wegener, J. L., Forliti, D. J., Leyva, I. A., Talley, D. G., "Receptivity of a Cryogenic Coaxial Liquid Jet to Acoustic Disturbances," ILASS Americas 26th , Portland, OR, May 2014 (Appendix C3)

[4] Wegener, J. L., Forliti, D. J., Leyva, I. A., Talley, D. G., "Receptivity of a Cryogenic Coaxial Gas-Liquid Jet to Acoustic Disturbances," 50th AIAA/ASME/SAE/ASEE Joint Propulsion, July 28-30, 2014, Cleveland, OH (Appendix C4)

[5] Roa, M., Forliti, D., Badakshan, A., and Talley, D., "Acoustically Forced Coaxial Hydrogen/Liquid Oxygen Jet Flames," ILASS Americas 28th , Dearborn Mi, May 2016 (Appendix C5)

[6] Roa, M., Schumaker, S. A., Talley, D. G., "Cryogenic Impinging Jets Subjected to High Frequency Transverse Acoustic Forcing in a High Pressure Environment," 52nd AIAA/SEA/ASEE

Joint Propulsion Conference, Salt Lake City, Utah, July 25-27 2016 (Appendix C6)

[7] Badakshan, A., Danczyk, S., Forliti, D., Leyva, I., and Talley, G., "Nano-ignition Torch Applied to Cyrogenic H2/O2 Coaxil Jet," 54th AIAA Aerospace Sciences Meeting, 4-8 Janauary 2016, San Diego, Ca (Appendix C7)

Accepted/Submitted for Publication:

D. J. Forliti, I. A. Leyva, D. G. Talley, J. I. Rodriguez, S. Teshome, J. L. Wegener, M. Roa, and, A. R. Karagozian, " Forced and unforced shear coaxial mixing and combustion at subcritical and supercritical pressures," AIAA Book Chapter in Editing (Appendix C9)

Invention Disclosures and Patents Granted:

Badakhshan, A., and Danczck, S. "Self-Contained Photo-Ignition Torch as Combustion Initiator and Gas Generator," invention disclosure and patent application 62/073,552 (2014).

Invited Lectures, Presentations, Talks, etc:

Forliti, D., Wegener, J., Leyva, I., and Talley, D., "Dynamics of High Pressure Reacting Shear Flows," AFOSR Contractor's Meeting, 16-17 Dec 2013.

Wegener, J., Leyva, I., Forliti, D., and Talley, D., "Shear-coaxial Jets Under the Influence of Acoustic Excitation," RQR Basic Research Program Review, 28-30 January 2014.

Forliti, D., Badakhshan, A., Wegener, J., Leyva, I., and Talley, D., "Dynamics of High Pressure Reacting Shear Flows, Nanoenergetics/combustion instability workshop, UCLA, Jan 2015.

Badakhshan, A., Talley, D., and Danczyk, S., "Energetic Materials for Controlling the Ignition of Liquid Fuel Spray at Elevated Pressures (0-750 psi)," Nanoenergetics/combustion instability workshop, UCLA, Jan 2015.

Roa, M., Forliti, D., Badakhshan, A., and Talley, D., "Dynamics of High Pressure Reacting Shear Flows," Space Power and Propulsion Contractor's Meeting, 2 October 2015.

Professional Activities (editorships, conference & society committees, etc):

Talley, D., Editor-in-Chief, AIAA Journal of Propulsion and Power, 2014-2016.

Talley, D., Chair, Institute of Liquid Atomization and Spray Systems – Americas, 2015-2017

Leyva, I., Chair, AIAA Liquid Propulsion Tech Committee, 50 world leaders in propulsion, 2015-

Honors Received:

Ivett Leyva, Technology Rising Star, Women of Color STEM conference, 2015

Ivett Leyva, STEM Military & Civilian Heroes – Hispanic Engineer National Achievement Awards Conference, 2015

Jeffrey Wegener – Doctorate from UCLA, 2014

Ivett Leyva, AFOSR Civilian of the Quarter, DR II through IV, Oct-Dec 2014

WR Marshall best paper award, ILASS Americas, for the paper "Receptivity of a Cryogenic Coaxial Liquid Jet to Acoustic Disturbances," by Wegener, J. L., Forliti, D. J., Leyva, I. A., and Talley, D. G., ILASS Americas 26th , Portland, OR, May 2014.

Appendix B: Technology Assists, Transitions, or Transfers—Detailed Listing

Task Title	Performance Period	AFOSR Program Manager	TD Performer	Customer	Research Results	Application	From	To	Application
14RQ21COR	2014-2016	Birkan	Talley, AFRL	Doug Talley, AFRL, douglas.talley@us.af.mil, DSN 525-6174	Basic understanding, validation data, for ALREST program	Combustion stability design code	L	AF	Pd
14RQ21COR	2014-2016	Birkan	Talley, AFRL	Johanna Lopez, SMC johanna.lopez.1@us.af.mil, DSN 633-3404	Basic understanding, validation data, for VISP program	Combustion stability design code	L	AF	Pd
14RQ21COR	2014-2016	Birkan	Talley, AFRL	Doug Lynch, Aerojet-Rocketdyne, Edward.Lynch@rocket.com, (818) 586-1597	Validated production code	AR-1 engine development program	L	I	Pd

This Page Intentionally Left Blank

Appendix C: Published Papers

J. Fluid Mech. (2016), *vol.* 790, *pp.* 5–32.
doi:10.1017/jfm.2016.2

Dynamic-mode decomposition based analysis of shear coaxial jets with and without transverse acoustic driving

Jia-Chen Hua[1], Gemunu H. Gunaratne[1], Douglas G. Talley[2], James R. Gord[3] and Sukesh Roy[4,†]

[1]Department of Physics, University of Houston, Houston, TX 77204, USA

[2]Aerospace Systems Directorate, Air Force Research Laboratory, Edwards Air Force Base, CA 93524, USA

[3]Aerospace Systems Directorate, Air Force Research Laboratory, Wright-Patterson Air Force Base, OH 45433, USA

[4]Spectral Energies, LLC, Dayton, OH 45431, USA

(Received 26 May 2015; revised 21 October 2015; accepted 30 December 2015)

Modal decompositions of unperturbed and acoustically driven injector flows from shear coaxial jets are implemented using dynamic-mode decomposition, which is a natural approach in the search for collective oscillatory behaviour in nonlinear systems. Previous studies using proper orthogonal decomposition had revealed the most energetic pairs of coherent structures in injector flows. One of the difficulties in extracting lower-energy coherent structures follows from the need to differentiate robust flow constituents from noise and other irregular facets of a flow. The identification of robust features is critical for applications such as flow control as well, since only they can be used for the tasks. A dynamic-mode decomposition based algorithm for this differentiation is introduced and used to identify different classes of robust dynamic modes. They include (1) background modes located outside the injector flow that decay rapidly, (2) injector modes – including those presented in earlier studies – located in the vicinity of the flow, (3) modes that persist under acoustic driving, (4) modes responding linearly to the driving and, most interestingly, (5) a mode whose density exhibits antiphase oscillatory behaviour in the observation plane and that appears only when J, the outer-to-inner-jet momentum flux ratio, is sufficiently large; we infer that this is a projection of a mode rotating about the symmetry axis and born via a spontaneous symmetry breaking. Each of these classes of modes is analysed as J is increased, and their consequences for the flow patterns are discussed.

Key words: jets, low-dimensional models, nonlinear dynamical systems

1. Introduction

Shear coaxial jets, in which a circular jet flows inside an annular jet, are canonical flows found in many applications, for example liquid rocket engines. Despite the

† Email address for correspondence: roy.sukesh@gmail.com

simplicity of the geometry, the flows exhibit very complex dynamical behaviour and non-trivial interactions with the dynamics of their surroundings (Hopfinger 1998; Hong *et al.* 2006), one important interaction being with coherent acoustic waves. They are important, for instance, in combustion chambers experiencing combustion-induced acoustic instabilities (Miesse 1955; Wicker & Eaton 1994; Villermaux, Rehab & Hopfinger 1998; Davis & Chehroudi 2006, 2007; Leyva *et al.* 2007; Teshome 2012). If the acoustic–jet interaction is such that pressure fluctuations become phase coherent with heat-release fluctuations, the acoustics can amplify temperature gradients and cause damage to the combusting system. Thus, it is important to gain an understanding of how different geometries and flow conditions affect the nature of the coupling between acoustic waves and coaxial jets.

Teshome (2012) studied the simplified case of acoustic waves interacting with non-reacting shear coaxial jets. He performed modal decomposition of high-frequency high-resolution shadowgraph imaging. Because applications usually have complex geometries, it is inefficient to perform such decompositions using predetermined basis functions. It is more appropriate to use techniques such as proper orthogonal decomposition (POD) (Lumley 1967; Sirovich 1987*a*,*b*,*c*; Berkooz *et al.* 1993), in which the basis functions are derived as part of the analysis. This approach was used by Teshome (2012); however, only the nature of the primary POD modes in the flows was reported.

In the present study, we extend the analysis of Teshome's data using an alternative decomposition based on Koopman eigenfunctions (Mezic & Banaszuk 2004; Rowley *et al.* 2009; Mezic 2013; Motheau *et al.* 2013). Koopman decomposition (Mezic & Banaszuk 2004; Rowley *et al.* 2009; Budišić, Mohr & Mezić 2012; Mezic 2013) is a natural approach to search for collective oscillatory behaviour and is based on the Koopman operator theory (Rowley *et al.* 2009; Schmid 2010; Mezic 2013), which generalizes eigendecomposition to nonlinear systems. Koopman modes are a generalization of normal modes (Mezic 2013), and each mode represents a global collective motion within a flow. Importantly, spectral properties of the flow will be contained in the spectrum of the Koopman operator (Rowley *et al.* 2009; Mezic 2013). A fast algorithm proposed by Schmid (2010) and referred to as dynamic-mode decomposition (DMD) can be used for computing approximately (a subset of) the Koopman spectrum from the time series of snapshots of the flow.

Each Koopman mode is associated with a complex eigenvalue whose real and imaginary parts represent the growth rate and frequency of the mode respectively. These eigenvalues can be used to address a critical issue in the analysis of nonlinear flows, namely how to differentiate robust features of the flow from noise and other non-robust characteristics. As we contend (Roy *et al.* 2015), comparison of Koopman spectra from nominally identical experiments can be the basis of this differentiation. The starting point is a search for reproducible Koopman modes, i.e. those that persist in different experiments. The differentiation is based on the following conjecture: robust characteristics of the flow can be associated with reproducible Koopman modes. Only robust features are expected to be useful in applications such as flow control.

Injector flows are introduced in § 2, and Koopman mode analysis and the relevant computational techniques are summarized in § 3. The results of the modal decomposition of injector flows for a series of control parameters are presented in § 4. Section 5 contains a discussion of the implications of our results.

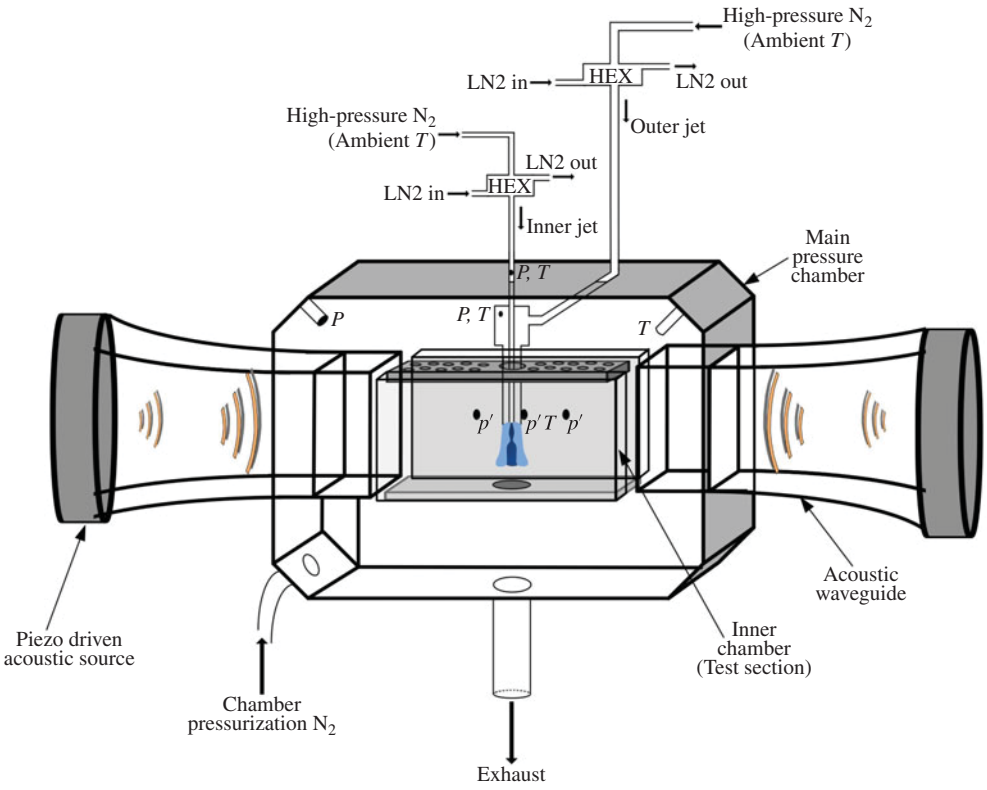

FIGURE 1. (Colour online) Schematic of the chamber and peripheral lines. The light long arrows point to constituents of the device and the heavy short arrows give the flow directions of gasses. Courtesy of Teshome (2012).

2. Injector flows

The experiments in the non-reactive shear coaxial study were conducted in the Cryogenic Supercritical Flow Facility (EC-4) at the Air Force Research Laboratory located at Edwards Air Force Base, CA. The fluid used in these studies was N_2 at ambient conditions tapped from a high-pressure supply line. Liquid N_2 was used for temperature control (Teshome 2012). The pressure within the chamber could be as high as 36 atm. A schematic of the experimental facility is shown in figure 1.

Injector flows were observed with shadowgraph imaging using diffuse backscattering and recorded using Phantom v7.1 and v710 high-speed cameras (Teshome 2012). High-density regions appeared dark. The flow was analysed through a modal decomposition implemented through Koopman mode analysis, described below.

The shear coaxial injector consisted of concentric straight tubes, where the inner jet flowed through the centre tube and the outer jet flowed through the annulus. A schematic of a sectional view of the entire injector assembly is shown in figure 2.

The inner jet was introduced through the top inlet hole of the assembly and entered a small plenum, which served as a settling chamber for the flow. The outer jet was introduced into a settling chamber through two ports located on the side of the assembly. Two parameters were varied for the two types of injectors constructed from 316 stainless steel: (1) the ratio of the inner-jet tube thickness to the diameter of

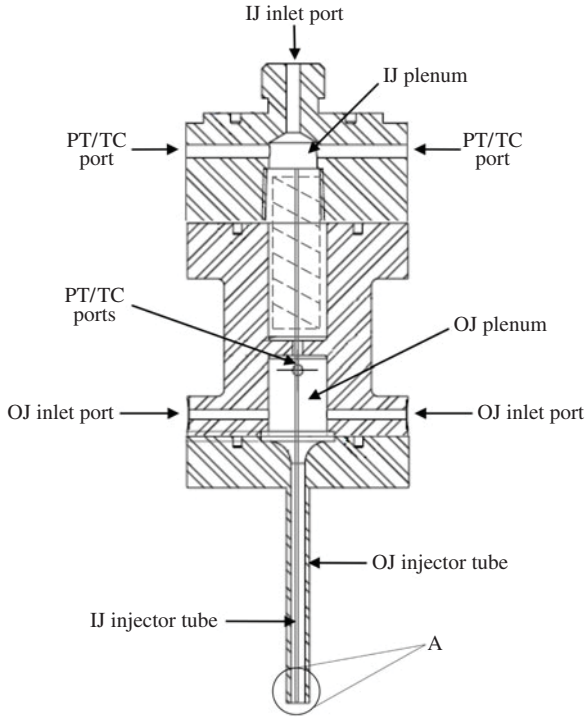

FIGURE 2. Schematic of the shear coaxial injector assembly (for expanded view of A, see figure 3) (from Teshome 2012).

the inner-jet tube and (2) the ratio of the outer-jet to inner-jet cross-sectional areas. Figure 3 is a schematic of the dimensions of the injector exit. The first injector with the large area ratio (LAR) and thin inner-tube post is labelled 'LAR-thin', while the second injector with the small area ratio (SAR) and thick post is labelled 'SAR-thick'. The results reported here are for the LAR-thin configuration; flows in the other injector tube set-up are similar but contain significantly higher levels of noise. For the same reason, we focus on subcritical-chamber-pressure experiments. The dimensions of the injector cross-section for the LAR-thin configuration were $D_1 = 0.70$ mm, $D_2 = 0.89$ mm, $D_3 = 2.44$ mm and $D_4 = 3.94$ mm.

The physical parameters of the coaxial jet flow were based on the injector exit flow properties. They are characterized by J, the outer-to-inner-jet momentum flux ratio, $\rho_o U_o^2/\rho_i U_i^2$, where ρ and U are the density and velocity of the flow respectively. For 'LAR-thin-subcritial' experiments, the available values of J are 0.1, 0.5, 2.1, 5.2, 11, 14 and 20.

The experimental set-up for injector flows in the absence of additional perturbations (referred to as baseline flows) was rotationally invariant about the axis of the flow. We also analysed flows that were subjected to transverse acoustic perturbations imposed using a waveguide attached to each side of a rectangular test section, as shown in figure 1. These perturbations break the rotational symmetry of the experimental configuration. Two types of acoustic driving were performed in the experiments: (1) those where the injector was placed at a pressure antinode (PAN) and (2) those where it was placed at a pressure node (PN). We focus on injector flows subjected to PAN driving; they contain lower levels of noise.

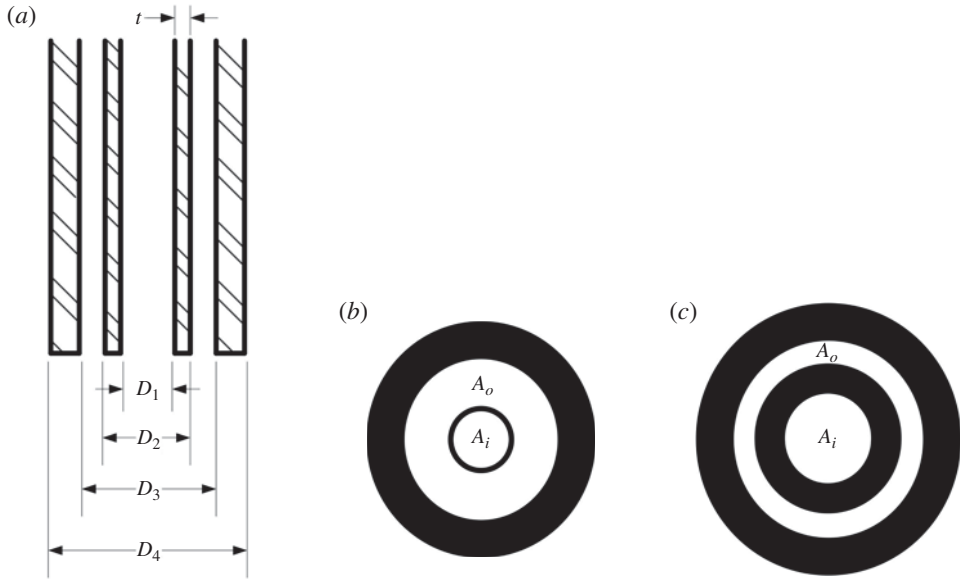

FIGURE 3. Schematic of the shear coaxial injector exit (from Teshome 2012): (*a*) expanded view of A in figure 2; (*b*) LAR-thin; (*c*) SAR-thick.

Each image was recorded on a grid of 192×302 with a resolution of 22 μm; thus the image dimensions are 4.2 mm × 6.6 mm. The image capture began close to the initiation of the injector flow and transients could be observed through the Koopman mode analysis, as seen below. The transients were especially long for smaller values of J.

3. Koopman modes and dynamic-mode decompositions

3.1. *Modal decomposition*

Proper orthogonal decomposition (Lumley 1967; Sirovich 1987*a*,*b*,*c*) has been used to analyse patterns within injector flows (Teshome 2012; Tirunagari *et al.* 2012*a*,*b*). The analyses provide the structure of proper orthogonal modes and the relative contributions to the flow from each mode. Typically, modes with larger contributions are associated with the regular constituents of the underlying flow and those with lower contributions are assumed to be noise and other irregular facets of the flow. However, there has not been a verification of this flow differentiation. Previous DMDs of sprays (Tirunagari *et al.* 2012*b*) have also not addressed the issue. The analysis reported here is motivated by an approach introduced in Roy *et al.* (2015) and outlined below which differentiates robust and non-robust constituents of a flow using Koopman mode analysis (Rowley *et al.* 2009; Schmid 2010; Mezic 2013). As we observe from figures 15 and 24 below, robust and non-robust constituents of injector flows cannot be differentiated using their contributions to the flow alone.

Koopman mode analysis of spatio-temporal fluid density fields is included for completeness and follows Lumley (1967), Sirovich (1987*a*,*b*,*c*), Rowley *et al.* (2009), Schmid (2010) and Mezic (2013). Suppose that the state of a dynamical system is z and that its dynamics is given by

$$\dot{z} = \mathscr{F}(z), \tag{3.1}$$

with constraints and restrictions such as an appropriate set of boundary conditions. The dynamics evolves from the initial state z_0 of the system to $z_t \equiv \boldsymbol{S}^t(z_0)$ at time t. In the case of fluid dynamics of injector flows, $\mathscr{F}$ consists of the Navier–Stokes equations with, perhaps, no-slip boundary conditions. Although this is the most compact representation of the flow, it is difficult to solve the system under realistic conditions, especially for high Reynolds numbers. On the other hand, high-quality empirical data are available on various secondary fields associated with the dynamical system, e.g. the density field of the injector flows. Let us represent one such (observable) secondary field (associated with z) by $u[z](\boldsymbol{x})$, where $\boldsymbol{x}$ represents the grid points on which the observations are made. As the state of the system evolves from z_0 at time $t = 0$ to z_t at time t, the secondary field evolves from $u[z_0](\boldsymbol{x})$ to $u[z_t](\boldsymbol{x})$. When the context is clear, one can simplify the notation by writing $u(\boldsymbol{x}, t)$ for $u[z_t](\boldsymbol{x})$.

Koopman analysis (Mezic & Banaszuk 2004; Rowley *et al.* 2009; Budišić *et al.* 2012; Mezic 2013) of the system is conducted on the 'observable' $\boldsymbol{u}[z](\boldsymbol{x}, t)$. An initial function $\boldsymbol{u}[z_0](\boldsymbol{x}, t = 0)$ evolves to a function $\boldsymbol{u}[z_t](\boldsymbol{x}, t)$ at time t. The transformation between the functions is given by the Koopman (or composition) operator, which is defined as

$$U^t{:}\boldsymbol{u}[z_0](\boldsymbol{x}, t = 0) \rightarrow \boldsymbol{u}[z_t](\boldsymbol{x}, t). \tag{3.2}$$

It should be noted that even when $\boldsymbol{S}^t$ is finite-dimensional and nonlinear, the Koopman operator U^t is infinite-dimensional and linear (Rowley *et al.* 2009; Mezic 2013). Since both $\boldsymbol{S}^t$ and U^t describe the same flow, one expects common features in the descriptions. For example, if the injector flow were uniform in time, z_0 would be a fixed point of $\boldsymbol{S}^t$ and $\boldsymbol{u}[z_0](\boldsymbol{x}, t = 0)$ would be a fixed point of U^t. In periodic flows, the periodicity will be reflected in the spectra of z_t as well as in the spectra of $\boldsymbol{u}[z_t](\boldsymbol{x}, t)$. In fact, it is known that spectral properties of $\boldsymbol{S}^t$ are contained in the eigenspectrum of U^t. Eigenvalues of U^t form the Koopman spectrum, and the corresponding eigenfunctions are referred to as Koopman eigenfunctions. Coefficients in the projection of $\boldsymbol{u}[z_t](\boldsymbol{x}, t)$ to the Koopman eigenfunctions form the Koopman modes of the state (Rowley *et al.* 2009). As the system evolves under $\boldsymbol{S}^t$, the kth Koopman mode evolves as $\mathrm{e}^{\mu_k t}$, where μ_k is the associated eigenvalue. Thus, the Koopman formalism is a generalization of normal form analysis and is a natural approach to searching for collective cyclic behaviour in spatio-temporal data.

Dynamic-mode decomposition (Bagheri *et al.* 2009; Schmid 2009, 2010) is an efficient algorithm for computing approximations for the eigenvalues and eigenvectors of U^t from empirical snapshots collected at uniform time intervals δt. Since $U^{\delta t}$ is independent of the state $u(\boldsymbol{x}, t)$, one can approximate the transformation of the field during the time interval $[t, t + \delta t]$ as

$$u(\boldsymbol{x}, t + \delta t) \approx \boldsymbol{A}u(\boldsymbol{x}, t), \tag{3.3}$$

where $\boldsymbol{A} \equiv \boldsymbol{A}(\delta t)$ is a matrix of size $HW \times HW$ in the case of a field of two spatial dimensions presented on a grid of size $H \times W$. If one denotes by u_k the field corresponding to the snapshot taken at time $t = k\delta t$, (3.3) can be rewritten as $u_{k+1} \approx \boldsymbol{A}u_k$. Thus,

$$\mathbb{U}_1 \equiv [u_1, u_2, \ldots, u_n] \approx \boldsymbol{A}[u_0, u_1, u_2, \ldots, u_{n-1}] \equiv \boldsymbol{A}\mathbb{U}_0. \tag{3.4}$$

With sufficiently large n, singular-value decomposition of $\mathbb{U}_0 = \boldsymbol{V}\boldsymbol{S}\boldsymbol{W}^{\mathrm{T}}$ can be used to compute the spectrum of $\boldsymbol{A}$ (or equivalently of $\boldsymbol{V}^{\mathrm{T}}\boldsymbol{A}\boldsymbol{V}$) by noting that $\boldsymbol{V}^{\mathrm{T}}\boldsymbol{A}\boldsymbol{V} =$

$\boldsymbol{V}^{\mathrm{T}}\mathbb{U}_1\boldsymbol{W}\boldsymbol{S}^{-1}$ (Schmid 2009). Eigenvectors of $\boldsymbol{A}$ are referred to as dynamic modes of the spatio-temporal dynamics (Bagheri *et al.* 2009; Schmid 2009, 2010). Dynamic-mode decomposition provides an approximation to a subset of the Koopman spectrum Λ_n, and the corresponding eigenfunctions $\Phi_n(\boldsymbol{x})$ approximate Koopman modes.

It should be noted that since $\boldsymbol{A}$ is not symmetric, the eigenvalues Λ_n and the eigenfunctions $\Phi_n(\boldsymbol{x})$ are, in general, complex-valued. Furthermore, the eigenfunctions are not orthonormal. Eigenvalues of the Hermitian conjugate $\boldsymbol{A}^{\dagger}$ of $\boldsymbol{A}$ are $\Lambda_n^* t$. The corresponding eigenfunctions $\tilde{\Phi}_n(\boldsymbol{x})$ are orthogonal to the $\Phi_n(\boldsymbol{x})$ – specifically, with an appropriate normalization $\int \mathrm{d}\boldsymbol{x}\, \tilde{\Phi}_m(\boldsymbol{x})\Phi_n(\boldsymbol{x}) = \delta_{mn}$.

The spatio-temporal flow field $u(\boldsymbol{x}, t)$ can be expanded as

$$u(\boldsymbol{x}, t) = \sum a_k(t)\Phi_k(\boldsymbol{x}), \tag{3.5}$$

where the sum is performed over the DMD modes. Variations in $u(\boldsymbol{x}, t)$ can be quantified using $V \equiv \mathbb{E}[(u(\boldsymbol{x}, t))^2]$, where the expectation is over the grid points and snapshots. By the orthonormality introduced above, $a_k(t) = \int \mathrm{d}\boldsymbol{x}\, \tilde{\Phi}_k(\boldsymbol{x})u(\boldsymbol{x}, t)$. If necessary, the field can also be expanded in the basis $\{\tilde{\Phi}(\boldsymbol{x})\}$ as $u(\boldsymbol{x}, t) = \sum \tilde{a}_k(t)\tilde{\Phi}_k(\boldsymbol{x})$. Now the variations in the spatio-temporal dynamics reduce to $V = \sum a_k\tilde{a}_k$, and one can interpret the quantity $L_k = a_k\tilde{a}_k$ as the contribution (or 'energy') from the kth mode. It should be noted, however, that because DMD modes are not orthogonal, L_k is not strictly positive; hence, in defining $\beta_n = \sum_{k=0}^{n-1} L_k / \sum_{k=0}^{HW-1} L_k$, where larger values of β_n correspond to better approximations of the data, one must sum absolute values. It should be noted, however, that with this definition, β_n may exceed 1 in some rare cases.

Prior to computing dynamic modes, the density of each frame is rescaled by removing the mean and setting the standard deviation to 1. Unlike mean subtraction (Chen, Tu & Rowley 2012), this rescaling does not change the DMD eigenvalues or dynamic modes. The intensity of the dynamic modes (i.e. the fluctuations) can be compared with the mean density.

3.2. *Robust modes*

The (nonlinear) Navier–Stokes equations, especially in the presence of many distinct modes, can amplify noise and other irregular facets of the injector flow (Cross & Hohenberg 1993). Consequently, features of a flow may differ among multiple realizations of an experiment or a simulation. Thus, the ability to extract robust characteristics from an injector flow is critically important. We use the following conjecture for the selection: configuration-independent (or robust) features of spatio-temporal dynamics can be captured through dynamic modes that are reproduced in multiple experiments. We also assume that different subgroupings of the full set of snapshots can be used for this purpose. In contrast, dynamic modes representing noise and non-robust flow constituents depend on the specific experimental realization. The corresponding differentiation in POD based methods relies on irregular features having lower energies than the regular flow facets. The results of the injector flow analysis, outlined in the next section, indicate that this differentiation may not be valid (Roy *et al.* 2015). It should also be noted that in constructing reduced-order models or in developing techniques to control the flow, one must focus on the robust features of the flow. Non-robust features cannot be used for this purpose; however, their statistical features or dynamical invariants may be necessary to complete the flow characterization.

In the experiment, injector flows were recorded at 25 kHz; thus, imaginary values of the Koopman spectrum lay in the range $(-2.5\pi \times 10^4, 2.5\pi \times 10^4)$. As discussed earlier, Koopman eigenvalues are either real or appear in complex conjugate pairs. To search for robust modes, we subgrouped the snapshots from each experiment into even-numbered and odd-numbered frames and implemented dynamic-mode computations for these subgroups as well. (Had the data not included transients, it would have been possible to include results from the first and second halves of snapshots as well.) We then searched for (nearly) identical Koopman eigenvalues among the different groups and investigated whether the corresponding Koopman modes were close. Specifically, reproducible dynamic modes of the flow were defined using the following criteria.

(1) The imaginary parts of the eigenvalues from multiple groups should be sufficiently close; specifically,

$$\max_g(|\mathrm{Im}(\Lambda_i) - \mathrm{Im}(\Lambda_j^{(g)})|) \leqslant \delta_I, \tag{3.6}$$

where g represents different subgroupings and δ_I is a cutoff.

(2) The real parts of an eigenvalue identified from the first condition should not vary significantly among the subgroups; specifically,

$$\max_g(|\mathrm{Re}(\Lambda_i) - \mathrm{Re}(\Lambda_j^{(\mathrm{g})})|) \leqslant \delta_R, \tag{3.7}$$

for a cutoff δ_R. Typically, the real parts of the eigenvalues exhibit larger variation; thus, the cutoff δ_R is larger than δ_I. For the work reported here we select $\delta_R \approx 1.5\delta_I$.

(3) Eigenmodes from the different groupings that satisfy the earlier conditions should be close. Specifically, if $\Phi_i(\boldsymbol{x})$ and $\Phi_j^{(g)}(\boldsymbol{x})$ are normalized eigenfunctions associated with proximate eigenvalues, then

$$\max_g\{\min_\theta |\exp(\mathrm{i}\theta)\Phi_i(\boldsymbol{x}) - \Phi_j^{(g)}(\boldsymbol{x})|\} \leqslant \Delta, \tag{3.8}$$

for a cutoff Δ. Here, we have noted that eigenfunctions computed from different experimental realizations may differ in phase.

At this point, we do not have a unique and unambiguous set of cutoff values δ_I, δ_R and Δ for injector flows; in fact, they may depend on the level of experimental and observational noise. Since the left-hand side of (3.8) is known to $\in (0, 2)$, Δ is selected first. For the results reported here Δ was chosen to be near 0.6. Its suitability is validated by visual inspection of modes from the different groups of snapshots. Next, δ_I and δ_R are simultaneously increased from 0 and the number of modes N_m satisfying the three criteria is recorded. We find that N_m increases initially as δ_I and δ_R are increased, and subsequently reaches a plateau. Modes in the plateau are assumed to be robust.

3.3. *Reconstruction of flow constituents*

Dynamic modes are associated with unique eigenvalues Λ_n, the growth rate and the frequency of the nth mode. One can use this observation to address an important issue: a constituent of the injector flow may not be captured by a single dynamic mode; rather, several such modes may be required to reconstruct a typical constituent

(Roy *et al.* 2015). Analysis of simulated and experimental data suggests approaches for identifying multiple modes that may be associated with a single flow constituent. Specifically, their eigenvalues are found to lie on a smooth curve in the complex plane (Bagheri *et al.* 2009; Schmid 2009, 2010). An alternative scheme is as follows. We recall that the primary dynamic mode (i.e. that with the highest energy) has a single frequency -2π times the imaginary part of the corresponding Λ. One may expect dynamic modes with harmonics of this frequency to be associated with the same flow constituent.

Once dynamic modes associated with a flow constituent are identified, the constituent and its evolution can be reconstructed using

$$u_{const.}(\boldsymbol{x}, t) = \sum a_i(t)\Phi_i(\boldsymbol{x}) + \text{c.c.}, \tag{3.9}$$

where 'c.c.' denotes complex conjugation, and the summation is over the modes associated with the constituent.

4. Results

4.1. *A classification of robust dynamic modes*

Analyses of injector flows for J values of 0.1, 0.5, 2.1, 5.2, 11.0, 14.0 and 20.0 show that robust dynamic modes fall into several distinct classes based on their locations, symmetries and dynamics. We outline the classification before presenting the results from the Koopman mode analysis.

(1) *Background modes* are spatially disordered, and their primary features lie outside the injector flow. They are transient and decay for all values of J. The robust mode 4 of the baseline flow at $J = 0.1$, shown in figure 4, is an example of a background mode. As observed here, the spatial structure of a background mode is disordered. Although these modes are robust within subgroupings of the snapshots in a single experiment, we suspect that their spatial structures differ between experiments.

(2) *Injector modes* have a well-defined spatial structure within the injector flow and exhibit high-frequency dynamics. Their coefficients $a(t)$ have sharp spectra. For a given subgrouping, their amplitudes exhibit either slow decay or slow growth; as can be seen from figure 16(*b*), the real part of their eigenvalue is statistically consistent with zero growth. Robust mode 72 of the baseline flow at $J = 0.1$, shown in figure 5, is an example of an injector mode. The projection shown in figure 5(*a*) supports the assertion that the mode contains successive high- and low-density annular regions, and that the planes of these annuli are, in general, not normal to the symmetry axis. (Injector modes that are symmetric about the axis are also found.) The dynamics of the flow in the complex plane, shown in figure 5(*c*), lies on an outward moving spiral.

(3) *Rotating modes* are observed for values of J larger than 5.2. The reconstruction of the dynamics for one such mode (robust mode 7 for $J = 11$) reveals that the densities of points on either side exhibit antiphase oscillatory behaviour, as observed in figure 8. Since the injector and the flow at the inlet are axially symmetric, this observation indicates that the underlying mode is an azimuthally modulated rotating mode generated via spontaneous symmetry breaking.

The stroboscopic depiction creates a visual illusion in figure 6(*c*). The dynamics follows an inward moving spiral and the angular position of the orbit nearly returns to its original value following 93 time steps. Consequently, the set of discrete points on the orbit appears to consist of 93 radial lines. However, joining successive points

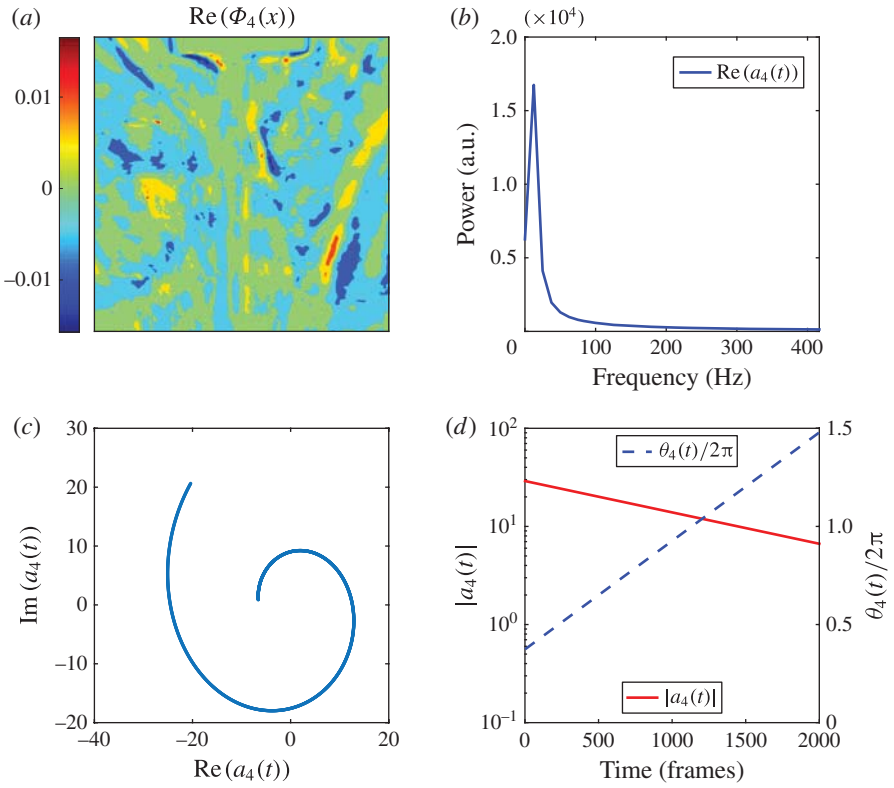

FIGURE 4. (Colour online) Background modes (*a*) are spatially disordered and located outside the injector flow. (*b*) Their coefficients $a(t)$ exhibit low-frequency dynamics. The amplitudes of the modes decay exponentially, as can be observed from the dynamics on the complex plane (*c*) or from $|a(t)|$ (*d*). The phase of $a(t)$, representing downstream motion of the mode, progresses uniformly, as observed in (*d*). The remaining figures will be presented in the same format.

during a small time interval, as shown in figure 7, reiterates that the orbit is a single inward moving spiral.

Similarly, the orbit shown in figure 5(*c*) lies on an outward moving spiral. That the motion is outward is confirmed by the (slow) growth of $|a_{72}(t)|$ in figure 5(*d*). Following 24 iterations, the angular and radial positions of the orbit have returned to slightly higher values than in their initial state. Consequently, the stroboscopic image appears to consist of 24 equally spaced arcs.

Reconstruction of the dynamics associated with the rotating mode, presented in figure 8, shows a periodic flipping (left to right) of the high-/low-density regions in the viewing plane. It is uncorrelated to any of the injector modes, as can be established using phase dynamics. Experimental noise and irregularities in the flow cause fluctuations in the coefficients of the dynamic modes. Interestingly, angular changes of the phase-space orbit are highly robust, and the irregularities are restricted to the radial component (Roy *et al.* 2015). The phase of the coefficient $a_k(t)$ of a dynamic mode $\Phi_k(\boldsymbol{x})$ is defined as

$$\theta_k(t) = \tan^{-1}[\mathrm{Im}(a_k(t))/\mathrm{Re}(a_k(t))]. \tag{4.1}$$

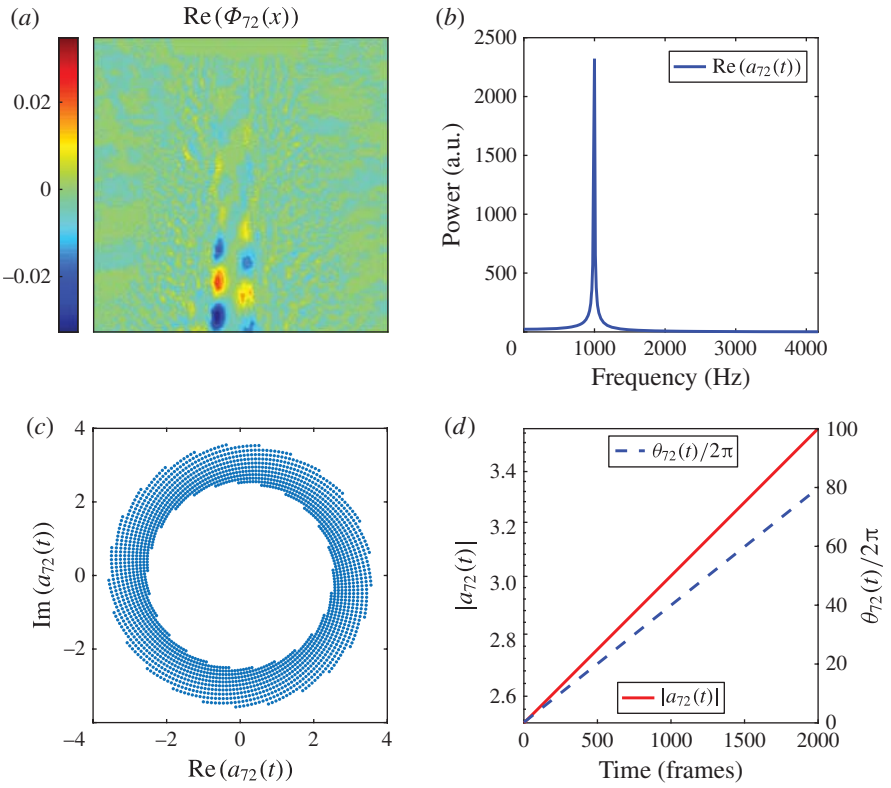

FIGURE 5. (Colour online) Injector modes (*a*) are located primarily within the injector flow, and (*b*) their coefficients $a(t)$ exhibit sharp spectra. As observed in (*c*,*d*), the amplitude of the mode for the selected subgrouping exhibits slow growth, while the phase progresses uniformly. It should be noted that (*c*) shows a single trajectory; the illusion of multiple trajectories is caused by the stroboscopic sampling.

The relationship between the phases of two dynamic modes can be illustrated using Lissajous figures, such as figure 9, which relate phases of a pair of modes through their sine functions (Roy *et al.* 2015). Specifically, when the ratio of angular velocities for two phases θ_i and θ_j is a (low-order) rational number, pairs of points $\{\sin\theta_i(t), \sin\theta_j(t)\}$ lie on a curve; otherwise, the points fill the space. As an example, figure 9 compares the phase dynamics of the rotating mode with one of the injector modes. Their frequencies (figure 9*a*) and phase dynamics (figure 9*c*) are not related, and the motion in the Lissajous figure (figure 9*d*) is space filling. Thus, it is inferred that the modes are uncorrelated.

(4) *Linear response modes* are located primarily in the neighbourhood of the injector flow and have an eigenvalue whose imaginary part is the ratio of the acoustic driving frequency and 2π. Figure 10 contains an example of such a mode.

(5) *Persistent modes* are those observed in PAN driven injector flows that have a structure and period similar to those of corresponding baseline injector modes. For example, as seen from figure 11, mode 83 of the PAN driven flow at $J = 0.1$ has a structure and dynamics qualitatively similar to mode 92 of the baseline flow. However, the amplitude of the latter is nearly unchanged in time while that of the former is found to decay.

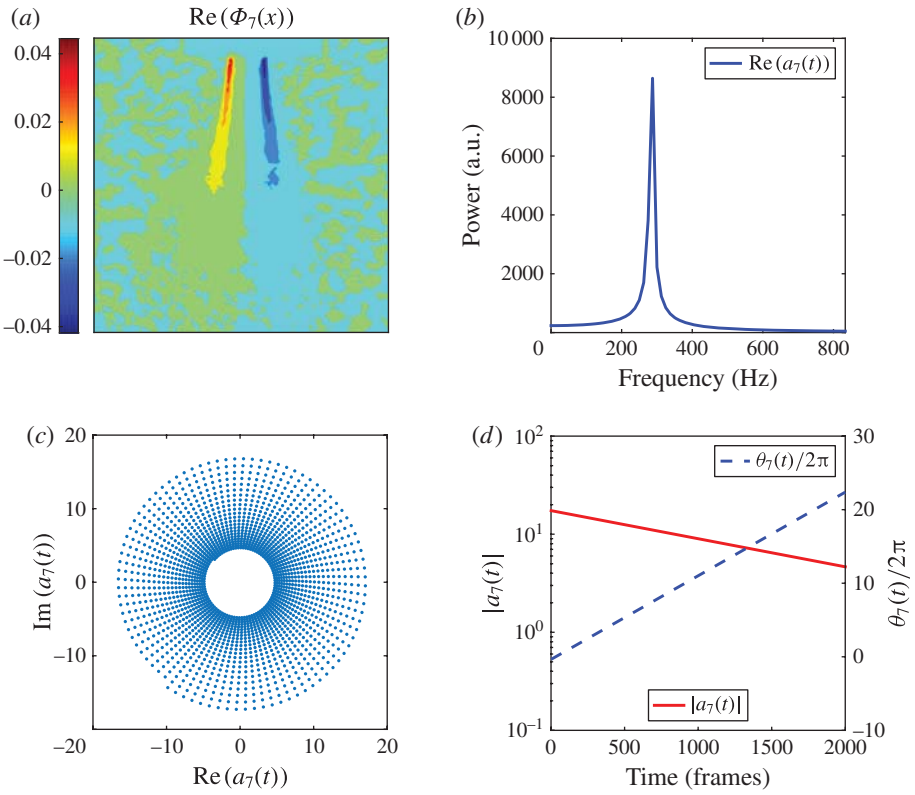

FIGURE 6. (Colour online) Projections of rotating modes (a) are asymmetric, and (b) their coefficients $a(t)$ have sharp spectra. As observed in (c,d), they exhibit uniform angular progression. Once again, (c) shows a single trajectory; the illusion of multiple (apparently radial) trajectories is caused by the stroboscopic sampling. Their magnitudes $|a(t)|$ exhibit a slow decay. We propose that the underlying three-dimensional flow is an azimuthally modulated rotating mode.

The correlation between persistent modes can be illustrated using their phase dynamics. The frequencies of the time coefficients of the modes (figure 12a) and their phase dynamics (figure 12c) are identical. The orbit in the Lissajous figure (figure 12d) is nearly a closed curve (its width is presumably due to irregularities and experimental noise). Thus, it is inferred that persistent modes are correlated.

The discussion is concluded with a recapitulation (figure 13) of the classes of robust modes identified in injector flows.

4.2. *Injector flows for low J ($J \leqslant 2.1$)*

The major features of the robust modes for injector flows for $J \leqslant 2.1$ are similar, and their characteristics will be illustrated using the results for $J = 0.1$.

4.2.1. *Baseline injector flows for $J = 0.1$*

Figure 14 shows a series of images of the baseline flow at $J = 0.1$. The injector can be seen at the centre near the top of each image. Figure 15 shows the energies of the 100 DMD modes of the injector flow at $J = 0.1$, with energies as defined in

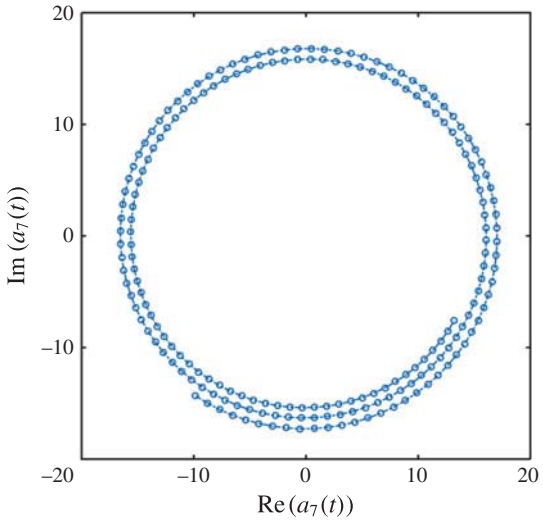

FIGURE 7. (Colour online) The dynamics of $a_7(t)$ in the complex plane follows an inward moving spiral. The corresponding motion for growing modes is on outward moving spirals.

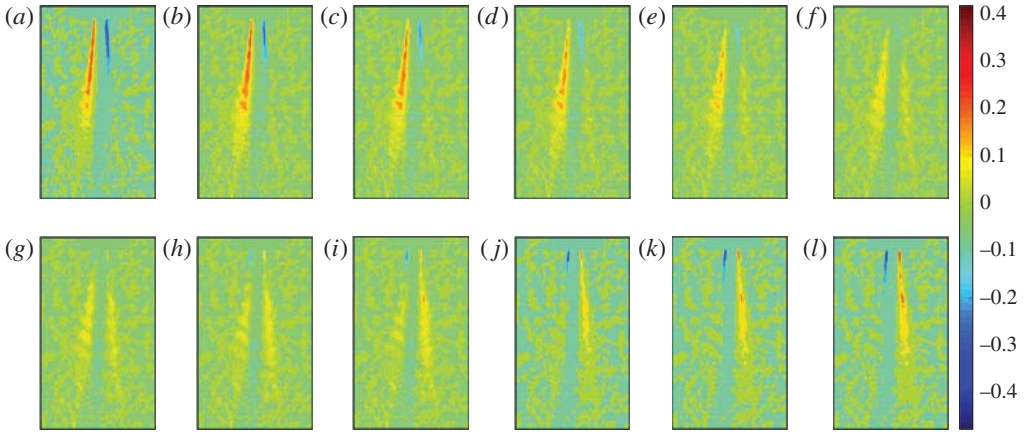

FIGURE 8. (Colour online) Several snapshots of reconstruction of mode 7 for $J = 11$, illustrating the antiphase oscillations of the projection: (*a*) 26.44 ms, (*b*) 26.48 ms, (*c*) 26.52 ms, (*d*) 26.56 ms, (*e*) 26.60 ms, (*f*) 26.64 ms, (*g*) 26.68 ms, (*h*) 26.72 ms, (*i*) 26.76 ms, (*j*) 26.80 ms, (*k*) 26.84 ms, (*l*) 26.88 ms.

§ 3.1. It can be observed, as we have already alluded to, that robust and non-robust modes cannot be partitioned using their energies (associated with DMD). The ability to differentiate robust modes from non-robust modes is one of the more significant advantages of DMD. It can be noticed also that the energy of the 'mean' mode $\Phi_0(\boldsymbol{x})$ is two orders of magnitude larger than the rest. Consequently, the variations of the spatio-temporal velocity field associated with the remaining modes are at least an order of magnitude smaller than those associated with $\Phi_0(\boldsymbol{x})$, as can be deduced from the definition of energy (§ 3.1). Figure 16(*a*) shows the corresponding DMD spectra for modes with non-negative imaginary parts.

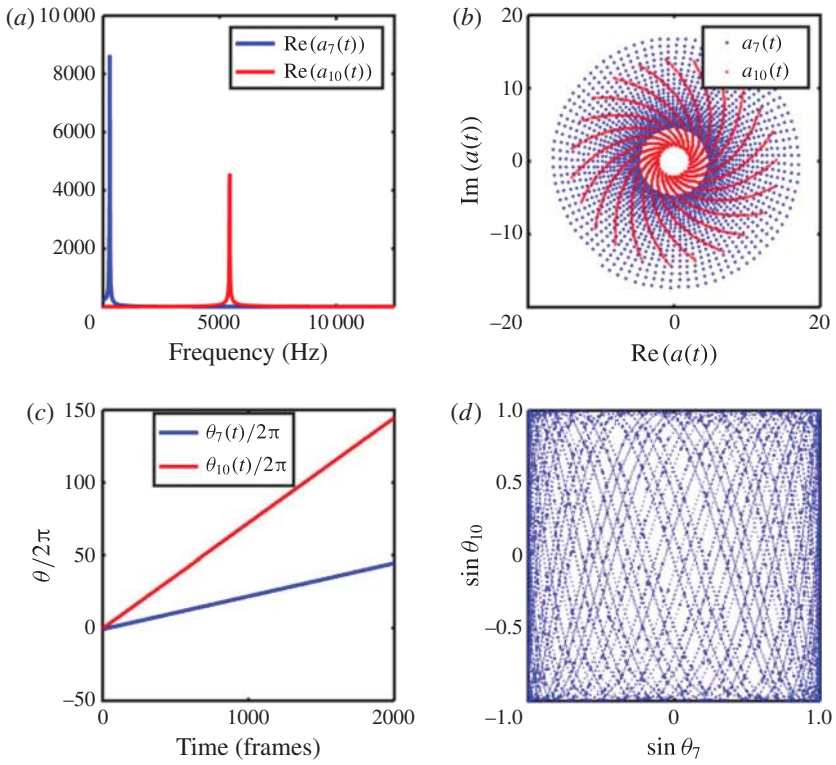

FIGURE 9. (Colour online) Comparison of the dynamics of the rotating mode $\Phi_7(\boldsymbol{x})$ and an injector mode $\Phi_{10}(\boldsymbol{x})$ for injector flow at $J = 11$. Their frequencies (*a*), complex-plane dynamics (*b*) and phase dynamics (*c*) are different. (As in figure 5, (*b*) shows two trajectories for $a_7(t)$ (points) and $a_{10}(t)$ (solid); the illusion of multiple trajectories is caused by the stroboscopic sampling.) (*d*) The orbit in the Lissajous figure appears to be a space filling curve. Here, $\lambda_7 = -16.49 + 1786.03\mathrm{i}$, and $\lambda_{10} = -23.96 + 34127.42\mathrm{i}$.

Reproducible modes of the flow are defined using cutoff values $\delta_I = 36$, $\delta_R = 54$ and $\Delta = 0.58$. The modes are partitioned into two groups according to their frequency (imaginary parts of the eigenvalues) and the location of the eigenfunctions. The low-frequency robust modes ($\mathrm{Im}(\Lambda) \leqslant 2000$), shown in figure 16(*c*), are background modes. They are transient; i.e. their amplitudes decay exponentially, as observed in figure 4. The imaginary parts of almost all of the background modes are observed to be (nearly) integer multiples of $\mathrm{Im}(\Lambda_4)$, suggesting that they are harmonics of $\Phi_4(\boldsymbol{x})$. Together, they will form a single flow constituent. Figure 17 shows several snapshots of the reconstructed spatio-temporal dynamics.

The high-frequency ($\mathrm{Im}(\Lambda_i) > 2000$) robust modes, shown in figure 16(*b*), are located near the injector flow. The dynamic modes associated with each group along with their energies are illustrated in figure 15. The contrast between the background flow and the injector flow (robust mode 48) becomes apparent on comparing the reconstructed flows shown in figures 17 and 18.

For $J = 0.1$, the robust injector modes, whose spectra are shown in figure 16(*b*), decay exponentially and are observed to flow downstream. Symmetric and asymmetric injector modes are found, examples of which are given in figures 19 and 20. Since the

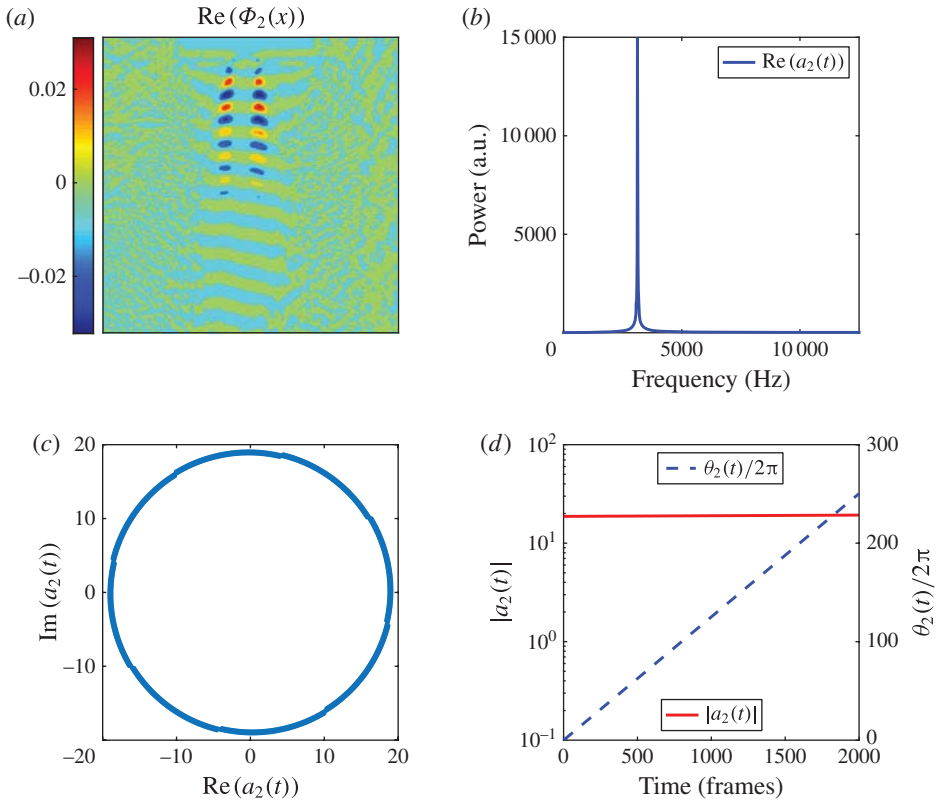

FIGURE 10. (Colour online) Robust mode 2 for $J = 0.1$ of the acoustically driven flow is a linear response mode. The imaginary part of its eigenvalue equals the ratio of the driving frequency and 2π.

amplitudes of the modes shown decay in time, the plot of the real versus imaginary parts follows an inward spiralling path.

4.2.2. *Acoustically driven injector flows for* $J = 0.1$

Figure 21 shows a series of images of the acoustically driven flow at $J = 0.1$ when the injector is placed at a PAN of the acoustic driving. The flow has considerably more structure than the corresponding baseline flow. The DMD spectrum and robust modes are shown in figure 22. Robust modes were selected using the criteria $\delta_I = 23$, $\delta_R = 15$ and $\Delta = 0.4$. The modes in figure 22(*c*) capture the spatio-temporal dynamics of the background flow, while those in figure 22(*b*) represent the injector flow, with some of them having analogues in the baseline flow, as exemplified by the modes shown in figure 11.

A new robust dynamic mode (mode 2) whose frequency is that of the acoustic driving is found. The imaginary part of Λ_2 is the PAN driving frequency divided by 2π, suggesting that it is the linear response of the flow field to the acoustic perturbation. The real part of the eigenvalue is nearly zero, indicating, as seen in figure 10, that $a_2(t)$ maintains its magnitude in time. The wavelength of the linear response mode is similar to the modulation in the flow seen in figure 21, and the

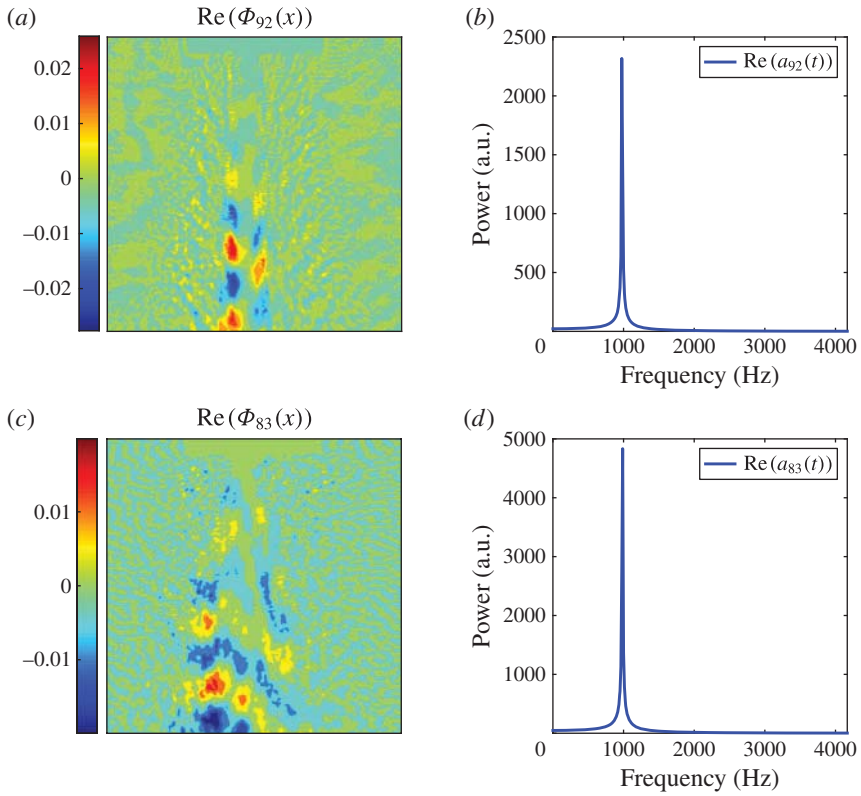

FIGURE 11. (Colour online) Robust mode 83 of the PAN driven flow, shown in (*c*), has a structure similar to the robust baseline mode 92 shown in (*a*). Their spectra, shown in (*d*) and (*b*) respectively, are similar as well.

large energy associated with the mode (seen in figure 22) is related to the large amplitude of the modulation.

It can be noticed that the real part of mode 61 is positive, indicating that it grows for the duration of the experiment. We suspect that it saturates at later times; the expectation needs to be verified in longer experimental runs.

4.3. *Injector flows for large J* ($J \geqslant 5.2$)

The injector flows for $J \geqslant 5.2$ present additional robust modes, which are illustrated through the results analysis of the flow for $J = 11$.

4.3.1. *Baseline injector flows for* $J = 11$

Figure 23 shows several snapshots of the injector flow at $J = 11$. It can be noticed that the high-density injector flows diffuse into the ambient fluid earlier at this high J. Figure 24 shows the 100 dynamic modes of the flow with the highest energies. As in the case of $J = 0.1$, the energy of the mean mode $\Phi_0(\boldsymbol{x})$ is more than two orders of

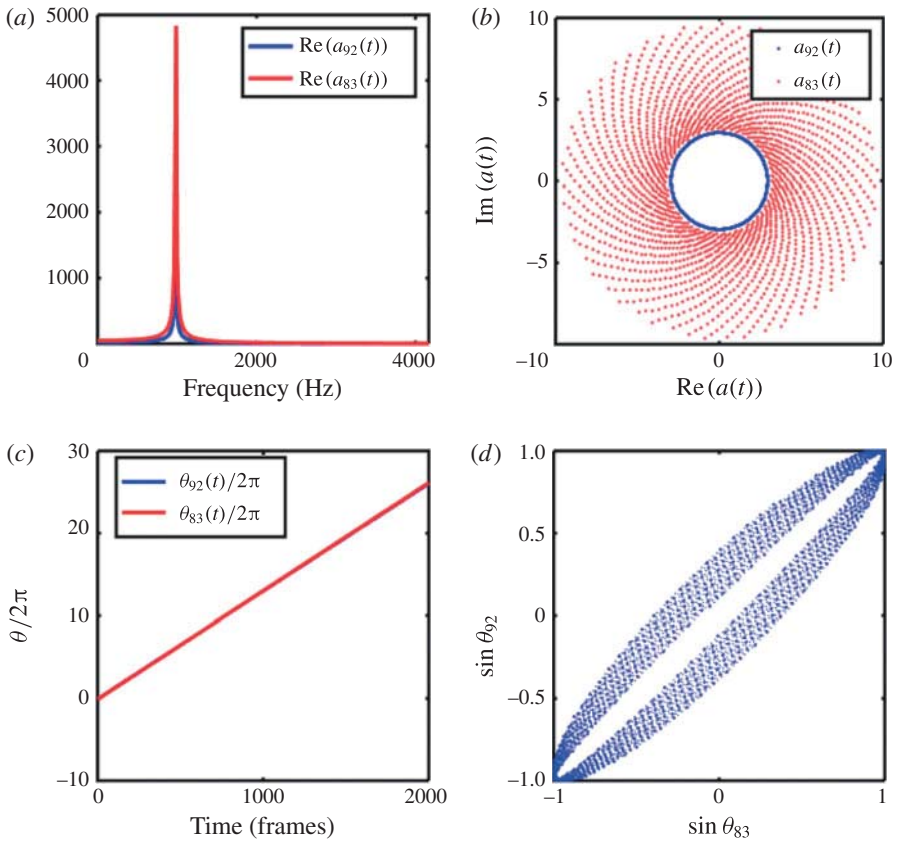

FIGURE 12. (Colour online) The eigenvalues of the two modes compared here are $\lambda = 0.05 + 6155.52\mathrm{i}$ and $\lambda = 13.95 + 6177.75\mathrm{i}$. Comparison of the dynamics of $\Phi_{92}(t)$ for the baseline flow and $\Phi_{83}(t)$ for the PAN driven flow. The (*a*) spectra and (*c*) angular progressions of the dynamics of the two modes are identical. (*b*) The magnitude $|a_{92}(t)|$ of the baseline flow is nearly unchanged (the inner solid line) in time while $|a_{83}(t)|$ for the PAN driven flow decays in time (the inward spiralling points). The Lissajous figure, shown in (*d*), is nearly a closed curve, thus reiterating the correlation between the persistent modes.

magnitude higher than the energies of the remaining modes. It can be observed that there are only a very few robust modes at $J = 11$. This is consistent with the presence of large variations in the flow, as illustrated in figure 23.

Figure 25(*a*) shows the DMD spectrum for the flow and figure 25(*b*) that for the robust modes; as before, the error bars are standard deviations of the set of eigenvalue real parts derived from distinct subgroupings of snapshots selected to represent the same dynamic mode. No robust low-frequency background modes are present in this flow. Furthermore, all injector modes in this flow are asymmetric. As mentioned in § 4.1, when J goes beyond 5.2, a rotating mode emerges in the baseline flow. The projection of this mode and the reconstructed dynamics were shown in figures 6 and 8. In addition, the rotating mode is not correlated with any of the injector modes, as illustrated in figure 9.

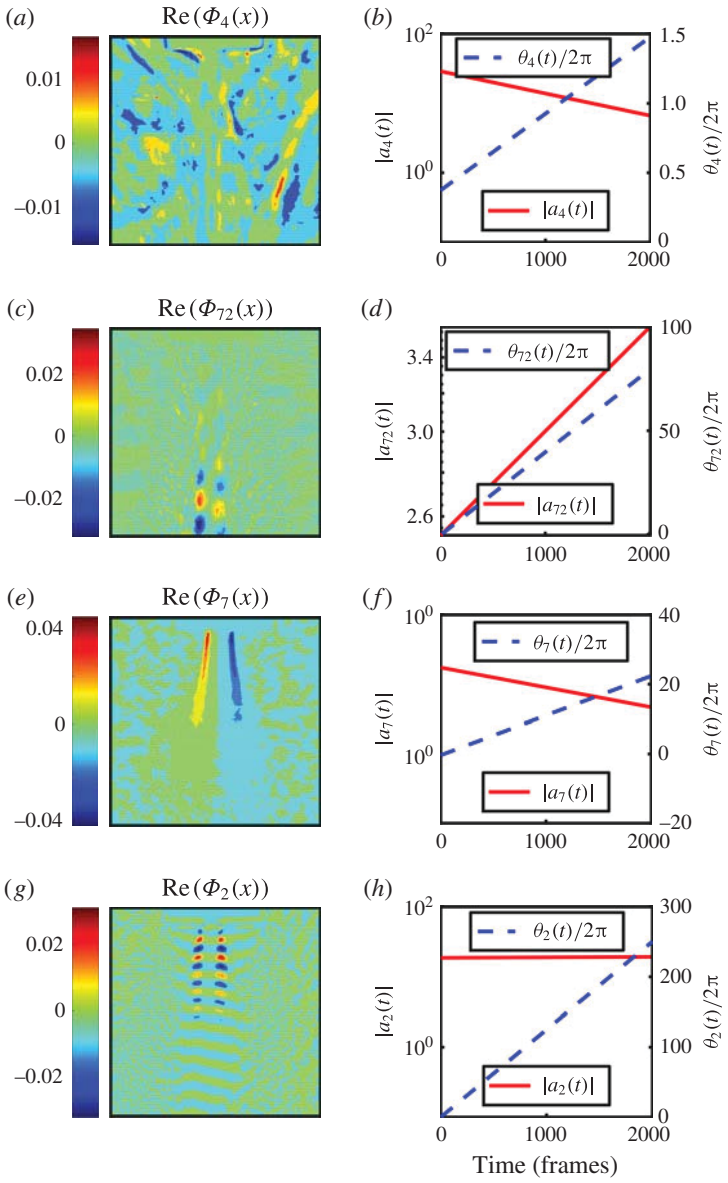

FIGURE 13. (Colour online) The four classes of robust modes found in injector flows and the dynamics of their coefficients: (*a*,*b*) a background mode, (*c*,*d*) an injector mode, (*e*,*f*) a rotating mode and (*g*,*h*) a linear response mode.

4.3.2. *Acoustically driven injector flows for* $J = 11$

Qualitatively, the acoustically driven flow at $J = 11$ is similar to the corresponding baseline flow. As in the case of low J, robust modes of the baseline flow persist when the injector is placed at a PAN of acoustic driving. The driving also initiates a linear response mode, as shown in figure 26. As seen from figure 26(*d*), the amplitude of $a_1(t)$ decays slowly for the selected subgrouping; the dynamics of the real versus imaginary parts of $a_1(t)$ follows an inward spiralling curve.

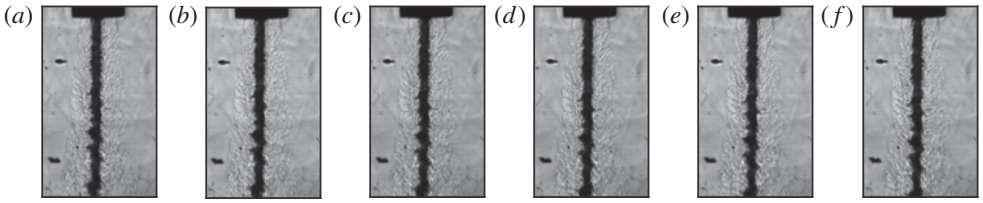

FIGURE 14. Several snapshots of the baseline injector flow at $J = 0.1$: (*a*) 3.96 ms, (*b*) 4.08 ms, (*c*) 4.20 ms, (*d*) 4.32 ms, (*e*) 4.44 ms and (*f*) 4.56 ms.

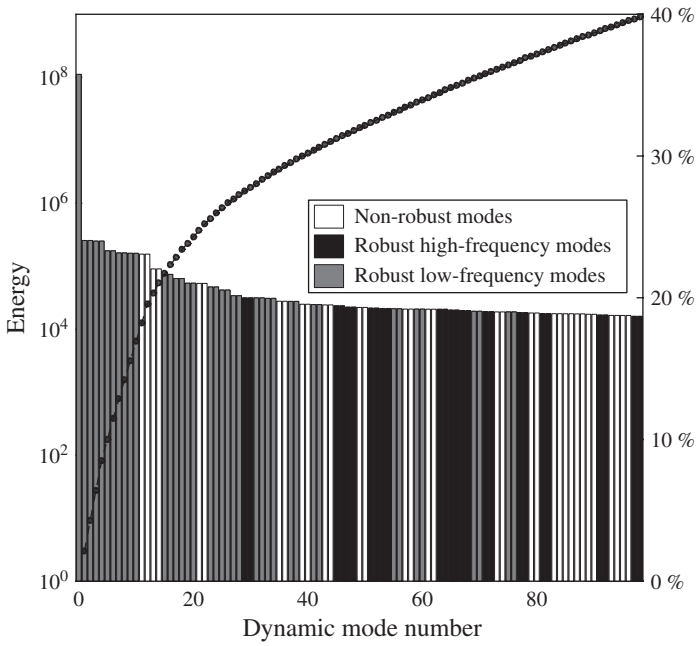

FIGURE 15. Energies of the 100 DMD modes with the highest energies for the full set of snapshots. Non-reproducible modes of the flow are shown in white. Reproducible modes are partitioned into high-frequency and low-frequency modes, shown in black and grey respectively.

5. Conclusions

Despite their apparent simplicity, shear coaxial jets can exhibit highly complex dynamical behaviour. Since theoretical analysis of realistic injector flows is difficult, an alternative approach to unravel the complexity is needed. Here, we proposed the use of modal decompositions of high-resolution high-frequency experimental data to perform this task. Teshome (2012) and Tirunagari *et al.* (2012*a*,*b*) implemented modal decompositions using POD. These studies only reported the most significant modes in the flows.

Strongly driven injector flows appear to be highly disordered and contain significant levels of non-reproducible constituents. One disadvantage of POD is the absence of techniques to differentiate these non-reproducible constituents from the robust dynamical features of the flow. In this paper, we used Koopman mode analysis, a natural approach to search for oscillatory modes (Mezic & Banaszuk 2004; Rowley

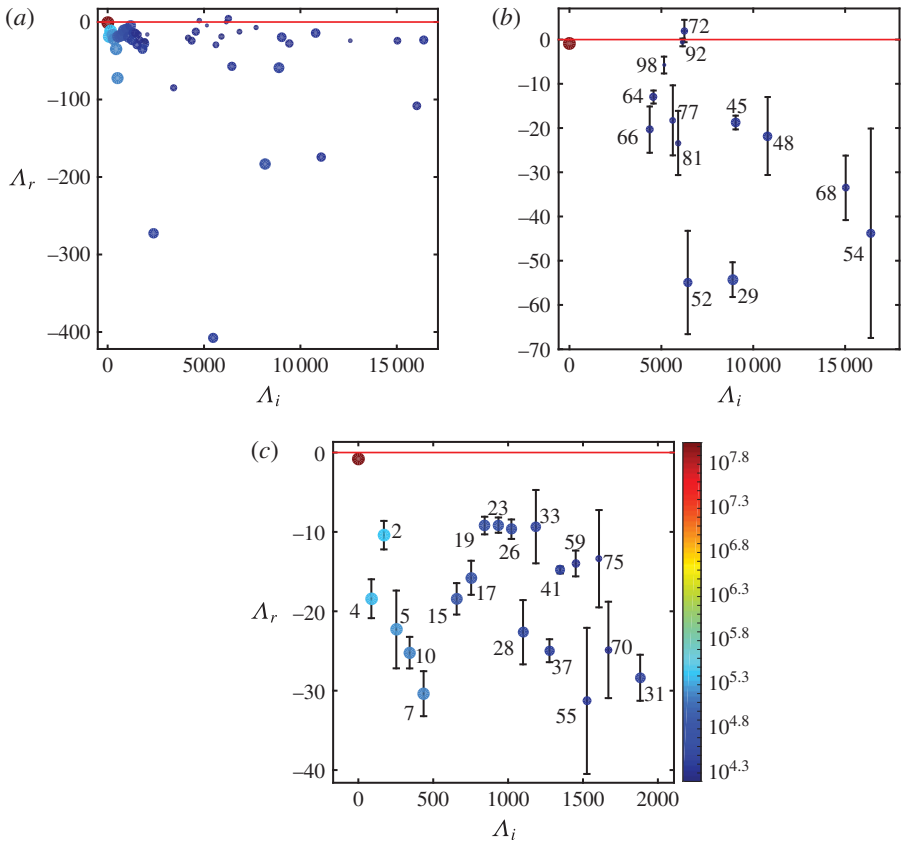

FIGURE 16. (Colour online) The DMD spectrum of $J = 0.1$ baseline flow. (*a*) The 100 modes with the highest energies and positive imaginary parts. The high-frequency ($\mathrm{Im}(\Lambda_i) > 2000$) robust modes, shown in (*b*), are located near the injector flow. The error bars are standard deviations for a set of eigenvalue real parts from different subgroupings that were identified as representing the same eigenmode. Modes 64, 66, 77, 92, 72, 52, 45, 48, 98, 81 and 68 are asymmetric (e.g. figure 20); modes 29 and 54 are symmetric about the axis. (*c*) Low-frequency ($\mathrm{Im}(\Lambda_i) \leqslant 2000$) robust modes that represent the background flow. The colour of the points represents the energies of the modes, according to the colour bar.

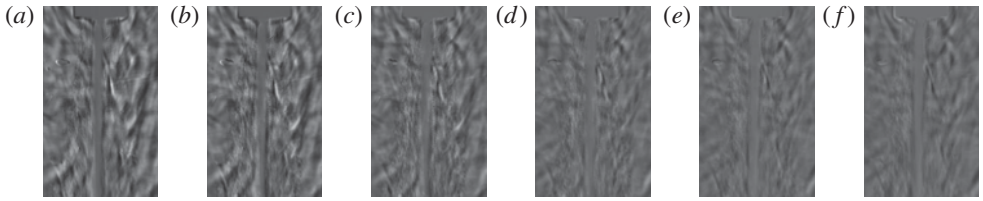

FIGURE 17. Several snapshots of the reconstructed background flow, which lies outside the injector flow and fails to exhibit a well-defined spatial structure: (*a*) 4 ms, (*b*) 6 ms, (*c*) 8 ms, (*d*) 10 ms, (*e*) 12 ms and (*f*) 14 ms.

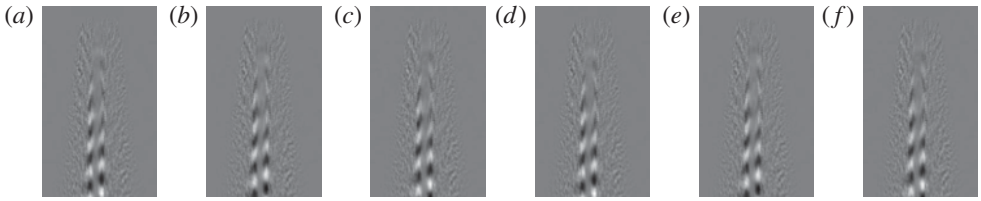

FIGURE 18. Several snapshots of the reconstructed flow for the robust asymmetric mode 48: (*a*) 4 ms, (*b*) 4.2 ms, (*c*) 4.4 ms, (*d*) 4.6 ms, (*e*) 4.8 ms and (*f*) 5 ms. The mode is seen to flow downstream.

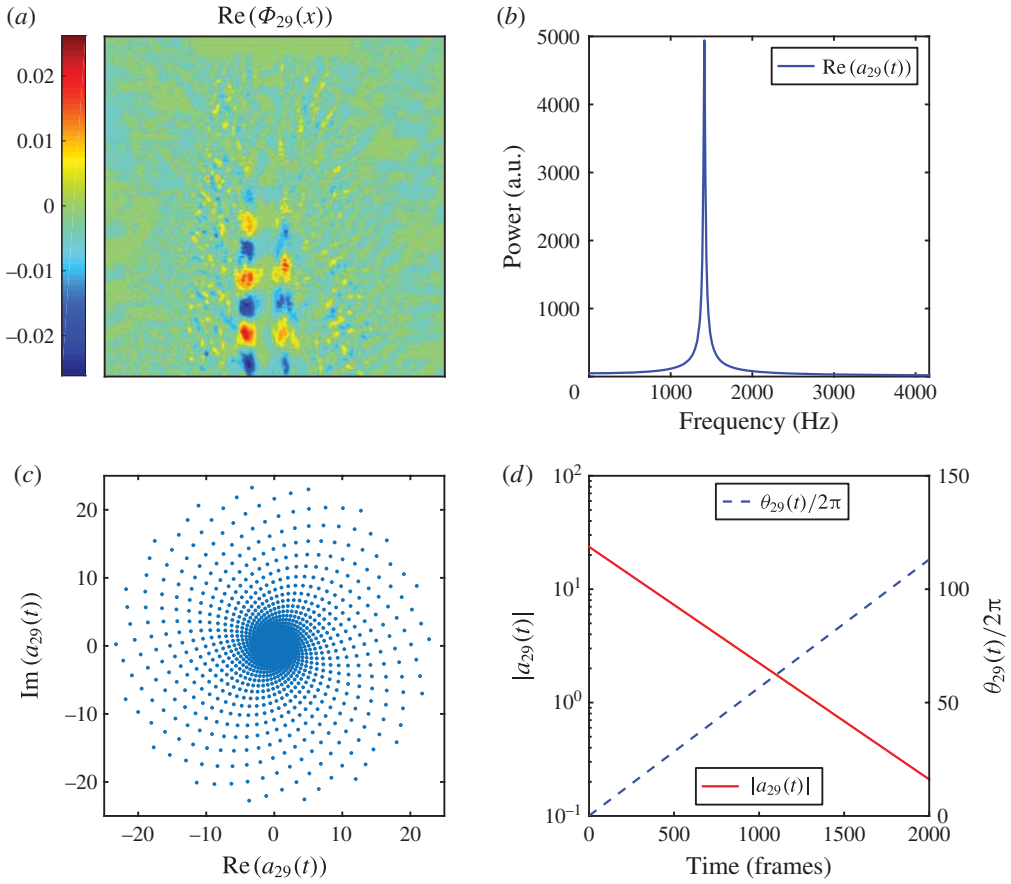

FIGURE 19. (Colour online) Robust symmetric mode Φ_{29}.

et al. 2009; Budišić *et al.* 2012; Mezic 2013), to decompose injector flows. The difficulty was that even non-cyclic and stochastic constituents of a finite data set may be interpreted as a sum of periodic dynamics. However, the deconvolution of these irregular dynamical facets is non-robust, i.e. they depend on the specific data set. Thus, we proposed an approach for differentiating robust and non-robust features in the flow that is based on identifying the former with reproducible Koopman modes, i.e. those that persist in distinct subgroupings of the data (Roy *et al.* 2015). It was

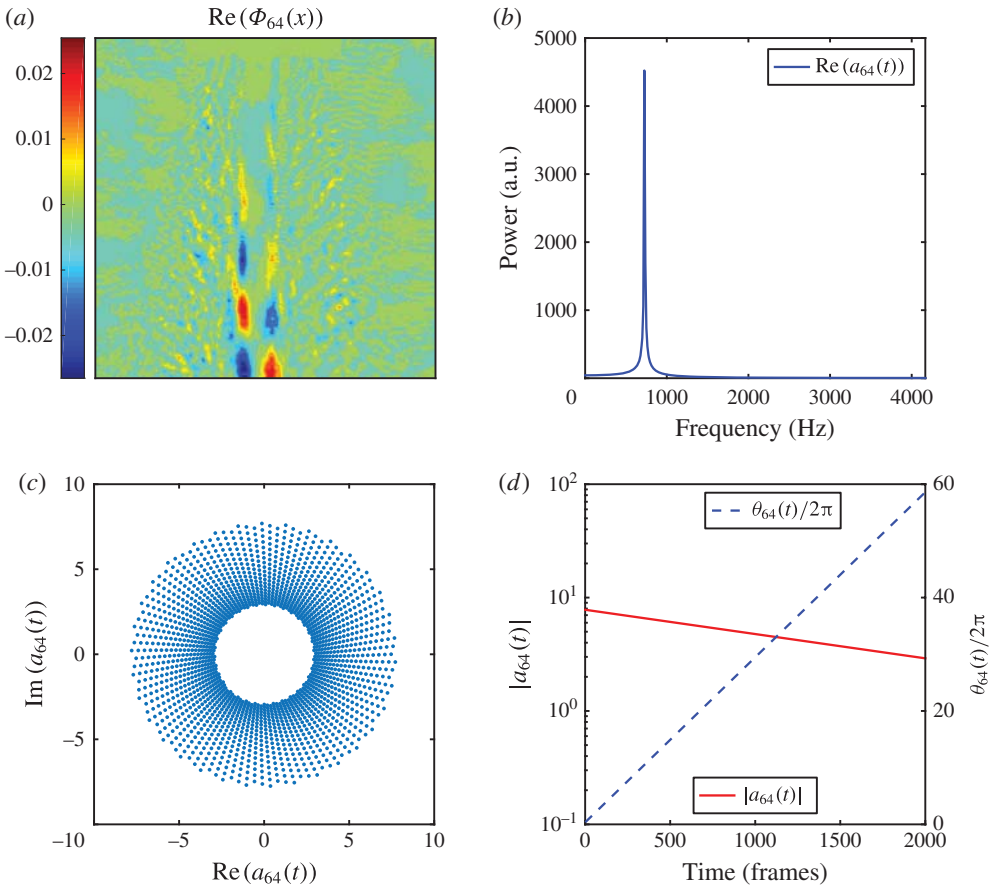

FIGURE 20. (Colour online) Robust asymmetric mode Φ_{64}.

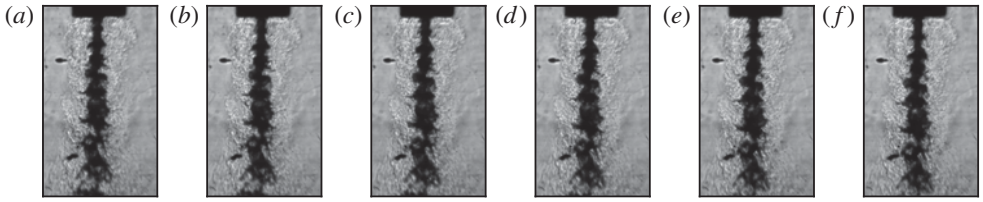

FIGURE 21. Several snapshots of the acoustically driven flow at $J = 0.1$ when the injector is placed at a PAN of the acoustic driving: (*a*) 3.96 ms, (*b*) 4.0 ms, (*c*) 4.04 ms, (*d*) 4.08 ms, (*e*) 4.12 ms and (*f*) 4.16 ms.

thus possible to study all relevant modes of the flow. It is important to note that only these robust features are expected to be useful in applications such as flow control.

The studies reported here were conducted on injector flows of N_2 under high pressure into an ambient N_2 background. The flows were observed with shadowgraph imaging using diffuse backscattering. The high-density injector flows could be observed as darker regions of the visual field. Koopman mode analysis of the density field in baseline flows (those not subjected to additional perturbations) and

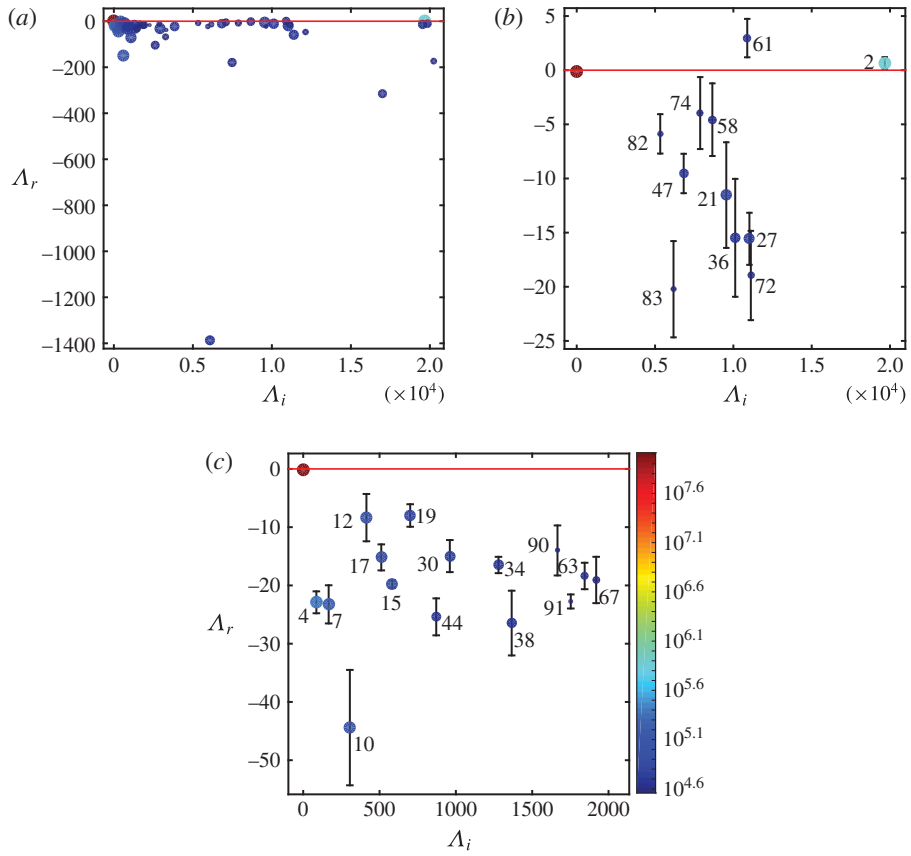

FIGURE 22. (Colour online) The DMD spectrum for the flow at $J = 0.1$ when the injector is placed at a PAN of the acoustic driving. (*a*) The first 100 modes with positive imaginary parts. (*b*) High-frequency ($\mathrm{Im}(\Lambda_i) > 2000$) robust modes with mode number i labelled. The error bars are identical to those defined in figure 16. Mode 2 is the linear response to the driving. (*c*) The low-frequency robust modes ($\mathrm{Im}(\Lambda_i) \leqslant 2000$) represent the background flow.

acoustically excited flows revealed several classes of robust dynamic modes. The modulations of the density field imposed by each of these modes were at least an order of magnitude smaller than the spatial variations in the time-averaged flow.

Several distinct groups of robust dynamic modes characterized by their spatial locations and dynamics were identified in the baseline flows. The first group contained a set of low-frequency excitations located outside the primary injector flow that exhibited rapid decay, as can be observed in figure 4 and the Koopman spectrum in figure 16(*c*). Reconstruction of the flow associated with background modes (figure 17) showed that this flow constituent has no well-defined structure. Although background modes are common between different subgroupings of snapshots in a single experiment, it is expected that they will differ among experiments. Background modes are not found for larger values of the control parameter J, presumably because they have decayed to insignificant levels during the experiment.

The second group of modes are referred to as injector modes because of their location near the primary injector flow. Unlike background modes, they have

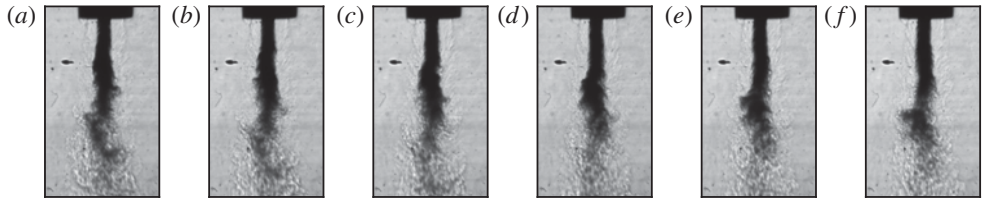

FIGURE 23. Several snapshots of the baseline injector flow at $J = 11$: (*a*) 3.96 ms, (*b*) 4.0 ms, (*c*) 4.04 ms, (*d*) 4.08 ms, (*e*) 4.12 ms and (*f*) 4.16 ms.

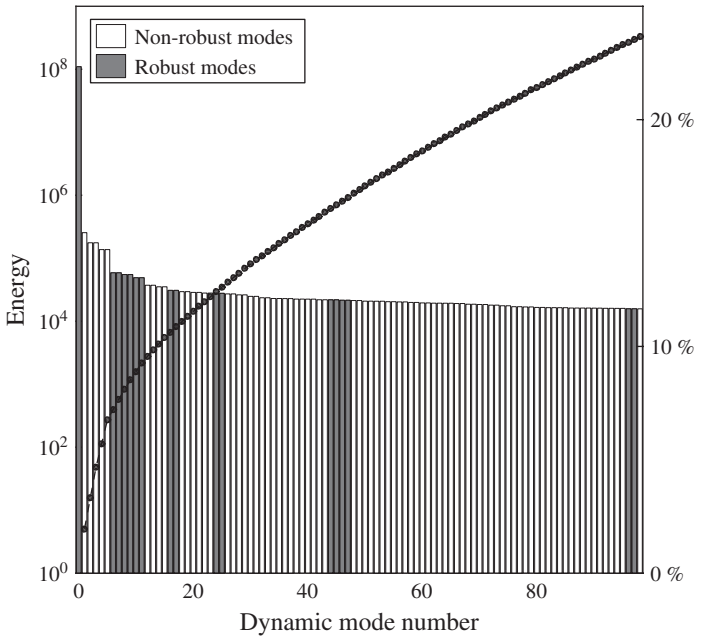

FIGURE 24. The energies of the 100 DMD modes with the highest energies for the full data set of the injector flow for $J = 11$. Non-reproducible modes of the flow are shown in white.

a well-defined structure, an example of which is shown in figure 5; they are high-frequency modes, propagate along the flow (see figure 18) and decay at a significantly slower rate. The wavelength of injector modes is comparable to the modulations of the flow, seen in figure 14, and is likely to be the origin of the latter. The spectrum of injector modes and their error estimates, shown in figure 16(*b*), suggest that some of these may persist beyond the initial transients. This suggestion needs to be validated in longer experimental runs. The broad features of injector modes remain unchanged under acoustic perturbation (figure 22) and for higher values of J (figure 25). While injector modes for small J can be either symmetric (figure 19) or asymmetric (figure 20) in the viewing plane, those for large values of J are antisymmetric. It is possible that the high-/low-density regions in these modes are spirals. They are the only modes reported by Teshome (2012).

Acoustic driving generates additional small-wavelength modulations of the injector flow, as can be seen in figure 21. These appear to be caused by a new robust mode,

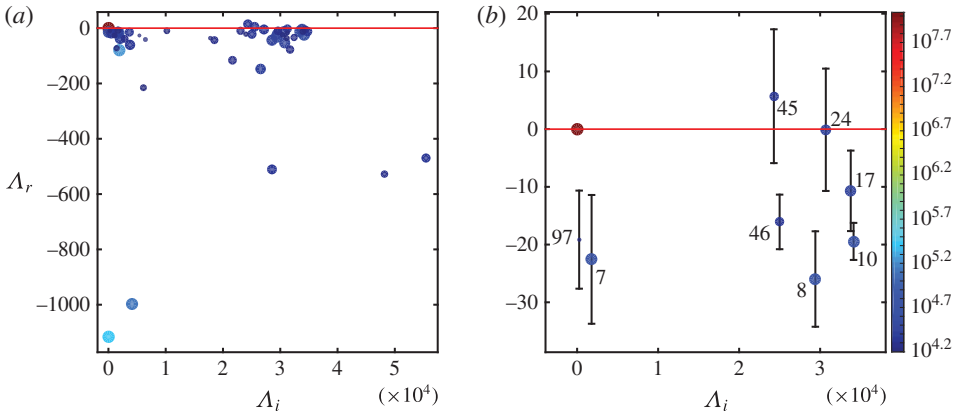

FIGURE 25. (Colour online) The DMD spectrum of $J = 11$ baseline flow. (*a*) The 100 modes with the highest energies and positive imaginary parts and (*b*) robust modes. Mode 7 is the new rotating mode, while modes 45, 46, 8, 24, 17 and 10 are asymmetric injector modes.

which we referred to as a linear response mode; the imaginary part of its eigenvalue is identical to the driving frequency (divided by 2π). Their dynamics exhibits a very sharp spectrum, and their magnitude is (nearly) uniform in time, as seen from figures 10 and 26. For the acoustic driving studied, the spatial periodicity of the linear response mode is smaller than that of injector modes, resulting in the smaller wavelength modulations observed in figure 21. As seen from figure 22, the linear response mode has a large energy, which is correlated with the increased amplitude of modulations of the flow. Linear response modes are found for PAN driven flows at all values of J.

A class of robust dynamic modes of the baseline flow retain their structure and dynamical features under acoustic perturbation. A pair of such modes is shown in figure 11, and the comparison of dynamics of a baseline mode and the corresponding PAN driven persistent mode is shown in figure 12. These modes, referred to as persistent modes, were found for all values of J studied.

The most interesting class of modes was termed rotating modes, as shown in figure 6, and only observed for $J > 5.2$. The projection of their density fields exhibits antiphase oscillatory behaviour. The reconstruction of the spatio-temporal dynamics, illustrated using several snapshots in figure 8, highlights a periodic flipping of the high-/low-density regions. Since the injector and the inlet flow are axisymmetric and the viewing plane has no special stature, the flipping observed in the viewing plane can only be described as a projection of an azimuthally modulated rotating mode, generated via a spontaneous symmetry breaking (Cross & Hohenberg 1993) similar to the rotating modes in uniform flame fronts (Palacios *et al.* 1997). The modes persist under acoustic perturbation, although in this case the system is not axisymmetric, and the symmetry breaking may not be spontaneous.

The roles played by robust modes at different values of J, the outer-to-inner-jet momentum ratio, can be quantified by figures 15 and 24. Injector flows for small values of J (when the outer-jet momentum is relatively large) contain only a few non-robust modes, while those for large values of J consist mostly of non-robust modes. The implication is that large-J flows are more irregular, an observation consistent with

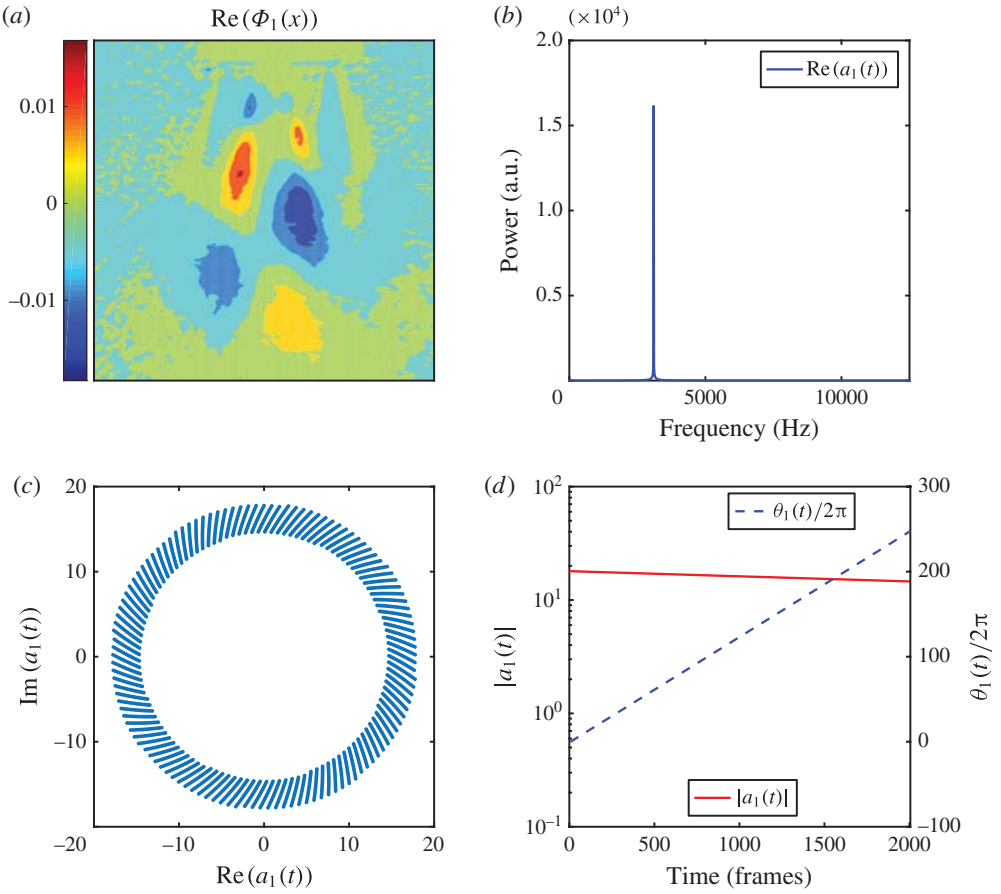

FIGURE 26. (Colour online) Linear response mode (mode 1) for PAN driving of the flow at $J = 11$. The imaginary part of its eigenvalue is identical to the driving frequency divided by 2π.

figures 14 and 23. The energy distributions also reaffirm that it may not be possible to differentiate robust and non-robust flow constituents using their energies alone.

The modal decompositions of injector flows presented here highlight the need for additional investigations. One issue is to identify robust Koopman modes that persist beyond the initial transient stage, i.e. those relevant for long-term flows. For example, our analysis of injector flows suggests that while the background modes are transient, many of the injector modes will persist. The task of differentiating the two groups can be implemented in one of two ways. The first is to conduct and analyse longer experimental runs where transients have decayed. An alternative computational approach is to conduct a sparsity-promoting DMD introduced recently (Jovanovic, Schimid & Nichols 2014). Sparsity-promoting DMD performs the extraction of dynamic modes associated with persistent flows, even when transients have larger energy.

The formation of rotating modes for $J \geqslant 5.2$ is another extremely interesting observation and requires further investigations. It would be especially important to validate the mode with supplementary measurements, study its onset in detail, and

analyse flows appearing in injectors with other geometries and under different classes of acoustic perturbations. Finally, it will be beneficial to determine whether additional classes of dynamic modes are present in the corresponding combustion flows.

Acknowledgement

Funding for this research was provided by the Air Force Research Laboratory under contract nos. FA8650-13-C-2440 and FA9300-13-M-1503. The paper has been cleared for public release by the Air Force Research Laboratory (no. 88ABW-2015-3171).

REFERENCES

BAGHERI, S., SCHLATTER, P., SCHMID, P. J. & HENNINGSON, D. S. 2009 Global stability of a jet in crossflow. *J. Fluid Mech.* **624**, 33–44.

BERKOOZ, G., HOLMES, P. & LUMLEY, J. L. 1993 The proper orthogonal decomposition in the analysis of turbulent flows. *Annu. Rev. Fluid Mech.* **25**, 539–575.

BUDIŠIĆ, M., MOHR, R. M. & MEZIĆ, I. 2012 Applied Koopmanism. *Chaos* **22** (4), 047510.

CHEN, K. K., TU, J. H. & ROWLEY, C. W. 2012 Variants of dynamic mode decomposition: boundary condition, Koopman and Fourier analysis. *J. Nonlinear Sci.* **22**, 887–915.

CROSS, M. C. & HOHENBERG, P. C. 1993 Pattern-formation outside of equilibrium. *Rev. Mod. Phys.* **65** (3), 851–1112.

DAVIS, D. W. & CHEHROUDI, B. 2006 Shear-coaxial jets from a Rocket-like injector in a transverse acoustic field at high pressures. In *44th AIAA Aerospace Sciences Meeting Reno, NV, Jan. 9–12, 2006*.

DAVIS, D. W. & CHEHROUDI, B. 2007 Measurements in an acoustically driven coaxial jet under sub-, near-, and supercritical conditions. *J. Propul. Power* **23** (2), 364–374.

HONG, L., FUSETTI, A., DE ROSA, M. & OSCHWALD, M. 2006 Experimental investigation on the acoustic characteristics of LOZ/CH4 flame. In *ICLASS-2006, 10th International Conference on Liquid Atomization and Spray Systems, Kyoto, Japan, Aug. 27–Sept. 1, 2006*.

HOPFINGER, E. J. 1998 Liquid jet instability and atomization in a coaxial gas stream. In *Advances in Turbulence VII* (ed. U. Frisch), Fluid Mechanics and its Applications, vol. 46, pp. 69–78; *7th European Turbulence Conference (ETC7), St. Jean Cap Ferrat, France, Jun. 30–Jul. 03, 1998*. Springer.

JOVANOVIĆ, M. R., SCHMID, P. J. & NICHOLS, J. W. 2014 Sparsity-promoting dynamic mode decomposition. *Phys. Fluids* **26**, 024103.

LEYVA, I. A., RODRIGUEZ, J., CHEHROUDI, B. & TALLEY, D. 2007 Preliminary results on coaxial jet spread angles and the effects of variable phase transverse acoustic fields. In *46th AIAA Aerospace Sciences Meeting and Exhibit Reno, NV, Jan. 7–10, 2008*.

LUMLEY, J. L. 1967 The structure of inhomogeneous flow. In *Atmospheric Turbulence and Radio Wave Propagation*, pp. 166–176. Publishing House Nauka.

MEZIC, I. 2013 Analysis of fluid flows via spectral properties of the Koopman operator. In *Annual Review of Fluid Mechanics, Vol. 45* (ed. S. H. Davis & P. Moin), Annual Review of Fluid Mechanics, vol. 45, pp. 357–378.

MEZIC, I. & BANASZUK, A. 2004 Comparison of systems with complex behavior. *Physica* D **197** (1), 101–133.

MIESSE, C. C. 1955 The effect of ambient pressure oscillations on the disintegration and dispersion of a liquid jet. *J. Jet Propulsion* **25** (10), 525–530.

MOTHEAU, E., MERY, Y., NICOUD, F. & POINSOT, T. 2013 Analysis and modeling of entropy modes in a realistic aeronautical gas turbine. *Trans. ASME J. Engng Gas Turbines Power* **135** (9), 092602.

PALACIOS, A., GUNARATNE, G. H., GORMAN, M. & ROBBINS, K. A. 1997 Cellular pattern formation in circular domains. *Chaos* **7** (3), 463–475.

ROWLEY, C. W., MEZIC, I., BAGHERI, S., SCHLATTER, P. & HENNINGSON, D. S. 2009 Spectral analysis of nonlinear flows. *J. Fluid Mech.* **641**, 115–127.

ROY, S., HUA, J.-C., BARNHILL, W., GUNARATNE, G. H. & GORD, J. R. 2015 Deconvolution of reacting-flow dynamics using proper orthogonal and dynamic mode decompositions. *Phys. Rev.* E **91** (1), 013001.

SCHMID, P. J. 2009 Dynamic mode decomposition of experimental data. In *Proceedings of 8th International Symposium on Particle Image Velocimetry, PIV09-0141, Melbourne, Victoria*.

SCHMID, P. J. 2010 Dynamic mode decomposition of numerical and experimental data. *J. Fluid Mech.* **656**, 5–28.

SIROVICH, L. 1987*a* Turbulence and the dynamics of coherent structures. 1. Coherent structures. *Q. Appl. Maths* **45** (3), 561–571.

SIROVICH, L. 1987*b* Turbulence and the dynamics of coherent structures. 2. Symmetries and transformations. *Q. Appl. Maths* **45** (3), 573–582.

SIROVICH, L. 1987*c* Turbulence and the dynamics of coherent structures. 3. Dynamics and scaling. *Q. Appl. Maths* **45** (3), 583–590.

TESHOME, S. 2012 Droplet combustion and non-reactive shear-coaxial jets with transverse acoustic excitation. PhD thesis. UCLA Electronic Theses and Dissertations.

TIRUNAGARI, S., HULKKONENE, T., VUORINEN, V., KAARIO, O. & LARMI, M. 2012*a* Proper orthogonal decomposition analysis of cross sectional fuel spray data. In *ICLASS 2012, 12th Triennial International Conference on Liquid Atomization and Spray Systems, Heidelberg, Germany, September 2–6, 2012*.

TIRUNAGARI, S., VUORINEN, V., KAARIO, O. & LARMI, M. 2012*b* Analysis of proper orthogonal decomposition and dynamic mode decomposition on LES of subsonic jets. *CSI J. Comput.* **1** (3), 20–26.

VILLERMAUX, E., REHAB, H. & HOPFINGER, E. J. 1998 Shear instabilities in the near field of coaxial jets. *Phys. Fluids* **10** (9), S2; *15th Annual Fluid Mechanics Photo Contest at the Meeting of the American Physical Society Division of Fluid Dynamics, San Francisco, CA, Nov. 1997*.

WICKER, R. B. & EATON, J. K. 1994 Near-field of a coaxial jet with and without axial excitation. *AIAA J.* **32** (3), 542–546; *AIAA 31st Aerospace Sciences Meeting, Reno, NV, Jan. 11–14, 1993*.

AIAA SciTech
13-17 January 2014, National Harbor, Maryland
52nd Aerospace Sciences Meeting

Development of a Facility for Combustion Stability Experiments at Supercritical Pressure

Jeffrey L. Wegener[1]
University of California at Los Angeles, CA 90095

Ivett A. Leyva[2]
AFRL/RQRE, Edwards AFB, CA 93524

David J. Forliti[3]
Sierra Lobo, Inc. supporting AFRL/RQRC, Edwards AFB, CA 93524

and
Douglas G. Talley[4]
AFRL/RQRC, Edwards AFB, CA 93524

Combustion instability in liquid rocket engines can have severe consequences including degraded performance, accelerated component wear, and potentially catastrophic failure. High-frequency instabilities, which are generally the most harmful in liquid rocket engines, can be driven by interactions between disturbances associated with transverse acoustic resonances and the combustion process. The combustion response to acoustic perturbation is a critical component of the instabililty mechanism, and is in general not well understood. The current paper describes an experimental facility at the Air Force Research Laboratory (AFRL) at Edwards Air Force Base that is intended to investigate the coupling between transverse acoustic resonances and single/multiple liquid rocket engine injector flames. Critical aspects of the facility will be described, including the capability to operate at supercritical pressures that are relevant to high-performance liquid rocket engines, accurately-controlled and cryogenically-conditioned propellants, and optical access to facilitate the use of advanced diagnostics. The transverse acoustic resonance is induced through the use of carefully-controlled piezoelectric sirens, allowing monochromatic excitation across a range of amplitudes at a number of discrete frequencies. The location of the flame within the acoustic resonance mode shape can also be varied through relative phase control of the two acoustic sources. The operating space of the facility, for oxygen and hydrogen operation, will be described. Preliminary nonreacting and reacting data will also be presented to demonstrate the quality of operation of this facility. It is anticipated that future results generated using this facility will provide both fundamental insight into the acoustic-flame interactions as well as provide a database useful for validating combustion instability models.

Nomenclature

A	=	area
c	=	speed of sound

[1] Graduate Student, Department of Mechanical and Aerospace Engineering, UCLA, Los Angeles, CA 90095 student member.
[2] Technical Advisor, AFRL/RQRE, 4 Draco Drive, Building 8351, Edwards AFB, CA 93524, Associate Fellow.
[3] Research Scientist, Sierra Lobo, Inc., 4 Draco Drive, Building 8451, Edwards AFB, CA 93524, senior member.
[4] Lead, Combustion Dynamics Group, AFRL/RQRC., 4 Draco Drive, Building 8451, Edwards AFB, CA 93524, Associate Fellow.

D_1 = inner injector inner diameter
D_2 = inner injector outer diameter
D_3 = outer injector inner diameter
D_4 = outer injector outer diameter
dt = time step
f_F = acoustic frequency
m = waveguide flare constant
p_c = mean chamber pressure
p' = acoustic pressure perturbation amplitude
t = inner post thickness
u' = acoustic velocity perturbation amplitude
x = streamwise (longitudinal) coordinate axis
y = spanwise (transverse) coordinate axis
z = depthwise coordinate axis

I. Introduction

LIQUID rocket engines exhibit challenging scientific problems which have been the subject of extensive efforts over several decades. A fundamental understanding of these problems remains incomplete for several phenomena, with combustion instability being a critical example. This lack of understanding has caused delays and budget increases in rocket engine development programs. The inability to predict combustion instabilities in particular, requires expensive iterative testing as part of the development cycle.

Physics-based modeling and understanding of the problem have potential to improve the prediction of combustion instability, leading to a simplified design cycle requiring fewer redesign iterations. Verification and validation of numerical models for combustion stability require advanced bench-scale experiments to serve two primary purposes. First, these experiments must improve fundamental knowledge of the underlying physics of combustion instability. Combustion instability has been investigated in a wide range of scenarios and typically involves a coupling between hydrodynamic instabilities, unsteady heat release, and acoustic disturbances[1]. Liquid rocket engine (LRE) injectors create non-premixed flames, relying on turbulent mixing within shear layers which exhibit velocity and heat release oscillations that can couple with chamber acoustics. Characterizing these oscillations in terms of frequencies and amplitudes from detailed experimental measurements and data analysis will improve the ability to predict these values, and indicate the likelihood of an oscillation giving rise to combustion instability. Second, these experiments must provide data for validation of computational models. This requirement drives the need for high-fidelity measurements and well-characterized boundary conditions.

Fundamental experiments exploring combustion stability in conditions similar to that of a liquid rocket engine (LRE) require challenging systems, including cryogenic propellants and supercritical chamber pressure operation, among others. To meet these requirements, a new combustion stability experimental facility was recently constructed at the Air Force Research Laboratory (AFRL) at Edwards Air Force Base. The development of this facility was based on experience gained from an existing nonreactive facility at AFRL[2-4]. Insight was also gained from a small number of existing combustors which create LRE conditions in sub-scale tests. These tests involve total mass flow rates which are often orders of magnitude lower than a typical LRE and contain five or fewer injector elements. But, in order to employ detailed experimental methods, such as high-speed diagnostics and acoustic control systems, a variety of hardware designs have been used. Five modern combustors are particularly relavant for comparison with the new combustion stability facility. These are the Multi-injector Combustor (MIC) and the Very High Amplitude Modulator (VHAM) facility, both operated jointly by ONERA and CNRS, the Common Research Combustor (CRC) operated jointly by CNRS and DLR, the BKH combustor operated by DLR, and the Continuously Variable Resonance Combustor (CVRC) operated by Purdue University.

The CRC originated in 2002 from the efforts of a German-French working group which now operates identical experimental combustors at the Research Institute for Equilibrium Systems (IRPHE) in Marseilles, France and DLR in Lampoldshausen, Germany. The CRC injects propellant from one side of a flat, cylindrically shaped chamber through a single injector which is $1/10^{th}$ scale of a typical LRE injector. With high-speed shadowgraphy and OH* chemiluminescence imaging, the dynamics of a single LOx/H_2 flame were investigated to fundamentally relate spatial and temporal heat release oscillations to pressure oscillations controlled by external acoustic forcing. A single injector element though, provides only partial representation of thermoacoustic instabilities occurring in LREs that contain multiple injectors and interactions between adjacent flames.

The BKH combustor is part of a recently constructed facility at DLR Lampoldshausen, Germany, which focuses on high-frequency combustion instability for LO_x/H_2 conditions[5,6]. This combustor includes five shear coaxial injectors in a cross formation to investigate interactions between neighboring flames. The MIC, located in Paris, France, shares many design features with the BKH combustor. The MIC uses multiple injectors, but in a linear arrangement to isolate interactions between pairs of flames using two-dimensional imaging[7,8]. Unless utilizing laser sheet flame illumination, a cross formation prevents one from distinguishing between foreground and background flames when viewing OH* emission images.

The VHAM facility is a modified version of the MIC which creates much greater acoustic pressure amplitudes in an effort to replicate the high-amplitude oscillations documented in actual LRE combustion instabilities[9]. The VHAM facility uses a toothed wheel to periodically block gas flow through exhaust nozzles, creating high-pressure amplitudes inside the combustion chamber. The toothed-wheel exhaust nozzle technique is also employed in the MIC, BKH, and CRC designs for the same purpose. With this method, the periodic nozzle imposes an acoustic boundary condition on the chamber wall, where the acoustic frequency is controlled by the wheel speed. The resulting pressure perturbation amplitude though, is not independently controlled, and is instead determined by hardware geometry such as nozzle diameter and tooth profile design. In the MIC, BKH, and CRC configurations, the toothed wheel is placed over a secondary exhaust nozzle which is located on the side of the chamber, perpendicular to the primary exhaust nozzle. The VHAM does not use secondary nozzles and two primary exhaust nozzles located at the end of the chamber are periodically blocked by a common toothed wheel. This alternative design was used to create pressure amplitudes as high as 20% of p_{cc} in the VHAM, whereas previous experience with the smaller amplitudes of the MIC design yielded limited flame response[9].

Controlled acoustic excitation in the manner described above allows a partial decoupling of a portion of the combustion instability feedback loop. Without an external acoustic source, chamber pressure perturbations exist due to combustion instabilities alone, and these natural changes in pressure cause further pulsations in combustion and heat release rate via oscillations in propellant flow and mixing rates. This mechanism is best represented in three steps as shown in Fig. 1. As flow oscillations represented by u' create fluctuations in propellant mixing, unsteady heat release is produced, represented by q' in Fig. 1. Then, unsteady heat release induces acoustic pressure perturbations which may resonate within the combustion chamber. Acoustics may influence the propellant mixing process and create a feedback mechanism. In this way, the flame serves as a source. But, when controlled acoustic excitation contributes to chamber acoustics, feedback dependencies are partly disassociated because a second source of acoustics is added. This allows one to investigate the effects of acoustic waves on fluid dynamic instability and unsteady heat release by varying acoustic pressure amplitude and frequency. With this strategy, the degree to which perturbation amplitudes and their inherent frequencies can be varied is highly dependent on the specific design used for external acoustic forcing.

In contrast to the nozzle modulation method used by all four aforementioned combustors, the CVRC of Purdue uses an acoustic control system relying on variable injector geometry[10]. By altering the size of the oxidizer plenum, the resonant frequency of the injector flow is controlled such that chamber pressure amplitudes range from less than 10% to 60% of the chamber pressure were achieved. The highest pressure amplitudes are achieved when the oscillation frequency of the injector matches the chamber pressure oscillation frequency, whereas a mismatch dampens the chamber mode. Thus, the CVRC design forgoes the electro-mechanical system of a typical acoustic source, and instead relies on injector flow oscillations to create heat release oscillations in the reaction zone. A family of chamber geometries can be investigated; some are stable and some are not. This method reliably induces high-amplitude instability, but requires mindful choice of fuel species and propellant flow conditions to indirectly manipulate the preferred frequency and amplitude of the instability.

The current endeavor concentrates on operational flexibility. The importance of variable injector configurations, propellant flow conditions, and acoustic excitation motivated the combustion stability facility design to offer a wide range of conditions in these three areas. A single injector is used in a modular flange, allowing for multiple injectors in future work. Second, propellant temperatures, and thus densities, are widely variable by employing cryogenic heat exchangers to cool ambient temperature gaseous propellants to the desired temperatures. Lastly, a pair of piezoelectric sirens serve as acoustic sources with variable acoustic pressure amplitudes and a range of forcing frequencies. This approach allows for separate control of amplitude and frequency.

II. Experimental Facility

The combustion stability facility takes on the complexities of a complete LRE test stand at subscale. All data acquisition and control system (DACS) hardware and user interfaces are located in a remote control room. Thus, the infrastructure, plumbing, and electrical designs necessary to realize this facility are extensive. This description

though, will be limited to features having a direct influence on the experimental environment. These include the combustion chamber, cryogenic heat exchangers and propellant supply systems, the acoustic excitation system, and high-speed imaging.

A. Combustion Chamber

Similar to the previously existing chamber used in nonreactive AFRL work[2,11], the chamber is designed as a chamber within another chamber. The inner chamber creates a near ideal environment for one-dimensional acoustic wave resonance, but is not sealed from the surrounding volume. This surrounding volume is the outer chamber, which has the structural integrity to withstand operating pressures of 1500 psi (=10.34 MPa). Thick walls and windows are not necessary for the inner chamber, allowing more freedom for placing injectors and integrating new injector designs. A CAD rendering of the chamber assembly is shown in Fig. 2, and a photograph of the completed facility is shown in Fig. 3 with the chamber integrated into the apparatus.

The outer chamber is fabricated from a forged Naval brass alloy and has an octagon shape to offer optical access from multiple views. The current configuration contains six windows, which includes large windows in the front and rear walls of the chamber and four smaller windows located at each corner of the outer chamber. The large windows are made of sapphire, while the smaller windows are made of quartz. Large opening in the two remaining chamber side walls are used for acoustic excitation attachments. The injector assembly and exhaust port are located at the top and bottom of the outer chamber, respectively, creating downward propellant flows which exit the combustor through a 4.8 mm exhaust orifice, the chamber's only exhaust path.

The central part of the inner chamber, where the injector is located, is a rectangular volume open to transverse acoustic excitation from the left and right. The inner chamber depth is 20.32 mm and the height is 36.07 mm, making room for subscale injectors only. The transverse width is much larger, reaching 0.82 m from the left acoustic source to the right acoustic source. This dimension makes the inner chamber volume large in comparison to the size of the combustion zone. One should also note that although the inner chamber cross sectional area is 20.32 mm × 36.07 mm near the injector, the far left and far right areas of the inner chamber expand to a large circular area in order to house each acoustic driver.Two quartz inner chamber windows separate the inner chamber from the outer chamber, and because these windows need not withstand a large pressure differential, small holes are located throughout the rear inner window. Hence dynamic pressure transducers and thermocouples are placed in these holes to diagnose the region near the flame by way of placement directly through the window. At the upper wall of the inner chamber, a gaseous nitrogen plenum provides two flows parallel to propellant flows. First, window cooling flows enter the inner chamber through slotted holes above the windows. Second, a propellant coflow system provides gaseous nitrogen to the region surrounding the flame by entering the chamber through dozens of 0.48 mm holes in a circular pattern around the injector.

B. Fluid Supply Systems

In a facility where propellant density control is crucial in achieving a set of experimental objectives, propellant temperature and pressure are paramount. In this case, the propellant pressure at the injector exit is treated as equal to the chamber pressure. The propellant temperature, though, is determined by the oxygen and hydrogen supply systems. Liquid rocket engine propellant tanks often hold fuel and oxidizer at cryogenic states, but this facility instead relies on ambient temperature propellant tanks providing high-pressure oxygen and hydrogen. Cryogenic heat exchangers then cool the propellants to the desired state. Thus, fluid supply system descriptions will focus on chamber pressurization techniques and cryogenic heat exchangers in order to understand propellant systems as a whole.

As in an LRE, similar experimental systems[5,9] have relied on combustion for chamber pressurization. But, when using subscale injectors and propellant flow rates of 10 g/s or less, combustion alone will not produce the high pressures seen in actual LREs. The current endeavor indeed maintains low flow rates, and also utilizes a relatively large chamber volume as explained in the previous section. Thus, an added source of mass flow must exist in order to achieve desired pressures and densities, which is a more precise technique to control the mean chamber pressure, rather than with combustion alone. A nitrogen chamber pressurization system serves this purpose by entering the chamber through multiple ports in the outer chamber wall, and chamber pressure is set using a variable control valve in the nitrogen supply system. Flow out of the chamber is restricted by the exhaust orifice. This technique adds freedom for designing a large array experimental conditions, because chamber pressure is controlled independent of propellant flow conditions. The source of chamber pressurization is partly decoupled from the combustion process.

With propellant pressure determined by chamber pressure, propellant flow rate and temperature are left to be controlled by the propellant feed system. First, flow rate is set using a remote needle valve followed by a mass flow meter (Porter 123 series), and both of these components are located upstream from the heat exchangers such that

these components operate on gaseous propellants at nominal room temperature. Maximum mass flow rates are 0.7 g/s and 10 g/s for hydrogen and oxygen, respectively. Downstream of the flow meters, hydrogen and oxygen pass through individual heat exchangers. Both heat exchangers operate under similar principles where propellant flow passes through a coiled tube which is cooled by liquid nitrogen. The oxygen heat exchanger is shown in Fig. 4 and the hydrogen heat exchanger is shown in Fig. 5. In the case of the oxygen heat exchanger, the propellant tube is coiled inside of a casting which also contains a coiled tube for liquid nitrogen flow. Electric heaters are mounted to the aluminum casting to offer additional energy in the event that the casting is chilled below the target temperature. The heating system consists of six heater elements individually controlled by a closed-loop control system written in LabVIEW. In this way, coolant control valves are set to slightly sub-cool the casting using liquid nitrogen, reducing the process gas to a temperature 2 to 5 K below the target temperature. The heater power is then manually applied and automatically adjusted to hold the process fluid outlet temperature equal to the target temperature with an accuracy of ±1 K. The oxygen heat exchanger was designed and constructed by Sierra Lobo, Inc. For the hydrogen heat exchanger, the propellant tube is immersed directly within a liquid nitrogen bath and heaters are not included. The temperature of the process fluid in each heat exchanger is controlled by individually regulating liquid nitrogen flow rates through each system with separate control valves. Although the propellant heat exchangers offer variable control of temperature, a conditioning process is required to cool plumbing hardware prior to achieving a desired, stable temperature. The temperature conditioning process is performed using nitrogen as a surrogate process fluid in order to minimize propellant usage.

To characterize the capability of each heat exchanger, the minimum achievable temperature was measured for a range of chamber pressures. This was done by utilizing high liquid nitrogen flow rates over a long period of time to cool the hardware of each system. Thus, the injector flow temperature for each process fluid was minimized, representing a low temperature limit on the facility operating space. The results from this effort are shown in Fig. 6 for oxygen, where minimum temperature is shown to have a small dependence on chamber pressure. An oxygen density contour is the background of Fig. 6, showing that a liquid phase is achievable for $p_c < p_{crit,Ox}$, where $p_{crit,Ox}$ = 731 psia (=5.04 MPa). Mass flow rate is shown to have a negative correlation with temperature. Similar measurements were made with the hydrogen propellant system, but to perform these tests safely, helium was used as a surrogate. Minimum helium temperatures are shown in Fig. 7, superimposed on a hydrogen density contour map. For both oxygen and hydrogen, the minimum achievable temperature falls between 110 and 120 K with a primary dependence on propellant flow rate and a minor dependence on chamber pressure.

To formalize a range of possible operating conditions for the new facility, a parametric map of propellant density ratio S versus chamber pressure p_c is shown in Fig. 8. The oxygen and hydrogen density limits required to calculate S were determined using temperature limits from a heat exchanger characterization study. The upper temperature limit was taken as room temperature, while the lower limit is the minimum achievable propellant temperature ascertained from the heat exchanger characterization study, i.e. Figs. 6 and 7. To create Fig. 8, the resulting limits of S were then plotted for two-phase LO_x-GH_2 flow, single-phase GO_x-GH_2 flow, and flows in which $p_c > p_{crit,Ox}$.

The injector consists of a single shear-coaxial element designed for hydrogen flow in the annulus and oxygen flow in the center. In terms of total cross-sectional area, the injector is $1/10^{th}$ scale of the J-2 engine, for example. An injector of this size is challenging to manufacture, but is used here to achieve jet velocities and Reynolds numbers with an order of magnitude similar to an actual LRE while maintaining much smaller propellant mass flow rates. The cross sectional dimensions of the injector are shown in Fig. 9. The outer to inner jet area ratio is 1.68. The inner post thickness to inner diameter ratio t/D_1 has a value of 0.27, which prevents the inner shear layer from behaving purely as the meeting of co-flowing fluids. Instead, a recirculation zone is expected to form at the exit of the injector between the outer and inner jets. The length of the inner and outer injectors are sufficient to create fully developed turbulent flow at the exit for all conditions of interest here.

A comparison of the inner jet Reynolds number Re_{ij} and the outer jet Reynolds number Re_{oj} for similar research combustors is shown in Fig. 10, with operating points of actual oxygen-hydrogen LREs. Operating spaces of four other combustion instability research facilities are shown, including the BKH combustor of DLR, Germany, the Common Research Combustor (CRC) of CNRS, France and DLR, Germany, the Multi-Injector Combustor (MIC) of ONERA and CNRS, France, and the Cryogenic Combustion Laboratory (CCL) of Pennsylvania State University, USA. These facilities were specifically chosen for comparison because detailed flow conditions for oxygen-hydrogen stability experiments for shear-coaxial jets are available in published literature[5,7,8,12,13], but one must be cognizant that apparatuses such as these often see multiple modifications in only a few years time. As a result, Fig. 10 should be considered a general guide for comparison, because Re values for the facility concerned here, as well as the others in Fig. 10, can be revised with simple hardware modifications.

C. Acoustic Characterization

A challenging task required to complete the facility design was the development of an acoustic excitation system. An ideal design will offer free control of amplitude over a wide range of acoustic frequencies. But, as seen in the acoustic control systems of existing facilities[6], this proves to be difficult. Designs must often sacrifice either control of frequency or amplitude in order to achieve high pressure amplitudes on the order of those manifested by LRE combustion instabilities. This facility utilizes a pair of piezoelectric acoustic sirens, where pressure amplitude is variably controlled with input voltage amplitude until reaching the sirens maximum safe amplitude of approximately 600V. The chamber integrates the sirens using stainless steel waveguides mounted to the left and right sides of the outer chamber as shown in Fig. 2.

The waveguides act as horns which focus acoustic energy from the 100 mm diameter sirens to the smaller rectangular inner chamber. This acoustic horn technique facilitates the production of high pressure amplitudes at the point of interest, the flame. The waveguides' shape must provide a smooth transition from a 11.24 cm diameter circlular flange to a 2.03 cm × 3.61 cm rectangular cross-section. To minimize two-dimensional and three-dimensional waves, the circle-to-rectangle transition must be void of abrupt area changes and sharp corners. This requirement, combined with material stress from high chamber pressures, make design and fabrication challenging.

The area reduction from circle to rectangle follows a quasi-one-dimensional model for sound propagation in a rigid-walled duct, which is derived beginning with the acoustic wave equation,

$$\nabla^2 p - \frac{1}{c^2}\frac{\partial^2 p}{\partial t^2} = 0\,, \tag{1}$$

which is then integrated for acoustic pressure p for a three-dimensional segment of the duct. A coordinate system is adopted where x is the jet streamwise direction, y is the transverse direction, and z is the depthwise direction. Thus, a perfectly-shaped waveguide will prevent acoustic wave propagation in the x and z directions and concentrate 100% of the energy from each siren to produce waves in the y direction. Gauss's theorem is then used to convert the volume integral of $\nabla^2 p$ to a surface integral. Then, apply the boundary condition that $\nabla p \cdot n = 0$ at the inner wall of the waveguide, divide by Δy, and take the limit as $\Delta y \to 0$ ($\Delta y = \partial y$). One obtains

$$\frac{\partial}{\partial y}\iint_A \frac{\partial p}{\partial y}\,dA - \frac{1}{c^2}\frac{\partial^2}{\partial t^2}\iint_A p\,dA = 0\,. \tag{2}$$

With the exception of a thin acoustic boundary layer near the inner wall of the waveguide, p is uniform over any given cross section, i.e. $\frac{\partial p}{\partial x} = \frac{\partial p}{\partial z} = 0$. The equation above then reduces to

$$\frac{1}{A}\frac{\partial}{\partial y}\left(A\frac{\partial p}{\partial y}\right) - \frac{1}{c^2}\frac{\partial^2 p}{\partial t^2} = 0\,, \tag{3}$$

which is known as Webster's horn equation, after Arthur G. Webster[14]. Following Pierce[15], Webster's horn equation can be simplified as

$$\left\{\frac{\partial^2}{\partial y^2} + \frac{1}{4A^2}\left[(A')^2 - 2AA''\right] - \frac{1}{c^2}\frac{\partial}{\partial t^2}\right\}A^{1/2} p = 0\,. \tag{4}$$

This is a nonlinear ordinary differential equation with respect to A which can be used to describe the optimal area of an expanding or constricting waveguide. The general solution is

$$A = A_{th}\left(\cosh my + T\sinh my\right)^2. \tag{5}$$

The specific solution is found for the catenoidal horn shape[15] for $T = 0$ using boundary conditions enforced by the chosen siren diameter, inner chamber area, and waveguide length in order to determine the throat area A_{th} and flare constant m. Finally, the specific solution was used to model the inside wall of each waveguide according to a prescribed area function. The CAD rendering in Fig. 11 shows the left waveguide in a cut-away view. With an identical assembly on the right of the chamber, the acoustic system produces high-amplitude pressure waves, $p'/p_c \sim 0.01$, traveling in the y direction.

Acoustic pressure amplitudes induced by this system are largely governed by the resonant modes of the chamber and the piezoelectric sirens. The chamber geometry will allow resonant modes for a particular set of acoustic frequencies, which are also dependent on the speed of sound for a given thermodynamics state. The sirens, on the other hand, have resonant frequencies of their own. Below 6 kHz, the sirens exhibit only three resonant frequencies and operating far from these three frequencies results in inefficient sound production and low pressure amplitudes. Thus the maximum achievable amplitudes are dependent on frequency as it relates to resonance of two independent phenomena.

Regarding the resonant chamber modes, an analytical examination reveals a broad array of frequencies. The analytical relationship between chamber length L, acoustic frequency f_F, and the speed of sound c follows as

$$L = \frac{n}{2}\lambda = \frac{n}{2}\left(\frac{c}{f_F}\right) \tag{1}$$

where even values of n create resonant conditions for acoustic sources operated in-phase (φ =0°) and odd values of n create resonant conditions for acoustic sources operated out-of-phase (φ =180°). In the same regard, sources operated in-phase will create a pressure antinode (PAN) at the center of the chamber and sources operated out-of-phase will create a pressure node (PN) at the center of the chamber. Due to the waveguides long span, ten transverse resonant frequencies occur at less then 6 kHz. Unlike convective waves, a resonant condition will form acoustic waves which are symmetric with respect to both space and time. Spatially, an isothermal volume subject to transverse resonance will produce evenly spaced PNs and PANs. This places the injector at a location of known acoustic perturbation gradients $\frac{\partial p'}{\partial y}$ and $\frac{\partial u'}{\partial y}$, where $\frac{\partial p'}{\partial y} = 0$ for a PAN condition (φ =0°) and $\frac{\partial u'}{\partial y} = 0$ for a PN condition (φ =180°). Temporally, the acoustic waves reveal a symmetric waveform lacking the abnormalities present when waves of unequal amplitude or phase interact and maintain a traveling wave component.

Second, the resonant frequencies of the sirens must be determined experimentally, as each unique siren will have its own characteristic peak amplitudes. This is best investigated using a frequency sweep method with each siren removed from the chamber. In this way, acoustic pressure is measured without regard to chamber resonance. An experimental frequency sweep was performed for 0 to 6 kHz and two peaks are observed at 3076 Hz and 5200 Hz for the left siren and 3084 Hz and 5101 Hz for the right siren. Wider bands of high sound production also exist at 1638-1915 Hz for the left siren and 1620-1860 for the right siren. These isolated frequencies offer three separate narrow bands of high amplitude acoustic excitation for each siren, while operating outside these bands results in much lower amplitudes.

Finally, a combined acoustic characterization of both sirens mounted inside the chamber must be completed to understand the system's performance. A frequency sweep from 0 to 6 kHz was employed with operation of sirens in-phase. To measure the frequency response of pressure oscillations within the chamber, a dynamic pressure transducer (Kulite model XCE-093-50D) was placed at the center of the chamber. When operating acoustic sources in-phase the chamber's center location represents a PAN, and is an excellent measure of the maximum pressure amplitude for a given frequency. The results of these measurements are shown in Fig. 11 for a chamber pressure of 400 psia (=2.76 MPa). Not all ten transverse chamber modes are identified in Fig. 12, with transverse resonance peaks only located near the sirens' optimum frequency bands. Although 1T and 2T modes exist for the chamber, for example, 1T and 2T modes do not appear in the comprehensive frequency sweep in Fig. 12 due to siren limitations, demonstrating the combined result of chamber and siren resonance.

In conclusion, the acoustic system demonstrates advantages over other techniques, but also has limitations. The piezoelectric sirens are useful only for select frequency bands. The pressure amplitudes achievable within these frequency bands are approximately equal to 1% of the mean chamber pressure. Although the pressure oscillations of LRE combustion instabilities can reach amplitudes far greater than 1% of the mean chamber pressure, the amplitudes obtained by this acoustic system are sufficient for inducing a significant response in the coaxial jet, as will be shown in the results and as shown in previous nonreacting experiments[16,17]. Further, by decoupling the

source of chamber pressurization from propellant flow rates, it becomes advantageous to scale p' with a the coaxial jet dynamics rather than the mean chamber pressure. For example, p' may be scaled by the jet dynamic pressure. At any rate, the acoustic system provides three key advantages over other techniques. First, by spacing the sirens very far apart (0.82 m), several different T modes can be achieved below 6 kHz. For example, Fig. 12 shows that a mean chamber pressure of 400 psia allows one to produce a resonant mode at 1543 Hz (3T) and also at 3169 Hz (6T). Second, the pressure amplitude is directly controlled by altering the voltage input to the sirens, similar to a traditional loudspeaker. Last, both a PN and a PAN can be located at the jet by operating the sirens out-of-phase and in-phase, respectively.

D. High-Speed Imaging

Jet flow visualization is the primary diagnostic tool for studying nonreactive flow dynamics, provided by back-lit high-speed images. A variable power Newport model 66986 power supply controls a 300 W Xe lamp, which emits light in the near ultraviolet spectrum. This beam is projected through the rear window as a back-light source. Although the beam is not collimated, this back-lighting technique produces sufficient contrast at fluid interfaces. Differences in the refractive index of the jets and the surrounding medium provide the necessary distinction between the fluids of interest. The low temperature, liquid nitrogen inner jet appears as a dark column of fluid as viewed by the high-speed camera placed on the opposite side of the light source.

A Phantom v7.10 high-speed camera is used to visualize the fast dynamical processes inherent to an unforced coaxial jet flow as well as those present during high-frequency acoustic forcing. A 200 mm Nikon MicroNikkor lens is used with a no. 1 close-up lens attachment, giving a spatial resolution of 30 μm per pixel. Image framing rates of 10 kHz or greater are used in order to avoid aliasing up to 5 kHz, which is much greater than the highest forcing frequency used in this study, 2600 Hz. An external trigger from the facility control system is used to start recording the image frames, which are synchronized with all other data using the coordinated universal time (UTC) stamp from an IRIG-B timecode generator.

The reactive imaging set up is designed to capture ultraviolet bands of flame radiation in order to isolate chemiluminescence of excited hydroxyl radicals near a wavelength of 308 nm. An oxygen-hydrogen flame also emits light in the visible spectrum due to photon emission from H_2O radicals, which is blocked using a UV bandpass filter with a center wavelength of 307.2 nm with a FWHM of 11.7 nm and peak transmission of 16.0%. The filter is mounted to a 105 mm Nikon UV-Nikkor lens. After passing through the filter and lens, light is captured using a Lambert Instruments HiCATT image intensifier, and the photocathode of the image intensifier was chosen to have a high quantum efficiency in the UV range. In order to project the intensified light onto the Phantom v7.10 high-speed camera, a relay lens is mounted in between the image intensifier and the camera.

III. Results

Results will be shown that demonstrate the facility capability for both nonreactive and reactive tests at a mean chamber pressure of 400 psia. First, nonreactive tests are performed using liquid nitrogen (LN_2) as the inner jet and gaseous helium (GHe) as the outer jet, which creates a outer-to-inner jet density ratio S similar to an oxygen-hydrogen LRE. The inner and outer jet temperatures are set to be approximately 120 K and 275 K, respectively, which gives S = 0.009. Sample images are shown in Fig. 13 for an unforced jet with an outer-to-inner momentum flux ratio J of 2. Fig. 13 demonstrates many shear-coaxial jet features using a series of snapshots which were acquired at a frame rate of 10 kHz, and a small field of view is added to increase the clarity of structures near the injector exit.

At the exit of the injector, a recirculation zone is easily distinguishable. Moving in the radial direction from the center of the jet, one first observes an interface between the liquid nitrogen inner jet and the recirculation zone formed between the inner and outer jets. This feature is labeled as (1) in Fig. 13. The width of the recirculation zone is equal to the inner post thickness t at the exit of the injector and converges to zero as the recirculation zone extends downstream. The recirculation zone results from a finite inner post thickness, separating near-field stability of this geometry from that of classical co-flowing streams (t=0) commonly used in linear stability theory[18,19].

Advancing farther in the radial direction, an outer shear layer is identified between the gaseous helium outer jet and the surrounding gaseous nitrogen. Although this interface is less distinguishable in analogous LN_2-GN_2 jet experiments[3,4], the LN_2-GHe jet shown in Fig. 13 reveals significant contrast between the light outer jet and the more dense ambient nitrogen ($\rho_c \approx 7\rho_{oj}$). At this interface, an outer shear layer instability is formed. Preliminary analysis of LN_2-GHe jets also indicates unique stability characteristics for the inner and outer shear layers, making this imaging technique particularly valuable when accompanied by image analysis techniques such as proper orthogonal decomposition[11,20] and dynamic mode decomposition[21,23].

Immediately downstream of the recirculation zone, a dynamic interface forms between the inner and outer jets. This interface, labeled as (4) in Fig. 13, is the most important feature of the jet for this particular set of experiments due to its importance in inner jet atomization and mixing. This region may be called the mixing layer or the inner shear layer, and the latter term is used here for continuity with other works. Additionally, the extreme contrast between the liquid inner jet with $\rho_{ij} \approx 500$ kg/m^3 and the light outer jet with $\rho_{oj} \approx 5$ kg/m^3 makes for straightforward image analysis because pixel intensity gradients are most steep at the inner shear layer. Near the recirculation zone, the inner shear layer appears as well-defined interfacial waves. Further downstream, the shear layer thickness increases and these waves develop into vortices.

Regarding coaxial jet behavior in acoustically forced conditions, Figs. 14 and 15 show several image samples for PN and PAN forcing, respectively. Comparing Fig. 14 and Fig. 15 reveals the qualitative differences between forcing a jet located at a PN and PAN, and the value of an experimental facility which can create each condition. A jet located at a PN, when responsive to acoustic forcing, is exposed to a periodic transverse velocity with an amplitude of u'. This caused the jet to take a sinusoidal shape[2,11]. The inner and outer jets are swept to the left during one-half of the acoustic period and then to the right during the remaining half of the acoustic period. A PAN, on the other hand, causes the jet to adopt an axisymmetric instability due to injector pulsation in the outer jet[3,17,23]. Preliminary results show that jets located at a PN are more susceptible to transverse acoustic forcing than jets located at a PAN.

The preliminary results shown in Figs. 13-15 are for $J = 2$, which is also used for preliminary reactive tests to offer a comparison. Reactive tests are performed using liquid oxygen (LO_x) as the inner jet and gaseous hydrogen (GH_2) as the outer jet, with an equivalence ratio φ of 1.36, which is equivalent to a mixture ratio MR of 5.9. As described earlier, a temperature conditioning process is required in order to reach stable, desired inner and outer jet temperatures. To begin a reactive test, this temperature conditioning process is performed using nitrogen as a surrogate in order to conserve propellant.

Fig. 16 shows a time-series plot of a LO_x-GH_2 test which begins after achieving stable temperatures in the inner and outer jet. Remote valves are used to switch from the nitrogen simulant supply to the propellant supply. Due to differences in viscosity, density, and heat conduction constants, alternating between nitrogen simulant flow and propellant flow causes small changes in mass flow rate and temperature. The difference between the process fluid temperature at the injector before and after the species transition was found to be highly dependent on both chamber pressure and mass flow rate. As can be seen by the propellant valve operations in Fig. 16, an oxygen "lead" technique is used at the beginning of the automated test sequence. More than 10 s after the oxygen supply valve is opened, the hydrogen supply valve is opened prior to triggering the ignitor. The time at which each propellant valve is opened is chosen such that each propellant reaches the injector, and thus replaces the nitrogen surrogate, at the desired point in time. Only milliseconds after hydrogen reaches the injector, a torch ignitor is triggered to ignite the propellant mixture. Note that since the chamber pressure is largely determined by a nitrogen chamber pressurization system, propellants are ignited after the chamber is pressurized. To ignite the propellant mixture at elevated pressures, a novel photoignition technique is used, and will be described in subsequent publications. After a burn duration of 6 s, the hydrogen valve is closed first, causing the flame to extinguish.

The test firing represented in Fig. 16 was captured with OH* chemiluminescence imaging, and Fig. 17 includes several image samples acquired near t =19.5 s. These images clearly resolve the evolution of burning structures as they convect downstream. The near-field region produces a non-premixed flame caused by the diffusion of hydrogen and oxygen at the inner shear layer. In the far downstream region, structures may break away from the main body of the flame, as shown in the fourth image of Fig. 17. Of utmost importance in combustion stability studies are the burning structures produced near the exit of the injector, which represent localized pockets of intense OH* chemiluminescence. Although OH* chemiluminsescence has been shown to be proportional to heat release[24], more recent studies highlight sources of inaccuracy when using OH* chemiluminescence to quantify heat release to turbulent flames[25]. Still, Fig. 17 allows one to conclude that unsteady heat release exists, and OH* chemiluminescence such as these may be used to make approximate conclusions regarding flame standoff distance and instability frequencies using image analysis algorithms, for example.

IV. Conclusion

A new facility has been constructed at the Air Force Research Lab at Edwards AFB, CA to experimentally investigate combustion stability for cryogenic propellants at high pressure. A widely variable test matrix may be achieved for nonreactive as well as reactive conditions by utilizing precise control of inner and outer jet temperatures and chamber pressure. Temperatures are controlled with an accuracy of ±1 K in a range spanning from 110 K to room temperature, while the mean chamber pressure is controlled using a secondary chamber

pressurization flow which partially decouples chamber pressure from combustion. A pair of piezoelectric sirens is used to create acoustic pressure oscillations which simulate the pressure oscillations an LRE combustion instability. Proper control of the phase difference and frequency of the sirens allows one to produce transverse standing waves with a pressure node (PN) or pressure antinode (PAN) located at the coaxial jet. The response of a coaxial jet to this environment is studied using high-speed diagnostics in the form of dynamic pressure transducers, backlit imaging, and OH* chemiluminescence imaging. These experimental capabilities, as well as ongoing facility advancements, will allow researchers to fundamentally investigate combustion instabilities in a manner which is comparable to very few other facilities in existence today.

Acknowledgments

Support was provided by the Air Force Office of Scientific Research, project officer Mitat Birkan, and by AFRL Laboratory Revitalization Funds. Significant technical contributions to the design and construction of the facilty are gratefully acknowleged from Randy Harvey, Al Badakhshan, Foster Beasley, Claudia Heflin, John Hasier, Todd Newkirk, Jeff Muss, and Rory Davis. Advanced Mobile Propulsion Test (AMPT) LLC provided significant expertise in the design and implementation of the data acquisition and control system and Sierra Lobo, Inc on the design and construction of the oxygen heat exchanger.

References

[1]Schadow, K., and Gutmark, E., "Combustion instability related to vortex shedding in dump combustors and their passive control," *Progress in Energy and Combustion Science* Vol. 18, No. 2, 1992, pp. 117-132.

[2]Leyva, I.A., Chehroudi, B., and Talley, D., "Dark core analysis of coaxial injectors at sub-, near-, and supercritical pressures in a transverse acoustic field," *43rd AIAA/ASME/SAE/ASEE Joint Propulsion Conference and Exhibit*, Vol. 5, 275–282, 2007-5456.

[3]Leyva, I.A., Rodriguez, J.I., Davis, B.W., and Chehroudi, B., "Preliminary results on coaxial jet spread angles and the effects of variable phase transverse acoustic fields," *46nd AIAA Aerospace Sciences Meeting & Exhibit*, Reno, NV, 2008.

[4]Teshome, S., "Droplet Combustion and Non-Reactive Shear-Coaxial Jets with Transverse Acoustic Excitation," PhD thesis, University of California, Los Angeles, Department of Mechanical and Aerospace Engineering, March 2012.

[5]Hardi, J., "Experimental Investigation of High Frequency Combustion Instability in Cryogenic Oxygen-Hydrogen Rocket Engines," PhD thesis, The University of Adelaide, School of Mechanical Engineering, June 2012.

[6]Hardi, J., Oschwald, M., and Dally, B., "Acoustic characterisation of a rectangular rocket combustor with liquid oxygen and hydrogen propellants," *Proceedings of the Institution of Mechanical Engineers, Part G: Journal of Aerospace Engineering*, Vol. 227, No. 3, 2013, pp. 436–446.

[7]Richecoeur, F., "Experiments and numerical simulations of interactions between transverse acoustic modes and cryogenic flames," PhD thesis, Ecole Centrale Paris, November 2006.

[8]Richecoeur, F., Ducruix, S., Scouflaire, P., and Candel, S., "Effect of temperature fluctuations on high frequency acoustic coupling," *Proc. of the Combustion Institute*, Vol. 32, 2009, 1663–1670.

[9]Mery, Y., Hakim, L., Scouflaire, P., Vingart, L., Ducruix, S., and Candel, S., "Experimental investigation of cryogenic flame dynamics under transverse acoustic modulations," *Comptes Rendus Mecanique*, Vol. 341, 2013, 100–109.

[10]Yu, Y.C., Koeglmeier, S.M., Sisco, J.C., and Anderson, W.E., "Combustion instability of gaseous fuels in a continuously variable resonance chamber (CVRC)," 44th Joint Propulsion Conference and Exhibit, AIAA 2008-4657, 2008.

[11]Teshome, S., Leyva, I.A., and Talley, D.G., "Proper orthogonal decomposition analysis of shear-coaxial injector flows with and without transverse acoustic forcing," *JANNAF Joint Subcommittee Meeting*, Huntsville, AL, 2011.

[12]Hulka, J. and Hutt, J.J., Instability phenomena in liquid oxygen/hydrogen propellant rocket engines. V. Yang and W.E. Anderson, editors, *Progress in Astronautics and Aeronautics: Liquid Rocket Engine Combustion Instability*, pages 39–72. AIAA, 1995.

[13]Woodward, R.D., Pal, S., Farhangi, S., Jensen, G.E., and Santoro, R.J., "LOx/GH2 shear coaxial injector atomization studies: effect of recess and non-concentricity," *45th AIAA Aerospace Sciences Meeting and Exhibit*, pp. 1–22, 2007-571.

[14]Webster, A.G., "Acoustical impedence, and the theory of horns and of the phonograph," *Proceedings of the National Academy of Sciences*, Vol. 5, 1919, pp. 275–282.

[15]Pierce, A. D. *Acoustics: An Introduction to Its Physical Principles and Applications*. Acoustical Society of America, 1991.

[16]Graham, J., Leyva, I.A., Rodriguez, J.I., and Talley, D., "On the effect of a transverse acoustic field on a flush shear coaxial injector," AIAA 2009-5142.

[17]Rodriguez, J.I., Leyva, I.A., Graham, J., and Talley, D., "Mixing Enhancement of Liquid Rocket Engine Injector Flow," AIAA 2009-5143.

[18]Jendoubi, S. and Strykowski, P.J., "Absolute and convective instability of axisymmetric jets with external flow," *Physics of Fluids*, Vol. 6, 1994, 3000–3009.

[19]Yecko, P., Zaleski, S., and Fullana, J.-M., "Viscous modes in two-phase mixing layers," *Physics of Fluids*, Vol. 14, No. 12, 2002, 4115–4122.

[20]Arienti, M. and Soteriou, M.C., "Dynamics of free jets submitted to upstream acoustic modulations," *Physics of Fluids*, Vol. 21, No. 112104, 2009.
[21]Schmid, P.J., "Application of the dynamic mode decomposition to experimental data," *Experiments in Fluids*, Vol. 50, 2011, pp. 1123–1130.
[22]Jovanovic, M.R., Schmid, P.J., and Nichols, J.W., "Low-rank and sparse dynamic mode decomposition," *Center forTurbulence Research, Annual Research Briefs*, 2012, pp. 139–152.
[23]Baillot, F., Blaisot, J.-B., Boisdron, G., and Dumouchel, C., "Behaviour of an airassisted jet submitted to a transverse high-frequency acoustic field," *J. of Fluid Mechanics*, Vol. 640, 2009, pp. 305–342.
[24]Marchese, A.J., Dryer, F.L., Nayagam, V., and Colantino, R.O., "Hydroxyl radical chemiluminescence imaging and the structure of microgravity droplet flames," *Twenty-sixth Symposium (International) on Combustion*, 1996, pp. 1219–1226.
[25]Kojima, J., Ikeda, Y., and Nakajima, T., "Spatially resolved measurement of OH*, CH*, and C*2 chemiluminescence in the reactio zone of laminar methane/air premixed flames," *Proc. Comb. Inst.*, Vol. 28, 2000, pp. 1757–1764.

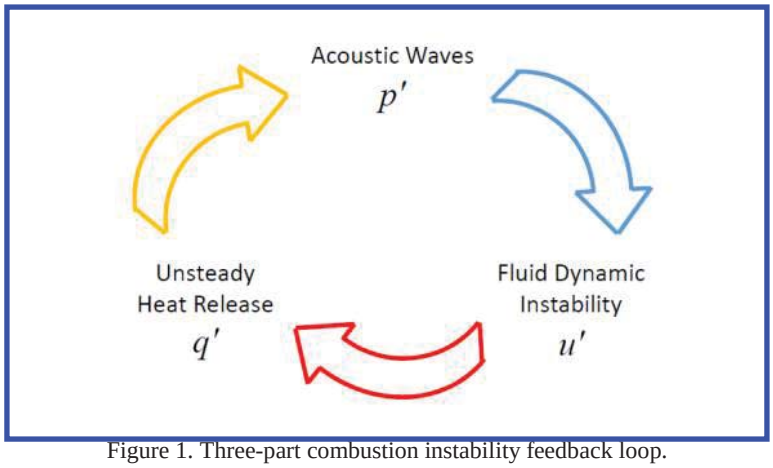

Figure 1. Three-part combustion instability feedback loop.

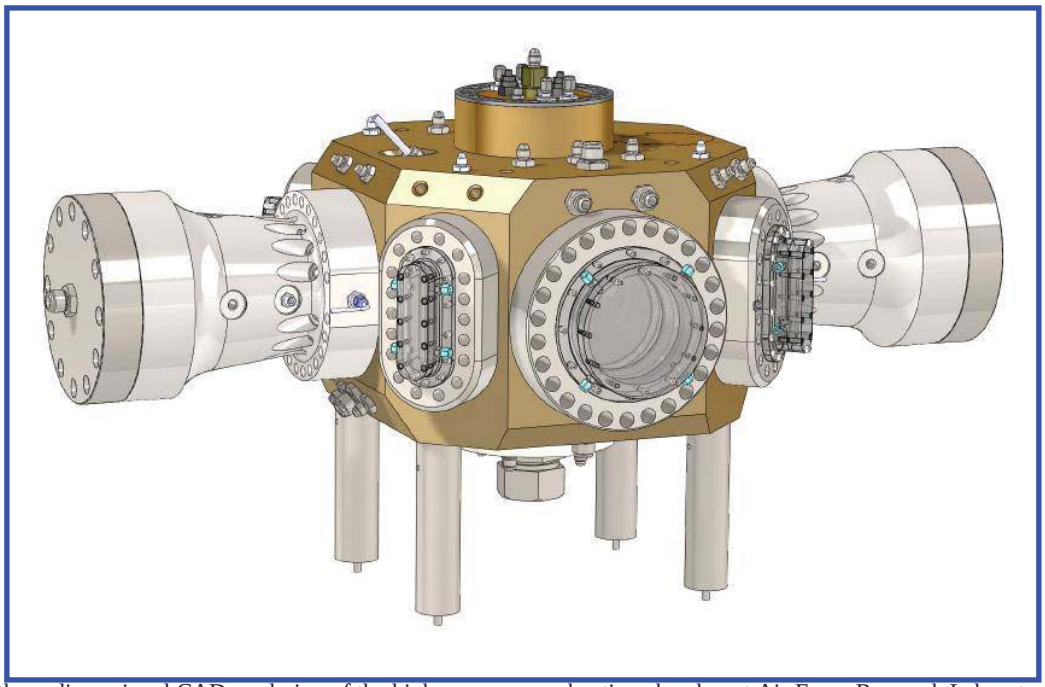
Figure 2. A three-dimensional CAD rendering of the high pressure combustion chamber at Air Force Research Laboratory at Edwards AFB, CA.

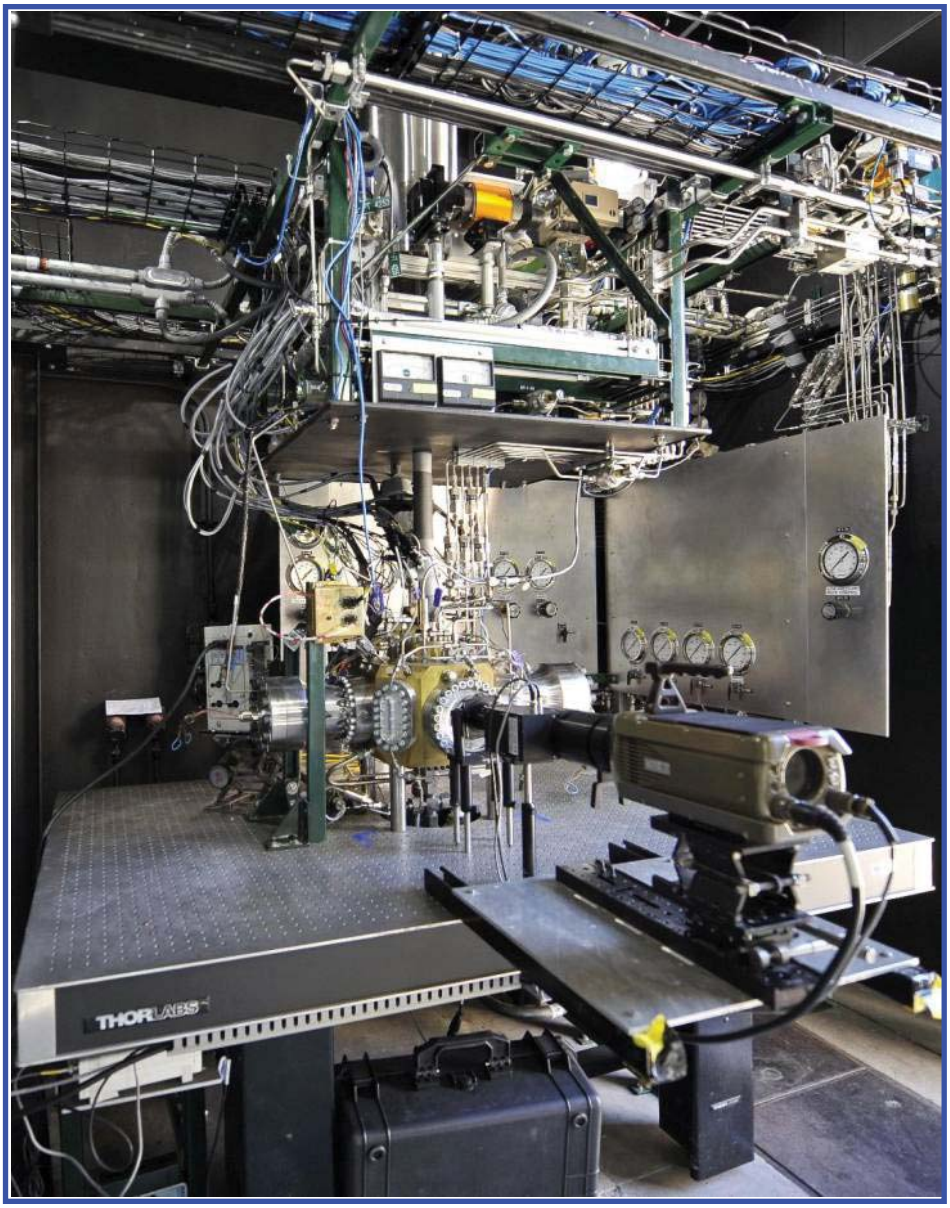

Figure 3. Photograph of the completed apparatus.

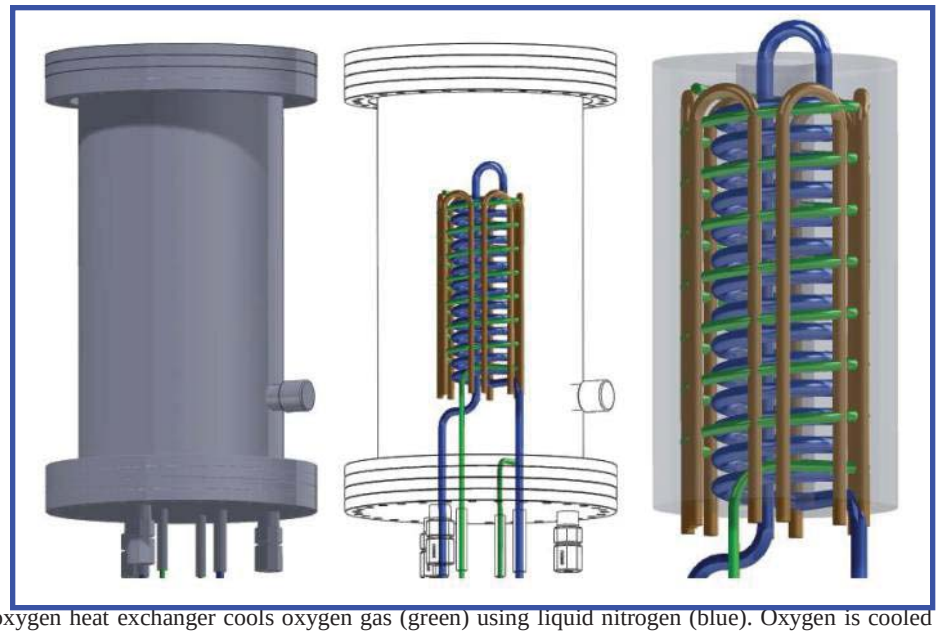

Figure 4. The oxygen heat exchanger cools oxygen gas (green) using liquid nitrogen (blue). Oxygen is cooled below the target temperature and electric heaters (brown) bring oxygen to the target temperature with a control resolution of ±1 K. Insulation is provided by a vacuum jacket (shown in left view, outlined in center view). An aluminum casting surrounds the plumbing assembly (shown in right view, gray).

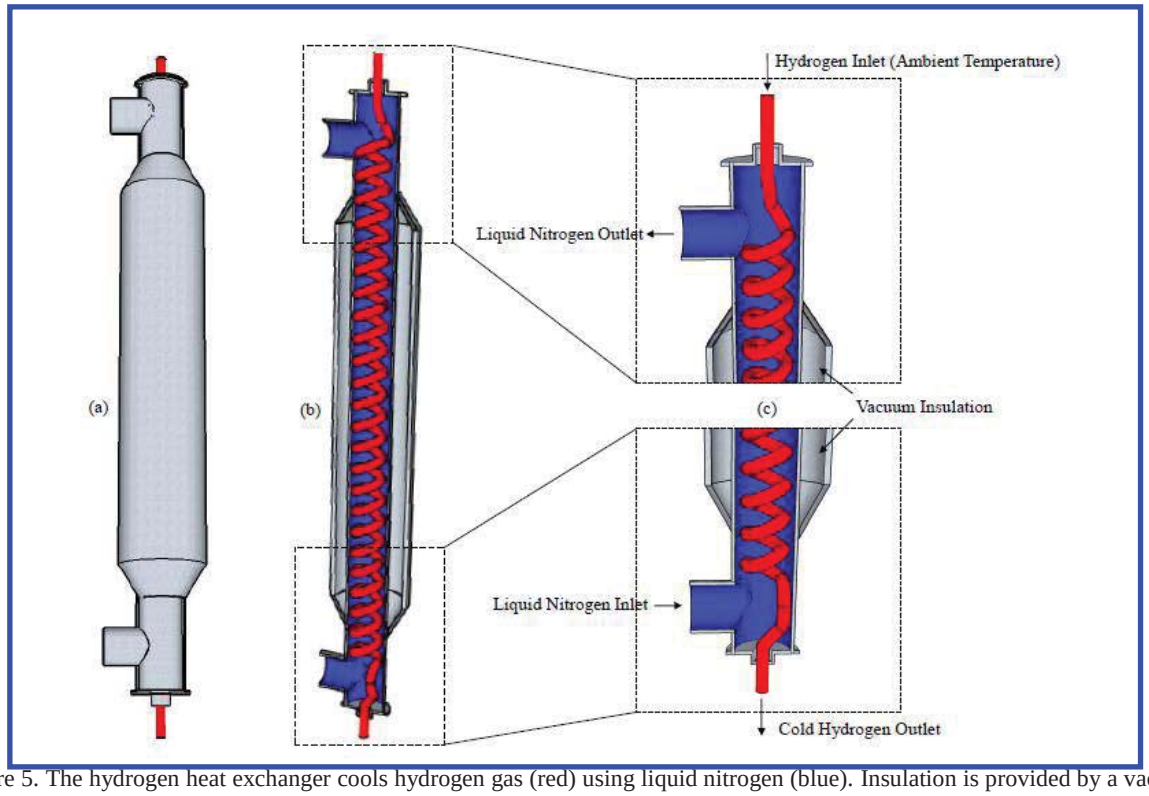

Figure 5. The hydrogen heat exchanger cools hydrogen gas (red) using liquid nitrogen (blue). Insulation is provided by a vacuum jacket.

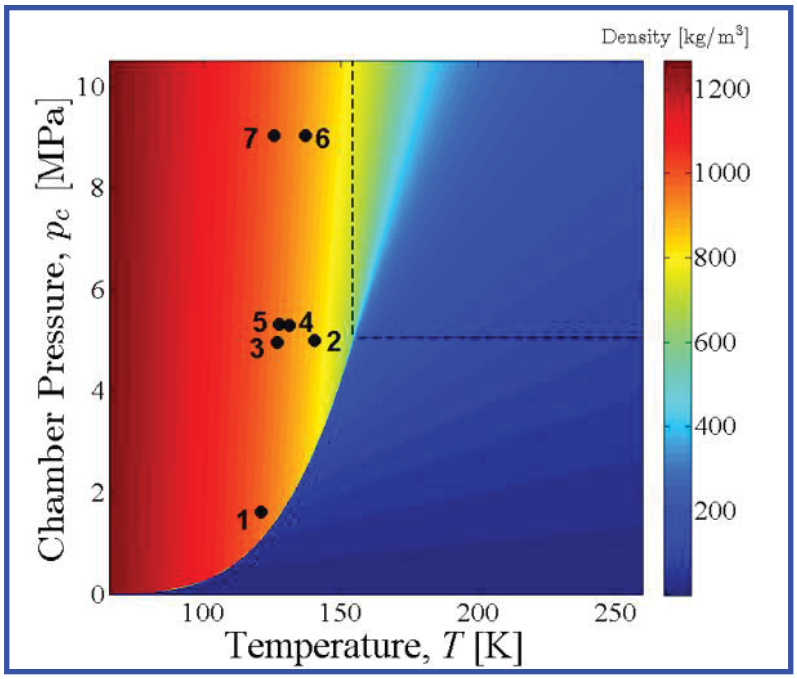

Figure 6. The facility's minimum achievable oxygen temperatures are plotted with an oxygen density contour overlay. Both chamber pressure and mass flow rate are controlled while temperature is measured. (1) 3.7 g/s (2) 2.6 g/s (3) 9.3 g/s (4) 3.0 g/s (5) 11.1 g/s (6) 2.7 g/s (7) 10.4 g/s

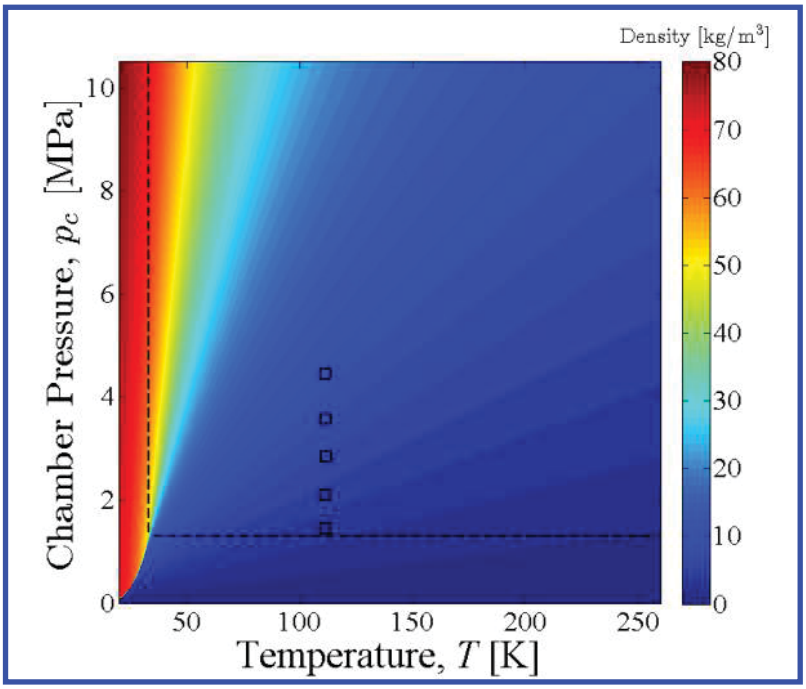

Figure 7. The facility's minimum achievable helium temperatures are plotted with a hydrogen density contour overlay. Helium is used as a surrogate gas, and is representative of minimum hydrogen achievable hydrogen temperatures in the outer jet. The nominal outer jet flow rate is approximately 1.3 g/s.

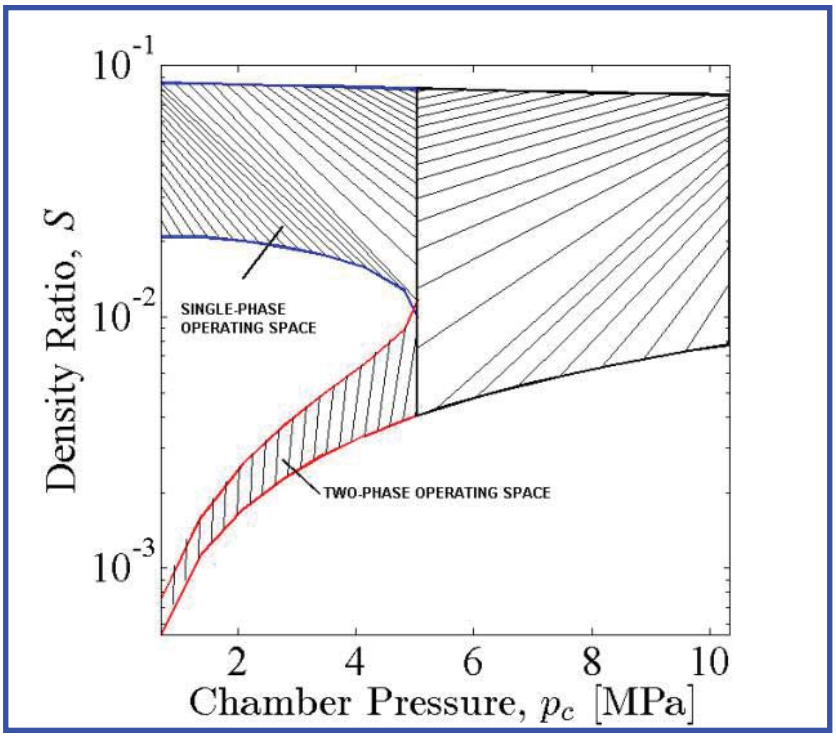

Figure 8. The facility's range of possible density ratios plotted versus chamber pressure.

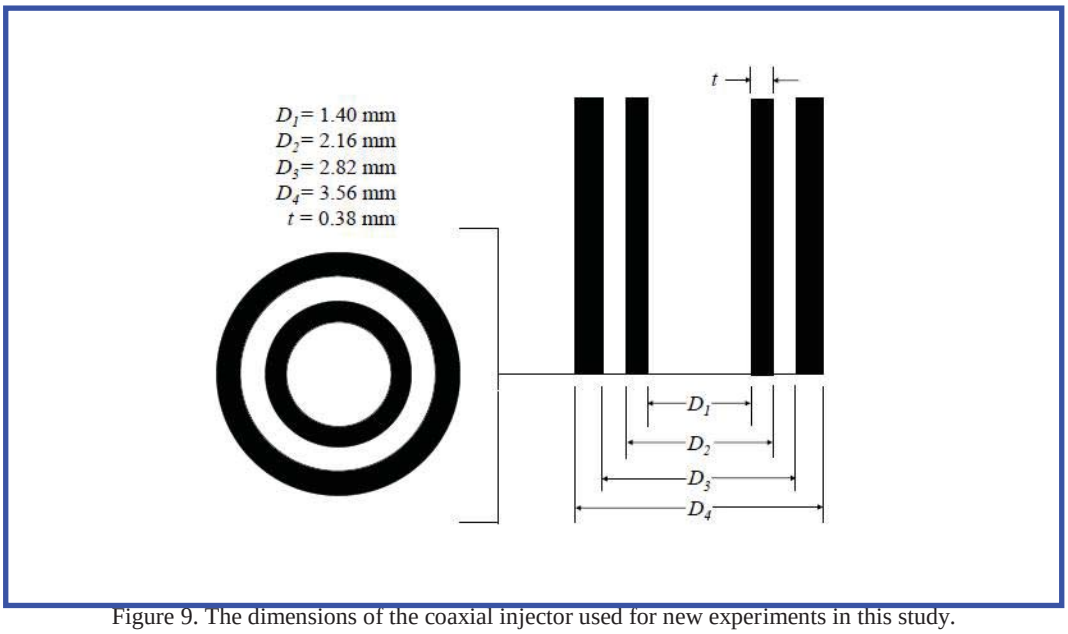

Figure 9. The dimensions of the coaxial injector used for new experiments in this study.

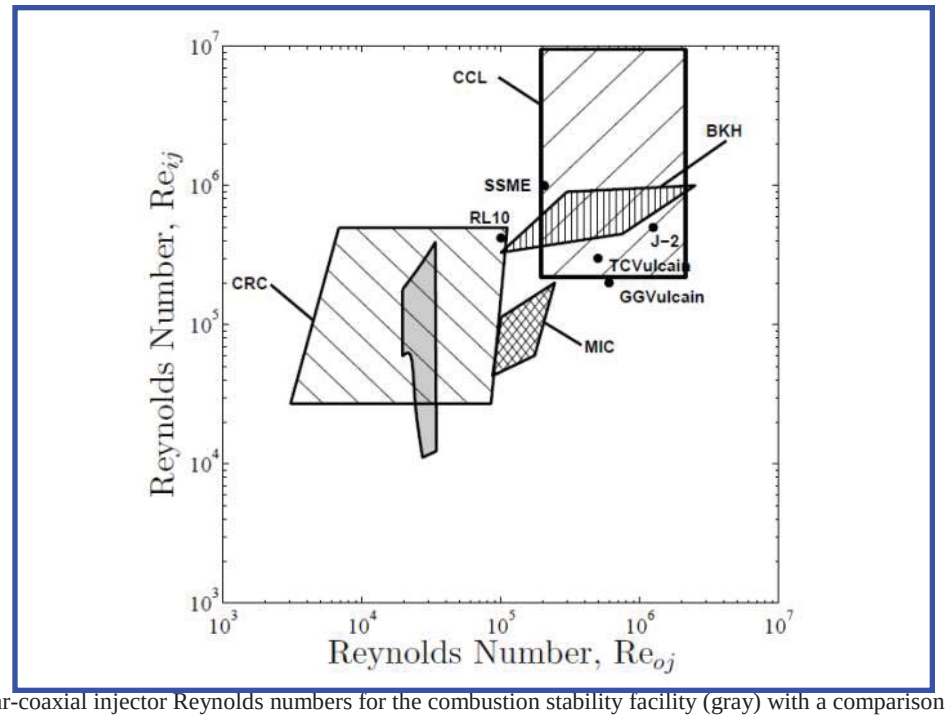

Figure 10. Shear-coaxial injector Reynolds numbers for the combustion stability facility (gray) with a comparison to other experimental facilities and liquid rocket engines with H2-O2 flows. Data is included for the Vulcain Gas Generator (GGVulcain), Vulcain Main Thrust Chamber (TCVulcain), RL10 engine, Space Shuttle Main Engine (SSME), J-2 engine, BKH combustor and Common Research Combustor (CRC) of DLR in Germany, Cryogenic Combustion Laboratory (CCL) of Pennsylvania State Univ., and the Mutli-Injector Combustor (MIC) of ONERA and CNRS in France.

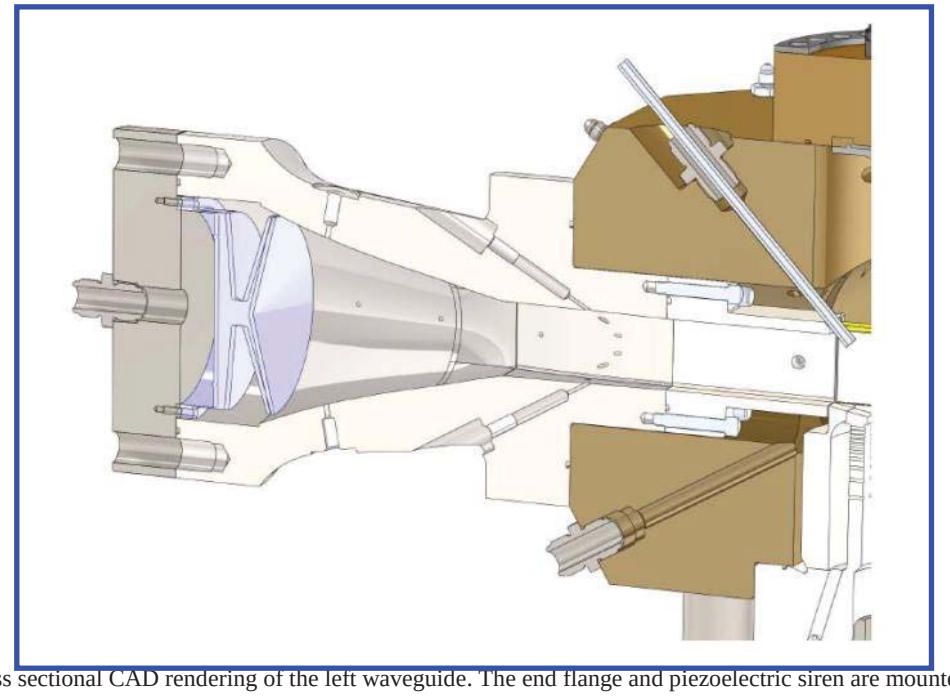

Figure 11. Cross sectional CAD rendering of the left waveguide. The end flange and piezoelectric siren are mounted on the left, and the waveguide assembly is mounted to the brass outer chamber on the right. The ignitor barrel enters through a diagonal port in the top left corner of the outer chamber wall.

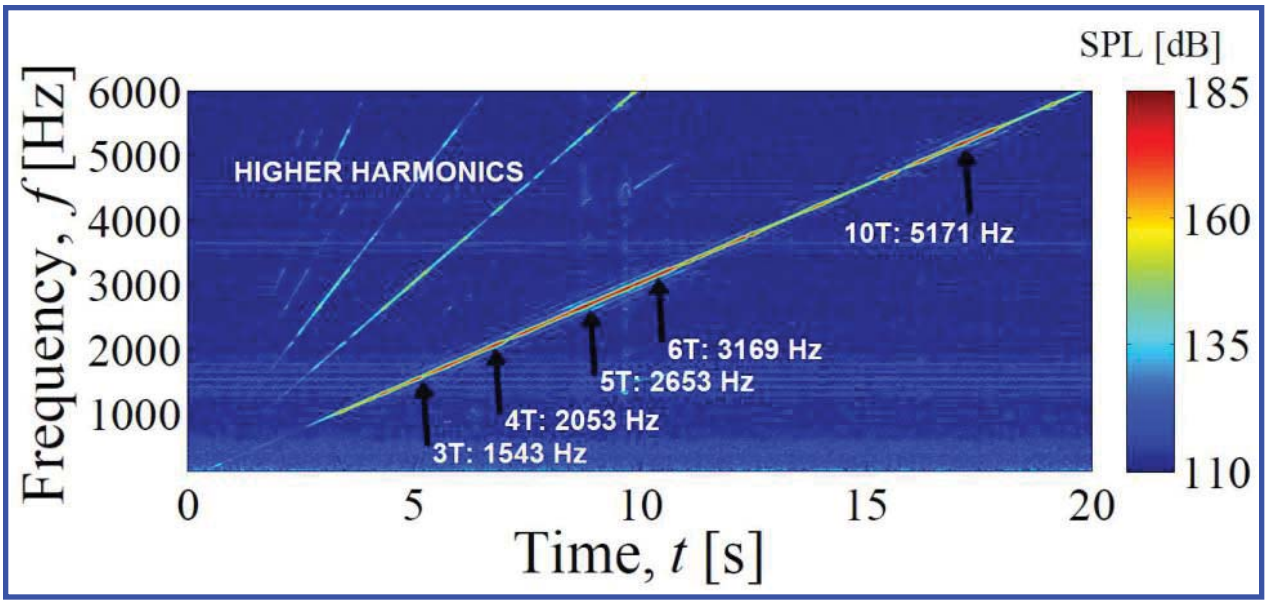

Figure 12. Acoustic pressure spectra results for a PAN condition measured using a pressure transducer in the center of the chamber. Magnitude is scaled with a sound pressure level (SPL) colormap, and key regions of transverse resonance are annotated. 1T, 2T, 7T, 8T, and 9T modes do not create appreciable pressure amplitudes, because these frequencies are outside of the useable frequency bands of the acoustic siresn. This study seeks to use one-dimensional, transverse waves only. Longitudinal modes and longitudinal-transverse mixed modes are ignored in this plot. p_c=400 psia = 2.76 MPa

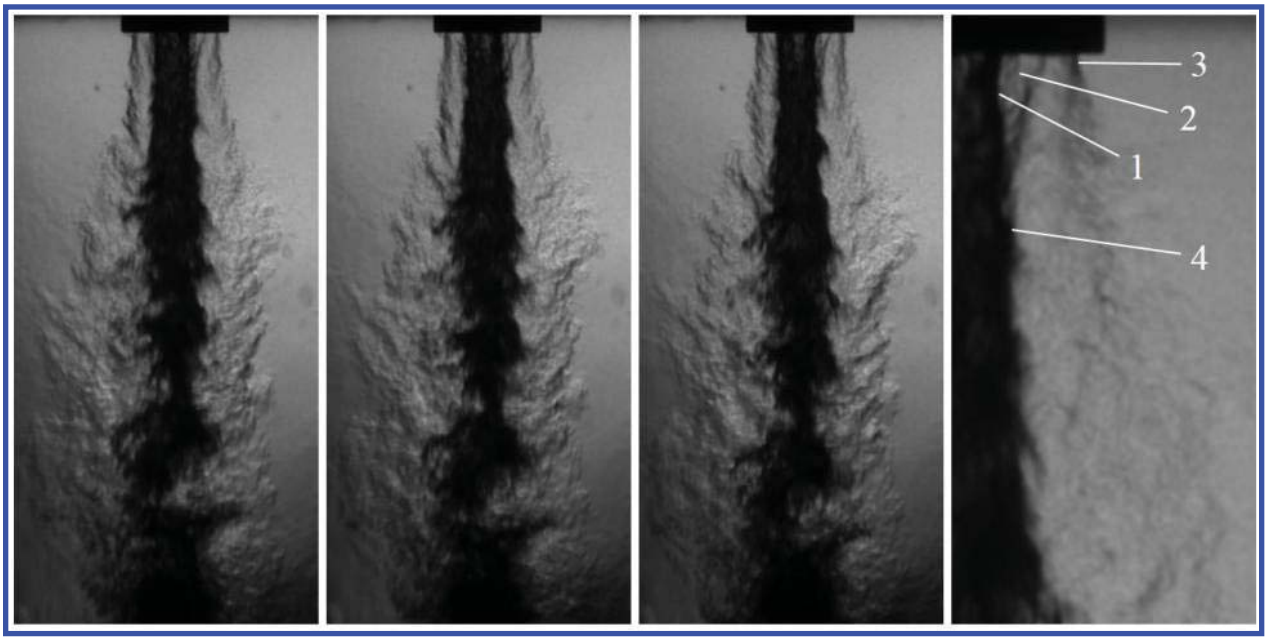

Figure 13. Liquid nitrogen-gaseous helium shear-coaxial jets without acoustic forcing. Three consecutive images are taken from a set of high speed images acquired at 10 kHz. A fourth image is shown with a reduced field of view to show the (1) interface between the inner jet and recirculation zone (2) recirculation zone (3) outer shear layer and (4) inner shear layer.
J = 2, p_c = 400 psia = 2.76 MPa

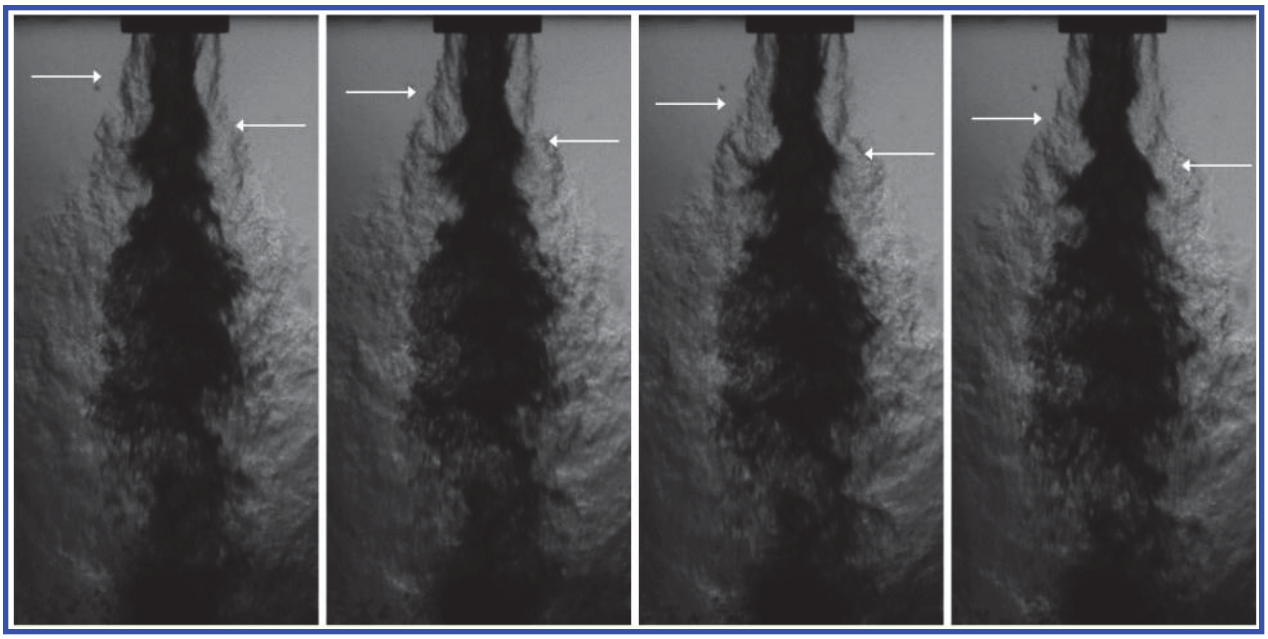

Figure 14. Liquid nitrogen-gaseous helium shear-coaxial jets exposed to external, transverse acoustic forcing at a pressure node. Four consecutive images are taken from a set of high speed images acquired at 10 kHz. An antisymmetric instability forms as periodic spanwise motions caused by the acoustic velocity perturbation u'. $J = 2$, $p_c = 400$ psia = 2.76 MPa, $f_F = 1700$ Hz, $u' = 0.43$ m/s

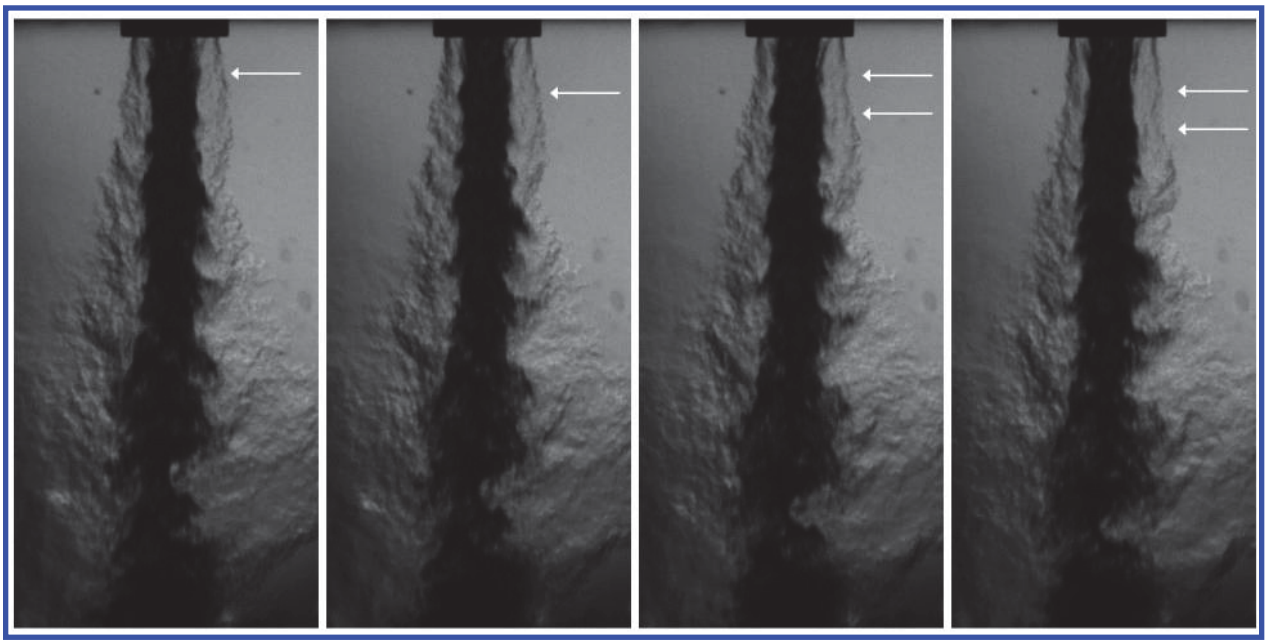

Figure 15. Liquid nitrogen-gaseous helium shear-coaxial jets exposed to external, transverse acoustic forcing at a pressure antinode. Four consecutive images are taken from a set of high speed images acquired at 10 kHz. An axisymmetric instability forms due to outer jet flow pulsations caused by the acoustic pressure perturbation p'. $J = 2$, $p_c = 400$ psia = 2.76 MPa, $f_F = 1700$ Hz, $p' = 1.53$ psi

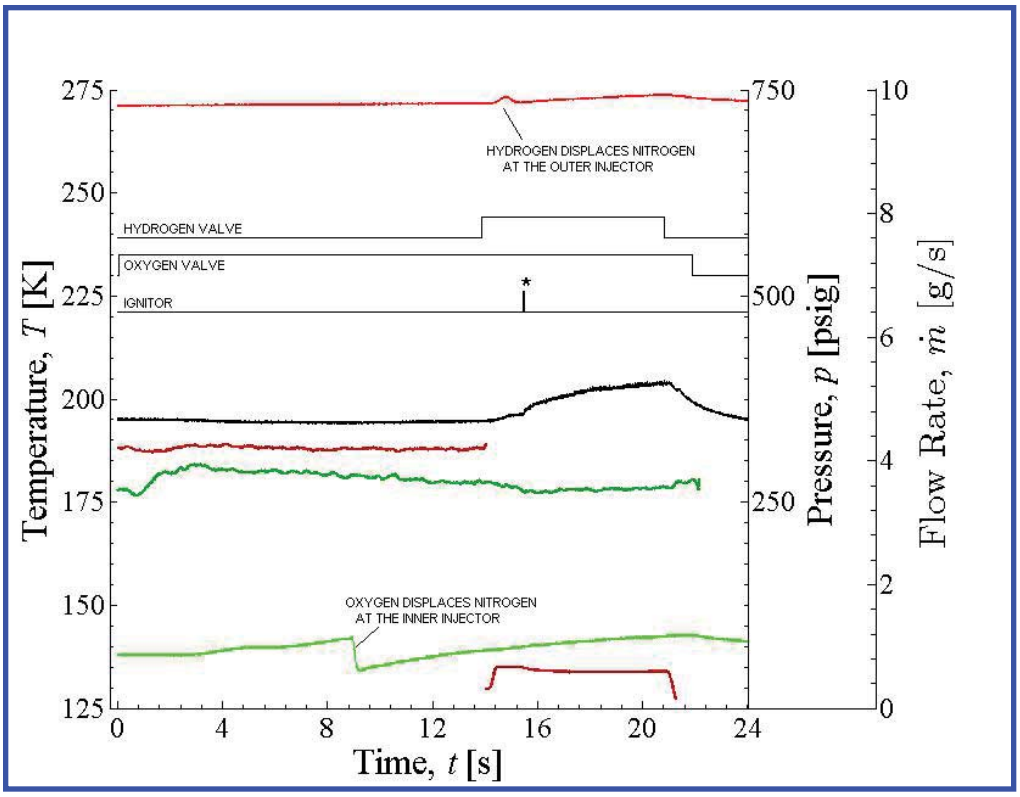

Figure 16. Time series plot of a typical reactive test using oxygen as the inner jet and hydrogen as the outer jet. The transition from a nitrogen simulant to the propellant occurs after the propellant valve is opened. A step change in outer jet mass flow rate occurs near t = 14 s, where nitrogen flow rate of approximately 4.2 g/s changes to a hydrogen mass flow rate of 0.65 g/s (dark red). The inner jet mass flow rate shows a species change near t = 1s, where a nitrogen flow rate of 3.6 g/s is overtaken by an oxygen mass flow rate of approximately 3.9 g/s. Inner jet temperature (light green), outer jet temperature (light red), and chamber pressure (black) are also shown. MR = 5.9 (φ=1.36), J = 2

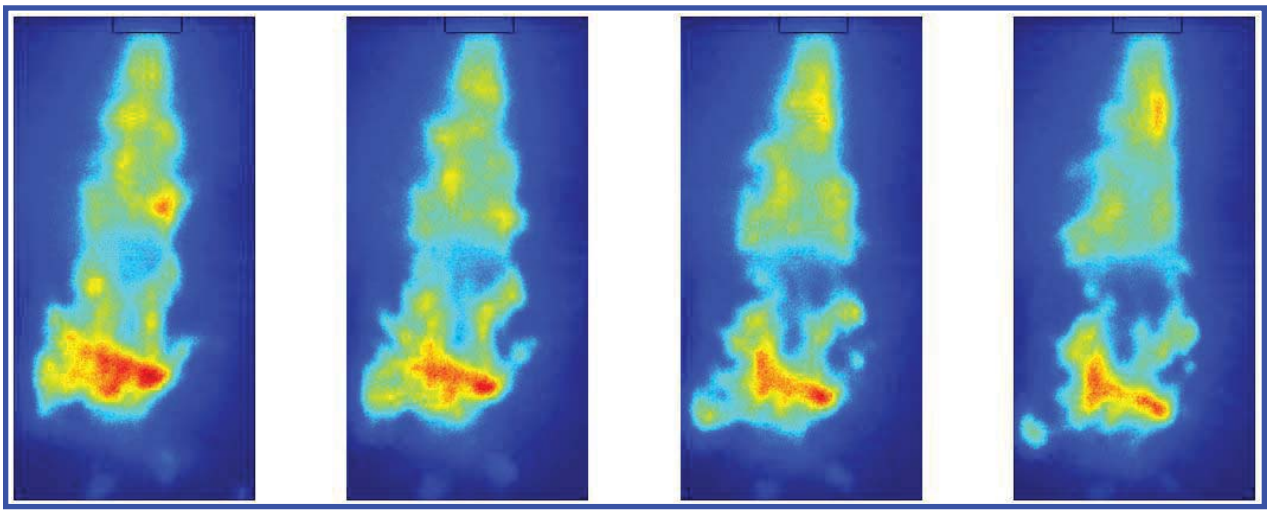

Figure 17. Liquid oxygen-gaseous hydrogen shear-coaxial jet flames without acoustic forcing. Four consecutive images are taken from a set of high speed images acquired at 16 kHz. The intensifier gate duration, which is essentially the camera exposure time, is set to 61 μs. Flame structures form near the injector exit and evolve as they travel downstream.
MR = 5.9, J = 2, $p_c \approx$ 400 psia = 2.76 MPa

Receptivity of a Cryogenic Coaxial Liquid Jet to Acoustic Disturbances

J. L. Wegener
Department of Mechanical Engineering
University of California at Los Angeles
Los Angeles, CA 90095 USA

D. J. Forliti*
Sierra Lobo, Inc.
Edwards AFB, CA 93524 USA

I.A. Leyva
AFRL/RQRE
Edwards AFB, CA 93524 USA

and
D.G. Talley
AFRL/RQRC
Edwards AFB, CA 93524 USA

Abstract

The receptivity of cryogenic coaxial gas-liquid jet flows to transverse acoustic disturbances has been explored experimentally. Liquid nitrogen in the inner jet and cooled helium in the outer annular jet were used to simulate an oxygen/hydrogen liquid rocket engine injector. The flow is submerged in a chamber that experiences a transverse acoustic resonance. The shear coaxial jet is exposed to a variety of acoustic conditions including different frequencies, amplitudes, and locations within the resonant mode shape. High-speed back-lit images were captured to record the behavior of the natural (unforced) and forced coaxial jets. Proper orthogonal decomposition and spectral analysis were used to extract natural and forced modes. Convective modes are extracted, and a new Strouhal number is used to characterize the strongest natural convective mode that is analogous to the preferred mode in free jets. The threshold of receptivity was found for a number of different injector flows and acoustic forcing conditions. The results indicate that the dimensionless frequency plays an important role, and there exists a finite forcing amplitude at which the threshold of receptivity occurs. The receptivity threshold provides useful insight on the suitability of a given injector design for specific rocket combustion chamber conditions.

*Corresponding author: david.forliti.ctr@us.af.mil

Approved for public release; distribution unlimited
PA case number 14132

Introduction

Combustion instability remains one of the key challenges in the development of robust and high-performance propulsion and energy systems. In liquid rocket engines (LREs), combustion instability can lead to degraded performance, severe wear, and catastrophic damage to the propulsion system. Unfortunately, combustion instability phenomena are not sufficiently understood to allow solution at the design stage. Thus full-scale testing and potentially multiple design cycle iterations may be required to satisfy the stability requirements. The development of high-fidelity design tools offers much promise in this regard, although data under a variety of relevant conditions are still needed to validate emerging computational tools.

The Air Force Research Laboratory (AFRL) at Edwards AFB has investigated the mixing properties of cryogenic single and coaxial jets under both sub- and supercritical thermodynamic pressure operating conditions.[1-3] These flows have also been exposed to a range of transverse acoustic forcing conditions.[4-6] A new experimental facility for reacting coaxial jet flows has been developed and is described in detail by Wegener et al.[7] The present paper describes nonreacting data that was collected with this new facility. Although a large quantity of data has been collected in the past for nonreacting conditions, the current effort considers a new framework for characterizing the forcing response of coaxial jets. Past studies have generally placed emphasis on investigating different injector conditions, including injector geometry, momentum flux ratio, and chamber pressure. The current study focuses on a single injector geometry in a two-phase (i.e. subcritical) regime, and focuses on the role of forcing frequency and amplitude.

Background

Single and coaxial jets at high Reynolds number are known to be spectrally broadband. Near the nozzle exit, shear layer instabilities and turbulent initial conditions will in general develop high-frequency oscillations. As the shear layers grow with increasing downstream distance, the spectra shifts to lower frequency.[8] Further downstream, the shear layers have grown to a point where a merger occurs, and typically the most intense fluctuations are encountered in this region. In single free jets, the fluctuations at the shear layer merging location, also referred to as the end of the potential core, are of global relevance and these fluctuations are referred to as the jet preferred mode.[8-11] Crow and Champagne conducted a classic study on forced free jets, and observed that the flow response was highly sensitive to the forcing frequency relative to the preferred mode frequency. More recently, Birbaud et al.[12] conducted a flow control study of a single free jet and considered the dependency of the forcing frequency relative to two characteristic frequencies; the initial high frequency associated with the initial shear layer and the low frequency preferred mode associated with the fluctuations at the end of the potential core. Having one (or more) characteristic frequency provides a useful reference in which to examine the effects of forcing, as different relative frequencies will influence the jet/shear layer structure through different mechanisms.

The coaxial jet contains more spatial and spectral complexity than the single jet, due to the presence of additional length and velocity scales. Figure 1(a)

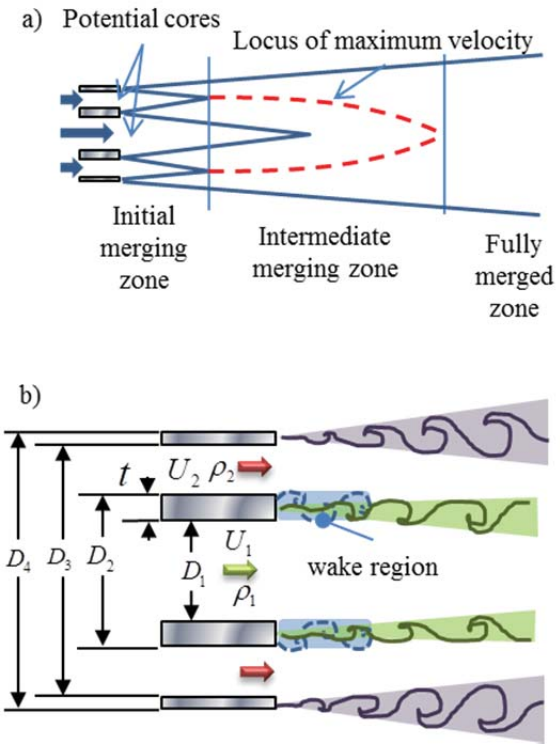

Figure 1. The a) global and b) near-field features of the coaxial jet.

shows the spatial development of the coaxial jet as described by Ko and Kwan.[13] There are a number of fluctuation sources including multiple shear layers and potential core zones. A schematic of the near-field region is shown in Fig. 1(b). The injector geometry is characterized by a set of diameters that can be non-dimensionalized to form two parameters, the area ratio *AR* and dimensionless post thickness t/D_1. Several near-field instabilities may be present, including an inner and outer shear layer, and a potential wake instability associated with the flow downstream of the inner post. The inner shear layer and wake modes overlap and thus these instabilities compete with one another. The acoustic disturbances are likely to couple with the

flow field in the near-field region where the flow is most unstable and sensitive to perturbations.

The coaxial jet flow is dependent on a large number of dimensionless groups. As mentioned above, the geometry can be characterized by the outer-to-inner area ratio *AR*, and the normalized post thickness t/D_1. There are two Reynolds numbers, one for the inner and outer flow. The momentum flux ratio *J*, defined outer to inner, is generally considered the primary independent parameter of the coaxial jet. Each of the two flows have characteristic velocities and densities, allowing the ability to define the velocity and density ratio across each shear layer. The shear flow is also very sensitive to the injector exit conditions, including profiles of mean and fluctuating velocity, and spectral characteristics of turbulence or other background disturbances. If the two streams differ in phase, then the Weber number is also a parameter of importance.

The behavior of the acoustically-excited coaxial jet will depend on all of the parameters mentioned above, in addition to the characteristic scales of the forcing conditions. The forcing can be characterized by the forcing frequency and amplitude; the amplitude may be measured by the magnitude of the pressure and/or velocity fluctuations. The interaction mechanisms differ when the coaxial jet is placed in a fluctuating pressure environment versus a fluctuating velocity environment. Thus the response of a given coaxial jet flow to acoustic perturbations will depend on the relative frequency, relative amplitude, and location within the acoustic resonance mode shape.

The purpose of the current study was to explore the receptivity of cryogenic two-phase coaxial jets to acoustic disturbances in the form of a transverse resonance; a flow is considered to be receptive to perturbations if detectable changes occur in the flow field. This study considered new parameters, the normalized frequency and amplitude. The conditions at which forcing dominates the natural coaxial jet behavior was documented.

Experimental Facility

The experiments were conducted in the Combustion Stability Lab at the Air Force Research Laboratory (AFRL) at Edwards Air Force base. A new facility, capable of high-pressure reacting flows, was used in the current study. Figure 2 shows both a schematic and three-dimensional rendering of the test chamber. Two acoustic sources, piezo sirens from Piezo Systems, Inc., are located symmetrically offset from the injector region. Waveguides shown in Fig. 2(a) are used to excite transverse resonances within the chamber. The acoustic frequency and amplitude are controlled via a signal generator/amplifier combination that drives the sirens. The sirens operate either in phase or with 180° shift to generate the pressure antinode (PAN) and pressure node (PN), respectively; the pressure node case is associated with an acoustic velocity antinode, but will be referred to as pressure node.

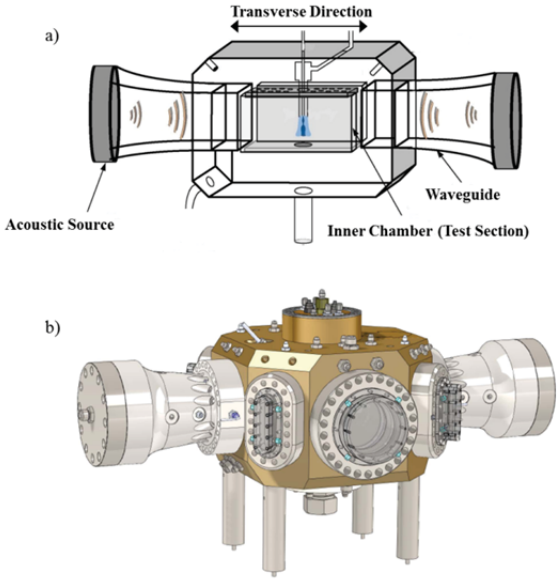

Figure 2. a) Conceptual and b) schematic of the Combustion Stability Lab experimental facility.

The chamber is divided into inner and outer chambers that are not sealed relative to one another. A high flow of gaseous nitrogen in the outer chamber is used to cool the combustion products under combustion conditions, and the combined flow is choked through an exit orifice. The gaseous nitrogen flow is used to set the chamber pressure. The facility is equipped with heat exchangers to allow cooling of the inner and outer injector flows. Further details on the experimental facility can be found in Wegener et al.[7]

A single coaxial jet injector was used for the experiments. The dimensions of the injector are summarized in Table 1. The outer-to-inner area ratio *AR* is

Parameter	Value (mm)
D_1	1.40
D_2	2.16
D_3	2.82
D_4	1.68

Table 1. Geometry of the injector.

1.68 and the dimensionless post thickness t/D_1 is 0.27; both parameters are within the lower range of previous studies at AFRL.[5, 6] The injector flow passages are sufficiently long to ensure fully-developed turbulent flow at the exit of the injector. Similar to previous work, the inner jet is liquid nitrogen. The outer jet in

the current study is cooled helium. The use of helium allows for a closer match to the density ratio as would occur for oxygen/hydrogen operation in a cryogenic rocket engine. The chamber pressure was 2.8 MPa (400 psi) for all experiments. Further details on the experimental conditions are given in Table 2.

Parameter	Values
T of inner jet (N_2)	~ 120 K
T of outer jet (He)	~ 275 K
J	2, 6
Re_1	~ 1.5×10^4
Re_2	~ 1.0×10^4
We	>100

Table 2. Injector operating parameters.

As shown in the table, two momentum flux ratios were considered. Due to the unique combination of fluids and conditions, surface tension values are not available to the authors' knowledge. Based on the visualizations shown later and the results of Farago and Chigier[14], the current experiments appear to be in the fiber-type regime and the Weber number is expected to be approximately 100 or higher.

The primary diagnostic of the coaxial jet involves high-speed backlit imaging. A Phantom v7.10 camera was used to capture images at 10 kHz. The acoustic resonance is characterized through several high-speed Kulite pressure sensors flush mounted in the test section area including the waveguides. A pressure sensor located in the center of the test section and coincident with the axis of the coaxial jet is used to measure the peak pressure fluctuation for the PAN cases. For the PN operation, the peak pressure fluctuation is estimated from measurements at off-node locations using an assumed mode shape, and the maximum acoustic velocity magnitude is estimated from the linear acoustics equation,

$$u' = \frac{p'}{\rho_c c} \tag{1}$$

where u' is the magnitude of the velocity fluctuation in the velocity antinode region, p' is the magnitude of the pressure fluctuation in the pressure antinode region, ρ_c is the density of the ambient gas in the chamber, which is nominal room temperature nitrogen, and c is the speed of sound. The injector flow species and temperatures will definitely alter the properties of the acoustic resonance, thus Eq. 1 is an approximation. The acoustic sirens were used to drive a transverse acoustic resonance ranging from the 3rd to 7th mode. See Wegener et al. for more details on the acoustic characteristics.[7]

Results

The first phase of the research was focused on understanding the properties of the unforced coaxial jets.

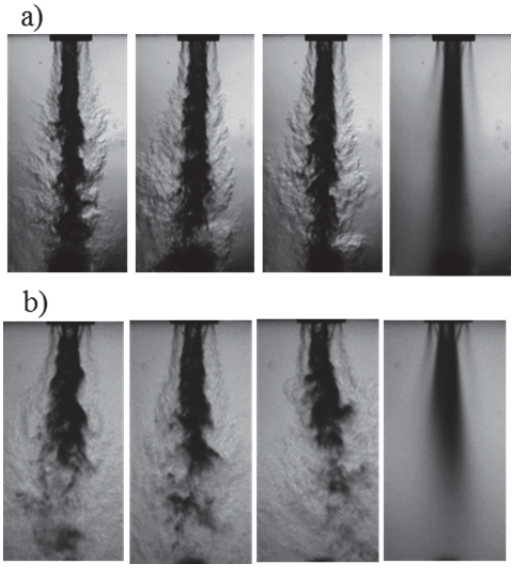

Figure 3. Instantaneous and mean backlit images of the coaxial jet for momentum flux ratio J of a) two and b) six.

Figure 3 shows instantaneous and mean images of the cryogenic coaxial jets at the two momentum flux ratios J of two and six. Although there are frequencies present in both the inner and outer shear layer, the strong contrast between the liquid inner flow and gaseous outer flow dominates the images. One can see some structure within the inner shear layer, although the turbulent inflow conditions result in a highly disturbed interface between the liquid and gas. As expected, the higher momentum flux ratio case has a shorter dark core length.[3] The triangular feature near the injector exit, more readily seen in the $J = 6$ case, is the recirculation zone downstream of the inner tube post. Some asymmetries are also apparent and are caused by manufacturing tolerances and the small scale of the injector components. Separate analyses of each side of the injector indicate similar spectra content (see Wegener[15] for details). It is thus expected that the general trends of the current results are representative of the symmetric case, although this will be validated in future studies.

As mentioned earlier, there is a need to identify the preferred mode of the coaxial jet. A frequency scaling variable, the Strouhal number, may be developed for use in a preferred mode scaling law. There are a number of choices available in defining the length and velocity scale for the Strouhal number. The length scale is a relatively straightforward choice of jet diameter as used for the single jet. In the case of a coaxial jet with

finite (or large) post thickness t/D_1, previous studies show, at least for moderate to high J, that the shear layer will more or less be centered near the middle of the post.[6] Thus the average of D_1 and D_2 are used as the length scale. Further data would need to be considered for different geometries to find the length scale that provides the best collapse across different injector designs.

The velocity scale is more subjective. For the free jet, the convention is to use the mean jet exit velocity. Guidance for an alternative choice is provided through studies of shear layers. Huerre and Monkewitz conducted a linear stability study of variable velocity ratio shear layers.[16] They found that the most unstable frequencies nominally collapse on a single value when the frequency is normalized by the mean velocity of the two streams. For variable density shear layers, the frequency of the most unstable mode will more likely scale with the convection velocity. Thus the convection velocity is proposed as an appropriate velocity scale.

The convection velocity of the coherent structures in a shear layer may be estimated in a variety of ways. Linear stability analysis may be used, for instance. Dimotakis developed a model for the spreading rate of planar shear layers, and included in the model development is an estimate of the convection velocity based on freestream conditions [17]. The model uses the assumption that in the reference frame of the shear layer structure, the dynamic pressure of the two freestreams is equal. This leads to a form of the convection velocity of

$$U_{c,\,Dimotakis} = \frac{\rho_1^{1/2} U_1^2 + \rho_2^{1/2} U_2^{1/2}}{\rho_1^{1/2} + \rho_2^{1/2}}, \qquad (2)$$

where ρ and U are the density and velocity of the freestreams. It should be mentioned that this expression was defined for single-phase shear layers.

In order to evaluate the validity of the Dimotakis model, the convection velocity is directly measured from the time-resolved images. Figure 4(a) shows the mean image for the $J = 6$ case. A line along the middle of the inner shear layer is defined through user input, and the intensities of these pixels are plotted as a function of time as shown in Fig. 4(b). As inner fluid structures convect along this trajectory, they trace diagonal lines in the s/D_1 versus time domain. This technique has been used in the past to visualize organized motion in jets.[18] The slope of the diagonal line represents the mean convection velocity; s is the distance along the shear layer ray. Ten samples are extracted and the mean convection velocity determined. The change in slope near s/D_1 of unity is coincident with the end of the triangular recirculation zone associated with the post wall thickness. As expected, the convection velocity increases downstream of the recirculation zone due to the presence of the high-speed coflow of the outer jet fluid; the outer-to-inner velocity ratio for this case is 25. This convection velocity analysis was conducted

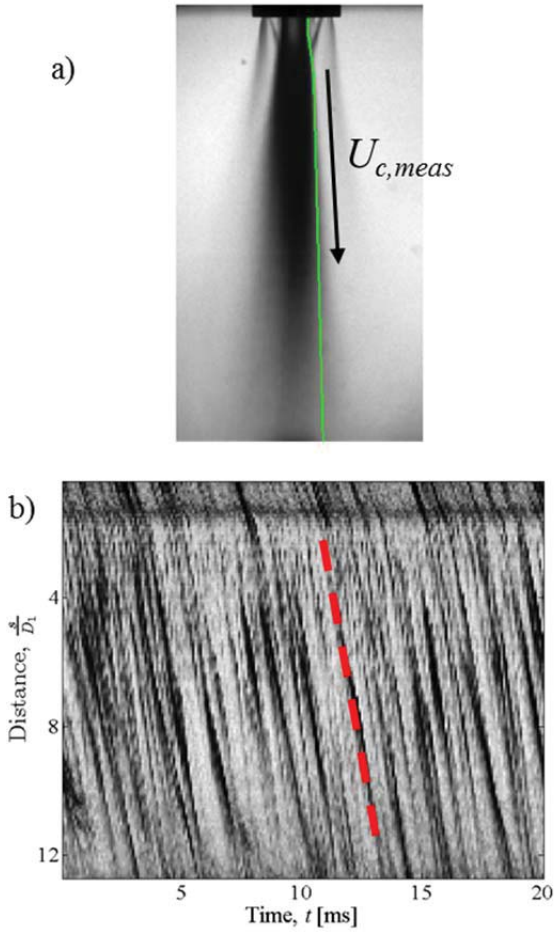

Figure 4. The (a) piecewise linear domain used to construct the (b) axial versus time maps for evaluating the convection velocity.

for several sets of data for the two momentum flux ratios and for two flow rates.

Figure 5 shows predicted versus measured convection velocities for the two momentum flux ratios. Data was collected for nominal and a higher flow rate for both momentum flux ratios. The conditions for the two momentum flux ratios were selected to keep the convection velocity predicted using Eq. 2 fixed, hence the overlap of points for both momentum flux ratios. The agreement is quite good, indicating that the Dimotakis model may be employed for the current flow conditions. A deviation is observed at higher flow rates (high convection velocities) and is likely due to heat transfer within the injector. Measurement of temperature upstream of the injector is used to evaluate density,

thus errors in temperature will result in errors in densi-

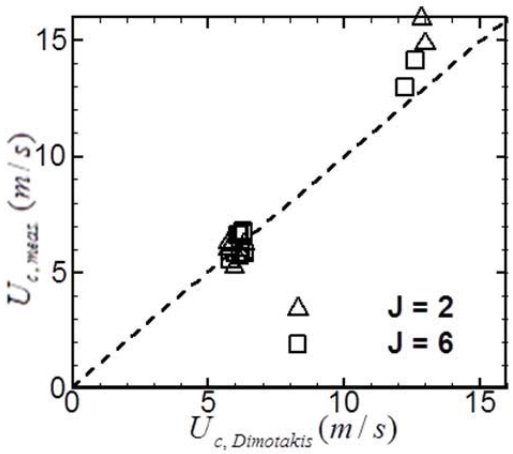

Figure 5. Measured versus predicted convection velocity.

ty. The velocity is estimated using the calculated density and the measured flow rate, thus creating further error due to temperature uncertainty. The subsequent measurements were all done at the lower flow rate associated with a convection velocity near 6 m/s.

In order to calculate the Strouhal number, the natural frequency of the jet must be extracted from the data. As would be expected for a spreading shear flow, the spectra depend on axial position. The global frequency of the jet is evaluated using the proper orthogonal decomposition (POD) of the image data. This approach places more emphasis on the larger-scale organized motions which make higher contributions to the total variance of the data. The POD is calculated for an image that spans an axial distance of approximately $12D_1$. The POD is calculated using singular value decomposition (SVD), the details of which can be found in Wegener.[15] The POD is applied to sets of 2000 images.

The application of POD to 2000 images yield the same number of variance-contributing modes, thus the POD spectrum is inherently broadband, especially for highly-turbulent flows of the type in the present study. Thus a criteria must be defined for extracting important dynamics from the POD results. Arienti and Soteriou provide a criteria for identifying convective modes from POD data.[19] First the POD spectrum, meaning the eigenvalues as a function of mode number, is constructed and pairs of modes with similar eigenvalues are sought. Once a candidate mode pair is identified, the cross-power spectral density (CPSD) and phase difference is calculated between the temporal coefficients of the mode pair. Once this has been done, the mode pair can be determined to be representing a convecting mode if:

1. the peak in the CPSD is coincident with a region of ± 90° phase shift;
2. the spatial distribution of the POD eigenfunctions are similar with features that are shifted nominally half a wavelength in the convection direction.

If a mode pair satisfied these conditions, a convective dynamic mode has been identified and the frequency of the particular convective mode is associated with the peak in the CPSD. In this study, the preferred mode is associated with the convective mode having the most energetic POD mode pair (i.e. has the highest eigenvalues). The singular values from the SVD process are used to evaluate the variance, as the singular values are equal to the square root of the eigenvalues. It is likely that multiple convective modes are present in the unforced cases of the present study. Other convective modes with lower singular values are not considered as representing preferred modes.

Figure 6(a) shows an example of a POD spectrum

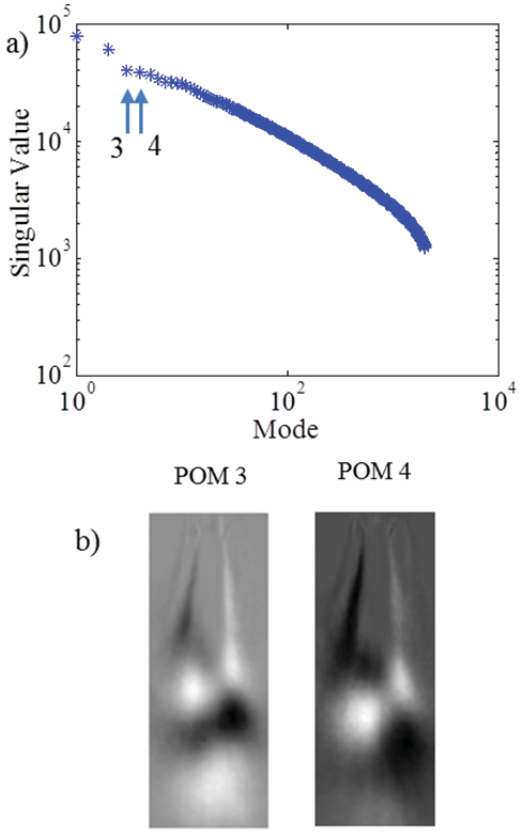

Figure 6. Proper orthogonal decomposition a) spectrum and b) eigenfunctions of mode pair candidate proper orthogonal modes (POM) 3 and 4 for $J = 2$.

(in terms of singular values) as a function of mode number. The most energetic mode pair with similar

singular values is associated with modes three and four. Figure 6(b) shows the proper orthogonal modes (POMs), or eigenfunctions, associated with the mode pair. This figure shows that the spatial distribution is similar, while mode four appears to have features that are slightly shifted downstream relative to mode three. Reconstructing these two modes with the temporal coefficients will represent a convective process. It may be seen that modes seven through nine also have similar singular values, thus a second convective mode may be present. This mode was not evaluated due to the lower variance contribution.

Figure 7 shows the CPSD and phase difference for

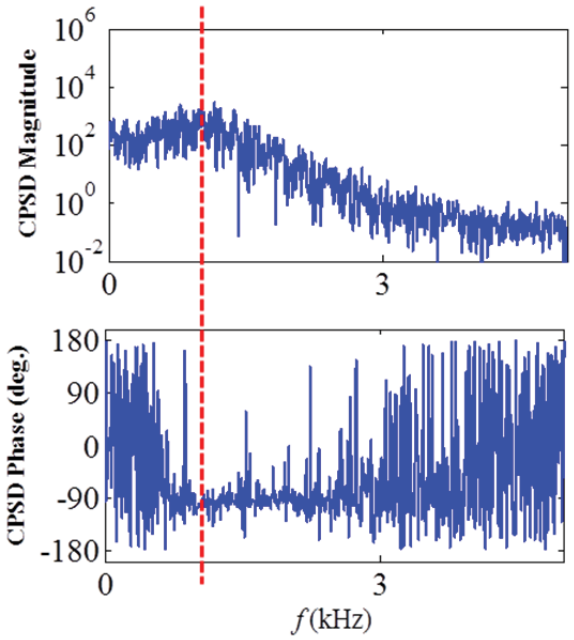

Figure 7. Cross-power spectral density amplitude and phase for modes three and four for $J = 2$.

modes three and four shown in Fig. 6. There is a broad peak on the low-frequency side of the spectrum. The peak is defined within the broad CPSD peak but also requires the phase to be near ± 90°. The frequency is near 1 kHz.

The process described above to identify the preferred mode frequency of the coaxial jet was applied to a number of data sets for both momentum flux ratios and nominal and high flow rates. The Strouhal number defined as

$$St = \frac{f_{nat}(D_1 + D_2)/2}{U_{c,meas.}}, \qquad (3)$$

where f_{nat} is the preferred mode frequency, was calculated for all data sets. The Strouhal number as a function of momentum flux ratio is shown in Fig. 8. The measured convection velocity provides a slightly reduced level of scatter compared results using Eq. 2. The trend represents a nominally constant value for *St* of 0.3. Spectra near the potential core end for

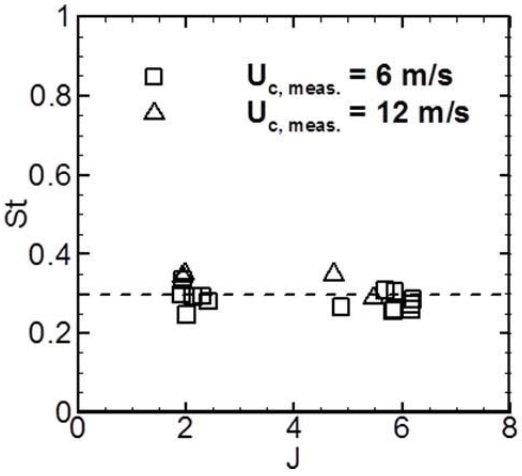

Figure 8. Strouhal number versus momentum flux ratio *J*.

the free jet data of Ko and Davies[20] and coaxial jet data of Ko and Kwan[13], when recast in the form of Eq. 3, fall within the scatter around 0.3. Both nominal and higher flow conditions (i.e. higher convection velocities) fall nominally near 0.3.

The scaling law in Fig. 8 was used to define baseline flow conditions for a predetermined frequency. Since the geometry is fixed, the preferred mode is determined by the convection velocity. For the present study, the unforced flow conditions were defined to result in a preferred mode frequency of approximately 1 kHz. One of the primary forcing parameters is the frequency ratio *F*, defined as

$$F = \frac{f_{forcing}}{f_{nat}}, \qquad (4)$$

where $f_{forcing}$ is the forcing frequency and f_{nat} is the natural preferred mode of the coaxial jet. The current study considered frequency ratios near 1.7, 2.0, and 2.6. The amplitude normalization will be discussed for both the PAN and PN forcing conditions.

Figure 9 shows instantaneous images of the $J = 2$ case for baseline and max PAN/PN forcing. The outer flow and inner shear layer are clearly perturbed under forcing conditions. In particular, the PN forcing results in highly antisymmetric structure in the outer annular flow with antisymmetric structures on the inner jet boundary. The instantaneous image for the PAN case

shows large-scale structures on the inner jet surface, while it is not apparent whether the structure is symmetric or antisymmetric.

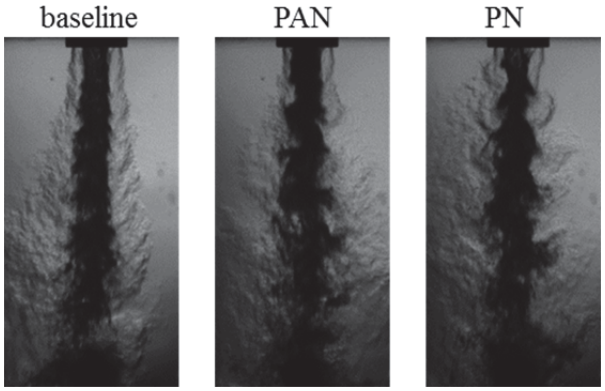

Figure 9. Instantaneous images for the baseline and maximum forced cases for PAN and PN, $J = 2$.

One of the primary goals of the research was to identify the conditions of forcing receptivity as a function of dimensionless forcing frequency and amplitude. The POD technique is used to detect the receptivity and relative importance of the forced and natural modes. Figure 10 shows the first eight POMs for the baseline,

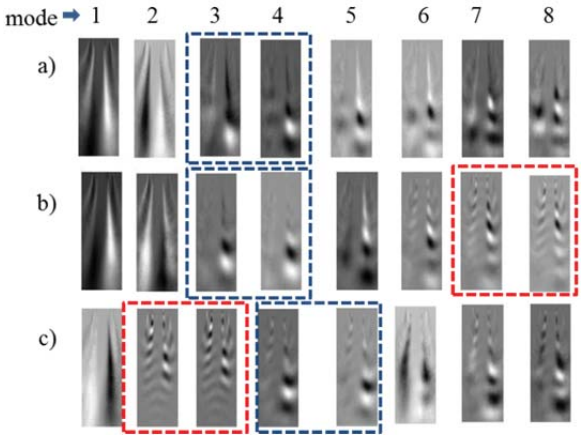

Figure 10. Proper orthogonal modes for $J = 2$, PAN, and $F = 2.7$ for a) unforced, b) $p' = 1.15$ psi, and c) $p' = 1.88$ psi.

and two forcing amplitudes of 1.15 and 1.88 psi for the PAN case for $J = 2.0$ and $F = 2.6$. The dashed blue box represents the natural preferred mode, which is present for all cases. The $p' = 1.15$ psi case shows the emergence of a new high frequency convective mode pair for modes 7 and 8. This force mode is highlighted by the red dashed box. When the amplitude was increased to 1.88 psi, the forced mode contributes more to the image variance as indicated by the order within the POD array. For the forced dominated case in Fig. 10(c), the natural mode persists but is somewhat contaminated with small scale instabilities from the forcing.

For PAN forcing, the injector is essentially exposed to an unsteady back pressure. Thus the coupling is likely to be related to unsteady flow rates caused by a fluctuating pressure drop across the injector. Due to the high density of the inner jet, the impact of the unsteady pressure drop is reduced because of the inertia of the mass within the injector passage. The outer jet is much more responsive to the unsteady back pressure due to the lower mass in the outer jet passage. Thus fluctuating back pressure drives a fluctuating flow rate in the outer jet. The accompanying velocity pulsations will disturb both the inner and outer shear layer. This description is consistent with the explanation given by Baillot et al.[21]

The above mechanism provides for some guidance for normalization of the forcing amplitudes for PAN conditions. The unsteadiness generated in the outer flow will depend on the ratio of the unsteady back pressure to the dynamic pressure of the flow. The magnitude of the induced velocity fluctuation will also depend on the frequency (see Wegener[15] for analysis). For a fixed pressure drop across the injector passage, high-frequency fluctuations have shorter periods in which the fluid can accelerate. Thus it is expected that higher-frequency fluctuations are less likely to couple for PAN forcing, although the hydrodynamic stability considerations also play a factor in how velocity fluctuations of a particular frequency lead to wrinkling of the inner jet column.

Figure 11 shows the inception and dominance boundaries of the PAN forcing conditions for both momentum flux ratios at the three frequency ratios. The empty symbols represent the conditions in which a new forced POM mode pair was observed, but was lower in variance contribution than the natural mode. The filled symbol represents the condition in which the forced mode is dominant over the natural mode. The grey shaded area has not been sampled, although the transition between natural and forced dominance occurs in this region.

It is interesting to note that the inception of receptivity occurs at a nominal dimensionless amplitude of unity. This is consistent with the arguments of Baillot et al.[21] It is unclear why the $J = 2$ case appears to be less receptive to high-frequency fluctuations.

Figure 12 shows the receptivity behavior for the PN forcing conditions. Here the amplitude of the forcing is given in units of m/s. The perturbation velocity is estimated using Eq. 1. The general trend of increasing receptivity with amplitude is once again demonstrated. The mechanism for the response is less evident. The velocity perturbation magnitude is much lower than the outer jet velocity (~ 40 m/s). It is thus unlikely that the

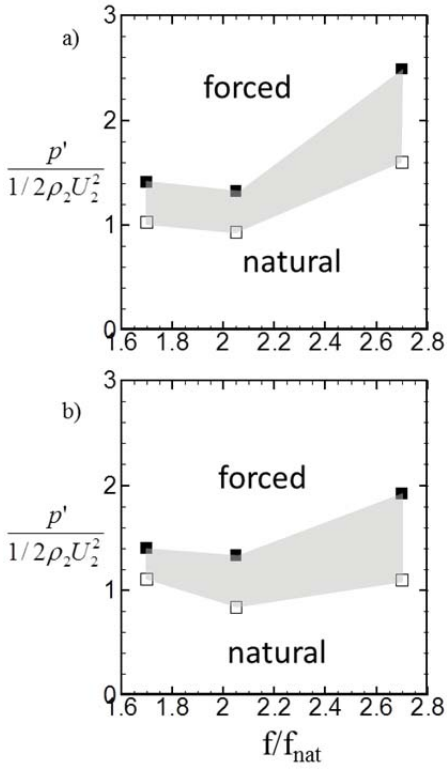

Figure 11. Receptivity regimes for PAN forcing as a function of frequency ratio for a) $J = 2$ and b) $J = 6$.

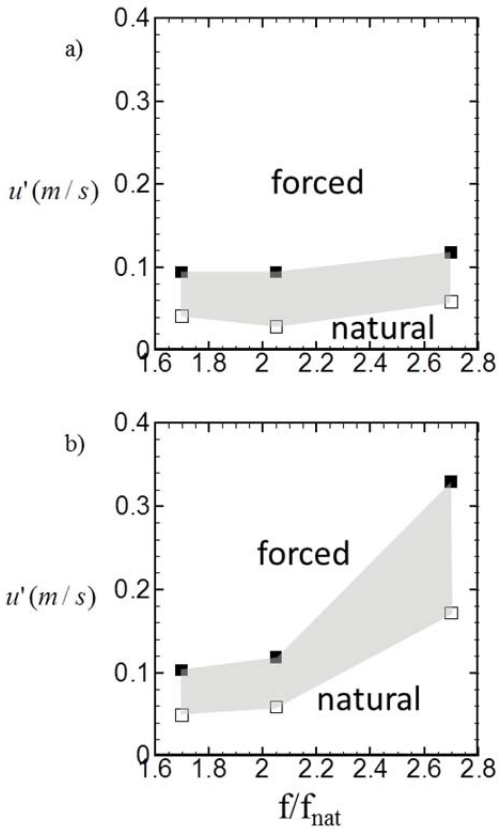

Figure 12. Receptivity regimes for PN forcing as a function of frequency ratio for a) $J = 2$ and b) $J = 6$.

perturbations are directly disturbing the inner jet surface as these low-level disturbances would be insignificant relative to the inflow turbulence.

Further insight may be gained through analysis of the images in the first few diameters of the coaxial jet. In this region, the flow is very unstable due to the high velocity gradients, thus this is the most likely region where the acoustic perturbations can disturb the flow. Figure 13 shows the near field of the coaxial jet for the baseline unforced case as well as highly-forced PAN and PN cases. These images are also representative for the results at $J = 6$. The near field of the dominant convective mode is also shown on the right of the figure. The PAN mode, as supported by the POM, is symmetric (although the thickness and intensity is not symmetric). This would be supportive of the pulsed outer flow mechanism, although this is not nearly as clear in the instantaneous images. The PN case shows very dramatic effects in the near field. In particular, the outer jet appears to be experiencing intense transverse motions that are out of phase. The antisymmetric nature is also supported by the POM. Recall from Fig. 12

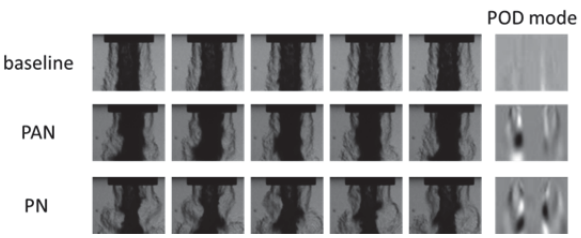

Figure 13. Instantaneous images of the near field of the coaxial jet under forced and unforced conditions for $J = 2$.

that the estimated acoustic velocity is much smaller than the outer jet velocity. The flapping nature of the jet, and the involvement of the jet as a whole, suggests the possibility of excitation of a helical jet column mode. The transverse velocity disturbance is not of sufficient magnitude to cause a drag force leading to such dramatic motion. Future analysis will be required to gain further insight into the coupling mechanism for PN conditions.

Conclusions

An experimental study has investigated the receptivity of two-phase coaxial jet flows to transverse acoustic perturbations. It was found, over the range of conditions considered, that the shear flow structures along the inner jet convect at a speed well predicted by the model developed by Dimotakis.[17] A new Strouhal number definition is proposed that appears to provide reasonable collapse of the frequency of convective modes as extracted from POD analysis of the potential core region of the coaxial jet. Coaxial jets at two different momentum flux ratios were subsequently forced through exposure to variable frequency and amplitude acoustic environments, including PN and PAN conditions.

The PAN forcing appears to generate a pulsation in the outer jet flow rate that subsequently excites instabilities in the flow. The receptivity of the flow field to PAN forcing occurs near the condition where $p' \sim 1/2 \rho_2 U_2^2$, independent of momentum flux ratio. This mechanism will also be sensitive to the inertance properties of the injector design, and therefore sensitive to frequency.

The PN forcing results in a strong coupling even at very low acoustic velocities. The relative magnitudes of the acoustic velocity to the characteristic velocities of the coaxial jet make it unlikely that the acoustics directly generate disturbances in the shear flow. A potential mechanism involves the coherent transverse velocity fluctuations in the acoustic field exciting a helical mode in the outer jet. Further research will be required to further explore the coupling mechanism for PN forcing.

Nomenclature

AR	outer-to-inner area ratio
c	speed of sound
D	diameter
f	frequency
F	normalized frequency
J	outer-to-inner momentum flux ratio
m	mass
p	pressure
p'	pressure fluctuation amplitude
St	Strouhal number
t	inner jet post thickness
U	mean velocity
u'	velocity fluctuation amplitude
ρ	density

Subscripts

c	convection
1	inner jet fluid
2	outer jet fluid

References

1. Chehroudi, B., D. Talley, and E. Coy, *Visual characteristics and initial growth rates of round cryogenic jets at subcritical and supercritical pressures.* Physics of Fluids, 2002. **14**(2): p. 850-861.
2. Oschwald, M., et al., *Injection of fluids into supercritical environments.* Combustion Science and Technology, 2006. **178**(1-3): p. 49-100.
3. Leyva, I., B. Chehroudi, and D. Talley, *Dark Core Analysis of Coaxial Injectors at Sub-, Near-, and Supercritical Conditions in a Transverse Acoustic Field*, in *43rd AIAA/ASME/SAE/ASEE Joint Propulsion Conference & Exhibit.* 2007, American Institute of Aeronautics and Astronautics: Cincinnati, OH.
4. Davis, D.W., *On the behavior of a shear-coaxial jet, spanning sub-to supercritical pressures, with and without an externally imposed transverse acoustic field*, in *Mechanical Engineering*. 2006, The Pennsylvania State University: University Park, PA.
5. Rodriguez, J.I., *Acoustic excitation of liquid fuel droplets and coaxial jets*, in *Aerospace Engineering*. 2009, University of California, Los Angeles: Los Angeles, CA.
6. Teshome, S., *Droplet Combustion and Non-Reactive Shear-Coaxial Jets with Transverse Acoustic Excitation*, in *Mechanical Engineering*. 2012, University of California, Los Angeles: Los Angeles, CA.
7. Wegener, J., et al., *Development of a facility for combustion stability experiments at supercritical pressure*, in *52nd AIAA Aerospace Sciences Meeting.* 2014: National Harbor, MD.
8. Yule, A., *Large-scale structure in the mixing layer of a round jet.* Journal of Fluid Mechanics, 1978. **89**(3): p. 413-432.
9. Crow, S. and F. Champagne, *Orderly structure in jet turbulence.* Journal of Fluid Mechanics, 1971. **48**: p. 547-591.
10. Gutmark, E. and C.M. Ho, *Preferred modes and the spreading rates of jets.* Physics of Fluids (1958-1988), 1983. **26**(10): p. 2932-2938.
11. Drubka, R.E. and H.M. Nagib, *Instabilities in near field of turbulent jets and their dependence on initial conditions and Reynolds number*, in *AFOSR Scientific Report AFOSR-TR-0962*. 1981.

12. Birbaud, A.-L., et al., *Dynamics of free jets submitted to upstream acoustic modulations.* Physics of Fluids, 2007. **19**: p. 013602.
13. Ko, N. and A. Kwan, *The initial region of subsonic coaxial jets.* Journal of Fluid Mechanics, 1976. **73**: p. 305-332.
14. Chigier, N. and Z. Farago, *Morphological classification of disintegration of round liquid jets in a coaxial air stream.* Atomization and Sprays, 1992. **2**(2).
15. Wegener, J., *Multi-phase Combustion and Transport Processes Under the Influence of Acoustic Excitation*, in *Mechanical Engineering*. 2014, University of California, Los Angeles: Los Angeles, CA.
16. Monkewitz, P.A. and P. Huerre, *Influence of the velocity ratio on the spatial instability of mixing layers.* Physics of Fluids, 1982. **25**: p. 1137.
17. Dimotakis, P.E., *Two-dimensional shear-layer entrainment.* AIAA Journal, 1986. **24**(11): p. 1791-1796.
18. Dahm, W.J. and P.E. Dimotakis, *Mixing at large Schmidt number in the self-similar far field of turbulent jets.* Journal of Fluid Mechanics, 1990. **217**: p. 299-330.
19. Arienti, M. and M.C. Soteriou, *Time-resolved proper orthogonal decomposition of liquid jet dynamics.* Physics of Fluids (1994-present), 2009. **21**(11): p. 112104.
20. Ko, N. and P. Davies, *The near field within the potential cone of subsonic cold jets.* Journal of Fluid Mechanics, 1971. **50**(01): p. 49-78.
21. Baillot, F., et al., *Behaviour of an air-assisted jet submitted to a transverse high-frequency acoustic field.* Journal of Fluid Mechanics, 2009. **640**: p. 305-342.

This Page Intentionally Left Blank

Propulsion and Energy Forum
July 28-30, 2014, Cleveland, OH
50th AIAA/ASME/SAE/ASEE Joint Propulsion Conference

Receptivity of a Cryogenic Coaxial Gas-Liquid Jet to Acoustic Disturbances

Jeffrey L. Wegener[1]
University of California at Los Angeles, CA 90095

David J. Forliti[2]
Sierra Lobo, Inc. supporting AFRL/RQRC, Edwards AFB, CA 93524

Ivett A. Leyva[3]
AFRL/RQRE, Edwards AFB, CA 93524

and
Douglas G. Talley[4]
AFRL/RQRC, Edwards AFB, CA 93524

An experimental study has been conducted at the Air Force Research Laboratory at Edwards Air Force Base to explore the receptivity of cryogenic coaxial jet flows to transverse acoustic disturbances. The shear coaxial jet flow employed liquid nitrogen in the inner jet and cooled helium in the outer annular jet to represent the nominal fluid dynamical conditions of an oxygen/hydrogen liquid rocket engine injector. The injector flow is submerged in a chamber that experiences a monotonic transverse acoustic resonance characteristic of a rocket chamber in the presence of combustion instability. The coaxial jet is exposed to a variety of acoustic conditions including different frequencies, amplitudes, and locations within the resonant mode shape. High-speed back-lit images were captured to record the behavior of the natural (unforced) and forced coaxial jets. Proper orthogonal decomposition and spectral analysis were used to extract natural and forced modes. Convective modes are extracted, and a new Strouhal number is used to characterize the dominant natural convective mode that is analogous to the preferred mode in free jets. The threshold of receptivity was found for a number of different injector flows and acoustic forcing conditions. The results indicate that the dimensionless frequency plays an important role, and there exists a finite forcing amplitude at which the threshold of receptivity occurs. The receptivity threshold and post receptivity response provides useful insight on the suitability of a given injector design for specific rocket combustion chamber conditions.

[1] Graduate Student, Department of Mechanical and Aerospace Engineering, UCLA, Los Angeles, CA 90095 student member. Currently at Physical Sciences, Inc., Andover, MA 01810.
[2] Research Scientist, Sierra Lobo, Inc., 10 E. Saturn Blvd, Building 8451, Edwards AFB, CA 93524, senior member.
[3] Technical Advisor, AFRL/RQRE, 4 Draco Drive, Building 8351, Edwards AFB, CA 93524, Associate Fellow.
[4] Lead, Combustion Dynamics Group, AFRL/RQRC., 10 E. Saturn Blvd, Building 8451, Edwards AFB, CA 93524, Associate Fellow.

Nomenclature

AR	=	outer-to-inner area ratio
c	=	speed of sound
D	=	diameter
f	=	frequency
F	=	normalized frequency
J	=	outer-to-inner momentum flux ratio
m	=	mass
p	=	pressure
p'	=	pressure fluctuation amplitude
St	=	Strouhal number
t	=	inner jet post thickness
U	=	mean velocity
u'	=	velocity fluctuation amplitude
ρ	=	density

Subscripts

c	=	convection
meas	=	measured
Dimotakis	=	the Dimotakis[1] convection velocity model
1	=	inner jet fluid
2	=	outer jet fluid

I. Introduction

COMBUSTION instability phenomena has been and remains one of the key challenges in the development of robust and high performance propulsion and energy systems. In the liquid rocket engine (LRE) application, combustion instability can lead to degraded performance, severe wear, and rapid catastrophic damage to the propulsion system. Unfortunately, combustion instability phenomena are not sufficiently understood to allow solution at the engine design stage. Thus full-scale testing and potential multiple design iterations may be required to satisfy the stability requirement. The development of high-fidelity design tools offers much promise in this respect, although data under a variety of relevant conditions are still needed to validate emerging computational tools.

The Air Force Research Laboratory (AFRL) at Edwards AFB has extensively investigated the mixing properties of cryogenic single and coaxial jets under both sub- and supercritical thermodynamic pressure operating conditions.[2, 3] These flows have also been exposed to a range of transverse acoustic conditions.[4-6] A new experimental facility for reacting coaxial jet flows has been developed as described by Wegener et al.[7] The present paper describes preliminary nonreacting data that was collected using this new facility. Although a large quantity of data has been collected in the past for nonreacting conditions, the current data considers a new framework in which to explore the forcing response of coaxial jets. Past studies have generally placed emphasis on investigating different injector conditions, including injector geometry, momentum flux ratio, and chamber pressure. The current study focuses on a single injector geometry in a two-phase (i.e. subcritical) regime, and focuses on the role of forcing frequency and amplitude.

II. Background

The free jet is known to contain a broad range of frequencies, ranging from the shear layer instabilities near the nozzle exit, to the large-amplitude fluctuations near the end of the potential core, and continuing into the weak far field fluctuations.[8-11] Although the global spectral features of the free jet are extremely broad band, the peak frequencies near the end of the potential core are generally selected as being a representative characteristic of the jet.[8] The approach adopted by Birbaud et al. is also highly appropriate in selecting two frequencies that represent the near field ranging from the nozzle trailing edge to the end of the potential core.[12] Having one (or more) characteristic frequency provides a useful reference in which to examine the effects of forcing, as different relative frequencies will influence the jet/shear layer structure through different mechanisms.

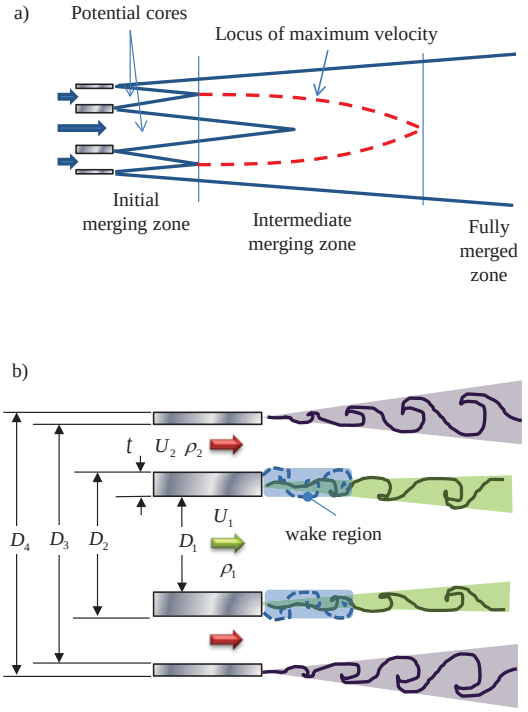

Figure 1. The a) spatial regions of the coaxial jet flow field and b) the potential unsteady structure in the initial merging zone.

The coaxial jet is a highly complex flow due to the presence of multiple shear layers and potentially a splittler plate wake instability in the near field as shown in Fig. 1. Figure 1(a) shows the spatial development of the coaxial jet as described by Ko and Kwan.[13] Figure 1(b) shows the potential shear flow regions in the initial merging zone including an inner and outer shear layer, and a possible wake instability associated with the flow downstream of the inner nozzle trailing edge. This wake instability has been found to occur within certain velocity ratio ranges for coaxial jets and shear layers.[14-20] The role of density ratio on the competition between the shear layer and wake modes has not been thoroughly explored, in particular in the small density ratio (outer to inner stream) regime associated with the conditions of interest at AFRL.

Ko and coworkers have studied the flow and spectral properties of coaxial jets spanning a broad range of conditions.[13, 21-23] They employed two different Strouhal number definitions for the inner and outer shear layer. The inner shear layer Strouhal number definition compensates for the presence of the outer flow, which has a tendancy to increase the frequency through a higher instability convection velocity. For the application of interest at AFRL, the frequencies in the inner shear layer region are of primary interest, as this will be the location of the flame under reacting flow conditions. Thus hydrodynamic instabilities in this region are most likely to generate coherent heat release fluctuations that are known to participate in thermoacoustic instability mechanisms. In this context, a representative preferred mode of the coaxial jet would be be based on the frequency of the inner shear layer structures (which may be dominated by the wake instability) near the end of the inner jet potential core where fluctuations are most intense. Although this preferred mode is likely to generate heat release fluctuations, one must remain cognizant that higher frequency fluctuations closer to the injector trailing edge might play a very key role in driving combustion instability. This aspect will be a subject of future reacting flow research at AFRL.

The coaxial jet flow is dependent on a large number of dimensionless groups. The geometry can be characterized by the outer-to-inner area ratio *AR*, and the normalized post thickness t/D_1. There are two Reynolds numbers, one each for the inner and outer flow. The momentum flux ratio *J*, defined outer to inner flow, is generally considered the primary independent flow parameter of the coaxial jet. Each of the two flows have characteristic velocities and densities, allowing the ability to define the velocity and density ratio across each shear layer. The shear flow is also very sensitive to the injector exit conditions, including profiles of mean and fluctuating velocity, and spectral characteristics of turbulence or other background disturbances. If the two streams differ in phase, then the Weber number is also a parameter of importance.

The behavior of the acoustically-excited coaxial jet will depend on all of the parameters mentioned above, in addition to the characteristic scales of the forcing conditions. The forcing can be characterized by the acoustic frequency and amplitude; the amplitude may be measured by the magnitude of the pressure and/or velocity fluctuations. The interaction mechanisms differ when the coaxial jet is placed in a fluctuating pressure environment versus a fluctuating velocity environment.[24] Thus the response of a given coaxial jet flow to acoustic perturbations will depend on the relative frequency, relative amplitude, and location within the acoustic resonance mode shape.

The purpose of the current study was to explore the receptivity of cryogenic two-phase coaxial jets to disturbances of the form of an acoustic transverse resonance; a flow is considered to be receptive to perturbations if detectable changes occur in the flow field. This study considered new parameters, the normalized frequency and amplitude. The conditions at which forcing dominates the natural coaxial jet behavior were documented.

III. Experimental facility and methods

The experiments were conducted in the Combustion Stability Lab at the Air Force Research Laboratory (AFRL) at Edwards Air Force base. A new facility, capable of high-pressure reacting flows, was used for the current study. Figure 2 shows both a schematic and three-dimensional rendering of the test chamber. Two acoustic sources, piezo sirens from Piezo Systems, Inc., are located symmetrically offset from the injector region. Waveguides shown in Fig. 2(a) are used to connect the acoustic sources to the injector flow region. The acoustic frequency and amplitude are controlled via a signal generator/amplifier combination that drives the sirens. The sirens operate either in phase or with 180° shift to generate the pressure antinode (PAN) and pressure node (PN) at the middle of the chamber; the pressure node case is associated with an acoustic velocity antinode, but will be referred to as pressure node.

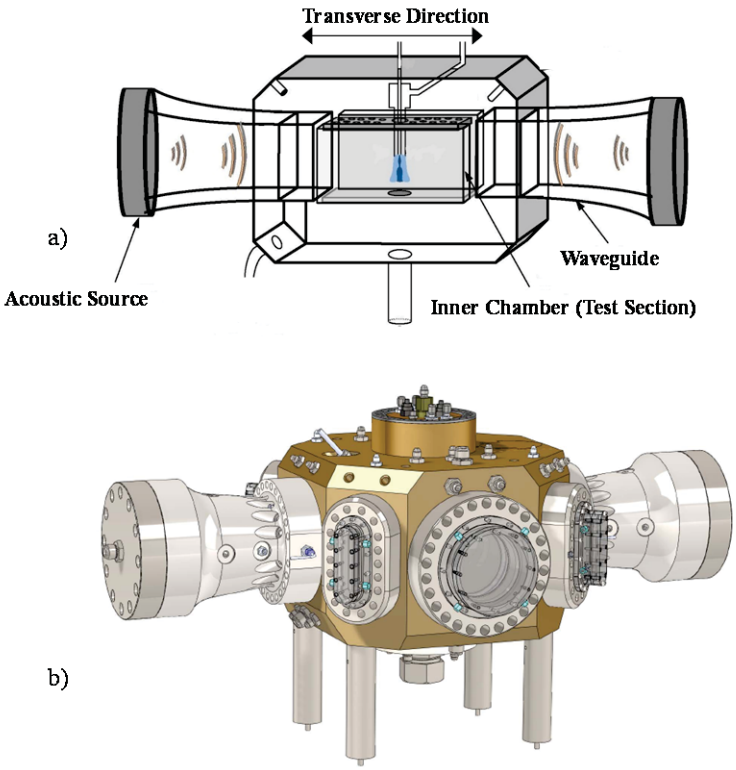

Figure 2. a) Conceptual and b) schematic of the Combustion Stability Lab experimental facility.

The chamber is divided into inner and outer chambers that are not completely sealed relative to one another. A high flow of gaseous nitrogen in the outer chamber is used to cool the combustion products under reacting flow conditions, and the combined flow is choked through an exit orifice. The gaseous nitrogen flow is used to control the chamber pressure. The facility is equipped with heat exchangers to allow cooling of the inner and outer injector flows. Further details on the experimental facility can be found in Wegener et al.[7]

Table 1. Geometry of the injector.

Parameter	Value (mm)
D_1	1.40
D_2	2.16
D_3	2.82
D_4	3.56

A single coaxial jet injector was used for the experiments. The dimensions of the injector are summarized in Table 1. The outer-to-inner area ratio *AR* is 1.68 and the dimensionless post thickness t/D_1 is 0.27; both parameters are within the lower range of previous studies at AFRL.[4, 6] The injector flow passages are sufficiently long to ensure fully-developed turbulent flow at the exit of the injector. Similar to previous work at AFRL, the inner jet is liquid nitrogen. The outer jet in the current study is cooled helium. The use of helium allows for a closer match to the density ratio as would occur for oxygen/hydrogen operation in a cryogenic rocket engine. The chamber pressure was 2.8 MPa (400 psi) for all experiments. Further details on the experimental conditions are given in Table 2.

Table 2. Injector operating parameters.

Parameter	Values
T of inner jet (N_2)	~ 120 K
T of outer jet (He)	~ 275 K
J	2, 6
Re_1	~$1.5x10^4$
Re_2	~ $1.0x10^4$
We	> 100

As shown in the table, two momentum flux ratios were considered. Due to the unique combination of fluids and conditions, surface tension values are not available to the authors' knowledge. Based on the visualizations shown later and the results of Farago and Chigier[25], the current experiments appear to be in the fiber-type regime and the Weber number is expected to be approximately 100 or higher.

The primary diagnostic of the current experimental study involves high-speed backlit imaging. A Phantom v7.10 camera was used to capture images at 10 kHz. The acoustic resonance is characterized through several high-

speed Kulite pressure sensors flush mounted in the test section area including the waveguides. A pressure sensor located in the center of the test section and coincident with the axis of the coaxial jet is used to measure the peak pressure fluctuation for the PAN cases. For the PN operation, the peak pressure fluctuation is estimated from measurements at off-node locations using an assumed mode shape, and the maximum acoustic velocity magnitude is estimated from the linear acoustics equation,

$$u' = \frac{p'}{\rho_c c} \tag{1}$$

where *u'* is the magnitude of the velocity fluctuation in the velocity antinode region, *p'* is the magnitude of the pressure fluctuation in the pressure antinode region, ρ_c is the density of the ambient gas in the chamber, which is nominally room temperature nitrogen, and *c* is the speed of sound. The injector flow species and temperatures will definitely alter the properties of the acoustic resonance, thus Eq. (1) is an approximation. The acoustic sirens were used to drive a transverse acoustic resonance ranging from the 3rd to 7th mode. See Wegener et al. for more details on the acoustic characteristics.[7]

IV. Results

The first phase of the research was focused on understanding the properties of the unforced coaxial jet. Figure 3 shows instantaneous and mean images of the cryogenic coaxial jet at the two momentum flux ratios *J* of two and six.

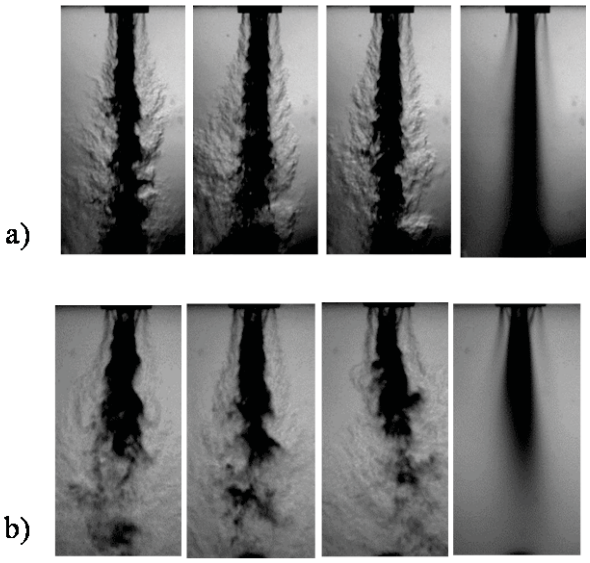

Figure 3. Instantaneous and mean (far right) backlit images of the coaxial jet for momentum flux ratio *J* of a) two and b) six.

Although there are dynamics present in both the inner and outer shear layers, the strong contrast between the liquid inner flow and gaseous outer flow dominates the images. One can see some structure within the inner shear layer, although the turbulent inflow conditions result in a highly disturbed interface between the liquid and gas. As expected, the higher momentum flux ratio case has a shorter dark core length.[26] The triangular feature near the injector exit, more readily seen in the $J = 6$ case, is the recirculation zone downstream of the inner tube post. Some asymmetries are also apparent and are caused by manufacturing tolerances and the small scale of the injector components. Separate analyses of each side of the injector flow field indicate similar spectra content (see Wegener[27] for details). It is thus expected that the general trends of the current results are representative of the symmetric case, although this will be validated in future studies.

As mentioned earlier, there is a need to identify the preferred mode of the coaxial jet. A frequency scaling variable, the Strouhal number, may be developed for use in a preferred mode scaling law. There are a number of choices available in defining the length and velocity scale for the Strouhal number. The length scale is a relatively straightforward choice of jet diameter as used for the single jet. In the case of a coaxial jet with finite (or large) post thickness t/D_1, previous studies show, at least for moderate to high *J*, that the shear layer will more or less be centered near the middle of the post.[6] Thus the average of D_1 and D_2 are used as the length scale. Further data would need to be considered for different geometries to find the length scale that provides the best collapse across different injector designs.

The velocity scale is more subjective. For the free jet, the convention is to use the mean jet exit velocity. Guidance for an alternative choice is provided through studies of shear layers. Huerre and Monkewitz conducted a linear stability study of variable velocity ratio shear layers.[28] They found that the most unstable frequencies nominally collapse on a single value when the frequency is normalized by the mean velocity of the two streams. For variable density shear layers, the frequency of the most unstable mode will more likely scale with the convection velocity. Thus the convection velocity is proposed as an appropriate velocity scale.

The convection velocity of the coherent structures in a shear layer may be estimated in a variety of ways. Linear stability analysis may be used, for instance. Dimotakis developed a model for the spreading rate of planar shear layers, and included in the model development is an estimate of the convection velocity based on freestream conditions.[1] The model uses the assumption that in the reference frame of the shear layer structure, the dynamic pressures of the two freestreams are equal. This leads to a form of the convection velocity of

$$U_{c,\,Dimotakis} = \frac{\rho_1^{1/2} U_1^2 + \rho_2^{1/2} U_2^{1/2}}{\rho_1^{1/2} + \rho_2^{1/2}}, \tag{2}$$

where ρ and U are the density and velocity of the freestreams. It should be mentioned that this expression was derived for single-phase shear layers.

In order to evaluate the validity of the Dimotakis model, the convection velocity is directly measured from the time-resolved images. Figure 4(a) shows the mean image for the $J = 6$ case. A line along the middle of the inner shear layer is defined through user input, and the intensities of these pixels are plotted as a function of time as shown in Fig. 4(b). As inner fluid structures convect along this trajectory, they trace diagonal lines in the s/D_1 versus time domain. This technique has been used in the past to visualize organized motion in jets.[29] The slope of a particular diagonal line represents the convection velocity for that structure; s is the distance along the shear layer ray. Ten samples are extracted and the mean convection velocity determined. The change in slope near s/D_1 of unity is coincident with the end of the triangular recirculation zone associated with the blunt post wall. As expected, the convection velocity increases downstream of the recirculation zone due to the presence of the high-speed coflow of the outer jet fluid; the outer-to-inner velocity ratio for this case is 25. This convection velocity analysis was conducted for several sets of data including two momentum flux ratios and two flow rate combinations.

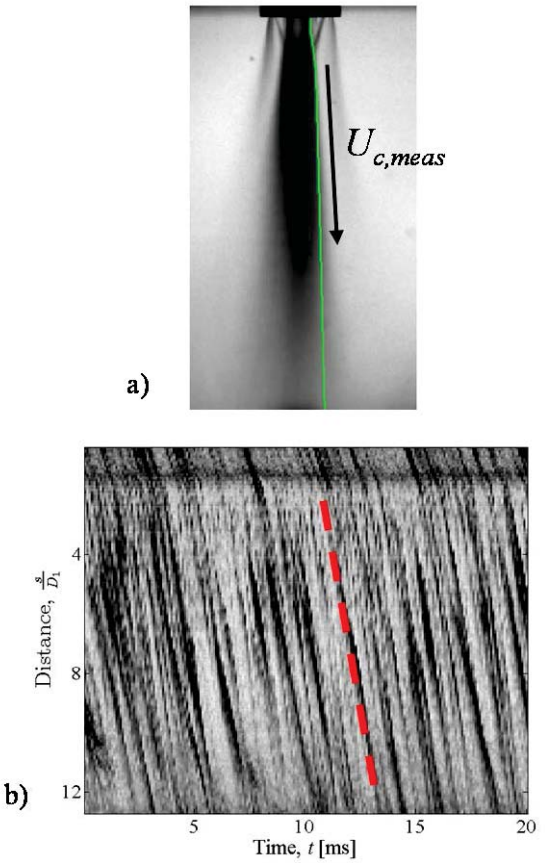

Figure 4. The (a) piecewise linear domain used to construct the (b) axial versus time maps for evaluating the convection velocity.

Figure 5 shows predicted versus measured convection velocities for the two momentum flux ratios. Data was collected for nominal and a higher flow rate for both momentum flux ratios. The conditions for the two momentum flux ratios were selected to keep the convection velocity predicted using Eq. (2) fixed, hence the overlap of points for both momentum flux ratios. The agreement is quite good, indicating that the Dimotakis model may be employed for the current flow conditions. A deviation is observed at higher flow rates (i.e. high convection velocities) and is likely due to heat transfer within the injector. Measurement of temperatures upstream of the injector is used to evaluate density for both flows, thus errors in temperature will result in errors in density. The velocity is estimated using the calculated density and the measured flow rate, thus creating further error due to temperature uncertainty. The subsequent measurements were all done at the lower flow rate associated with a convection velocity near 6 m/s.

In order to calculate the Strouhal number, the characteristic frequency of the jet must be extracted from the data. As would be expected for a spreading shear flow, the spectra depend on axial position. The global frequency of the jet is evaluated using proper orthogonal decomposition (POD) of the image data. This approach places more emphasis on the larger-scale organized motions which make higher contributions to the total variance of the data, thus will be biased towards dynamics in the downstream region. The POD is calculated for an image that spans an

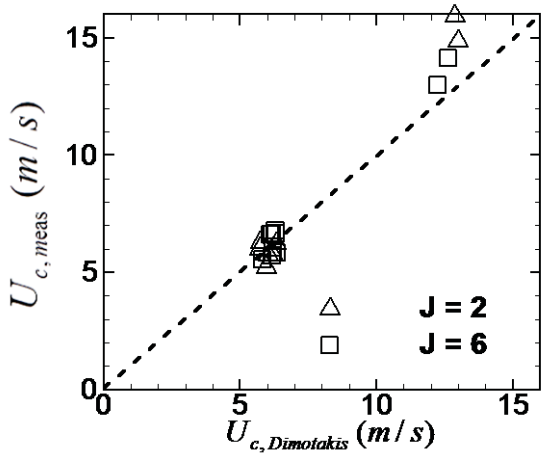

Figure 5. Measured versus predicted convection velocity.

axial distance of approximately $12D_1$. The POD is calculated using singular value decomposition (SVD), the details of which can be found in Wegener.[27] The POD is applied to sets of 2000 images.

The application of POD to 2000 images yield the same number of variance-contributing modes, thus the POD spectrum is inherently broadband, especially for highly-turbulent flows of the type in the present study. Thus a criteria must be defined for isolating important dynamics from the POD results. Arienti and Soteriou provide a criteria for identifying convective modes from POD data.[30] First, the POD spectrum, meaning the eigenvalues as a function of mode number, is constructed and pairs of modes with similar eigenvalues are sought. Once a candidate mode pair is identified, the cross-power spectral density (CPSD) amplitude and phase are calculated for the temporal coefficients of the mode pair. Once this has been done, the mode pair can be determined to be representing a convecting mode if:

1. the peak in the CPSD is coincident with a region of ± 90° phase shift;
2. the spatial distribution of the POD eigenfunctions are similar with features that are shifted nominally half a wavelength in the convection direction.

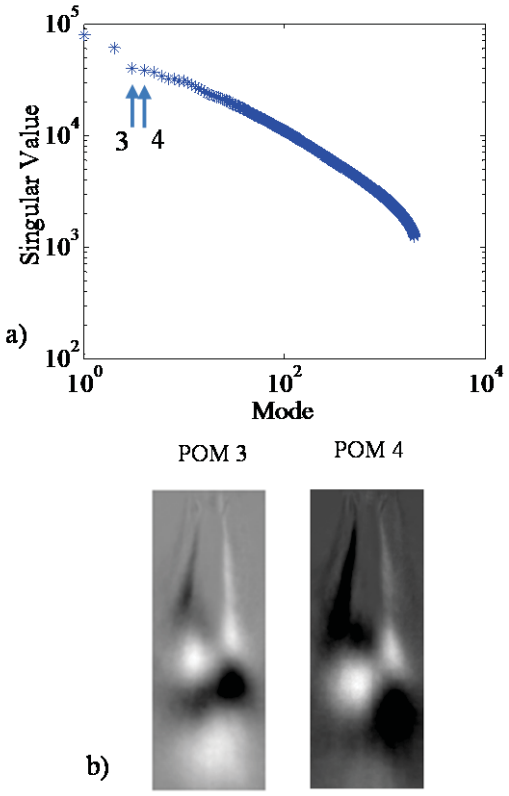

Figure 6. Proper orthogonal decomposition a) spectrum and b) eigenfunctions of mode pair candidate proper orthogonal modes (POM) three and four for J = 2.

If a mode pair satisfies these conditions, a convective dynamic mode has been identified and the frequency of the particular convective mode is associated with the peak in the CPSD. In this study, the preferred mode is associated with the convective mode having the most energetic POD mode pair (i.e. has the highest eigenvalues). The singular values from the SVD process are used to evaluate the variance, as the singular values are equal to the square root of the eigenvalues. It is likely that multiple convective modes are present in the unforced cases of the present study. Other convective modes with lower singular values are not considered as representing preferred modes.

Figure 6(a) shows an example of a POD spectrum (in terms of singular values) as a function of mode number. The most energetic mode pair with similar singular values is associated with modes three and four. Figure 6(b) shows the proper orthogonal modes (POMs), or eigenfunctions, associated with the mode pair. This figure shows that the spatial distribution is similar, while mode four appears to have features that are slightly shifted downstream relative to mode three. Reconstructing these two modes with the temporal coefficients will represent a convective process. It may be seen that modes seven through nine also have similar singular values, thus a second convective mode may be present. This mode was not evaluated due to the lower variance contribution.

Figure 7 shows the CPSD and phase difference for modes three and four shown in Fig. 6. There is a broad peak on the low-frequency side of the spectrum. The peak is defined within the broad CPSD peak but also requires the phase to be near ± 90°. The frequency is near 1 kHz.

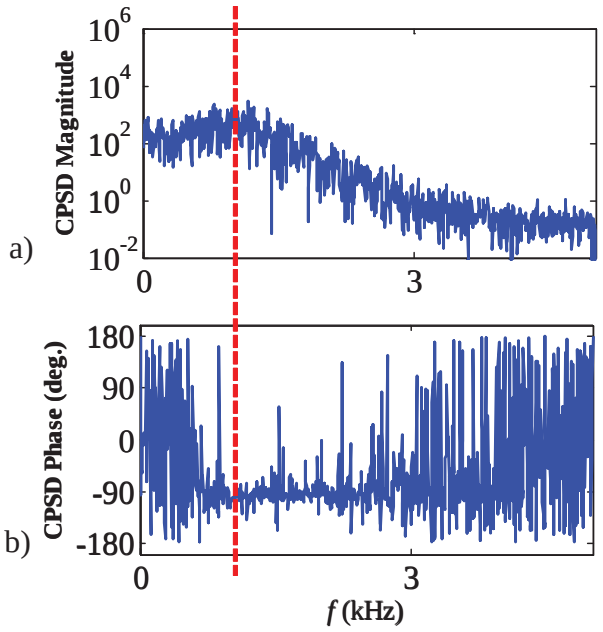

Figure 7. Cross-power spectral density a) amplitude and b) phase for modes three and four for J = 2.

The process described above to identify the preferred mode frequency of the coaxial jet was applied to a number of data sets for both momentum flux ratios and nominal and high flow rates. The Strouhal number defined as

$$St = \frac{f_{nat}(D_1 + D_2)/2}{U_{c,meas}}, \tag{3}$$

where f_{nat} is the preferred mode frequency, was calculated for all data sets. The Strouhal number as a function of momentum flux ratio is shown in Fig. 8. The measured convection velocity provides a slightly reduced level of scatter compared results using Eq. (2). The trend represents a nominally constant value for St of 0.3. Spectra near the potential core end for the free jet data of Ko and Davies[9] and coaxial jet data of Ko and Kwan[13], when recast in the form of Eq. (3), fall within the scatter around 0.3. Both nominal and higher flow conditions (i.e. higher convection velocities) fall nominally near 0.3.

The scaling law in Fig. 8 was used to define baseline flow conditions for a predetermined frequency. Since the geometry is fixed, the preferred mode is governed by the convection velocity. For the present study, the unforced flow conditions were defined to result in a preferred mode frequency of approximately 1 kHz.

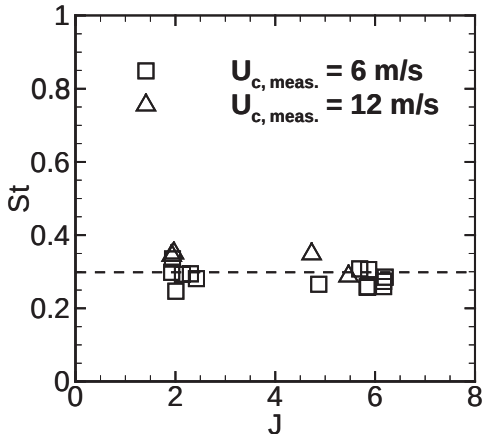

Figure 8. Strouhal number versus momentum flux ratio J.

One of the primary forcing parameters is the frequency ratio F, defined as

$$F = \frac{f_{forcing}}{f_{nat}}, \tag{4}$$

where $f_{forcing}$ is the forcing frequency and f_{nat} is the natural preferred mode. The current study considered frequency ratios near 1.7, 2.0, and 2.6. The amplitude normalization will be discussed for both the PAN and PN forcing conditions.

Figure 9 shows instantaneous images of the J = 2 case for baseline and max PAN/PN forcing. The outer flow and inner shear layer are clearly perturbed under forcing conditions. In particular, the PN forcing results in highly antisymmetric structure in the outer annular flow with antisymmetric structures on the inner jet boundary. The instantaneous image for the PAN case shows large-scale structures on the inner jet surface, while it is not apparent whether the structure is symmetric or antisymmetric.

One of the primary goals of the research was to identify the conditions of forcing receptivity as a function of dimensionless forcing frequency and amplitude. The POD technique is used to detect the receptivity and relative importance of the forced and natural modes. Figure 10 shows the first eight POMs for the baseline unforced case, and two forcing amplitudes of 1.15 and 1.88 psi for the PAN case for J = 2.0 and F = 2.6. The dashed blue box represents the natural preferred mode, which is present for all cases. The p' = 1.15 psi case shows the emergence of a new high frequency convective mode pair for modes 7 and 8. This force mode is highlighted by the red dashed box. When the amplitude was increased to 1.88 psi, the forced mode contributes more to the image variance as indicated by the order within the POD array. For the forced dominated case in Fig. 10(c), the natural mode persists but is somewhat contaminated with small-scale instabilities from the forcing.

For PAN forcing, the injector is essentially exposed to an unsteady back pressure. Thus the coupling is likely to be related to unsteady flow rates caused by a fluctuating pressure drop across the injector. Due to the high density

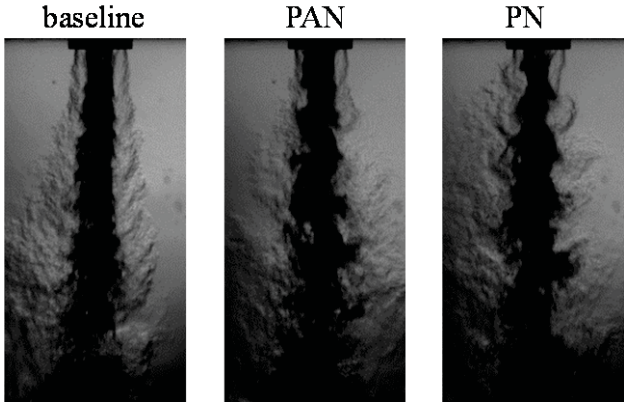

Figure 9. Instantaneous images for the baseline and maximum forced cases for PAN and PN, J = 2.

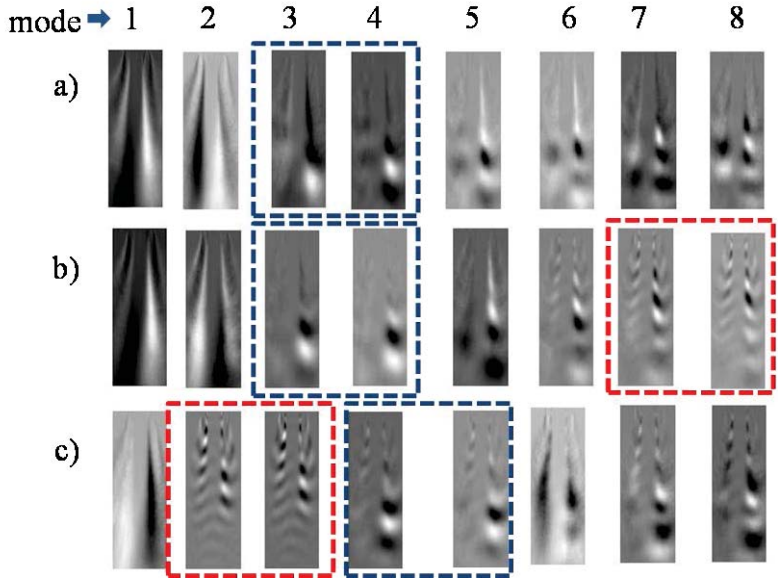

Figure 10. Proper orthogonal modes for J = 2, PAN, and F = 2.7 for a) unforced, b) p' = 1.15 psi, and c) p' = 1.88 psi.

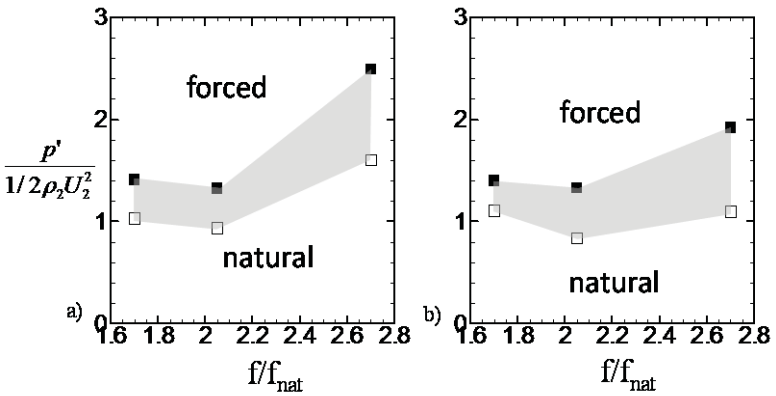

Figure 11. Receptivity regimes for PAN forcing as a function of frequency ratio for a) J = 2 and b) J = 6.

of the inner jet, the impact of the unsteady pressure drop is reduced because of the high inertia within the injector passage. The outer jet is much more responsive to the unsteady back pressure due to the lower mass in the outer jet passage. Thus fluctuating back pressure drives a fluctuating flow rate in the outer jet. The accompanying velocity pulsations will disturb both the inner and outer shear layer. This description is consistent with the explanation given by Baillot et al.[24]

The above mechanism provides for some guidance for normalization of the forcing amplitudes for PAN conditions. The unsteadiness generated in the outer flow will depend on the ratio of the unsteady back pressure to the dynamic pressure of the flow. The magnitude of the induced velocity fluctuation will also depend on the frequency (see Wegener[27] for analysis). For a fixed pressure drop across the injector passage, high-frequency fluctuations have a shorter time period in which the fluid can accelerate. Thus it is expected that higher-frequency fluctuations are less likely to couple for PAN forcing, although the hydrodynamic stability considerations also play a factor in how velocity fluctuations of a particular frequency lead to wrinkling of the inner jet column.

Figure 11 shows the inception and dominance boundaries of the PAN forcing conditions for both momentum flux ratios at the three frequency ratios. The empty symbols represent the conditions in which a new forced POM mode pair was observed, but was lower in variance contribution than the natural mode. The filled symbol represents the condition in which the forced mode is dominant over the natural mode. Other test points above and below these points are not included for clarity. Between five and seven amplitudes were tested for each frequency ratio. The grey shaded area has not been sampled, although the transition between natural and forced dominance occurs in this region.

It is interesting to note that the inception of receptivity occurs at a nominal dimensionless

amplitude of unity. This is consistent with the arguments of Baillot et al.[24] It is unclear why the $J = 2$ case appears to be less receptive to high-frequency fluctuations, both in terms of initial detection of receptivity and the amplitude required for the force mode to dominate the natural mode. The $J = 6$ case appears to be less sensitive to frequency ratio in the range explored.

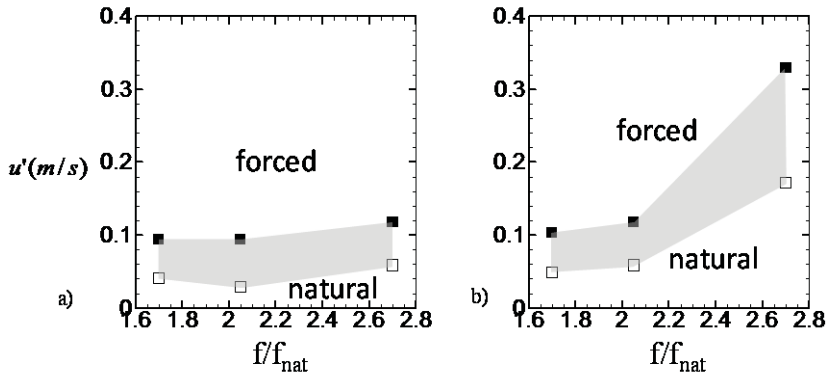

Figure 12. Receptivity regimes for PN forcing as a function of frequency ratio for a) $J = 2$ and b) $J = 6$.

Figure 12 shows the receptivity behavior for the PN forcing conditions. Here the amplitude of the forcing is given in units of m/s. The perturbation velocity is estimated using Eq. (1). The general trend of increasing receptivity with amplitude is once again demonstrated. The mechanism for the response is less evident. The velocity perturbation magnitude is much lower than the outer jet velocity (~ 40 m/s). It is thus unlikely that the perturbations are directly disturbing the inner jet surface as these low-level disturbances would be insignificant relative to the inflow turbulence. Interestingly, the higher momentum flux ratio case exhibits stronger frequency dependence including degraded receptivity at high frequency.

Further insight may be gained through analysis of the images in the first few diameters of the coaxial jet. In this region, the flow is very unstable due to the high velocity gradients, thus this is the most likely region where the acoustic perturbations can disturb the flow. Figure 13 shows the near field of the coaxial jet for the baseline

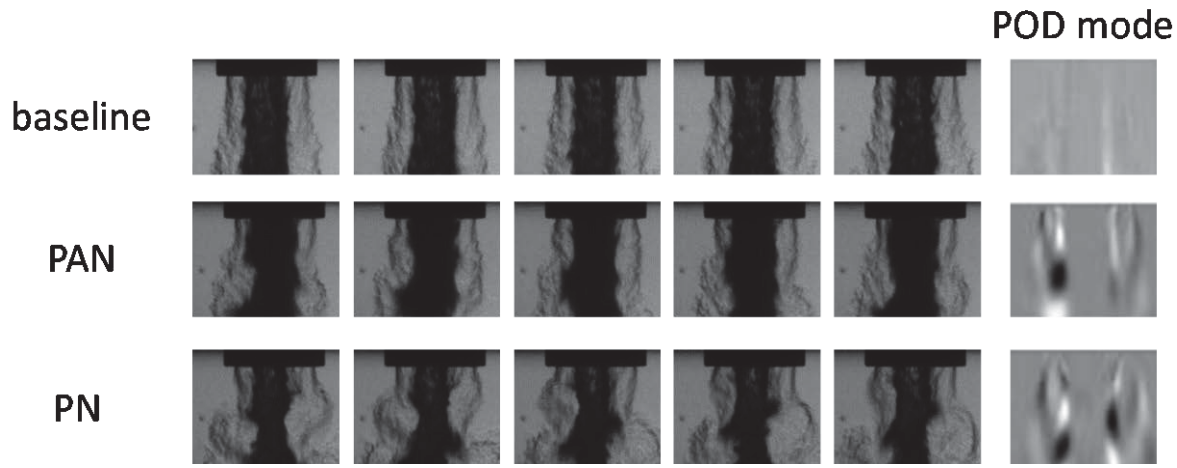

Figure 13. Instantaneous images of the near field of the coaxial jet under forced and unforced conditions for $J = 2$.

unforced case as well as highly-forced PAN and PN cases. These images are also representative for the results at $J = 6$. The near field of the dominant convective POM modes are also shown on the right of the figure. The PAN mode, as supported by the POM distribution, is symmetric (although the thickness and intensity is not symmetric). This would be supportive of the pulsed outer flow mechanism, although this is not nearly as clear in the instantaneous images. The PN case shows very dramatic effects in the near field. In particular, the outer jet appears to be experiencing intense transverse motions that are out of phase. The antisymmetric nature is also supported by the POM. Recall from Fig. 12 that the estimated acoustic velocity is much smaller than the outer jet velocity. The flapping nature of the jet, and the involvement of the jet as a whole, suggests the possibility of excitation of a helical jet column mode (or multiple modes). The transverse velocity disturbance is not of sufficient magnitude to cause a

drag force leading to such dramatic motion. Future analysis will be required to gain further insight into the coupling mechanism for PN conditions.

V. Conclusions

An experimental study has investigated the receptivity of two-phase coaxial jet flows to transverse acoustic perturbations. It was found, over the range of conditions considered, that the shear flow structures along the inner jet convect at a speed well predicted by the model developed by Dimotakis.[1] A new Strouhal number definition is proposed that appears to provide reasonable collapse of the frequency of convective modes as extracted from POD analysis of the potential core region of the coaxial jet. Coaxial jets at two different momentum flux ratios were subsequently forced through exposure to variable frequency and amplitude acoustic environments, including pressure node and pressure antinode conditions.

The pressure antinode forcing appears to generate a pulsation in the outer jet flow rate that subsequently excites instabilities in the flow. The receptivity of the flow field to pressure antinode forcing occurs near the condition where $p' \sim 1/2 \rho_2 U_2^2$, independent of momentum flux ratio, with the exception of highest frequency case for $J = 2$. This mechanism will also be sensitive to the inertance properties of the injector design, and therefore sensitive to frequency. The receptivity charactersitics are different for the two momentum flux ratios, even though the frequency of the preferred modes were the same. This suggests more subtle differences in the hydrodynamics between the two momentum flux ratios play a role in the receptivity characteristics.

The pressure node forcing results in a strong coupling even at very low acoustic velocities. The relative magnitudes of the acoustic velocity to the characteristic velocities of the coaxial jet make it unlikely that the acoustics directly generate disturbances in the shear flow. A potential mechanism involves the coherent transverse velocity fluctuations in the acoustic field exciting one or multiple helical modes in the outer jet. Further research will be required to further explore the coupling mechanism for pressure node forcing. Once again, the receptivity trends were different for the two momentum flux ratios, suggesting again the presence subtle hydrodynamic effects in the receptivity mechanism. Interestingly, the lower momentum flux ratio case is less receptive at high frequency for the pressure antinode forcing while the higher momentum flux ratio case is less receptive for the pressure node forcing.

Acknowledgments

Support was provided by the Air Force Office of Scientific Research, project officer Mitat Birkan, and by AFRL Laboratory Revitalization Funds. The authors thank Randy Harvey and Todd Newkirk for their assistance in conducting the experiments.

References

1. Dimotakis, P. E., "Two-dimensional shear-layer entrainment," *AIAA Journal*, Vol. 24, No. 11, 1986, pp. 1791-1796.

2. Chehroudi, B., Talley, D., and Coy, E., "Visual characteristics and initial growth rates of round cryogenic jets at subcritical and supercritical pressures," *Physics of Fluids*, Vol. 14, No. 2, 2002, pp. 850-861.

3. Oschwald, M., Smith, J., Branam, R., Hussong, J., Schik, A., Chehroudi, B., and Talley, D., "Injection of fluids into supercritical environments," *Combustion Science and Technology*, Vol. 178, No. 1-3, 2006, pp. 49-100.

4. Davis, D. W., "On the behavior of a shear-coaxial jet, spanning sub-to supercritical pressures, with and without an externally imposed transverse acoustic field," Ph.D., Mechanical Engineering, The Pennsylvania State University, 2006.

5. Rodriguez, J. I., "Acoustic excitation of liquid fuel droplets and coaxial jets," Ph.D., Aerospace Engineering, University of California, Los Angeles, 2009.

6. Teshome, S., "Droplet Combustion and Non-Reactive Shear-Coaxial Jets with Transverse Acoustic Excitation," Ph.D., Mechanical Engineering, University of California, Los Angeles, 2012.

7. Wegener, J., Leyva, I., Forliti, D., and Talley, D., "Development of a facility for combustion stability experiments at supercritical pressure," 52nd AIAA Aerospace Sciences Meeting, National Harbor, MD, 2014.

8. Crow, S., and Champagne, F., "Orderly structure in jet turbulence," *Journal of Fluid Mechanics*, Vol. 48, 1971, pp. 547-591.

9. Ko, N., and Davies, P., "The near field within the potential cone of subsonic cold jets," *Journal of Fluid Mechanics*, Vol. 50, No. 01, 1971, pp. 49-78.

10. Yule, A. J., *Two-dimensional self-preserving turbulent mixing layers at different free stream velocity ratios*, Aeronautical Research Council 1972.

11. Drubka, R. E., and Nagib, H. M., "Instabilities in near field of turbulent jets and their dependence on initial conditions and Reynolds number," *AFOSR Scientific Report AFOSR-TR-0962*. 1981.

12. Birbaud, A.-L., Durox, D., Ducruix, S., and Candel, S., "Dynamics of free jets submitted to upstream acoustic modulations," *Physics of Fluids*, Vol. 19, 2007, p. 013602.

13. Ko, N., and Kwan, A., "The initial region of subsonic coaxial jets," *Journal of Fluid Mechanics*, Vol. 73, 1976, pp. 305-332.

14. Boldman, D., Brinich, P., and Goldstein, M., "Vortex shedding from a blunt trailing edge with equal and unequal external mean velocities," *Journal of Fluid Mechanics*, Vol. 75, 1976, pp. 721-735.

15. Segalini, A., and Talamelli, A., "Experimental analysis of dominant instabilities in coaxial jets," *Physics of Fluids*, Vol. 23, No. 2, 2011, pp. 024103-1-024103-7.

16. Talamelli, A., and Gavarini, I., "Linear instability characteristics of incompressible coaxial jets," *Flow, Turbulence and Combustion*, Vol. 76, No. 3, 2006, pp. 221-240.

17. Talamelli, A., Segalini, A., Örlü, R., and Buresti, G., "A note on the effect of the separation wall in the initial mixing of coaxial jets," *Experiments in Fluids*, Vol. 54, No. 3, 2013, pp. 1-7.

18. Tian, V., McKeon, B., and Leyva, I. A., "Split stream flow past a blunt trailing edge with application to combustion instabilities," 46th AIAA/ASME/SAE/ASEE Joint Propulsion Conference and Exhibit, 2012.

19. Wallace, D., and Redekopp, L., "Linear instability characteristics of wake-shear layers," *Physics of Fluids A: Fluid Dynamics*, Vol. 4, No. 1, 1992, pp. 189-191.

20. Sarpotdar, S., and Raman, G., "Investigation of the Inner Nozzle Wake on Kelvin Helmholtz Instabilities in a Coannular Jet," *International Journal of Flow Control*, Vol. 3, No. 2, 2011, pp. 67-86.

21. Kwan, A., and Ko, N., "The initial region of subsonic coaxial jets. Part 2," *Journal of Fluid Mechanics*, Vol. 82, 1977, pp. 273-287.

22. Ko, N., and Au, H., "Coaxial jets of different mean velocity ratios," *Journal of Sound Vibration*, Vol. 100, 1985, pp. 211-232.

23. Au, H., and Ko, N., "Coaxial jets of different mean velocity ratios. II," *Journal of Sound Vibration*, Vol. 116, 1987, pp. 427-443.

24. Baillot, F., Blaisot, J.-B., Boisdron, G., and Dumouchel, C., "Behaviour of an air-assisted jet submitted to a transverse high-frequency acoustic field," *Journal of Fluid Mechanics*, Vol. 640, 2009, pp. 305-342.

25. Chigier, N., and Farago, Z., "Morphological classification of disintegration of round liquid jets in a coaxial air stream," *Atomization and Sprays*, Vol. 2, No. 2, 1992.

26. Leyva, I., Chehroudi, B., and Talley, D., "Dark Core Analysis of Coaxial Injectors at Sub-, Near-, and Supercritical Conditions in a Transverse Acoustic Field," 43rd AIAA/ASME/SAE/ASEE Joint Propulsion Conference & Exhibit, Cincinnati, OH, 8-11 July, 2007.

27. Wegener, J., "Multi-phase Combustion and Transport Processes Under the Influence of Acoustic Excitation," Ph.D., Mechanical Engineering, University of California, Los Angeles, 2014.

28. Monkewitz, P. A., and Huerre, P., "Influence of the velocity ratio on the spatial instability of mixing layers," *Physics of Fluids*, Vol. 25, 1982, p. 1137.

29. Dahm, W. J., and Dimotakis, P. E., "Mixing at large Schmidt number in the self-similar far field of turbulent jets," *Journal of Fluid Mechanics*, Vol. 217, 1990, pp. 299-330.

30. Arienti, M., and Soteriou, M. C., "Time-resolved proper orthogonal decomposition of liquid jet dynamics," *Physics of Fluids (1994-present)*, Vol. 21, No. 11, 2009, p. 112104.

Acoustically Forced Coaxial Hydrogen / Liquid Oxygen Jet Flames

M. Roa* and D. Forliti[1]
Sierra Lobo, Inc.
Edwards, Ca 93524 USA

Al Badakhshan
ERC Inc.
Edwards AFB, CA 93524 USA

Doug Talley
Air Force Research Laboratory
Edwards AFB, CA 93524 USA

Abstract

Combustion instabilities can pose serious problems in the development of liquid rocket engines. In order to understand and predict them, it is necessary to understand how representative liquid rocket injector flames react to acoustic waves. In this study, a representative coaxial gaseous hydrogen / liquid oxygen (LOX) jet flame is visualized for both reacting and nonreacting cases. The jet flame was studied unforced, without acoustics, and forced, with transverse acoustic waves in a pressure node and a pressure antinode configuration. For unforced flames, reactions are found to cause a significantly more expanded plume due to the vaporization and expansion of the LOX. Flame holding is established at the lip with a particularly dominant LOX recirculation zone. Nonreacting convective structures propagate downstream at relatively constant velocity, while reacting structures start at a slow speed and gradually accelerate with downstream distance. These structures never reach the velocity of the nonreacting structures. Reactions shift the spectral content to lower frequencies, consistent with trends observed in the linear stability literature. For forced flames, acoustics do not appear to affect the flame holding. Dynamic mode decomposition detects jet response not only at the fundamental frequency but at higher harmonics as well. Reactions produce inconsistent trends in the harmonics: reactions promote harmonics at a pressure antinode while they damp harmonics at a pressure node.

*Corresponding author: Mario.roa.ctr@us.af.mil
[1]Now at University of St. Thomas, St. Paul, Minnesota

Introduction

Combustion instability associated with liquid rocket engines has been responsible for degradation of engine performance, increase in engine component stresses, and under extreme conditions, catastrophic engine failure. High-frequency instabilities, which are generally the most harmful in liquid rocket engines, can be driven when the disturbances associated with transverse acoustic resonances couple with the combustion process to form a feedback loop. In order to understand and predict combustion instabilities, it is necessary to understand how representative liquid rocket injector flames react to acoustic waves. In general, the thermoacoustic instability phenomenon is understood to be an interaction between acoustic waves and unsteady combustion. The unsteady heat release can amplify the acoustic field if the conditions are favorable. Due to the broadband nature of hydrodynamic instabilities, avoiding a detrimental coupling between acoustics and fluid dynamic mixing is challenging.

One way to try to mitigate the instabilities is to design an injector that does not couple with acoustic perturbation while it still provides the necessary mixing to sustain combustion. One such injector, used extensively for liquid rocket applications, is the shear coaxial injector [1-5]. In this injector configuration liquid oxidizer is injected surrounded by a gaseous fuel, as shown in Figure 1. The aerodynamic interactions at both fluid interfaces bring about hydrodynamic instabilities and atomize the liquid oxidizer into small droplets. These droplets evaporate and mix with the surrounding fuel and react.

There have been many models and efforts [6-9] to describe the atomization process with most being linear in nature and supported with empirical approximations to existing data. The models provide approximate liquid core lengths, time scales associated with growth rates of small disturbance, and droplet sizes and distributions. Due to the highly nonlinear nature of atomization, these models are limited in their range application and do not take reactions and the effects of high pressures into consideration. Accurate predictions of nonlinear, reacting high pressures atomization are left for intense computational studies.

In an effort to further understand high pressure atomization and combustion of a shear coaxial injector, experimental efforts have been carried at academic and national laboratories [10-12]. From these studies, there have been several proposed models of the breakup and dynamics of the liquid core of the shear coaxial injector under relevant rocket engine conditions. One such model is the classical phenomenological break up mod-

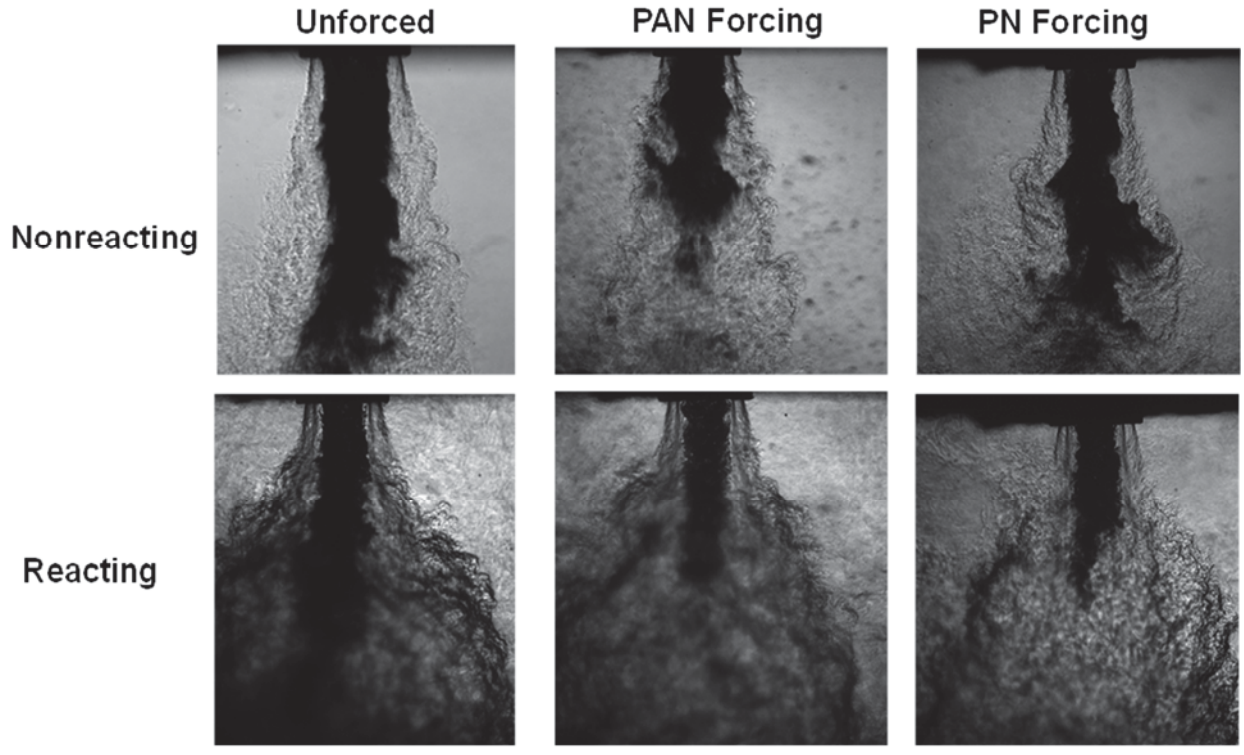

Figure 1. The shear coaxial flow of a LOX center surrounded by gaseous hydrogen. The first row shows the unreacting condition under same acoustic amplitude (0.34 bar) in a PAN and PN configuration. The second row shows the same conditions but reacting.

el by Reitz and Bracco [6]. In this model, the intact liquid core has ligaments and droplets continually shed due to surface instabilities, with the rate of liquid atomization dependent on momentum flux and velocity ratios between the liquid and the gas. This model has been typically used for rocket applications. Experimental and computational results have since raised questions of Reitz and Bracco model on its applicability to coaxial jets at rocket relevant conditions [13-15]. Another model is the core fragmentation model [16] where helical instabilities distort and breakup the liquid core. It is this helical mode that is responsible for some the large scale breakup of the LOX core observed for this investigation.

Since the LOX core has been observed to be the most prominent feature of shear coaxial injectors and with studies suggesting that combustion instabilities couple with LOX-post acoustics [17], an experimental effort was undertaken to study LOX core dynamics and breakup using a shear coaxial configuration subjected to high frequency acoustic forcing. A near field view at the injector exit was studied, limited to 6 LOX diameters, to capture the onset of the LOX core instabilities. The shear coaxial injector was studied both at reacting and nonreacting conditions. High frequency pressure anti-node (PAN) and a pressure node (PN) acoustic forcing was applied at the injector exit. Dynamic mode decomposition (DMD) was used to extract frequencies and spatial modal shape of the LOX response to the acoustic forcing under reacting and nonreacting conditions. There were differences in LOX core convective speeds and LOX core length between the reacting and nonreacting conditions for the acoustically unforced conditions. The LOX core behaved similarly under reacting and nonreacting conditions for the PAN acoustic forcing. A coupling of hydrogen (GH2) and LOX core shear layers occurred and a LOX core helical model was observed for the PN acoustic forcing for both reacting and nonreacting cases.

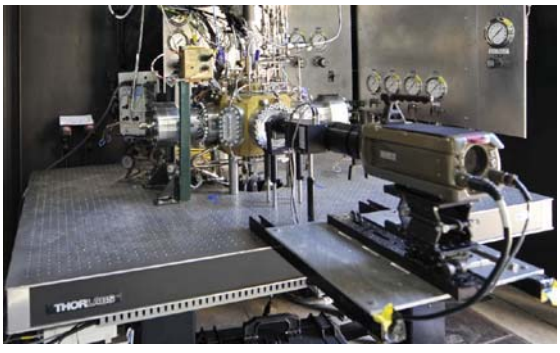

Figure 2. The experimental chamber and high speed camera.

Experimental Setup and Conditions

The experimental facility at the Air Force Research Laboratory (AFRL) at Edwards Air Force Base was used to investigate the coupling of transverse acoustic resonances with a single, shear coaxial, LOX/GH2 flow with varying acoustic perturbation amplitudes. Figure 2 shows the experimental chamber. The features of this facility were documented by Wegener et al. [12]. The injector geometry was the same as studied by Wegener et al [12]. Experiments were done at a mean chamber pressure of 34.45 bars (500 Psia). Nominal flow rates of liquid oxygen and hydrogen were 4.2 and 0.7 g/s, respectively, with a jet momentum ratio (GH2 to LOX) of 2.2. Both fluids had a Reynolds number on the order of 10^4. The LOX core had a Weber number on the order of 10^4. The LOX core was kept at constant temperature of 140 K and the GH2 at 250 K. The transverse acoustic resonance was induced through the use of carefully-controlled piezo-sirens, allowing excitation across a range of pressure amplitudes for discrete resonant chamber frequencies. The amplitude of the acoustic perturbations was varied incrementally from 0 bar (i.e. no acoustic forcing) to 0.34 bar (5 Psi). The pressure fluctuations were measured via Kulite high-speed pressure transducers (model XCL -100) located at different transverse locations, including the middle of the chamber which is the location of the injector. The mode shape of the acoustic field was altered through the phase relationship between the two acoustic drivers. The control of the mode shape allows for the PAN and PN regions of the acoustic mode to be placed at the exit of the injector. Resonant chamber frequencies of 3060Hz for PAN forcing and 2890 Hz for PN were selected. Previous studies on nonreacting experiments have shown a dramatic difference in the coupling mechanism depending on the local acoustic environment [18].

Shadowgraphy was selected as the basis of flow visualization due to the focus on the LOX core dynamic response to the acoustics, while providing an indirect view of the flame through the locations of density variations. A collimated light source and Vision Research v710 Phantom camera were used to acquire the high-speed shadowgraph images. The images were acquired at a 25 kHz frame rate with an exposure of 5 microseconds. The high-speed shadowgraph images were then analyzed using dynamic mode decomposition (DMD), similar to that described by Schmid [19], to identify when and how the LOX core and its shear flow responded to acoustic perturbations with and without heat release.

Results

Figure 1 shows instantaneous shadowgraph images of unforced and acoustically-forced cases under both unreacting and reacting conditions. The presence of the

flame has a dramatic effect on the topology of the LOX surface. For nonreacting, unforced conditions, the interface is highly blurred and appears to be in a fibrous atomization regime, consistent with Farago and Chigier [20] diagram of fiber type of atomization for the given Reynolds and Weber numbers. Evidence of large scale breakup of the LOX core length for the nonreacting and unforced condition, shown on the upper left in Figure 1, is evident 6 diameters away from the exit. Although the breakup is evident, a frequency cannot be determined nor a breakup length since the core extended beyond 6 diameters for the majority of shadowgraph images collected.

The shape of the acoustic forcing is shown in figure 3, with PAN forcing having the maximum pressure oscillations and the PN having the maximum velocity oscillations. For the acoustic forcing conditions, the same blurred and fibrous atomization was observed for both the PAN and PN conditions at the LOX shear layer, but a dramatic reduction of the LOX core length was observed, as shown in Figure 1. Massflow variations were observed of the LOX core subjected to PAN forcing. PN forcing resulted in a helical mode of the LOX core. For the PAN condition, the massflow variations are due to the increase and decrease of back pressure the injector experiences. In the PAN forcing, the shear coaxial flow is subjected to large pressure fluctuations. Using a simple Bernoulli argument, as the back pressure raises there is reduction in mass flowrate out of the injector and as the pressure dips an increase in LOX flowrate is achieved. These pressure fluctuations results in periodic surges of LOX mass flowrates, with large intact LOX fragments shedding away from the main core at the same acoustic forcing of 3060 Hz. For the PN condition the velocity perturbations are at their maximum. These velocity perturbations impart a helical movement on the LOX core given by the wavy or snake-like pattern of the LOX core. This wavy pattern has been reported previously by Boniface et al [10] and Woodward et al [21]. It is this instability that is responsive for the breakup of the LOX core closer to the nozzle exit under PN forcing compared to the acoustically unforced condition.

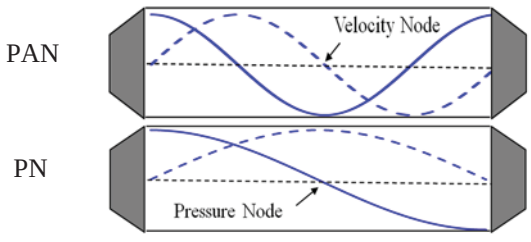

Figure 3. An instant in time of PAN and PN forcing. The solid line is the pressure fluctuations and the dash line is the velocity fluctuations. In PAN forcing, the injector experiences maximum and minimum pressure fluctuations. In PN forcing, the velocity fluctuations are maximum.

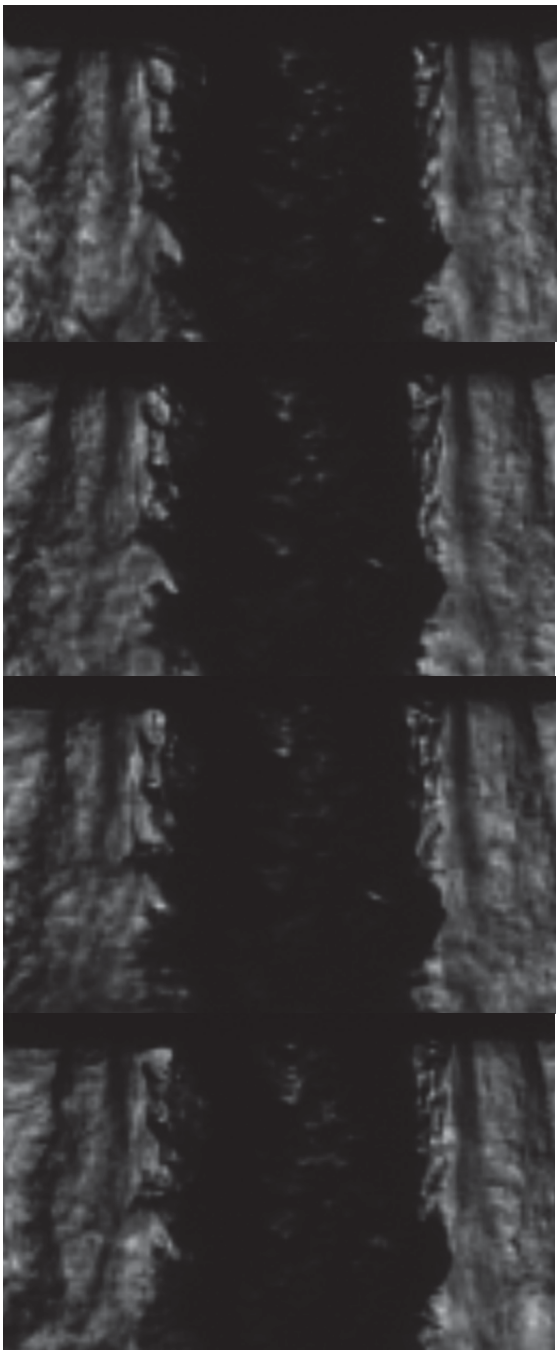

Figure 4. Sequential shadowgraph images demonstrating ligaments being shed off the LOX core for reacting cases. The time step between each image is 0.04 ms.

For the reacting conditions the presence of the flame results in a dramatic reduction in the fibrous nature of the surface, as expected, due to evaporation pro-

cesses as shown in closed up images in figure 4. The presence of the flame also shortens the length of the LOX core, which is again driven in part by the enhanced vaporization regardless of the acoustic forcing. Similarly, an expanded plume exists downstream due to the vaporization and expansion of the LOX, as shown in Figure 1. In the reacting flow cases, small ligaments were observed to be shed off the LOX core near the exit. These small ligaments are then entrained into a recirculation zone established below the LOX post. The ligament shedding close to the nozzle exit can be observed in figure 4, where the sequential images show ligaments on the either side of the LOX core being shed off. These ligaments get entrained into the LOX post recirculation zone if they are shed off within one LOX diameter. If shed past one LOX diameter, the ligaments convect with the rest of the LOX core. Figure 4 also shows an attached flame to inner lip of the GH2 exit.

No local flame extinction was observed regardless of the acoustic forcing amplitude. It has been experimentally observed when the strain rates associated with acoustic forcing is high enough [22], local extinction of the flame and the flame holding regions can occur. The extinction and re-ignition of the flame produces a flow field with uneven heat release that can couple with acoustic forcing, leading to a combustion instability limit cycle. Flame extinction and re-ignition events were not observed for any of the acoustic forcing conditions.

By extracting a column of pixels at each time step along the shear layer edge, dark streaks lines with constant slope represent convecting liquid structures can been seen in figure 5. These dark streaks, which are LOX core structures were observed to be traveling at constant velocity. For the unreacting case with no acoustic forcing, the shear layer between the LOX and the GH2 was approximate to Dimotakis [23] shear layer velocity. In the reacting condition, the shear layer velocity is not constant. Since the flame is attached to inner lip of the GH2 exit, there is a reduction in density between the interface between the LOX core and GH2. This reduced density pulls less on the LOX core, thus

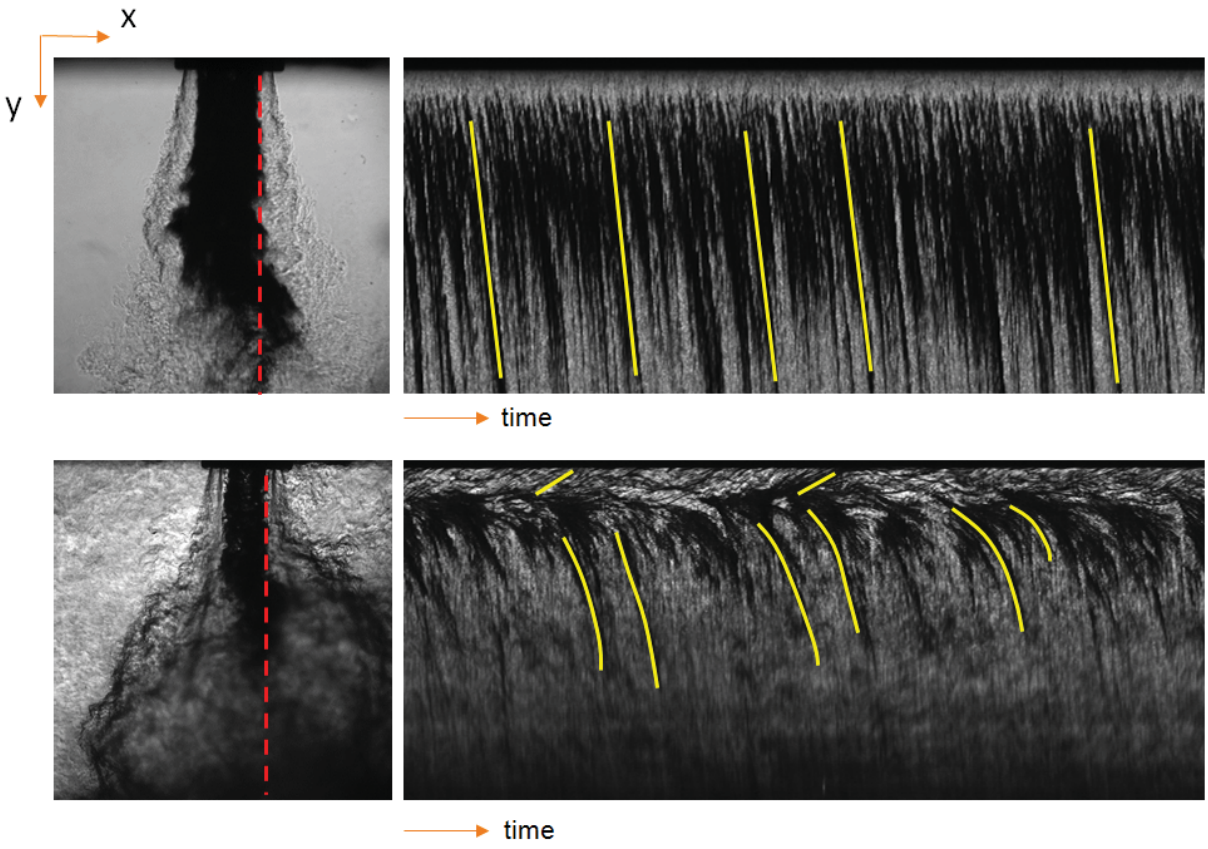

Figure 3. Extracted column of pixels at each time step along shear layer edge as a function of time. The dark streaks, traced with yellow lines, represent convecting liquid structures. The top is the unreacting condition and the bottom is the reacting condition. LOX core structures convect at a constant velocity for the nonreacting, acoustically unforced case. For the reacting condition, the LOX core exits at a low velocity and accelerates after one LOX core diameter away from the exit. The shear layer for the reacting condition never attains the same velocity as the unreacted condition.

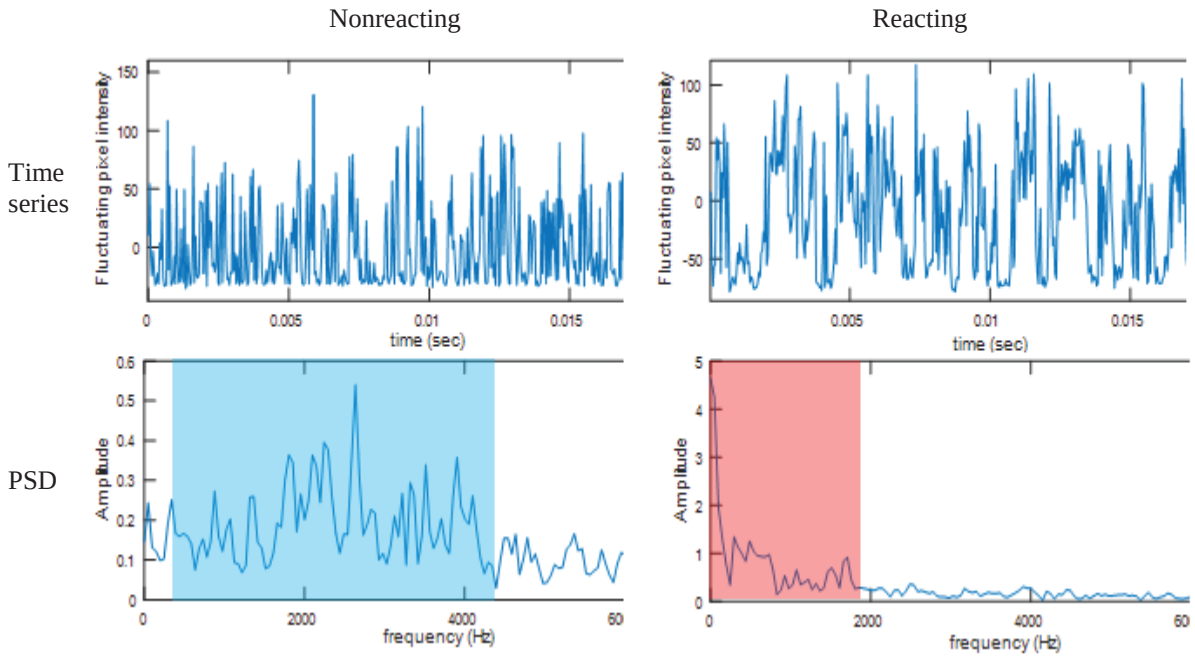

Figure 4. The pixel intensity of a pixel 2 diameters away from the exit along the shear layer, with its corresponding PSD. There is general shift to lower frequencies when the flame is present, consist with linear stability theory.

effectively convects slower compared to the nonreacting LOX core. Beyond the first diameter though, the LOX core starts to accelerate, as shown in figure 5 with the curved dark streaks, but never achieves the same convective velocity as the nonreacting condition. When the acoustic forcing was present the LOX core shape was too distorted to extract velocity information. Figure 5 also shows streaks with opposite flow orientation, illustrating the recirculation of the ligaments that were shed off within the first diameter as demonstrated in figure 4.

Although the trend in spectral content is highly dependent on the specific velocity and heat release profile, the presence of a flame is, in general, expected to result in a stabilizing effect and a shift to lower frequencies (e.g. Mahalingam et al. [24]). Spectral analysis of the measured intensity fluctuations in the near field of the inner shear layer (between the LOX core and GH2) shows there is a general shift of spectral content to lower frequencies when the flame is present. By analyzing the intensity fluctuations at a point 2 diameters away from the nozzle exit along the shear layer and performing a power spectral density, the general shift towards lower spectral content is observed, as shown in figure 6.

Dynamic mode decomposition (DMD) was used to identify the spectral content of both the forced and unforced cases. For the nonreacting case without acoustic perturbations, good agreement was found between the frequency associated with a convective mode and established scaling laws for shear coaxial jets [25]. For the

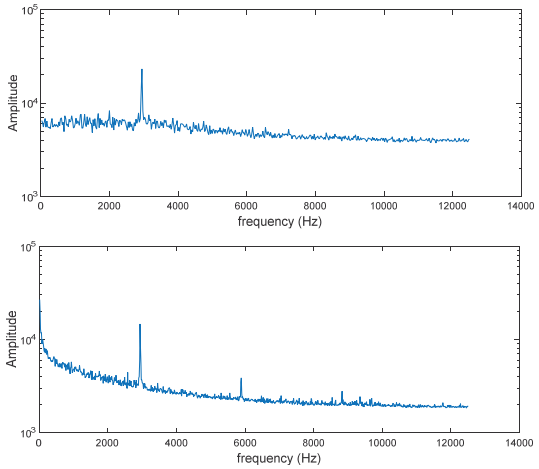

Figure 5. The DMD spectrum for the PAN nonreacting (top) and reacting (bottom) conditions. For the reacting condition, higher harmonics are present in the DMD analysis.

reacting condition without acoustic perturbations, there was no significant dominant mode, although a weak coupling between the inner and outer shear layers was observed at high frequencies.

Figure 7 shows the DMD spectrum for the maximum amplitude forcing condition with the injector placed at the PAN. It is evident from the DMD analysis that physical flow is coupled with the acoustic perturbation at the same driving frequency of 3060Hz. The case shown in figure 7 is for both reacting and nonreacting

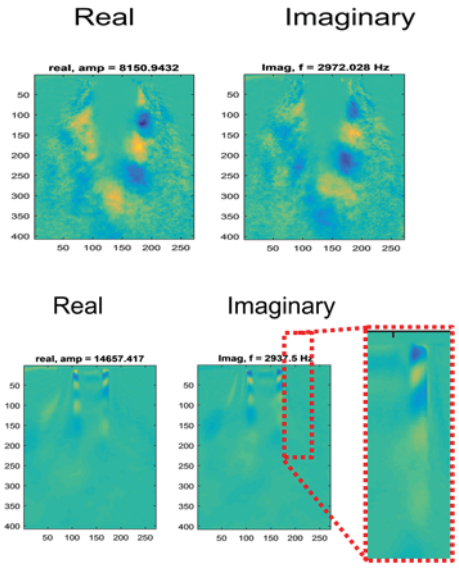

Figure 9. The DMD shape mode of the PAN unreacting (top) and reacting (bottom) condition.

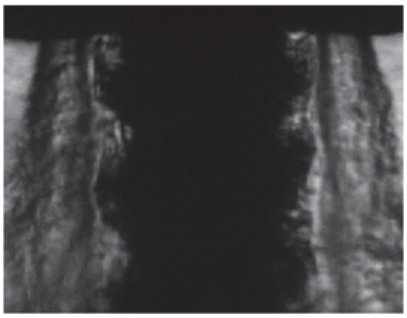

Figure 10. Organized motion of the LOX core under PAN perturbations and reacting.

conditions. The peak-to-peak pressure amplitude for this case was approximately 0.36 bar (5.3 psi). For the reacting condition there is a clear indication of coupling between the acoustics and the inner shear layer instability, including coupling at higher harmonic frequencies, but this coupling is not evident in the nonreacting case. Figure 8 shows the DMD spatial modes. The DMD spatial mode illustrates a symmetric shear layer response of the LOX core, as indicated by the axially aligned positive (yellow) and negative (blue) intensity fluctuations in the DMD spatial mode shapes. This symmetry is expected as the mechanism that is associated with PAN forcing relates to azimuthally-coherent mass flow fluctuations in the LOX core flow as discussed earlier. Although the LOX core response is symmetric, the scales of the axisymmetric structures are not the same. For the reacting case these structures are smaller compared to the nonreacting condition shown in Figure 1. Figure 10 shows a shadowgraph image of

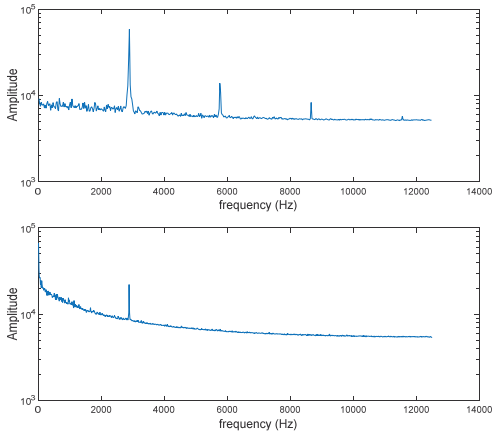

Figure 11. The DMD spectrum for the PN nonreacting (top)and reacting conditions (bottom). For the unreacting condition, higher harmonics are present in the DMD analysis.

the injector near field, and a vertical row of shear layer structures can be seen at the LOX core boundary. These structures are thought to be smaller because the LOX core velocity is slower compared to the nonreacting case, resulting in reduced massflow variations. The LOX core also experiences roll-up motion that is in the opposite direction then would be expected based on the presence of the high-speed GH2 flow. The LOX core rollup travels upstream, opposite of the both the GH2 and LOX core flow, into the wake and recirculation region underneath the LOX post. The observed vorticity orientation suggests the inner shear layer is interacting with the LOX post's low-speed wake region. The combination of the reduced interfacial density, as discussed earlier, and the low-speed wake region effectively slows the LOX core resulting in a decrease in massflow variations subjected PAN forcing. The PAN interactions are first detected when the acoustic perturbation amplitude is approximately 0.13 bar (2 psi). The coherent organized motion, shown in figure 10, at the surface of the LOX core is also first observed at this amplitude.

Figure 11 shows the DMD spectrum for the maximum forcing amplitude PN forcing, similar to figure 7. Similar to the PAN condition, a coupling of the shear layers at a frequency of 2890 Hz was observed for the PN acoustic forcing. There is a reversal of the harmonics detected for the nonreacting and reacting conditions. For the nonreacting condition subjected to PN forcing higher harmonics are detected. The higher harmonics are dampen for the reacting condition. This results is opposite of the PAN results. Figure 12 shows the DMD spatial modes associated with the peak frequencies in figure 11. In the figure 12, the large alternating blue and yellow pattern shows a helical mode excitation of the LOX core when perturbed by PN forcing. A coupling between the inner and outer shear layers, as observed

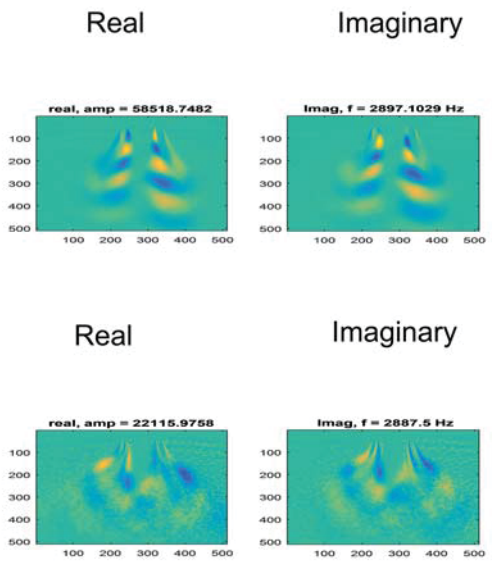

Figure 12. The DMD shape mode of the PN nonreacting (top) and reacting (bottom) condition.

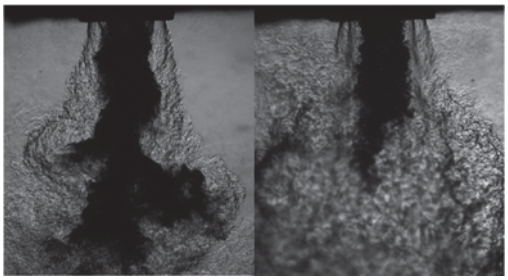

Figure 13. Full field images of the nonreacting (left) and reacting (right) PN forced condition. For the reacting condition there is very little LOX core motion.

by Dahm et al [26], is present when the flow is unreacting, with the LOX core shear layer dominating. The slim alternating blue and yellow streaks to either side of the LOX core illustrate the coupling of GH2 shear layer to the LOX core shear layer. This coupling between the inner and outer shear layer was not observed for PAN conditions when no reaction was present. A coupling was observed when a flame was present. For the reacting condition, an anti-symmetric structure with coherent coupling between the outer and inner shear layers was present.

Figure 13 shows side by side images of the nonreacing and reacting PN forced conditions. For the nonreacting condition, the LOX core responses dramatically to the PN forcing and a helical mode is observed in figure 13. For the reacting condition, the LOX core is slow to respond to the PN forcing. It was observed that GH2 shear layer was in phase with acoustic forcing and LOX core was out of phase with the respect to the incoming acoustic wave. From figure 13 the helical shape of the nonreacting LOX core begins close to the nozzle exit, unlike reacting condition where helical turning starts further away from the nozzle exit compared to nonreacting case. It is believed that the anchored flame at the exit of the nozzle dampens the velocity perturbation at the nozzle exit for the PN forcing, but not for the pressure perturbations in the PAN conditions. The higher harmonics are believed to be dampen because of the LOX core delayed reaction to PN perturbations and the helical shape is not as pronounced under reacting conditions.

Conclusion

The near field of shear LOX/GH2 coaxial flow was investigated under relevant rocket conditions; both reacting and nonreacting conditions were subjected to acoustic forcing. Under reacting conditions, the rapid expansion and vaporization of the LOX core caused an expanded plume that was presented for all acoustic forcing conditions. A LOX recirculation zone was present downstream of the LOX post. In the reacting condition, ligaments where shed off from the LOX core and entrained into the LOX post recirculation zone. Flame holding was established at the inner lip of the GH2 exit. Convective velocities of the LOX core were constant under nonreacting conditions but not in the reacting conditions, where the flow started at a slow speed and gradually accelerated. A shift of spectral content to lower frequencies occurred when a flame was present.

Dynamic mode decomposition captured the physical response of the LOX core under different acoustic forcing. For PAN forcing the LOX core experienced variations of the mass flowrates for both nonreacting and reacting conditions, but the liquid structures differed greatly in size. For PN forcing the nonreating case, a LOX core helical mode was present and the inner outer shear layer coupled together. For the reacting case, the LOX core response was out of phase with respect to the acoustic forcing. Given the physical differences and responses of the nonreacting flows compared to the reacting flows to low amplitude, high frequency acoustic perturbation, it is vital these differences be understood to better control combustion instabilities.

Nomenclature

DMD	Dynamic mode decomposition
GH2	Gaseous Hydrogen
LOX	Liquid Oxygen
PAN	Pressure Anti-node
PN	Pressure Node

Acknowledgements

This work was funded by Airforce Office of Scientific Research.

References

1. Juniper, M.P., and Candel, S.M., *Journal of Fluid Mechanics* 482:257-269 (2003)
2. Hakim, L., Schmitt, T., Ducruix, S., and Candel, S., *Combustion and Flame* 162:3482-3502 (2015)
3. Ibraim, E.A., Kenny, R.J., and Walker, N.B., 42nd *AIAA/ASME/SAE/ASEE/ Joint Propulsion Conference*, Sacramento, Ca, USA, July 2006
4. Puissant, C., and Glogowski, M.J., *Atomization and Sprays* 7:467-478 (1997)
5. Yang, V., and Anderson, W., *Liquid Rocket Engine Combustion Instability*, American Institute of Aeronautics and Astronautics, Inc. 1995, p. 46.
6. Reitz, R.D., and Bracco, F. V., *Physics of Fluids* 25:1730-1742 (1982)
7. Lin, S.P., and Lian, Z.W., *AIAA Journal* 28:120-126 (1990)
8. Mohanta, L., Cheung, F., and Bajorek, S.M., *Physica A*443:333-346 (2016)
9. Lin, S.P., and Ibrahim, E.A., *Journal of Fluid Mechanics* 218:641-658 (1990)
10. Boniface, Y., Reeb, A., Woodard, R., Pal, S., and Santoro, R. J., *Proceedings of the 11th Annual PERC Symposium on Propulsion*,University Park, PA, USA, November 1999,. pp 110-119
11. Pal, S., Moser, M.D., Ryan, H.M., Foust, M.J., and Santoro, R.J., *Atomization and Sprays* 6:227-244 (1996)
12. Wegener, J.L., Leyva, I.A., Forliti, D.J., and Talley, D.G., *52nd AIAA Aerospace Sciences Meeting*, National Harbor, MD, USA, January 2014
13. Oefelein, J.C., and Yang, V., *Journal of Propulsion and Power*, (14): 843-857 (1998)
14. Yang, V., *Symposium (International) on Combustion*, (28) :925-941 (2000)
15. Zong, N., and Yang, V., C*ombustion Science and Technology*, (178): 193-227 (2006)
16. Andrews, M. J., *Atomization and Sprays* 3:29-54 (1993)
17. Locke, J.M., Pal, S, Woodard, R.D., and Santoro R.J, 46th *AIAA/ASME/SAE/ASEE/ Joint Propulsion Conference*, Nashville, TN, USA, July 2010
18. Forliti, D.J., Badakhshan, A., Wegener, J.L., Leyva, I.A., and Talley, D.G *53rd AIAA Aerospace Sciences Meeting*, Kissimmee, FL, USA January 2015.
19. Schmid, P. J., *Journal of Fluid Mechanics* (656):5-28 (2010)
20. Farago, Z., and Chigier, N., *Atomization and Sprays* 2:137-153 (1992)
21. Woodard, R.D, Pal, S., Farhangi, S., and Santoro, R.J., 42nd *AIAA/ASME/SAE/ASEE/ Joint Propulsion Conference*, Reno, NV, USA, January 2001
22. Chaouki, G, Smith, O. I., and Karagozain, A. R,. 39th *AIAA Aerospace Science Meeting S*acramento, Ca, USA, July 2006
23. Dimotakis, P.E., *Am. Inst. Aeronaut. Astronaut. J.* 24(11):1791-1796
24. Mahalingam, S., Cantwell, B.J. and Ferziger. J.H., *Physics of Fluids A: Fluid Dynamics* (3):1533-1543 (1991)
25. Schumaker, S, A., *An experimental investigation of reacting and nonreacting coaxial jet mixing in laboratory rocket engine*, Thesis, (2009)
26. Dahm, W.J.A, Frieler, C.E. and Tryggvason, G., *J. Fluid Mech*.(241):371-402 (1992)

This Page Intentionally Left Blank

Propulsion and Energy Forum
July 25-27, 2016, Salt Lake City, UT
52nd AIAA/SAE/ASEE Joint Propulsion Conference

Cryogenic Impinging Jets Subjected to High Frequency Transverse Acoustic Forcing in a High Pressure Environment

Mario Roa[1]
Sierra Lobo, Inc. Air Force Research Laboratory, Building 8451, Edwards AFB, CA, 93524

S. Alexander Schumaker[2] and Douglas G. Talley[3]
Air Force Research Laboratory, Building 8451, Edwards AFB, CA, 93524

An experimental study has been conducted to explore the coupling between the impact waves created by impinging jets and high frequency acoustic pressure perturbations. High speed, backlit imaging was used to capture the physical response of impact waves present on impingement sheet formed by two like on like impinging jets. Dynamic mode decomposition was used to extract the natural frequencies of impact waves and isolate the spatial structures response present on the impingement sheet due to the transverse acoustic forcing. Chamber pressure and jet velocity were varied until impact waves became visually prominent. After impact waves became visually prominent, the impingement sheet was subjected to incremental pressure amplitudes in a pressure anti-node (PAN) and pressure node (PN) configurations. The results indicate that impact waves appear to vanish once a certain pressure amplitude is reached. When subjected to PAN forcing the impingement sheet size grows and decays and in-plane flapping is generated under a PN forcing.

Nomenclature

DMD	=	Dynamic Mode Decomposition
PAN	=	Pressure Anti-Node
PN	=	Pressure Node

I. Introduction

Impinging jet injectors are one of the many injectors type used for liquid propellant atomization in rocket engines[1-2]. Liquid rocket engines like the F-1 have successfully used like-on-like impinging jet injectors and are a preferred injector type for hypergolic and gelled-propellants[3-4]. Figure 1 shows a schematic of the flow field formed by a like-on-like impinging jets injector. In Figure 1 two cylindrical liquid jets strike each other at an angle 2Θ and form an impingement sheet. Impact waves or surface waves travel along the surface of the impingement sheet, detach, and form ligaments and droplets. These injectors are favored due to inherently simple design, potential high flow rate operation, and low manufacturing costs[1-2]. Although great operation success has been achieved with like on like impinging injectors, they do suffer from some major drawbacks. One such drawback is the high machining tolerance needed for like-on-like impingement of the two cylindrical jets. Another drawback, perhaps the most critical, is that rocket engine using impinging jets sacrifice performance in order to achieve an acceptable level of high frequency combustion instability[1].

[1]Research Scientist, Sierra Lobo, Inc. 10 E. Saturn Blvd, Building 8451, Edwards, CA 93524, Member
[2]Research Engineer, AFRL/RQRC., 10 E. Saturn Blvd, Building 8451, Edwards, CA 93524, Senior Member
[3]Lead, Combustion Dynamic Group, AFRL/RQRC., 10 E. Saturn Blvd, Building 8451, Edwards, CA 93524, Associate Fellow

Extensive experimental and theoretical studies have been performed on understanding the spray characteristics of these injectors, with particular attention given to the shape of the impingement sheet, the breakup length of liquid impingement sheet, and mean droplet size and distribution[4-8]. It has been well documented that the impingement sheet shows several physical characteristics depending on the operating Reynolds and Weber number[5, 9]. These physical characteristics or modes of the impingement sheet are: closed-rim, open-rim, and fully developed. Transition to either of these modes is dependent on jet velocity. Present on these modes are unstable hydrodynamic waves usually referred to as impact waves. It is theorized that these impact waves are the dominant mechanism in the impingement sheet breakup and atomization.

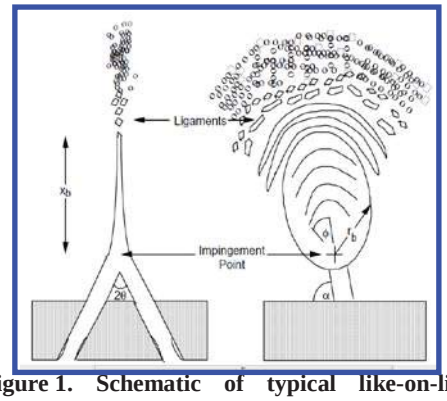

Figure 1. Schematic of typical like-on-like impinging jet injector. Figure is reproduced from Anderson[9].

Heidmann *et al*[4] and Dombrowski *et al*[5] performed extensive studies on impinging jets under atmospheric conditions. From these studies, two mechanisms were identified as the responsible mechanism to impingement sheet breakup. One mechanism is the superposition of aerodynamic waves. The second is when waves are produced at the point of impingement, which results in ripples[8] emanating from this point. These ripples are referred to as impact waves. Impact waves were observed even in near vacuum conditions and exhibit nonlinear behavior that cannot be fully predicted by linear stability theory. Heidmann *et al* arrived at these two breakup mechanisms by systemically studying the effect of orifice diameter, jet velocity, impingement angle, pre-impingement length, and jet viscosity by using different liquid combinations of glycerol and water. Heidmann *et al* concluded that jet velocity was the parameter of choice to describe the spray structures produced by the impinging jets. Guided by Heidmann *et al* results, Dombrowski *et al* studied the disintegrations of the impingement sheet. Their results show that the disintegration of the impingement sheet usually resulted from the formation of unstable waves, either aerodynamic or hydrodynamic in origin. Their results indicate there is a transition to when impact waves control breakup of the impingement sheet. This transition occurs when the liquid jets are above a critical Weber number. This critical Weber number when impact waves start to appear lies between 65 and 165[5, 9], defined as We $=\frac{\rho v^2 D}{\sigma}$, where ρ is the jet density, v is the jet velocity, D the jet diameter, and σ is the surface tension. It should be noted that Dombrowski *et al* results are dependent on the jets being either laminar or turbulent.

Anderson *et al*[10] performed experiments on impinging jets using water at atmospheric conditions to characterize the effect of impact waves on the atomization process. Anderson *et al* measured atomization frequency from the impingement sheet using high-speed videos. They did this by monitoring a fixed point in the high speed videos and checking if ligaments and droplets passed through. They discovered that impact waves are formed with a characteristic wavelength of about one jet diameter. The experimental results also suggested that impact waves seem to dominate the atomization process over most of the conditions relevant to rocket engines and are responsible for the atomization frequency. Although, these observations was made only when jet velocities were low. Anderson *et al* also reported that the experimental results are dependent if the jets are laminar or turbulent, similar to Dombrowski *et al*.

Chen *et al*[10] performed a numerical study on the physical mechanism of impact waves and mixing process, and atomization of impinging jets. Chen *et al* carried out his numerical studies by varying Reynolds number, surface tension, and impingement sheet thickness. Chen *et al* concluded that impact waves form when the impinging jets have a Strouhal value of 0.86. Their results show that impact waves are caused by the interfacial shear stress which form capillary waves on the either side of the impingement sheet.

A single like-on-like impinging jet injector, machined at relevant dimensions for liquid rockets engines, was studied under acoustic perturbations. Cryogenic nitrogen was used as the working fluid. The study focused on identifying the conditions when visibly impact waves were formed by the like-on-like injector at elevated pressures. After identifying where the impact waves were easily identified, dynamic mode decomposition (DMD) was used to extract the natural frequency associated with the impact waves. The same condition was then subjected to high frequency acoustic forcing with incremental pressure amplitudes in both the PAN and PN configurations. High speed backlit imaging was used to capture the effect of acoustic forcing has on the impact waves. DMD analysis was performed to identify the dominate mode frequencies and structures.

II. Experimental Set-up and Methods

The experiment was performed at Air Force Research Laboratory (AFRL), Edwards. A schematic of the experimental facility can be found in previous research conducted using shear coaxial injectors[12-13]. The same windowed pressure chamber from the previous shear coaxial injector studies was used for these studies. The impingement jet injector was manufacture as a cap disk that attaches to small reservoir. High machining tolerances were kept on the cap to ensure proper jet impingement. A drawing of the cap and reservoir is shown in Figure 2. The natural acoustic frequencies of the reservoir are 16 kHz longitudinally and 35 kHz radially, both are higher than the forcing frequencies that were used for these studies. The impinging jet injector selected for this study has a jet diameter of 0.5 mm (0.02 in) with a half angle between exit holes of 30 degrees. Cryogenic nitrogen was used as the working fluid. The injector has a flow passage length of l/d of 8 within the injector. After exiting the injector, the fluid travels a pre-impingement length of 2.3 jet diameters. The jet velocity was controlled by varying the mass flow rate fed into the reservoir. A Porter mass flow meter (model 123-DKASVDAA) was used to measure the gaseous nitrogen flow. The gaseous nitrogen then traveled to a liquid nitrogen heat exchanger, where the gaseous nitrogen was converted to liquid nitrogen before entering the injector. An E type thermocouple on a piezo-electric translating stage (AttoCube ANS Scanners) was used to measure the temperature of the liquid impingement sheet prior to testing to ensure the temperature of the liquid nitrogen emerging from the injector was at steady state condition. A xenon arc lamp was used to provide the illumination for the back lit images. A high speed Phantom v710 CMOS camera, set at 25 kHz frame rate, was used to capture impact waves from the impingement sheet.

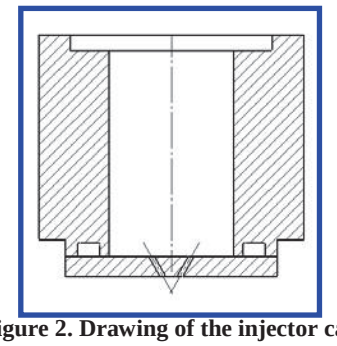

Figure 2. Drawing of the injector cap attached to the liquid nitrogen feed reservoir.

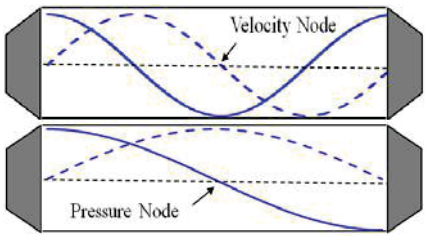

Figure 3. An instant in time of PAN and PN forcing. The solid line is the pressure fluctuations and the dash line is the velocity fluctuations. In PAN forcing, the injector experiences maximum and minimum pressure fluctuations. In PN forcing, the velocity fluctuations are maximum.

The acoustic waves used for the acoustic forcing portion of the study were generated by a Fluke 292 arbitrary waveform generator. The signal generator was then fed to two Trek PZD2000A high-voltage amplifiers that drove two piezo-sirens and generate a standing wave. The impingement sheet was then subjected to the acoustic forcing from the piezo-sirens tuned to the resonance chamber frequency for a PAN or PN configuration. Both the PAN and PN where centered at the middle of the impingement sheet. The shape of the PAN and PN forcing and be seen in Figure 3. For PAN forcing the pressure fluctuations are maximum and the velocity fluctuations are maximum for the PN forcing. Three differential pressure transducers (Kulite CCQ-093) were used to measure both the shape and amplitude of the acoustic forcing to ensure that a PAN and PN was achieved for each test condition. The chamber resonance for the PAN configuration was measured and driven at 2950 Hz and 3110 Hz for the PN. The impingement sheet was then subjected to incremental pressure amplitudes and the physical response was then visually recorded with the high speed camera. Dynamic mode decomposition (DMD), as outlined by Peter Schmid[14], was then used to extract the natural frequency of the impact waves in the unforced and forced conditions and their corresponding spatial response and structures.

III. Results

A. Velocity and Chamber Pressure Parametric Sweeps

For the first portion of the experiment, both jet velocity and chamber pressure were varied until visible impact waves became prominent on the impingement sheet. Impact waves appeared in a narrow range of conditions. Impact waves were observed at low jet velocities within the range of 2 to 5 m/s and at a chamber pressure of 1 to 1.37 MPa (150 to 200 PSIA) corresponding to jet Reynolds numbers of 7000 to 20000 and Weber numbers of 220 to 760, respectively. Figure 4 shows the spray formed by the impinging jets at several test conditions. Each column in Figure 4 corresponds to the same jet velocity of 5, 7, and 10 m/s. The first row in Figure 4 is at a chamber pressure

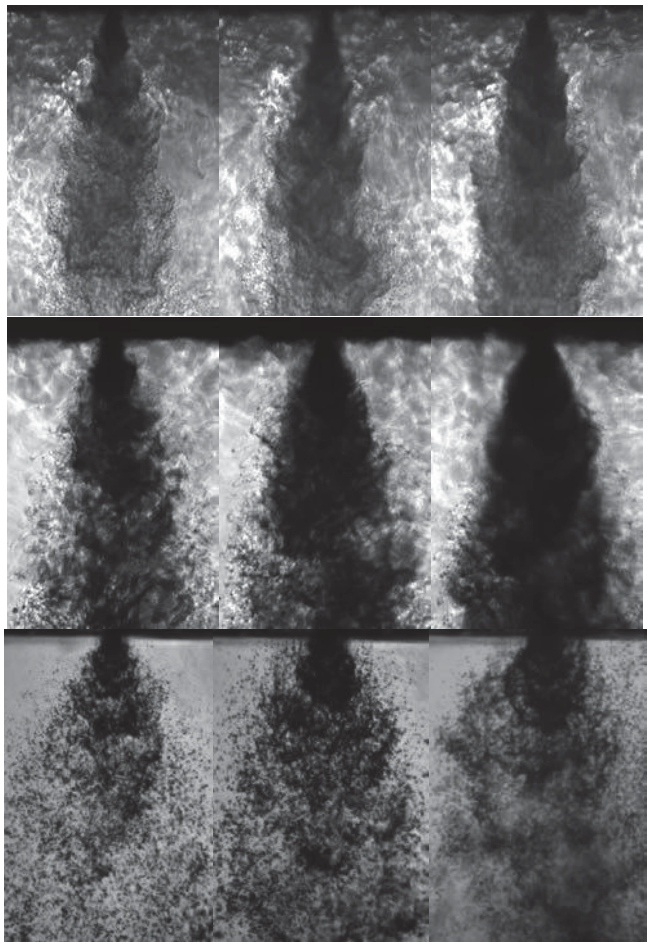

Figure 4. The spray formed by the impinging jets. Each column the jet velocity if the same of 5, 7, and 10 m/s. The first row of images was taken at a supercritical chamber pressure of 4.8 MPa (700 Psia), the second and third row at subcritical pressures of 2.5 MPa (375 Psia) and 1.37 MPa (200 Psia).

of 4.8 MPa (700Psia), above the supercritical pressure of nitrogen of 3.39 MPa (492 PSIA). The middle row and third row were taken at a subcritical chamber pressures of 2.5 MPa (375 PSIA) and 1.37 MPa (200 PSIA), respectively. At the supercritical chamber pressure a fine mist was formed regardless of the jet velocity and no evidence of impact waves was observed. As the chamber pressure is reduced to subcritical conditions, droplets and ligaments were observed to be shed off from the impingement sheet. No such identifiable droplets or ligaments were observed in the supercritical condition. As the jet velocity was increased for subcritical chamber pressure of 2.5 MPa, finer droplets were formed and eventually a dense mist was observed. A similar behavior was observed for the 1.37 MPa chamber pressure condition, but a dense mist similar to the 2.5 MPa and 10 m/s condition was never observed. It is apparent from these instantaneous images that there are different regimes of atomization for impinging jets which are dependent on several factors. At the supercritical condition it is possible that the aerodynamic forces on the cylindrical jets promptly atomize and form a fine mist or at these conditions the injection can no longer be regarded as an atomization or spray formation process. Further work will be require to understand how the interface between the low temperature jet and the supercritical nitrogen play a role, since the Weber number at these conditions approaches infinity and the mist formed is not as dense as the subcritical cases. At the subcritical conditions, chamber pressure or density ratio of the jet and the chamber gas plays a large role in promptly atomizing the impingement sheet, since it is evident that mist is formed at 10 m/s for the 2.5 MPa chamber pressure condition and not 1.37 MPa.

For the higher chamber pressure conditions above 1.4 MPa no discernible impact waves or frequencies were detected. It was only when the jet velocities were at 5 m/s and below and at 1.37MPa and below chamber pressures did impact waves became visually prominent. Figure 5 shows impact waves originating from the impingement point for the subcritical chamber pressures of 1 and 1.37 MPa at a constant jet velocity of 2 m/s. Similar to the higher jet velocity conditions, as the chamber pressure is increased, evidence of impact wave structures on the impingement sheet breaks down and a dense mist is formed. It was also observed that there was lack of structure at the lower chamber pressures, evident in the lowest chamber pressure shown in Figure 5. From low jet velocity conditions, chamber pressures between 1 and 1.37 MPa produced the most prominent impact waves, particularly at 1 MPa shown in Figure 5. Although from Figure 5 the chamber pressure condition at 1 MPa shows evidence of impact wave atomization, the chamber pressure of 1.37 MPa was selected for further analysis with a constant jet velocity at 2 m/s. Based on the jet diameter the jet Reynolds number was 7800 and a jet Weber of 270, meeting the critical Weber number criteria calculated by Heidmann *et al*. The jet exit temperature was kept at a constant 95 K.

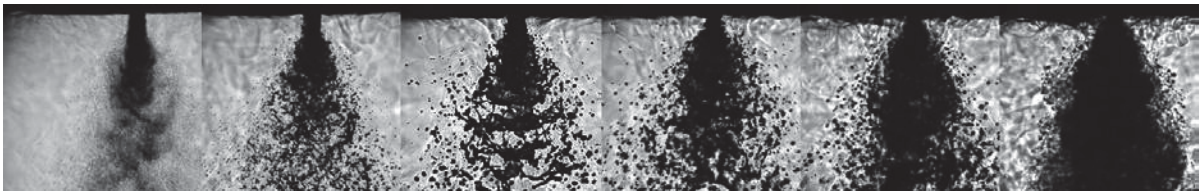

Figure 5. Instantaneous images of the flow field of the impingement sheet at a constant jet velocity of 2 m/s and increasing chamber pressure. From left to right the chamber pressure if 0.34, 0.68, 1, 1.37, 2.06, 2.75 MPa. A density ratio of jet over chamber of 165, 78, 53, 38, 25, 19.

B. Acoustic Forcing Results

Figure 6 is an instantaneous image of the impingement sheet without any acoustic forcing for a chamber pressure of 1.37 MPa and a jet velocity of 2 m/s. The impact waves and subsequent ligaments formed are shown to be emanating from the impingement sheet. This condition, with no acoustic forcing, served as a reference to compare to the acoustic forcing conditions. Dynamic mode decomposition was used to extract the natural frequencies of the impact waves emanating from the impingement sheet. The DMD analysis was apply to red square section shown in Figure 6. The DMD amplitude spectrum is shown below in Figure 7. Although no dominant mode was detected by the DMD analysis, the natural frequency of the corresponding to impact waves was measured to 4822 Hz, based on visually inspecting the spatial DMD modes.

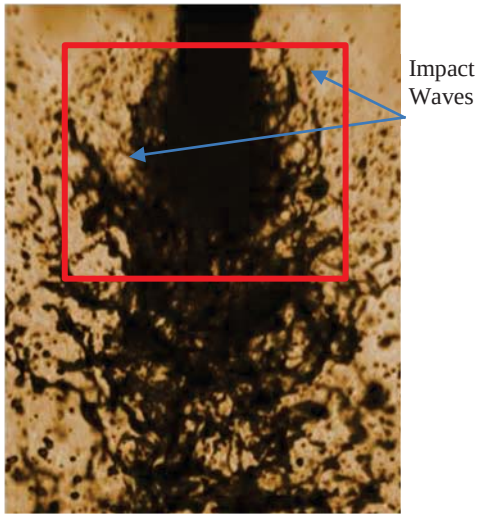

Figure 6. Instantaneous image of the impingement with impact waves emanating from the impingement sheet.

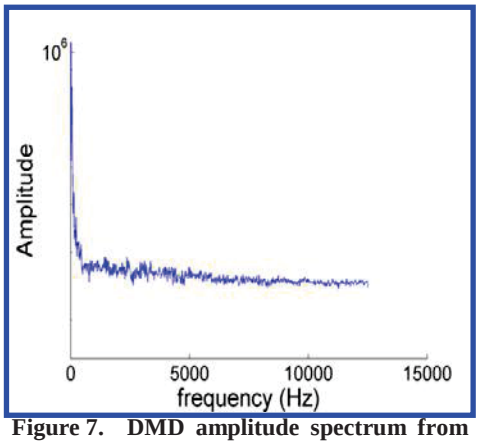

Figure 7. DMD amplitude spectrum from the no forcing base condition.

The DMD spatial mode corresponding to the impact waves for the base condition is shown in Figure 8. The alternating red and blue bands correspond to light intensity fluctuations due to dark liquid nitrogen impact waves passing on the exterior of the impingement sheet. It is currently suspected that variations in the impact wave's convective speeds or droplets shed along the exterior of the impingement sheet dampen the spectral content associated with impact waves and hence weak spectral frequency is picked up by the DMD analysis. The impact wave velocity is suspected because based on the high speed images, impact wave's velocity decelerates the further away they are from

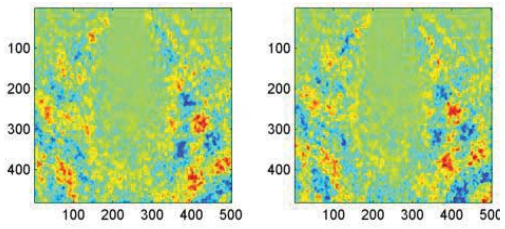

a) b)

Figure 8. DMD spatial for the base condition at 4822Hz. a) is the real portion and b) is the imaginary portion.

the impingement point. There is also a great degree of variation as to when the impact wave detach from the impingement sheet and is shed as ligaments. This variation of the breakup length of the impingement sheet seems to affect the impact wave velocity. A similar observation was made by Heidmann *et al* depending if the impingement sheet was closed or open rim. Heidmann *et al* also made an observation that the breakup length of the impingement sheet had a large variation in the fully develop mode and that the breakup length cannot be measured with any certainty. Similar mechanisms are likely responsible for the weak DMD amplitude of the impact waves since the impingement sheet in Figure 7 is in the fully developed regime, although further study will be needed to address the weak spectral strength.

Table 1 shows the acoustic test conditions with the pressure amplitude (P') the impingement sheet was subjected. Table 1 also has P' normalized to the dynamic pressure of the jets. For the PAN conditions, a total of 5 conditions were tested and a total of 4 conditions were tested for the PN configurations. For the PAN conditions, at the low P' (PAN 1 condition) acoustic forcing, the impingement sheet doesn't couple with the acoustic forcing. As P' is increased, the impingement sheet starts to couple with the acoustic forcing. This transition can be observed in the DMD amplitude spectrum shown in Figure 9. The corresponding DMD spatial mode is also shown. From Figure 9, PAN 1 condition is relatively unchanged when subjected to low P' PAN acoustic forcing. The DMD amplitude spectrum appears similar to the based unforced condition shown in Figure 7. The DMD spatial mode in Figure 9a also appears similar to the Figure 8 with the wave like pattern. Both PAN and the base condition have similar frequencies associated with the wave like pattern with frequencies of 4730 Hz and 4822 Hz, respectively, indicating this low level of acoustic forcing has little influence the dynamics of the impingement sheet and the frequency of the impact waves. The transition to where the impingement sheet couples with the acoustic forcing can be readily seen in the PAN 2 condition. Figure 9b shows the DMD amplitude spectrum with a peak centered at 2957 Hz, close to the acoustic forcing frequency of 2950 Hz. The DMD spatial mode, shown in Figure 9b, also demonstrates the transition with the impingement sheet. The alternating red and blue bands have grown larger and across the entire impingement sheet. This is different when from the base condition having the alternating bands only on exterior of the impingement sheet. What this transition seems to indicate that there is a coupling between the injector mass flow rate and the acoustic field. The impingement sheet under goes a surge of mass flow when the PAN forcing dips in the negative direction due to its sinusoid nature, it results in a temporally larger differential pressure This localized larger pressure differential drives a larger volume of mass flow through the injector. The impingement sheet also contracts in size when the PAN forcing is at its greatest and resulting in a small differential pressure between chamber and injector, thus restricting mass flow.

Table 1. Acoustic Test conditions with relevant parameters.

	No Forcing	**PAN 1**	**PAN 2**	**PAN 3**	**PAN 4**	**PAN 5**	**PN 1**	**PN 2**	**PN 3**	**PN 4**
P'(Psi)	0	1.75	2.97	4.5	6.6	11	1.5	2.7	6.2	7.6
$P'/\frac{1}{2}\rho u^2$	0	9.13	15.52	23.4	34.3	58.1	9.13	15.52	37.6	40

This coupling effect can be readily noticed for the PAN 5 condition, where the impingement sheet has fully coupled with the acoustic forcing. Both the DMD amplitude spectrum and spatial mode are shown in Figure 10. A strong peak centered at 2925 Hz, within less than 1% error of the acoustic forcing frequency of 2950Hz, is readily noticeable in Figure 10a, along with a higher harmonic. In Figure 10b demonstrates the large physical expansion and contraction of the impingement sheet, due to the surges of mass flow rates the injector is experiencing. It is at this condition that no traces of the impact waves were readily visible. Instead, what was observed was a large group of droplets shedding at the acoustic forcing frequency from the impingement sheet. This is indicative of a klystron effect, where faster moving fluid particles overtake slower liquid particles. This event is captured in the phase average images shown in Figure 11. The phased average images were false colored to best demonstrate both large group of droplets being shed and the klystron effect. As the pressure increases locally below the injector, there is a temporarily reduction in mass flow and jet velocity, afterwards the liquid jets

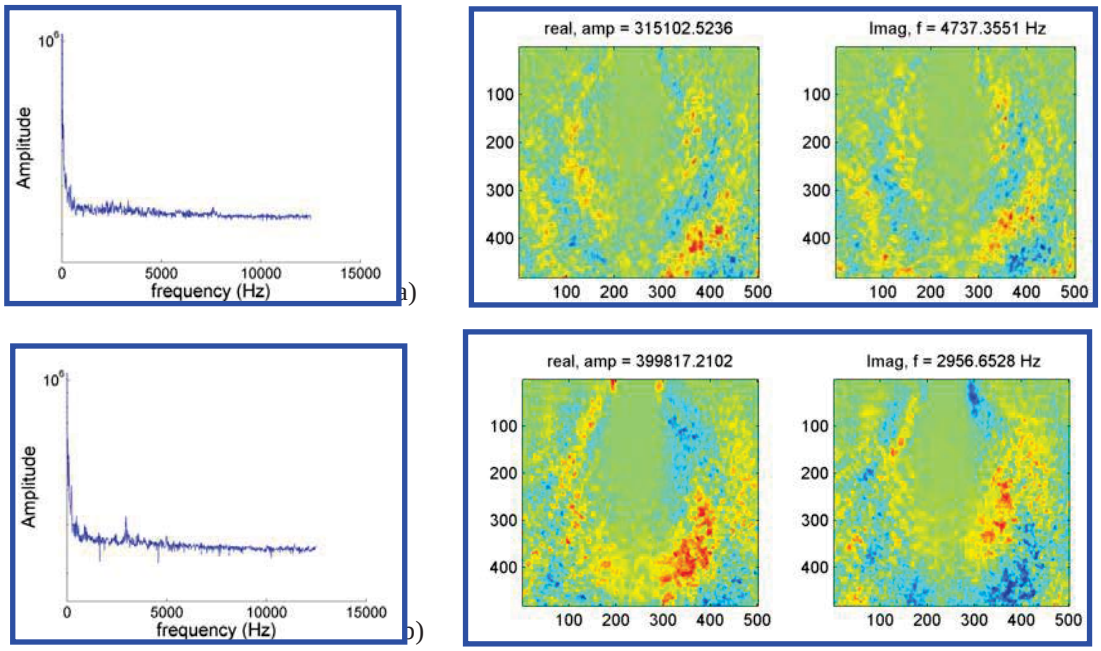

Figure 9. The DMD amplitude spectrum with the corresponding spatial mode. A) is the DMD amplitude spectrum and spatial mode for PAN 1 condition. B) is the DMD amplitude spectrum and spatial mode for PAN 2 condition.

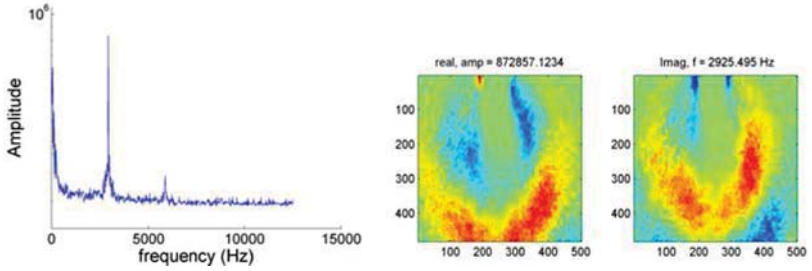

Figure 10. DMD output for PAN 5. A) is the DMD amplitude spectrum and b) is the corresponding spatial mode of 2925 Hz.

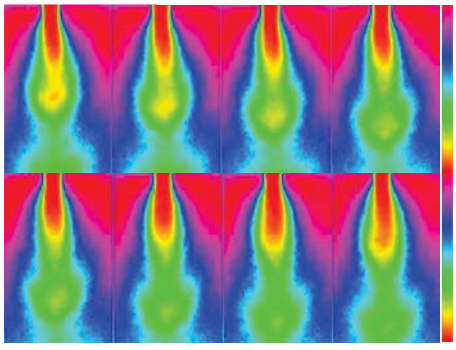

Figure 11. False colored, phased average images of the PAN 5 condition. A large small of liquid nitrogen is shown being shed off.

surge when the pressure amplitude dips. This dip in pressure temporally increases both the mass flow and jet velocity. This also gives the instantaneous images a "Christmas tree[15]" appearance (Appendix A). It is after when the pressure dips that the impingement sheet is observed to expand to its maximum width and shed large group of droplets. It is this condition where the atomization regime is dominant by the coupling of injector with the imposed acoustic field and not by impact waves. Based on observation of the high speed images no impact waves where formed when the injector fully couple with the acoustic field. A similar coupling between the propellant feed system and the acoustic field has been identified since the Apollo era[8].

For the PN conditions, the velocity fluctuations are maximum, unlike the PAN conditions where the pressure fluctuations are maximum. For the PN conditions coupling between the acoustic perturbations and impingement sheet occurred at a lower pressure

amplitude. Figure 12 demonstrates this coupling at a lower pressure amplitude. Shown in Figure 12 is the DMD spectrum and spatial mode for the PN 1 and PN 4 conditions. Unlike the PAN conditions, the velocity perturbations produce an in plane flapping motion of the impingement sheet. Both PN conditions spatial modes share the same characteristic shape. As the pressure amplitude is increased the in plane flapping motion becomes more pronounce as shown from Figure 12b for PN 4 condition. Although the PN spatial modes appear similar to the base case condition, fundamentally they represent a different mode of operation. In the base condition the alternating red and blue pattern are symmetric along the impingement sheet. This is physically representative of impact waves travelling down along the impingement sheet. In the PN forcing, the spatial modes have an alternating patterns that are asymmetrical. Physically what is occurring is that in a PN acoustic field the two cylindrical jets swing in phase with the velocity perturbations. As they swing, the impingement point is physically displaced and hence the impingement sheet is also displaced resulting in the in plane flapping motion.

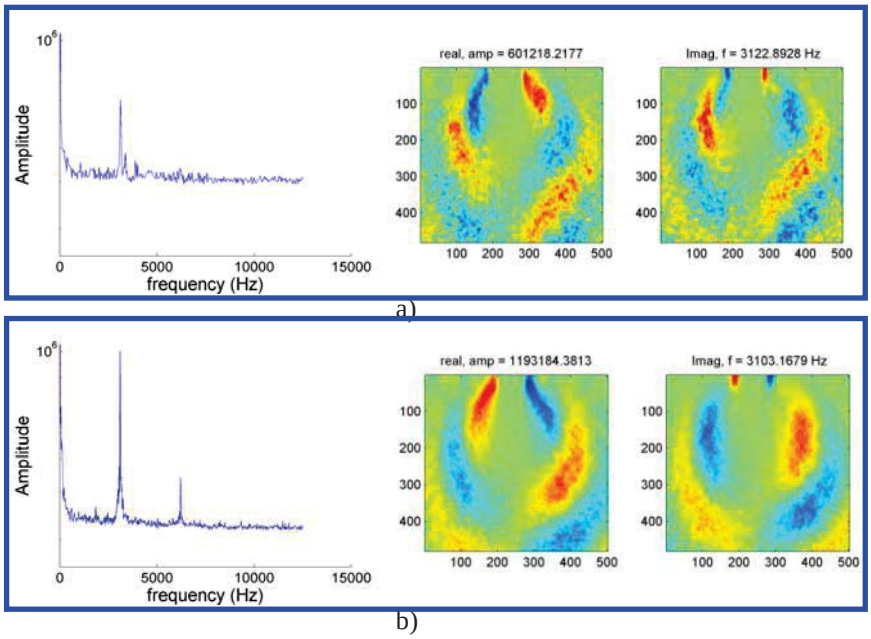

Figure 12. The DMD spectrum and spatial mode for a) PN 1 and b) Pan 4.

This in plane flapping motion is observed in the phased average images of PN 4 condition in Figure 13. Unlike the PAN forcing conditions where the cyclic mass flow variations produce a symmetric impingement sheet, PN forcing produces an S-shape curvature along the impingement sheet. S-shape curvature is indicative of the impingement point being periodically displaced. What was also observed was that ligaments would be shed in the direction of the incoming acoustic wave (Appendix A). This is a different mode of atomization when compared to the base condition. In the base condition the dynamic pressure of the liquid jets are used to overcome the surface tension force and atomize into droplets, but prior to becoming droplets, impact waves form on the impingement sheet and subsequently detach as ligaments and form droplets. Instead in a PN acoustic field, the edges of the impingement sheet are stripped off as ligaments and form a swig-swag pattern downstream. It is this mode of atomization that dominates the impingement sheet and not impact waves. Similar to PAN 5 condition, no impact waves were observed when the jets fully coupled with the acoustic field. It is believe that after a certain pressure amplitude associated with both PAN and PN acoustic forcing is reached, the impingement sheet is never fully developed, and hence limits any influence or traces of impact waves on the impingement sheet.

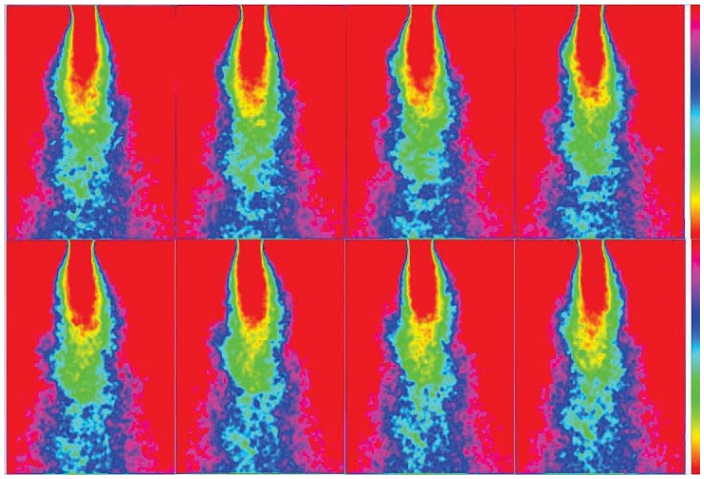

Figure 13. False colored, phased average images of the PN 4 condition. An in plane flapping is generated with PN forcing.

IV. Conclusion

Cryogenic nitrogen impinging jets were studied under a high pressure environment and subjected to an acoustic perturbations. High speed, backlit imaging was used to capture the physical response of the impact waves to the acoustic forcing present on impingement sheet form. For the first phase of the study**,** jet velocity and chamber pressure were varied until impact waves were visually prominent on the impingement sheet. Chamber pressures, up to 4.8 MPa, and jet velocity, 2 to 10 m/s, were investigated. It was observed that impact waves became visually prominent in a narrow range of chamber pressures and jet velocities, particularly when both jet velocity and chamber pressure are low. At supercritical pressures, no droplets or ligaments were ever observed to form, instead the flow field resemble a fine mist. In subcritical pressure both ligaments and droplets were observed to be shed from the impingement sheet. In the subcritical pressures there appears to be an influence of jet to chamber gas density ratio. It was observed for the same jet velocity a transition to a fully atomize, when a dense mist is formed, occurs sooner at higher chamber pressures.

After the conditions that led to impact waves being visually prominent were identified, dynamic mode decomposition was used to extract the natural frequencies of impact waves and isolate the spatial structures, both the unforced and force conditions at a constant chamber pressure and jet velocity. For the forces conditions the pressure amplitude was incrementally increased until the injector and the acoustic field fully coupled. The results indicate that impact waves influence appear to vanish once a certain pressure amplitude is reached. When subjected to PAN forcing the impingement sheet size grows and decays and a large group of droplets are shed. For the PN forced conditions, in-plane flapping is generated and ligaments are stripped of the impingement sheet.

References

[1]Anderson, W. E., Ryan, H. M., Pal, S., and Santoro, R. J., "Fundamental Studies of Impinging Liquid Jets," *30th Aerospace Sciences Meeting & Exhibit, AIAA Paper 92-0458, Reno, NV*.

[2]Anderson, W. E., Ryan, H. M., and Santoro, R. J., "Impinging Jet Injector Atomization," Liquid Rocket Combustion Instability, edited by V. Yang and W. E. Anderson, Progress in Astronautics and Aeronautics, vol. 169, AIAA, Washington D.C., 1995, pp. 215-246

[3]James, M. D., Kubal, T. D., Son, S. F., Anderson, W. E., and Poutpoint, T. L., " Calibration of an Impinging Jet Injector Suitbale for Liquid and Gelled Hypergolic Propellants," *45th AIAA/ASME/SAE/ASEE Joint Propulsion Conference & Exhibit*, Denver, Co, AIAA 2009-4882, 2009

[4]Fakhri, S., Lee, J. G., and Yetter, R. A., "Atomization and Spray Characteristics of Gelled-Propellant Simulants Formed by Two Impinging Jets," *45th AIAA/ASME/SAE/ASEE Joint Propulsion Conference & Exhibit*, Denver, Co, AIAA 2009-5241, 2009

[4] Heidmann, M. F., Priem, R. J., and Humphrey, J. C., "A Study of Sprays Formed by Two Impinging Jets," NACA TN-3835, 1957.

[5] Dombrowski, N., and Hooper, P. C., " A Study of the Sprays Formed Imping Jets in Laminar and Turbulent Flow," *Journal of Fluid Mechanics*, vol. 18, no. 3, 1964, pp. 392-400.

[6] Anderson, W. E., Ryan, H. M., and Santoro, R. J., "Impinging Jet Injector Atomization," Liquid Rocket Combustion Instability, edited by V. Yang and W. E. Anderson, Progress in Astronautics and Aeronautics, vol. 169, AIAA, Washington D.C., 1995, pp. 215-246

[7] Anderson, W. E., Ryan, H. M., Pal, S., and Santoro, R. J., "Spray Formation Processes of Impinging Jet Injectors," NASA Propulsion Engineering Research Center, vol. 2, N94-23042, 1993, pp.69-74.

[8] Li, R., and Ashgriz., "Characteristics of liquid sheets formed by two impinging jet," *Physics of Fluids*, Vol. 18, No. 8, 2006, pp. 087104-1, 087104-13

[9] Ciezki, H. K., Tiedt, T., Von Kampen, J., and Bartels, Nora., "Atomization Behavior of Newtonian Fluids with an Impinging Jet Injector in Dependence upon Reynolds and Weber Numbers" *41th AIAA/ASME/SAE/ASEE Joint Propulsion Conference and Exhibit*, Tucson, AZ, AIAA 2005-4477, 2005.

[10] Anderson, W. E., Ryan, H. M., and Santoro, R. J., "Impact Wave-Based Model of Impinging Jet Atomization," *Atomization and Sprays*, Vol. 16, No. 7, 2006, pp. 791-806

[11] Chen, X., Ma, D., and Yang, V., "Mechanism Study of Impact Wave in Impinging Jets Atomization," *50th AIAA Aerospace Sciences Meeting*, Nashville, TN, AIAA 2012-1089, 2012

[12] Teshome, S., Leyva, I. A., Talley, D, G., and Karagozian, A. R., "Cryogenic High-Pressure Shear-Coaxial Jets Exposed to Transverse Acoustic Forcing," *50th Aerospace Sciences Meeting*, Nashville, TN, AIAA2012-12665, 2012

[13] Graham, J. J., Leyva, I. A., Rodriguez, J. I., and Talley, D. G., "On the Effect of a Transverse Acoustic Field on a Flush Shear Coaxial Injector," *45th AIAA/ASME/SAE/ASEE Joint Propulsion Conference and Exhibit*, Denver, CO, AIAA 2009-5142, 2009

[14] Schmid, P. J., "Dynamic mode decomposition of numerical and experimental data," *Journal of Fluid Mechanics*, Vol. 656, 2010, pp. 5-28

[15]Harrje D. T., and Reardon, F. H., "Liquid Propellant Rocket Combustion Instability," NASA SP-194, 1972

V. Appendix A

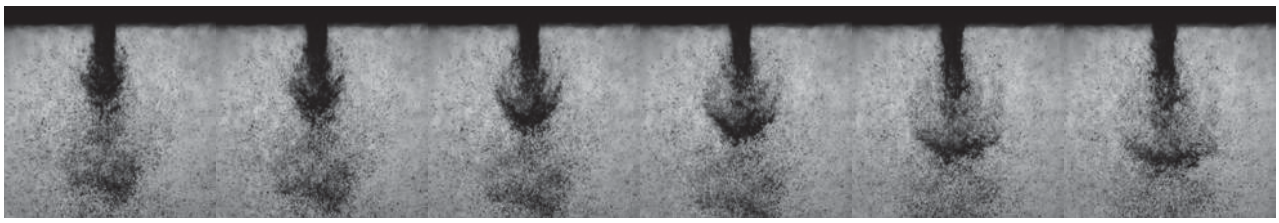

Figure A1. Instantaneous images of an acoustic cycle for the PAN 5 condition. A large group of droplets are shed and no impact waves were ever observed. The klystron effect produces the Christmas tree shape in the far left image.

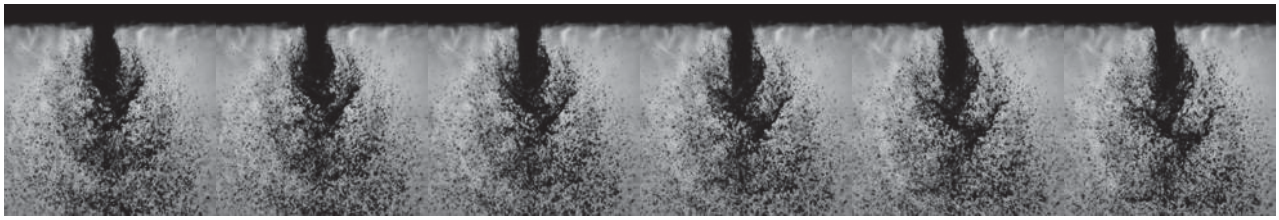

Figure A2. Instantaneous image of an acoustic cycle for the PN 4 condition. A swig-swag pattern of ligaments being shed off the impingement sheet can be observed in the downstream flow. No impact waves were ever observed in this condition.

AIAA SciTech
4-8 January 2016, San Diego, California, USA
54th AIAA Aerospace Sciences Meeting

Nano-ignition Torch Applied to Cryogenic H2/O2 Coaxial Jet

A. Badakhshan[1]
ERC Inc., Edwards AFB, CA 93524
Stephen Danczyk[2]
Air Force Research Lab, Edwards AFB, CA 93524
David Forliti[3]
Sierra Lobo Inc., Edwards AFB, CA 93524
Ivett Leyva[4] and Douglas Talley[5]
Air Force Research Lab, Edwards AFB, CA 93524

Abstract

A high-pressure photoignition torch has been developed which takes advantage of the photoignition properties of single wall carbon nanotubes (SWNTs). The goal was to initiate combustion in a cryogenic O_2-H_2 coaxial injector at about 35 atm (~520 psi) at O_2 temperature of about 130 K with SWNT-based "solid fuel mixtures". Our investigation includes the effects of chamber pressure, the presence of different solid oxidizers such as $BKNO_3$ and $KMnO_4$, as well as solid fuels and solid propellants, on the functionality of the photoignition torch. We have shown that the ignition parameters such as burn temperature, burn duration and the ignition byproducts can be tailored to meet different ignition requirements. It is anticipated that photoignition provides a suitable method for ignition of systems that require the start of combustion at a high pressure up to about 135 atm (2000 psi) as well as ignition of certain thrusters and liquid rocket engines that require an extremely small and light weight torch igniter. This ignition method can be applied to large combustion chambers such as gas turbines, gas generators, liquid rocket engines and possibly multi grain solid rocket motors.

I. Introduction

THERE are a number of properties that are desirable for an ignition system. Ideally an ignition system should be robust, efficient, reliable, simple, low cost, and flexible. Ideally, an ignition system should initiate combustion under a broad range of conditions in order to maximize the operational flexibility of energy and propulsion systems. When ignition systems rely on high reactivity additives, such as hypergolic or pyrophoric reactants, handling and storage of these specialized chemicals

[1] Research Scientist, ERC Inc., Combustion Devices Group, 10 Saturn Blvd., Edwards AFB, CA 93524
[2] Research Scientist, RQRC, Combustion Devices Group, 10 Saturn Blvd., Edwards AFB, CA 93524
[3] Research Scientist, Sierra Lobo Inc., Edwards AFB, CA 93524
[4] Aerothermodynamics PO, AFOSR/RTE, 875 N Randolph St, Arlington, VA 22242, AIAA Associate Fellow
[5] Research Scientist, Combustion Devices Group, 10 Saturn Blvd., Edwards AFB, CA 93524, AIAA Fellow

may be complicated by safety and health concerns. Thus there is a need for novel ignition technologies that satisfy the numerous requirements while maintaining simplicity.

Ajayan et al. first reported the photoignition of single-wall carbon nanotubes (SWNTs) by a camera flash in 2002.[1] It was suggested that Fe nanoparticles within SWNTs play an important role in the photoignition process.[2] Subsequently, others reproduced some of the aforementioned results[3] and we suggested that SWNTs could be used as an ignition agent for a variety of fuels, including those of interest in liquid rocket engines.[4-6] Other applications of photoignition of SWNTs have also been reported.[7-10] More recently, research on the photoignition of gaseous fuel and air mixtures showed distributed ignition.[11,12] Photoignition of graphene oxide for fuel burning applications has also been demonstrated.[13]

An ignition torch that is based on the photoignition of carbon nanotubes was developed and ignition of liquid fuel sprays by the torch has been achieved. In this report, we will describe the experimental procedure for producing ignition that is induced by a compact Xe-flash, including the results for photoignition of a simple fuel spray in air as well as ignition of a coaxial injector flow with cryogenic propellants. The application for the current effort is liquid rocket engines, but the reported photoignition torch has a range of other possible applications beyond propulsion systems.

II. Experimental Setup

Samples of SWNT with different nanoparticle Fe content used in this study were obtained from Unidym Inc., Houston, Texas. The samples were as-grown SWNTs with a high concentration of impurities as byproducts of CNT syntheses. Based on the evidence presented by the vendor the carbon nanotubes believed to be predominantly SWNT. The as-grown samples typically contain substantial impurities, (about 50% by weight in the reported samples) mostly Fe nanoparticles and amorphous carbon.[3,14] The term CNT is used for the samples in this report in order to indicate that they were as-grown SWNT samples and they were not purified in any way. Contrary to photoignition, most applications of CNTs require high concentration of CNTs and low concentration of Fe, which explains the need for the often elaborate purification process. However, purified samples show considerably higher photoignition threshold as tested, thus ill-suited for photoignition applications. The same batch of CNT was used for all photoignition experiments reported here, the CNT samples with nanoparticle Fe content of 51 wt.%, as stated by the vendor. In most cases some solid additives (to be described later) were used along with CNTs, which are collectively referred to as a "CNT mixture."

The ignition light source was a modified version of the compact Xe-flash that is used in a disposable camera. This type of light source proved to be quite reliable and the Xe-flash bulb was found to have sufficient structural integrity for high pressure applications, and survived many pressure cycles between 1to 135 atm. Also, the same Xe-flash unit was repeatedly used for ignition at elevated pressures up to about 50 atm.

Figure 1 shows the preferred configuration of a self-contained Xe-flash light source, the related electronics, and a transparent ignition capsule that is partially filled with the CNT mixture. Similar ignition

capsules were used in all of the configurations reported here. When used within a pressure vessel, the Xe-flash and the ignition capsule were usually placed next to each other under high pressure and connected through sealed feed-through electrical wires to the rest of the electronics outside.

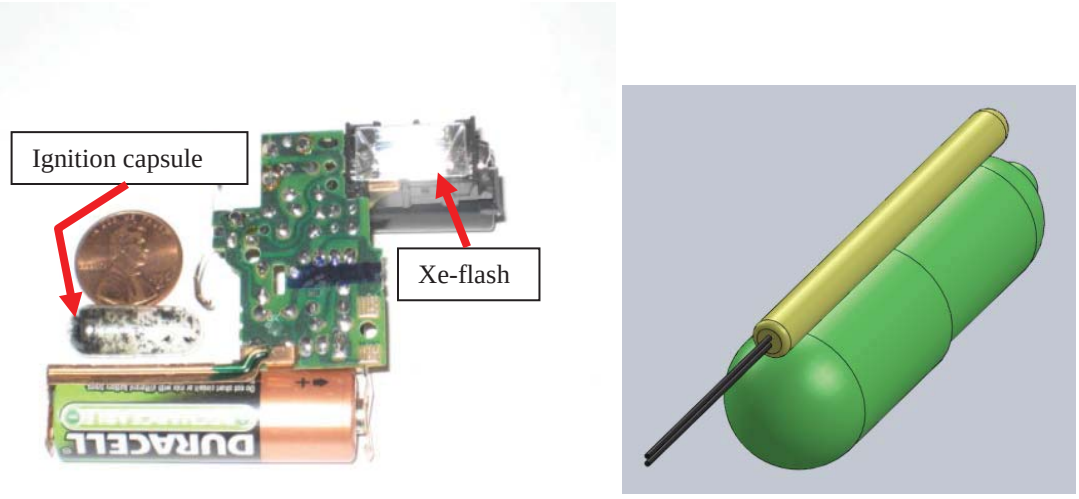

Figure 1 – The photographic image of a complete hardware of a self-contained photoignition device that was used in most of the reported ignition systems and torches. The ignition capsule that is shown below the penny is 5-10% filled with 30-70 mg of the nanostructured solid fuel mixture. Normally the capsule is placed alongside of the Xe-flash that is shown at the top right where it receives the maximum exposure.

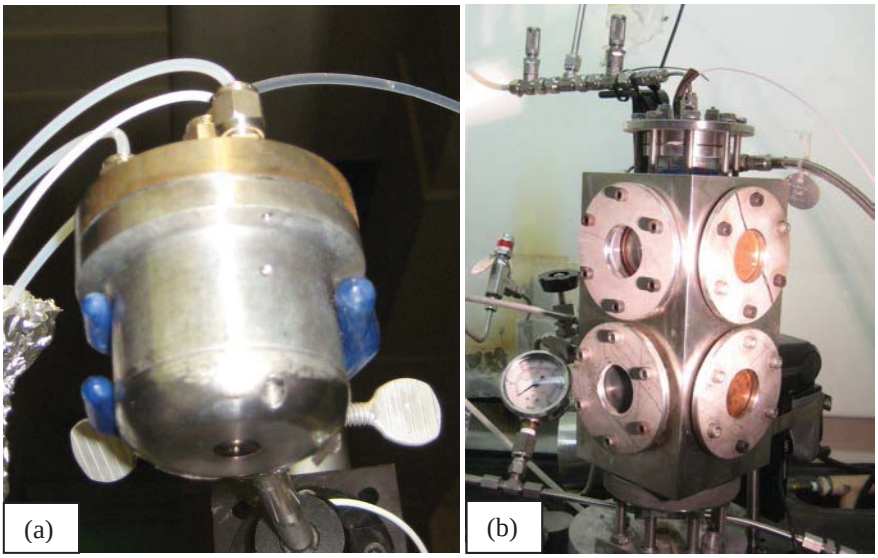

Figure 2 – (a) The customized ultrasonic atomizer (OD=6 cm) that was used as the fuel injector at atmospheric pressure and at an intermediate pressure up to about 30 atm (~450 psi). (b) The mid-pressure combustion chamber for photoignition test up to about 30 atm (440 psi) of pressure with the ultrasonic fuel injector at the top of it. . In this case the light source is located outside of the chamber aginst the lower back window (D=5 cm, L=2.5 cm) and the ignition torch sits inside the chamber and aginst the same window.

Experimental Setup for Fuel Spray Ignition

Three different setups were utilized for the fuel ignition experiments. The first one was used for observation of the dynamics of the photoignition process at atmospheric pressure with an unhindered view of the ignition source and the ignition process. Figure 2 shows a picture of the ultrasonic atomizer that was used to produce an injector flow for some of the ignition studies. It also shows the second fuel ignition setup, a mid-pressure test chamber that was utilized to observe the torch function up to about 30 atm. The pressurizing gas was N_2, air, or a combination of the two for reduced oxidation capability, and it included both stagnant and flowing conditions.

The third setup was a compact high-pressure ignition torch (HPIT) chamber that was made of brass and was designed for photoignition experiments up to about 135 atm of pressure. Figure 3 shows a schematic diagram of HPIT along with photographic image of the HPIT as it is attached to high pressure combustion chamber that uses HPIT through a 30 cm long connecting tube. The HPIT was utilized to ignite the O_2-H_2 at different pressures and temperatures.

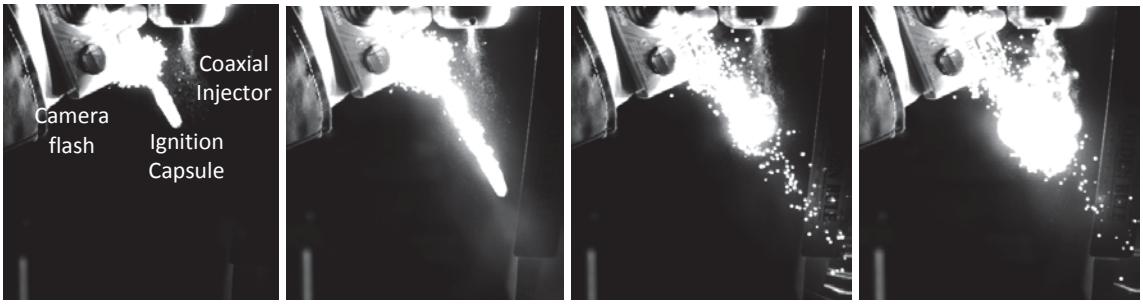

Figure 3 – Photoignition of RP1 spray by a nano-ignition capsule containing about 5 mg of CNT shows the process through the sequence of images. In this case the ignition capsule is taped on the flash of a disposable camera that is also shown. The time reference of t=0 indicates the peak of the illumination of the disposable camera flash with a duration of about 1 ms. The fuel injector is the customized ultrasonic atomizer that is shown in Figure 2(a). These images were captured at 2000 fps.

III. Instrumentation

A high-speed pyrometer, model KGA 740 HS from Mikron Infrared Inc., covering a temperature range from 300-2300 C was used to determine the instantaneous temperature of the sample during the process leading to photoignition of the CNTs, as well as for measuring burn temperature of other ingredients such as aluminum nanoparticles and solid rocket fuel particles. It should be noted that the pyrometer produces a curve of the instantaneous temperature of a focused spot of the sample that is about 2 mm in diameter that also provides a reasonable estimate of the maximum burn temperature of the sample. As such the reported values are a rough measure of maximum burn temperature of the spot on the surface of the sample and they may not represent the true temperature of the entire sample.

A high-speed Phantom V7.1 camera from Vision System capable of capturing up to 4800 frames/s (fps) at full-frame (800x600) was utilized in most of the experiments to record the sequence of ignition events, including fast moving photoignition byproducts. In the HPIT experiments, a different high-speed camera, model Phantom V710 from Vision System (7500 fps at 1280x800) was utilized.

IV. Experimental Procedure

The motivation for this project was to use CNTs as photoignition agents for initiation of combustion in subscale liquid rocket fuel injectors. The general approach is to take advantage of the exothermic photoignition of carbon nanotubes to initiate combustion within reactants mixed with the nanotubes. The current approach goes beyond the general practice and involves an ignition chamber which is separate from but connected to the combustion chamber.

A. The Need for Encapsulated CNT

Previous proof-of-concept experiments indicated that this could be a viable approach. However, it was observed that samples that were partially wet due to exposure to the mist from the liquid fuel spray required a substantially higher light fluence (energy per unit area) for photoignition. The high fluence requirement made photoignition of fuel sprays very difficult to implement for most applications, because the CNT sample is usually located close to the fuel spray in order to induce ignition.

In order to overcome the problem two methods were devised to keep the CNT samples dry. The first method was encapsulation of CNT mixture in a transparent container/capsule, and the second one was lamination of CNTs along with a solid oxidizer in thin layers of a transparent polymer. Both methods proved to be effective, but the encapsulation is more reproducible and it is easier to implement for high-pressure applications. Thus encapsulation of CNTs along with solid energetic additives, referred to as CNT mixture was employed as the method of choice for igniting liquid fuel/oxidizer flows. Examples of CNT mixtures are presented in Table 1 and a detailed description of the purpose and properties of different CNT mixtures will be discussed later in this report.

The ignition capsules were prepared by placing CNT mixtures in a transparent gel cap size 00 (about 0.75 cm^3 in volume, D=7 mm and L=20 mm). Figure 1shows a typical ignition capsule partially loaded with CNT mixture. Numerous tests indicated that if there was sufficient material in the container, typically a few milligrams, the gaseous byproducts of the photoignition of CNT (mostly CO_2 and CO) would pressurize the capsule beyond its 2 atm (~30 psi) limit, causing it to burst and release its burning contents to ignite the fuel spray.

V. Results and Discussions

Photoignition of Different Materials

We studied ignition characteristics of CNT and a number of other nanoparticles or nanostructured materials in order to identify those parameters that are particularly useful in photoignition process. The parameters of interest are minimum ignition energy (MIE) and burn temperature for different materials, as

listed in Table 1. We also studied photoignition properties of other materials such as multi-walled CNT, C60 fullerenes and SWNT and multiwall carbon nanotubes from different vendors as well as carbon black, metallic and nonmetallic fine particles, and ball milled metallic thermites with mixed results. Table 1 only includes materials that are well characterized and showed a more consistent photoignition effect. The stated error figures are the measured statistical variations for the first four samples and they are the estimated uncertainty for the last three samples.

Table 1 – MIE for different nanostructured materials and their corresponding burn temperatures

nanoparticle samples	**particle size/ smallest dimensional size**	**Min. ignition Energy/area, Fluence (mJ/cm^2)**	**ignition/burn temperature* (^0C)**
CNT(51% Fe)	< 30 nm	64 ± 8	490 ± 30
CNT(18% Fe)	< 30 nm	182 ± 13	420 ± 50
Graphene Oxide Foam/Nanoplatelets	< 30 nm thick platelets	500 ± 60	370 ± 100
Al-nanoparticles	18 nm	290 ± 50	1100 ± 150
Fe, Carbon coated	~ 40 nm	220 ± 35	250 ± 30
Fe powder	~ 30 nm	150 ± 25	220 ± 30
Pd powder	~ 12 nm	530 ± 60	320 ± 40

*this is the temperature of a focused spot on the sample and may not be representative of the entire sample

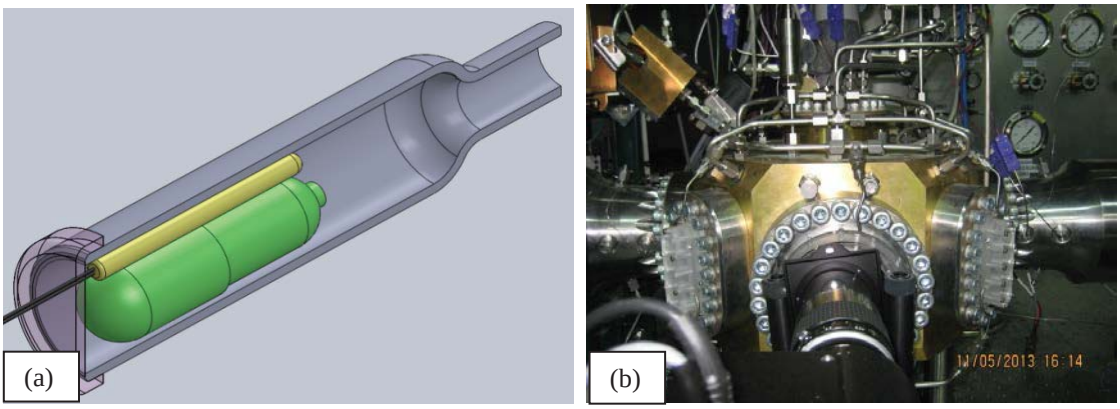

Figure 4 – (a) The schematic diagram of the drop-in 135 atm (2000 psi) ignition torch. The ignition capsules are loaded from the back and hot gas and burning particles rush through the tube (OD=6 mm) in front of the torch. (b) The O_2-H_2 combustion chamber that is designed for combustion instability studies at pressures up to about 100 atm. The high-pressure ignition torch, the brass cube on the top left corner of this photographic image is coupled to the combustion chamber via a 35 cm long tube with OD=6mm.

Realization of the Photoignition Torch

In preliminary tests, nano-ignition capsules were used to ignite a fuel spray by allowing the two-part capsule to burst open in the vicinity of the fuel spray. In this report the term fuel spray is used in its most general sense so that it includes injector flow as well, though from technical point of view they may not be the same as it is related to the presence or flow of the oxidizer. Further investigations of fuel ignition process revealed that a 2-3 mm size hole in an ignition capsule may prevent it from exploding due to over pressurization, if the burn rate was kept sufficiently

low. In such cases the capsule would discharge burning byproducts and burning particles directly through the hole as the pressure is built up in the capsule. Hence it produces a miniature ignition torch. An example of the application of photoignition torch for fuel spray is shown in Figure 4.

At atmospheric pressure, a typical photoignition torch may burn close to 0.5 second depending on the burn rate and the amount of fuel in the capsule, and it typically discharges a combination of hot gas, flame, and burning particles that extends 15-30 cm away from the ignition capsule. As the ambient pressure is increased beyond about 10 atm, the burn rate gradually increases and the burn duration decreases, so that at about 30 atm the burn duration is no more than half of what it is at 10 atm for most CNT mixtures. This trend is expected to continue as the pressure is increased beyond 30 atm.

Table 2 – Ingredients for a photoignition torch for different chamber pressures.

CNT, main Photoignition Agent (Wt%)	Fuel Al_NP 18/80nm (Wt%)	Fuel SRF (Wt%)	Oxidizer $BKNO_3$ (Wt%)	Oxidizer $KMnO_4$ (Wt%)	Observations and Comments On the Relative Effects of Additives
Sample 0 100%					Short burn duration & low burn Temp. (~800K)
Sample 1 10%			90%		Improved ignition reliability & burn Temp.
Sample 2 10%				90%	Reliable ignition only $\gtrsim$10 atm
Sample 3 ~3%		~97%			Unreliable ignition of SRF associated with a long ignition delay (ratio doesn't matter)
Sample 4 3%	7-12%	85-90%			More reliable ignition, burns at higher T & is more energetic than samples 2 & 3
Sample 5 3%	7%	45%		45%	Less reliable ignition than the above unless the chamber Pres. $\gtrsim$10 atm
Sample 6 3%	7%	50%	40%		Improved flash sensitivity & ignition + generate a lot of gas & smoke
Sample 7 1%	9%	80%	10%		Best ignition sensitivity, reliability & burn duration for chamber Pres. $\gtrsim$7 atm
Sample 8 2%	8%	70%		20%	Comparable to sample 7 only for chamber Pres. $\gtrsim$15 atm
Sample 9 2%	8%	70%	20%		Improved ignition reliability and burn duration
Sample 10 1%	15%	75%	9%		As good as the above at atmospheric pressure, but burns too fast $\gtrsim$ 15 atm

B. Fuel Mixtures for a Photoignition Torch

While we were able to ignite a fuel spray with an ignition capsule that contained only CNTs, such an ignition capsule exhibited a number of drawbacks. These are due to the fact that CNTs do not burn long and hot enough and the amount of gas generated may not be sufficient for an effective ignition torch for most applications. The solution was to add small amounts of granulated solid fuel/propellants and oxidizers to the ignition capsule. The CNTs would ignite these additives and then the much more robustly burning

additives could be used to ignite something else. Table 2 shows examples of ingredients of a typical ignition capsule along with the weight percentage of each of the ingredients in the capsule. Comments about the relative advantages and possible disadvantages of each specific mixture are also stated in Table 2.

It should be mentioned that each material in Table 2 is from the same batch and the total content of the photoignition torches were typically 30-70 mg. CNT samples with no add material as well as samples with added energetic materials such as aluminum nanoparticles (Al-NP) solid rocket fuel (SRF) and solid oxidizers were used as fuel for the photoignition torch. The different CNT mixtures exhibited different ignition properties depending on their ingredients. A rough measure of burn temperature and qualitative burn duration of various CNT mixtures were determined through the pyrometer as described previously. The burn duration of most photoignition torches were also measured by the high-speed camera, which is a more reliable approach.

All of the ingredients that are listed in Table 2 are commercially available except for the solid rocket fuel (SRF), also known as solid propellant, which is formulated and prepared in-house. The SRF is typically 87% solid loaded composite propellant composed of hydroxyl-terminated polybutadiene (HTPB) as a binder, ammonium perchlorate as an oxidizer and aluminum powder as a fuel. The granulated SRF was used in the ignition capsules that are reported here and they were made from rubber-like solid chunks of SRF that is mixed from solid powders and polymerized through a proprietary process at the Air Force Research Lab, Edwards AFB. It is possible to use commercially available model rocket fuels (MRF) instead of SRF. While MRF is easier to ignite and it typically produces more gas than SRF, it also produces black smoke and leaves behind a film residue on the nearby surfaces. Moreover, MRF in powdered form burns too fast at elevated pressures and it may be hard to produce properly sized particles from this material if it is not polymerized.

At elevated pressures, it may be necessary to push the photoignition byproducts from the ignition chamber into the combustion chamber with pressurized air/gas before they burn out. This is not necessary when the photoignition torch is placed inside the combustion chamber. In ignition experiments with HPIT, an air pressure of 2-4 at above the combustion chamber pressure was used in order to carry ignition byproducts to the high-pressure combustion chamber before they were extinguished. The best photoignition torch for 20-50 at pressure has been generated by samples 7 through 10 in Table 1, respectively.

A typical nano-ignition capsule has a total mass of no more than 200 mg, of which about 130 mg is due to the empty capsule and the rest is the CNT mixture. The amount of CNT in the mixture is typically 1-3 mg. The function of the solid oxidizer is to speed up the propagation of ignition to other solids. For the solid oxidizer, boron–potassium nitrate ($BKNO_3$) and potassium permanganate ($KMnO_4$) were used. While technically BKNO3 is not merely an oxidizer, but a mix of fuel (boron) and oxidizer (KNO3), we used it as an oxidizer.

The role of Al-NP is to make sure that the temperature increases rapidly enough and gets high enough (exceeding 1500 K) to ignite the SRF. We used Al-NP in powdered form with nominal sizes of 18 nm and 80 nm and found both of them to be equally effective as additives for the reported application. The only

notable difference between the two is that the former exhibits photoignition without CNT and latter does not show such a property up to the maximum fluence that was available to us, about 3 J/cm^2. SRF is the main ingredient that provides a burn duration beyond 200 ms and burn temperature well beyond 2000 K. We were able to achieve burn durations approaching 1 s at atmospheric pressure by utilizing the same capsule size of Figure 1 and the same ingredients of Table 2 with no more than 150 mg of CNT mixture. A typical photoignition torch has about 30-70 mg of CNT mixture and burns for 200-400 ms at atmospheric pressure and for 50-100 ms at about 50 atm.

C. Fuel Spay Ignition at Ambient Condition

The setup of Figure 2(a) was used for fuel spray ignition in open air under a fume hood. In the liquid fuel burning experiments, an ignition capsule was positioned close to the path of fuel spray from the ultrasonic atomizer, such that upon ignition and rupture of the nano-ignition capsule the fuel and the burning particles impinge upon one another. The camera flash was located very close to the ignition capsule so that it received sufficient energy from the flash to induce photoignition of the CNT mixture. The photoignition and subsequent fuel ignition and burning process were captured by a high-speed camera, at a rate of 500-2000 frames/second (fps). Figure 3 shows still images of a fuel burning experiment at atmospheric pressure after the activation of the camera flashed. Within 10 ms the combustion of the fuel spray is in progress through the expanding fireball that is about 4 cm in diameter. The flame speed is several meters per second, depending on the fuel and within 15 ms the entire combustible mixture is in flame.

D. Ignition Torch for Combustion of Injector Flow at Elevated Pressures

The setup of Figure 2(b) was used to study photoignition at an elevated pressure up to about 30 atm. In this case, the compact Xe-flash light source was outside of the chamber and the ignition capsule was inside, and the light coupling was made available through a 5 cm wide quartz window at a bottom port opposite to the high-speed camera. The byproducts of the ignition were directed upward toward the fuel spray and the injector flow. The ultrasonic atomizer was modified to accept a pressurized fuel line. The pressure in the chamber was provided by a high pressure air bottle. The exhaust port was at the bottom of the chamber directing the flow and hot gas through a cold trap. Ignition of different types of fuels with this set up was demonstrated including isopropyl alcohol (IPA), methanol and RP1, a category of aerospace fuel similar to kerosene.

In order to use a photoignition torch for high pressure applications, a high-pressure ignition torch (HPIT) with a separate ignition chamber was designed and built. Figure 4 shows a schematic diagram of a HPIT that is capable of sending hot/reacting gases and burning particles beyond 35 cm from the ignition capsule. The body of HPIT is made of brass in order to safely operate at high pressure in an oxygen-rich environment up to about 135 atm (2000 psi). High pressure air is introduced to the HPIT from a K-bottle through an inlet such that the pressure within the ignition chamber stays 2-3 atm above the pressure in the combustion chamber. This excess pressure provides a continuous gas flow in order to carry the hot photoignition byproducts into the combustion chamber and provide the opportunity for fuel ignition at the

combustion chamber. The entire system was housed in an explosion proof facility with the remote operation capability that provided control signals for the different remote operated values and electrical firing sequence with millisecond accuracy.

We have successfully applied the HPIT system to generate ignition of an O_2-H_2 coaxial shear injector flow at elevated pressures up to ~35 atm. The coaxial shear flow had liquid oxygen in the center tube and gaseous hydrogen in the annular outer tube. Figure 5 shows an example of initiation of O_2-H_2 combustion that is made possible by a photoignition torch. In a typical high-pressure O_2-H_2 combustion experiment, the timing sequence is controlled such that the burning particles arrive at the coaxial jet region within a few milliseconds before H_2 enters the chamber in order to prevent the accumulation of unburned fuel within the chamber. Typically the combustion of fuel happens within a few milliseconds after burning particles first show up in the combustion chamber and the combustion is typically limited to a few seconds in order to avoid overheating and possible melt down of the injector. However combustion can be sustained as long as it is needed for the study, up to 12 s as tested, with no sign of any damages to the injector.

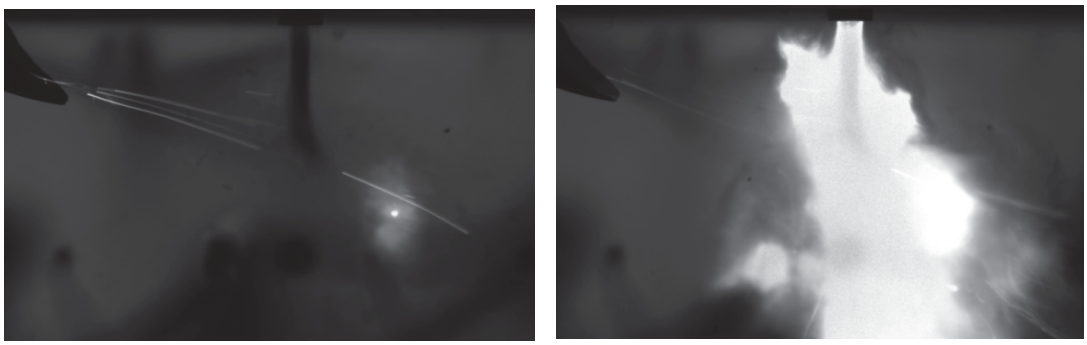

Figure 5 – Snapshots of combustion in LOX/H_2 coaxial jet that was induced by a photoignition torch at ~32 atm and ~133K. The exit point of the burning particles from the 35 cm long tube of the ignition torch is located at the top left corner of the image. These images show t= T+1 ms and T+2 ms after firing of a Xe-flash that has a pulse duration of 1 ms, where T=25-30 ms is the delay between ignition signal and the burning particles entering the combustion chamber. The field of view is about 7 cm across and the images are captured at 1000 fps.

E. Tailoring Ignition Parameters for Fuel Ignition Applications

The function of CNTs is to provide photoignition at a low light level (less than 0.1 J/cm^2), while producing substantial amount of gas to pressurize the capsule.[6.15] This event sets off a chain reaction that ruptures the two part capsule that typically bursts open at about 2 atm of static pressure. Aluminum nanoparticles (Al-NP) in the fuel was easily ignited by burning CNTs (about 800 K) and it produced a high burning temperature (exceeding 1500 K), which lasted more than 100 ms.[15] It is worth mentioning that 18 nm Al-NPs showed photoignition at high enough fluence (> 0.6 J/cm^2) without any CNTs.[15] However Al-NPs produce very little gaseous byproducts, certainly not enough to contribute to the pressure build up within the ignition capsule.

Aluminum nanoparticles burn much longer than CNTs and burn at a high enough temperature to ensure the ignition of SRF particles. In turn SRF particles burn at a very high temperature, well above 2000 K,

they produce a substantial amount of gas and burn for a substantially longer time, exceeding 500 ms, depending on their size and their surface to volume ratio. Through many tests, it was verified that a combination of the ingredients in Table 1 provides the capability of tailoring the burn temperature, pressure ramp up and burn duration for different applications.

A 200 mg photoignition torch can release numerous burning particles at the exit tube of the torch that is 35 cm away from the ignition capsule. The smallest torch that was able to produce consistent ignition contained about 10 mg of fuel mixture and was able to introduce hot/reacting gases and burning particles 10-15 cm away from the ignition capsule. Burn duration of an ignition capsule is adjustable between 50-1000 ms at atmospheric pressure depending on the type and the amount of its ingredients. A noticeable reduction in burn duration has been observed at elevated pressures beyond 10 atm.

VI. Conclusions

A miniature photoignition torch using an encapsulated CNT-based fuel mixture was created. The photoignition torch has been tested up to about 135 atm (2000 psi) of pressure and its suitability for spray ignition demonstrated up to ~50 atm (~735 psi). Application of the photoignition torch for initiation of combustion in a cryogenic O_2-H_2 shear coaxial flame at high pressure was demonstrated at an oxygen temperature of about ~130 K and a pressure of ~32 atm (~470 psi). The photoignition torch as described is suitable for high pressure ignition applications. It also offers the following advantages:

-Light weight and compact: A typical self-contained ignition system has a mass of less than 25 g without the battery and it occupies less than 30 cm^3 of space. The ignition capsule is about 200 mg and it contains 50-70 mg of fuel.

-Safety: The photoignition torch is battery operated and optically coupled so that there is no electrical contact between the ignition source and the ignition charge or fuel. This makes a photoignition system relatively insensitive to electromagnetic interference and electrostatic discharge.

-Reliability: The photoignition torch is based on the mature technology of a compact battery operated Xe-flash lamp and ignition of solid propellants. Over the course of 4 years of testing, the Xe-flash has shown no reliability problem.

-Scalability: While the photoignition torch has been demonstrated here only at small scales, the photoignition system can be easily scaled up to much larger sizes with a relatively small penalty in the ignition delay.

Acknowledgements:

Funding support for this work was made possible by a grant from the Nanoscience and Technology program of the Air Force Office of Scientific Research (SFOSR). We would like to thank Dr. Scott Gilje and Dr. Bruce Chehroudi for the helpful discussions.

References

1. Ajayan PM, et al. “Nanotubes in a Flash: Ignition and Reconstruction”, *Science* 296, pp 705, (2002).
2. Braidy N, Botton GA, and Adronov A, Nanoletters 2 (11), pp. 1277-1280, (2002).
3. Smits J, and Wincheski B, “Response of Fe powder, purified and as-produced HiPCo SWNT to flash exposure”, Materials Science and Engineering A, 358, pp. 384-389, (2003).
4. Chehroudi B., Danczyk S, Morgan C, and Badakhshan A, “Ignition Characteristics of Single-Walled Carbon Nanotubes (SWNTs) Utilizing a Camera Flash for Distributed Ignition of Liquid Sprays”, Tech. Rep. DTIC, Online Information for Defense Community, ADA511240, Oct 2008.
5. Badakhshan A, Danczyk S, Wirth D, and Pilon L, “Ignition of Liquid Fuel Spray and Simulated Solid Rocket Fuel by Photoignition of Carbon Nanotube Utilizing a Camera Flash”, Conf. paper, DTIC, Online Information for Defense Community, ADA571240, Dec 2011.
6. Badakhshan A, and Danczyk, “Photo-ignition of Carbon Nanotube for Ignition of Liquid Fuel Spray and Solid Fuel” Conf. paper, DTIC, Online Information for Defense Community, ADA573322, Mar 2012.
7. Manaa R, Mitchell A, and Garza R, “Flash ignition and initiation of explosives−nanotubes mixture”, Journal of the American Chemical Society 127 (40), pp. 13786-13787, (2005).
8. Tseng S, et al., **“**Ignition of carbon nanotubes using a photoflash”, Carbon, 45, pp. 958-964 (2007).
9. Abboud, J., Jiang, N., Zhang, Z., Roy S., Gord, J.R., *Comb and Flame* **2013,** 160 (9), 1842–1847.
10. Ohkura, Y, Weisse J. M., Cai L, and Zheng X., *Nano Lett.*, **2013**, *13* (11), 5528–5533.
11. Berkowitz AM, and Oehlschlaeger MA, "The PhotoInduced Ignition of Quiescent Ethylene/Air Mixtures Containing Suspended Carbon Nanotubes," *Proceeding of the Combustion Institute*, 33, pp. 3359-3366 (2011).
12. Loomis MP, Lee JG, Yetter RA, “Characterization of photoignition of single walled carbon nanotubes”, Fall Technical Meeting of the Eastern States Section of the Combustion Institute, University of Maryland, October 18-21, (2009).
13. Gilje S, et al., “Photothermal Deoxygenation of Graphene Oxide for Patterning and Distributed Ignition Applications”, Adv Mat, 22, pp. 419–423, (2010).
14. See for example http://www.nano-c.com/nanoprod.html, more detailed images of SWNT and impurities are found at: Safarova et al., *Modern Res. Educ. Topics in Microscopy* **2007**, A. Méndez-Vilas and J. Díaz (Eds.).

Peer Reviewed

Title:
Multi-phase Combustion and Transport Processes Under the Influence of Acoustic Excitation

Author:
Wegener, Jeffrey Lewis

Acceptance Date:
2014

Series:
UCLA Electronic Theses and Dissertations

Degree:
Ph.D., Mechanical Engineering 0330UCLA

Advisor(s):
Karagozian, Ann R

Committee:
Smith, Owen I, Leyva, Ivett A, Eldredge, Jeff D, Anderson, Chris R

Permalink:
http://escholarship.org/uc/item/5kq1238x

Abstract:

University of California

Los Angeles

Multi-phase Combustion and Transport Processes Under the Influence of Acoustic Excitation

A dissertation submitted in partial satisfaction

of the requirements for the degree

Doctor of Philosophy in Mechanical Engineering

by

Jeffrey L. Wegener

2014

Abstract of the Dissertation

Multi-phase Combustion and Transport Processes Under the Influence of Acoustic Excitation

by

Jeffrey L. Wegener

Doctor of Philosophy in Mechanical Engineering

University of California, Los Angeles, 2014

Professor Ann R. Karagozian, Chair

This experimental study examined the coupling of acoustics with reactive multi-phase transport processes and shear flows. The first portion of this dissertation deals with combustion of various liquid fuels when under the influence of externally applied acoustic excitation. For this study, an apparatus at the Energy and Propulsion Research Laboratory, UCLA, used a horizontal waveguide to create a standing acoustic wave, wherein burning fuel droplets were positioned near pressure nodes within the waveguide. Alcohol fuels (ethanol and methonal) as well as aviation fuel replacements (Fischer-Tropsch (FT) synfuel and an FT blend with JP-8) were studied here. During acoustic excitation, the flame surrounding the droplet was observed to be deflected in a manner consistent with the direction of a theoretical acoustic radiation force, analogous to a buoyancy force, acting on the burning system. Based on this degree of deflection, a method was developed for experimentally quantifying the acoustic acceleration and relating it to the theoretical acoustic acceleration. This technique employed phase-locked optical imaging of the flame in the ultraviolet band in order to capture hydroxyl radical (OH*) chemiluminescence as an indication of the flame structure and shape. The flame was observed to be deflected in a bulk manner, but also with micro-scale oscillations in

time. The bulk or mean flame alteration was used to determine an experimental value of the acoustic acceleration for a range of different fuels and excitation conditions. This investigation showed experimentally determined acoustic accelerations which were quite consistent qualitatively with theory, but which were quantitatively inconsistent with theoretical predictions. Observed flame deformations were greatest for a droplet situated immediately next to a pressure node, in contrast to the theory, while milder flame deflections were observed for droplets positioned closer to a pressure antinode. These observations were consistent among all fuels studied, qualitatively and with the same mean qualitative trends. Phase-locked OH* chemiluminescence imaging revealed significant differences in the amplitude of flame oscillation based on the applied frequency and droplet location. Low frequency acoustic excitation and proximity to the pressure node produced higher amplitude flame oscillations, suggesting an enhanced degree of acoustically-coupled combustion that could be responsible for qualitative differences between theory and experimental measurements of acoustic acceleration.

The second portion of this dissertation utilized a similar, but more advanced facility which was recently constructed at the Air Force Research Laboratory, Propulsion Directorate (RQR). These experiments explored the interaction between acoustics and nonreactive shear-coaxial jets under high chamber pressure, acoustically resonant conditions, using liquid nitrogen as the inner jet and gaseous helium as the outer jet. The shear-coaxial jet was placed within the chamber, for which piezoelectric sirens could create a standing wave. The coaxial jet could thus be situated at either a pressure node or a pressure antinode location, and backlit high-speed imaging was used to resolve the naturally unstable mixing layer between the inner and outer jets. For jets with and without exposure to acoustic forcing, two different reduced basis methods were applied to the gray-scale pixel intensity data in order to extract instability frequencies and mode shapes from image sets; these included proper orthogonal decomposition (POD) and dynamic mode decomposition (DMD). A new POD-based method was used to quantify the

susceptibility of coaxial jets to external acoustic forcing by comparing the pixel intensity variance induced by the acoustic mode to the total variance of pixel intensity caused by fluctuations in jet mixing. A novel forcing susceptibility diagram was then created for coaxial jet momentum flux ratios of 2 and 6 for both pressure node and pressure antinode locations. Measurements of the critical forcing amplitude were made to quantify the acoustic perturbation amplitudes required in order for the forced mode to overtake the natural mode as the most dominant instability in the jet, which is generally classified as "lock-in" to the applied mode. It was found that, for forcing frequencies greater than the natural frequency of the jet, an increase in the forcing frequency caused the jet to be less susceptible to applied acoustic disturbances, thus requiring higher acoustic forcing to achieve "lock-in". This relationship held true for both pressure node and pressure antinode conditions. The shear layer instability characteristics of unforced jets were also investigated, and a theoretical convection velocity which depends on inner and outer jet velocities and densities was validated for the range of experimental flow conditions used in this study. An extensive description of the design of the experimental reactive facility is also offered, including preliminary results for oxygen-hydrogen coaxial jet flames acquired using high-speed OH* chemiluminescence imaging.

The dissertation of Jeffrey L. Wegener is approved.

Christopher R. Anderson

Jeffrey D. Eldredge

Ivett A. Leyva

Owen I. Smith

Ann R. Karagozian, Committee Chair

University of California, Los Angeles

2014

to Samantha and Ian

Table of Contents

List of Figures

List of Tables

Nomenclature

Symbols or Abbreviations

$\mathbf{A}$	matrix form of pixel intensities for an image set
$\widetilde{\mathbf{A}}$	matrix form of mean pixel intensities for an image set (POD)
a	set of pixel intensities for an image set
c	speed of sound
$\mathbf{D}$	eigenvalue matrix (DMD)
f	frequency
f_F	acoustic forcing frequency
f_{nat}	natural jet instability frequency
g_a	acoustic acceleration
g_o	gravitational acceleration
I	acoustic intensity
J	outer-to-inner jet momentum flux ratio
K	burning rate constant
L	distance between acoustic drivers
M	number of pixels in one image
MR	oxygen-to-fuel mixture ratio
N	number of images
Oh	Ohnesorge number
p_c	mean chamber pressure
p'	pressure perturbation

Symbols or Abbreviations (continued)

Q_v	volumetric flow rate
R	outer-to-inner jet velocity ratio
$\mathbf{R}$	covariance matrix (POD)
Re	Reynolds number
S	outer-to-inner jet density ratio
$\widetilde{\mathbf{S}}$	companion matrix (DMD)
St	Strouhal number
T_∞	ambient temperature
$\mathbf{U}$	orthogonal matrix containing temporal information (POD)
U_∞	bulk flow velocity
U_c	shear layer convection velocity
u_k	vector of temporal amplitude coefficients for mode k (POD)
u'	velocity perturbation
$\mathbf{V}$	orthogonal matrix containing spatial information (POD)
v_k	vector of proper orthogonal mode k (POD)
We	Weber number
z_a	acoustic impedance

Greek Symbols

α	density difference correction factor
ϕ	phase
ϕ_f	flame deflection angle
$\phi_{f/o}$	fuel-to-oxygen equivalence ratio
$\mathbf{\Lambda}$	product of the singular value matrix and its transpose (POD)
λ	acoustic wavelength
ω	complex eigenvalues (DMD)
ρ	density
$\mathbf{\Sigma}$	diagonal matrix singular values (POD)

Subscripts

B	buoyancy
$eqvs$	equivalent volume of a sphere
exp	experimental
f	flame
i	imaginary
ij	inner jet
oj	outer jet
p	hot combustion products
R	acoustic radiation
r	real
s	surface
th	theoretical
II	image intensifier

Acknowledgments

The shear-coaxial jet experimental work was sponsored by the Air Force Office of Scientific Research (AFOSR), Laboratory Task 11RZ07COR, under Dr. Mitat Birkan, program manager, and facility development support was provided by AFRL Commander's Revitalization Funds. AFOSR must also be thanked for the equipment grant that allowed the Energy and Propulsion Laboratory at UCLA to purchase the NanoStar Camera, without which ultraviolet imaging of burning droplet experiments would not be possible. I am also thankful for the departmental fellowship I received from the UCLA Mechanical and Aerospace Engineering Department, which allowed me to begin full-time graduate study in the 2009-2010 academic year. The department also supported me as a Teaching Assistant for the 2010-2011 academic year.

I owe Drs. Doug Talley and Ivett Leyva for this opportunity. I was entrusted with a tremendous amount of responsibility during the construction of this facility, and as a result, I am better prepared for what lies ahead. Many of my tasks involved on-the-job training, which required patience on their part. Much of this on-the-job training occurred under the watch of Randy Harvey. Randy is a technician with the analytical approach of an engineer. Working with Randy, I was confident someone was always watching over me and ready to catch my engineering mistakes. Together, Randy and I built a spectacular machine which will bear fruit for many years. I am also indebted to Dr. David Forliti for emphasizing scientific education and fundamental research where basic engineering and facility validation often took precedence. Thanks to his emphasis, this dissertation contains merit with regard to both scientific research and facility engineering. Finally, I thank Prof. Ann Karagozian for trusting me and my abilities, even when progress was much slower than expected. Her encouragement was a boost of confidence when I needed it the most.

Vita

2003	High School Diploma, Raytown High School, Raytown, MO
2007	B.S. Mechanical Engineering, Missouri Univ. of Science and Technology (ST)
2007-2009	Departmental Fellowship, Mechanical and Aerospace Engineering Department, Missouri ST
2009	M.S. Mechanical Engineering, Missouri ST
2009	Propulsion Research Scientist, Air Force Research Laboratory (AFRL), Edwards AFB, CA
2009-2010	Departmental Fellowship, Mechanical and Aerospace Engineering Department, UCLA
2010	Teaching Assistant, Mechanical and Aerospace Engineering Department, UCLA. MAE 157 - Basic Mechanical Engineering Laboratory
2011	Teaching Assistant, Mechanical and Aerospace Engineering Department, UCLA. MAE 150C - Combustion
2011	M.S. Aerospace Engineering, UCLA
2011-2013	Graduate Student Researcher, AFRL, Edwards AFB, CA
2013	American Institute of Aeronautics and Astronautics (AIAA) Liquid Propulsion Student of the Year

Publications and Presentations

J.L. Wegener, I.A. Leyva, D.J. Forliti, and D.G. Talley, Development of a Facility for Combustion Stability Experiments at Supercritical Pressure, 52nd AIAA Aerospace Sciences Meeting, National Harbor, MD, January 13-17, 2014.

C.I. Sevilla-Esparza, J.L. Wegener, S. Teshome, J.I. Rodriguez, O.I. Smith, and A.R. Karagozian, Droplet Combustion in the Presence of Acoustic Excitation, to be published in Combustion and Flame.

J.L. Wegener, C. Sevilla, J. Smolke, A. Sung, K. Chen, O.I. Smith, and A.R. Karagozian, Transient OH* Chemiluminescence Imaging of Acoustically Coupled Fuel Droplet Combustion, APS/DFD Meeting, Baltimore, MD, November 20-22, 2011.

H. Lan, J.L. Wegener, B.F. Armaly, and J.A. Drallmeier, Simulations and Measurements of 3-D Gravity Driven Liquid Film Flow, J. Fluids Eng., Vol. 132, 081301, 2010.

J.L. Wegener and J.A. Drallmeier, Measurement of Thin Liquid Film Characteristics using Laser Focus Displacement Instruments for Atomization Applications, 22nd Annual ILASS-Americas Conference, Cincinnati, OH, May 16-19, 2010.

J.L. Wegener, M.A. Friedrich, J.A. Drallmeier, and B.F. Armaly, Experimental Validation of a Film Separation Criterion, 11th Triennial ICLASS Conference, Vail, CO, July 26-30, 2009.

CHAPTER 1

Introduction and Background

Acoustic fluctuations are coupled to condensed phase combustion in an array of important power generation and propulsion applications, including liquid rocket engines (LREs), gas turbine engines, and other air-breathing engines. Although each combustion system exhibits unique problems caused by acoustic fluctuations, a broad view of the field reveals an inability to suppress combustion instabilities due to a lack of fundamental knowledge regarding the coupling of combustion and acoustics. The inability to control these instabilities has led to engine and engine component failures in the case of liquid rocket and gas turbine engines, and a consequential increase in combustion instability research.

This study contributes to this field by isolating the problem in two ways. First, a set of alternative fuel combustion experiments performed at the UCLA Energy and Propulsion Research Laboratory investigate the behavior of burning droplets placed within standing acoustic waveforms. Second, a study at the advanced experimental facility of the Air Force Research Laboratory at Edwards AFB, CA explores coaxial, cryogenic non-reactive and reactive jets in the presence of strong acoustic forcing in a high pressure chamber. Each respective study concentrates effort towards behaviors which have a direct impact on the instabilities observed in the predominant applications (gas turbine engines and LREs). Such behaviors include but are not limited to acoustically altered fuel burning rates, droplet flame deformations, and acoustically enhanced jet mixing and atomization. These phenomena hold paramount importance in that they impact

performance, efficiency, and robustness of the system.

1.1 Combustion Instabilities

Combustion instabilities are characterized by large amplitude oscillations of one or more acoustic modes or injector modes of a combustion chamber. The pressure and velocity perturbations produced by these instabilities are problematic because they result in thrust oscillations, severe vibrations that interfere with control system operation, increased heat transfer and thermal stresses to combustor walls, oscillatory mechanical loads that fatigue hardware components, and flame blowoff or flashback [1]. This study provides an overview of combustion instability by first describing the physical mechanisms which fundamentally create the phenomena. The physical mechanisms section is followed by discussion of instability in two primary power systems. A brief background of combustion instabilities in gas turbine engines is given first, due to its relevance to the fuel droplet combustion results in chapter 3. This is followed by a historical summary of LRE combustion instability, which is directly related to the shear-coaxial jet research of chapter 5. A literature review is then presented for fundamental research of fuel droplet combustion and shear-coaxial jets.

1.1.1 Physical Mechanisms

In the most fundamental sense, a system's stability relies on competing mechanisms of driving and damping. The stability of a combustion system and its associated heat release as shown in Fig. 1.1 is determined by acoustic feedback, which can cause driving or damping. The genesis of acoustics though, often lies in unsteady heat release generated by changes in local propellant reaction rates. These changes in reaction rate can also be governed by fuel-oxidizer mixing fluctuations in the flame region. In this case a third

mechanism, fluid mixing, is the origin of unsteady heat release and thus, the production of acoustic energy [2]. A discussion on the combustion instability feedback loop, then, will begin here with a fluid dynamics mechanism.

This physical sequence of events is depicted in Fig. 1.2, which is a detailed version of the more common bimodal representation in Fig. 1.1 [3–5]. The thermoacoustic feedback loop is reduced to three major phenomena, a graphical representation also utilized by Candel [6] and others [7, 8]. These three are represented by oscillations in fluid velocity u', heat release q', and acoustic pressure p' in Fig. 1.2, which are perturbations from the time averaged value, i.e.

$$u = \overline{u} + u' \tag{1.1}$$

$$q = \overline{q} + q' \tag{1.2}$$

$$p = \overline{p} + p' \tag{1.3}$$

Reactive flows can exhibit velocity oscillations due to several perturbation sources, many of which naturally occur in the absence of the acoustic fluctuations. Fluid dynamic instability inherent to a reactive flow instigates the existence of thermoacoustic instability, and only after the onset of acoustic pressure perturbations will acoustic waves act upon the propellant velocity u to complete the instability feedback loop. Natural fluid dynamic instabilities can be provoked by large-scale events such as inlet flow oscillations [9], engendering shear layer instability [10] or vortex development, whereas small scale events like droplet formation and atomization can also have an important role through enhanced mixing and entrainment. High Reynolds number flows supply broadband turbulence to the flame region [11], enhancing molecular mixing processes. Flow instabilities with distinct frequencies often accompany broadband noise, asserting high amplitude velocity fluctuations, and thus mixing oscillations, in the flame region.

Ultimately, these mixing fluctuations will alter flame location and shape via changes in species concentration. This relationship is the link between "Fluid Dynamic Insta-

bility" and "Unsteady Heat Release" in Fig. 1.2. For example, inlet flow oscillations of fuel or oxidizer can globally alter mixture ratio and flame strain rates to the point of extinction [12]; this behavior is shown to be influenced by pressure [13]. Shear flow instabilities produce locally unsteady heat release due to continually changing species mass fractions and densities [14, 15], and heat release fluctuations may adopt the instability frequency naturally occurring in the shear layer. Vortex shedding may result from the puffing behavior of inlet flow oscillations [16] or from shear layer vorticity. In the case of two-phase flow, oscillatory behavior can results from differences in times scales associated with breakup, vaporization, and mixing processes. The extent to which chemical reaction processes and fluid mechanical/mixing processes control combustion is described by the Dahmkohler number

$$Da = \frac{\tau_m}{\tau_{ch}} \tag{1.4}$$

which is a ratio of the characteristic fluid mixing time τ_m and the characteristic reaction time τ_{ch}. For large-scale fluid structures, τ_m is often large in comparison to reaction time scales, hence combustion is limited by reactant mixing of diffusive processes. For small-scale mixing such as that which occurs during droplet atomization and reaction, τ_m is often small compared with reaction rates, and as such are instead limited by kinetics (τ_{ch}). Overall, both fluid mechanics and chemical kinetics must be considered to ascertain the controlling factor in an unsteady combustion system.

In acoustically-coupled combustion, the flame will significantly impact the fluid dynamics, making this interaction two-way coupled. The natural instability frequencies of different types of two-phase shear flows have been shown to be dependent on density, velocity, and viscosity gradients [10], which are manipulated by a flame's temperature distribution when in the presence of a reaction. In addition, the flame's elevated temperatures introduce rapid dilatation and alter the pressure and density distributions which can produce vorticity through baroclinic torque. Subsequently, the interdependence of

fluid dynamics and the flame create a strong coupling which is critical in combustion stability.

As spatio-temporal flame oscillations cause unsteady heat release, thermal expansion and contraction will be concomitant with pressure oscillations which propagate through the surrounding media at the speed of sound. In Fig. 1.2, the enhancement of acoustics by unsteady heat release is represented by the link between "Unsteady Heat Release" and "Acoustic Waves". Increasing pressure perturbations may result when heat release oscillation frequencies equal resonant modes of the combustion chamber. Resonant chamber modes can be radial, tangential, longitudinal, or a mixture of the three, and are determined by geometric chamber dimensions [8, 17–19]. Acoustic pressure oscillations alone may have little direct effect on combustion processes. For example, this is supported by experiments of droplet combustion [20–22] at velocity nodes, i.e. locations of maximum pressure perturbation and zero velocity perturbation in a standing acoustic wave. In this example, there is little coupling between acoustic waves and unsteady heat release, exemplified by minimal changes in burning rate and flame shape.

However, acoustic perturbations in general have an influence on fluid dynamic processes. Both pressure nodes (PNs) ($p' = 0$, $u' = u'_{max}$) and pressure antinodes (PANs) ($p' = p'_{max}$, $u' = 0$) have a unique effect on fluid dynamic processes. Large tangential acoustic velocity oscillations at a PN act to increase mixing and vorticity by inducing additional velocity perturbations within the shear flow, and the natural mode of a shear layer may be overtaken by that of external acoustic forcing [23, 24], especially if the shear layer is convectively unstable [25]. In the case of coaxial jets, a PN condition may also intensify mixing [16, 19, 26] and create a sinuous yet cohesive jet shape [27–30]. If located at a PAN, an incoming flow may be impeded by a periodic rise in chamber pressure [16]. The resulting flow rate pulsations induce a time dependent mixture ratio MR, and large-scale yet relatively symmetric chugging instability. Flow rate pulsations

may also occur for traveling waves which can result in behaviors representative of both a PAN and a PN.

Hence, acoustic feedback serves to amplify or attenuate unsteady heat release through both pressure and velocity perturbations which affect the flow field. Past studies have described this relationship via the well-known the Rayleigh criterion [31]. The Rayleigh criterion addresses the problem using the phase relationship between pressure and heat release oscillations. This two-part approach reduces the complexities described above by including only the pressure oscillation amplitude p' and the heat release oscillation amplitude q', and is often explained using the bimodal diagram in Fig. 1.1 [3–5]. Amplification is said to occur if the pressure perturbation p' occurs in-phase with the heat release perturbation q'. Damping occurs when p' and q' are out-of-phase. The associated Rayleigh index G is given by

$$G(x) = \frac{1}{T}\int_T p'(x,t)q'(x,t)\mathrm{d}t \tag{1.5}$$

which integrates the pressure and heat release oscillations over the time period T to quantify the extent to which the instability is amplified ($G > 0$), or the system experiences damping ($G < 0$). The Rayleigh index is a valuable tool for measuring the coupling of acoustics and combustion or lack thereof, but it does not describe the underlying physics of combustion instability. Utilization of the Rayleigh criterion for measuring the coupling of acoustics and combustion has been used in an experimental dump combustor study by Smith and Zukoski [32] which later inspired more detailed work by Yu *et al.* [33] and Schadow and Gutmark [34] in similar geometries, where low frequency convective modes in the combustion chamber triggered pulsating inlet flow rates which resulted in uncontrolled p' amplification and positive values of the Rayleigh index G. McManus *et al.* [2] and Candel [6] review the Rayleigh criterion's use within other unsteady combustion systems. The Rayleigh criterion is an appropriate quantitative gauge of acoustic-flame coupling, but is particularly valuable in explaining causality when also

accompanied by a investigation of fluid dynamic instability in a three-part approach including heat release, pressure perturbations, and fluid mixing associated with velocity perturbations.

1.1.2 Gas Turbine Engines

The 1980s marked the start of a momentous increase in the importance of instabilities in gas turbine engines. Added attention arose from the challenges of meeting NOx emission standards, chiefly the Gas Turbine New Source Performance Standards (NSPS) in 1979 and the EPA's Best Available Control Technology (BACT) approach in 1987, which were followed by the more broad Clean Air Act Amendments of the 1990s [35, 36]. Formation of nitrogen oxides (NO_x) most commonly has an exponential dependence on temperature via the 'thermal' NO mechanism, and thus NOx reduction requires a decrease in combustor flame temperatures [37]. This is often achieved with leaner fuel-air mixtures [37], which can create lower flame temperatures. Lower flame temperatures bring the combustor closer to the lean blowout condition, where small temporal variations in fuel-air ratio can significantly affect the heat release rate, burning rate, and flame position and shape. Leaner conditions are often associated with pulsations in the flow field. The ensuing combustor pressure oscillations in gas turbines can reach amplitudes as high as 6 psi (rms). Resulting problems have included cracking of combustion chambers, fretting of the outside of the fuel injector, intolerable noise, and other damage [38, 39].

Premixing or partially-premixing of fuel and air has also been employed in gas turbine engines to reduce NOx by eliminating localized high temperatures characteristic of the presence of local diffusion flames. Yet the premixing technique has also shown to contribute to instabilities. Thus, combustion guidelines are being developed for new diffusion flame combustor concepts to eliminate potential instability problems [39]. Consequently, the renewed value of research in non-premixed flames in the presence of acous-

tics calls for salient relationships describing the behavior of jet and droplet/spray flames within acoustic flow fields. These relationships depend on fuel type, which is gaining recognition due to the increasing popularity of alternative fuels for aircraft engines [40].

1.1.3 Liquid Rocket Engines

Historically, only one propulsion method has been used for a vehicle to escape the earth's gravitational field and travel into outer space. Currently and in the near future, this technique remains chemical propulsion. Solid motors, liquid rocket engines (LREs), and hybrid engines, or a combination thereof, have been incorporated into multiple stages to provide the necessary thrust for successful launch vehicles to date [41]. Liquid rocket engines are part of the foundation of any launch vehicle's propulsion system due to their ability to endure long periods of operation with the required levels of thrust. Pairing LREs with high thrust solid rocket boosters to constitute a vehicle's first stage is a common configuration for providing greater acceleration early in flight, followed by disposal of the spent solid motors. For example, the Atlas V uses this technique, as well as the Ariane 5 and the Delta IV, shown in Fig. 1.3.

Liquid rocket engines typically achieve higher specific impulses than their solid and hybrid counterparts, but at the cost of more complexity. An LRE stores propellants as a liquid and uses a system of pipes, valves, manifolds, and injectors to feed fuel and oxidizer into the combustion chamber. In the most simple design, high pressure propellant tanks supply propellants to the chamber. The pressure-fed cycle though, requires thick-walled propellant tanks, limited chamber pressure, or a combination thereof in order to produce the required propellant flow rates. The pressure-fed cycle can be used for upper stage engines, where heavy tanks are acceptable because the upper stage constitutes a relatively small portion of the launch vehicle's total weight at low altitudes. On the other hand, first stage LREs often adopt turbopumps to drive high propellant supply

pressures and combustion chamber pressures while using low pressure tanks. There are exceptions to this rule though, and one example is the upper stage RL10 engine, driven by turbopumps. One type of pump-fed system is the gas-generator engine cycle, which is discussed here as an exemplary illustration of the intricacies within an LRE.

In a gas-generator cycle, a small amount of fuel and oxidizer flow is diverted to produce energy to drive the propellant pumps. The "gas generator" of this engine cycle burns a propellant mixture with a small flow rate and spins a turbine with the hot exhaust products before diverting the exhaust outside the engine. The pre-burner, an alternative to the gas-generator, serves a similar purpose but routes the turbine exhaust into the main combustion chamber. The fuel pump and oxygen pump can be placed on the same shaft such that both propellant pumps are driven by a single turbine, thus minimizing weight and complexity. This configuration is shown in the flow diagram in Fig. 1.4. Alternatively, the gas-generator exhaust can drive two separate turbines, one for each pump. Fuel is commonly used as a chamber and nozzle coolant by routing cold fuel through channels in the chamber and nozzle walls prior to flowing into the injector plenum. In the J-2 engine used in the Apollo program, for example, hydrogen at less than 25 K traveled through tubes welded to the outside of the nozzle wall and was subsequently heated to 110 K before reaching the hydrogen injector distribution dome [42].

These propellant feed systems, as well as the chamber's acoustic modes and the engine structure, can interact with chamber pressure oscillations to sustain instability. The existence of pressure amplitudes exceeding the amplitude of the noise floor is considered combustion instability, and in this sense, a liquid rocket engine is never perfectly smooth. Pressure fluctuations having peak-to-peak magnitudes less that 5% of the chamber pressure, $\frac{p'}{p_c} < 0.05$, are considered "smooth" and larger amplitudes generally designate "rough" combustion [41]. However, payload considerations often can only tol-

erate combustion instabilities having amplitudes much less than 5% of p_c. Furthermore, the nondimensional value of $\frac{p'}{p_c}$ has become the most common method for quantitative evaluation of combustion instability in LREs.

Combustion instabilities are also classified with regard to frequency. Frequencies less than 400 Hz are considered low frequency instabilities, also termed "chugging" instabilities. Interaction between injector feed systems and the combustion chamber is often the cause of low frequency instability [3], whereby chamber pressure momentarily rises above the propellant supply pressure(s), impeding inlet flow and initiating pulsations in propellant flow rate. Frequencies between 400 Hz and 1000 Hz are intermediate frequency instabilities and are commonly related to vibrations of the engine structure, but can also be caused by combustion processes. High frequency instability occurs at frequencies greater than 1000 Hz. Instabilities of this type, called "screeching" instabilities, generally involve excitation of acoustically resonant chamber modes and can rapidly amplify to destructive magnitudes; this makes diagnosis and prevention very challenging.

For LREs, early recognition of combustion instabilities has lead to a vast history of research. By the 1950s, German rocket technology from the Peenemuende program had literally been moved to France, the Soviet Union, and also the United States, where slight modifications to existing German V-2 and V-4 rockets exhibited combustion instability. After changing the concave injector face of the V-4 to a flat injector arrangement for the Navaho engine [43], the Navaho was unstable until injector baffles were added in 1960 [44]. During the same period of time, the X-1 engine was developed strictly for scientific exploration by an experimental engines group in the US Department of Defense. This program identified stability problems during staged startup tests and throttling tests [45], an issue which still occurs in modern engine development programs [44].

One of the first major campaigns in the engine stability discipline occurred in the

1960s, largely motivated to suppress vibrations in human-carrying flights to the moon [46]. Of the 3200 full-scale tests of the Saturn V's F-1 engines from 1962-1966, about 2000 of these tests were principally focused on combustion instability as part of a program called Project First [47]. It was learned that injector design, which controlled interactions between jets of fuel and oxidizer, was of utmost importance. The F-1 engine, in particular, used impinging style injectors where two jets of fuel and two jets of oxygen converge on a single impingement point to atomize and burn. Injector configurations which were originally deemed as producing 'absolutely' stable engine conditions were later shown to have less stability for different fuels and flow conditions [46, 48], revealing an incomplete understanding of the problem.

In parallel, the J-2 engine was also developed in the 1960s, but with key design differences from the F-1 and much better stability characteristics. The J-2 was one of the first successful hydrogen fueled rocket engines, whereas the F-1 used kerosene based fuel (RP-1). The J-2 also utilized shear-coaxial injectors [42]. The engine's first tests resulted in high frequency instability, but was reduced to an acceptable level using radial baffles. Particular conditions also resulted in low frequency chugging, which was eliminated using a metering orifice at the inlet of the oxygen tube. This technique effectively made oxygen flow insensitive to chamber pressure perturbations by increasing the pressure drop across the injector, but did not alter the high frequency instability margin [45]. Thus, although high and low frequency modes coexisted, tolerable high frequency instability endured from its own prevailing cause. This inadequate state of the practice resulted in inefficient approaches involving many expensive tests, often in a trial-and-error method. New programs specifically dealing with combustion instabilities in liquid rockets did not appear again in the U.S. until the 1980s, which coincided with a comprehensive research program in France following the failure of an Ariane vehicle due to combustion instability in a Viking engine [49].

LRE instability testing and abatement empirical techniques have improved since the extensive tests of the F-1, but a lack of reliable design criteria has made use of these techniques a requirement for new engine development programs. As mentioned above, acoustic baffles were an early choice for unstable engines, but additional hardware was avoided due to cost and weight. Instead, engineers adopted the injector, injector plenum geometry, and acoustic cavities as primary variables to control mixing while preventing propellant flow oscillations. Margins of stability were found to be sensitive to small changes in the geometry of shear-coaxial injectors. For example, in a subscale engine study a mild recess of the oxygen tube was found to shift the range of operating conditions in which the engine was stable [50]. Fig. 1.6 shows the numerous ways in which the oxygen tube or "LO_x post" has been manipulated in the past, and one or more of these designs is still used today [45]. Stability testing, on the other hand, has been aimed at identifying three areas of operations: stable, dynamically unstable, and spontaneously unstable. When the engine is subject to an initial, controlled perturbation, or "bomb", measured pressure oscillations will return to original levels if the engine is stable. In such tests, the chamber is required to reach stability within a limited time, which is calculated as a function of frequency. Conversely, a dynamically unstable engine will sustain significant chamber pressure oscillations after the perturbation subsides. An operating point is deemed spontaneously unstable if the engine is self-excited [51]. Finally, hydrogen temperature ramping is a stability testing method that should be mentioned due to its relevance to this study. A range of fuel temperatures is included while testing gas generator cycle and expander cycle LREs, because variables such as run time and throttle set point will determine the amount of heat energy added to the fuel upstream of the injector. Hydrogen temperature ramping has been used extensively in LH_2-LO_x engines, which is reviewed by Hulka and Hutt [45]. Hydrogen temperature variations dynamically alter fuel density, viscosity, and injector feed pressure, which can result in instability for a specific temperature band as shown in Fig. 1.5, for example.

Thus, hardware designs and stability verification tests provide the answers needed, but require a trial-and-error approach. Stability verification tests are intended for engine qualification, not engine development. Results indicate whether an engine is stable or unstable without explaining why, and this information is gathered and applied after engine development is complete. To reduce the number of design iterations and improve computational combustion tools, the community must turn to scientific research of the underlying physics.

1.2 Fuel Droplet Combustion

1.2.1 Alternative Fuels

Rapid rise in the demand for fossil fuels, combined with constricting emission regulations, is resulting in expanded interest in alternative fuel sources. Although long term goals focus on reducing dependence on crude oil, the current infrastructure requires near term solutions which involve hydrocarbons [52]. As a result, the U.S. is witnessing tremendous growth in the use of biofuels in automotive transportation, while the aircraft industry is exploring the use of fuels derived from a range of sources (coal, natural gas, etc.) from the Fischer-Tropsch (FT) process [53].

Ethanol and biodiesel have led the recent expansion of the biofuel industry. Since 2000, global ethanol and biodiesel production has increased by more than 200% and 500%, respectively, with the largest growth occurring in the U.S. [54]. Alcohols, such as ethanol and methanol, serve as gasoline substitutes with less pollutant emissions and higher octane performance [55]. However, the use of pure alcohols is unfeasible without significant changes to current engine designs. Gasoline-biofuel blends, on the other hand, maintain characteristics similar to those of gasoline and can be used in existing internal combustion (IC) engines with zero or few modifications. These blends are effective

in the current transportation infrastructure, which is cultivating a global market for blends of gasoline and 10% ethanol (E10) and 85% ethanol (E85). Thus, there remains an immediate demand for understanding the behavior of these fuels in the presence of acoustic forcing as their usage is increasingly diversified. Although the IC engine, the most popular biofuels application, features acoustic pressure waves in the intake manifold and ports [56], the term "combustion instability" is used in the realm of IC engines to describe unwanted cycle-to-cycle variation in cylinder pressures, temperatures, and species concentrations. Therefore, the effects of sound waves on IC engine combustion are quite different from that of a gas turbine combustor or liquid rocket combustion chamber. Still, suppressing or exploiting acoustics within intake systems is desired for IC engines [57], presenting a need to explore the behavior of biofuels in the presence of acoustic flow fields.

For aircraft propulsion, the use of Fischer-Tropsch (FT) fuels is seeing increased use as an alternative fuel. These synthetic fuels are produced by converting carbon based materials into liquid fuels using the Fischer-Tropsch process [58], and the USAF plans to meet half of domestic fuel needs with FT fuel by 2016. Progress toward this goal is being achieved by using a 50-50% by volume blend of JP-8 and FT fuel, and nearly the entire USAF fleet has been certified for use with this FT blend [53, 59].

Thus, near term progress in the search for alternative fuel sources is being made using multiple fuel types and blends thereof. However, increased use of these fuels must be accompanied by a better fundamental understanding of the fuels' performance in typical engine operating conditions. As discussed previously, typical conditions often involve resonant acoustic waves, which have repercussions unique to the fuel being used. The diffusive, convective, and reactive time scales affiliated with one fuel will differ from another, altering the effects of flow instabilities on the combustion process. Therefore, the successful proliferation of alternative fuels requires studies which define the relationship

between acoustic fluctuations and combustion processes for each fuel.

1.2.2 Fundamental Droplet Combustion

Droplet combustion plays a role in a significant portion of condensed phase combustion applications. Fuel injectors may create dilute sprays of tiny droplets, or instead liquid jets which form free ligaments and then break up into large droplets [60, 61]. In either scenario, the combustion of the field of droplets is largely governed by the combustion of individual droplets. Therefore, fundamental studies of the combustion of a single droplet offer conclusions which apply to a field of many burning droplets in a fuel spray. Such studies involve spherical or semi-spherical droplets, which are placed in quiescent flow or convective flow with slip. A diffusion flame front forms away from the droplet surface where fuel vapor, evaporated from the droplet surface, diffuses into and reacts with the oxidizer, usually air. Aside from sprays, droplet combustion is often used as a model for heterogeneous combustion in general [62].

Droplet sizes and lifetimes for quasi-steady droplet burning are described by the well-known d^2 law [63, 64]:

$$d^2(t) = d^2(t=0) - Kt \tag{1.6}$$

where the square of the droplet diameter d varies linearly with time t according to the burning rate constant K. The d^2 law has been shown to accurately describe droplet burning for spherical droplets in micro-gravity environments and semi-spherical droplets in normal gravity, but in the latter case the scaled diameter of an equivalent spherical droplet is required [65], as described below.

Micro-gravity droplet burning experiments provide ideal conditions for application of the d^2 law. Without gravitational forces, the droplet and the surrounding flame both maintain a spherical shape. This setting provides for straightforward determination of the droplet diameter d and thus the burning rate constant K. Experimental validation

of the d^2 law in micro-gravity conditions is shown by Law and Faeth [62] and Marchese *et al.* [66, 67], among many others. Work by Marchese *et al.* also includes imaging of electronically excited hydroxyl (OH*) radical chemiluminescence for the flame surrounding the droplet in order to validate the accuracy of a droplet combustion model, but more importantly, to confirm OH* chemiluminescence as an appropriate flame location indicator. For both fuels used, methanol and n-heptane, this is confirmed as an appropriate technique. To the knowledge of the current author, work by Dattarajan *et al.* [22] is the only set of experiments utilizing OH* chemiluminescence imaging for burning droplets in acoustically forced conditions. This technique is used for micro-gravity and normal gravity conditions, and Dattarajan et al. also successfully uses the d^2 law in quantifying burning rate constants for both sets of experiments.

Both micro-gravity and normal gravity environments require additional steps in the application of the d^2 law due to alterations in the shape of the droplet and flame. A more ellipsoidal droplet shape is formed by the balance of weight (for normal gravity) and surface tension, and is addressed by using an equivalent diameter d_{eqvs}, which is determined as the diameter of a sphere with a volume equal to that of the non-spherical droplet [65]. In normal gravity, the natural convection caused by thermal buoyancy creates an elongated flame shape with variations in flame standoff distance. Thus, the droplet combustion phenomena in normal gravity require understanding of steady flow effects even in the absence of forced convection. Still, the d^2 law has shown accuracy for droplets in non-quiescent flows [68, 69] when d_{eqvs} is used.

1.2.3 Effects of Acoustics on Fuel Droplet Combustion

Burning droplets exhibit salient changes in behavior when exposed to acoustic forcing. First and foremost, this has been documented by several experimental works which show burning rate constants increased by surrounding acoustic flow fields. Early observation

of the influence of acoustic forcing on burning rate is documented by Kumagai and Isoda [68], where an increase in the burning rate is thought to occur due to greater mass and heat transfer rates at the droplet surface due to steeper temperature gradients and species concentration gradients. This relationship has since been further explored by several others, including various studies by Saito *et al.* [70, 71]. Saito *et al.* [70, 71] record the effects of burning kerosene droplets in a normal gravity environment when the droplet is positioned near a pressure node (PN) or pressure antinode (PAN) of a standing acoustic wave. Locations of maximum and minimum velocity perturbations coincide with the location of a PN and PAN, respectively. Results show evaporation and burning rate constants of the burning droplet near a PN which are more than twice that of the unforced case, while positions near a PAN yield no significant alteration of these behaviors when compared to the unforced case.

Experiments performed in micro-gravity environments, on the other hand, lack the natural convective flow caused by thermal buoyancy, and thus isolate the effects of acoustic forcing. Burning droplets in zero gravity conditions are examined by several experimentalists [20–22, 72, 73]. Okai *et al.* [72] explore the influence of frequency and oscillation amplitude for n-octane single droplets and droplet pairs. Results show burning rates having a dependence on amplitude, with burning rates increasing with amplitude until flame extinction occurs, which is an event requiring more detailed inspection conducted by others [74, 75]. Experiments by Tanabe *et al.* [20, 21] confirm the burning rate conclusions noted above for both micro-gravity and normal gravity with n-decane droplets. Their studies situate the droplet at a pressure node, or between a pressure node and antinode of a standing acoustic wave. Moreover, their work reveals flame deformations in the presence of acoustic forcing, captured by flame imaging in the visible spectrum, and thus visualization of soot in the flame. Qualitative observations show flame deflections toward a PAN, or away from a PN.

To explain and predict this behavior, Tanabe *et al.* [20] propose an acoustic radiation force theory. Acoustic radiation forces are studied in a multitude of theoretical and experimental works extending back several decades. These forces are theorized and physically manifested by the existence of acoustic streaming, steady flow induced by an oscillating flow. Early experimental and theoretical study of acoustic streaming dates back more than one century [76, 77], which later allowed for theoretical formulations of the acoustic radiation force [78–80]. Expanding acoustic radiation force theory into the realm of combustion, Tanabe *et al.* [20] treat the region of hot products surrounding the droplet as a sphere of density ρ_p, which is less than the density of the gas surrounding the flame ρ_o. This discrimination between lighter and heavier gases permits a formulation from the work of Nyborg [79], where an equation is derived for the acoustic radiation force on a sphere of different density than that of the surrounding gas. Adding the assumption that $\rho_p << \rho_o$, Tanabe et al. reach an expression for the acoustic radiation force, F_R, acting on a sphere of hot products

$$F_R = \alpha(\rho_p - \rho_o)V\frac{\partial\overline{u'^2}}{\partial x} \tag{1.7}$$

where V is the volume of the sphere containing the hot products, x is the displacement of the droplet from the pressure node or pressure antinode location, and $\overline{u'^2}$ is the mean of the square of the local perturbation velocity u'. The coefficient α is defined as

$$\alpha = \frac{3\rho_o}{2(2\rho_p + \rho_o)} \tag{1.8}$$

The formulation in equation (1.7) is remarkably similar to that of a buoyancy force, which led Tanabe *et al.* to treat the acoustic radiation force acting on a burning droplet as analogous to a buoyancy force. In testing this theory, the flame behaviors observed in their imaging experiments affirm the prediction of the direction of flame deflection, where the acoustic radiation force calls for the hot products to shift towards a PAN. These experiments utilize a horizontal waveguide configuration, and thus involve only

horizontal acoustic radiation forces (i.e. parallel with sound wave propagation). The same group also tested this theory in a vertical waveguide configuration, generating forces which act upward, against thermal buoyancy forces [73]. Droplet combustion imaging in this experiment showcases a flame adopting a more spherical shell surrounding the droplet and claims gravitational forces are effectively "cancelled", but further evidence of this behavior is unavailable.

Droplet burning rate and flame orientation are also subject to extensive study in works performed at UCLA with regard to normal gravity [75, 81, 82], and experiments led by the same group in the micro-gravity facility at the NASA Glenn Research Center [22]. These phenomena were experimentally investigated using a horizontally oriented, long cylindrical waveguide, or Kundt's tube, either with a loudspeaker positioned at both ends or with one loudspeaker replaced by a sound reflector. Work by Dattarajan *et al.* [22] used the speaker and reflector configuration to create standing acoustic waves for methanol droplet experiments in micro-gravity. Similar to results discussed above, burning rates measured by Dattarajan et al. exhibit an increase over the unforced case when the droplet is located near a PN. In fact, for sound pressure levels of 135 dB, burning rate constants are as much as 200% greater than the unforced value for droplets situated near a PN. A smaller increase of 75% is shown for droplets near a PAN. For the same apparatus in normal gravity at 138 dB a smaller relative increase of 11-15% is measured for droplet near a PN, and the burning rate shows no alteration for droplets positioned near a PAN. With regard to flame deformation, the same study notes a trend in the direction of flame direction, where flames consistently deflect away from the approximate location of the PN, consistent with the theory of Tanabe *et al.* [20]. This flame deflection behavior is seen for both micro-gravity and normal gravity experiments, but with the micro-gravity conditions revealing a more obvious flame deflection direction due to the absence of thermal buoyancy.

Studies conducted solely in normal gravity by Rodriguez *et al.* [75] and Teshome *et al.* [82] offer results which agree with experiments above over a wider range of acoustic frequencies and for an array of fuels (ethanol, methanol, pure FT, and a JP-8/FT blend), but with more detail concerning the location of the burning droplet relative to the PN. Whether using a speaker-reflector configuration or a speaker-speaker configuration, the speaker assembly was moved as a unit within the waveguide while holding the droplet location constant. In this fashion, the location of the droplet could be varied with respect to the acoustic waveform. Further details on this technique are included in Section 2.1.

This technique exposes a trend of increasing burning rate as the droplet is moved from a PAN to a PN, with increases in the burning rate constant of up to 20%. These studies also give attention to the amount of flame deflection captured by imaging. Flame orientation generally agrees qualitatively with the theory of Tanabe *et al.* and with other pertinent experiments, but quantifying flame deflection brings light to certain unexplainable behavior. Imaging shows the largest deflections immediately next to a PN, with a dramatic switch in flame orientation when comparing results to the left and right of a PN. Teshome *et al.* [82] quantifies these deflections by measuring the flame deflection angle relative to the unforced, vertically oriented flame. To relate deflection angle measurements to the acoustic radiation force of Tanabe *et al.*, Teshome *et al.* balances the acoustic radiation force with the buoyancy force for the flame surrounding the droplet using a technique to be described further in 2.4.2. The resulting comparisons show that although equation (1.7) predicts flame orientation accurately, experimental results show significant quantitative differences. The trends and actual quantities evidenced by experiment are not captured by the same theory, and this is explored further in the present studies.

1.3 Shear-Coaxial Jets

A variety of coaxial jets have been used for injection of reactants in LREs. These include swirl coaxial jets, gas-centered coaxial jets, and impinging coaxial jets (shown in Fig. 1.6), to name a few. Unless otherwise noted, this study focuses hereafter on *parallel* shear-coaxial jets with an outer, annular jet of fuel and an inner jet of oxidizer, or an inert simulant in the inner jet and/or outer jet for a nonreactive configuration. Other coaxial jet types have been successful in LREs to date, but the parallel shear-coaxial jet still offers the most ideal condition for fundamental research due to its simplicity in injector design and exit flow conditions.

1.3.1 Nonreactive Shear-Coaxial Jets

1.3.1.1 General Characterization

The shear-coaxial jet involves three separate bodies of fluid in a concentric arrangement, creating two different shear layers. First, the inner jet and outer jet form the inner shear layer, where the traditionally denser fluid of the inner jet is disturbed by the surrounding outer jet, often at a higher velocity than the inner flow. A mixing layer is formed near the injector exit and increases in thickness in the streamwise direction, entraining more of the two fluids into the inner shear layer. Meanwhile, the outer shear layer forms between the outer jet and the ambient gas having zero bulk velocity. Each shear layer can exhibit large differences in velocity, density, and temperature, and as a result, become separate independent sources of instability which may interact. The two phenomena mentioned here, mixing and instability, are the primary foci of this discussion.

The streamwise development of these two shear layers was characterized in early research by Kwan and Ko [83] as shown in Fig. 1.7. Three zones are used to appropriately differentiate between regions containing an intact outer jet core, inner jet core, or the

existence of a single, fully merged jet. The region near the injector exit consists of both an intact inner jet core and outer jet core, and the downstream end of the outer jet core defines the end of the *initial merging zone*. The *intermediate zone* then, is defined as the region downstream of the outer potential core tip, but where distinguishable outer and inner mixing layers still exist. Primary vortices of the inner shear layer with convective velocity U_{c1} and secondary vortices of the outer shear layer with convective velocity U_{c2} reside in the initial merging zone, and then begin to interact in the intermediate zone. Last, the *fully merged zone* covers the region where the mixed jet behaves and appears as an equivalent singe jet of equal thrust.

Important nondimensional numbers and their definitions include the outer-to-inner density ratio $S \equiv \frac{\rho_{oj}}{\rho_{ij}}$, velocity ratio $R \equiv \frac{U_{oj}}{U_{ij}}$, and the momentum flux ratio $J \equiv \frac{\rho_{oj} U_{oj}^2}{\rho_{ij} U_{ij}^2}$. These three values are the most common measures for mixing and stability relationships and traditionally, $S \ll 1$ due to the jet's denser inner core. Additionally, with comparable mass flow rates ($\dot{m}_{oj} \sim \dot{m}_{ij}$), the outer jet velocity is much greater than that of the inner jet. This is certainly true for LO_x/GH_2 applications, as well as many of the nonreactive experiments of interest in this section. Consequently, at sub-critical pressure the shear forces at the inner shear layer cause a liquid inner jet to break up in a classical cascade of ligament and droplet formation, and finally atomization. For nonreactive jets, the break up process is characterized by J, the inner jet Reynolds number $\mathrm{Re}_{ij} \equiv \frac{U_{ij} D_1 \rho_{ij}}{\mu_{ij}}$, and the gaseous Weber number $We \equiv \frac{\rho_{oj} U_{oj}^2 D_1}{\sigma}$, where D_1 is the inner jet exit diameter and σ is the surface tension. These parameters can be used to identify multiple regimes of recognizably different break up processes [16]. Instantaneous images of inner jet break up for high We flows are shown in Fig. 1.8 due to their direct relevance to this study. More detailed characterization of mixing and stability is still subject to research.

1.3.1.2 Near-field Mixing

The earliest purported experimental study of coaxial jets was done by Forstall and Shapiro [84] for single-phase flow, where firm qualitative trends were established for the mixing of the gas inner and outer jets at atmospheric pressure. As the velocity of the air outer jet was increased, it was shown that the helium-air inner jet was less distinct. The boundary between the two jets eventually became ambiguous with downstream distance, and the streamwise position at which this occurred advanced upstream as the jet's velocity ratio increased.

Chigier and Beer [85] confirmed the general conclusions of Fortall and Shapiro [84] by quantitatively investigating the velocity distributions of air inner and outer jets issuing into quiescent air. Velocities were calculated using differential pressure measurements to give radial velocity distributions at several axial positions from the injector exit to $8D_1$ downstream. The injector used by Chigier and Beer [85] contracted the inner diameter and outer annulus near the exit rather than using a parallel shear-coaxial element. Velocity ratios ranging from 0.024 to ∞ were used to span from conditions nearly equal to a single jet and an annular jet, respectively. For a low velocity ratio, $R = 0.085$, the outer jet completely merged with the inner jet within a distance $D_2 - D_1$ from the exit and the central potential core extended far downstream similar to a single air jet. For a larger velocity ratio, $R = 2.35$, the potential core to end at a distance was just $3D_1$ from the exit.

In the 1970s, several bodies of work investigated near-field mixing of coaxial jets with attention to area ratio $AR \equiv \frac{A_{oj}}{A_{ij}}$ as well as R (Champagne and Wygnanski [86], Ko and Kwan [87], and Ko and Kwan [88]). Again, these experiments used air jets injected from contracting coaxial nozzles into air, with Reynolds numbers as high as 10^5 for each nozzle. Champagne and Wygnanski [86] noted that when increasing the outer diameter of the annulus to increase AR from 1.28 to 2.94 while holding R constant, an

increase in the outer jet potential core length was observed. However, this length was not affected by changes in R for the flow conditions used in their work ($0< R\leq 10$). The inner jet behavior though, depended on both AR and R. In this respect, Champagne and Wygnanski [86] deduced that the outer jet core length acts similar to a single jet in the ambient gas, having little sensitivity to changes in the inner jet. Ko and Kwan [88] also compared the coaxial jet to a single jet, but clearly defined regions for each class of flow. The outer shear layer was called the *secondary mixing region*, which was deemed equivalent to a single jet in potential core length and spreading behavior. The inner shear layer was called the *primary mixing region*, which was said to function like the layer between a single jet in a co-flowing ambient gas as opposed to a co-flowing stream of finite thickness. But, experimental conditions in Ko and Kwan [88] were limited to $R < 1$ (R=0.3, 0.5, 0.7). The results of both groups reaffirmed the finding of previous researchers that the velocity difference ($|U_{oj} - U_{ij}|$) is positively correlated with mixing due to enhanced shear between the inner and outer jets.

An extensive array of analytical derivations and experiments on coaxial jet and two-dimensional shear layer mixing were pursued by Dimotakis [89], and later by Dahm and Dimotakis [90], Dimotakis [91], and Dahm *et al.* [92]. These works aim to describe mixing layers by quantifying mass entrainment, shear layer convection velocity, circulation, and vortex size, to name a few. Dimotakis [89] used empirical relations to derive an expression for the volume flux entrainment ratio E_v and the mean vortex spacing to position ratio $\frac{l}{x}$. More importantly, a relation for shear layer convection velocity was derived by applying the Bernoulli equation to a two-dimensional shear layer. Dimotakis [89] asserted that a stagnation point must exist between vortices when in the Galilean rest frame of the vortices, and thus, Bernoulli's equation would apply along a line through this point. Following this frame of reference in Fig. 1.9, neglecting gravity, and assuming that differences in static pressure can be ignored, then the dynamic

pressures in each free stream were matched, i.e.

$$\rho_1 \left(U_1 - U_c\right)^2 \approx \rho_2 \left(U_c - U_2\right)^2 \tag{1.9}$$

Solving for the convection velocity, as in Dahm *et al.* [92], yields

$$U_c \approx \frac{U_{ij}\rho_{ij}^{\frac{1}{2}} + U_{oj}\rho_{oj}^{\frac{1}{2}}}{\rho_{ij}^{\frac{1}{2}} + \rho_{oj}^{\frac{1}{2}}} \tag{1.10}$$

for a shear-coaxial jet. In contrast to prior studies of isodensity jets, this relation accounts for different densities as well as velocities, and is far more pertinent to bi-propellant applications and research thereof. Other studies have since validated and applied eqn. 1.10 for this reason [92, 93].

Modern coaxial jet research has sought to account for an even larger body of variables to describe mixing and break up, in addition to velocity and density. These include chamber pressure, outer and inner jet temperature, viscosity, and surface tension forces present in two-phase flows. Reactive experiments are often the most holistic approach for research of combustion systems, but construction and maintenance of combustion facilities remains costly, especially for cryogenic applications such as LREs. In terms of scientific value, nonreactive experiments can also simplify the physics of otherwise complex flows, clarifying the results. Therefore, nonreactive experiments have remained an excellent research strategy throughout the 1990s, 2000s, and today.

During this period, a significant effort was made to categorize two-phase coaxial jets according to the break up process of the inner liquid core. Chigier and Farago [94] used Re_{ij} and We to characterize several regimes of inner jet break up, and Lasheras and Hopfinger [95] extended their work to include the effects of J and the Ohnesorge number $Oh \equiv \mu_{ij}/(\rho_{ij}\sigma D_1)^{\frac{1}{2}}$. The culmination of this work is shown in Fig. 1.10, where five regimes of break up for air-water jets at atmospheric pressure are shown to occur according to the values of Re_{ij}, We, J, and Oh. These five regimes are axisymmetric

and nonaxisymmetric Rayeigh break up, shear break up, membrane break up, and fibre-type break up. The latter two regimes are of particular interest here, because LRE flow conditions often exhibit high We values produced by high velocity gas in the outer jet which strips the outer perimeter of the denser inner jet. Membrane and fibre-type break up were characterized in Lasheras and Hopfinger [95] as having an inner core length L_b less than $8D_1$. Under the action of the gaseous jet turbulence, the liquid core breaks into clusters and ligaments near the injector exit and atomization can occur less than $2D_1$ from the exit for $We{\sim}1000$. Their experiments support the correlation

$$\frac{L_b}{D_1} = \frac{6}{\sqrt{J}} \left(\left| 1 - \frac{1}{R} \right| \right)^{-1} \tag{1.11}$$

for use in LREs, but devise a separate relation for low We flows not in the fibre-type regime. Extensive experiments by Baillot *et al.* [16] not only support the numerous regime boundaries in Fig. 1.10, but also support the $L_b{\sim}J^{-\frac{1}{2}}$ relationship, despite using an impinging inner jet shear-coaxial injector (see Fig. 1.6c). However, their experiments also included tests at very slightly elevated chamber pressure. At just 2.16 and 3.6 kPa above atmospheric pressure, the Re_{ij} and We values for break up regime boundaries were clearly altered, revealing the importance of pressure in shear-coaxial jet break up and atomization.

The effects of pressure are particularly important to the LRE community, where high chamber pressures are desired in order increase specific impulse. Although, supercritical pressure introduces less understood physics into the mixing process. The well-known features of liquid jet break up (e.g., ligaments, droplets, and atomization) are replaced with indiscernible fluid interfaces and obscure lumps rather than droplets. The first apparent set of experiments on jets in supercritical environments was done by Newman and Brzustowski [96] in 1971. Their experiments involved backlit shadowgraphy of single jets of liquid CO_2 in a gaseous nitrogen environment. With the chamber pressure above the critical pressure of CO_2 and the temperature below the critical temperature of CO_2,

i.e. $p_c > p_{crit,CO_2}$ and $T_c < T_{crit,CO_2}$, CO_2 droplet sizes were observed. As T_c approached T_{crit,CO_2}, droplets became smaller until the liquid-gas interfaces became unobservable for $T_c \geq T_{crit,CO_2}$. At this point, the flow could no longer be described as heterogeneous two-phase flow.

Since the work of Newman and Brzustowski [96], a large body of work has supported and expanded upon their findings. A number of studies have been done at both the U.S. Air Force Research Laboratory (AFRL) and the German Aerospace Center (DLR), and a thorough review of their advancements prior to 2006 is found in Oschwald *et al.* [97]. Nonreactive, near-critical and supercritical experiments at AFRL began with single liquid nitrogen (LN_2) jets in a quiescent nitrogen environment and later experiments added a nitrogen outer jet in a shear-coaxial configuration. For the single jet, drops at the liquid-gas interface were no longer detected when the chamber pressure reached $\frac{p_c}{p_{crit,N_2}} = 1.03$. Instead, finger-like entities were seen at the interface. Chamber pressures greater than $2.5p_{crit,N_2}$ were eventually tested, and the continuous shrinking of the dense liquid core was observed as pressure increased to and beyond this point, as well as the suppression of droplet production for single jets and coaxial jets [97–99]. Chehroudi *et al.* [98] also showed quantitative evidence of gas jet behavior to support the gas-like appearance of the jet in supercritical environments for a specific range of jet densities.

Meanwhile, nonreactive experiments at DLR by Telaar *et al.* [100] and Mayer and Smith [14] used LN_2 and gaseous helium (GHe) coaxial jets to better replicate the density ratios of LO_x-GH_2 rocket engines. A sample of their shadowgraphy results is shown in Fig. 1.11. These results reinforced the LN_2-GN_2 results noted above, even for species with very different critical pressures and temperatures. The development of the inner jet was said to be dependent on its own fluid properties. Complementary experiments were performed with LN_2-GH_2 flows by Oschwald *et al.* [101] using Raman scattering for quantitative density measurements. This diagnostic technique provided Raman signals of

nitrogen and hydrogen at two different wavelengths and appropriately filtered the signals to effectively measure the species fraction of each. The results were analyzed to measure a streamwise location at which the jet was completely mixed with the background gas, culminating in salient evidence of mixing or lack thereof. This was the first study measuring species fractions in sub and supercritical pressure environments.

Since the composite review by AFRL and DLR in Oschwald *et al.* [97], further backlit image analysis of coaxial jets at AFRL has accumulated strong indications of a correlation to predict inner core length L_b for a wide range of flow conditions. First, Davis and Chehroudi [102] and Davis [103] used low speed imaging (< 1 kHz) to optically measure L_b, and organized a large amount of data from the literature to create a comprehensive review of the dark core length's dependence on chamber pressure. Leyva *et al.* [29] advanced this study to include variations in J and the influence of acoustic forcing, both of which were found to have a significant impact on L_b and jet spread angle. With the use of high speed imaging (> 10 kHz), coherent jet oscillations were also recognized when acoustic forcing was applied. For example, L_b measured for jets at a PN location in the chamber were found to be less than those measured for jets at a PAN location [75, 81]. Rodriguez [75] also included variations in injector area ratio AR in a study which was expanded to include a recessed inner post by Graham *et al.* [104]. In conclusion, an array of variables encompassing injector geometry, density ratio S, velocity ratio R ($J = SR^2$), chamber pressure, and acoustic forcing conditions have been shown by works at AFRL to alter shear-coaxial jet mixing as evidenced by variations in dark core length.

Experimental data from testing of two shear-coaxial injectors, sub and super-critical pressures, and J values ranging from 1 to 23 was used by Teshome [23] to find an empirical correlation for L_b. This new data was supplemented with experimental data from studies mentioned above ([23, 75, 104, 105]) to create an empirical solution to

predict L_b. Injector geometry and momentum flux ratio were combined to create the nondimensional parameter G, which takes the form

$$G = c_1 J^{c_2} \left(\frac{t}{D_1} \right)^{c_3} (AR)^{c_4} \tag{1.12}$$

where t is the wall thickness of the coaxial injector's inner tube. The constants c_1, c_2, c_3, and c_4 were chosen to fit the data of four injectors, all having different combinations of large or small values for $\frac{t}{D_1}$ and AR. Again, this study demonstrated the importance of chamber pressure through the difficulty in producing a correlation applicable both above and below the critical pressure. Teshome [23] was instead forced to choose two unique sets of constants; the first set was chosen to fit L_b vs. G data for sub-critical pressure and a second set was required for super-critical pressure. Although a physics-based approach may identify the missing factors necessary to predict dark core length across a range of pressures in the future, this correlation remains the most comprehensive empirical formula to quantify mixing for LRE-like coaxial injectors by including the majority of the variables identified in the studies cited above. Future work at AFRL will explore the effects of these variables for reactive propellants.

1.3.1.3 Stability Consideration

Early jet turbulence researchers recognized that many combustion systems are diffusion-controlled, having chemical kinetics which are so rapid that the reaction rate is entirely dictated by turbulent mixing [86]. When isolating these mixing processes in nonreactive experiments, these researchers also recognized the existence of high amplitude modes of fluid instability which would completely dominate the mixing processes of a combustion system. Several key studies will be discussed here which give attention to the frequencies and amplitudes of these coherent instabilities rather than chaotic turbulence.

Crow and Champagne [106] characterized the natural instability of single jets according to the Strouhal number St and explored the relationship between instability

amplitude and St. The Strouhal number is a nondimensional measure of frequency f generally defined as

$$St = \frac{fx}{u} \tag{1.13}$$

where x is a characteristic length scale and u is a characteristic velocity scale. Crow and Champagne [106] explored single jets of water, and later air, and defined x as the jet exit diameter D which was held constant while the mean jet exit velocity U_e was controlled. The jet spectra was probed at various positions downstream of the exit, and a natural oscillation was found to occur at $St = 0.30$. This mode was amplified downstream of the exit until reaching a peak amplitude at x/D=9.5. Crow and Champagne then used a loudspeaker upstream of the jet exit to force the jet at a controlled frequency, unequal to the jet's natural frequency. In this way, St was controlled using f and U_e to employ a range of $0.15 < St < 0.60$. They found that the forcing frequency could be measured and controlled in the near-exit region $x/D < 8$, but the natural mode, or "preferred" mode, dominated and saturated in the region $x/D > 8$ regardless of the forcing frequency. This conflicted with existing linear stability theory which failed to predict $St = 0.30$, but rather asserted an increasing instability amplitude for increasing St. A significant conclusion of Crow and Champagne's study was that linear stability theory could not be used to predict the jet's dominant mode because nonlinearity established the preferred mode of $St = 0.30$. This is a classical work in single jet instability due to its clear demonstration that jet instability has a preferred mode which can be scaled using St.

Since the work of Crow and Champagne, single jet preferred modes have been shown to adopt different values of St and definitions thereof. As an example, the systematic experimental study by Birbaud *et al.* [107] defined a preferred mode Strouhal number for both the jet and the shear layer existing between the jet column and the surrounding quiescent gas, St_D and St_θ, respectively. St_D was defined using the jet exit diameter D and St_θ was defined using the initial momentum thickness θ_0, a measured quantity. For low Reynolds number air jets at atmospheric pressure, the jet mode frequency f_D and

the shear layer mode frequency f_θ were measured for natural jets and for jets subject to upstream acoustic forcing at f_0. This study not only asserted that two natural modes can exist in single jets, but also that the values of the preferred Strouhal numbers, St_D^p and St_θ^p, can be used to predict the response of jets to acoustic forcing. Particularly, when f_0 was chosen to be near the preferred mode f_p, the jet adopted and amplified the forced mode as the convective instability moved downstream. When f_0 was much greater than f_p, the jet was insensitive to upstream modulations and did not display evidence of the forced mode. This study represents the field's advancement since the work of Crow and Champagne, demonstrating that even without the added complexities of a coaxial jet, single jet natural modes feature several key behaviors. Mainly, St can be intuitively defined by parameters characteristic of the source of the instability, such as θ_0, and a jet is more likely to amplify a forced mode if the forcing frequency is near that of the natural jet instability.

Coaxial jets may also manifest the same principles as single jets, albeit with more complexity. In early work by Kwan and Ko [83] and Ko and Kwan [88], similar concepts were explored for shear-coaxial jets. Velocity fluctuation measurements revealed two modes in the initial merging zone; a low frequency mode was measured from primary vortices in the inner shear layer and a high frequency mode was measured from secondary vortices in the outer shear layer. In the intermediate zone the low and high frequency vortices merged and one overtook the other to dominate the fully merged zone. Like Crow and Champagne [106], Ko and Kwan [88] described modes according to St and attempted to find one St value to predict the jet's preferred mode over a range of flow conditions. However, Ko and Kwan acknowledged that the complexity of a coaxial jet not only required different length and velocity scales than the single jet, but also called for separate length and velocity scales for the inner shear layer and the outer shear layer.

These two definitions followed as

$$St = \frac{fD_1}{\left[0.6\left(U_{ij} - U_{oj}\right) + U_{oj}\right]/0.6} \tag{1.14}$$

$$St = \frac{fD_3}{U_{oj}} \tag{1.15}$$

where eqns. 1.14 and 1.15 applied to the inner shear layer mode and outer shear layer mode, respectively. Experimental validation in Kwan and Ko [83] and Ko and Kwan [88] supported these definitions. Although the experiments were limited to $R < 1$, this work clearly described two sources of shear layer instability in coaxial jets and stark differences between them. The definition of eqns. 1.14 and 1.15 is the earliest attempt to differentiate multiple sources of coaxial jet instability with individual scaling laws. Other researchers have since defined St to include variables such as jet exit boundary layer thickness and a combined jet mean velocity to reach a St scaling which holds for greater values of R [108, 109].

Advances in stability theory have since isolated additional sources of instability in two-dimensional shear layer mixing, which can provide insight to possible sources of instability in three-dimensional coaxial jets. The field of linear stability theory has seen vast development and application since its ineffectiveness in explaining the results of Crow and Champagne, and could be reviewed to designate flows which are accurately and inaccurately predicted by stability theory. A lengthy review of this kind will not be offered here. However, a few select studies of this kind will be discussed, because despite the shortcomings of linear stability theory when treating LRE-like flows with complex geometry and nonlinear effects, *linear stability results offer intuition for scaling laws such as St*.

A straightforward classification of modes was included in a theoretical stability study by Yecko *et al.* [10], where a two-dimensional, liquid-gas shear layer of unequal density, velocity, and viscosity was subject to temporal stability calculations. The common

Kelvin-Helmholtz instability was identified resulting from a velocity deficit at the interface, as expected. Inviscid theory will capture this mode, which is said to be the cause of instability in the experiments of Crow and Champagne (Talamelli and Gavarini [108]), but will not capture Tollmien-Schlichting (T-S) type modes. A liquid T-S mode and a gas T-S mode were identified by Yecko *et al.* [10] as the result of Reynolds stress at a liquid-gas or liquid-liquid interface, which cannot be neglected in the cryogenic flows of rocket engines. Later experimental work by Matas *et al.* [93] showed that viscous models often predict higher frequencies in spatial stability calculations though, and a correct estimation of the shear layer convection velocity U_c is more critical for obtaining accurate frequencies. Their own calculations assumed the formula of eqn. 1.10 for U_c from Dimotakis [89]. Lastly, Matas *et al.* [93] noted that instability frequencies between streams with finite thicknesses would be even more difficult to estimate, because the modes of multiple shear layers will communicate.

The presence of global instability in a number of different types of shear flows is well known [25]. As noted by [110], evidence in the spatial evolution of the disturbance amplitude for a nonlinear global mode in an infinite domain consists of a sharp front located at the upstream boundary of the absolute instability region, where the disturbance amplitude abruptly increases and stays high as one moves downstream. Under such conditions the flow behaves as an oscillator rather than a noise amplifier. Flows that can become globally unstable include low density axisymmetric jets in quiescent surroundings below a critical jet-to-surroundings density ratio [111, 112], countercurrent mixing layers above a critical velocity difference [113, 114], and wake flows above a critical Reynolds number [115, 116]. The evidence for such transitions includes phenomena that have already been documented for the transverse jet [117], e.g., (1) clear changes in the spectral character of the shear-layer, with strong oscillations at narrow spectral peaks for global instability, representing pure tones with higher harmonics, (2) a rather dramatic alteration in the value of the Strouhal number associated with the initial insta-

bility as the influencing flow parameter is brought into the range for globally unstable flow, and (3) little spectral alteration of the globally unstable flow in response to low to moderate flow excitation, in contrast to significant spectral alteration of the convectively unstable flow during such excitation. Additional phenomena associated with a transition to globally unstable conditions include: (4) a rather abrupt increase in the amplitude of the disturbance within and near the shear-layer as one approaches the critical flow parameter, consistent with the characteristics of the Landau equation [25, 113], and (5) a reduction in the energy transfer from fundamental to subharmonic frequencies along the shear-layer, and hence a reduction in the strength of subharmonics and corresponding inhibition of the vortex pairing process after the transition. In addition, for the low density free jet it has been shown that very strong external sinusoidal excitation can be used to overcome the fundamental instability mode for globally unstable conditions [118, 119]. These findings are consistent with theoretical work [120] which suggests that for spatially developing flows, external forcing upstream of the transition from convective to absolute instability can overwhelm the naturally occurring absolute instability. The low density jet experiments show that at forcing frequencies f_F that are relatively close to the global instability frequency f_{nat} and/or at very high amplitude forcing, the global frequency is not observed at all, and the forcing frequency dominates the flow's spectral character, with the capacity to either reduce or enhance jet mixing. The excitation amplitude at which the flow "locks" on to the forcing frequency f_F increases in proportion to $\mid f_{nat} - f_F \mid$, consistent with the flow transition to a global mode via a Hopf bifurcation [25, 110]. The capacity for strong sinusoidal forcing to alter the global instability is viewed as a means of controlling the low density jet.

Jendoubi and Strykowski [121] used inviscid, spatio-temporal stability theory to describe the modes created by axisymmetric jets with ambient co-flow and counter-flow. This study focused on the behavior of two particular modes with regard to large changes in the density ratio and velocity ratio. "Mode I" was described as a shear layer insta-

bility, having peak velocity perturbations at the interface which were not felt in the center of the jet nor at a position far from the jet. "Mode II" was deemed a jet column mode, because peak perturbations were located at the shear layer as well as the jet centerline. These two modes were found to not only produce convectively unstable modes, but for a specific range of velocity and density ratios each mode predicted absolute instability. The transition from convective to absolute instability was the focus of Jendoubi and Strykowski [121]. This transition is important because should a mode become absolutely unstable, it becomes time-amplifying in a localized area and basically self-excited, whereas convective modes develop as the waves are conveyed downstream. If an LRE, for example, sustained absolutely unstable propellant flows, then the self-excited mixing of reactants may become insensitive to acoustic feedback. To explore this possibility, a plot from Jendoubi and Strykowski [121] is presented in Fig. 1.12, showing convective-absolute transition lines calculated as a function of the velocity and density ratio. The operating conditions of a typical LO_x-GH_2 LRE are added, showing that absoulte instability brought on by these particular modes is unlikely.

Absolute instability is especially relevant to combustion instability when considering its resistance to external forcing. This feature has been investigated experimentally for single jets by Getsinger *et al.* [122], among others [115, 118, 123]. For low density jets in crossflow, Getsinger *et al.* [122] found an absolutely unstable jet to be resistant to upstream forcing in a way which was dependent on the jet-to-crossflow momentum flux ratio and the forcing frequency. It was observed that as the forcing amplitude increased, a "lock-in" amplitude was eventually reached such that the formerly absolutely unstable jet adopted a convective instability with a frequency equal to the forcing frequency. The lock-in amplitude was found to be dependent on momentum flux ratio and linearly dependent on the nondimensional forcing frequency F, defined as a ratio of the forcing frequency f_F to the jet's natural frequency f_0. Other lock-in experiments of single jets have also observed this relationship, namely nonreactive work by Sreenivasan *et al.* [123]

and nonreactive and reactive experiments recently presented in Juniper *et al.* [118]. To the author's knowledge, the first experimental evidence of the lock-in phenomenon was shown in Provansal *et al.* [115] for the wake behind a cylinder. If applied to coaxial jets, this concept could aid investigators when diagnosing an acoustically forced flow condition as absolutely or convectively unstable or when classifying flows according to their resistance to said forcing, which is the foremost objective of the present study.

From a theoretical standpoint, to predict absolute or convective instability for coaxial jet flow conditions requires that the results of Jendoubi and Strykowski [121] be supplemented with an analysis specific to coaxial jets. The analysis must account for sources of instability in the outer shear layer and the inner post wake, both of which were not present in Jendoubi and Strykowski's study. Their results indicate that LRE coaxial jets are far from the convective-to-absolute transition due to high speed co-flow and dense inner jets, preventing both the jet column and shear layer modes from reaching absolute instability. This is supported by Fig. 1.12. But, a finite thickness inner post creates a potential source of absolute instability in the wake region.

In a more recent theoretical study by Talamelli and Gavarini [108], the outer shear layer as well as a finite inner post thickness were included in an effort to explore these two regions as possible sources of absolute instability. Three unstable modes were identified: one in the outer shear layer and two associated with the inner post wake. For a small but nonzero wake velocity, one of the wake modes was shown to become locally absolutely unstable. It is also notable that the absolutely unstable mode could be described by $St \approx 0.24$ when St was calculated using the wake thickness and mean free stream velocity, i.e. $(U_{ij} + U_{oj})/2$. Further inspection of this mode showed that the absolute instability exists for a limited range of R, and the extent of this range depended on the assumed momentum thickness θ and the wake velocity. Specifically, a significant amount of reverse flow in the wake increased the likelihood of absolute instability. As

will be shown later, wake induced modes are particularly important in the present study due to the injector's finite inner post thickness t, which creates a visually identifiable recirculation zone in the near-field.

Although inviscid and incompressible assumptions were made in Talamelli and Gavarini's analysis, LRE coaxial jets may manifest the absolutely unstable wake mode described above. Teshome [30] extended the previously discussed work at AFRL [75, 81, 104, 105] by measuring natural and acoustically forced coaxial jet instability frequencies for sub- and near-critical chamber pressures, simulating the cryogenic propellants of LREs in a nonreactive LN_2-GN_2 configuration. Images from high-speed shadowgraphy were used to determine the frequencies most representative of a range of flow conditions, both acoustically forced and unforced. This was achieved by extracting spectral information from image sets using a partial orthogonal decomposition (POD) algorithm to reconstruct modes with a high energy content garnered from fluctuating image intensities. Separate spectra plots were obtained for each flow condition. It was observed that for high J and $AR(\equiv \frac{A_{oj}}{A_{ij}})$ the jet appeared to sustain its natural instability frequency even when acoustically forced, displaying absolutely unstable behavior. Conversely, low J and AR conditions were sensitive to forcing, adopting a instability frequency equal to f_F. In this study, high amplitudes of acoustic forcing were used to replicate the severity of an actual engine instability rather than the low level forcing technique of Getsinger *et al.* [122], for example. Thus, an absolutely unstable wake mode may be present in the experiments of Teshome [30], and a more detailed alteration of forcing amplitudes to confirm frequency lock-in could be performed as reinforcement.

Due to the limited amount of experiments regarding forcing of absolutely unstable coaxial jets, it is difficult to anticipate the appearance of this phenomenon. The behavior of convectively unstable jets though, is well documented for experiments where these flows are subject to transverse acoustic forcing, and a short list of studies will be discussed

here to classify the expected results. The earliest experiments of this kind were reported by Miesse [124] and Buffum and Williams [27], both of which involved two-phase flow. Miesse [124] recorded a definite jet response to external acoustic forcing, regardless of whether wave propagation was parallel (longitudinal) or perpendicular (transverse) to the jet axis. Buffum and Williams [27] focused on single water jets exposed to transverse, standing acoustic waves. When placed at a pressure node (PN) for frequencies less than 500 Hz, a whipping motion was observed which is analogous to a jet injected into an oscillating crossflow. For SPL>161 dB, increased atomization was also recorded. Subsequent studies focused on the increased break up and atomization caused by acoustic forcing. For example, Carpentier *et al.* [26] also studied single liquid jets in transverse acoustic fields, but noted steady jet flattening for acoustic frequencies ranging from 500 to 1864 Hz. The jet was constricted in the wave propagation direction and stretched in the direction perpendicular to wave propagation, a phenomenon also reported for high pressure in Chehroudi *et al.* [98]. However, Carpentier *et al.* [26] did not observe the sinuous jet motions as in Buffum and Williams [27], and used a simple analytical model to explain the existence of both regimes of jet response, primarily categorized by frequency. In conclusion, their model mathematically explained that if the values of the acoustic velocity u' and $1/(f_F D_1)$ are large, then sinuous jet forms can result. Otherwise, an acoustic radiation force F_R similar to that discussed in section 1.2.3 induces steady flattening and fanning in the plane of the PN.

When tested for coaxial jets, these conditions produce quite different results. Baillot *et al.* [16] tested liquid-gas coaxial jets with regard to the relationships stated by Carpentier *et al.* and discerned different behaviors at PNs and PANs. At a PN, Baillot *et al.* [16] also observed jet flattening, but noted that for a sufficient amount of outer jet flow no flattening occurred. Again, this phenomenon was also observed by Leyva *et al.* [29] and Chehroudi *et al.* [98] for elevated pressures. At a PAN, jet break up was only influenced by acoustics if in the presence of outer jet flow, which is a feature that

emerged as a result of outer jet flow pulsations. By periodically impeding outer jet flow with chamber pressure fluctuations at a PAN, acoustics increased mixing and breakup via the formation of axisymmetric vortices. Although the nonreactive experiments cited above exclude the effects of speed of sound gradients inherent in high temperature combustion systems, many of these rules hold true for acoustic forcing of reactive flows, as discussed below.

1.3.2 Reactive Shear-Coaxial Jets

1.3.2.1 General Characterization

The flame of a reactive coaxial jet adds complexity to fluid instability and mixing, but many key features are retained from nonreactive jets. As shown in Fig. 1.13, the vortex structures at the inner shear layer manipulate the reaction zone, creating a wrinkled flame. A ring shaped flame forms a distance x_f downstream from the inner post, and its flame thickness δ_f grows in the streamwise direction x until the flame merges to become a single, broad flame downstream of the liquid core tip. An attached flame corresponds to $x_f = 0$. Near the reaction zone, steep temperature gradients promote a rapid density reduction of both the liquid oxygen core and the outer gaseous fuel, a process controlled by convective transport of hot gases. Thus, the state of the dense inner jet is significantly altered by the wrinkled flame, and if reaction rates are controlled by mixing or liquid vaporization then this can generate combustion instability. Analysis by Snyder *et al.* [125] confirmed that combustion of LO_x-GH_2 coaxial jets in LREs is indeed a oxygen vaporization limited process, because the characteristic vaporization time scale t_v is longer than both the characteristic chemical and mixing time scales, t_c and t_m, i.e. $t_c < t_m < t_v$ (see also Candel *et al.* [126]). Therefore, the interfacial instabilities of the liquid oxygen core and measure of its length, L_b, are paramount for understanding combustion instability.

As a direct result of the added heat release of a combustion system, fluid mixing and instability cannot be easily isolated as in the nonreactive flows discussed heretofore. Measures of mixing such as L_b are consequently studied concurrent with instability, because fluid mechanics are difficult to decouple from unsteady heat release and the ensuing chamber acoustics of a combustion instability feedback loop, shown in Fig. 1.2. Suitably, the following section reviewing reactive coaxial jet research is ameliorated by discussing mixing and stability phenomena together in light of their close coupling in reactive flows.

1.3.2.2 Propellant Mixing and Stability Consideration

Although LO_x-GH_2 engines were thoroughly tested by engineers as early as the 1950s and '60s, little fundamental research was done during this period. At the Lewis Laboratory (now the NASA Glenn Research Center) in 1958, Baker and Steffen [127] used a bench scale thrust chamber with multiple propellant combinations to measure high frequency pressure chamber pressure fluctuations for various chamber lengths. Little high frequency instability was observed for hydrogen-oxygen propellants in particular, and in experiments with coaxial injectors no instability was present. Other propellant combinations brought about significant longitudinal modes.

Early experiments of this kind were limited to direct probe measurements as opposed to optical techniques. A later set of experiments from Heidmann [128] at the same laboratory in 1965 included some of the first images with evidence of mixing alterations caused by combustion instability. For a small shear-coaxial injector ($D_1 = 0.7$ mm) LO_x-GH_2 combustion images resolved the outline of the liquid core, and the core length L_b was shown to respond to transverse waves. Their imaging technique could not resolve break up and vaporization, but clearly displayed a reduced L_b in the presence of transverse acoustic modes, a behavior likened to a liquid jet in gaseous cross-flow.

Numerous other experiments of small-scale thrust chambers by NASA in the 1960s confirmed Baker and Steffen's conclusion that LO_x-GH_2 coaxial jets produce stable conditions relative to their marginally stable LO_x-Hydrocarbon counterpart. In fact, it was the Apollo program's difficulty with combustion instability in the kerosene based F-1 engine that largely motivated the surge in research during this period. Meanwhile, the J-2 engine, a hydrogen fueled upper stage engine flown during Apollo missions, exhibited minor instabilities which were quickly abated (see section 1.1.3). Oxygen-hydrogen coaxial jets were being adopted as a stable configuration by both the engineering and the scientific communities. At the conclusion of NASA's subscale campaign of experiments at the Lewis Laboratory, it was even stated that ". . . all liquid oxygen-hydrogen staged combustion tests in the U.S. have been stable at high frequency." [45] The knowledge acquired up to this time was consolidated in NASA SP-194, *Liquid Rocket Engine Combustion Instability.*

Motivation for fundamental research in this area then subsided until two in-flight incidents of combustion instability occurred for engines of the European Ariane rocket [3]. These unexpected events renewed research activity in the field, and several key research groups have developed new test facilities to experimentally replicate the complex flows of LREs while using modern imaging techniques. These facilities attempt to reproduce the hazardous, high-pressure conditions of LREs at subscale while also applying novel concepts for high-fidelity acoustic control. Below, this review highlights the diverse experiences of five modern combustors which are particularly relevant to this study. These are the Multi-injector Combustor (MIC) and the Very High Amplitude Modulator (VHAM), both operated jointly by the French Aerospace Research Agency (ONERA) and the French National Center for Scientific Research (CNRS), the Common Research Combustor (CRC) operated jointly by CNRS and DLR, the BKH combustor operated by DLR, and the Continuously Variable Resonance Combustor (CVRC) operated by Purdue University.

The CRC originated in 2002 from the efforts of a German-French working group which now operates identical experimental combustors at the Research Institute for Equilibrium Systems (IRPHE) in Marseilles, France and DLR in Lampoldshausen, Germany. The CRC injects propellants from one side of a flat, cylindrically shaped chamber through a single injector which is 1/10th scale of a typical LRE injector. With high-speed shadowgraphy and OH* chemiluminescence imaging, the dynamics of a single LO_x/GH_2 flame can be isolated to fundamentally relate spatial and temporal heat release oscillations to pressure oscillations controlled by external acoustic forcing from a secondary nozzle. A single injector element though, provides only partial representation of thermoacoustic cycles occurring in LREs with multiple injectors and interactions between adjacent flames.

The BKH combustor is part of a recently constructed facility at DLR Lampoldshausen, Germany which focuses on high frequency combustion instability for LO_x/GH_2 and LO_x/LH_2 combustion. Simultaneous high speed backlit shadowgraphy and OH* chemiluminescence imaging was used to measure liquid core length L_b in addition to flame shape, both of which had a strong response to external acoustic forcing. Dark core length L_b values were reduced by up to 70% when forced at resonant chamber frequencies, and a curve-fit between L_b/D_1 and a nondimensional acoustic pressure amplitude predicted core length with reasonable accuracy for the conditions used in Hardi [24]. The pressure amplitude p' was nondimensionalized by the chamber pressure, i.e. p'/p_c, in one attempt to collapse L_b data into a single relationship. A second nondimensionalization method used the dynamic pressure of the outer jet, which followed as

$$\frac{\rho_c u'^2}{\rho_{oj} u_{oj}^2} \tag{1.16}$$

where ρ_c is the chamber gas density and the acoustic velocity amplitude u' is calculated from p' measurements. Both attempts to scale acoustic perturbation amplitudes with dark core length showed promise.

Hardi [24] also describes linear and nonlinear instability events which occurred during high frequency acoustic excitation. First, pressure measurements of unforced coaxial jet combustion confirmed the system's natural excitation of the first longitudinal (1L) and first transverse (1T) modes via small increases in p' values at those frequencies. Second, transverse forcing at the 1T frequency (≈4 kHz) strongly excited this mode while also creating low frequency chugging far from the excitation frequency. A similar event occurred when forcing at the 1L1T frequency. The chugging mode only occurred during high frequency excitation of transverse modes, and was said to occur due to nonlinear effects.

The BKH combustor also includes five shear-coaxial injectors in a cross formation to investigate interactions between neighboring flames. Although Hardi [24] was unable to give flame interaction detailed attention, this feature is expected to be investigated in future work. The MIC, located in Paris, shares many design features with the BKH combustor. The MIC also uses multiple injectors, but always in a linear arrangement to isolate interactions between pairs of flames when using two-dimensional imaging. Unless utilizing laser sheet flame illumination as in OH-PLIF, a cross injector formation prevents one from distinguishing between foreground and background flames when viewing OH* emission images. But, even OH-Planar Laser Induced Fluorescence (PLIF) imaging in these configurations has been challenging because it is difficult to penetrate the dense oxygen jet with a laser sheet [129, 130].

The VHAM is a modified version of the MIC which creates much greater acoustic pressure amplitudes in an effort to replicate the high amplitude oscillations documented in actual LRE combustion instabilities. The VHAM uses a toothed wheel to periodically block gas flow through exhaust nozzles, creating high pressure amplitudes inside the combustion chamber. The tooth wheel exhaust nozzle technique is also employed in the MIC, BKH, and CRC designs for the same purpose [18, 131]. With this method, the

periodic nozzle imposes an acoustic boundary condition on the chamber wall, where the acoustic frequency is controlled by the wheel speed. The resulting pressure perturbation amplitude though, is not controlled, and is instead determined by hardware geometry such as nozzle diameter and tooth shape. In the MIC, BKH, and CRC configurations, the toothed wheel is placed over a secondary exhaust nozzle which is located on the side of the chamber, perpendicular to the primary exhaust nozzle. In the VHAM though, zero secondary nozzles exist and two primary exhaust nozzles located at the end of the chamber are excited by a single toothed wheel. The VHAM design was recently used to create pressure amplitudes as high as 20% of p_c in Mery *et al.* [19]. Consequently, the VHAM induced a strong flame response whereas previous tests with smaller amplitudes in the MIC design yielded very little flame response.

The MIC used LO_x-GH_2 propellants in early experiments but quickly moved to LO_x-CH_4 propellants in an effort to achieve a more dramatic flame response to acoustic forcing. Again, this was linked to low amplitude acoustic pressure created by the single toothed wheel. Eventually, LO_x-CH_4 tests of subcritical and supercritical chamber pressure revealed a notable flame response to external forcing. A Ph.D. thesis by Richecoeur [8] presents results with similarity to Heidmann [128], mainly an increased spread angle caused by a shortened mixing region. Also, the combustor's five element injector arrangement showed evidence of interaction of adjacent flames. The VHAM is expected to produce a substantial flame response, even with LO_x-GH_2 propellants, and these results may be publicized in the future.

Controlled acoustic excitation in the manner described above allows experimentalists to partially decoupled a portion of the combustion instability feedback loop. Without an external acoustic source, chamber pressure perturbations exist due to combustion instabilities alone. But, when user-controlled acoustic excitation contributes to chamber acoustics, dual feedback dependencies exist as shown in Fig. 1.14. This configuration

allows one to isolate the effects of acoustic waves on fluid dynamic instability and heat release by controlling acoustic pressure amplitude and frequency. With this strategy, the degree to which perturbation amplitudes and their inherent frequencies can be varied is highly dependent on the specific hardware design used for external acoustic forcing. However, if the flame is self-excited then added acoustic forcing will compete with naturally occurring modes, and the experimentalist forfeits *complete* control over chamber acoustics. An analytical comparison of the excited acoustic energy and combustion energy was made by Rey *et al.* [132] and this relationship will be considered for the chamber used in the present study.

In contrast to the nozzle modulation method used by all four aforementioned combustors, the CVRC of Purdue uses an acoustic control system relying on variable injector geometry [17]. By altering the size of the oxidizer plenum, the resonant frequency of the injector flow is controlled such that chamber pressure amplitudes range from less than 10% to 60% of the chamber pressure. The highest pressure amplitudes are achieved when the oscillation frequency of the injector matches a chamber resonant frequency, whereas a mismatch dampens the chamber mode. Thus, the CVRC design forgoes the electro-mechanical system of a typical acoustic source [8, 23, 24], and instead relies on injector flow oscillations to create unsteady heat release. This method reliably induces high amplitude instability, but requires mindful choice of fuel species and propellant flow conditions to manipulate the preferred frequency and amplitude of the instability.

The lessons learned from the experimental facilities described above were instrumental in the design and construction of the shear-coaxial jet combustion facility used in this study. Many concepts introduced here are revisited in section 4.3, with new observations regarding the stability of O_2-H_2 flames.

1.4 Present Studies

The goal of the present studies is to explore acoustically-coupled combustion and transport processes in two fundamental configurations. One involves a continuously burning liquid fuel droplet exposed to acoustic excitation in a cylindrical waveguide at background atmospheric pressure. These experiments have been conducted at UCLA in the Energy and Propulsion Research Laboratory. The other configuration involves a coaxial jet of transcritical fluid injection into a high pressure (2.75 MPa) chamber at AFRL, also with exposure to acoustic excitation, and with the ultimate goal of exploring reactive flow. A detailed exploration of each system helps to shed light on important phenomena associated with acoustically-coupled combustion instabilities.

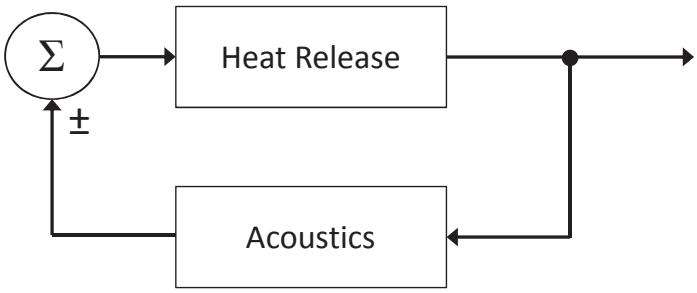

1.1: The bimodal combustion instability feedback loop [4, 5].

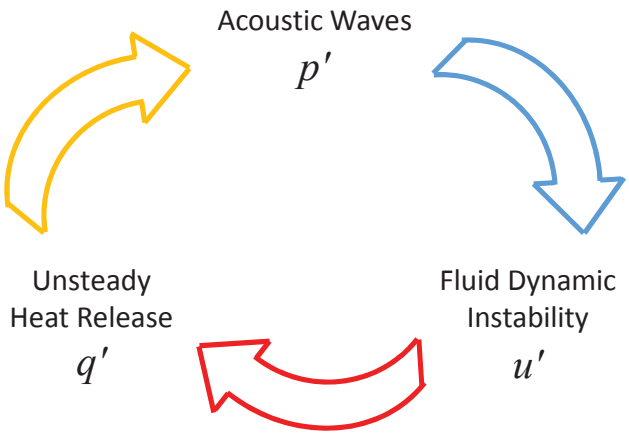

1.2: Three-part combustion instability feedback loop.

1.3: Modern launch vehicles using O_2-H_2 LREs. Delta IV (left, ULA 2011) Ariane 5 (right, ESA 2013)

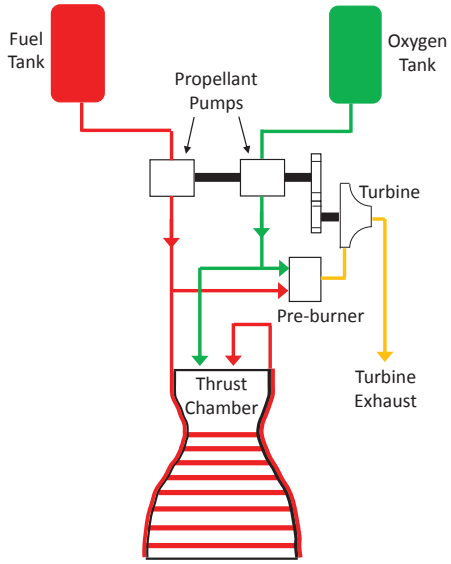

1.4: Diagram of the gas generator cycle in a liquid rocket engine.

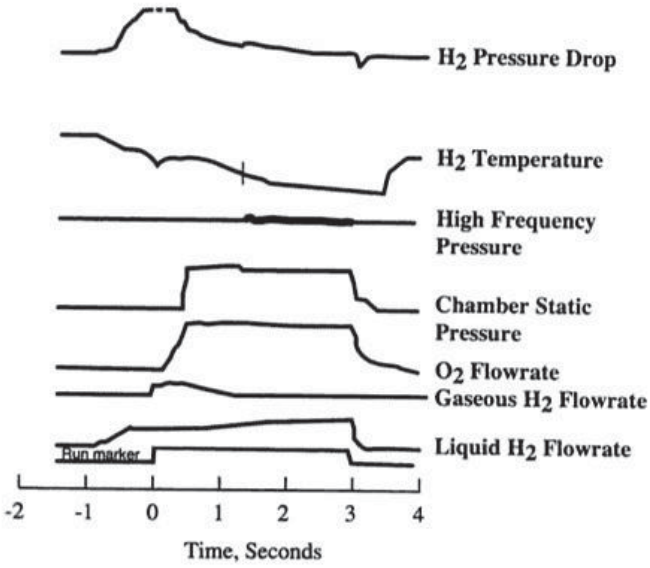

1.5: Fuel temperature ramping has been a common technique for verifying LRE stability for a wide range of fuel properties in hydrogen-oxygen engines. This plot, taken from Hulka and Hutt [45], reveals an instability occurring after a temperature drop engendered a lower hydrogen supply pressure.

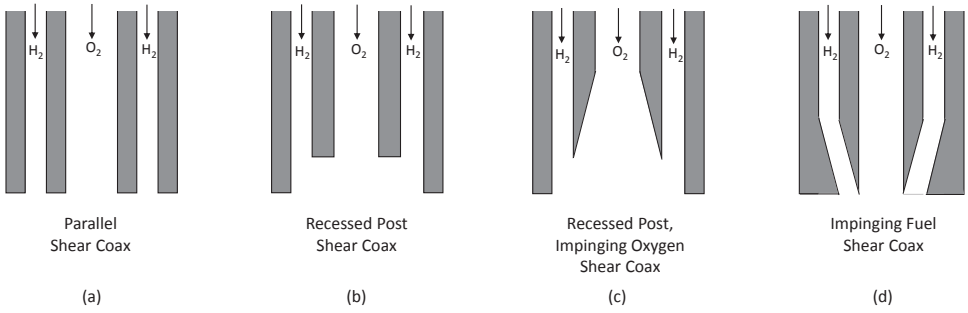

1.6: As early as the 1960s, multiple configurations of the shear-coaxial injector had been used to enhance mixing and prevent instability in hydrogen-oxygen LREs.

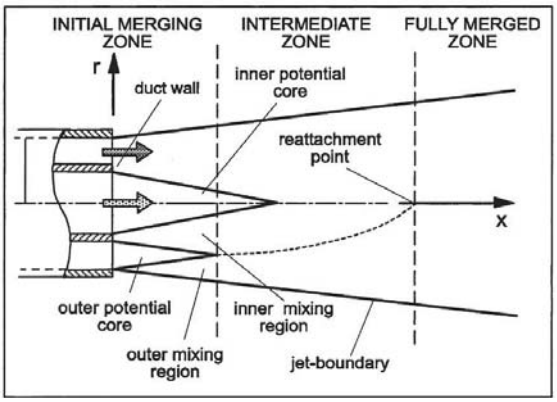

1.7: The mixing of the nonreactive shear-coaxial jet is characterized by three merging zones and two mixing regions. (diagram by Talamelli and Gavalini [108], adopted from Ko and Kwan [88])

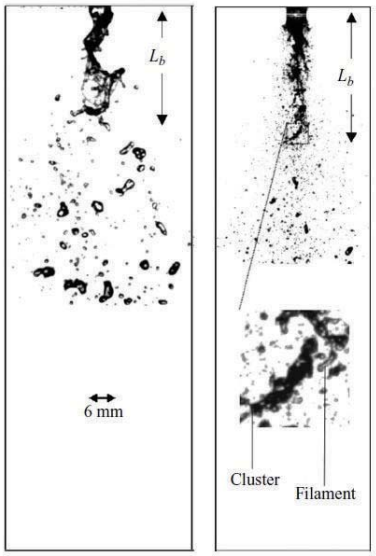

1.8: Coaxial jet images from Baillot *et al.* [16] show the membrane break up regime (left) and the fibre-type break up regime (right).

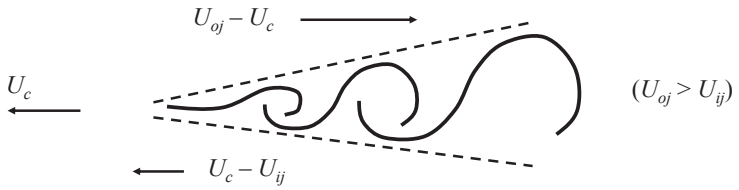

1.9: A convective shear layer diagram drawn in the vortex frame of reference.

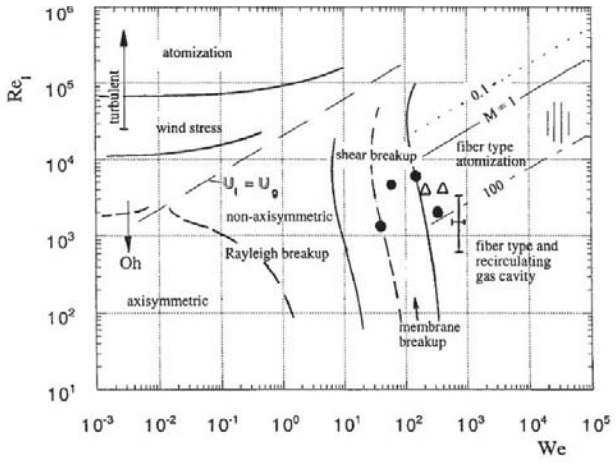

1.10: Break up characteristics of liquid-gas coaxial jets separated into five regimes (axisymmetric Rayleigh, antisymmetric Rayleigh, shear, membrane, and fibre-type break up) according to liquid Reynolds number and Weber number. M is the momentum flux ratio. (plot from Lasheras and Hopfinger [95])

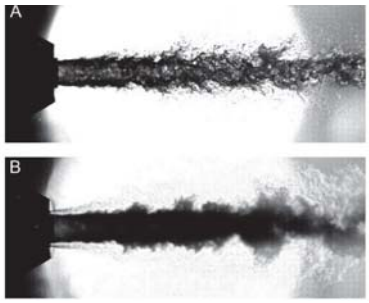

1.11: Shear-Coaxial jets of liquid nitrogen and gaseous helium issuing into high pressure chambers. $D_1 = 1.9$ mm, $U_{ij} = 5$ m/s, $U_{oj} = 100$ m/s, $T_{ij} = 97$ K, $T_{oj} = 280$ K (A) 1.0 MPa (B) 6.0 MPa (Mayer and Smith [14])

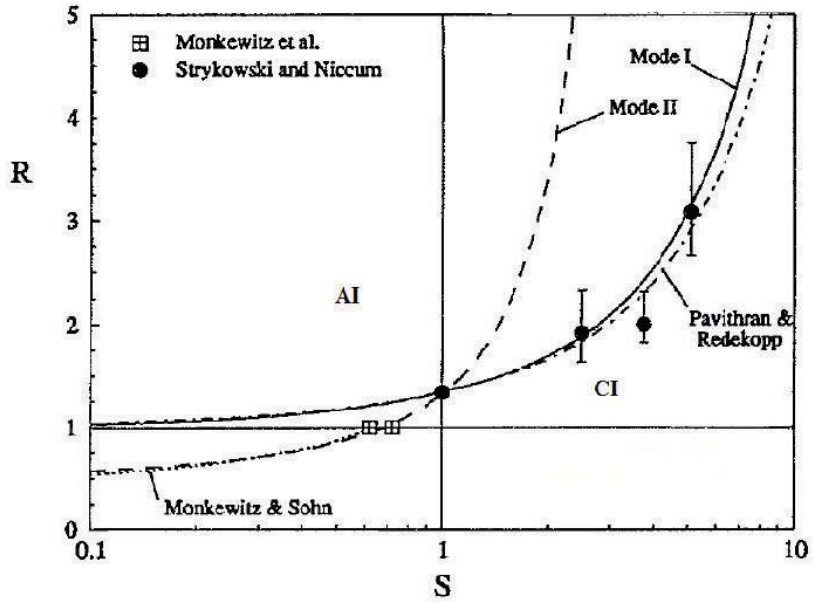

1.12: Absolute-convective instability transition lines from Jendoubi and Strykowski [121] with results from several others [113, 114, 133, 134]. The upper left region represents absolutely unstable operating space, and the lower right region represents convectively unstable operating space. Following the definitions of [121] for the x and y axes, $R > 1$ represents ambient counter-flow and $R < 1$ represents co-flow ($R \equiv (U_1 - U_2)/(U_1 + U_2)$). $S > 1$ represents jets *heavier* than the surrounding fluid, and $S < 1$ represents jets *lighter* than the surrounding fluid ($S \equiv \rho_1/\rho_2$). The typical conditions of a LO_x-GH_2 shear-coaxial jet lie in the convective instability operating space for $R < 0$, not shown here.

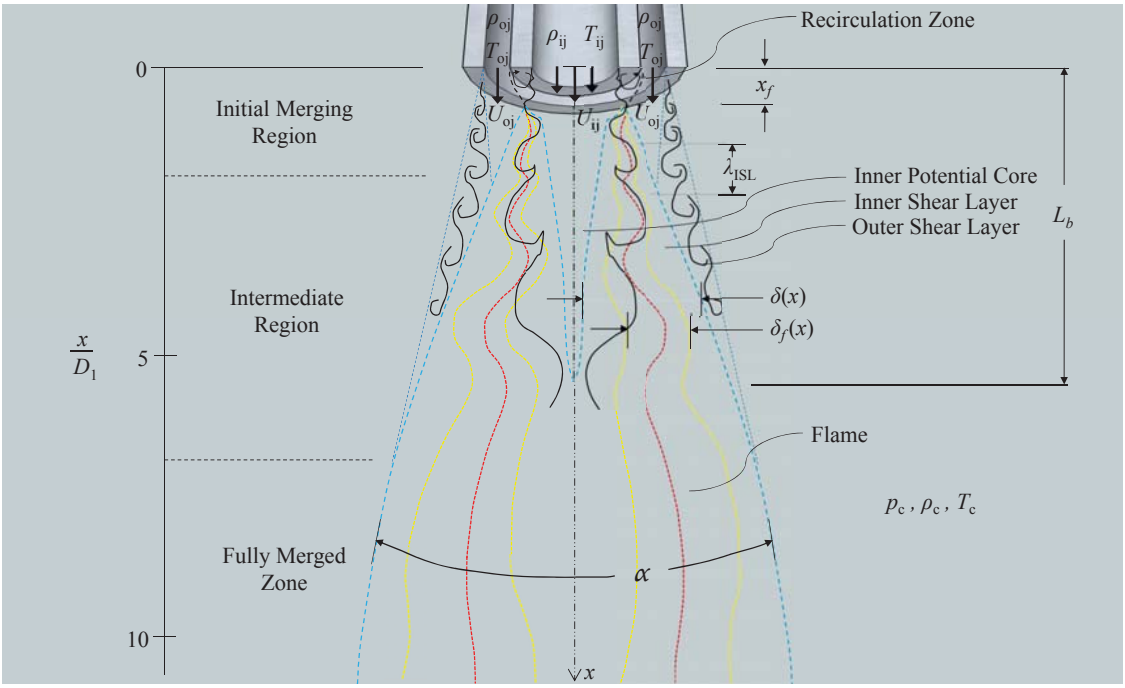

1.13: Flow diagram of a reactive shear-coaxial jet.

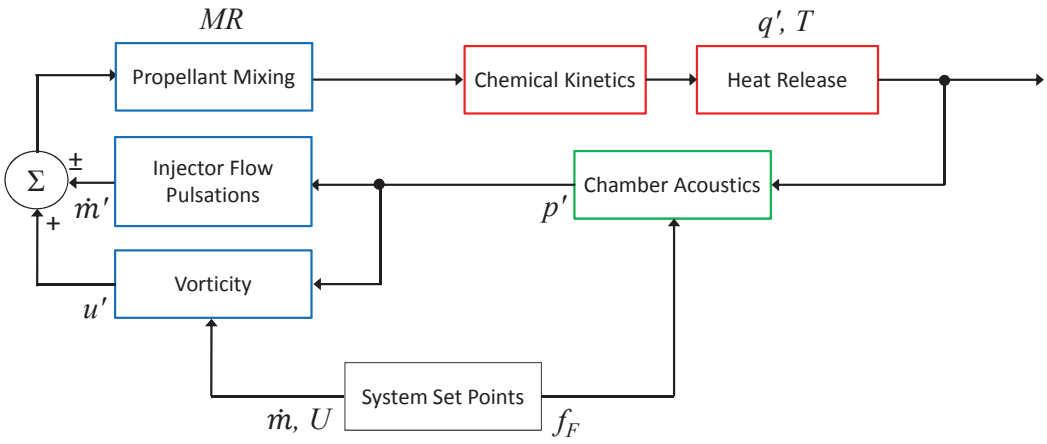

1.14: An expanded portrayal of the three part combustion instability feedback loop showing fluid mechanical features in blue, reactive features in red, and acoustic pressure oscillations in green. User-controlled acoustic forcing acts as an additional input to chamber pressure oscillations. Injector exit flow conditions act as a potential control of shear layer vortex structures.

CHAPTER 2

Experimental Facility and Methods - Acoustically Coupled Fuel Droplet Combustion

The experimental apparatus in these studies is the same as that used by Dattarajan *et al.* [22] and Rodriguez *et al.* [75], with several modifications. Modifications include, but are not limited to, the pressure perturbation measurement system and the flame imaging system, both of which will be described in this chapter.

2.1 Acoustic Waveguide

A long, cylindrical waveguide, similar to a Kundt's tube, was used to create standing acoustic waves by placing a loudspeaker at each end. The system was operated at atmospheric background pressure and room temperature. A continuosly fed, burning fuel droplet was situated at the center of the waveguide. The waveguide was made of aluminum tubing with an inner diameter of 11.4 cm and a full length of 90 cm, and quartz windows placed in the side of the waveguide nearest the droplet allowed for optical access. The 8 Ω woofer loudspeakers were connected using three long rods, allowing the pair to be moved as an assembly while remaining a constant distance apart. The same apparatus was also used in a speaker-reflector configuration by replacing one speaker with an aluminum reflector plate. The complete apparatus is shown in Figure 2.1.

Using a function generator, a sinusoidal signal was sent to each loudspeaker with

the two signals in-phase ($\Delta\phi = 0°$) or out-of-phase ($\Delta\phi = 180°$). Due to a constant waveguide length L the loudspeaker frequency, or acoustic frequency f_a, is the controlling parameter in creating a resonant standing waveform within the waveguide. Theoretically, f_a can be chosen such that the waveguide length L is an integral multiple of half the acoustic wavelength, $\lambda/2$, that is,

$$L = \frac{n}{2}\lambda = \frac{n}{2}(\frac{c}{f_a}), \tag{2.1}$$

where c is the speed of sound. Regardless of the value of the f_a and n, speakers operated out-of-phase ($\Delta\phi = 180°$) will create a PN at the center of the waveguide and speakers operated in-phase ($\Delta\phi = 0°$) will create a PAN at the center [135]. But, to create an acoustically resonant condition with maximum pressure perturbations, then f_a must take on a value such that n is an integer. More specifically, for speakers operated out-of-phase, if f_a is chosen to give an odd value of n then the pressure amplitude is maximized in the waveguide. For speakers operated in-phase, if f_a is chosen to give an even value of n then the pressure amplitude is maximized in the waveguide. Thus, resonant conditions hold for a select few frequencies, but for any frequency the center of the waveguide will take on a PN or PAN condition for $\Delta\phi = 180°$ and $\Delta\phi = 0°$, respectively. These conclusions assume the perturbation amplitudes created by the speakers to be identical. In the special case where one speaker is instead replaced with a rigid wall, eqn. (2.1) still holds true. Theoretically, in this speaker-reflector configuration odd values of n produce a PN at the waveguide center, and even values of n produce a PAN at the waveguide center.

Experimental acoustic characterization relied on point-like pressure measurements made using a Kulite XCE-093-50D miniature pressure transducer with an output resolution 0.29 mV/kPa and diameter of 2.4 mm. The sinusoidal pressure transducer output signal was amplified and then used to find the pressure perturbation amplitude p'. With the sensor placed at the center of the waveguide, the most ideal f_a was determined by

sweeping through a wide range of frequencies in search of p' minima (PN) for $\Delta\phi = 180°$ or p' maxima (PAN) for $\Delta\phi = 0°$. The result of this frequency sweep technique is shown in Figures 2.2 and 2.3 for $\Delta\phi = 180°$ and $\Delta\phi = 0°$, respectively. Pressure measurements at the speaker are also shown, which will exhibit maxima for all resonant frequencies. Along these lines, a speaker-reflector frequency sweep was performed with a pressure sensor located at the reflector, and results are shown in Figure 2.4. All three frequency sweeps presented here can be used to extract experimental resonant wave frequencies, which can then be compared to theoretical resonant frequencies calculated using eqn. (2.1). This comparison is shown in Table 2.1.

Experiments by Dattarajan *et al.* [22] and Rodriguez *et al.* [75] employed a speaker-reflector configuration, but Teshome *et al.* [82] improved upon this by instead using the speaker-speaker configuration, citing a more symmetric pressure distribution about the center. This claim is explored more thoroughly here by measuring p' throughout the axial length of the waveguide for each frequency of interest. The resulting collection of pressure versus waveguide location plots is divided into speaker-reflector conditions in Figure 2.5, speaker-speaker out-of-phase conditions in Figure 2.6, and speaker-speaker in-phase conditions in Figure 2.7. Comparison with theoretical pressure distributions are also shown, with the pressure maximum based on matching of theory and experiment at the closest peak to the waveguide center.

First considering the speaker-reflector pressure distributions, the amplitudes are shown to be generally symmetric for frequencies near the theoretical values of Table 2.1. Figure 2.7 includes two frequencies which produce a PN at the waveguide center, 308 Hz and 784 Hz, and one other frequency which produces a PAN at the center, 562 Hz. Upon closer inspection though, the pressure distribution is mildly asymmetric for the lowest frequency, 308 Hz. The correspondingly longer wavelength associated with 308 Hz appears to exacerbate any asymmetric speaker boundary conditions, having a

greater impact on the distribution at the center. Moreover, previous work has shown conditions producing a distinct PN at the waveguide center to also produce a quite asymmetric velocity distribution according to hot wire measurements [75].

For the speaker-speaker results shown in Figure 2.6, operating the speakers 180^o out-of-phase creates standing waves at the waveguide center regardless of acoustic frequency. For five different frequencies ranging from 332 Hz to 1500 Hz the primary difference is instead the maximum measured pressure amplitude. Similar plots are found in Figure 2.7 for speakers in-phase, which produces a PAN near the center for all five frequencies explored here. Also, when comparing two conditions with an equal speaker input voltage but different frequencies, choosing a frequency close to the resonant frequency will provide a larger pressure amplitude. For example, contrasting Figures 2.7(c) for 898 Hz and 2.7(d) for 1088 Hz shows a much larger amplitude for 1088 Hz. This principle holds true for all frequencies explored here, such that the difference in sound pressure level between a resonant and non-resonant flow condition could be easily detected by the human ear. The same body of work revealing asymmetric velocity distributions for the speaker-reflector configuration measured a very symmetric velocity distribution for the speaker-speaker configuration, largely motivating previous [82] and current experiments to employ a two speaker configuration. With this established, one must also note that additional hot wire measurements are needed to complete the current acoustic characterization and confirm the assumption that VAN locations indeed coincide with PN locations and vise versa. Hotwire measurements in Teshome *et al.* [82] were uncalibrated and preliminary, but did show a symmetric velocity profile with a VAN at the waveguide center.

2.2 Droplet Generation and Ignition

The fuel delivery system consisted of a hollow borosilicate glass capillary and a KDS Model 100 syringe pump. The fuel droplet was suspended within the waveguide at the tip of the glass capillary of approximately 0.37 mm outer diameter. Liquid fuel was delivered to the capillary during droplet combustion at a constant volumetric flow rate Q_v, set by the syringe pump. The volumetric flow rate and the droplet size were used to determine the burning rate constant K, as will be described below. A protective copper shroud was placed above the end of the glass capillary in order to prevent vaporization of the fuel within the glass capillary just above the droplet. The distance between the end of the shroud and the end of the tip of the capillary was fixed at 3.2 mm, a regime for which the droplet burning rate constant did not depend on this length [22]. The droplet was ignited by means of a resistive heating Ni-Cr wire mounted on a push-type solenoid. A TattleTale Model 8 data logger/controller board was used to synchronize the extenstion of the solenoid arm and the passage of current in the ignitor wires. This mechanism created an efficient means for igniting the droplet remotely without having to open, manually ignite, and close the waveguide. After ignition, the flame remained intact unless extinguished by strong convective flow or by a fuel vapor jet formed at the capillary exit due to overheated incoming fuel. This ignition technique was identically performed for all fuels, which are listed in Table 2.2 with their respective properties.

2.3 Imaging

Flame imaging was performed using an intensified camera and image acquisition system designed to capture OH* chemiluminescence at various instants within an acoustic cycle. This imaging system is discussed in several parts. First, the optical train assembled to capture OH* chemiluminescence is described, including a quantitative estimation of

transmission versus wavelength. Second, a description of the components, communications, and controls required to coordinate image acquisition will include equipment specifications and variables set by the user, with justification. Last, a timing system based upon the acoustic pressure cycle is explained.

2.3.1 Optics

There are several well-documented reactions occurring within hydrocarbon flames which produce chain carriers in route to the final combustion products. If sufficiently energetic, such reactions will produce radicals in electronically excited states which then undergo deexcitation through one of two mechanisms. More specifically, hydrocarbon flames commonly exhibit the reaction

$$CH(^2\Pi_u) + O_2(^3\Sigma_g) \rightarrow CO(^1\Sigma^+) + OH^*(^2\Sigma^+) \tag{2.2}$$

where electronically excited hydroxyl radicals (OH*) then experience spontaneous radiative deexcitation (chemiluminescence) or collisional deexcitation (quenching). The exact proportions of quenched OH* and OH* which produces chemiluminescence are governed, for example, by fuel type (e.g. carbon to hydrogen ratio) and flow conditions (e.g. pressure). Regardless of these precise quantities though, regions of OH* chemiluminescence are shown to coincide with primary reaction zones and lie close to, if not coincide with, maximum temperature [66, 136]. This correlation between OH* chemiluminescence and flame topology has limitations with turbulent premixed flames or flames near extinction [137], but is quite sufficient for laminar diffusion flames in steady state conditions. Thus, for droplet combustion this study tracks light emission created via the deexcitation reaction

$$OH^*(^2\Sigma^+) \rightarrow OH(^2\Pi) + h\nu \tag{2.3}$$

which is observed in the ultraviolet (UV) band at approximately 308 nm.

The optical arrangement passes a span of UV wavelengths to isolate this particular source of chemiluminescence. Figure 2.8 shows the receiving optics from the flame to the camera. The quartz waveguide window and the UV lens (UV-Nikkor 105 mm f/4.5) pass with over 70% transmission for low UV to high infrared (IR) wavelengths, while the camera photocathode is designed for best capture with low wavelengths. The UV bandpass filter provides 88% maximum transmission centered around 320 nm, and also transmits 20-50% of IR light. The camera photocathode (NanoStar S20 type) achieves greatest quantum efficiencies for 200-450 nm. The combined transmission of the receiving optics is quantified in Figure 2.9. To confirm capture of OH* chemiluminescence and blocking of other sources of chemiluminescence, results from the work of Kojima *et al.* [138] are shown for comparison. The transmission range is consistent with this prior work for methane.

2.3.2 Image Acquisition

Acquiring and storing flame images for specific parts of an acoustic cycle is made possible by the interconnection of image acquisition equipment shown in Figure 2.1. The function generator which controls loudspeakers sends a second signal, equal to the first in phase and frequency, to a Programmable Timing Unit (PTU) for camera control. This parallel control of the acoustic and imaging systems by a single function generator permits image capture which is phase-locked to a short span of time within the acoustic cycle.

The PTU sends a signal to the camera which can be custom manipulated within LaVision's software interface, but always maintains a frequency equal to the acoustic frequency. Custom manipulations include specifying the image intensifier gate width, image intensifier gain, number of intensifier pulses within one image frame (burst count), and the phase angle marking the start of the intensifier gate. For all imaging in this study, the gate width time is set equal to 1/64 of the acoustic period, $T_a/64$, while the

intensifier gain and burst count must be varied to ration the total intensity captured by the CCD sensor. For example, high luminosity flames such as JP-8 require a lower intensifier gain and burst count than low luminosity flames such as methanol. Otherwise, the CCD sensor will be damaged by over-exposure. Depending on fuel type, the intensifier gain and burst count range from 30/100 to 80/100 and 20 to 200, respectively. Other specifications are listed in Table 2.3. Last, the phase angle marking the start of the intensifier gate is specified by a repeating loop of 18 different phase angles, $\phi_{II} = 20\colon 20\colon 360$. However, this phase angle sequence is in reference to the PTU output signal, which is not in phase with the acoustic pressure cycle due to time delays caused by components within both the acoustic system and the imaging system. Thus, these time delays, or phase delays, must be measured in order to convert ϕ_{II} to its equivalent value referenced by the acoustic pressure cycle ϕ_p.

2.3.3 Acoustics-Imaging Synchronization

Reformatting ϕ_{II} in terms of ϕ_p is possible by comparing two signals and their associated phase delays. First, the pressure perturbation signal is measured by a pressure transducer and observed via oscilliscope, creating phase delays due to the transducer unit and pressure transducer amplifier. Second, the camera produces a TTL output pulsed with the image intensifier gate, thus providing a pulsed signal corresponding to the actual time period captured by the camera. Relating these two signals allows one to identify the exact slice of time within the acoustic pressure cycle which is captured by the camera. Moreover, this technique strategically avoids individual measurement of the phase delays associated with each individual compenent within the acoustic and imaging systems (e.g. speaker amplifier, loudspeakers, sound travel, PTU, etc.).

Specifically, the problem is represented as $\phi_p = \phi_{II} + \Delta\phi$. Setting $\phi_{II} = 0$ and measuring $\Delta\phi$ gives a solution for ϕ_p. $\Delta\phi$ is uniquely determined for each forcing

frequency as the difference between the two signals listed above plus pressure transducer and pressure transducer amplifier phase delays, as listed above. The pressure transducer phase delay is $< 1^o$, and negligible. The pressure transducer amplifier phase delay is measured as part of a complete frequency response measurement, thus recording both the amplifier gain and phase delay as a function of frequency. The camera's TTL output representing the image intensifier gate is delayed by 20 ns and the delays associated with all wiring are ~ 1 ns, both negligible.

2.4 Measurement Methods

2.4.1 Burning Rate Constant

From continuity for a spherical droplet of diameter d, the instantaneous burning rate constant K may be evaluated as

$$K = \frac{4Q_v}{\pi d(t)} - 2d\dot{d} \tag{2.4}$$

A constant volumetric flow rate Q_v provided by the syringe pump was chosen in order to maintain a roughly constant droplet size. This technique makes the first term in eqn. (2.4) the dominant term, while the second term is close to zero. This is the opposite of the typical "non-fed" burning droplet governed by the d^2 law when $Q_v = 0$ [63, 64]. Due to the normal gravity environment of the present experiments, eqn. (2.4) required a droplet diameter equivalent to that of a sphere with volume equal to the oblong droplet volume, as done by Struk *et al.* [65] and described in section 1.2.2. A custom image processing MATLAB^{TM} algorithm was used to fit an ellipse to the droplet in each image, thus providing the data needed to calculate d_{eqvs} for each image and $\dot{d}_{eqvs}$ for a set of images. Additional LED back-lighting provided ample contrast between the liquid fuel and the back-light in order for the image processing algorithm to detect the silhouette of the droplet. Time-averaged K values were then computed according to eqn. (2.4)

for a complete flow condition. The same calculation could be performed for a given acoustic phase angle within a flow condition, but this task reveals fuel droplet sizes to be independent of phase and thus K values also independent of phase. Investigation of burning rate versus acoustic phase could instead require utilizing chemiluminescence intensity variations with respect to acoustic phase, which has not been explored in previous works.

2.4.2 Acoustic Acceleration

In the absence of acoustic forcing the only net force is the buoyancy force, acting on the volume V of hot products with density ρ_p. When surrounded by a cooler gas of density ρ_o the buoyancy force follows as $F_B = (\rho_p - \rho_o)Vg_o$, which results in a vertically oriented, symmetric flame. With acoustic excitation, the flame orientation became aligned with the resultant force due to buoyancy and an analogous acoustic radiation force, $F_R = (\rho_p - \rho_o)Vg_a$, where g_a is the acoustic acceleration. This type of behavior is shown in Figure 2.10. According to the theory suggested by Tanabe *et al.* [21], based on the work of Nyborg [79], the acoustic acceleration g_a depends on the position of the droplet with respect to the PN or PAN. In light of the preceding relationship, this study experimentally determines acoustic acceleration as done by Teshome *et al.* [82]. The actual acoustic acceleration at the location of the droplet is estimated using the measured deflection angle ϕ_f and gravitational acceleration

$$g_{a,exp} = g_o \tan \phi_f \tag{2.5}$$

The degree of flame deflection ϕ_f was estimated by measuring the average change in angle between the tangent lines of an unforced and forced flame edge, as shown in Figure 2.10. For extreme cases of flame deflection where the flame is nearly horizontal, more uncertainty can be attributed to ϕ_f because the plume region turns upward in the far wake of the flame.

2.4.3 Flame Standoff Distance

A burning droplet in normal gravity is encompassed by a quasi-ellipsoidal flame front as shown by Figure 2.10, an image for the special case of an acoustically excited burning droplet. For both unforced and forced burning droplets, the flame standoff distance δ_f is clearly a function of the angle θ measured from the positive x-axis in the x-y plane. One should also deduce that unlike the unforced case, the acoustically forced flame is not axisymmetric because δ_f is also a function of the out-of-plane angle ϕ. But, for the two-dimensional standoff distance measurements discussed here, this descrimination will not bear importance.

Flame standoff distance is defined as the difference between the flame and droplet radii, $\delta_f = r_f - r_s$, each of which is measured by image analysis algorithms. First, r_s is defined as a function of θ using the droplet ellipse fit technique identical to that employed in d_{eqvs} measurements. Second, r_f is defined as the distance from the center of the droplet to the location of maximum OH* chemiluminescence intensity for a given value of θ. This particular definition of the "flame" is common to many experimental works in the fields of both diffusion and premixed flames [66, 67, 137, 138]. Several other definitions have been used as a reliable measure of flame topology, including the point of maximum temperature, maximum C_2* or CH* chemiluminescence, or maximum HCO mole fraction. Moreover, different flame measurement methods can provide conflicting results in the realm of turbulent premixed flames or flames near the extinction strain limit. Extinction studies have actually revealed shortcomings in the traditional OH* chemiluminescence technique when carbon-based chain carriers sustain reaction where a lack of OH* chemiluminescence would otherwise predict extinction [137]. The questions arising from these inconsistencies are highly motivated by combustion instability research and imply a loss of robustness for this study's r_f definition. But, the set of results analyzed here avoid extinction for even the strongest convective and oscillating

flows. In conclusion, the maximum OH* chemiluminescence flame definition is imperfect, but quite effective for a diffusion flame in the current flow conditions, where a lack of extinction and turbulent flame structure provide for an unbroken flame front in all flame images.

Finally, δ_f data analysis will focus attention on the upstream side of the flame, the location of which is determined by acoustic flow conditions. For example, Figure 2.10 shows a stagnation point on the flame's right side. A different droplet position though, can switch flame orientation and move the stagnation point, thus moving the area of interest. Therefore, it is important to clarify that δ_f is measured on the upstream side only. These measurements include $\delta_f(\theta = 0^o)$ and $\delta_f(\theta = 180^o)$, depending on flame orientation. Other valuable analysis includes minimum standoff distance created by natural convection $\delta_f(\theta = 270^o)$ and standoff distance at the stagnation point $\delta_f(\theta = \alpha_f)$, but little study of these points is included in this body of work.

2.5 Experimental Procedure

Upon beginning a set of experiments, a clean syringe was loaded with the desired fuel and connected to the glass capillary by a rubber tube. The flow rate maintained by the syringe pump was chosen to achieve quasi-steady droplet burning for a given fuel and flow condition. For all experiments in this study, fuel flow rate fell within the range 53.3 mL/hr $< Q_v <$ 63.3 mm^3/s. The acoustic amplitude for a given condition was identified using p' measured at the PAN with the smallest positive x location, which required knowledge gained from pressure distributions shown in Section 2.1. This amplitude is represented as p'_{max}, i.e. $p'_{max}(f_a = 332 \text{ Hz}) = p'(x = 28 \text{ cm})$, $p'_{max}(f_a = 898 \text{ Hz}) = p'(x = 10 \text{ cm})$, $p'_{max}(f_a = 1500 \text{ Hz}) = p'(x = 5 \text{ cm})$. Finally, before each ignition, the waveguide was purged with air to remove combustion products from prior experiments.

Droplet ignition was performed using the heater wire and push-type solenoid assembly, and ignition was immediately followed by initiating the acoustics. Under the steady conditions used here, burning droplets could be sustained for as long as 10 minutes without flame extinction. Within this burning period an image recording loop cycled through 18 different phase-locked acoustic phase angles, $\phi_{II} = 20 : 20 : 360$, acquiring 5 images at each phase before proceeding to the next. This method of capturing 90 images was performed 4 times to complete 1 recording session, which required 2 to 5 minutes of recording. Each image was immediately digitized in .im7 file format with an associated clock time. The imaging procedure was completed by acquiring a set of 50 background images with the capillary and shroud removed from the field of view, and thus the LED creating the only source of light and variations thereof.

The experiment was followed by two steps of image processing. First, a flame image was processed using LaVision's DaVis software, where the average of 50 background images was subtracted from the flame image. Second, the resulting pair of flame images (original and background subtracted) were reoriented and analyzed using a MATLAB^{TM} algorithm. The original image was utilized only to detect the droplet edge, and then calculate the position and dimensions of an ellipse coinciding with the droplet silouette. Using the pixel coordinates of the ellipse center, the background subtracted image was converted from cartesian coordinates to cylindrical coordinates with an origin at the ellipse center, and this final image was used for all remaining flame analysis. It should be noted that imperfections in the background subtraction technique arise because although the shroud, capillary, and droplet shield backlighting, the backlight is still subtracted from these areas, creating biased regions in the final flame image. The pixel intensities of these regions are lower than actual intensities, but this bias error does not interfere with the conclusions of this study.

2.6 Measurement Uncertainties

2.6.1 Precision Uncertainty

The sources of precision uncertainty in the measured values of the burning rate constant K in eqn. (2.4) stem from uncertainties in the fuel volumetric flow rate Q_v and determining the equivalent sphere diameter d_{eqvs} for the droplet. The technique for calculating the uncertainty in d_{eqvs} is similar to the method used by Dattarajan *et al.* [22] which utilizes the principles of uncertainty propagation in Mills and Chang [139], but with improved resolution due to a reduced pixel view. First, the equivalent sphere diameter is found in terms of the major and minor axes of the droplet ellipse, resulting in $d_{eqvs} = 2a^{\frac{2}{3}}b^{\frac{1}{3}}$. Then, if the uncertainty in the axes lengths, a and b, are equal, then the method cited above follows as

$$\begin{aligned}
\Delta d_{eqs} &= \sqrt{\left(\frac{\partial d_{eqs}}{\partial a}\Delta a\right)^2 + \left(\frac{\partial d_{eqs}}{\partial b}\Delta b\right)^2} \\
&= \sqrt{\left(\frac{2}{3}\frac{2b^{\frac{1}{3}}}{a^{\frac{1}{3}}}\Delta a\right)^2 + \left(\frac{1}{3}\frac{2a^{\frac{2}{3}}}{b^{\frac{2}{3}}}\Delta b\right)^2} \\
&= \sqrt{\left(\frac{4}{3}\Delta a\left[\frac{b}{a}\right]^{\frac{1}{3}}\right)^2 + \left(\frac{2}{3}\Delta b\left[\frac{a}{b}\right]^{\frac{2}{3}}\right)^2} \\
&= \Delta ab\sqrt{\frac{16}{9}\left[\frac{b}{a}\right]^{\frac{2}{3}} + \frac{4}{9}\left[\frac{b}{a}\right]^{-\frac{4}{3}}}
\end{aligned} \tag{2.6}$$

where it is assumed $\Delta a = \Delta b = \Delta ab$. Uncertainty in d_{eqvs} is then calculated using $d_{eqvs} \approx 1.5$ mm, $\Delta ab \approx 0.05$ mm, and $\frac{b}{a} \approx 1.5$, giving an uncertainty of $\frac{\Delta d_{eqvs}}{d_{eqvs}} \approx 5.4\%$. Uncertainty in Q_v though, is based solely in the precision uncertainty of the syringe pump. Thus, the manufacturer's rating of 0.1% is used for $\frac{\Delta Q_v}{Q_v}$.

The resulting uncertainties in K follow as

$$\begin{aligned}\Delta K &= \sqrt{\left(\frac{\partial K}{\partial Q_v}\Delta Q_v\right)^2 + \left(\frac{\partial K}{\partial d_{eqs}}\Delta d_{eqs}\right)^2} \\ &= \sqrt{\left(\frac{4\Delta Q_v}{\pi d_{eqs}}\right)^2 + \left(-\frac{4Q_v}{\pi d_{eqs}^2}\Delta d_{eqs}\right)^2} \\ &= \sqrt{\left(K\frac{\Delta Q_v}{Q_v}\right)^2 + \left(-K\frac{\Delta d_{eqs}}{d_{eqs}}\right)^2} \\ &= K\sqrt{\left(\frac{\Delta Q_v}{Q_v}\right)^2 + \left(\frac{\Delta d_{eqs}}{d_{eqs}}\right)^2}\end{aligned} \tag{2.7}$$

Therefore, $\frac{\Delta K}{K} = 5.4\%$ when $\frac{\Delta d_{eqvs}}{d_{eqvs}} \approx 5.4\%$ and $\frac{\Delta Q_v}{Q_v} = 0.1\%$, and the influence of fuel flow uncertainty has a negligible affect on total uncertainty in K. The transient term in eqn. (2.4) also has a negligible affect in this analysis and is not included here. Last, the precision uncertainty of time-averaged K values, which is of primary importance in this study, can be found by accounting for the minimum number of experimental points used to encompass the burning rate constant for one flow condition, 30. The resulting precision uncertainty in average K values is estimated to be $5.4\%/\sqrt{30} \approx 0.99\%$.

The source of precision uncertainty for pressure perturbation measurements, on the other hand, lies only in the accuracy rating of the pressure transducer. The XCE-093-50D has an output signal reproducibility of 0.5% of the full scale output, $\Delta V = (0.005)(\text{FSO}) = (0.005)(100\text{ mV}) = 0.5\text{ mV}$. With a signal resolution of 0.292 mV/kPa and a signal amplifier gain of 495, the calculation follows as

$$\begin{aligned}\Delta p' &= \sqrt{\left(\frac{\partial p'}{\partial V}\Delta V\right)^2} \\ &= \frac{\partial p'}{\partial V}\Delta V \\ &= \frac{\partial}{\partial V}\left(\frac{V}{\delta G}\right)\Delta V \\ &= \frac{0.5\text{ mV}}{\left(0.292\frac{\text{mV}}{\text{kPa}}\right)(495)} = 3.5\text{ Pa}\end{aligned} \tag{2.8}$$

For the pressure amplitude used most in this study, $p' = 150$ Pa, the precision uncertainty is $\frac{\Delta p'}{p'} \approx 2.31\%$.

2.6.2 Bias Uncertainty

Concerning K, sources of bias uncertainty include a 1% accuracy rating for Q_v, quoted from the syringe pump manufacturer, and bias due to pixel representation of the droplet edge. The latter form of uncertainty is present in all experiments where image analysis algorithms are used for edge detection. For this particular study, the camera's high spatial resolution results in a pixel view of 7.3 μm and therefore, droplet edge detection bias is negligibly small when compared to precision uncertainties and error from the droplet ellipse fit process. This ellipse fit technique, the third source of bias uncertainty discussed here, is largely connected to errors from equating the diameter of the droplet ellipse with the diameter of a sphere of equivalent diameter. Extensive analysis is included in Dattarajan *et al.* [22], where other techniques for choosing an appropriate droplet diameter d are quantitatively compared. Additional attention though, could be given to the accuracy of the ellipse fit itself. Surface tension and gravitational forces cause the droplet to form a teardrop-like shape, where an ellipse fit consistently matches the lower edge of the droplet, but over estimates the volume in the upper portion of the droplet. Ultimately, the burning rate constant K is under estimated by an enlarged droplet volume. Flame standoff distance measurements are uninfluenced by this effect because this study is interested in standoff distance for the lower hemisphere of the droplet, where the majority of burning occurs.

Although, the standoff distance measurement technique contains a second source of bias uncertainty. Droplet flame images represent a 3-D reaction zone in a 2-D manner, which misrepresents flame curvature. Well documented deconvolution methods, such as the Abel transform [140], can transform an axisymmetric image of a 3-D field into an

image representing a 2-D plane view. For example, an Abel transformed image of an unforced droplet flame is shown in Figure 2.11. Adversely, acoustically forced flames are non-axisymmetric, leaving the vast majority of images analyzed in this study subject to line-of-sight error. When defining the flame as the point of peak OH* chemiluminescence, as described in section 2.4.3, the measured flame standoff distance is less than the actual distance. Correction requires a value for flame curvature perpendicular to the image plane, which is unknown and unequal to the known flame curvature within the image plane for acoustically forced flames.

2.1: Experimental and Theoretical Resonant Frequencies

Speaker-Speaker				Speaker-Reflector			
$\Delta\phi = 0^o$ (PAN)		$\Delta\phi = 180^o$ (PN)		PN		PAN	
f_{exp} [Hz]	f_{th} [Hz]	f_{exp} [Hz]	f_{th} [Hz]	f_{exp} [Hz]	f_{th} [Hz]	f_{exp} [Hz]	f_{th} [Hz]
154		332	281.2	562	527.9	308	263.9
558	562.5	898	843.7	1108	1055.7	796	791.8
1132	1125.0	1500	1406.2		1583.6	1370	1319.7

2.2: Fuel Properties (alcohol fuels [64]; hydrocarbon fuels [141])

Fuel	Chemical Formula	Specific Heat Capacity	Thermal Conductivity	Heat of Vaporization	Lower Heating Value
		c_p [kJ/kg·K]	k [W/m·K]	h_{fg} [kJ/kg]	LHV [kJ/kg]
Ethanol	C_2H_5OH	2.815	0.0533	841	26952
Methanol	CH_3OH	2.531	0.0616	1104	19930
Pure FT	$C_{12}H_{25}$	2.793	0.00935	339	44136
JP-8/FT	$C_{11}H_{22}$	2.01	0.0134	297	43745

2.3: Camera Specifications

Maximum Frame Rate	8 Hz
Dynamic Range	4096
Active Image Area	1280 x 1024 pixels
Pixel Size	6.7 μm x 6.7 μm
Field of View	9.3 mm x 7.4 mm
Pixel View	7.3 μm x 7.3 μm
Depth of Field	2 mm
CCD Readout Noise	< 2 counts (RMS)

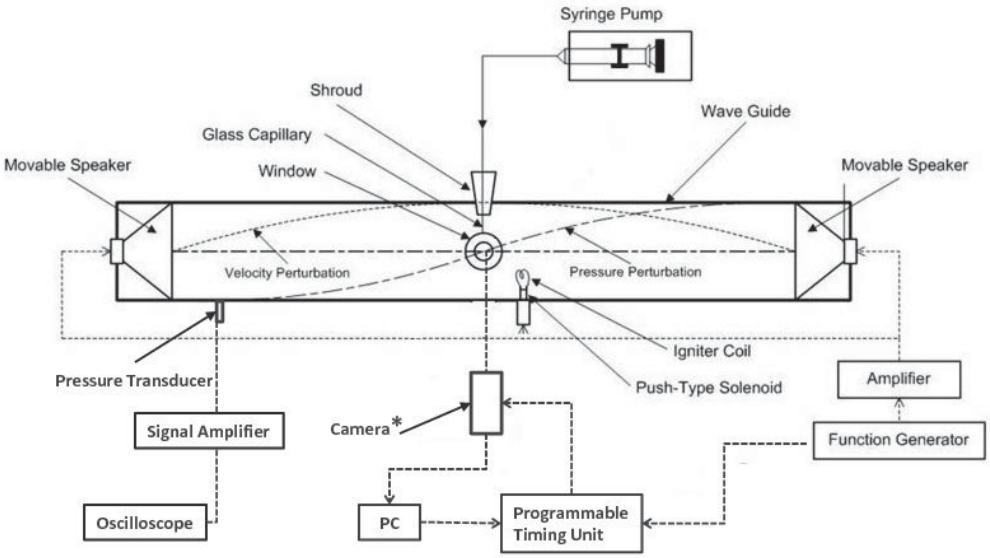

2.1: Experimental setup of the acoustic waveguide and feed droplet system.

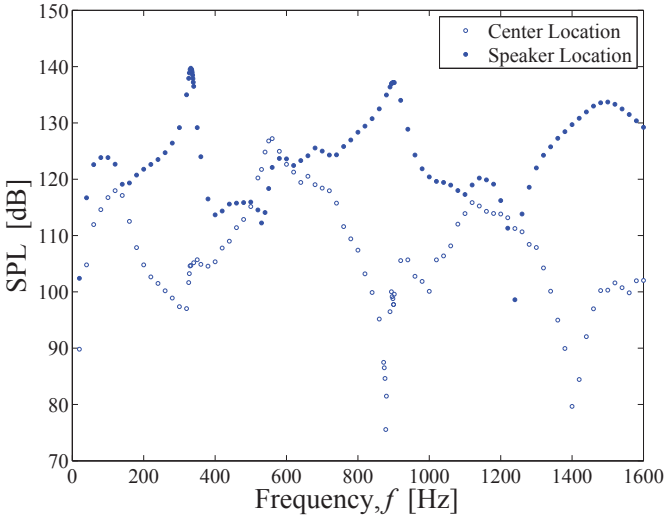

2.2: Frequency sweep for the speaker-speaker configuration with speakers operated 180^o out-of-phase and a PN occurring at the center of the waveguide. The distance between speakers is approximately 61 cm. Resonant frequencies are shown to occur near 332 Hz, 898 Hz, and 1500 Hz.

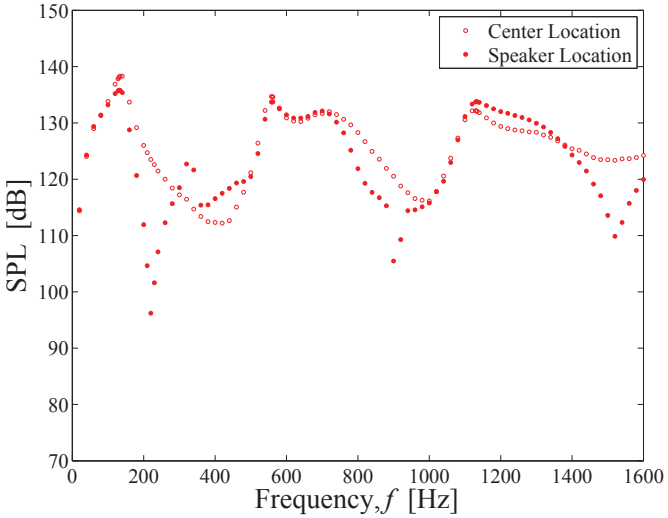

2.3: Frequency sweep for the speaker-speaker configuration with speakers operated in-phase (0^o) and a PAN occurring at the center of the waveguide. The distance between speakers is approximately 61 cm. Resonant frequencies are shown to occur near 134 Hz, 558 Hz, and 1132 Hz.

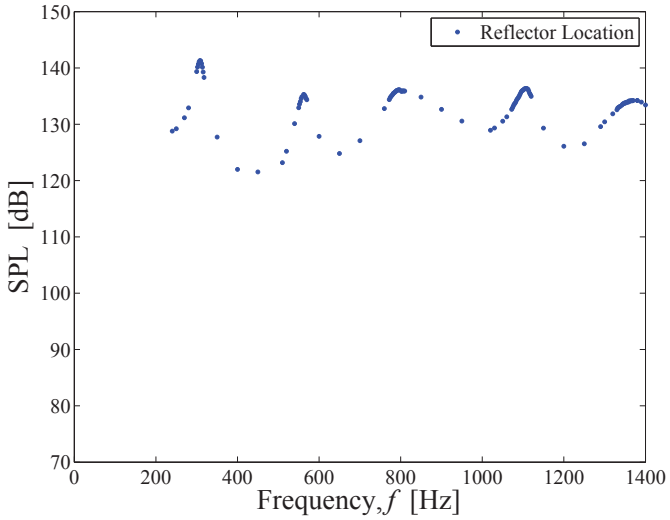

2.4: Frequency sweep for the speaker-reflector configuration. The distance between speaker and reflector is approximately 65 cm. Resonant frequencies are shown to occur near 562 Hz and 1108 Hz for a PAN occurring the waveguide center and 308 Hz, 796 Hz, and 1370 Hz for a PN occurring at the waveguide center.

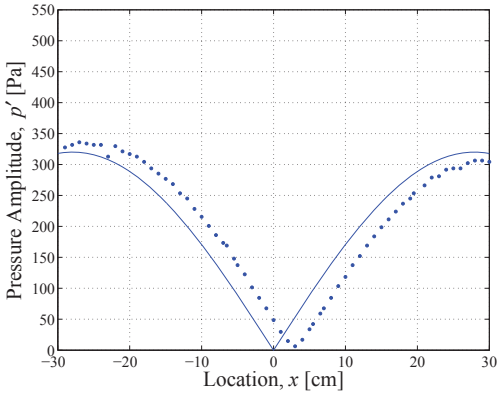

(a) 308 Hz PN (200 mV input)

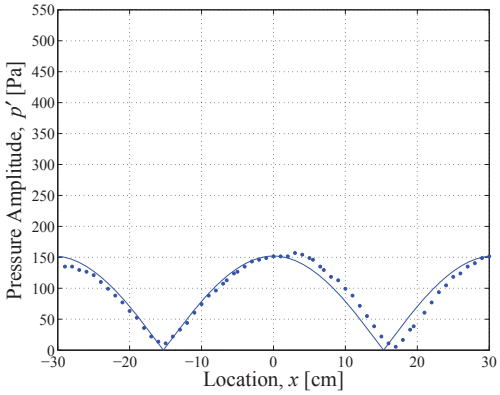

(b) 562 Hz PAN (200 mV input)

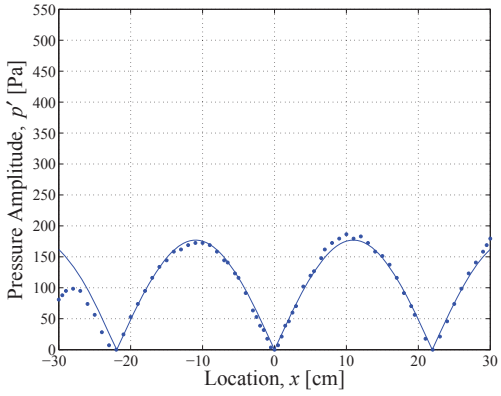

(c) 784 Hz approximate PAN (400 mV input)

2.5: Acoustic pressure amplitude measurements for the speaker-reflector configuration. The distance between speaker and reflector is approximately 65 cm, and the reflector is located at the positive end of the waveguide.

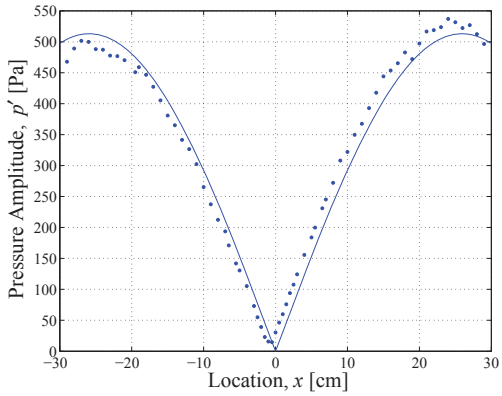

(a) 332 Hz PN

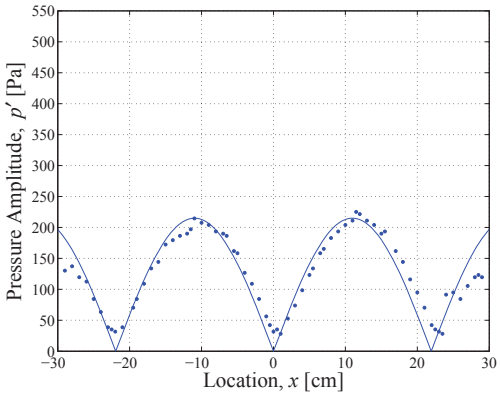

(b) 784 Hz

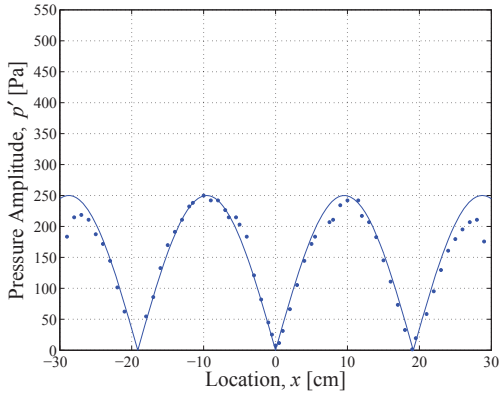

(c) 898 Hz PN

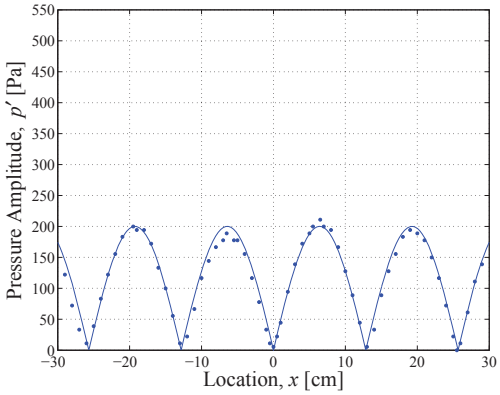

(d) 1340 Hz

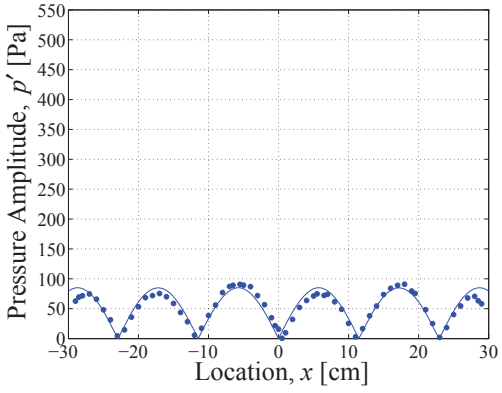

(e) 1500 Hz PN

2.6: Acoustic pressure amplitude measurements for the speaker-speaker configuration ($\phi = 180^o$). The distance between the speakers is approximately 61 cm. (200 mV speaker input)

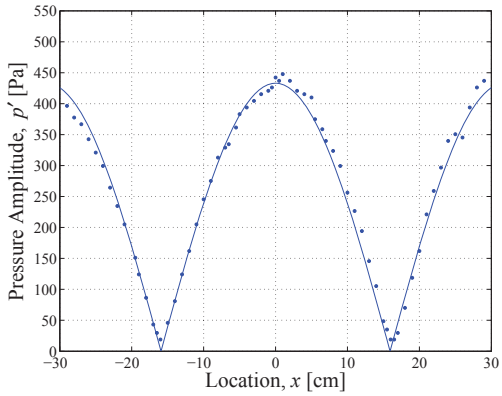

(a) 540 Hz PN

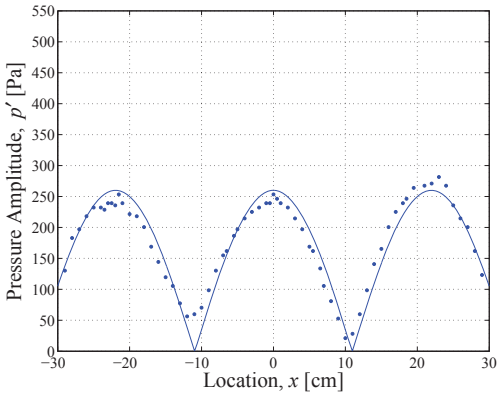

(b) 784 Hz

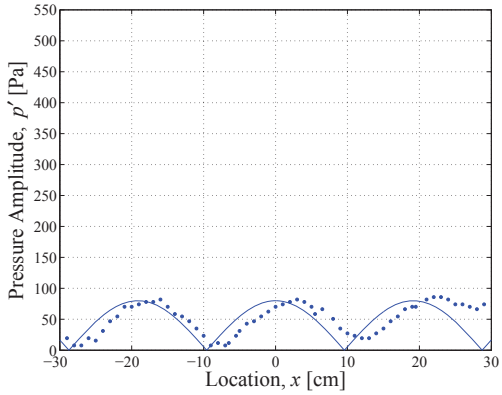

(c) 898 Hz PN

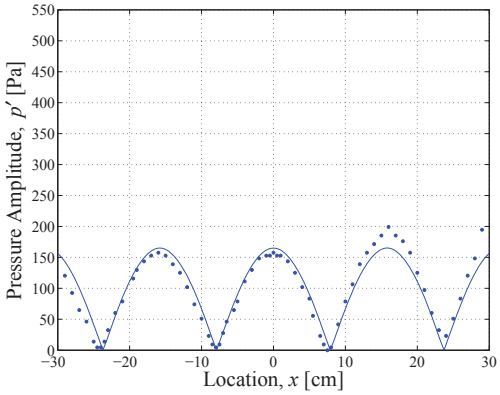

(d) 1088 Hz

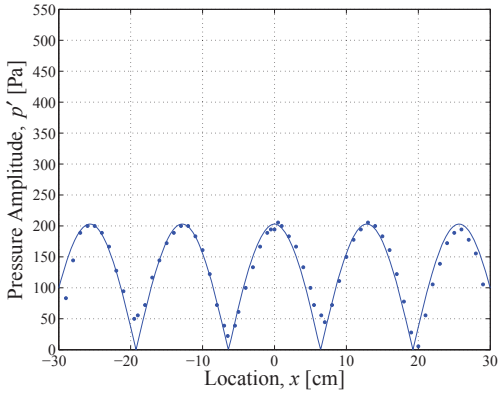

(e) 1340 Hz PN

2.7: Acoustic pressure amplitude measurements for the speaker-speaker configuration ($\phi = 0^o$). The distance between the speakers is approximately 61 cm. (200 mV speaker input)

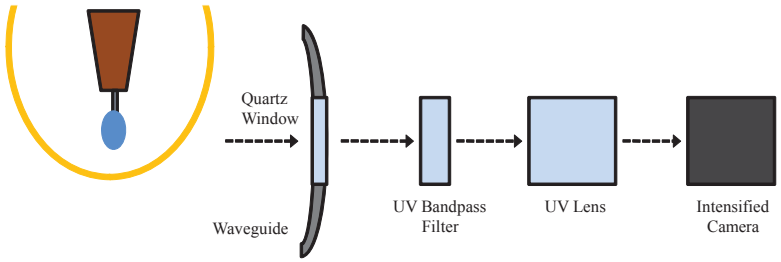

2.8: OH* chemiluminescence optics showing the path of light transmission from the flame source to the photocathode of the intensified camera.

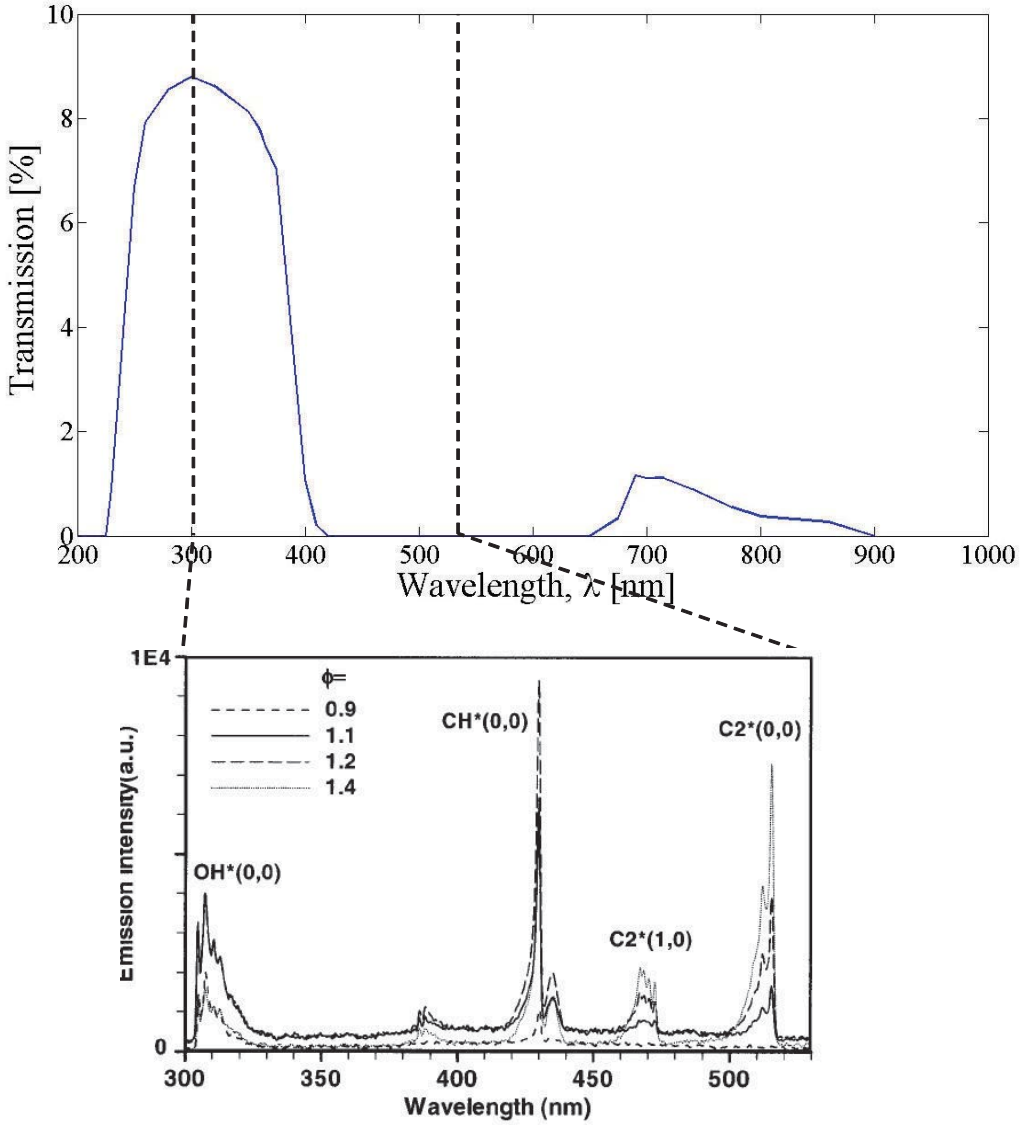

2.9: To confirm the isolation of OH* chemiluminescence, total light transmission was calculated for the complete optical arrangement. A comparison with experimentally measured excitation wavelengths of methane combustion from Kojima *et al.* [138] affirms the current bandpass range.

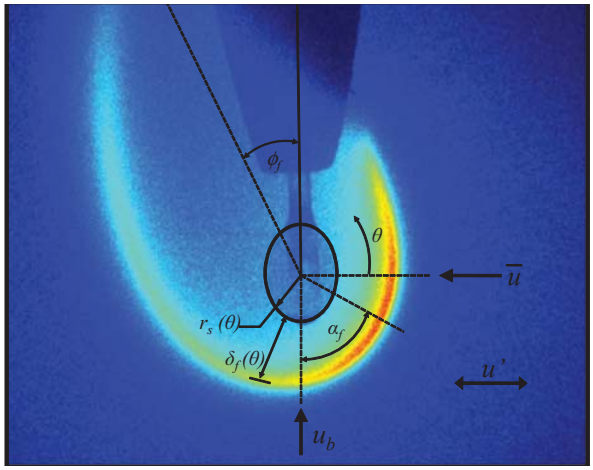

2.10: OH* chemiluminescence image for ethanol under acoustic forcing. The droplet radius r_s and flame radius r_f are dependent on the angle θ defined in a cylindrical coordinate system with an origin at the center of the droplet. Maximum chemiluminescence intensity occurs near the stagnation point, which is located at an angle α_f from the negative y-axis.

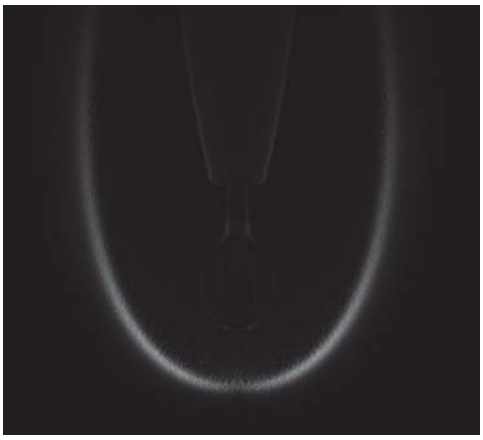

2.11: An ethanol flame in the absence of acoustic forcing is imaged by capturing light emitted from three-dimensional space, which can then be deconvoluted using the Abel transform [140] to create the image above, representing a two-dimensional slice of the axisymmetric flame.

CHAPTER 3

Results - Acoustically Coupled Fuel Droplet Combustion

3.1 Burning Rate Constant

Concerning the burning rate constant K, the primary interests are in the difference in K between unforced and acoustically forced conditions and the effect of various acoustic flow conditions on K. This portion of the study first presents baseline (unforced) burning rate constant measurements and comparisons with established values, then presents measurements for acoustically forced cases.

3.1.1 Baseline Burning Rate Constant

A sample image of chemiluminescence for the unforced burning droplet is shown in Figure 3.1 for each of the four fuels of interest. Gravitational forces give the fuel droplet an oblong shape and produce an elongated flame shape due to natural convection. Although not shown by UV chemiluminescence images, the alcohol and hydrocarbon fuels vary greatly in visible color. The alcohols, due to oxygenated chemical compounds, emit radiative energy mostly in lower wavelengths and appear blue. The hydrocarbons, on the other hand, appear bright yellow due to chemiluminescence in longer wavelengths dominated by electronically excited CH and C_2 radicals.

Baseline burning rate constants for all four fuels used in this study were measured

and compared with other available data, as shown in Table 3.1. Although not quantitatively discussed here, K decreased over long periods of time due to increasing product concentrations surrounding the reaction zone. A reduction in reaction rate can be expected for regions with concentrations saturated by hot products and thus a reduction in oxidizer mass fraction, and this process is especially significant for unforced conditions. For the acoustically excited case, forced convection prevents a large build up of products surrounding the flame and burning rate constants have negligible long term reductions within the time spans used here. To prevent adverse influence by this phenomenon, burning rate constants for unforced conditions were determined using only the first 30 seconds after ignition.

3.1.2 Effect of Acoustics on Burning Rate Constant

Burning droplets were placed at various locations relative to a PN within a standing wave, which allows one to investigate the difference between the forced and unforced K values as well as the changes which occur for different forced conditions. As discussed earlier, applying acoustic perturbations to the field surrounding the droplet will increase the burning rate constant [20–22, 72, 75, 82], but the following results aim to further quantify the increase occurring for various locations relative to the PN as done only by recent studies at UCLA [75, 82].

For acoustic frequencies of 332 Hz, 898 Hz, and 1500 Hz, PNs were located at the center of the waveguide by speakers 180^o out-of-phase. All results presented within this chapter were produced from these three frequencies, but nearly two hundred different acoustic flow conditions were tested by positioning the droplet in different locations within these three waveforms (see Figure 2.6a,c,e). Figures 3.2-3.13 present K values measured at these different locations, along with acoustic acceleration values, as discussed below.

The complete set of acoustically excited K measurements show values greater than or equal to baseline measurements. More specifically, positioning a droplet near the PN consistently produces burning rate constants higher than baseline values, while moving towards the PAN ($x \approx \pm\lambda/4$) produces burning rate constants closer to baseline values. These trends are manifested by three different frequencies and four different fuels, with a select few conditions producing burning rate constants as high as 20% greater than the baseline value near the PN. The higher frequency results show K values extending to PANs in both the positive and negative directions, which are precisely the locations where burning droplets consistently behave similar the unforced burning droplet. Much like previous works have shown, there is no appreciable difference in K at these locations [70, 71, 75, 82]. The increase in K towards the PN though, is believed to occur due to decreased flame standoff distance, causing steeper temperature gradients near the droplet surface and thus greater fuel evaporation rates. These topics are discussed in more detail with flame behavior results.

3.2 Flame Behavior

The imaging system provides the ability to measure flame behavior in multiple ways, ranging from deflection of the flame's plume to chemiluminescence intensity in the reaction zone. Using phase-locked imaging techniques described earlier, acoustic forcing is shown to alter the flame both in a constant manner and a time-dependent manner. In fact, examining flame front location with respect to acoustic phase reveals flame oscillation frequencies equal to the acoustic frequency f_a. These observations and others are illustrated in the following sections, including an interpretation of flame behaviors in terms of the acoustic radiation force.

3.2.1 Flame Deflection and Acoustic Acceleration

The most prevalent flame alteration induced by acoustic forcing is the deflection of the flame to one side. Deflection occurs primarily in the plume of the flame, and examples of this behavior are shown for ethanol in Figure 3.14. The observed deflections are independent of the micro-scale changes in time within each acoustic cycle. Instead, any infrequent changes in flame deflection occur throughout long periods, ~ 1 s. Recent experimental work at UCLA quantifies flame deflection to evaluate an acoustic radiation force theory [20] which has previously been validated qualitatively [21, 75, 82]. Further quantitative comparisons are presented here using the flame deflection measurement techniques of Teshome *et al.* [142].

For a standing wave, the acoustic radiation force equation can be expressed per the analysis of Tanabe *et al.* [20]:

$$F_R = (\rho_p - \rho_o)V[\pm 4\alpha(\frac{I}{z_a})(\frac{2\pi f_a}{c})\sin(\frac{2\pi x}{\lambda})\cos(\frac{2\pi x}{\lambda})] \tag{3.1}$$

Here I represents the acoustic intensity, which depends on the maximum sound pressure level (SPL) inside the waveguide, $z_a = \rho c$ is the acoustic impedance, and c represents the speed of sound. The term in square brackets represents an equivalent acoustic acceleration term, $g_a = \alpha\frac{\partial\overline{u'^2}}{\partial x}$, for a condition where a standing wave is present in the waveguide. The coefficient α defined in eqn. 1.8 is approximated as one in subsequent analyses. Concerning the plus-minus sign in eqn. 3.1, the minus sign corresponds to the case where a PN or VAN was positioned at the center of the waveguide, $x = 0$, whereas the plus sign corresponds to a PAN or VN at that location. Thus, the minus sign is used to calculate theoretical acoustic acceleration $g_{a,th}$ for the waveguide and flow conditions in this study. Inspecting eqn. 3.1, one observes that a burning droplet located to the left ($x < 0$) or right ($x > 0$) of the PN will experience a finite acoustic radiation force F_R due to a nonzero acoustic acceleration g_a. Then, Tanabe *et al.* concludes that the physical consequence of this force on a burning droplet would be flame deflection/deformation in

the opposite direction of F_R, assuming that the hot products with density ρ_p occupy a volume V and are separated from the surrounding gas with density ρ_o.

Noting the analogy between thermal buoyancy and the acoustic radiation force formulated above, Teshome *et al.* [142] utilize well known flame behaviors when buoyant from gravitational acceleration g_o in order to experimentally determine acoustic acceleration g_a. The two accelerations are interpreted as similar in effect, whereas gravitational acceleration is vertically orientated and acoustic acceleration is horizontal (i.e. in the direction of sound propagation). Using the definition of flame deflection angle shown in Figure 2.10, an experimental acoustic acceleration can be calculated as $g_{a,exp} = g_o \tan(\phi_f)$. The flame deflection angle ϕ_f is measured between the vertical axis and the semi-major axis of an ellipse which is fit to the elongated flame shape. In this way, $\phi_f = 45^o$ corresponds to an experimental acoustic acceleration equal to gravitational acceleration, while ϕ_f tending towards 90^o corresponds to an infinitely large experimental acoustic acceleration.

Figures 3.2-3.13 compare theoretical and experimental g_a values, including the absolute value of each ($|g_{a,exp}|$ and $|g_{a,th}|$) juxtaposed with burning rate constants for illustration. Both experimental and theoretical values exhibit a switch in sign near the PN, where experimental images reveal a distinct switch in deflection from leftward orientation for $x < 0$ and rightward orientation for $x > 0$ as shown in Figure 3.14. In this regard, the acoustic radiation force theory consistently agrees with experiments across a wide range of flow conditions and fuel types. These results confirm that acoustically forced flames will deflect away from the nearest PN, or towards a PAN. But, although theoretical values predict a maximum absolute acceleration at $x = \pm\lambda/8$, centered between a PN and PAN, $|g_{a,exp}|$ values reveal maximums closer to the PN. In fact, maximum flame deflections often occur immediately adjacent to the PN, engendering acoustic acceleration values which exceed 9.8 m/s^2 and are much larger than maxima estimated by

Tanabe's theory. If acoustic and gravitational acceleration constants are indeed similar mechanisms for deforming a volume of low density products, then $g_a > 9.8$ m/s^2 would presumably produce acoustic radiation forces which are greater than buoyancy forces. Tanabe *et al.* [21, 73] cite this relationship when producing droplet flames in a vertically oriented waveguide such that the acoustic radiation force and buoyancy force oppose one another, causing the flame to form a sphere-like shape similar to burning droplets in micro-gravity. This effective "cancellation" of gravity has not been reproduced by other experimentalists though, including several attempts by droplet combustion experiments at UCLA.

There are particular flow conditions though, where the location of flame switch does not coincide with a PN. Specifically for the lowest acoustic frequency, $f_a = 332$ Hz, flame switch occurs somewhat far from the PN. For all fuels tested in this study, this lower forcing frequency provides a less distinct flame switch and concurrently, the observed deflections are generally larger when oriented in the negative direction (i.e. leftward). Pressure distributions in Figure 3.2 show a waveform which is slightly asymmetric with a PN favoring the left side of the waveguide, which may contribute to the asymmetries evidenced by burning droplets. The same pressure distribution also shows maximum pressure perturbations which are nearly 10% larger on the waveguide's positive side. Therefore, acoustic pressure asymmetries combined with a lack of acoustic velocity measurements warrant further investigation to verify the absence of traveling waves, and in addition, determine the true waveform characteristic which causes flame switch. One should also note that all acoustic pressure fluctuations were measured at room temperature without combustion, but the temperature and species distribution alterations caused by a burning droplet may not be negligible.

3.2.2 Standoff Distance

3.2.2.1 Standoff Distance Oscillation

Using the phase-locked imaging techniques discussed in Section 2.3, the flame front position can be investigated as a function of acoustic phase. The resulting behavior is best understood by first viewing Figure 3.15, which shows a pair of flame images acquired at two different points within an acoustic cycle. Acoustic excitation manifests a difference in flame position between such a pair of images, and moreover, the flame position is found to oscillate at a frequency equal to the acoustic frequency f_a. In fact, the entire flame appears to maintain a constant global shape while moving horizontally in a sine-like manner, changing position relative to the droplet. Again, the acoustic waveforms used here are assumed to be one-dimensional, which is supported by a lack of vertical flame movement within microscale changes in time.

The flame standoff distance δ_f, defined in Figure 2.10, is dependent on the coordinate angle θ. As a result of the one-dimensional oscillation of the flame, the maximum standoff distance oscillation amplitude δ'_f occurs near $\theta = 0^o$ or $\theta = 180^o$. For example, Figure 3.15 shows a case where $\delta'_{f,max} = \delta'_f(\theta = 0^o)$. Note that the flame's wake region is not examined when investigating standoff distance. Rather, the hemisphere centered around the flame's stagnation point is of paramount interest because it is believed that maximum temperatures and mass burning rates occur in this hemisphere [61]. Then, focusing on the upstream side of the droplet, Figure 3.16 shows $\delta_f(\theta = 0^o)$ versus ϕ_p for each fuel and acoustic frequency at a select few locations within the waveguide. Four acoustic periods worth of phase-locked images show four distinct oscillation cycles for δ_f. The oscillation amplitude δ'_f varies with respect to position within the waveguide though, with effectively zero oscillation for droplets near a PAN (VN). Near a PN (VAN) on the other hand, high amplitudes are observed due to greater velocity perturbations. A greater velocity amplitude u' causes large changes in the total velocity $u = \overline{u} + u'$,

and thus greater changes in mass diffusion rates of air. Physically, these perturbations of oxidizer mass fraction within the reaction zone cause the fuel-air equivalence ratio to change, and the heart of the reaction zone, or flame, must move in order to maintain the prescribed mixture composition for peak reaction rates.

However, the chemical kinetics processes exhibit their own frequency response. Lower acoustic frequencies permit longer periods before flow is reversed at the minimum or maximum of u', and as a result, these lower frequencies (e.g. Figure 3.16a for $f_a = 332$ Hz) allow for greater values of δ'_f. Meanwhile, higher frequencies (e.g. Figure 3.16c for $f_a = 1500$ Hz) with a similar value of u' will prohibit large values of δ'_f due to shorter diffusion time scales relative to the kinetics time scale. Figure 3.17 demonstrates this relationship in a comprehensive manner in a plot of δ'_f versus waveguide location x. This broader perspective reveals a direct relationship between the acoustic period $T_a (= \frac{1}{f_a})$ and δ'_f for the acoustic intensities and frequencies used here, where a three-fold increase in T_a results in approximately the same relative increase in δ'_f. But, this relationship cannot hold for all frequencies. Also, amplitudes as high as 275 μm are observed for $f_a = 332$ Hz at a PN ($x = 0$), while amplitudes are approximately zero for droplets placed at a PAN ($x = \pm\lambda/4$). Thus, trends observed in δ'_f roughly coincide with the trends observed in the burning rate constant K, experimental acoustic acceleration $g_{a,exp}$, and the assumed trend in u', all of which exhibit maximum values at or near a PN. In contrast, there is not a correlation between flame oscillation amplitude and the theoretical acoustic acceleration $g_{a,th}$ of Tanabe *et al.* [20, 21, 73], which predicts a maximum effect mid-way between a PN and PAN, $x = \pm\lambda/8$.

3.2.2.2 Mean Standoff Distance

Acoustic radiation force theory [78, 79] descibes the time-averaged forces caused by acoustic fluctuations. Therefore, a more direct validation of the theory of Tanabe *et al.*

should inspect time-averaged flame behaviors rather than flame alterations occurring throughout microscale changes in time. The mean standoff distance $\overline{\delta_f}$ could offer a better correlation than the analysis above. If indeed the acoustic radiation force should act to displace or deform the droplet's surrounding flame as though it were a sphere of hot products, then the flame front will presumably shift towards the droplet surface on one side of the droplet and away from the droplet on the other side. This concept is partially captured in Section 3.2.1 by using flame deflection angle as a representation of the constant displacement generated by the combined forces of thermal buoyancy and the acoustic radiation force. Instead, a different flame angle can be produced by mean standoff distance measurements which focus on the time-averaged deformations occurring in the stagnation point region of the flame as opposed to the deflection angle of the flame's plume. The aforementioned technique, as well as other comparisons, will be discussed below in an effort to more confidently evaluate the theory of Tanabe *et al.*

First, consider Figure 2.10, where acoustic forcing has altered the location of the flame's stagnation point. The stagnation point is defined here as the location of minimum flame standoff distance and occurs at an angle α_f from the negative y-axis. Thus, $\alpha_f = 0^o$ for the unforced flame, which is governed only by natural convection represented by u_b in Figure 2.10. A second velocity component $\overline{u}$ is also shown, representing horizontal steady flow induced by the fluctuating component u'. In this discussion, the horizontal steady component $\overline{u}$ will be interpreted in two ways. First, this bulk flow can represent flow caused by an acoustic radiation force similar to buoyancy. In other words, high flame temperatures cause the surrounding gases to expand due to increasing temperature, then these low density gases are swept into the reaction zone at a velocity $\overline{u}$ by a buoyancy-like acoustic radiation force. The second interpretation considers $\overline{u}$ as an acoustic streaming velocity [80, 143, 144]. Acoustic streaming is not a result of temperature or density differences, but instead occurs throughout the entire waveguide as a result of wave attenuation near boundaries and dissipation in open space. Both interpretations call for

an increase in $\overline{u}$ as acoustic intensity increases, and therefore a decrease in $\overline{\delta_f}$ as more air diffuses into the reaction zone.

If the acoustic radiation force in eqn. (3.1) is indeed valid, then the minimum flame standoff distance $\overline{\delta_{f,min}}$ will occur at $x = \pm\lambda/8$. Whether the flame front is displaced by a shift of the entire sphere of hot gases contained within the flame or by a rise in oxidizer diffusion rates via $\overline{u}$, $\overline{\delta_{f,min}}$ will coincide with maximum $|g_{a,th}|$ if Tanabe *et al.*'s application of acoustic radiation force theory to flames is valid. The exact quantities one expects are obfuscated by gradual variations in temperature and density, but the qualitative expectations are clear. Figure 3.18 shows the relationship between $\overline{\delta_f}$ and waveguide location x when $\overline{\delta_f}$ is measured at either $\theta = 0^o$ or $\theta = 180^o$, depending on flame orientation. $\overline{\delta_{f,min}}$ is shown to occur near the PN ($x = 0$), as opposed to the predicted value of $x = \pm\lambda/8$ from eqn. (3.1). As the droplet is positioned closer to the PAN, $\overline{\delta_{f,min}}$ adopts the unforced value shown by dashed lines. This relationship disagrees with that of the prescribed theory, and this point is ameliorated by Figure 3.19. Figure 3.19 confirms a contradicting correlation between flame displacement and theoretical acoustic acceleration, where standoff distance increases with an increase in acoustic acceleration as calculated per the bracketed term in eqn. (3.1). It is thus clear that flame oscillations, which are not represented in the Tanabe theory, may in part be responsible for the discrepancy between theoretical and experimental values of acoustic acceleration.

For future work, a separate technique for comparing the effects of acoustic excitation to those of thermal buoyancy is proposed here. Utilizing the measured angle of minimum standoff distance α_f, a simple nondimensional velocity estimation is proposed

$$\frac{\overline{u}}{u_b} = \tan \alpha_f \tag{3.2}$$

where it is assumed that the steady flow velocity into the flame is equal to the combined magnitude of a vertical vector u_b and a horizontal vector $\overline{u}$. A preliminary plot of $\overline{\delta_f}$ ver-

sus the nondimensional velocity $\frac{\overline{u}}{u_b}$ can be found in Figure 3.20. Briefly, this comparison shows a relationship between standoff distance and convective velocity very similar to that predicted by the classical droplet combustion model with forced convection [61, 64]. In light of the shortcomings of the acoustic radiation force theory discussed above, this calculation is suggested for future analysis of this and similar burning droplet data with more focus allocated to predicting steady flow velocities such as $\overline{u}$, which could better explain the flow fields manipulating flame behavior.

3.1: Comparison of measured values of burning rate constant K for various fuel droplets in the absence of acoustic excitation.

Fuel	K, present (mm^2/s)	K, established (mm^2/s)
Ethanol	0.87-0.96	0.81-0.86 [60]
Methanol	0.94-1.04	0.85-1.2 [145, 146]
Pure FT	0.96-1.05	-
JP-8/FT	0.98-1.05	-

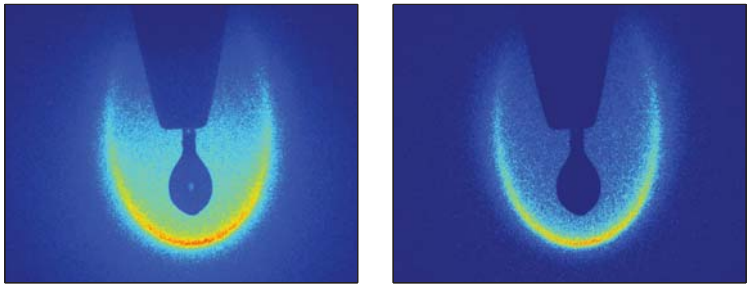

(a) Ethanol

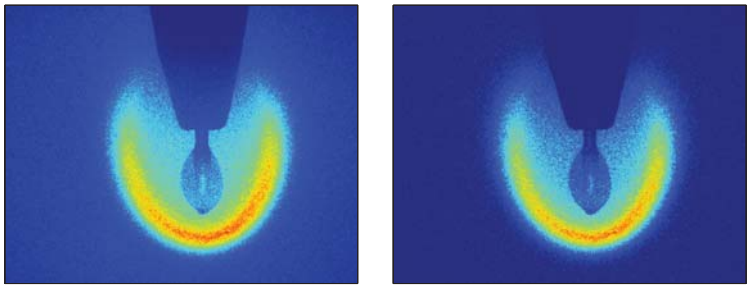

(b) Methanol

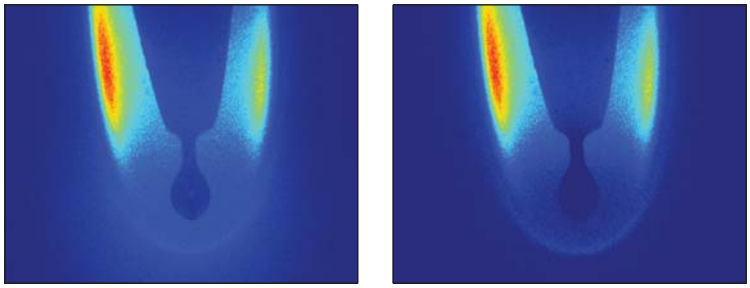

(c) Pure FT

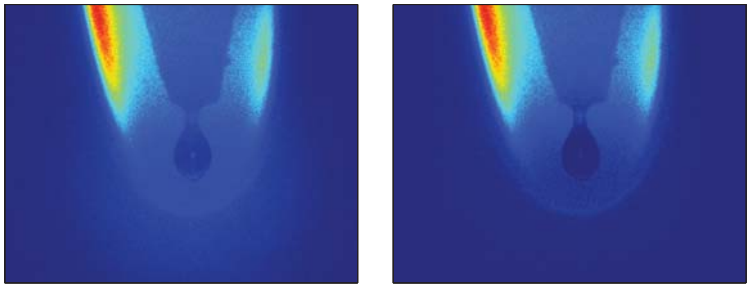

(d) JP-8/FT Blend

3.1: OH* chemiluminescence images of burning droplets in the absence of acoustic forcing. The left column shows an image as captured. The right column shows the same image after background light subtraction.

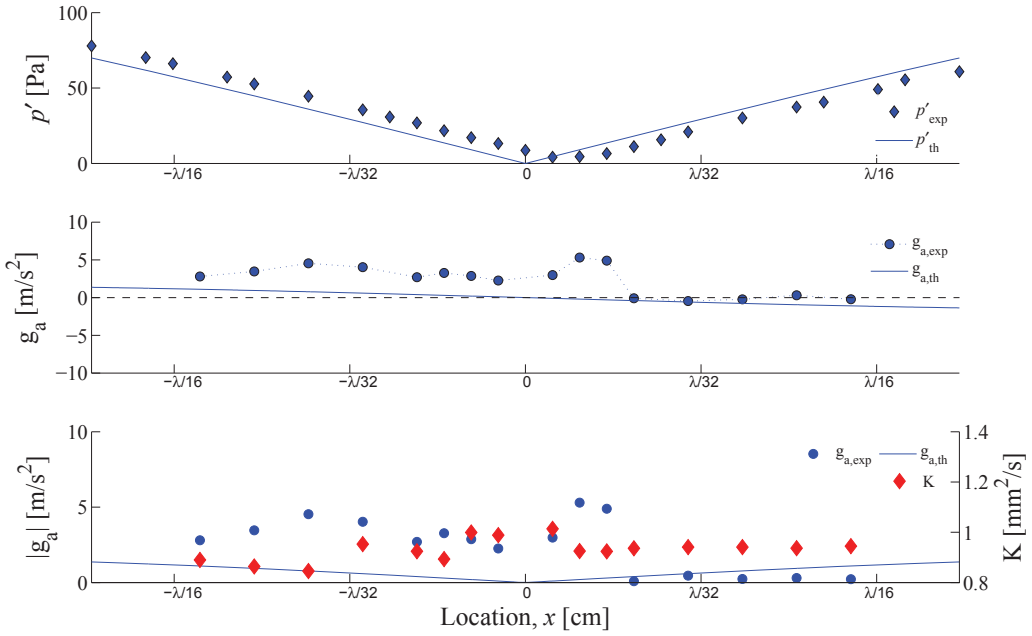

3.2: Pressure perturbations, estimated theoretical and actual acoustic accelerations g_a, and average burning rate constant K as a function of waveguide location for the ethanol droplet burning in the vicinity of a pressure node at a frequency of 332 Hz and $p'_{max} = 150$ Pa.

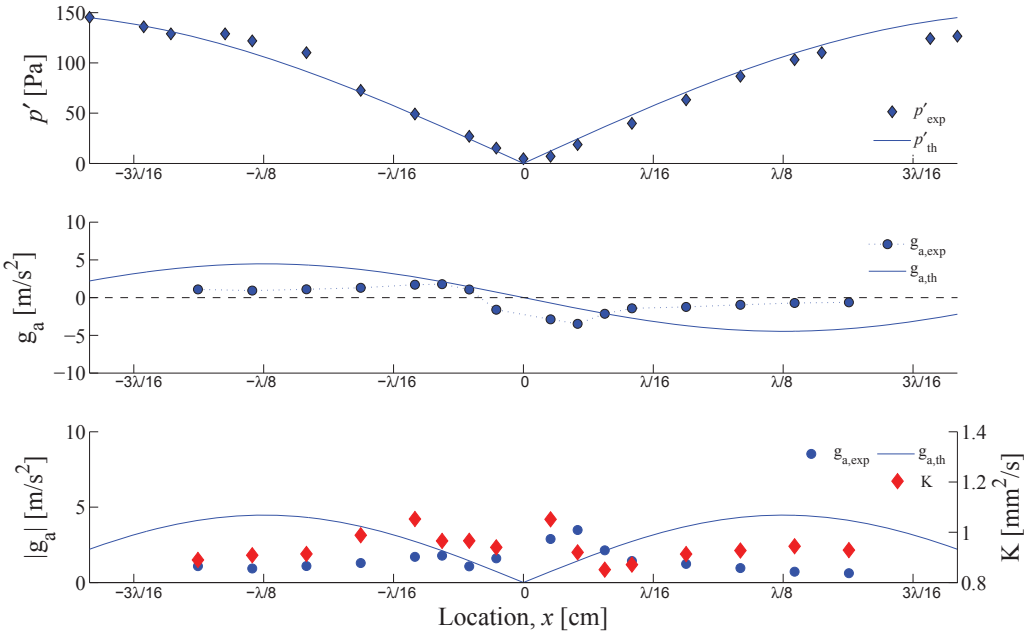

3.3: Pressure perturbations, estimated theoretical and actual acoustic accelerations g_a, and average burning rate constant K as a function of waveguide location for the ethanol droplet burning in the vicinity of a pressure node at a frequency of 898 Hz and $p'_{max} = 150$ Pa.

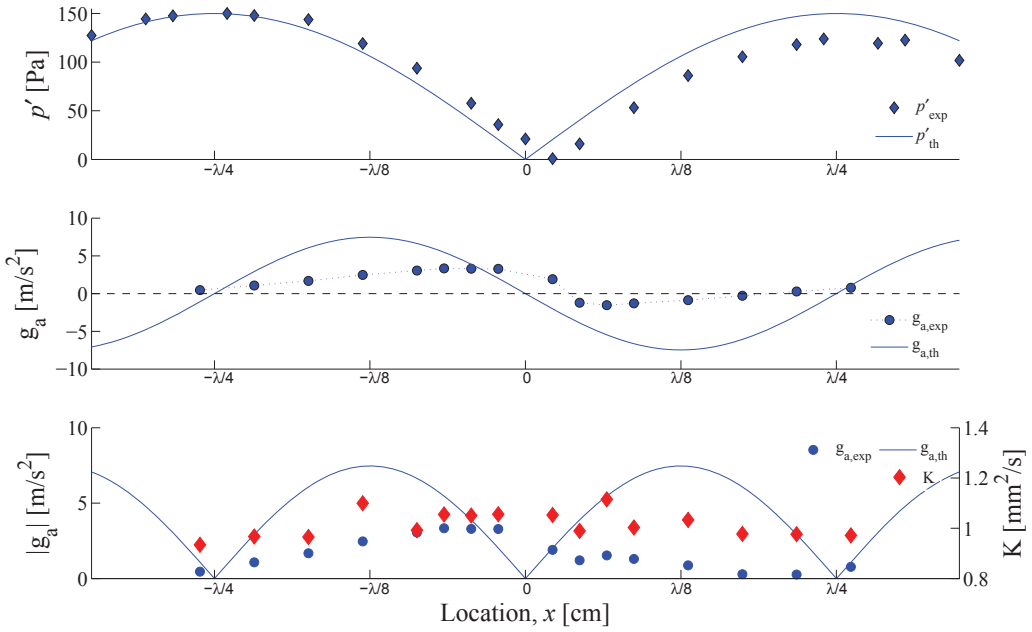

3.4: Pressure perturbations, estimated theoretical and actual acoustic accelerations g_a, and average burning rate constant K as a function of waveguide location for the ethanol droplet burning in the vicinity of a pressure node at a frequency of 1500 Hz and $p'_{max} = 150$ Pa.

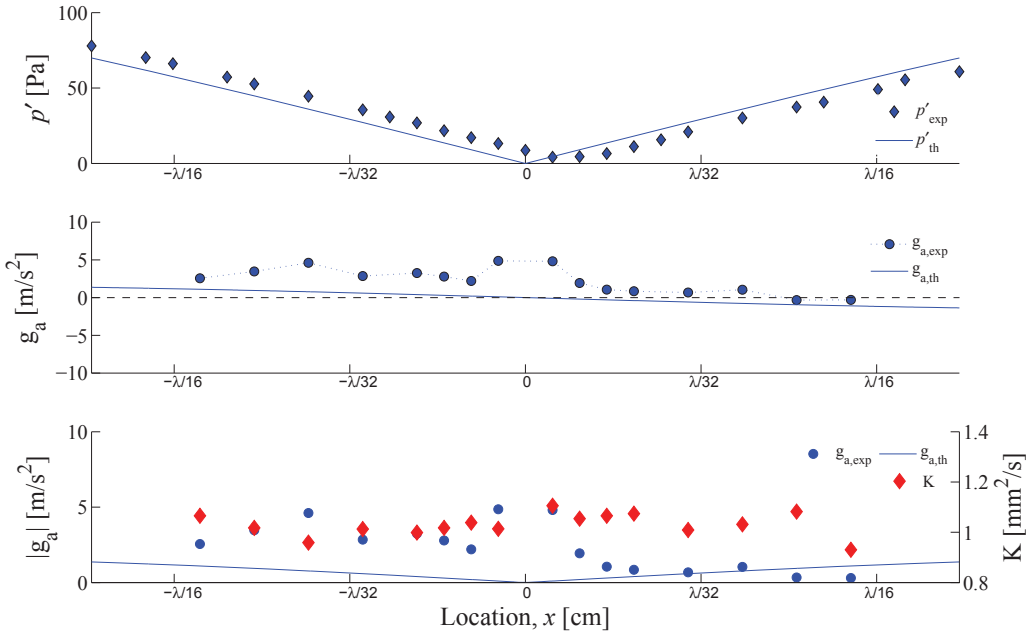

3.5: Pressure perturbations, estimated theoretical and actual acoustic accelerations g_a, and average burning rate constant K as a function of waveguide location for the methanol droplet burning in the vicinity of a pressure node at a frequency of 332 Hz and $p'_{max} = 150$ Pa.

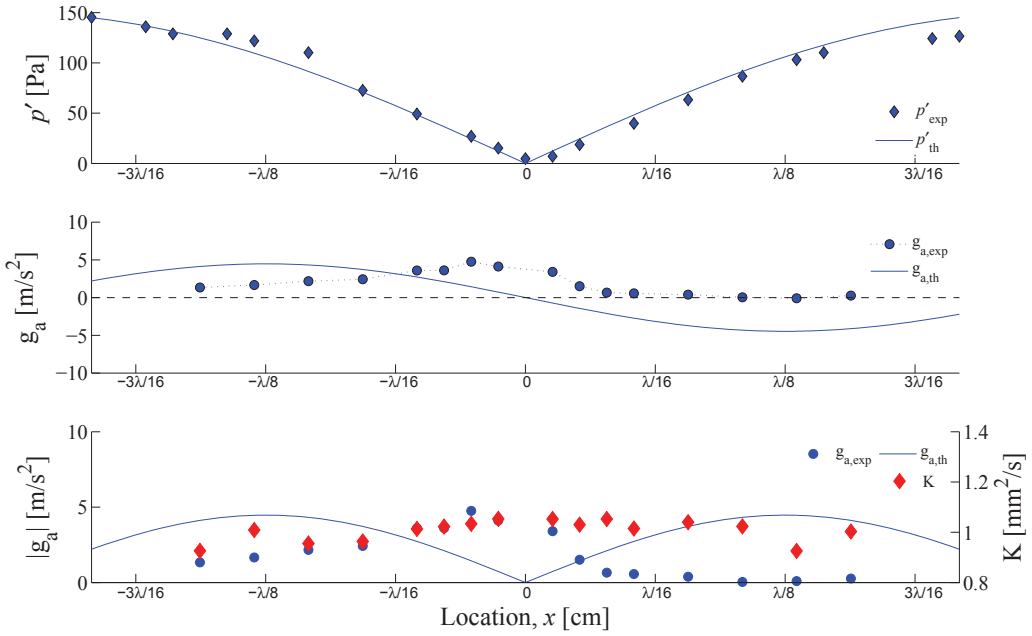

3.6: Pressure perturbations, estimated theoretical and actual acoustic accelerations g_a, and average burning rate constant K as a function of waveguide location for the methanol droplet burning in the vicinity of a pressure node at a frequency of 898 Hz and $p'_{max} = 150$ Pa.

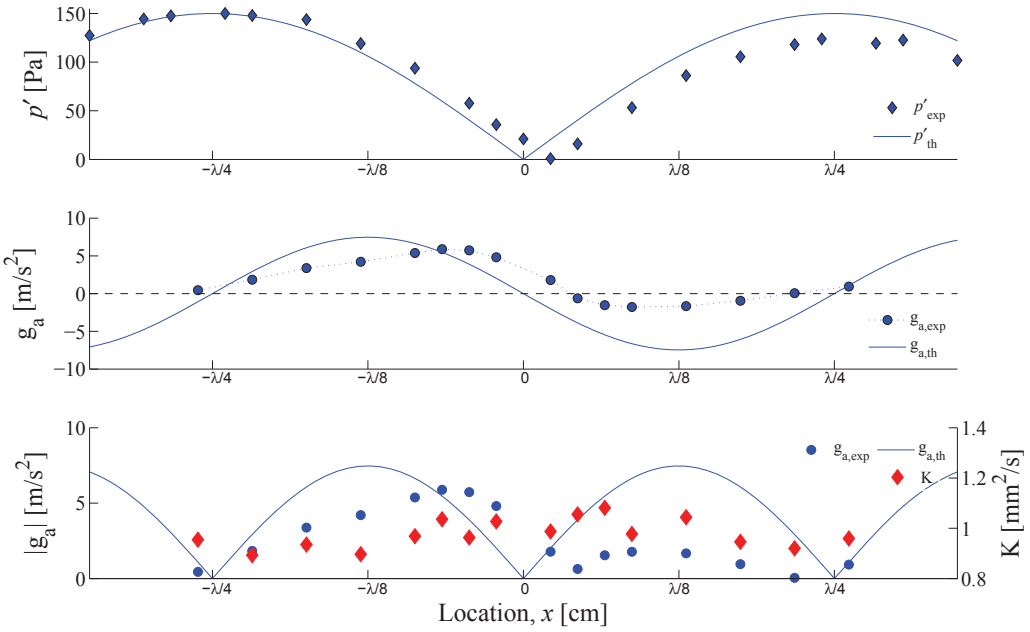

3.7: Pressure perturbations, estimated theoretical and actual acoustic accelerations g_a, and average burning rate constant K as a function of waveguide location for the methanol droplet burning in the vicinity of a pressure node at a frequency of 1500 Hz and $p'_{max} = 150$ Pa.

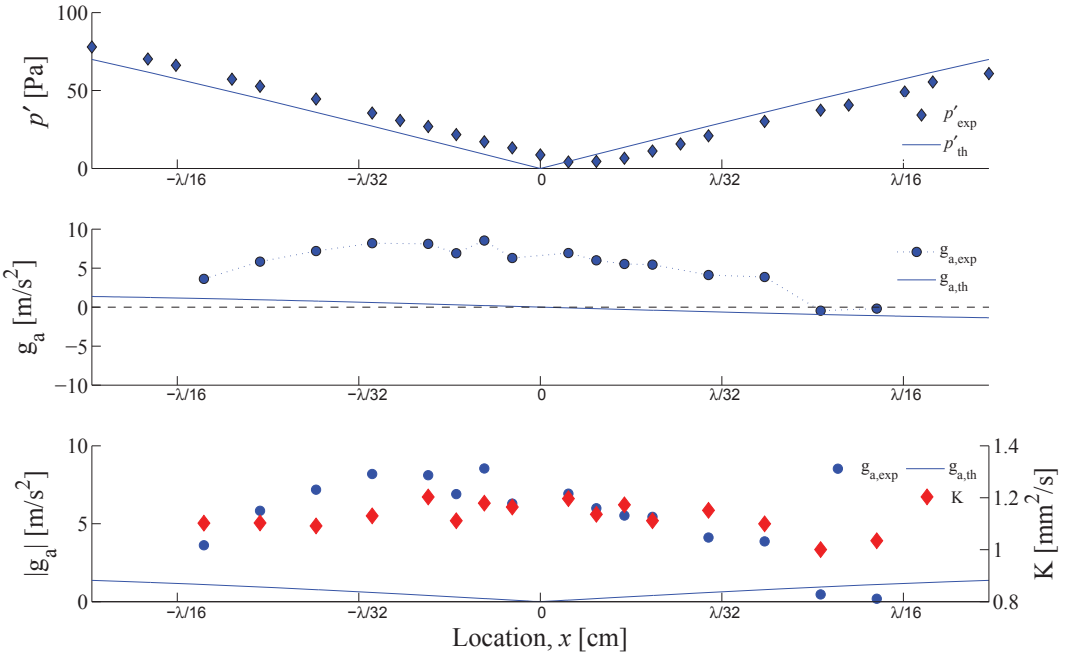

3.8: Pressure perturbations, estimated theoretical and actual acoustic accelerations g_a, and average burning rate constant K as a function of waveguide location for the FT droplet burning in the vicinity of a pressure node at a frequency of 332 Hz and $p'_{max} = 150$ Pa.

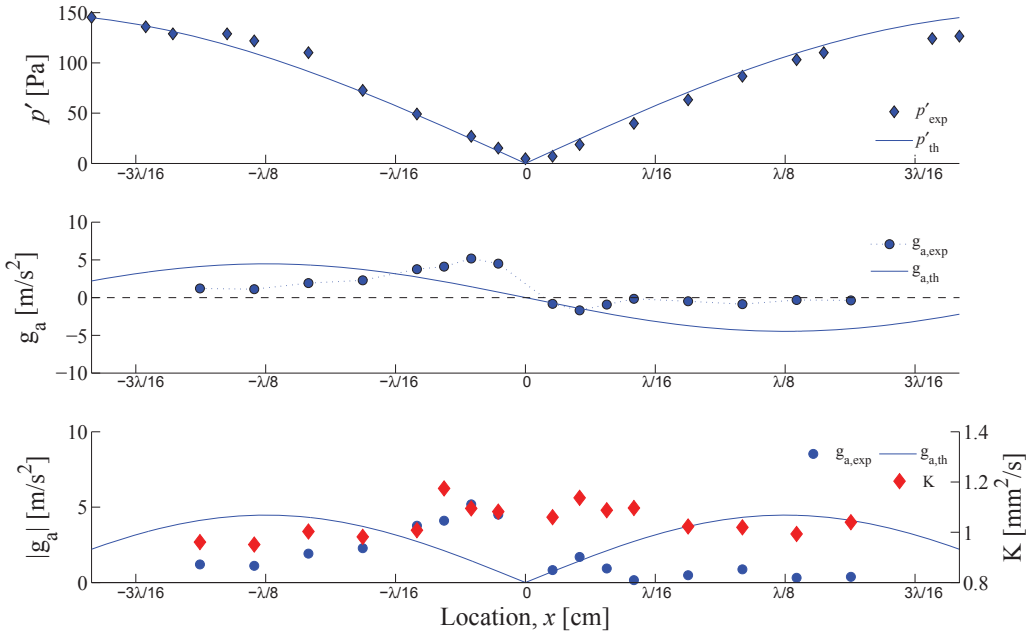

3.9: Pressure perturbations, estimated theoretical and actual acoustic accelerations g_a, and average burning rate constant K as a function of waveguide location for the FT droplet burning in the vicinity of a pressure node at a frequency of 898 Hz and $p'_{max} = 150$ Pa.

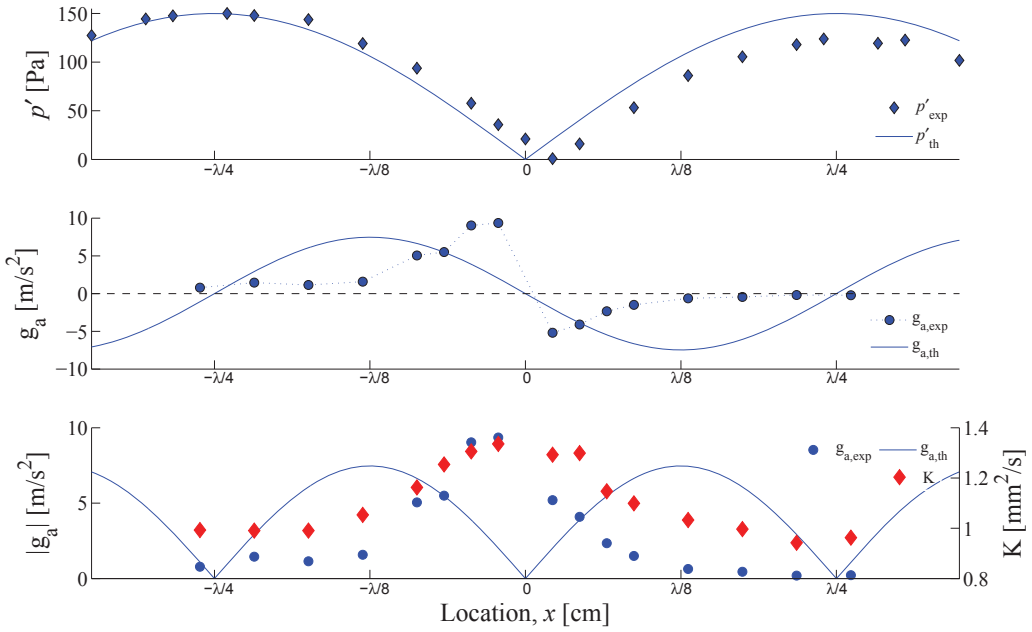

3.10: Pressure perturbations, estimated theoretical and actual acoustic accelerations g_a, and average burning rate constant K as a function of waveguide location for the FT droplet burning in the vicinity of a pressure node at a frequency of 1500 Hz and $p'_{max} = 150$ Pa.

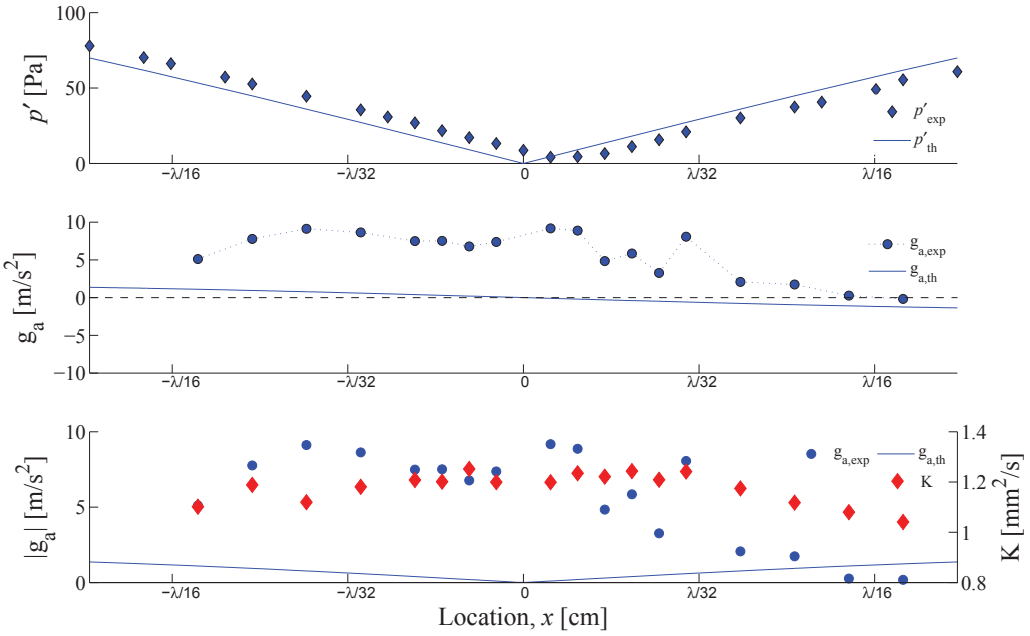

3.11: Pressure perturbations, estimated theoretical and actual acoustic accelerations g_a, and average burning rate constant K as a function of waveguide location for the JP8FT droplet burning in the vicinity of a pressure node at a frequency of 332 Hz and $p'_{max} = 150$ Pa.

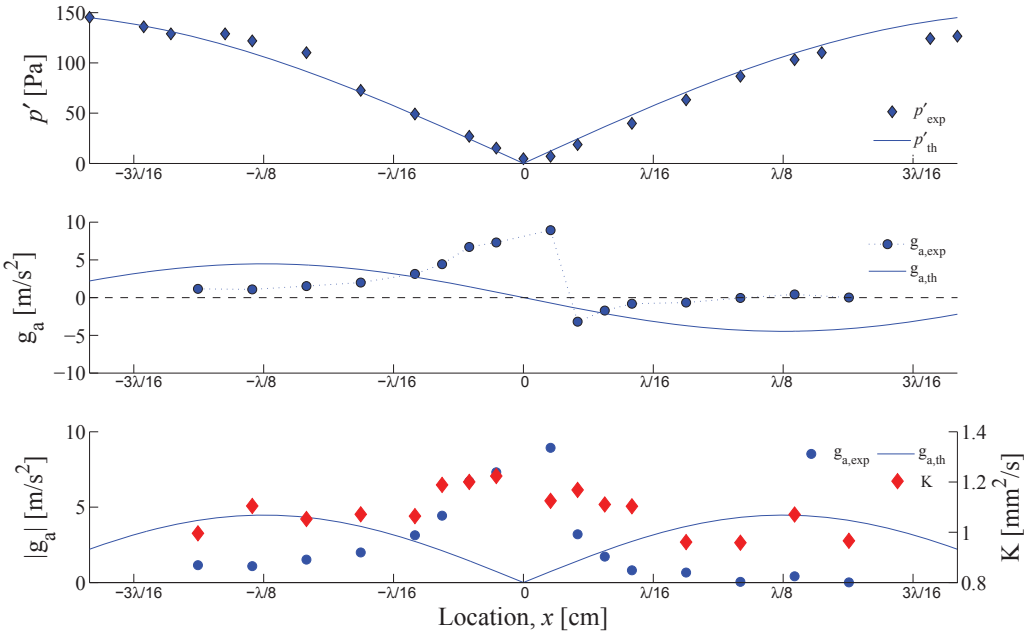

3.12: Pressure perturbations, estimated theoretical and actual acoustic accelerations g_a, and average burning rate constant K as a function of waveguide location for the JP8FT droplet burning in the vicinity of a pressure node at a frequency of 898 Hz and $p'_{max} = 150$ Pa.

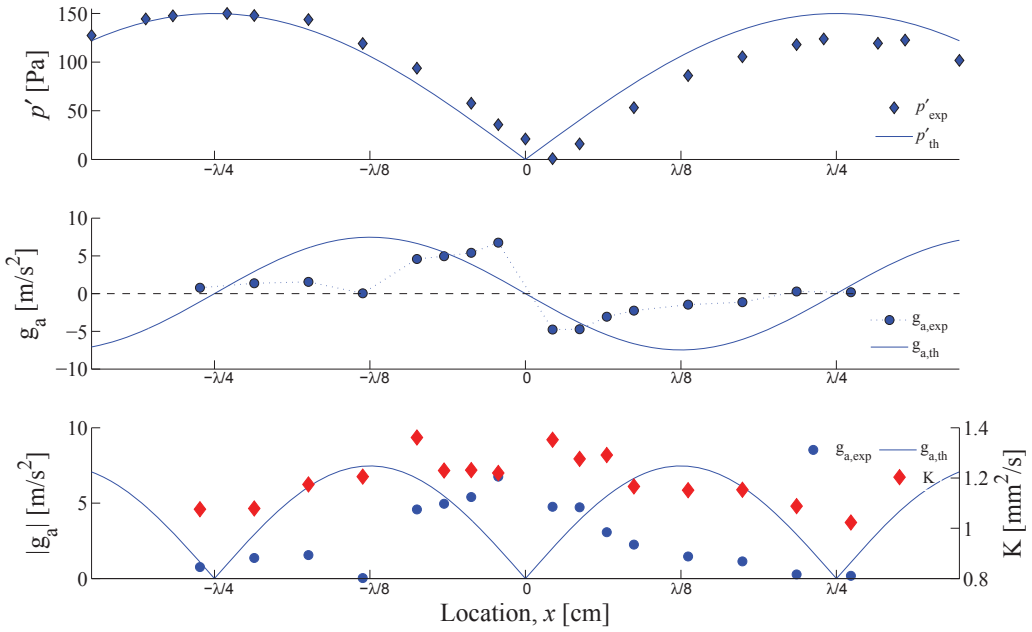

3.13: Pressure perturbations, estimated theoretical and actual acoustic accelerations g_a, and average burning rate constant K as a function of waveguide location for the JP8FT droplet burning in the vicinity of a pressure node at a frequency of 1500 Hz and $p'_{max} = 150$ Pa.

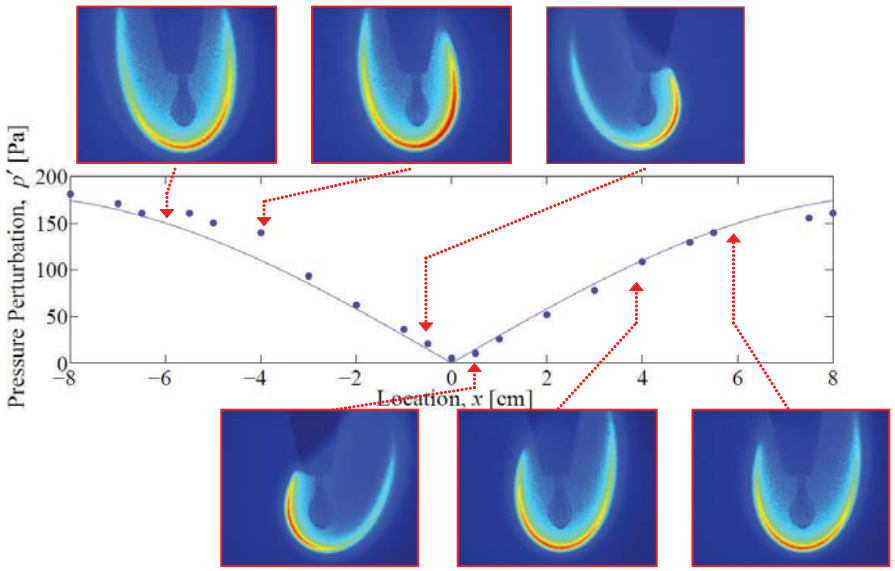

3.14: Ethanol flame images under the influence of acoustics. Flames are consistently deflected away from the pressure node (PN) with a flame "switch"' occurring near the PN.

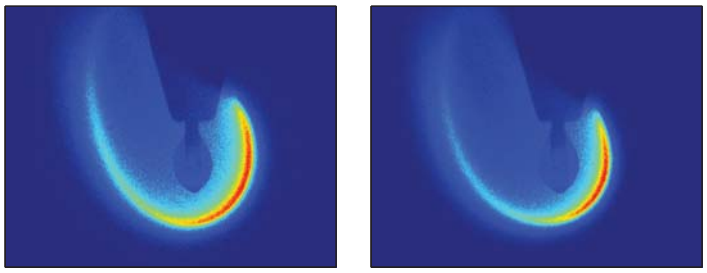

(a) (b)

3.15: A pair of ethanol flame images acquired at different points within the acoustic cycle. ((a) $\phi_p = 80^o$ (b) $\phi_p = 260^o$) Horizontal flame standoff distance δ_f oscillations cause the flame to exhibit a maximum δ_f in (a) and a minimum δ_f in (b) when viewing the right side of the flame.

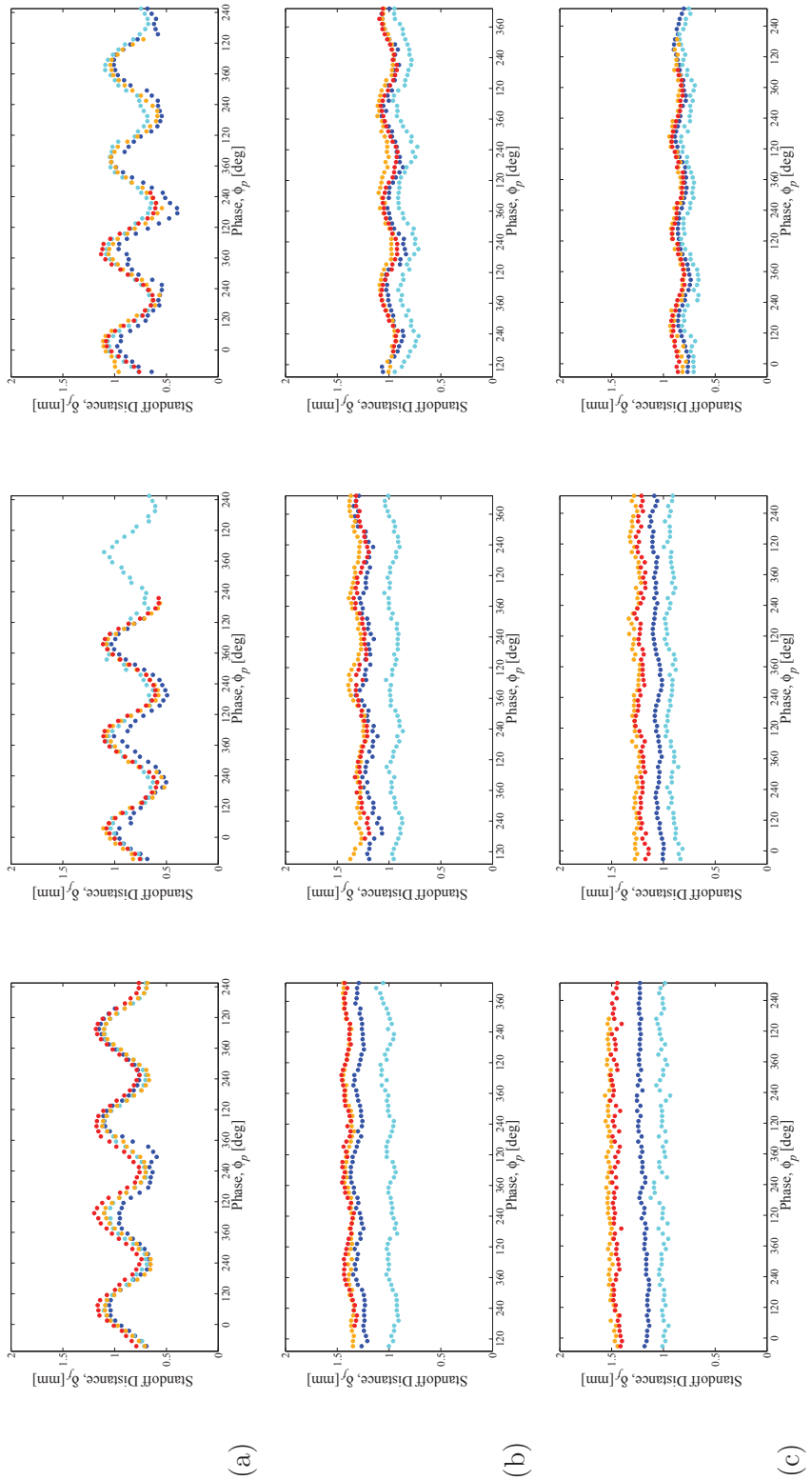

3.16: Horizontal flame standoff distance plotted versus the acoustic pressure phase. All fuels and acoustic frequencies are shown for three select waveguide locations. (rows: (a) $f_a = 332$ Hz (b) $f_a = 898$ Hz (c) $f_a = 1500$ Hz; columns: (left) $x = -6$ cm (middle) $x = -4$ cm (right) $x = -2$ cm; fuels: (●) ethanol (●) methanol (●) FT (●) JP-8/FT blend).

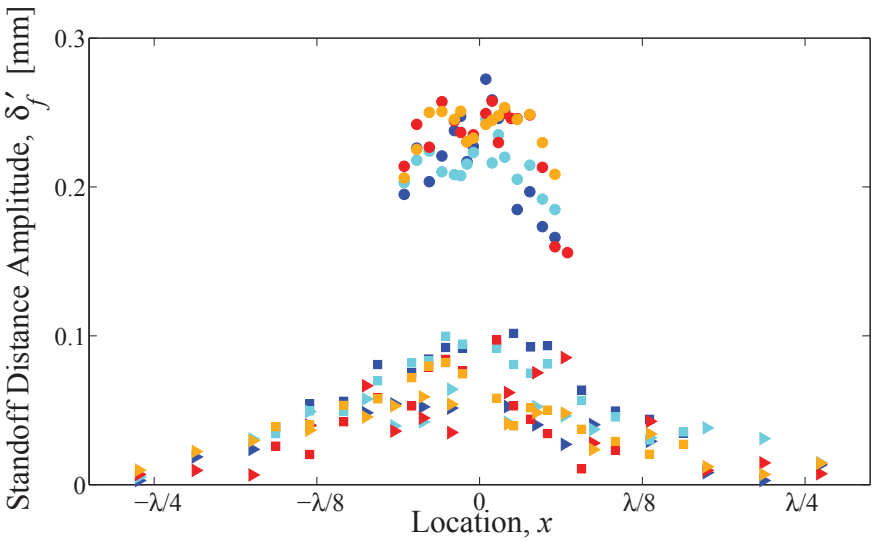

3.17: Standoff distance oscillation amplitude plotted versus waveguide location. (fuels: (●) ethanol (●) methanol (●) FT (●) JP-8/FT blend; frequencies: (●) $f_a = 332$ Hz (■) $f_a = 898$ Hz (▶) $f_a = 1500$ Hz).

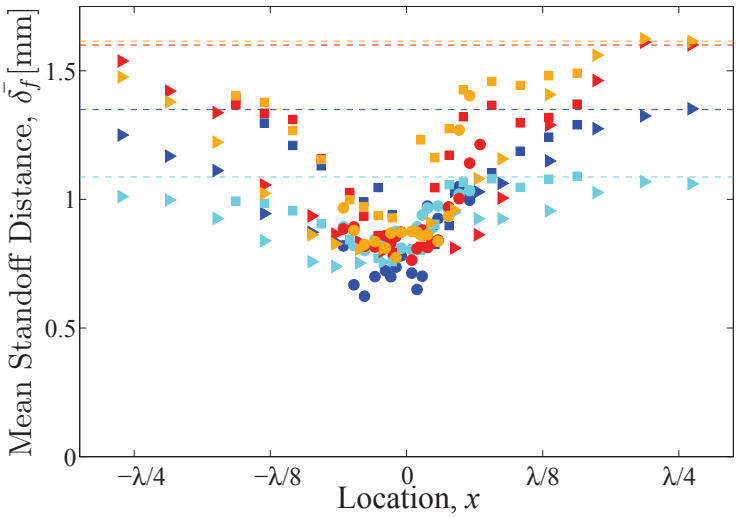

3.18: Time-averaged standoff distance plotted versus waveguide location. (fuels: (●) ethanol (●) methanol (●) FT (●) JP-8/FT blend; frequencies: (●) $f_a = 332$ Hz (■) $f_a = 898$ Hz (▶) $f_a = 1500$ Hz).

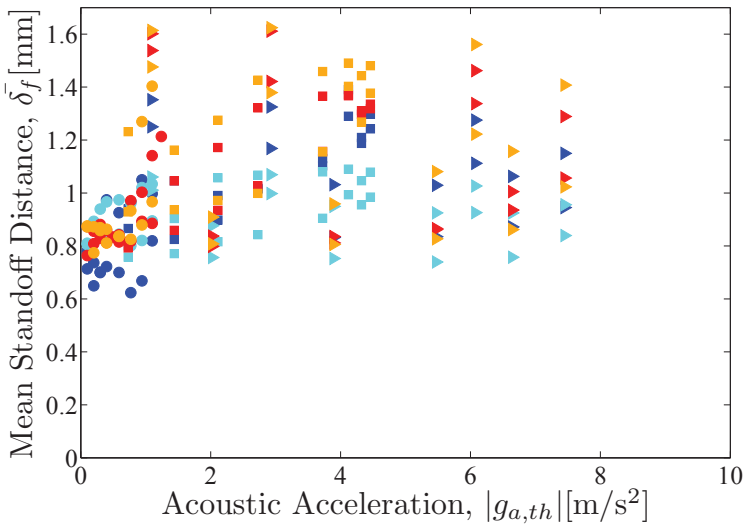

3.19: Time-averaged standoff distance plotted versus theoretcal acoustic acceleration. (fuels: (●) ethanol (●) methanol (●) FT (●) JP-8/FT blend; frequencies: (●) $f_a = 332$ Hz (■) $f_a = 898$ Hz (▶) $f_a = 1500$ Hz).

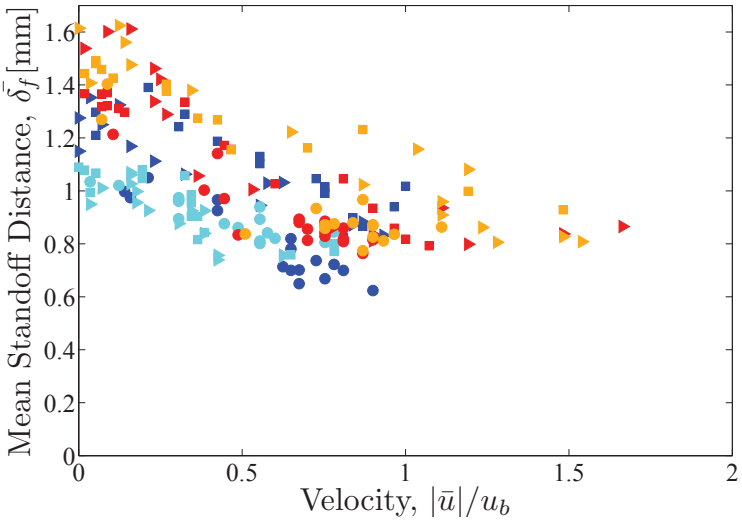

3.20: Time-averaged standoff distance plotted versus nondimensional horizontal velocity calculated using eqn. (3.2). (fuels: (●) ethanol (●) methanol (●) FT (●) JP-8/FT blend; frequencies: (●) $f_a = 332$ Hz (■) $f_a = 898$ Hz (▶) $f_a = 1500$ Hz).

CHAPTER 4

Experimental Facility and Methods - Shear-Coaxial Jets

To best describe the newly-constructed experimental facility used for the study on shear-coaxial jets at high pressures, the nonreactive apparatus used for previous super-critical jet experiments at AFRL must be mentioned. The two chambers lie on opposite sides of a single test cell, and in fact, the reactive chamber adopted many features from the existing nonreactive chamber in order to utilize experience gained from extensive nonreactive testing over many years. These features include the separation of inner and outer chamber volumes, heat exchangers to control propellant temperature, and generating sound using acoustic horns as waveguides. Unlike the nonreactive facility, the reactive facility must address the hazards associated with high pressure combustion of cryogenic oxygen and hydrogen, which requires remote control and sensing of the apparatus. The data acquisition system monitors over 200 sensors and the control system operates over 60 control devices. Thus, the complete system rivals the complexity of a rocket engine test stand, and navigating the intricacies of the entire facility is outside the scope of this chapter. To describe the complete capabilities of the facility though, parametric maps are provided which reach well beyond the experimental conditions explored in chapter 5.

4.1 High Pressure Chamber and Fluid Delivery Systems

4.1.1 Chamber

Similar to the previously existing apparatus used in nonreactive AFRL work [23, 75, 104], the chamber is designed as a chamber within a chamber. The inner chamber creates a near ideal environment for one-dimensional acoustic wave resonance, but is not sealed from the surrounding volume. This surrounding volume is the outer chamber, which has the structural integrity to withstand operating pressures of 1500 psi (10.34 MPa). Thick walls and windows are not necessary for the inner chamber, allowing more freedom when placing instrumentation and integrating new injector designs. A CAD rendering of the chamber assembly is shown in Fig. 4.1.

The outer chamber is fabricated from a forged naval brass alloy and has an octagon shape to offer optical access from multiple views. The current configuration contains six windows in the outer chamber wall, which includes large sapphire windows in the front and rear walls and four smaller quartz windows located at each corner. Large openings in the two remaining chamber side walls (left and right) are used for acoustic excitation sources. The injector assembly and exhaust port are located at the top and bottom of the outer chamber, respectively, creating downward propellant flows which exit the outer chamber through a cylindrical exhaust manifold. The exhaust manifold serves as a dilution and cooling point for the combustion products, and the resulting mixture exits the pressurized volume though a variable diameter exhaust orifice which is set to 4.8 mm, and is the chamber's only exhaust path.

4.1.2 Propellant Systems

To properly compose propellant density and velocity ratios, the oxygen and hydrogen feed systems must control the pressure, temperature, and flow rate of each. In this con-

text, the differential pressure between the injector exit and the chamber is assumed to be small, and the propellant pressure is simply taken as the chamber pressure. Temperature and flow rate though, are actively controlled upstream of the injector.

4.1.2.1 Propellant Flow Rate

Propellants are pressure fed by high pressure tanks located outside of the experimental cell, and flow rate is controlled by a remote needle valve for each propellant at ambient temperature. The needle valve often acts as a sonic nozzle, whereby flow rate remains constant although small changes in the downstream pressure occur, e.g. a rise in chamber pressure following ignition. To gather reliable propellant flow rates a Porter 123 series thermal mass flow meter is used in both the inner and outer jet systems, allowing maximum flow rates of 0.71 g/s, 2.02 g/s, 9.90 g/s, and 10.79 g/s for hydrogen, helium, nitrogen, and oxygen, respectively. Unique calibration data for each gas species is used when converting voltage output to mass flow rate for hydrogen, nitrogen, and oxygen, while helium mass flow rates are calculated using conversion factors published by Porter. These propellant flow rates, albeit low, create a flame similar to that of an O_2-H_2 LRE environment when used in conjunction with a sub-scale injector (see section 4.1.2.3) and considerable gaseous nitrogen flow to produce high chamber pressures (see section 4.1.2.4).

4.1.2.2 Heat Exchangers

Concerning temperature, LRE propellant tanks often hold fuel and oxidizer as a liquid, storing large masses of propellants within small cryogenic tanks. This is the case for many sub-scale test facilities as well [8, 24], and appropriate plumbing insulation allows propellants to be injected at temperatures only slightly above storage temperatures. For example, the BKH combustor maintains low hydrogen temperatures by submerging the

hydrogen supply lines in a liquid nitrogen bath between the liquid hydrogen tank and the test article [24]. Instead, this facility relies on ambient temperature propellant tanks storing gaseous oxygen and hydrogen at pressures exceeding 2000 psi (13.8 MPa). Thus, downstream of the flow meters, hydrogen and oxygen pass through separate cryogenic heat exchangers which cool propellants to the desired temperature.

Both heat exchangers operate under similar principles where propellant passes through a coiled tube which is cooled by liquid nitrogen. Liquid nitrogen is supplied from a 1500 gallon (5680 L) vacuum jacketed vessel pressurized to 90 psig (0.6 MPa). Approximately 9 m of vacuum jacketed tubing transfers liquid nitrogen from the vessel to the experimental cell, where the supply is split to deliver coolant to each individual heat exchanger. With this arrangement, the temperature of the process fluid is controlled by individually regulating liquid nitrogen flow rates through each system with separate control valves. A detailed drawing of the components and instrumentation of the heat exchangers can be found in the complete piping and instrumentation diagram in appendix A.

For the oxygen heat exchanger, which was designed and constructed by Sierra Lobo Inc., 2.82 m of inconel tubing is coiled on a vertical axis near the perimeter of an aluminum casting to carry process fluid. The casting also contains approximately 2 m of coiled tubing in the center of the casting for liquid nitrogen flow. In this way, heat energy from room temperature process gas enters the outer perimeter of the casting and transmits heat inward via conduction, where liquid nitrogen flow continually removes energy via convection. A vacuum jacket surrounds the assembly and is maintained at 10-100 mTorr. In its simplest form, this design can result in inaccurate control of fluid temperature, because liquid nitrogen flow rate control may be too coarse to obtain the desired process fluid temperature. For a test matrix in which propellant density ratio control is imperative, oxygen temperatures near the saturation point require accurate control to avoid large changes in density, caused by a large $\frac{\partial \rho}{\partial T}$. Inaccurate oxygen

temperatures also influence heat transfer phenomena in the flame region where propellant temperatures, as well as other thermodynamic variables such as chamber pressure, will engender a specific flame location and temperature.

As a direct result of these factors, the oxygen heat exchanger contains additional features to improve temperature control. First, a second coolant control valve is installed in parallel with the larger main control valve such that initial liquid nitrogen flow rates are set using the main control valve. Then, fine adjustments in liquid nitrogen flow rate are made with the small control valve as the process fluid outlet temperature approaches the target temperature. The flow capacity rating C_v is 2.0 for the main control valve and 0.075 for the small control valve. Second, electric heaters are mounted to the aluminum casting to offer additional energy in the event that the casting is chilled below the target temperature. The heating system consists of six heater elements individually controlled by a closed-loop control system written in LabVIEW. In this way, coolant control valves are set to slightly sub-cool the casting, reducing the process gas to a temperature 2 to 5 K below the target temperature. The heater power is then manually applied and automatically adjusted to hold the process fluid outlet temperature equal to the target temperature with an accuracy of ± 1 K. To achieve optimal accuracy, the heaters are used unless the target temperature is equal to the system's minimum possible temperature. Only four of the six heaters were used for the results shown in this study. A three-dimensional rendering of the oxygen heat exchanger is shown in Fig. 4.2.

The hydrogen heat exchanger, on the other hand, lacks many of these additional features. As shown in Fig. 4.3, the hydrogen heat exchanger consists of 2.5 m of process fluid tubing directly submerged in a liquid nitrogen bath. In this configuration, the flow direction of coolant is opposite that of the process fluid. This arrangement ensures a minimum process fluid temperature at the outlet region by encompassing said region with unheated coolant. Liquid nitrogen flow is regulated using a single control valve

downstream of the heat exchanger, and the position of this valve is the only variable directly controlled by the user for achieving the desired process fluid temperature. Process fluid outlet temperature then, is actively controlled by the user rather than employing an automatic control loop. Similar to the oxygen heat exchanger, the nitrogen bath is insulated by a vacuum jacket.

Although the propellant heat exchangers offer variable control of temperature, a cooling process is required to condition plumbing hardware prior to achieving a desired, stable temperature. The temperature conditioning process requires approximately 30 minutes and is performed using nitrogen not only as the coolant, but also as the process fluid in order to preserve propellant. When a stable temperature and flow rate are reached, remote valves are used to switch from the nitrogen simulant supply to the propellant supply. Due to differences in viscosity, density, and heat conduction constants, alternating between nitrogen simulant flow and propellant flow causes significant changes in mass flow rate and temperature. A time series plot of the transition from nitrogen simulant to propellant is shown for oxygen and hydrogen in Fig. 4.4. The difference between the process fluid temperature at the injector before and after the species transition was found to be highly dependent on both chamber pressure and mass flow rate.

To characterize the capability of each heat exchanger, the minimum achievable temperature was measured for a range of chamber pressures. This was done by utilizing high liquid nitrogen flow rates over a long period of time to cool the hardware of each system. Thus, the injector flow temperature for each process fluid was minimized, representing a limiting temperature condition for the facility. The results from this effort are shown in Fig. 4.5 for oxygen, where minimum temperature is shown to have a small dependence on chamber pressure. An oxygen density contour is the background of Fig. 4.5, showing that a liquid phase is achievable for $T_{ij} < T_{sat,ox}$ and $p_c < p_{crit,ox}$ and supercritical fluid

for $p_c > p_{crit,Ox}$. Temperature is shown to have a negative correlation with mass flow rate. Similar measurements were made with the hydrogen propellant system, but to perform these tests safely, helium was used as a surrogate. Minimum helium temperatures are shown in Fig. 4.6, superimposed on a hydrogen density contour map.

To quantify the heat exchangers capability for nonreactive experiments, minimum temperatures for nitrogen are plotted for both the inner and outer jets in Fig. 4.7. A nitrogen density contour is also shown. Reviewing temperature limitations for the outer and inner jets, one observes that two-phase flows can be realized for both reactive (LO_x-GH_2) and nonreactive (LN_2-GN_2) tests. Single-phase conditions can also be achieved with subcritical gas-gas jets where $T_{ij} > T_{sat,ox}$ for reactive tests and $T_{ij} > T_{sat,N_2}$ for nonreactive tests. If desired, liquid-liquid conditions can also be achieved for nonreactive tests where $T_{ij} < T_{sat,N_2}$ and $T_{oj} < T_{sat,N_2}$. Although heat exchanger performance is also dependent on process fluid mass flow rate, which is not characterized in Figs. 4.7, these results are a valuable tool for the design of experiments with known facility limitations.

The significance of propellant temperature limits is best understood by mapping the possible values for densitiy ratio S. For oxygen-hydrogen flows, Fig. 4.8 shows the range of achievable values for S as a function of chamber pressure. For $p_c < p_{crit,ox}$, single-phase flows allow for density ratios as high as 0.1. Two-phase LO_x-GH_2 flows though, restrict density ratios to a small range of values less than 0.01, which is comparable to a oxygen-hydrogen engine with regenerative nozzle cooling. Supercritical oxygen flows are characterized by a region with pressures greater than 5.04 MPa (731 psia), where oxygen is a supercritical fluid and a distinct phase change does not exist for oxygen.

4.1.2.3 Injector

The injector consists of a single shear-coaxial element designed for hydrogen flow in the annulus and oxygen flow in the center. In terms of total cross-sectional area, the injector

is $1/10^{th}$ scale of the J-2 engine, for example. An injector of this size is challenging to manufacture, but is used here to maintain jet velocities and Reynolds numbers with orders of magnitude similar to an actual LRE while maintaining much smaller propellant mass flow rates. This technique was also employed in the design of shear-coaxial injectors for the Common Research Combustor of CNRS and DLR. The cross-sectional dimensions of the injector are shown in Fig. 4.9, and dimensions for all recent AFRL injectors are shown in Table 4.1 for comparison. In comparison with previous AFRL shear-coaxial injectors, the current injector has a small area ratio, $\frac{A_{oj}}{A_{ij}} = 1.68$. The inner post thickness to inner diameter ratio $\frac{t}{D_1}$ has a value of 0.27, which prevents the inner shear layer from behaving purely as that of co-flowing fluids. Instead, a recirculation zone is expected to form at the exit of the injector between the outer and inner jets. A CAD image of the injector and top flange assembly is shown in Fig. 4.10.

A comparison of Re_{ij} and Re_{oj} for similar research combustors is shown in Fig. 4.11, with operating points of actual oxygen-hydrogen LREs. Operating spaces of four other combustion instability research facilities are shown, including the BKH combustor of DLR, Germany, the Common Research Combustor (CRC) of CNRS, France and DLR, Germany, the Multi-Injector Combustor (MIC) of ONERA and CNRS, France, and the Cryogenic Combustion Laboratory (CCL) of Pennsylvania State University, USA. These facilities were specifically chosen for comparison because detailed flow conditions for oxygen-hydrogen stability experiments for shear-coaxial jets are available, but one must be cognizant that apparatuses such as these often see multiple modifications in only a few years time. As a result, Fig. 4.11 should be considered only a general guide for comparison, because Re values for the facility concerned here, as well as the others in Fig. 4.11, can be revised with simple hardware modifications.

For all conditions shown in Fig. 4.11, two-phase flows lie in the membrane type breakup regime or the fibre-type breakup regime, characteristic of high Re and high

We flows as discussed in section 1.3.1.2. Reynolds numbers of this magnitude are often considered to create fully-developed turbulent conditions at the injector exit. Fully-developed flow at the injector exit is particularly advantageous for establishing a known and canonical velocity profile, imparting momentum boundary conditions for shear layer studies and providing a boundary layer thickness approximately equal to half of the diameter for a range of mean velocities. Rather than matching the design of a particular LRE injector where the fully-developed turbulence assumption may or may not be valid, the current injector design places priority on ensuring fully-developed turbulent flow for the entire effective range of Re values to provide confidence in experimental boundary conditions. A minimum injector length is required to make this assumption valid. According to the development length criterion of Munson *et al.* [147] the minimum nondimensional development length required for fully-developed turbulent flow is

$$\frac{L}{D} \geq 4.4 Re^{\frac{1}{6}} \tag{4.1}$$

where D is taken as D_1 for the inner jet and $D_3 - D_2$ for the outer jet. Using the complete range of values for Re_{ij} and Re_{oj} from Fig. 4.11, $\frac{L}{D} > 4.4 Re^{\frac{1}{6}}$ for all conditions and the fully-developed turbulence assumption is valid. One particular flow condition is represented by the diagram in Fig. 4.12, where the $1/7^{th}$ power law [148] is used to plot fully-developed velocity profiles for the inner and outer jets.

The injector design chosen here also deviates from popular LRE injector designs, because the inner jet lacks a recessed exit plane. A recessed inner post, as shown in Fig. 1.6b and 1.6c, is commonly used in LREs in order to enhance mixing in the initial merging zone via an increased transverse velocity of either the inner jet, outer jet, or both. The J-2 and SSME engines both used recessed inner posts for LO_x-GH_2 combustion, for example [45]. Thus, both the injector length and the exit geometry deviate from practical designs in order to create more well-known boundary conditions at the injector exit. This design also serves as a baseline geometry that could be used

for comparison with recessed injectors in the future.

A parametric map of the facility can be obtained by combining the density ranges discussed above with injector dimensions and propellant mass flow rates, but first a range of propellant mixture ratios must be defined to constrain the operating space. For oxygen-hydrogen mixtures, the stoichiometric mixture ratio is 8 and actual LREs operate fuel-rich in the range $4.5 < MR < 7.2$. In terms of the fuel-oxidizer equivalence ratio $\phi_{f/o} = \frac{\dot{m}_f/\dot{m}_o}{\left(\dot{m}_f/\dot{m}_o\right)_{st}}$, this range corresponds to $1.11 < \phi_{f/o} < 1.78$. A minimum MR of 2 is used here to capture the lower limit of mixture ratios for a practical specific impulse [149]. A maximum of 8 is taken to include stoichiometric conditions. Using a wide range of mixture ratios offers an expanded range of momentum flux ratios without changing the injector element, as shown in a parametric map of J versus MR in Fig. 4.13.

4.1.2.4 Exhaust

Rather than passing through a single exhaust nozzle, the chambers' exhaust path is staged. Upon exiting the inner chamber through a rectangular hole, the combustion products, which are mixed with nitrogen from the inner chamber, will enter a small manifold. This exhaust manifold serves as a dilution and cooling volume. The exhaust manifold is separated from the outer chamber by a cylindrical wall. Throughout the wall, 3.18 mm diameter holes allow gaseous nitrogen from the outer chamber to flow into the exhaust manifold. Thus, the combustion products are initially cooled and diluted by nitrogen present in the inner chamber and then experience further cooling and dilution due to additional nitrogen in the exhaust manifold.

Consequently, a supplementary flow system introduces gaseous nitrogen into the outer chamber to provide a positive pressure differential between the outer chamber and the exhaust manifold. In turn, this produces a continuous flow of exhaust dilutant into the product mixture. The ensuing nitrogen-rich mixture then exits the exhaust manifold

through a tube with a 22.1 mm inner diameter prior to being choked through a 4.8 mm diameter restricting orifice. Without altering the orifice size, the chamber pressure can be controlled independent of propellant flow rate by adjusting one of several nitrogen flow rates, and the orifice size was chosen to create the desired p_c for a given nitrogen mass flow rate. Assuming that inner chamber nitrogen flows, to be described below, are set according to the experimental needs of the scientifically sensitive region near the flame, the supplementary outer chamber nitrogen flow rate is appropriately used for adjusting the mean chamber pressure. Therefore, this supplementary nitrogen system is termed the chamber pressurization flow system although it also serves as an exhaust dilutant and coolant.

4.2 Inner Chamber

4.2.1 Inner Chamber Dimensions and Instrumentation

The inner chamber is a rectangular volume open to transverse acoustic excitation from circular acoustic drivers on the left and right. The inner chamber depth is 20.32 mm and the height is 36.07 mm, making room for sub-scale injectors only. The width is much larger, reaching 0.82 m from the left acoustic source to the right acoustic source, making the inner chamber volume large in comparison to the injector. One should also note that although the inner chamber cross-sectional area is 20.32 mm $\times$ 36.07 mm near the injector, the far left and far right areas of the inner chamber expand to a large circular area in order to house each acoustic driver. The waveguide design which is used to smoothly transition from a rectangular shape to a circular shape will be described in section 4.3.2. Two quartz inner chamber windows separate the inner chamber from the outer chamber, and because these windows need not withstand a large pressure differential, nine small holes are located throughout the rear inner window at an axial distance

of $12D_1$ from the injector exit, but at various spanwise locations. Three of these nine holes are occupied by dynamic pressure transducers; one of which is spanwise centered in the rear window ($p_{dyn,2}$), while two others are located 25.4 mm to the left and right of the center pressure transducer ($p_{dyn,1}$ and $p_{dyn,3}$). Thermocouples are located 6.35 mm to the left and right of each pressure transducer, totaling six thermocouples measuring temperature at the inside surface of the rear window. Hence, these instruments diagnose the region near the flame at $x = 12D_1$, and one final thermocouple is suspended in the center of the inner chamber exit to measure the flame temperature at $x = 30D_1$. By placing a thermocouple at $x = 30D_1$, the temperature near the end of the flame is measured without disturbing the region captured by high-speed imaging.

4.2.2 Inner Chamber Nitrogen Flows

At the top of the inner chamber, a nitrogen plenum provides two flows parallel to propellant flows. First, window cooling flows enter the inner chamber through slotted holes located immediately inside the top edge of the inner windows. Second, a propellant co-flow system provides gaseous nitrogen to the region surrounding the flame by entering the chamber through dozens of 0.48 mm diameter holes in a circular pattern around the coaxial injector. This co-flow system decreases coaxial jet recirculation in the inner chamber, and will be referred to as the flow straightener flow. The nitrogen used for both the window cooling and flow straightener systems is supplied at ambient temperature.

4.3 Waveguide Design and Characterization

The acoustic system design meets several key requirements. Most importantly, acoustic fluctuations in the transverse direction are maximized and fluctuations in the longitudinal and depth-wise directions are minimized to create approximately one-dimensional

waves. Second, it is possible to create acoustic pressure amplitudes with the same order of magnitude as an actual LRE combustion instability while still maintaining the ability to control and sustain low amplitudes, e.g. $p' < 0.01 p_c$. Last, the acoustic system allows for reliable establishment of standing waveforms with pressure nodes or velocity nodes located at the coaxial jet.

4.3.1 Acoustic Drivers

Similar to both the droplet combustion apparatus and the aforementioned nonreactive facility at AFRL, twin acoustic drivers are used in concordance with the general principles of a Kundt's tube. However, in the case of the system described here and the nonreactive facility at AFRL, drivers with a total area more than twice that of the inner chamber's cross sectional area are used. This feature establishes pressure amplitudes much higher than a traditional Kundt's tube when the waveguide shape is designed as a sound amplifying horn, which will be described in the following section. High acoustic pressure amplitudes are also enabled by using circular piezoelectric sirens as acoustic sources. The sirens are made entirely of aluminum, and the contruction of which is described further in appendix A.1. The sirens enable much higher amplitudes than classical loudspeakers, but piezoelectric sirens have one drawback to mention here.

As a result of their geometric form, the piezoelectric sirens exhibit a few resonant frequencies. Within the narrow bands located at each resonant frequency, high oscillation amplitudes occur in the siren's cone, and high-amplitude coherent sound is produced. Operating the sirens outside of these narrow bands of efficiency results in much lower amplitudes.

To quantify this limitation, sound pressure measurements were made with the sirens mounted outside of the chamber. In this manner, chamber resonance is avoided by allowing waves to propagate into an open room. Each siren was mounted firmly using

the same technique which is used when mounting the siren inside the chamber, and a dynamic pressure transducer (Kulite model XCE-093-50D) was placed 5 cm from the siren's diaphragm. A frequency sweep over a duration of 15 s was used to ramp the oscillation frequency of the siren from 100 Hz to 6000 Hz while acquiring data at a rate of 80 kHz. Results are shown in Fig. 4.14, revealing three frequency bands of peak performance for both the left and right sirens. A wideband at relatively low frequency occurs at 1638-1915 Hz for the left siren and 1620-1860 Hz for the right siren. Then, two distinct peaks occur at 3076 and 5200 Hz for the left siren, and 3083 Hz and 5100 Hz for the right siren. These resonant frequencies will indeed limit the usable range of chamber acoustic frequencies, but this factor must be considered hand in hand with chamber resonance to fully characterize the acoustic system.

4.3.2 Waveguide

As described above, the sirens have a circular shape while the inner chamber is rectangular. Thus, the waveguide's shape must provide a smooth transition from a 11.24 cm diameter circle to a 2.03 cm $\times$ 3.61 cm rectangular cross-section. To minimize two-dimensional and three-dimensional waves, the circle-to-rectangle transition must be void of abrupt area changes and sharp corners. This requirement, combined with material stress from high chamber pressures, make design and fabrication challenging.

The area reduction from circle to rectangle follows a quasi-one-dimensional model for sound propagation in a rigid-walled duct, which is derived beginning with the acoustic wave equation,

$$\nabla^2 p - \frac{1}{c^2}\frac{\partial^2 p}{\partial t^2} = 0, \tag{4.2}$$

which is then integrated for acoustic pressure p for a three-dimensional segment of the duct shown in Fig. 4.15. In agreement with the coaxial jet diagram in Fig. 1.13, x is the jet streamwise direction, y is the transverse direction, and z is the depthwise direction.

Thus, a perfectly shaped waveguide will prevent acoustic wave propagation in the x and z directions and concentrate 100% of the energy from each siren to produce waves in the y direction ($\frac{\partial^2 u}{\partial x^2} = \frac{\partial^2 u}{\partial z^2} = 0$). Gauss's theorem is then used to convert the volume integral of $\nabla^2 p$ to a surface integral, i.e.

$$\iiint_V (\nabla^2 p) dV = \oiint_S (\nabla p \cdot \hat{n}) dS. \tag{4.3}$$

Then, apply the boundary condition that $\nabla p \cdot \hat{n} = 0$ at the inner wall of the waveguide, divide by Δy, and take the limit as $\Delta y \to 0$ ($\Delta y = \partial y$). One obtains

$$\frac{\partial}{\partial y} \iint_A \frac{\partial p}{\partial y} dA - \frac{1}{c^2} \frac{\partial^2}{\partial t^2} \iint_A p dA = 0. \tag{4.4}$$

With the exception of a thin acoustic boundary layer near the inner wall of the waveguide, p is uniform over any given cross section, i.e. $\frac{\partial p}{\partial x} = \frac{\partial p}{\partial z} = 0$. The equation above then reduces to

$$\frac{1}{A} \frac{\partial}{\partial y} \left(A \frac{\partial p}{\partial y} \right) - \frac{1}{c^2} \frac{\partial^2 p}{\partial t^2} = 0, \tag{4.5}$$

which is known as Webster's horn equation, after Arthur G. Webster [150]. Following Pierce [151], Webster's horn equation can be simplified as

$$\left\{ \frac{\partial^2}{\partial y^2} + \frac{1}{4A^2} \left[(A')^2 - 2AA'' \right] - \frac{1}{c^2} \frac{\partial^2}{\partial t^2} \right\} A^{\frac{1}{2}} p = 0. \tag{4.6}$$

This is a nonlinear ordinary differential equation with respect to A which can be used to describe the optimal shape of an expanding or constricting waveguide as shown in Fig. 4.15. The general solution is

$$A^{\frac{1}{2}} = A_{th}^{\frac{1}{2}} (\cosh my + T \sinh my), \tag{4.7}$$

where $A_{th} = A(y = 0)$ and $A_{th}^{\frac{1}{2}} Tm = \frac{\partial (A^{\frac{1}{2}})}{\partial y} (y = 0)$. The specific solution is found for the catenoidal horn shape for $T = 0$ [151]:

$$A = A_{th} (\cosh my)^2. \tag{4.8}$$

The throat area A_{th} and flare constant m are unique constants which are found according to the boundary conditions of the waveguide. First, the throat area is set equal to the cross-sectional area of the inner chamber,

$$A_{th} = (\Delta x)\,(\Delta z) = (36.1\text{ cm})\,(2.03\text{ cm}) = 7.33\text{ cm}^2, \tag{4.9}$$

and finally, constraining the solution for a specific waveguide length L and siren area gives a value of 0.0910 cm^{-1} for m. Thus, the completed solution for a catenoidal horn area distribution is

$$A(y) = 7.33\cosh^2(.091y)\,. \tag{4.10}$$

This formula for $A = f(y)$ was used to calculate an appropriate transverse area distribution in square centimeters for the acoustic waveguides to the left and right of the chamber. The area distribution according to equation 4.10 is plotted in Fig. 4.16 with the inner chamber included in between the left and right waveguides. Thus, Fig. 4.16 represents the area distribution of the completed chamber.

However, Webster's horn equation is limited when applied to waveguides in this way. Effective use of waveguides as sound amplifiers requires an acoustic frequency above a minimum operating frequency, or cutoff frequency f_c, which is a function of the speed of sound c and the flare constant m. According to Pierce [151],

$$f_c = \frac{mc}{2\pi}, \tag{4.11}$$

which can be used to estimate an appropriate minimum acoustic frequency. This cutoff frequency is less important for horns with $mL \leq 1$ [151], but mL=3.3 for the waveguides used here. As an example, nitrogen at T=300 K gives f_c=511.5 Hz and f_c=552.0 Hz for p_c=0 psig and p_c=1500 psig (10.34 MPa), respectively. Although temperature variations may also alter the speed of sound, and large temperature variations exist near the jet, the temperature of gas in the waveguides was found to have a negligible effect on f_c. Therefore, the cutoff frequency criterion will be adhered to for the experiments in this study.

4.3.3 Resonant Frequencies

4.3.3.1 Acoustic Forcing Strategy and Analytical Consideration

Paired with the resonant modes of the acoustic drivers, the resonant modes of the chamber cavity are imperative in determining a useable set of frequencies for experiments involving high amplitude acoustics. A straightforward calculation predicting several transverse chamber modes is described below. Following theoretical discussion, experimental resonant frequencies are presented for a range of chamber pressures.

Akin to the cavity resonance analysis for the cylindrical waveguide discussed in section 2.1, the resonant frequencies of the more complex chamber geometry addressed here can be predicted by eqn. 2.1, which is listed here for convenience.

$$L = \frac{n}{2}\lambda = \frac{n}{2}(\frac{c}{f_F}) \tag{4.12}$$

Again, regardless of the value of f_F and n, speakers operated out-of-phase ($\Delta\phi = 180°$) will create a PN at the center of the chamber and speakers operated in-phase ($\Delta\phi = 0°$) will create a PAN at the center. To achieve maximum acoustic pressure and velocity amplitudes, f_F must take on a value in accordance with 2.1 where n is a positive integer. But, additional phenomena cause increased error when applying the following assumptions. First, the area changes within each waveguide are neglected when applying one-dimensional theory. Second, the speed of sound c is not constant, but rather is altered by chamber pressure and temperature. Thus, as a result of repeated cooling and firing cycles near the injector, the speed of sound for each experimental test should be considered unique. Temperature, for example, is a minimum at the center of the chamber where cryogenic flows cool the region after long periods of temperature conditioning prior to ignition. During this period, the chamber's maximum temperature is located at ends of each respective waveguide. After ignition though, a sharp temperature rise occurs in the flame region and a small pressure rise occurs due to combustion. Speed of

sound is a function of both time and space as a result of these variations in temperature and pressure.

A second phenomenon which increases error when applying the assumptions of eqn. 2.1 is a result of three-dimensional geometry variations in the waveguides. Although the shape of the internal waveguide walls was carefully designed according to the derivations in Section 4.3.2, resonant modes may occur in three different dimensions. These three are the transverse direction y spanning from the left waveguide to the right waveguide, the secondary transverse direction z spanning from the front window of the inner chamber to the rear window of the inner chamber, and the longitudinal direction x spanning from the upper wall of the inner chamber to the exhaust orifice. Each of these three mode types will be addressed differently.

The transverse modes occurring in the y direction navigate only smooth area changes within the waveguides. Thus, the transverse mode, or "T" mode, will be described using the approximate calculations of eqn. 2.1 using a value of c for pure nitrogen at the mean chamber pressure p_c and the mean chamber temperature T_c. By design, a transverse span of $L = 0.82$ m offers multiple frequencies less than 6000 Hz at which transverse resonance may occur. This mode type will be the focus of all acoustic forcing results presented in this study.

The secondary transverse modes occurring in the z direction will resonate within a very small span created by the depth of the inner chamber. This geometric boundary, created by the front and rear inner windows, is only 20.32 mm in length. Consequently, only very high frequencies are capable of producing resonant conditions in the z direction. A speed of sound of c=344 m/s and n=1, for example, will result in an acoustic resonant frequency of 8465 Hz. This frequency is far greater than the useable range of the piezoelectric sirens. Thus, secondary acoustic modes in the z direction are assumed to be negligible.

The longitudinal modes occurring in the x direction maneuver a series of abrupt area changes between the inner chamber and the exhaust tube. The inner chamber's exit is a rectangular exhaust gap which connects the rectangular inner chamber with the exhaust manifold. The exhaust manifold introduces additional gaseous nitrogen into the exhaust mixture, cooling the mixture before it exits the outer chamber through a 22.1 mm diameter hole, and then the 4.8 mm exhaust orifice. Thus, three interconnected volumes create a longitudinal space in which "L" modes may exist, but cannot be accurately predicted with brief analytical techniques due to two substantial area changes joining the inner chamber, exhaust manifold, and exhaust tube. For a three-dimensional computational analysis of chamber acoustics, ANSYS and COMSOL have been used to successfully resolve the influence of complex geometry and speed of sound variations [18, 24, 131]. Such an analysis is outside the scope of this work and will be considered in future analysis.

4.3.3.2 Experimental Characterization

Using a single dynamic pressure transducer within the inner chamber, acoustically resonant conditions can be identified for both PAN and PN conditions at the center of the chamber. This type of experimental characterization conveys the final result of merging acoustic resonance attributed to each siren with acoustic resonance attributed to chamber geometry. Due to the sirens' ability to produce high pressure amplitudes for only three limited frequency bands, it is expected that p' measurements will be high for a limited number of transverse chamber modes. Other transverse modes may be resonant, but acoustic chamber modes far from the effective frequency bands of the sirens will create low, unusable amplitudes. To demonstrate this balance, a frequency sweep was performed for PAN conditions.

To experimentally determine resonant PAN conditions, p' was measured at the center

of the chamber using a pressure transducer located in the center of the rear inner window, a distance $12D_1$ below the injector. The pressure measured at this point is $p_{dyn,2}$. A PAN condition was produced at this location by operating the sirens in-phase, i.e. $\Delta\phi = 0°$. Over a time span of 20 s, the sirens were linearly swept from an acoustic frequency of 100 to 6000 Hz while sampling pressure at a rate of 40 kHz. This procedure was repeated for ten different mean chamber pressures from 100 to 1000 psia (6.9 MPa) while at room temperature.

To provide a comparative representation of PAN frequency sweep results, time series data are transformed into a periodogram power spectral density estimate using a Hamming window function. Fig. 4.17 includes the results from each chamber pressure set point, and also includes theoretical lines calculated using eqn. 2.1 for comparison. For $f < 1400$ Hz, amplitudes remain negligible regardless of chamber pressure due to the sirens' ineffective sound production in this range. The 1T and 2T modes cannot be identified. For 1400 Hz $< f <$ 4000 Hz, several modes can be identified throughout the sirens' effective frequency range. When comparing the performance of the left and right sirens in Fig. 4.14 with the theoretical transverse resonance values, it is clear that an additional factor must be engendering other peak frequencies shown in Fig. 4.17 for 1400 Hz $< f <$ 4000 Hz. The additional factor may be a result of chamber resonance unaccounted for by transverse resonance calculations, such as longitudinal resonance. Unexpected spectral results may also be manifested by imperfect siren operation. For example, although the phase relationship of each siren control channel is set to zero ($\Delta\phi = 0°$), deviations in $\Delta\phi$ can occur over wide variations in frequency. For $\Delta\phi \neq 0°$, perfect resonance cannot be achieved and the PAN deviates from the center of the chamber [135]. These deviations result from the uniqueness of each siren signal amplifier, amounting to a phase difference of several degrees between each amplifier. Variations in $\Delta\phi$ were not corrected during the frequency sweep represented in Fig. 4.17. In conclusion, although significant amplitudes can be achieved near the 3T, 4T,

5T, 6T, and 7T modes, the exact frequency of each mode cannot be determined as a result of unidentifiable frequency peaks, and thus, Fig. 4.17 alone is an imperfect indication of transverse standing waves. Using the acoustic forcing system requires standing wave verification for each individual experimental condition, and this procedure will be described in appendix A.1.

4.4 Nonreactive Jet Imaging

Jet flow visualization was the primary diagnostic tool for studying LN_2-GHe flow dynamics, provided by back-lit high-speed images. A variable power Newport model 66986 power supply controlled a 300 W Xe lamp, which emitted light in the near ultraviolet spectrum. This beam was projected through the rear window as a back-light source. Although the beam was not collimated, this back-lighting technique produced sufficient contrast at fluid interfaces. Differences in the refractive index of the jets and the surrounding medium provided the necessary distinction between the fluids of interest. The low temperature, liquid nitrogen inner jet appeared as a dark column of fluid as viewed by the high-speed camera placed on the opposite side of the light source. The less dense gaseous helium outer jet was also distinguishable from the heavier gaseous nitrogen surrounding the coaxial jet.

A Phantom v7.10 high-speed camera was used to visualize the fast dynamical processes inherent to an unforced coaxial jet flow as well as those present during high frequency acoustic forcing. A 200 mm Nikon MicroNikkor lens was used with a no. 1 close-up lens attachment, giving a spatial resolution of 30 μm per pixel. Image framing rates of 10 kHz were used in order to avoid aliasing up to 5 kHz, which is much greater than the highest forcing frequency used in this study, 2600 Hz. An external trigger from the facility control system was used to start recording the image frames, which were synchronized with all other data using the coordinated universal time (UTC) stamp

from an IRIG-B timecode generator.

4.5 Reduced Basis Methods

Reduced basis methods are growing in popularity as a computational procedure to reduce the complexity of flow systems exhibiting periodic, coherent structures. For computational fluid dynamicists, reduced basis methods have been used to provide inlet flow boundary conditions which capture important flow instabilities without representing all, and thus insignificant, modes in order to increase computational efficiency [152]. For experimentalists, reduced basis methods have been particularly useful image analysis tools. In a study by Arienti *et al.* [153] the shape and instability frequencies of a jet in crossflow were captured using just a few modes which contain the highest energy contribution. Where experimental systems pose installation challenges for direct probing and sensing instruments, which may cause unwanted flow disturbances, reduced basis methods extract spatial and temporal information from images alone. This study uses proper orthogonal decomposition (POD) to determine the spectral content of the most significant modes in a shear-coaxial jet, and uses the same set of results to describe the qualitative shape of these modes. Also, a brief comparison is made between POD and a second reduced basis method, dynamic mode decomposition (DMD).

4.5.1 Proper Orthogonal Decomposition

When used as an image analysis algorithm for flow instability, POD uses high-speed imaging results to reconstruct an approximate representation of a flow using proper orthogonal modes (POMs) which are ranked according to their pixel intensity variations relative to the time-average. This method has been used by Arienti *et al.* [153] and Arienti and Soteriou [154] to determine the dominant vortex shedding frequencies in

jets in crossflow, and Teshome *et al.* [30] have been the first researchers to apply POD to shear-coaxial jet instabilities. In Teshome *et al.* [30], the natural jet instability and the acoustically forced jet instability was identified by truncating the resulting set of POMs to the highest ranked POM conjugate pair with the goal of representing the jet with a single mode. The present study holds a similar approach, and this section serves to describe POD accordingly.

First, the pixel intensity values for a set of images can be represented in continuous form as

$$a(x,t) = \sum_{k=1}^{N} u_k(t) v_k(x), \tag{4.13}$$

where u_k are vectors of temporal amplitude coefficients, v_k are vectors of proper orthogonal modes, k is the mode number, and N is the number of modes. In order to implement this method, the pixel intensities are arranged into a single aggregate data array for all image frames, giving a a single spatial dimension having a length M equal to the total number of pixels in a single $m \times n$ image. Thus, $M = mn$. First, this is achieved by forming a row vector consisting of all pixel intensity values of each image frame. The row vector is formed in order of increasing pixel columns followed by increasing pixel rows, as shown in Fig. 4.18. Row vectors are then combined for a sequence of N image frames, resulting in the complete matrix $\mathbf{A}$ consisting of N rows by M columns of intensity values. Thus, $\mathbf{A}$ is an array of N sets of M pixel intensities in a single matrix, as shown in Fig. 4.19.

In order to isolate the periodic fluctuations of coherent structures, the intensity fluctuations should be considered rather than the mean. Thus, the time-average of each pixel intensity is subtracted from the mean to produce a matrix of intensity fluctuations $\widetilde{\mathbf{A}}$. That is,

$$\widetilde{\mathbf{A}}_{ij} = \mathbf{A}_{ij} - \frac{1}{N} \sum_{i} \mathbf{A}_{ij} \tag{4.14}$$

where $i = 1...N$, $j = 1...M$. Figure 4.20a shows a single image frame, and Fig. 4.20b

shows the corresponding time-averaged image for $N = 100$ frames. Since a single image contains more than 100,000 pixels and the number of images is ∼1000, then $\widetilde{\mathbf{A}}$ is a rectangular matrix where $N < M$. A singular value decomposition (SVD) can be readily computed for this non-square matrix as opposed to eigenvalue decomposition, which is an alternative to SVD for computing a POD solution, but requires $\widetilde{\mathbf{A}}$ to be a square matrix. According to SVD, $\widetilde{\mathbf{A}}$ can be represented with the form

$$\widetilde{\mathbf{A}} = \mathbf{U}\mathbf{\Sigma}\mathbf{V}^T \tag{4.15}$$

This decomposition is used within POD to divide the complete matrix into a matrix containing temporal information $\mathbf{U}$, a matrix containing spatial information $\mathbf{V}$, and a scaling matrix $\mathbf{\Sigma}$. The product of $\mathbf{U}$ and $\mathbf{\Sigma}$ is representative of u_k in eqn. 4.13, and $\mathbf{V}$ is the matrix form of v_k. After removing unused rows in $\mathbf{U}$ in an economic SVD scheme, $\mathbf{U}$ is an $N \times N$ orthogonal matrix taking the form

$$\mathbf{U} = \begin{bmatrix} u_{11} & u_{12} & & \\ u_{21} & u_{22} & & \\ & & \ddots & \\ & & & u_{NN} \end{bmatrix}, \tag{4.16}$$

$\mathbf{V}^T$ is an $M \times M$ orthogonal matrix taking the form

$$\mathbf{V}^T = \begin{bmatrix} v_{11} & v_{21} & & & & \\ v_{12} & v_{22} & & & & \\ & & \ddots & & & \\ & & & \ddots & & \\ & & & & \ddots & \\ & & & & & v_{MM} \end{bmatrix}, \tag{4.17}$$

and $\mathbf{\Sigma}$ is an $N \times M$ diagonal matrix taking the form

$$\mathbf{\Sigma} = \begin{bmatrix} \sigma_1 & 0 & & & \\ 0 & \sigma_2 & & & \\ & & \ddots & & \\ & & & \sigma_N & 0 \quad \cdots \quad 0 \end{bmatrix} \tag{4.18}$$

which contains non-negative, real diagonal elements. With row operations, the structure of $\mathbf{\Sigma}$ was enforced to have the ranking $\sigma_1 \geq \sigma_2 \geq \ldots \geq \sigma_N \geq 0$. Thus, POD enforces not only that the singular values of $\mathbf{\Sigma}$ are arranged in descending order, but also enforces orthogonality in $\mathbf{U}$ and $\mathbf{V}$.

To explain why SVD is an appropriate method for completing POD, the following derivation will show that by enforcing orthogonality in $\mathbf{U}$ and $\mathbf{V}$ we have solved a simplified form of a covariance eigenvalue problem. Thus, this method allows one to approximate the eigenvalues and eigenvectors of the covariance which exists in the acquired data. Each eigenvalue and eigenvector will together represent a single mode of fluctuation which exists in $\mathbf{A}$. As will be discussed below, the constraints of SVD allow for an optimal reconstruction of $\mathbf{A}$ according to the covariance of each mode, which is a representation of the energy contribution of the spatio-temporal fluctuations of each mode present in the image. This estimate of energy contribution is with regard to pixel intensity variations only, and is not quantitatively correlated with energy. Therefore, this study will use singular values and eigenvalues as a measure of pixel intensity variance for a single mode rather than a measure of energy. First, consider the $M \times M$ covariance matrix $\mathbf{R} = \widetilde{\mathbf{A}}^T \widetilde{\mathbf{A}}$, or in continuous form

$$\mathbf{R}_{ij} = \sum_{k=1}^{N} a_{ki} a_{kj}. \tag{4.19}$$

$\mathbf{R}_{ij}$ is the product of the intensity fluctuations of the i^{th} pixel and the j^{th} pixel, hence $\mathbf{R}$ is the covariance of intensity throughout the image. When used within a POD algorithm,

the orthogonality constraint of SVD allows one to solve an eigenvalue problem for $\mathbf{R}$ with real, non-negative eigenvalues.

With $\widetilde{\mathbf{A}} = \mathbf{U}\mathbf{\Sigma}\mathbf{V}^T$, the covariance matrix can be rewritten as

$$\mathbf{R} = \mathbf{V}\mathbf{\Sigma}^T\mathbf{U}^T\mathbf{U}\mathbf{\Sigma}\mathbf{V}^T. \tag{4.20}$$

If we assume that $\mathbf{U}$ is orthogonal then $\mathbf{U}^T\mathbf{U}$ is equal to the identity matrix and

$$\mathbf{R} = \mathbf{V}\mathbf{\Sigma}^T\mathbf{\Sigma}\mathbf{V}^T. \tag{4.21}$$

Now, define $\mathbf{\Lambda}$ as the product of the singular value matrix and its transpose ($\mathbf{\Lambda} = \mathbf{\Sigma}^T\mathbf{\Sigma}$), which by definition is the diagonal matrix

$$\mathbf{\Lambda} = \begin{bmatrix} \sigma_1^2 & & & & & & \\ & \sigma_2^2 & & & & & \\ & & \ddots & & & & \\ & & & \sigma_N^2 & & & \\ & & & & 0 & & \\ & & & & & \ddots & \\ & & & & & & 0 \end{bmatrix}, \tag{4.22}$$

where $\mathbf{\Lambda}_{ij} = 0$ for $i > N$ or $j > N$ and the same form is reached by dropping zero columns from $\mathbf{\Sigma}$ to increase computational efficiency. Multiplying both sides of eqn. 4.21 by $\mathbf{V}$ and enforcing orthogonality in $\mathbf{V}$ leads to the desired eigenvalue problem

$$\mathbf{R}\mathbf{V} = \mathbf{V}\mathbf{\Lambda}, \tag{4.23}$$

which is the general form of an eigenvalue problem. An eigenvalue problem defines a non-zero vector that, when multiplied by a square matrix, yields a constant multiple of the non-zero vector. Here, the constant multiplier is $\mathbf{\Lambda}$, and the vector is $\mathbf{V}$. In other words, $\mathbf{V}$ contains the eigenvectors of $\mathbf{R}$ and $\mathbf{\Lambda}$ contains the eigenvalues. By the

definition of the covariance matrix ($\mathbf{R} = \widetilde{\mathbf{A}}^T\widetilde{\mathbf{A}}$), $\mathbf{R}$ is both real and symmetric, because $\widetilde{\mathbf{A}}$ contains real data. Also, following the proof in appendix A.2, $\mathbf{R}$ is positive semidefinite. For any eigenvalue problem where the square matrix $\mathbf{R}$ is real, symmetric, and positive semidefinite, the eigenvector solutions will be orthogonal, i.e. $\mathbf{V}$ is orthogonal. In addition, this state requires that the eigenvalues σ_i^2 are real and non-negative. Finally, this gives real, non-negative values for σ_i and allows rows of $\mathbf{\Sigma}$ to be ranked such that $\sigma_1 \geq \sigma_2 \geq \ldots \geq \sigma_N \geq 0$. The above derivation of the covariance eigenvalue problem is not part of the POD algorithm employed in this study, but can be used in other POD schemes which do not utilize SVD. The derivation is given here to explain why SVD provides a valid reconstruction of the data matrix $\widetilde{\mathbf{A}}$. By enforcing $\mathbf{U}$ and $\mathbf{V}$ to be orthogonal, SVD reaches a solution equivalent to the solution of the covariance eigenvalue problem, thus computing eigenvalues and eigenvectors of the covariance matrix.

4.5.2 Application of Proper Orthogonal Decomposition

Proper orthogonal decomposition was applied to shear-coaxial jet high speed image sets with three objectives:

- qualify the appearance of the most dominant mode
- quantify the frequency of the most dominant mode
- quantify the relative significance of the natural mode and the forced mode occurring within a single acoustically forced flow condition

To reach these objectives, a POD algorithm written in MATLAB was used to reach a solution for the orthogonal matrices $\mathbf{U}$ and $\mathbf{V}$ and the diagonal matrix of singular values $\mathbf{\Sigma}$ for a pixel data matrix $\mathbf{A}$. For a given flow condition, a set of back-lit images was reduced to capture only the pertinent portion of the field of view. The 320×640 field of view was reduced in width and height to only include the jet, thus decreasing

the number of columns M in the aggregate matrix $\mathbf{A}$ and reducing computational time. Figure 4.20 shows a snapshot example, as well as the cropped field of view. The image acquisition rate and duration were chosen to create instability frequency spectra for an appropriate frequency range and resolution. First, the image sampling rate was 10 kHz, which provides a Nyquist frequency of 5 kHz. Second, the number of rows N in matrix $\mathbf{A}$, i.e. the number of images, was 2000. This was chosen to maintain acceptable computational efficiency while providing sufficient frequency resolution, which was 2.5 Hz (=5000Hz/2000). After subtracting the average image from each instantaneous image frame as in eqn. 4.14, SVD was applied to $\widetilde{\mathbf{A}}$ to determine $\mathbf{U}$, $\mathbf{\Sigma}$, and $\mathbf{V}$, which must be analyzed further to obtain mode shapes and frequencies.

Following SVD of $\widetilde{\mathbf{A}}$, additional data reductions were applied to further reduce computational time. Since $N << M$, only the first N diagonal elements of $\mathbf{\Sigma}$ and the first N columns of $\mathbf{V}$ are non-zero. Consequently, $\mathbf{\Sigma}$ and $\mathbf{V}$ were reduced to $N \times N$ and $M \times N$ matrices, respectively. By convention, since the singular values are arranged in descending order of magnitude, the columns of $\mathbf{U}$ and $\mathbf{V}$, which represent an orthonormal bases set of the column and row space of $\widetilde{\mathbf{A}}$, respectively, were arranged to match the order of $\mathbf{\Sigma}$.

Moreover, each column of $\mathbf{Q} = \mathbf{U\Sigma}$, equivalent to $u_k(t)$ in eqn. 4.13, is a vector of time-dependent amplitude coefficients, while the columns of $\mathbf{V}$ are the proper orthogonal modes. The columns of $\mathbf{V}$ are eigenvectors, or can also be called eigenfunctions. Therefore, the first column of $\mathbf{Q}$ contains the temporal characteristics of the coherent flow structure of the first mode, which contained the highest variance contribution to the flow. Meanwhile, the first column of $\mathbf{V}$ contains the spatial distribution of the first mode, and so on, for subsequent columns of $\mathbf{Q}$ and $\mathbf{V}$. As an example, Fig. 4.21 shows a plot of the singular values for all modes in the image set of an acoustically forced flow. The set of eigenvalues for this flow condition is calculated as $\Lambda_i = \sigma_i^2$, and is plotted

in Figure 4.22, which can also be regarded as the energy spectrum for the image set, because each eigenvalue is a representation of variance magnitude for a single mode. For this case, the spatial distribution of the flow was reconstructed using only the first mode, corresponding to the mode with the maximum eigenvalue in Fig. 4.22. The reconstruction of mode-1 is shown in Fig. 4.23b using the first column of $\mathbf{V}$; this is called the proper orthogonal mode (POM) image, or eigenvector. The spatial distributions of subsequent modes could be constructed similarly from the remaining columns of $\mathbf{V}$. For example, the second column of $\mathbf{V}$ is used to reconstruct mode-2, and the POM image is shown in Fig. 4.23c. By subtracting out the average pixel intensities prior to SVD processing, POM images will reveal lobes of dark and light regions to indicate locations where fluid was present and absent as it emanated from the dense inner jet flow. The uniform regions colored gray indicate a mean level in a gray-scaled image. Intuitively, the POM images will provide qualitative results regarding symmetry or asymmetry for a given mode. A jet located at a PN, for example, adopts an antisymmetric instability as shown in Fig. 4.23.

Analysis of the time-dependent amplitude coefficients found in $\mathbf{Q}$ can be used to produce power spectral density (PSD) plots corresponding to each POM. Fig. 4.24 shows a PSD plot for mode-1 obtained from the first column of $\mathbf{Q}$. This is the same mode as shown in Fig. 4.23a. Similar to the measurement of experimental velocity oscillation frequencies using a hot-wire anemometer, Fig. 4.24 provides an indication of flow fluctuations, but only for a single mode. Rather than using an intrusive probe, POD allows one to study oscillations in flow as manifested by density gradients visualized in shadowgraph images. A peak in PSD denotes a recurring flow structure that originates from the inner shear layer with the associated peak frequency.

After forming POM images and PSD plots for a set of high-speed images, one must use both of these outcomes to find the most dominant, *convective* mode in the flow. To

be labeled as the most dominant mode, a solution must meet two requirements. First, its eigenvalue must be greater than those of other modes. In the most simple case, the first eigenvalue is the largest, and therefore the corresponding mode would be the most dominant. Although, a second requirement adds complexity and even subjectivity to the process of determining the most dominant mode. A convective shear-layer instability, or traveling vortex, will be represented by a conjugate POM pair rather than a single POM. Arienti and Soteriou [154] define conjugate mode pairs as any two modes whose cross power spectra magnitude peaks near a phase of 90° and are represented by similar lobe patterns. Following Arienti and Soteriou [154], the cross power spectral density (CPSD) of a conjugate mode pair with temporal amplitude coefficients, a_k and b_k was computed as

$$\text{CPSD} = \sum_{s=0}^{N-1} \text{corr}\left(a_k, b_k\right) e^{-i\omega s} \tag{4.24}$$

where $\text{corr}(a_k, b_k)$ represents the cross-correlation of a_k and b_k. For the same acoustically forced condition shown in Fig. 4.24, the CPSD magnitude of mode-1 and mode-2 is shown in Fig. 4.25 along with the phase difference. The magnitude spectra reveals a peak instability at the forcing frequency, $f_F = 2050$ Hz, and a phase difference of 90° also occurs at 2050 Hz. When choosing to pair mode-1 and mode-2 as a single flow instability, Fig. 4.23 can also be used to add confidence. In Fig. 4.23, the reconstructed POM images of mode-1 and mode-2 show the same visual features simply shifted 90′ in direction of convection, supporting the pairing of these modes as a single flow phenomenon. In conclusion, because this study seeks to describe convective waves within the jet, an instability having a large energy contribution to the flow must consist of a conjugate mode pair in addition to highly ranked eigenvalues.

Using the post-processing methods described above, the mode identified as most dominant will be described qualitatively by using the POM images from $\mathbf{V}$ and quantitatively by using the PSD of the conjugate mode pair. To meet the final objective

of comparing the significance of natural jet modes and acoustically forced jet modes, a measure of variance contribution will be calculated using the entire collection of N singular values. The pixel intensity variance contribution of a POM pair is calculated as

$$\Psi = \frac{\sigma_{k_1}^2 + \sigma_{k_2}^2}{\sum_{k=1}^{N} \sigma_k^2} \tag{4.25}$$

where $\sigma_{k_1}^2$ and $\sigma_{k_2}^2$ are the eigenvalues of mode-k_1 and mode-k_2 and the denominator is the sum of all eigenvalues. As noted earlier, the eigenvalue of a mode is equal to the square of the singular value for that mode ($\Lambda = \sigma^2$). Mode-k_1 and mode-k_2 are not necessarily mode-1 and mode-2. In conclusion, this method is used for comparing co-existing modes. In an acoustically forced flow system, a natural instability can maintain an energy contribution greater than or less than the mode asserted by forcing, and Ψ quantifies their relative importance.

4.5.3 Dynamic Mode Decomposition

Like POD, DMD allows one to reconstruct a data matrix in an approximate form, projecting large-scale motions onto a solution which neglects noise and maintains significantly fewer degrees of freedom. In eqn. 4.13, the pixel intensity values contained in a are organized to create an ordinary differential equation with temporal and spatial information separated in the variables u and v, respectively. To best describe DMD, a is written in a similar fashion, but with an amplitude coefficient included, i.e.

$$a(x,t) = \sum_{k=1}^{N} a'_k d_k(t) \phi_k(x). \tag{4.26}$$

In this form, d_k contains the temporal information, ϕ_k contains the spatial information or dynamic modes, and a'_k is the amplitude of each mode k. Note that the amplitude coefficient is only dependent on the mode number. The time-dependent function d_k takes a sinusoidal form as $d_k = \exp(\omega_k t)$, where ω_k represents the complex frequency of

mode k. ($\exp(ix) = \cos x + i\sin x$) Since sines and cosines are orthogonal, this form of d_k makes a DMD reconstruction orthogonal in *time*, whereas a POD reconstruction is orthogonal in *space* [152].

Dynamic mode decomposition proceeds by assuming that if $\mathbf{A}$ represents a series of snapshots $\mathbf{a}$ where $\mathbf{a}_1 = \mathbf{a}(x_1, t_1)$ from image 1 to image N. We can write $\mathbf{A}$ as

$$\mathbf{A} = \mathbf{A}_1^N = \{\mathbf{a}_1, \mathbf{a}_2, \mathbf{a}_3, \ldots, \mathbf{a}_N\}, \tag{4.27}$$

then a linear mapping $\mathbf{S}$ connects any flow field $\mathbf{a}_i$ to a subsequent flow field $\mathbf{a}_{i+1}$, that is,

$$\mathbf{S}\mathbf{a}_i = \mathbf{a}_{i+1}. \tag{4.28}$$

In complete form, eqn. 4.28 follows as

$$\begin{bmatrix} s_{11} & s_{12} & \cdots & s_{1M} \\ s_{21} & s_{22} & \cdots & s_{2M} \\ \vdots & & \ddots & \vdots \\ s_{M1} & s_{M2} & \cdots & s_{MM} \end{bmatrix} \begin{bmatrix} a_{1i} \\ a_{2i} \\ \vdots \\ a_{Mi} \end{bmatrix} = \begin{bmatrix} a_{1(i+1)} \\ a_{2(i+1)} \\ \vdots \\ a_{M(i+1)} \end{bmatrix}. \tag{4.29}$$

This linear mapping is assumed to be the same over the entire sampling interval $0 < t \leq (N-1)\,\Delta t$, which is a linear tangent approximation. If we apply the linear tangent approximation to the next flow field, then $\mathbf{a}_{i+2} = \mathbf{S}\mathbf{S}\mathbf{a}_i = \mathbf{S}^2\mathbf{a}_i$, or for all $i \geq 2$ we have $\mathbf{a}_i = \mathbf{S}^{i-1}\mathbf{a}_1$. Using this method for the entire sequence of N flow fields gives a Krylov sequence for $\mathbf{A}_1^N$,

$$\mathbf{A}_1^N = \left\{\mathbf{a}_1, \mathbf{S}\mathbf{a}_1, \mathbf{S}^2\mathbf{a}_1, \ldots, \mathbf{S}^{N-1}\mathbf{a}_1\right\}. \tag{4.30}$$

This formula allows one to predict an entire sequence of flow fields using only a single snapshot $\mathbf{a}_1$, but requires a known $\mathbf{S}$ ($M \times M$), which is a complete and exact mapping of the flow field. Although, when applying reduced basis methods to experimental imaging results, $\mathbf{S}$ is unknown. On the other hand, the entire flow field sequence $\mathbf{A}_1^N$ is known. Thus, rather than determining $\mathbf{A}_1^N$ using a complete $\mathbf{S}$ and a limited amount of data as

in eqn. 4.30, DMD determines a limited form of $\mathbf{S}$ using the known data matrix $\mathbf{A}_1^N$. To this end, eqn. 4.30 is rewritten to better utilize the data matrix and factor out the unknown $\mathbf{S}$. Namely,

$$\begin{aligned}\mathbf{A}_2^N &= \{\mathbf{a}_2, \mathbf{a}_3, \ldots, \mathbf{a}_N\} &&= \left\{\mathbf{S}\mathbf{a}_1, \mathbf{S}^2\mathbf{a}_1, \ldots, \mathbf{S}^{N-1}\mathbf{a}_1\right\} \\ &= \mathbf{S}\left\{\mathbf{a}_1, \mathbf{S}\mathbf{a}_1, \ldots, \mathbf{S}^{N-2}\mathbf{a}_1\right\} \\ &= \mathbf{S}\mathbf{A}_1^{N-1},\end{aligned} \tag{4.31}$$

which is the reduced form of the linear tangent approximation for the entire sequence of images. A DMD algorithm aims to extract the eigenvalues (time-dependent magnitudes), eigenvectors (spatial distributions), and amplitudes from the dynamical process described by $\mathbf{S}$ based on the pixel data contained in $\mathbf{A}_1^N$.

In addition to the linear tangent assumption, a second assumption is made. If the physical process represented by an experimental image set, or represented by a numerical flow field in the case of computational fluid dynamics, is periodic and steady in the mean, then after a critical number of flow field snapshots have been acquired there will not be new information presented in any of the following snapshots. Additional images will only contain phenomena already captured in the previous set of images. Mathematically, a critical number of snapshots $N-1$ is reached such that $\mathbf{a}_N$ is linearly dependent on the previous $N-1$ snapshots. Thus, each of the vectors $\mathbf{a}_1, \mathbf{a}_2, \ldots, \mathbf{a}_{N-1}$ are linearly independent, but $\mathbf{a}_N$ can be written as a linear combination of those vectors when the correct mapping is applied, i.e.

$$\mathbf{a}_N = g_1\mathbf{a}_1 + g_2\mathbf{a}_2 + \ldots + g_{N-1}\mathbf{a}_{N-1}. \tag{4.32}$$

Since the mapping coefficients $g_1, g_2, \ldots, g_{N-1}$ are scalars, eqn. 4.32 can written in

matrix form as

$$\begin{bmatrix} a_{1N} \\ a_{2N} \\ \vdots \\ \vdots \\ a_{MN} \end{bmatrix} = \begin{bmatrix} a_{11} & a_{12} & \cdots & a_{1(N-1)} \\ a_{21} & a_{22} & \cdots & a_{2(N-1)} \\ \vdots & & & \vdots \\ \vdots & & & \vdots \\ a_{M1} & a_{M2} & \cdots & a_{M(N-1)} \end{bmatrix} \begin{bmatrix} g_1 \\ g_2 \\ \vdots \\ g_{N-1} \end{bmatrix}, \tag{4.33}$$

or simply

$$\mathbf{a}_N = \mathbf{A}_1^{N-1}\mathbf{g}. \tag{4.34}$$

Note that the vector $\mathbf{g}$ is on the right of $\mathbf{A}_1^{N-1}$. Further, if we create a matrix $\widetilde{\mathbf{S}}$ then $\mathbf{A}_2^N$ can be written as

$$\begin{aligned} \mathbf{A}_2^N &= \{\mathbf{a}_2, \mathbf{a}_3, \mathbf{a}_4, \ldots, \mathbf{a}_N\} \\ &= \left\{\mathbf{a}_2, \mathbf{a}_3, \mathbf{a}_4, \ldots, \mathbf{A}_1^{N-1}\mathbf{g}\right\} \\ &= \mathbf{A}_1^{N-1}\widetilde{\mathbf{S}}, \end{aligned} \tag{4.35}$$

which is the reduced form of the linear combination assumption. This form may only be used when $\widetilde{\mathbf{S}}$ is taken as a companion matrix, meaning that all columns of $\widetilde{\mathbf{S}}$ serve as placeholders except for the last column containing the linear combination coefficients of $\mathbf{g}$. The complete companion matrix is

$$\widetilde{\mathbf{S}} = \begin{bmatrix} 0 & & & & g_1 \\ 1 & 0 & & & g_2 \\ & \ddots & \ddots & & \vdots \\ & & 1 & 0 & g_{N-2} \\ & & & 1 & g_{N-1} \end{bmatrix}. \tag{4.36}$$

where the coefficients $\{g_1, g_2, \ldots, g_{N-1}\}$ are unknown. The matrix form of 4.35 is

$$\begin{bmatrix} a_{12} & a_{13} & \cdots & a_{1N} \\ a_{22} & a_{23} & \cdots & a_{2N} \\ \vdots & & & \vdots \\ \vdots & & & \vdots \\ a_{M2} & a_{M3} & \cdots & a_{MN} \end{bmatrix} = \begin{bmatrix} a_{11} & a_{12} & \cdots & a_{1(N-1)} \\ a_{21} & a_{22} & \cdots & a_{2(N-1)} \\ \vdots & & & \vdots \\ \vdots & & & \vdots \\ a_{M1} & a_{M2} & \cdots & a_{M(N-1)} \end{bmatrix} \begin{bmatrix} 0 & & & & g_1 \\ 1 & 0 & & & g_2 \\ & \ddots & \ddots & & \vdots \\ & & 1 & 0 & g_{N-2} \\ & & & 1 & g_{N-1} \end{bmatrix}. \tag{4.37}$$

Finally, joining the linear combination assumption with the linear tangent approximation, $\widetilde{\mathbf{S}}$ is clearly an approximated version of the complete mapping $\mathbf{S}$, because

$$\mathbf{S}\mathbf{A}_1^{N-1} = \mathbf{A}_2^N = \mathbf{A}_1^{N-1}\widetilde{\mathbf{S}}. \tag{4.38}$$

With $\mathbf{A}_2^N$ as the single-stepped advancement of $\mathbf{A}_1^{N-1}$, the i^{th} column of $\mathbf{A}_2^N$ is equal to the $(i+1)^{th}$ column of $\mathbf{A}_1^{N-1}$ for $i = 1, 2, \ldots, N-2$. These two data matrices are used to find the last column of $\widetilde{\mathbf{S}}$, whose eigenvalues approximate some of the eigenvalues of $\mathbf{S}$. Hence, it is our objective to determine an approximate mapping $\widetilde{\mathbf{S}}$ which serves as a reduced version of $\mathbf{S}$.

At this point in the derivation, the remaining steps vary depending on the specific DMD algorithm employed. Regardless, the objective is to formulate and solve an eigenvalue problem for the approximate mapping matrix. The general version described here utilizes a proper orthogonal decomposition basis, whereas other DMD methods use entirely different steps in order to define an eigenvalue problem for the companion matrix $\widetilde{\mathbf{S}}$. Proceeding with the general method described by Jovanovic *et al.* [155], the displaced data matrix $\mathbf{A}_2^N$ and a singular value decomposition of the initial matrix $\mathbf{A}_1^{N-1}$ are used to evaluate a transformed arrangement of $\widetilde{\mathbf{S}}$. By definition, the SVD of $\mathbf{A}_1^{N-1}$ is

$$\mathbf{A}_1^{N-1} = \mathbf{U}\mathbf{\Sigma}\mathbf{V}^H, \tag{4.39}$$

where $\mathbf{U}$ and $\mathbf{V}$ are orthogonal and $\mathbf{\Sigma}$ represents the energy content for each mode, i.e.

singular values. Then, the right-hand portion of eqn. 4.38 can be written as

$$\mathbf{A}_2^N = \mathbf{U}\mathbf{\Sigma}\mathbf{V}^H\widetilde{\mathbf{S}}. \tag{4.40}$$

Multiplying eqn. 4.40 by $\mathbf{U}^H$ on the left and $\mathbf{V}\mathbf{\Sigma}^{-1}$ on the right gives

$$\mathbf{U}^H\mathbf{A}_2^N\mathbf{V}\mathbf{\Sigma}^{-1} = \mathbf{\Sigma}\mathbf{V}^H\widetilde{\mathbf{S}}\mathbf{V}\mathbf{\Sigma}^{-1}, \tag{4.41}$$

This equation is a new form of $\mathbf{A}_2^N = \mathbf{A}_1^{N-1}\widetilde{\mathbf{S}}$ which includes the singular value decomposition of $\mathbf{A}_1^{N-1}$. For this reason, the general version of DMD can be described as application of the POD modes of $\mathbf{A}_1^{N-1}$ onto the dynamic mode decomposition of $\mathbf{A}_1^N$.

Along these lines, the general version continues by redefining the approximate map, which was defined as $\widetilde{\mathbf{S}}$, as a transformation of $\widetilde{\mathbf{S}}$ using the POD modes of $\mathbf{A}_1^{N-1}$. Remember, $\widetilde{\mathbf{S}}$ is known from eqn. 4.37. As done in Jovanovic *et al.* [155], the transformed companion matrix is equivalent to the right hand side of 4.41, and will be called $\widetilde{\mathbf{S}}'$. In other words,

$$\widetilde{\mathbf{S}}' = \mathbf{\Sigma}\mathbf{V}^H\widetilde{\mathbf{S}}\mathbf{V}\mathbf{\Sigma}^{-1}. \tag{4.42}$$

Eqn. 4.42 provides a known $\widetilde{\mathbf{S}}'$ which allows one to readily formulate a general eigenvalue problem for $\widetilde{\mathbf{S}}'$ which is similar to the eigenvalue problem for $\mathbf{R}$ formulated for POD. The eigenvalue problem for $\widetilde{\mathbf{S}}'$ follows as

$$\widetilde{\mathbf{S}}'\mathbf{X} = \mathbf{X}\mathbf{D}, \tag{4.43}$$

where $\mathbf{D}$ is a matrix of the eigenvalues $d_k(t)$ as in eqn. 4.26. The matrix $\mathbf{X}$ contains eigenvectors which are used to form the dynamic modes $\phi_k(x)$. One can readily solve the eigenvalue problem to determine the time-dependent function $d_k(t)$ and the spatially dependent function $\phi_k(x)$, which are the outputs desired to complete a limited reconstruction of the flow field. To reach this point, constraints have not been placed on the eigenvectors and eigenvalues; both can be negative, imaginary, and need not be orthogonal. Instead, several other assumptions were made to obtain the correct form in eqn.

4.43. First, the linear tangent assumption was made to relate $\mathbf{A}_1^{N-1}$ with $\mathbf{A}_2^N$ using the linear mapping $\mathbf{S}$. Second, the mapping $\mathbf{S}$ was approximated as the companion matrix $\widetilde{\mathbf{S}}$ by way of the linear combination of a critical number of images N. Last, the initial data matrix $\mathbf{A}_1^{N-1}$ was decomposed using SVD as in the POD algorithm of the previous section. Since $\mathbf{S}\mathbf{A}_1^{N-1} = \mathbf{A}_2^N$, this step is referred to as a projection of the linear operator $\mathbf{S}$ onto a POD basis, which is advantageous for reasons discussed in section 4.5.4.

The preceding derivation of DMD is only one possible procedure for completing the decomposition. A second method of DMD, the full-rank method, utilizes a QR decomposition, $\mathbf{A}_1^{N-1} = \mathbf{QR}$, rather than SVD. Here, $\mathbf{Q}$ and $\mathbf{R}$ should not be confused with the nomenclature of section 4.5.1. The full-rank method though, does not provide an order to the identified modes. A magnitude of energy content is not distinguished in QR decomposition as in SVD. As will be shown in the following section, the computation of singular values in the general method enables the ranking of flow instability amplitude: a paramount objective of this study.

4.5.4 Application of Dynamic Mode Decomposition

Dynamic mode decomposition was employed with the same three objectives as the application of POD. Rather than use this algorithm to analyze all experimental flow conditions, a limited number of cases were analyzed using DMD with the primary purpose of comparing the effectiveness of DMD with that of POD. The conclusions gained from this comparison are offered in Section 5.2.

Similar to POD, an algorithm was written in MATLAB to process high speed image sets captured at a frame rate of 10 kHz and store the pixel intensity data in $\mathbf{A}$. In contrast to POD, DMD uses the raw gray-scale intensities to form $\mathbf{A}_1^{N-1}$ and $\mathbf{A}_2^N$ directly rather than subtracting the mean [152]. Then, the matrix $\widetilde{\mathbf{S}}'$ was found using eqns. 4.39 and 4.42, in that order. With a known $\widetilde{\mathbf{S}}'$, the eigenvalue problem in eqn. 4.43 was solved

using a MATLAB built-in function, giving the complex eigenvector matrix

$$\mathbf{X} = \begin{bmatrix} x_{r11} + ix_{i11} & x_{r12} + ix_{i12} & & \\ x_{r21} + ix_{i21} & x_{r22} + ix_{i22} & & \\ & & \ddots & \\ & & & x_{rnn} + ix_{inn} \end{bmatrix} \tag{4.44}$$

and complex eigenvalue matrix

$$\mathbf{D} = \begin{bmatrix} d_{r1} + id_{i1} & 0 & & \\ 0 & d_{r2} + id_{i2} & & \\ & & \ddots & \\ & & & d_{rn} + id_{in} \end{bmatrix}, \tag{4.45}$$

where $\{d_{r1} = d_{r2}, d_{r3} = d_{r4}, \ldots, d_{r(n-1)} = d_{rn}$ and $\{d_{i1} = -d_{i2}, d_{i3} = -d_{i4}, \ldots, d_{i(n-1)} = -d_{in}$. These two matrices are processed to form the complex frequencies and images which represent each mode.

As stated earlier, the matrix $\mathbf{D}$, made up of the individual eigenvalues d_k for each mode, is a periodic form of the frequency of mode k such that

$$d_k = \exp(\omega_k \Delta t). \tag{4.46}$$

Consequently, the complex frequency ω_k was calculated as

$$\omega_k = \omega_r + i\omega_i = \frac{\ln(d_k)}{2\pi\Delta t}, \tag{4.47}$$

and $\Delta t = 1/(10\text{ kHz}) = 0.1$ ms. The real component ω_r is the mode growth rate and the imaginary component ω_i is the mode frequency in Hertz. As depicted by the preceding calculation of ω_i, each mode is marked with a single frequency (a scalar) rather than a frequency spectrum (a vector). Meanwhile, the dynamic mode matrix $\mathbf{\Phi}$, made up of the dynamic modes ϕ_k for each mode, is determined using the eigenvector matrix $\mathbf{X}$ and $\mathbf{U}$. Simply stated,

$$\mathbf{\Phi} = \mathbf{UX}. \tag{4.48}$$

Each column of $\mathbf{\Phi}$ is a spatial distribution of the flow field for a single mode, and a linear combination of several columns of $\mathbf{\Phi}$ manifests a simplified reconstruction of the flow field neglecting all other modes and insignificant noise.

As a demonstration of this DMD algorithm, the same set of images used to create the POD results in Section 4.5.2 was analyzed with DMD. Because the flow field subject to analysis was acoustically forced, DMD is expected to reveal a coherent mode with $\omega_i = f_F$. In the top plot of Fig. 4.26 the wave growth rate ω_r is plotted versus ω_i for an LN_2-GHe flow condition coupled with acoustic forcing at a PN for $f_F = 2050$ Hz. The mode resulting from acoustic forcing is easily identified at 2050 Hz, with a slightly positive growth rate, identifying an unstable mode. With the exception of the mean flow represented by a point at the origin, all other modes are stable and are analogous to modes with low-ranked singular values as computed using POD. The spectrum of Fig. 4.26 is symmetric about the $\omega_i = 0$ axis, because all pixel intensity data contained real values. Complex data will generally result in an asymmetric appearance about the $\omega_i = 0$ axis.

For this study though, a measure of amplitude of pixel intensity fluctuations, or energy contribution, is more useful for identifying the significance of a given mode. Accordingly, amplitude was calculated using the method by Schmid [156], which follows as

$$\mathbf{a} = \frac{1}{\left\|\mathbf{V}\mathbf{\Sigma}^{-1}\mathbf{X}\right\|}, \tag{4.49}$$

which can be interpreted as a matrix containing magnitudes of each vector in the two-dimensional space created by the product $\mathbf{V}\mathbf{\Sigma}^{-1}\mathbf{X}$. The value of $\mathbf{a}$ is proportional to a'_k in eqn. 4.26. Most importantly, amplitude relies on the singular values created by SVD, a step not included in the full-rank version of DMD. Further, the foundation of DMD does not include a ranking of modes in the linear tangent approximation, nor in the linear combination assumption of eqn. 4.32. Thus, multiple mode ranking techniques

for DMD algorithms have been explored in an effort to simplify flows using only the most important modes. Singular values alone though, impart the energy contribution of an entire spectra as in Fig. 4.24, not the magnitude at a distinct frequency. Thus, eqn. 4.49 relates the energy contributions held in $\mathbf{\Sigma}$ to a single eigenvector in $\mathbf{X}$. As shown in the lower plot of Fig. 4.26, DMD results convey the highest amplitude for the mean flow, a result which is in agreement with other DMD studies [152, 156, 157]. High amplitudes are also observed at $|\omega_i| = f_F = 2050$ Hz. This is expected for an acoustically forced jet in which the shear layer adopts the acoustic instability as the dominant mode.

A final form of verification lies in the realm of visualization. Like the POM images created using POD, the dynamic mode images of DMD are used for qualitative conclusions, such as jet symmetry or lack thereof. As an example, Fig. 4.27 displays the reconstructed images of one unstable mode shown by the cyan point in Fig. 4.26 where $[\omega_i, \omega_r] = [2050, 6.022]$. Characteristic of PN forcing, Fig. 4.27 shows an antisymmetric jet [29, 30]. The real and imaginary eigenvector images corresponding to ϕ_r and ϕ_i, respectively, are shown to be inherently conjugate by the location of lobes in each image in Fig. 4.27, which are 90° out-of-phase. This pairing occurs for the real and imaginary values found in each column of $\mathbf{\Phi}$, and thus results from the algorithm rather than a choice made by the user. This is one of many differences between DMD and POD, as will be discussed in chapter 5.

4.6 Measurement Uncertainty

The experimental results presented in this study derive from three measured quantities: pressure, temperature, and mass flow rate. These three measurements determine density ρ, velocity U, momentum flux M, and the ratios thereof (S, R, J). Although injector geometry is also used to determine velocity and momentum flux, the uncertainty of injector dimensions was made negligible by using the "as machined" dimensions with

an uncertainty of 0.013 mm (0.0005 in). Also, the precision error of pressure, temperature, and mass flow rate will be ignored due to their small relevance in comparison to bias error. This simplification is valid for two reasons. First, high signal-to-noise ratios were maintained by constructing well-shielded data transfer cables. Second, this study's reported measurements are time-averaged for steady flow conditions. Unsteady measurements, mainly dynamic pressure, were phase-averaged to obtain a mean p' value over more than 10,000 acoustic cycles.

For the inner and outer jets, exit velocities were determined using the relation

$$U_k = \frac{\dot{m}_k}{\rho_k A_k}, \tag{4.50}$$

where k is ij for the inner jet and oj for the outer jet. Following propagation of uncertainty principles of Mills and Chang [139], the uncertainty of U_k can be calculated as

$$\delta U_k = U_k \sqrt{\left(\frac{\delta \dot{m}_k}{\dot{m}_k}\right)^2 + \left(\frac{\delta \rho_k}{\rho_k}\right)^2 + \left(\frac{\delta A_k}{A_k}\right)^2} = U_k \sqrt{\left(\frac{\delta \dot{m}_k}{\dot{m}_k}\right)^2 + \left(\frac{\delta \rho_k}{\rho_k}\right)^2} \tag{4.51}$$

and the uncertainty of the momentum flux, $M_k = \frac{\dot{m}_k^2}{\rho_k A_k}$, is

$$\delta M_k = M_k \sqrt{4\left(\frac{\delta \dot{m}_k}{\dot{m}_k}\right)^2 + \left(\frac{\delta \rho_k}{\rho_k}\right)^2 + \left(\frac{\delta A_k}{A_k}\right)^2} = M_k \sqrt{4\left(\frac{\delta \dot{m}_k}{\dot{m}_k}\right)^2 + \left(\frac{\delta \rho_k}{\rho_k}\right)^2}. \tag{4.52}$$

A combination of vendor calibrations and on-site calibrations provide the measurement uncertainties for each instrument. Temperatures measured with both type E and type R thermocouples will be reported with uncertainties according to data published by the manufacturer, Omega. For the range of temperatures measured here, type E thermocouples have a bias uncertainty of ± 1 K while the bias uncertainty of type R thermocouples is ± 1.5 K. The Porter mass flow meters had a nonlinearity error of 1% full scale output (FSO) and a repeatability error of .2% FSO, as reported by Porter calibrations. This creates a combined nonlinearity and repeatability (CNLR) rating of

1.02%, which is the square root of the sum of squares of each source of error. With only negligible error present due to thermal effects, the CNLR is the total error of the mass flow meters. The CNLR and CNLRH ratings are standard methods for determining the static accuracy of an instrument for data without and with hysteresis, respectively. Thus, a mass flow rate uncertainty was chosen as the total error for the gas species of interest, because the FSO of each mass flow meter, and thus the total error, is altered by a change in species. The uncertainties for oxygen, nitrogen, helium, and hydrogen are 0.130 g/s, 0.119 g/s, 0.024 g/s, and 0.009 g/s, respectively. CNLRH ratings for all GP:50 static pressure transducers and Kulite dynamic pressure transducers were determined in calibrations performed on-site with a high pressure Ruska calibrator. Three different pressure transducer models were used for the pressure data reported in this study, each being used for separate purposes. Acoustic pressure fluctuations were measured with the Kulite Model XCE-093-50D, static pressures at room temperature were measured with the GP:50 Model 7200-8475, and static pressures at cryogenic temperatures were measured with the GP:50 Model 7720-JA-8474. For each of these three classifications of pressure measurement and corresponding sensor model, the total error applied to each category was drawn from calibration results of the *least accurate* single pressure transducer within that group. Values are listed in Table 4.2.

The inner and outer jet densities were evaluated based on chamber pressure and temperatures measured immediately upstream of the injector, using NIST REFPROP tables [158]. As shown in Fig. 4.5, density is primarily dependent on temperature when operating away from the saturation temperature. In this region, since density has a much weaker dependence on pressure than on temperature, the uncertainty in density due to pressure variation was deemed negligible. Thus, for measurement error analysis in this study, $\rho(p,T) \approx \rho(T)$.

Lastly, the uncertainties in momentum flux ratio and velocity ratio were calculated

as

$$\delta J = J\sqrt{\left(\frac{\delta M_{ij}}{M_{ij}}\right)^2 + \left(\frac{\delta M_{oj}}{M_{oj}}\right)^2} \tag{4.53}$$

and

$$\delta R = R\sqrt{\left(\frac{\delta U_{ij}}{U_{ij}}\right)^2 + \left(\frac{\delta U_{oj}}{U_{oj}}\right)^2}, \tag{4.54}$$

respectively. In chapter 5, error bars are included in several key plots to ameliorate clarity as one measures the accuracy of conclusions in this study. Conclusions are reached with an awareness of imperfect measurement techniques, and these error bars serve to quantify imperfections for the reader.

4.1: Dimensions of shear-coaxial injectors* used in AFRL experiments [23, 75].

Inj.	t [mm]	D_1 [mm]	$\frac{t}{D_1}$	D_2 [mm]	D_3 [mm]	D_4 [mm]	D_{eff} [mm]	$\frac{A_{oj}}{A_{ij}}$
I	0.53	0.51	1.05	1.59	2.42	3.18	1.05	12.9
II	0.13	1.40	0.09	1.65	2.44	3.94	1.53	1.65
III	1.24	1.47	0.84	3.96	4.70	6.35	2.72	2.90
IV	0.09	0.70	0.13	0.89	2.44	3.94	0.80	10.6
V	0.38	1.40	0.27	2.16	2.82	3.56	1.78	1.68

* Injector V is used for new experimental results presented in this study, while injectors I-IV were used in previous nonreactive experiments at AFRL.

4.2: Pressure transducer uncertainty values*.

Mfr.	Model	Nonlinearity	Repeatability	Hysteresis	Static Accuracy	Thermal Error	Total Error
Kulite	XCE-093-50D	.09%	.16%	.12%	.22%	-	.22%
GP:50	7720-JA-8474	.05%	.12%	.10%	.16%	.37%	.53%
GP:50	7200-8475	.06%	.12%	.12%	.18%	-	.18%

* Uncertainty values are taken as the total error of the instrument, listed here for each of the three transducer models used in this study. Static accuracy is the CNLRH rating calculated using the square root of the sum of squares method, and is the total error in the absence of significant error due to changes in temperature. For example, CNLRH= $\sqrt{(.06\%)^2 + (.12\%)^2 + (.12\%)^2} = .18\%$, which is the total error of pressures measured with the GP:50 7200-8475 at room temperature.

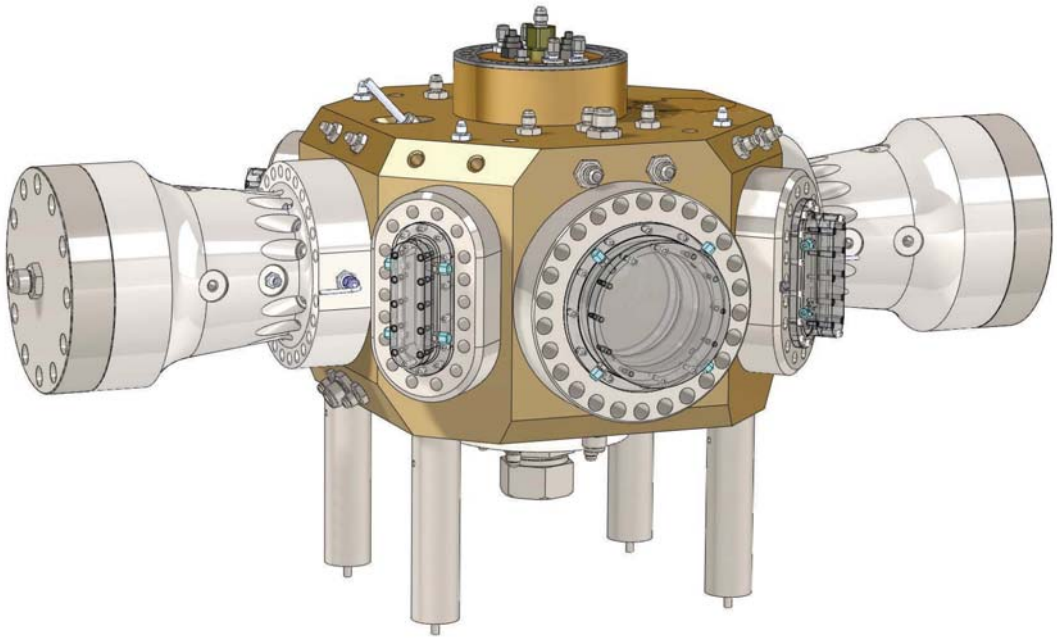

4.1: A three-dimensional CAD rendering of the high pressure combustion chamber at Air Force Research Laboratory at Edwards AFB, CA.

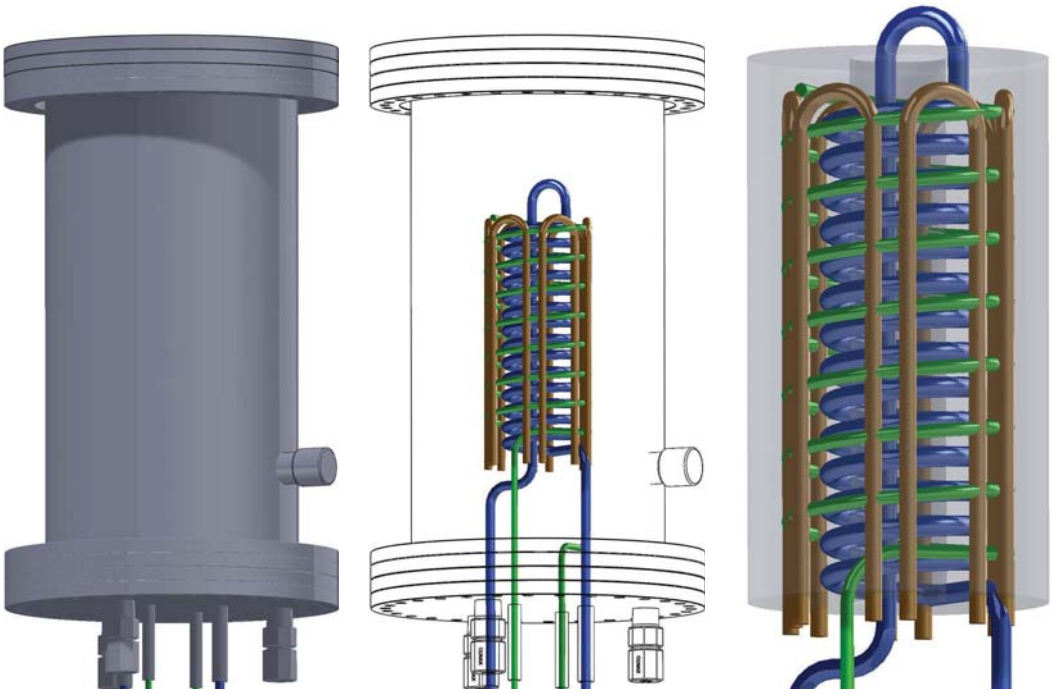

4.2: The oxygen heat exchanger cools oxygen gas (green) using liquid nitrogen (blue). Oxygen is cooled below the target temperature and electric heaters (brown) increase oxygen to the target temperature with a control resolution of ±1 K. Insulation is provided by a vacuum jacket (shown in left view, outlined in center view). An aluminum casting surrounds the plumbing assembly (shown in right view, gray). Courtesy of Sierra Lobo Inc.

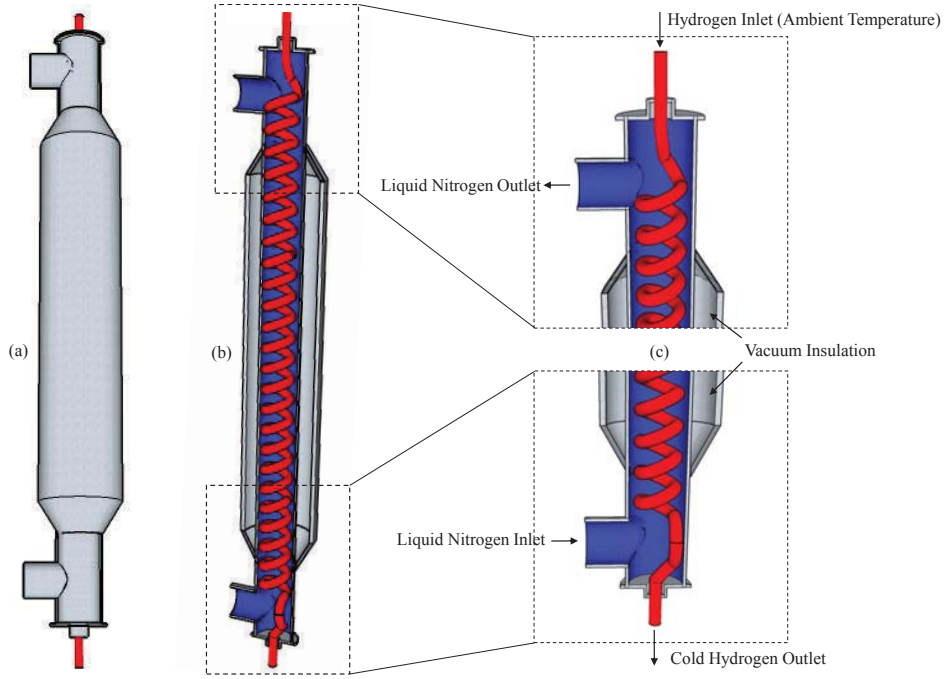

4.3: The hydrogen heat exchanger cools hydrogen gas (red) using liquid nitrogen (blue). Insulation is provided by a vacuum jacket.

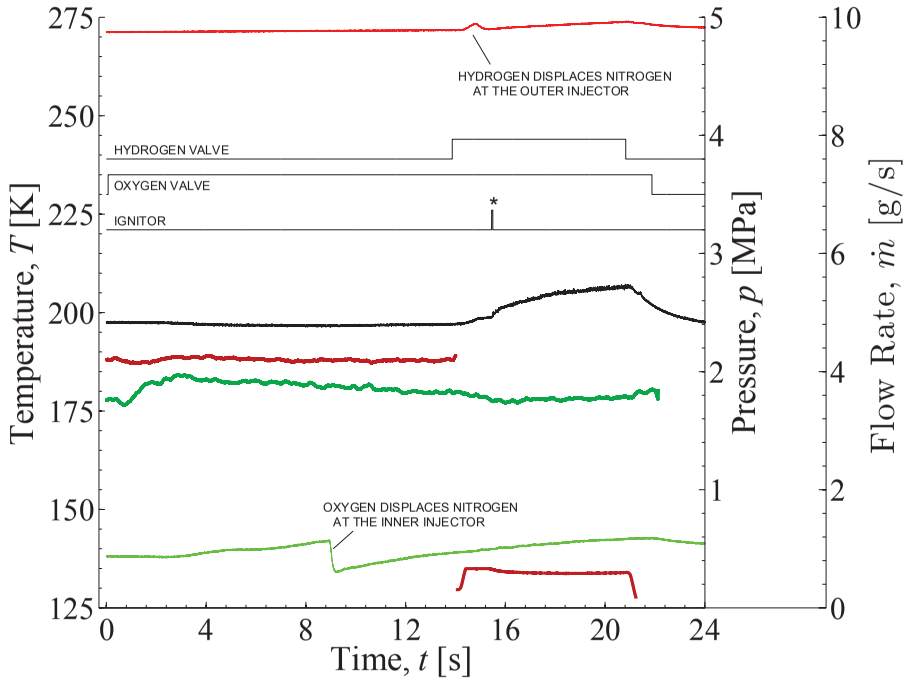

4.4: Time series plot of a reactive test using an oxygen and hydrogen. The transition from nitrogen simulant to propellant occurs after the propellant valve is opened. A step change in outer jet mass flow rate occurs near $t = 14$ s, where a nitrogen flow rate of ≈4.2 g/s changes to a hydrogen mass flow rate of 0.65 g/s (dark red). The inner jet mass flow rate shows a species change near $t = 1$ s, where a nitrogen flow rate of 3.6 g/s is overtaken by an oxygen mass flow rate of ≈3.9 g/s. Inner jet temperature (light green), outer jet temperature (light red), and chamber pressure (black) are also shown. $MR = 5.9$ ($\phi_{o/f} = 1.36$), $J = 2$

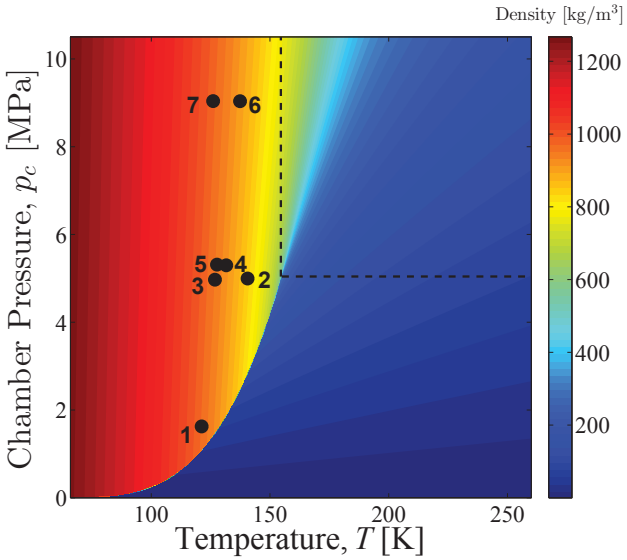

4.5: The facility's minimum achievable oxygen temperatures are plotted with an oxygen density contour overlay. A vertical line and a horizontal line represent the critical temperature and pressure, respectively. Both chamber pressure and mass flow rate are controlled while temperature is measured. (1) 3.7 g/s (2) 2.6 g/s (3) 9.3 g/s (4) 3.0 g/s (5) 11.1 g/s (6) 2.7 g/s (7) 10.4 g/s

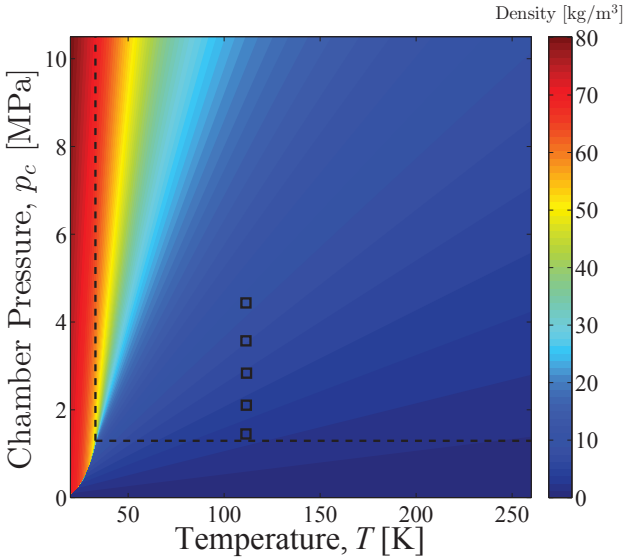

4.6: The facility's minimum achievable helium temperatures are plotted with a hydrogen density contour overlay. A vertical line and a horizontal line represent the critical temperature and pressure, respectively. Helium is used as a surrogate gas, and is representative of minimum hydrogen achievable hydrogen temperatures in the outer jet. The nominal outer jet flow rate is approximately 1.3 g/s.

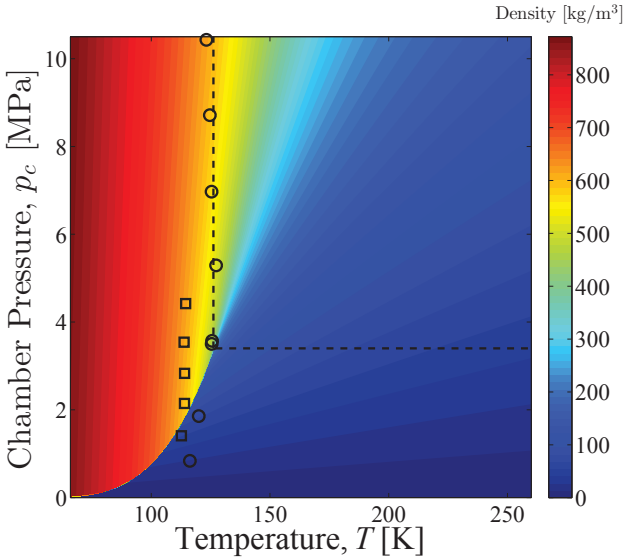

4.7: The facility's minimum achievable nitrogen temperatures for the inner and outer jets are plotted with an nitrogen density contour overlay. A vertical line and a horizontal line represent the critical temperature and pressure, respectively. Both chamber pressure and mass flow rate are controlled while temperature is measured. Flow rates of the inner and outer jets are approximately 9 g/s and 3 g/s, respectively. (○) Inner jet (□) Outer jet

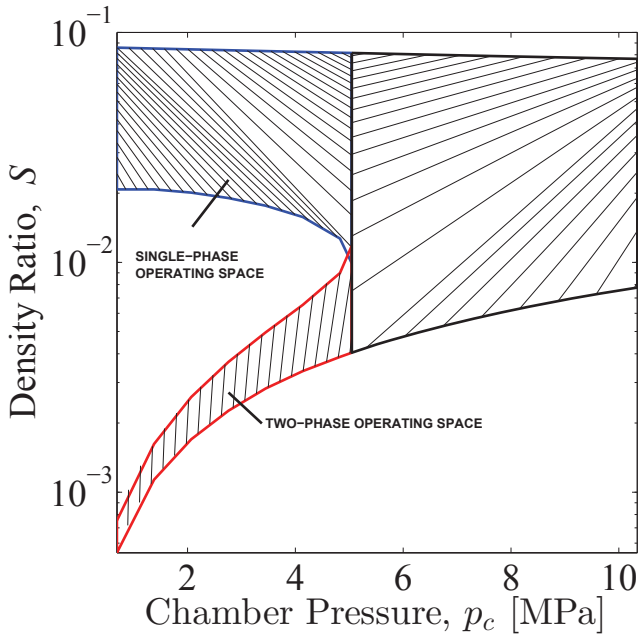

4.8: The facility's range of possible density ratios plotted versus chamber pressure for oxygen and hydrogen propellants.

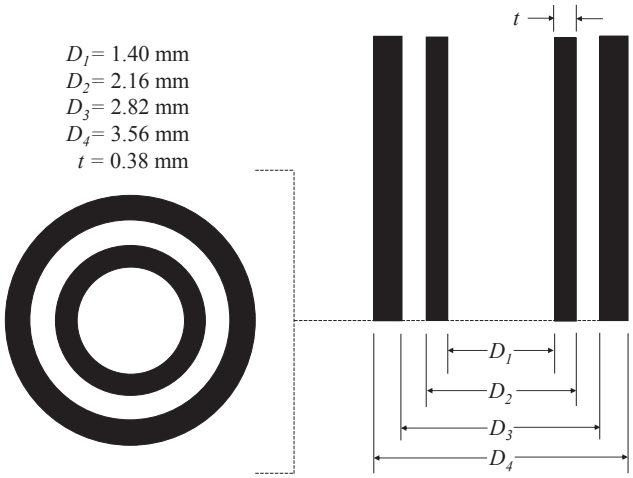

4.9: The dimensions of the coaxial injector used for new experiments in this study.

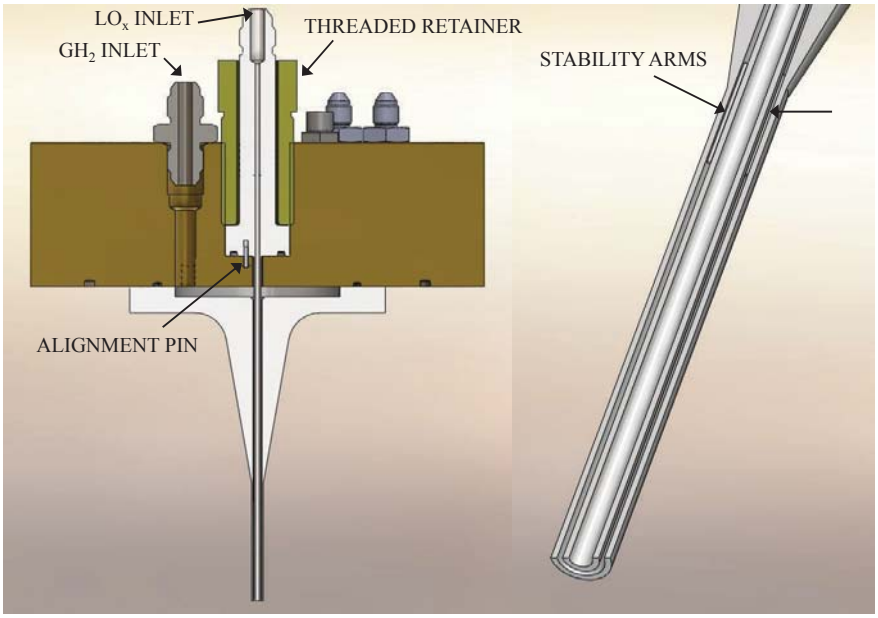

4.10: The inner injector body passes through the center of the brass top flange and is held in place using a retainer. For angular consistency between removal and re-installment, the inner injector is aligned with a dowel pin which is pressed into the top flange. To achieve concentricity between the inner and outer injectors, three stability arms are located on the outside surface of the inner tube (right). The outer injector fastens to the lower surface of the top flange, and an outer jet plenum is located between these two parts. Both the inner and outer injectors are machined from Monel 400 alloy.

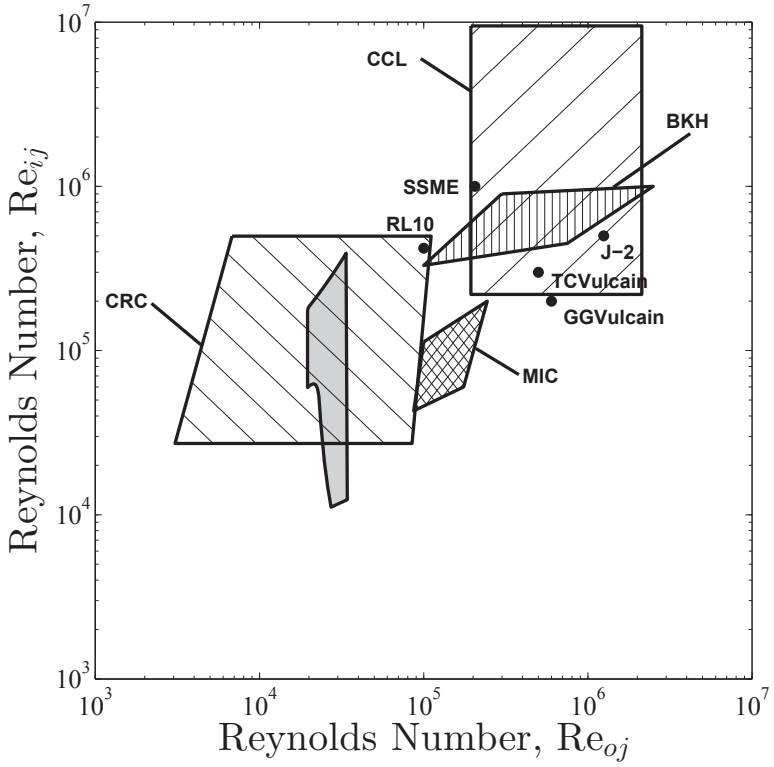

4.11: Shear-coaxial injector Reynolds numbers for the AFRL Combustion Stability Laboratory (gray) with a comparison to other experimental facilities and liquid rocket engines with H_2-O_2 flows. Data is included for the Vulcain Gas Generator (GGVulcain), Vulcain Main Thrust Chamber (TCVulcain), RL10 engine, Space Shuttle Main Engine (SSME), J-2 engine, BKH combustor and Common Research Combustor (CRC) of DLR in Germany, Cryogenic Combustion Laboratory (CCL) of Pennsylvania State Univ., and the Multi-Injector Combustor (MIC) of ONERA and CNRS in France [8, 24, 45, 131, 159].

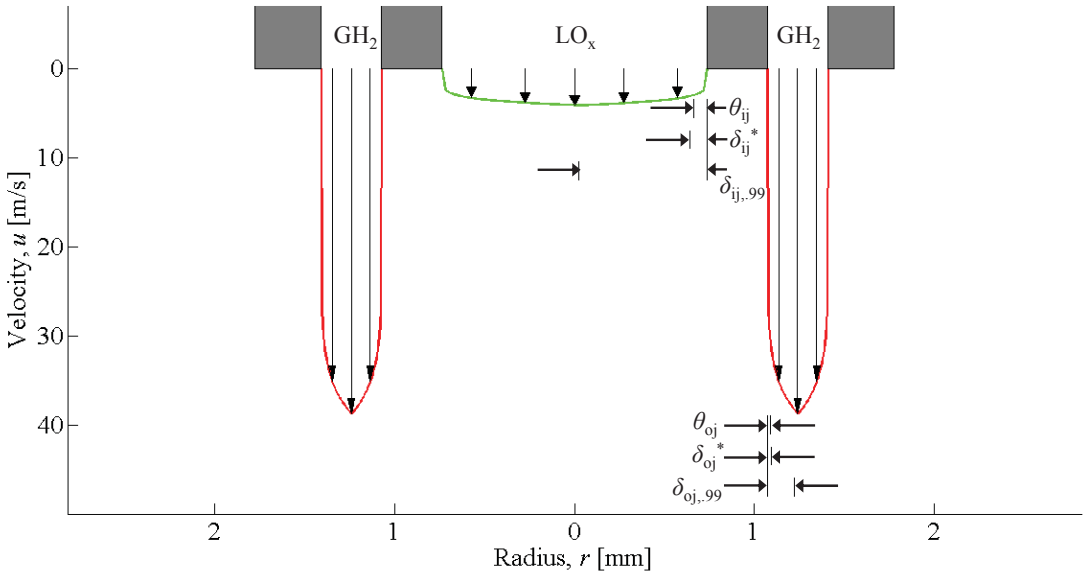

4.12: In a fully-developed turbulent flow, the exit velocity boundary layers of both the outer and inner jets are approximately equal to half the channel width. This particular diagram is an example of the fully-developed turbulent flow of gaseous hydrogen (outer jet) and liquid oxygen (inner jet) where $MR = 7$ ($\phi_{f/o} = 1.14$), $T_{oj} = T_{ij} = 145$ K, $p_c = 700$ psia (4.8 MPa), $\dot{m}_{oj} = 0.65$ g/s, and $\dot{m}_{ij} = 4.55$ g/s.

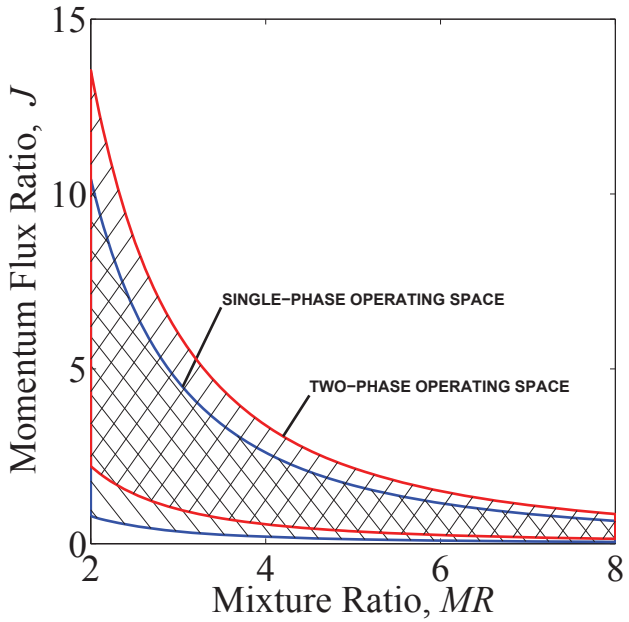

4.13: The facility's range of possible J values is best represented by a parametric map with MR. Single-phase flows (GO_x-GH_2) are bounded by blue lines and two-phase flows (LO_x-GH_2) are bounded by red lines. For reference, the stoichiometric condition for oxygen-hydrogen combustion occurs at $MR = 8$ and the fuel-oxidizer equivalence ratio $\phi_{f/o}$ for $MR = [2,4,6,8]$ is $\phi_{f/o} = [4,2,1.33,1]$.

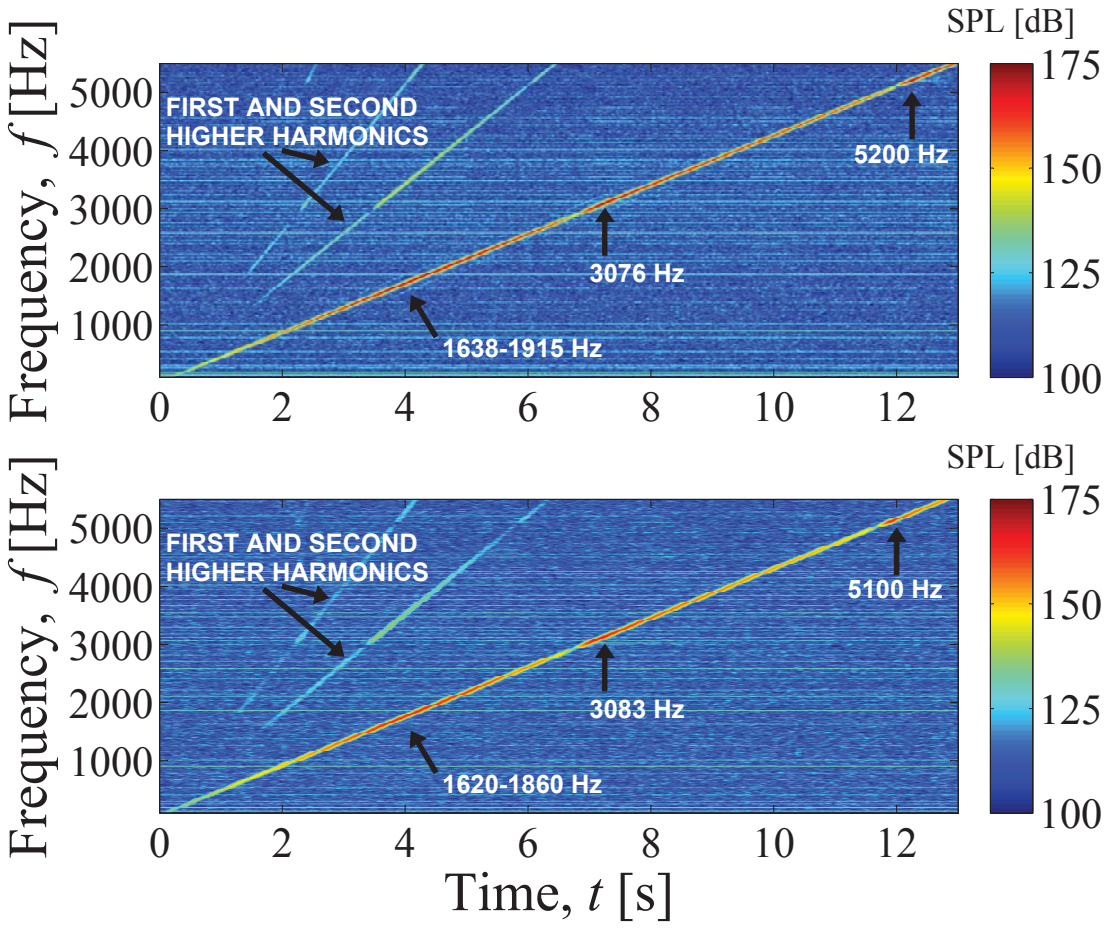

4.14: Acoustic pressure spectra results for the left piezo siren (top) and the right piezo siren (bottom). Magnitude is scaled with a sound pressure level (SPL) colormap, and key regions of piezo siren efficiency are annotated.

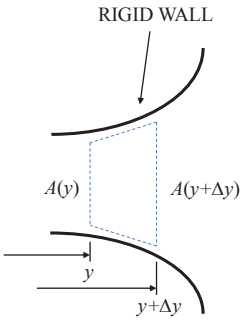

4.15: Area is a function of the transverse coordinate y, and this function is optimized for the design of acoustic waveguides such that wave amplitudes in the x and z directions are minimized while maximizing amplitudes in the y direction.

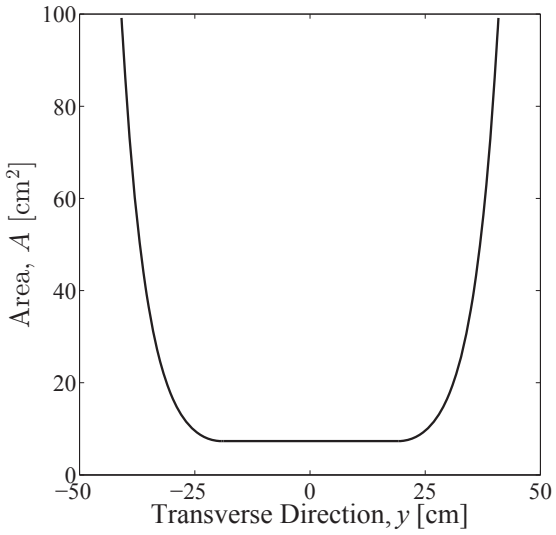

4.16: The left and right waveguides were fabricated according to the area distribution of a catenoidal horn [151]. The waveguides reduce a circular area of 99.18 cm^2 to a rectangular area of 7.33 cm^2 to match the inner chamber. The piezoelectric sirens are located at ± 40 cm.

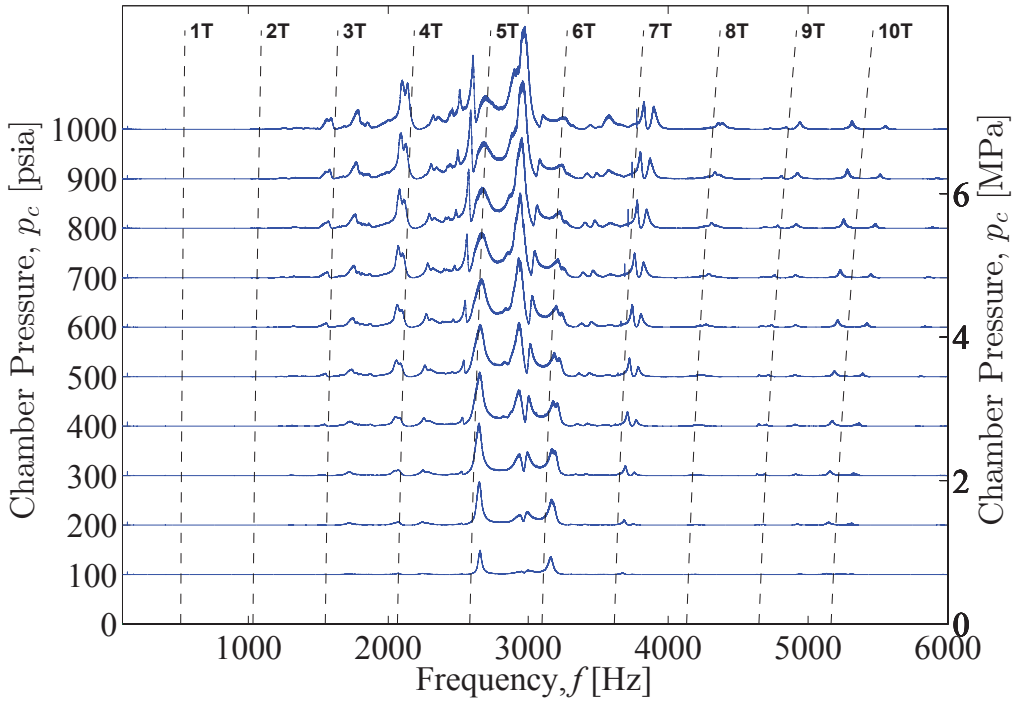

4.17: Acoustic frequency sweep results are plotted as power spectral density for PAN conditions at chamber pressures ranging from 100 to 1000 psia (6.9 MPa). Transverse modes 1T through 10T are identified with theoretical lines which transcend to higher frequency as the chamber pressure increases.

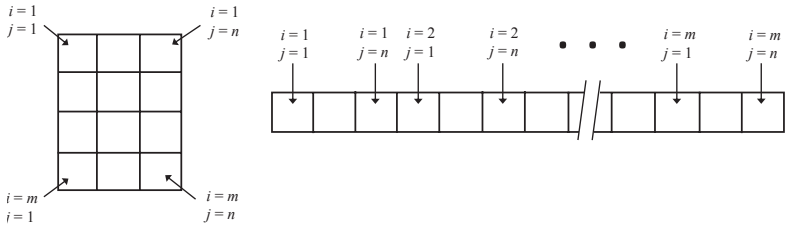

4.18: A single row of matrix **A** constructed from an $m \times n$ image for POD analysis.

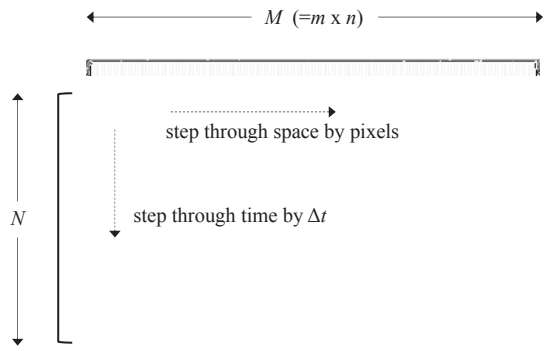

4.19: Prior to applying the POD algorithm, a complete set of images was conditioned to form a single data matrix **A** using N images and M pixels. Each row of **A** was formed by appending consecutive rows from the top row of pixels to the bottom row of pixels.

(a) (b) (c)

4.20: Sample images of a LN_2-GHe shear-coaxial jet for $J = 6$ without acoustic forcing. (a) instantaneous image (b) time-averaged image (c) cropped image used for data processing

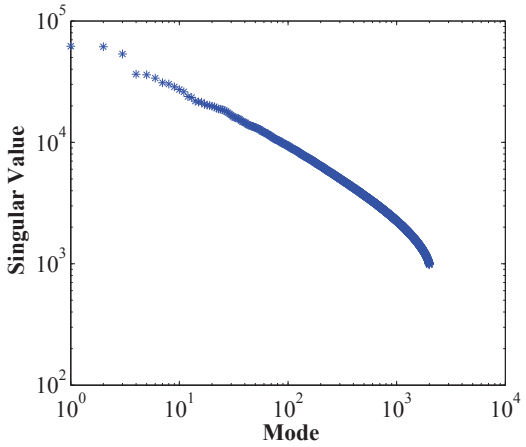

4.21: Singular values for an acoustically forced LN_2-GHe jet with $J = 2$ and $f_F = 2050$ Hz at a PN.

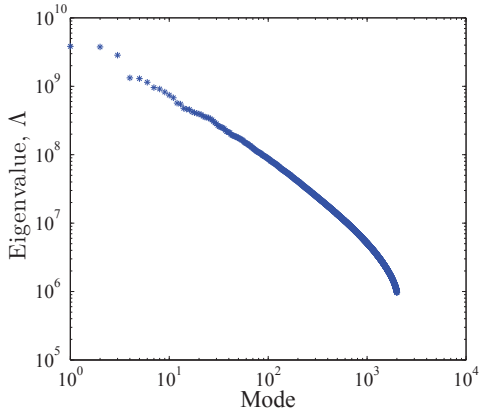

4.22: Eigenvalues for an acoustically forced LN_2-GHe jet with $J = 2$ and $f_F = 2050$ Hz at a PN. $\Lambda = \sigma^2$

(a) (b) (c)

4.23: A snapshot of an acoustically forced LN_2-GHe jet with $J = 2$ and $f_F = 2050$ Hz at a PN is shown in (a), and reconstructed POM images are shown for POD (b) mode-1 and (c) mode-2.

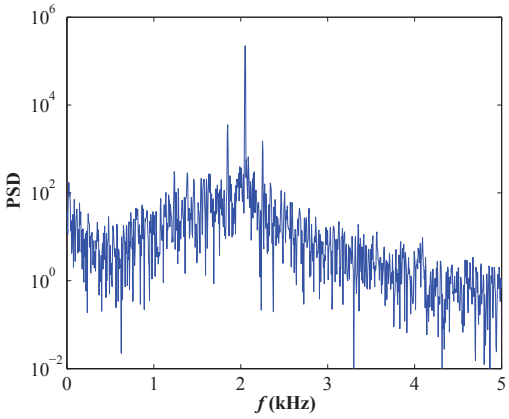

4.24: Power spectral density for mode-1 for an acoustically forced LN_2-GHe jet with $J = 2$ and $f_F = 2050$ Hz at a PN.

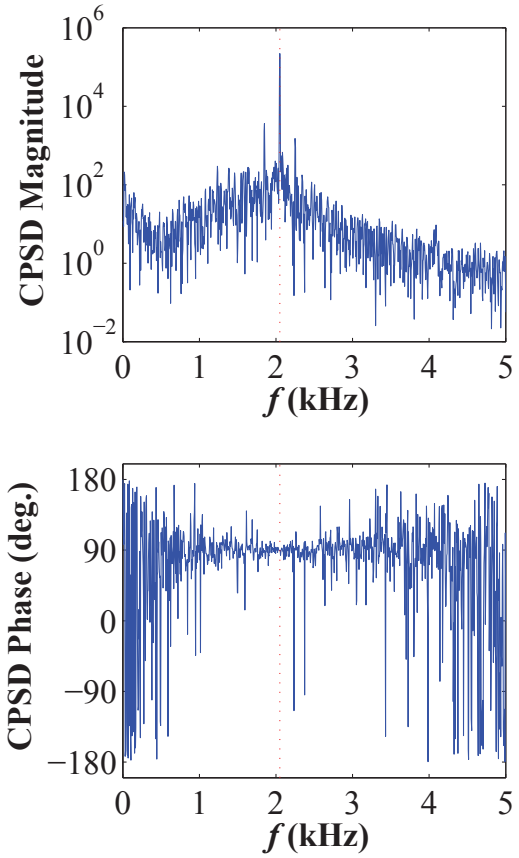

4.25: Cross power spectral density magnitude (top) and phase (bottom) for POD mode-1 and mode-2 for an acoustically forced LN_2-GHe jet with $J = 2$ and $f_F = 2050$ Hz at a PN. The vertical red line located at $f = 2050$ Hz represents the characteristic instability frequency for this condition.

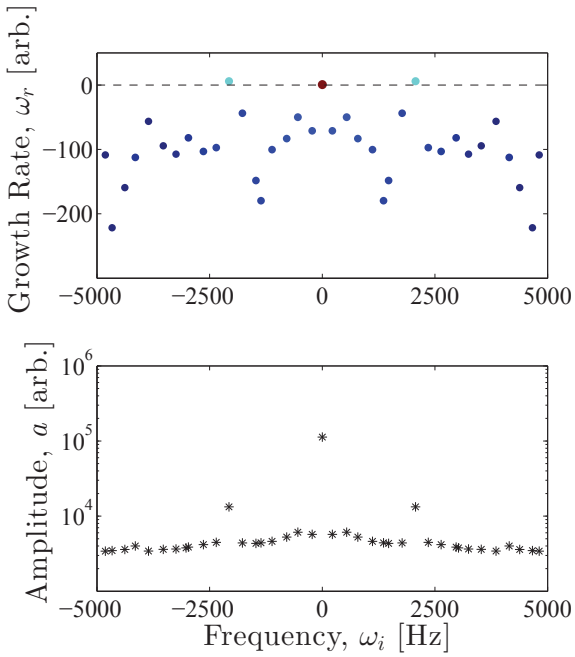

4.26: Top: Real eigenvalues ω_r (growth rate) and imaginary eigenvalues ω_i (frequency) plotted for DMD results computed for an acoustically forced LN_2-GHe jet with $J = 2$ and $f_F = 2050$ Hz at a PN. Each point represents a single mode identified by DMD, and the color and size of each point is scaled with the amplitude of each mode as calculated using eqn. 4.49. Bottom: Mode amplitudes plotted versus ω_i.

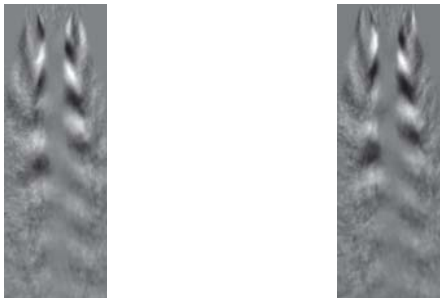

4.27: The DMD eigenvectors ϕ_r (left) and ϕ_i (right) for the unstable mode identified by cyan color in Fig. 4.26. $\lambda_i = f_F = 2050$ Hz

CHAPTER 5

Results - Shear-Coaxial Jets

5.1 Qualitative Observations of Liquid Nitrogen-Gaseous Helium Shear-Coaxial Jets

Prior to establishing quantitative conclusions from high-speed imaging results, several key qualitative observations must be mentioned. Figure 5.1 demonstrates many shear-coaxial jet features in a single snapshot, and a reduced field of view is used to increase the clarity of structures near the injector exit. Phenomena previously observed in other research studies appear in this snapshot, and are described below in order to bring to light the possible sources of shear-coaxial jet instability.

At the exit of the injector, a recirculation zone is easily distinguishable. Moving in the radial direction from the center of the jet, one first observes an interface between the liquid nitrogen inner jet and the recirculation zone formed between the inner and outer jets. This feature is labeled as (1) in Fig. 5.1. The width of the recirculation zone is equal to the inner post thickness t at the exit of the injector and converges to zero as the recirculation zone extends downstream. The recirculation zone results from a finite inner post thickness, separating the near-field features of this geometry from that of classical co-flowing streams ($t = 0$) commonly used in linear stability theory [10, 121] and other experimental studies of coaxial jets and shear layers. Note that a different injector geometry or range of flow conditions will result in a recirculation zone shape different from that observed here. Earlier work at AFRL has more thoroughly

explored the influence of t and the behavior of the recirculation zone [23, 81, 104] in nonreactive coaxial jets. As discussed earlier, when a finite value of t is used, the stability computations of Talamelli and Gavarini [108] predict not only that a wake instability can be produced, but also that the wake instability will be absolutely unstable for a small but nonzero wake velocity. Although wake velocity estimations are not included in this study and the results of Talamelli and Gavarini may not be directly applied, the existence of a recirculation zone gives potential for absolute instability.

Farther out in the radial direction, an outer shear layer is identified between the gaseous helium outer jet and the surrounding gaseous nitrogen. Although this interface is less distinguishable in analogous LN_2-GN_2 jet experiments [23, 29], the LN_2-GHe jet shown in Fig. 5.1 reveals significant contrast between the light outer jet and the more dense ambient nitrogen ($\rho_c \approx 7\rho_{oj}$). At this interface, an outer shear layer instability is formed. Since the outer and inner jets are fully turbulent at the exit, this would generally be expected to disrupt the coherence of large-scale structures in the shear layers. Early experimental conclusions by Ko and Kwan [88] found the outer shear layer to take on a different wavelength and instability frequency than those of the inner shear layer, and two different St definitions were used accordingly for the inner and outer shear layers. Far downstream, the shear layers are interact and merge, but they behave as isolated shear layers near the exit, as described by the separate St definition of Ko and Kwan. In support of defining a unique scaling law for each shear layer, preliminary POD analysis of LN_2-GHe jets also indicates different instability frequencies exist in each shear layer. This study focuses on the inner shear layer due to its direct relevance to fuel-oxidizer mixing and unsteady heat release, but a low-density outer jet provides the ability to track the outer shear layer with high-speed imaging, which is a valuable feature for future work.

Immediately downstream of the recirculation zone, a dynamic interface forms be-

tween the inner and outer jets. This interface, labeled as (4) in Fig. 5.1, is the most important feature of the jet for this particular set of experiments due to its importance in inner jet atomization and mixing. This region may be called the mixing layer or the inner shear layer, and the latter term is used here for continuity with other works. The extreme contrast between the liquid inner jet with $\rho_{ij} \approx 500\ kg/m^3$ and the light outer jet with $\rho_{oj} \approx 5\ kg/m^3$ makes for straightforward image analysis because pixel intensity gradients are most steep at the inner shear layer. Near the end of the recirculation zone, the inner shear layer appears as well-defined interfacial waves. Further downstream, the shear layer thickness increases and these waves develop into vortices. A vortex may form a ligament and break away from the dark core of the inner jet, or remain attached until reaching the end of the dark core ($x = L_b$) where large clumps and ligaments break up in the fully-merged zone. As will be shown by reduced basis methods results, these events occur within a broadband of frequencies accompanied by random noise, but a single characteristic frequency is adopted as the most significant natural instability.

An important observation was also made regarding jet symmetry. When viewing time-averaged images such as that in Fig. 4.20b, asymmetry is seen in the dark core. Upon close inspection of the injector, it was concluded that the observed jet asymmetry results from a lack of concentricity between the inner and outer streams either at the injector exit or in the upstream pathways of the injector. Following a series of efforts to achieve a perfectly symmetric jet, it was concluded that injector hardware adjustments were only sufficient to improve symmetry, but not completely eliminate the problem. Concerning application to LREs, injector asymmetry is considered a challenge, especially for propellant injection systems with dozens of injectors subject to high-volume manufacturing. Manufacturing variability is a likely cause of unpredictable behavior in LREs. Concerning the present research study, small asymmetries may be deemed acceptable if unavoidable and if asymmetric jet structures do not disrupt behaviors relevant to the scientific conclusions of the study. To this end, a verification test was performed to

inspect instability frequencies for the right and left sides of the jet. This study focused specifically on natural instability frequencies determined by POD, and compared f_{nat} for the mixing layer on the left side of the image with f_{nat} for the mixing layer on the right side of the image. For the range of conditions used in this study, the frequency difference was less than 80 Hz and the broadband spectra of each natural mode inhabited approximately the same range of frequencies. (The band of naturally excited frequencies was approximately 200 Hz, and was always found within the range from 720 Hz to 1140 Hz.) It was concluded that differences in spectral behavior are small, and further, these differences are not expected to have a significant effect on the susceptibility of the jet to external acoustic forcing. Future injector configurations should explore improved techniques for maintaining concentric inner and outer injectors without sacrificing the desired injector geometry, but the current injector configuration was accepted for this test campaign.

The natural instabilities of nonreactive shear-coaxial jets discussed above are subject to intense study due to their relevance to coaxial jet flames. As shown in Fig. 5.2, an unforced O_2-H_2 coaxial jet produces pockets of intense heat release rather than an evenly distributed flame. The images shown in Fig. 5.2 represent chemiluminescence of electronically excited OH radicals captured by blocking visible wavelengths using an optical bandpass filter. The bandpass filter was centered near 308 nm, which is the wavelength of peak radiation for OH* chemiluminescence. As discussed in chapter 2, OH* chemiluminescence is a good indication of heat release. Thus, from the sequence of high-speed images in Fig. 5.2, one can conclude that an unforced O_2-H_2 flame produces heat release which is highly dependent on both time and space, and which may experience natural acoustic coupling and/or absolutely unstable shear layer behavior [118] even in the absence of external excitation. Although the qualitative scientific conclusions of this study are limited to nonreactive jets, this sample of high-speed flame images reinforces the need to research naturally occurring instabilities in coaxial jets.

5.2 Comparisons of POD and DMD

Both proper orthogonal decomposition and dynamic mode decomposition are employed to extract organized structure from the visualization data. Although this study applies DMD to coaxial jet images for the first time, both methods have been used for a number of nonreactive and reactive experimental flows where optical techniques are the primary diagnostic tool. The following comparison weighs the advantages and disadvantages of each method such that future application of these methods may be done with specific limitations in mind.

To start the comparison, an argument should be made regarding simplicity. Although the derivations and procedures included in chapter 4 include lengthy details, the resulting code for both POD and DMD can be straightforward. In particular, POD is easier to implement in several ways. When written using singular value decomposition, the mathematical steps of POD are not as complicated as DMD, and creating a POD algorithm simply requires subtracting the time-averaged image from the image set and performing a SVD of the resulting image set. Alternatively, DMD requires separating the image set into $\mathbf{A}_1^{N-1}$ and $\mathbf{A}_2^N$, performing a SVD of $\mathbf{A}_1^{N-1}$, calculating the approximate mapping $\widetilde{\mathbf{S}}'$, solving the eigenvalue problem of $\widetilde{\mathbf{S}}'$, and finally one must use the eigenvalues and eigenvectors to calculate useful frequencies and mode shapes. This lengthy procedure is caused by a more extensive mathematical derivation, and results in DMD codes which are several steps longer than their POD counterpart. In addition, DMD requires more computational time. Using MATLAB, for example, several thousand images can be decomposed with POD in tens of minutes, but with DMD, the same image set will require hours. If instead only a few hundred images are deemed necessary to reconstruct the important modes, then either algorithm can be completed in minutes. But, interpreting the results of each tool brings to light more important differences between POD and DMD.

The most evident difference between POD and DMD is the solution of multi-frequency versus single-frequency results. Proper orthogonal decomposition describes the temporal dynamics of a mode using frequency spectra, whereas DMD represents each mode with a single frequency [152]. Dynamic mode decomposition is more advantageous in this regard. To identify the frequency of a coherent instability, the cross power spectral density from POD obfuscates the mode of interest by including magnitudes for an entire array of frequencies. Figure 5.3 shows the cross power spectral density magnitude and phase for the natural POM pair of an unforced condition at $J = 6$. The vertical red line in Fig. 5.3 is the frequency which best represents the natural mode, because this frequency has the greatest magnitude for a phase near 90°. Thus, this POM pair has a characteristic frequency of 945 Hz and is conjugate according to phase. But, this POM pair exhibits a broadband nature. The spectrum of the natural mode is broadband, and the POM pair also includes the energy of broadband turbulence, or noise, at higher frequencies. Thus, although cross power spectral density calculations were used to determine a single characteristic frequency for the dominant POM pair, each POM encompasses an array of frequencies by definition. Correctly pairing POMs and labeling pairs with a single characteristic frequency is a process which allows for user error in choosing two POMs to make a pair, and again allows for error when determining a single frequency from spectra. Some conditions pose more difficulty than the condition shown in Fig. 5.3. Several cases produced POMs which were particularly challenging to interpret, because a combination of natural and acoustically forced peaks created a spectra of "mixed" modes in a single POM. Dynamic mode decomposition, on the other hand, represents each mode with a single frequency.

As mentioned above, one disadvantage of POD lies in the potential error which results from choosing a pair of conjugate modes to form a single, physical mode. This issue is particularly relevant for unforced conditions or conditions with low levels of forcing, where the natural mode is the most dominant shear layer mode. In such a case,

although the natural mode variance is greater than that of lower ranked modes, the variance contribution is not as large as a forced mode variance contribution from high amplitude acoustic forcing, for example. Figure 5.4 shows a plot of the eigenvalues for the POD modes of an unforced jet; this plot represents the same condition as Fig. 5.3. With the exception of mode-1, there is a gradual decrease in the eigenvalue when viewing the log-log scale in Fig. 5.4. Remember, the eigenvalue of a single mode is proportional to the pixel intensity variance of that mode, as determined by POD ($\Lambda = \sigma^2$). For a very strong natural mode, a mode *pair* would appear with significantly higher eigenvalues which separate the coherent natural mode from other less significant modes. Instead, Fig. 5.4 shows only a single mode with a very large eigenvalue, and this mode merely contains low frequency (<5 Hz), steady-like motion without a conjugate mode pair. Although a coherent natural mode exists, this natural mode did not exhibit particularly strong dominance over other background modes and noise, making it challenging to identify the natural POM pair. One is left to analyze modes two and higher in search of a conjugate mode pair, rather than simply choosing a pair of highly ranked modes which stand out in an eigenvalue plot, such as mode-1 and mode-2 for the acoustically forced case in Fig. 4.22. For the experiments in this study, broadband turbulence contributes a significant amount of energy to the flow field of unforced jets, making the natural mode less distinctive.

In addition to eigenvalue plots, one must also utilize the eigenvector images and the power spectral density for each mode when searching for the conjugate mode pair. As an example, Fig. 5.5 displays the twelve highest ranked eigenvector images for the same unforced condition as Figs. 5.3 and 5.4. The POM ranking is based on eigenvalues, and therefore, is a ranking based on the variance content of each POM as defined using pixel intensity fluctuations from high-speed images sets. Since any mode pair creating a significant pixel intensity variance will be found within the highest ranked modes, Fig. 5.5 will contain the natural mode distributed between two images which have lobe

structures 90° out-of-phase in the direction of convection. The user must find the natural mode pair among these twelve POMs, as opposed to using the twenty highest ranked modes, for example. For the conditions of this study, exploring more than twelve modes was shown to consistently decrease efficiency without altering results. Although mode-1 and mode-2 contain the highest variance contribution, their eigenvector images in Fig. 5.5 do not show flow structures which are 90° out of phase, from simple qualitative inspection. Mode-1 and mode-2 represent two different phenomena. In fact, mode-1 represents low frequency (¡5 Hz) jet flapping, rather than a mixing instability. Mode-3 and mode-4, on the other hand, look very similar in lobe structure. Both contain a slightly antisymmetric inner shear layer instability manifested as dark and light lobes and mode-4 appears to be slightly shifted from mode-3. Indeed, these two modes share the same peak frequency, whereupon the pair has 90° phase difference. The PSD and eigenvector images for both mode-3 and mode-4 are shown side by side in Fig. 5.6. Upon reaching this conclusion, modes 5 through 12 need not be inspected for this particular case. Mode-3 and mode-4 represent the natural instability for $J = 6$ at $f_{nat} = 945$ Hz, and although secondary coherent modes may lie in modes 5 through 12, any other modes produce less pixel intensity variance and leave 945 Hz as the most significant natural instability in the jet. Further, a mode with a high pixel intensity variance is presumed to be a mode having a high energy contribution to the flow. A more difficult case requires CPSD inspection of many mode pairs in order to determine the natural instability mode pair. Clearly, this conclusion required thorough inspection and post-processing of the initial POD results.

In comparison, DMD does not require the pairing of modes in post-processing. Rather, the real and imaginary eigenvectors are inherently 90° out of phase, as was shown in Fig. 4.27, for example. As discussed earlier, the dynamic mode decomposition allows eigenvectors and eigenvalues to be negative and complex, whereas proper orthogonal decomposition constrains these matrices to be real and non-negative by en-

forcing orthogonality in $\mathbf{V}$. In DMD, the eigenvectors standalone as coherent modes by containing both real and imaginary components within a single dynamic mode $\mathbf{\Phi}$ which is tied to a single frequency ω. For this reason, many recent demonstrations of DMD [152, 156, 157] support the use of DMD in place of POD because instability information is often not known *a priori*, and one cannot discern the appropriate pairing of conjugate modes. This study supports the same conclusion.

Finally, for the same unforced condition presented in Figs. 5.3 - 5.5, DMD results are shown in Fig. 5.7. The x-axis is the frequency ω_i in Hertz while the y-axis is the growth rate ω_r and the amplitude a for the upper and lower plots, respectively. Each point in Fig. 5.7 represents a single mode which could be visualized by real and imaginary eigenvector images. As stated earlier, since the mean is not subtracted from the image set prior to implementing DMD, then the highest amplitude is a point at $\omega_i = 0$, which represents the mean. A point at $[\omega_i, \omega_r] = [0, 0]$ also represents the mean flow. Otherwise, significant amplitudes are not observed for any other modes. A significant amplitude could be expected at a frequency near f_{nat}, but obvious peaks in amplitude do not exist. Fig. 5.7 should also be compared to Fig. 4.26, where peak amplitudes were observed for an acoustically forced condition. For an unforced condition though, DMD is unable to clearly identify the significant amplitude of a natural mode for the conditions investigated here. If the natural mode consisted of a larger portion of the aggregate flow energy then perhaps a high value of a would be observed near f_{nat}, but such a condition does not exist for the current test matrix. This may be interpreted as an advantage of POD, whereby a mode characterized by a broadband peak from 800 to 1000 Hz is indiscernible in the single frequency dynamics of DMD, but the same natural mode is captured by a POD mode with broadband spectra. Further analysis is recommended prior to concluding that DMD cannot identify coherent structures with broadband frequencies.

In conclusion, the added complexity of DMD offers an algorithm better suited for identifying the dynamic modes in experimental image data. The *individual* modes of POD do not offer dynamic information, but only mode shapes. The eigenvectors of POD only contain a real component. The complex form of the eigenvectors of DMD inherently contains real and imaginary components which describe a single mode with two different points in phase, thus providing dynamic information regarding a single mode. Additionally, this mode is represented by a single frequency, making DMD more useful for experimental studies seeking to compare the amplitudes of different instability frequencies rather than compare the energy of complete frequency spectra, which includes random turbulence and background noise. When input data is in the form of experimental images, background turbulence is expected for high Re coaxial jets of this kind, and will indeed contribute to the result. Further investigation is needed to determine the proper technique for analyzing this flow regime. If the natural mode of interest is broadband, POD may be preferred in order to capture the complete spectra. Detailed refinement of the user inputs may also improve the performance of both DMD and POD. For example, noise filters may be applied as a pre-processing step or an ideal number of images may be shown to optimize identification of real flow dynamics. POD was sufficient for the objectives of this study, but a future implementation of DMD may offer more clarity to the results.

5.3 Susceptibility of Nitrogen-Helium Shear-Coaxial Jets to Acoustic Forcing

Utilizing the proper orthogonal decomposition, nonreactive shear-coaxial jet results are analyzed with respect to three variables at both a pressure antinode (PAN) and a pressure node (PN). These variables are the acoustic forcing amplitude, nondimensional forcing frequency $F = f_F/f_{nat}$, and outer-to-inner jet momentum flux ratio J. Low

and high values of J are used. An effort is made to separately investigate the influence of each of the these variables on the susceptibility of jets to external acoustic forcing. Specifically, for a given F and J, how will the jet respond to various amplitudes of acoustic forcing? What is the critical forcing amplitude required for the forced mode to overtake the natural mode and become the most dominant jet instability? If J is altered, will the critical forcing amplitude change? A test matrix which aims to answer these questions requires isolated control of each variable. In order to achieve this, unforced jets were first characterized for a range of flow conditions.

5.3.1 Unforced Shear-Coaxial Jets

To explore the influence of momentum flux ratio on shear-coaxial jet instabilities, the values $J = 2$ and $J = 6$ were chosen to span a range which is applicable to LREs and comparable to J values in analogous O_2-H_2 combustion experiments. To best isolate the effects of J, the dimensionless forcing frequency F should be held constant while J is varied. For the present experiments with limitations on applied frequencies associated with standing wave conditions, for a given set of acoustic forcing frequencies, the natural jet frequency f_{nat} for $J = 2$ would optimally be equal to that of $J = 6$. This is particularly challenging, because altering J requires a change in the velocities of the inner jet, outer jet, or both. Thus, shear layer instabilities may adopt different natural frequencies as a result of a modified velocity step $U_{oj} - U_{ij}$ and shear layer convective velocity U_c. Since F is dependent on f_{nat}, individually controlling J and F is challenging.

If the jet adopts a single value of St, as in the work of Birbaud *et al.* [107], Ko and Kwan [88], and others [83, 86, 87, 106], then St can be used to predict f_{nat}. When choosing characteristic velocity and length scales to define St, one must be mindful of the source of instability in a way similar to Ko and Kwan [88]. As done in eqns. 1.14 and 1.15, a Strouhal number which scales with an outer shear layer instability could

be defined with $D_h(=D_3 - D_2)$ and U_{oj}, for example. Conversely, a Strouhal number which scales with an inner shear layer instability should use a smaller diameter, such as D_1, and velocities such as U_{ij} or $(U_{ij} + U_{oj})/2$, which better characterize the inner shear layer region. As shown by works in linear stability theory [10, 121], a change in jet velocities or densities is likely to produce a change in f_{nat}. Thus, to use St as a tool for predicting f_{nat} of the inner shear layer the characteristic definition of St must account for the velocities *and* densities of both the inner and outer jets. Consequently, the shear layer convection velocity of eqn. 1.10 from Dimotakis [89] was chosen as a characteristic velocity for defining St and will be labeled as $U_{c,th}$ hereafter. The formula is included here for convenience.

$$U_{c,th} = \frac{U_{ij}\rho_{ij}^{\frac{1}{2}} + U_{oj}\rho_{oj}^{\frac{1}{2}}}{\rho_{ij}^{\frac{1}{2}} + \rho_{oj}^{\frac{1}{2}}}. \tag{5.1}$$

The dramatically different densities of liquid nitrogen and gaseous helium are included as ρ_{ij} and ρ_{oj}, respectively. By including ρ_{ij} and ρ_{oj}, the shear layer convection velocity better characterizes the present set of experiments. This approach aims to describe the velocity of inner shear layer instabilities represented by vortices which are observed as the most significant structures in the mixing region. For an isodensity shear layer, the convection velocity may be approximated by velocities alone. For example, the mean velocity $U_M = (U_{ij} + U_{oj})/2$ is a more appropriate approximation of U_c in that case, which is found by simply applying eqn. 5.1 for $\rho_{oj} = \rho_{ij}$. Instead, the two-phase flows of interest here ($\rho_{ij} \approx 100\rho_{oj}$) are expected to produce shear layer convection velocities dependent on the density difference as well as the velocity difference. Equation 5.1 is presumed to be an appropriate velocity scale if indeed the natural jet instability frequency matches that of the inner shear layer rather than another source of instability, e.g. the outer shear layer. If the preferred mode of the jet is produced at the outer shear layer or the wake of the recirculation zone, then a different definition of St will be required.

Finally, a definition of St requires a characteristic length scale. Again, to define St for natural jet instability which originates at the inner shear layer, the characteristic length scale is chosen to be approximately equal to the diameter at which the inner and outer jet meet. The exact location at which the outer and inner streams meet is dependent on flow conditions, thus an approximation is required. This characteristic length scale is taken as the average of the inner and outer diameters of the inner injector, D_1 and D_2, respectively, i.e.

$$D_{eff} = \frac{D_1 + D_2}{2}. \tag{5.2}$$

Traditionally, the most important length scale in shear layer instability is the shear layer thickness at the trailing edge, which is dictated by boundary layer thickness at the injector exit. For the present experimental conditions though, fully developed turbulence creates a boundary layer thickness which is approximately equal to the jet radius, making the diameter an appropriate length scale for this particular St definition. The Strouhal number is then defined as

$$St = \frac{f_{nat} D_{eff}}{U_{c,th}}. \tag{5.3}$$

With the assumption that this experimental configuration manifests a constant, preferred value of St for the unforced jet, this scaling law is used to predict f_{nat} values which will be adopted in experiments at $J = 2$ and $J = 6$. In principle, f_{nat} can be controlled by $U_{c,th}$ as one moves from $J = 2$ to $J = 6$.

The validity of this experimental approach and the assumption of constant Strouhal number is assessed by plots in Figs. 5.8 and 5.9. First, a plot of natural frequency versus $U_{c,th}$ is shown in Fig. 5.8. The values of f_{nat}, as determined by the most dominant POM pair, are shown to increase with $U_{c,th}$ as expected. A series of experiments were conducted for $U_{c,th} \approx 6$ m/s which produced $f_{nat} \approx 1$ kHz, and four additional cases were conducted for $U_{c,th} \approx 12$ m/s which produced a range of f_{nat} from 2 kHz to 3 kHz. More importantly, one must note that half of the points in Fig. 5.8 have a nominal

momentum flux ratio of $J = 2$, while half possess a nominal value of $J = 6$. Specifically, $U_{c,th}$ was held constant at 6 m/s while adjusting both the inner and outer jet velocities to achieve $J = 2$ and $J = 6$. This step was repeated for $U_{c,th} \approx 12$ m/s. Refer to appendix A for a table of results for all cases. Due to the repeatability achieved at 6 m/s, this condition was chosen for all acoustically forced flow conditions presented in the following section, where f_{nat}, and thus F, can be held constant while isolating the effects of J on the susceptibility of jets to acoustic forcing.

For the same data as in Fig. 5.8, a plot of St versus J is shown in Fig. 5.9. Although the collection of points has a calculated mean Strouhal number of 0.30, there is a significant amount of scatter, especially among cases where $U_{c,th} \approx 12$ m/s. Therefore, $St = 0.30$ may be a reasonable constant for the preferred mode, but an improved estimate of a characteristic velocity may reduce scatter in St and increase accuracy when predicting f_{nat}.

To test the validity of eqn. 5.1, shear layer convection velocities were experimentally measured via image analysis. Consider an array of pixels shown by the green curve in Fig. 5.10. The set of pixels along the green curve are chosen to represent the inner shear layer region, where vortices are located on the outer edge of the dark core. For a single pixel lying on the green curve, the pixel intensity will oscillate from low (dark) to high (light) as a pocket of dense fluid leaves the area. The oscillating behavior will continue as vortices pass this point in space over a duration in time. When the entire green curve is considered rather than a single point, then vortices will transcend through the array of pixels, creating areas of dark and light pixels which move in time. Fig. 5.11 demonstrates this concept. On the y-axis the shear layer curve coordinate s is nondimensionalized by D_1, while the x-axis is time in milliseconds. A diagonal streak illustrates the convection of inner shear layer vortices, or waves, which begin near the injector exit and travel downstream as time advances from one image to the next, and so on. Very close to

the injector, $\frac{s}{D_1} \approx 1$, a dark horizontal bar in Fig. 5.11 results as the signature of the end of the recirculation zone. The convection velocity upstream of this dark horizontal feature is less than the shear layer convection velocity downstream of the recirculation zone, where the much faster outer jet meets the inner jet. The streaks which appear at $\frac{s}{D_1} > 1$ are of interest here. The slope of a single streak, $\Delta s/\Delta t$, is the velocity of the coherent structure represented by the streak. To make an experimental estimate of the shear layer convection velocity $U_{c,meas}$, a collection of eight structures represented by dark diagonal lines in Fig. Fig. 5.11 were randomly chosen and their velocities were averaged to find a single estimate of $U_{c,meas}$ for each experimental condition.

Fig. 5.12 shows a plot of the experimental and theoretical convection velocities. For reference, a dashed line is plotted for $U_{c,meas} = U_{c,th}$. For low convection velocities, $U_{c,th}$ is an excellent approximation of the actual velocity. For a limited amount of data acquired for higher convection velocities though, $U_{c,th}$ under-predicts the velocity which is actually observed. This discrepancy may explain the scatter observed in St when defined using $U_{c,th}$. To confirm this, Fig. 5.13 shows a plot of St versus J using only experimentally measured values. The deviation previously caused by low estimates of U_c has been reduced, and the preferred mode of $St = 0.30$ is seen for both $J = 2$ and $J = 6$. Although Crow and Champagne [106] investigated single jets, they also observed a preferred mode of $St = 0.30$. This mode identified by their measurements may be analogous to the natural instability observed in this study, be it with different velocity and length scales used to define St. Further inspection would be required to reach a conclusion in this regard. Regardless, the LN_2-GHe shear-coaxial jet maintains a preferred instability scaling of $St \cong 0.30$ for the range of flow conditions explored in this study, and may be used to predict the most dominant natural jet instability frequency when an accurate inner shear layer convection velocity is used.

5.3.2 Shear-Coaxial Jets Subject to Acoustic Forcing

To explore the influence of acoustic forcing amplitude, nondimensional forcing frequency, and momentum flux ratio, results are organized to portray two important concepts. First, similar to lock-in diagrams created in Getsinger *et al.* [122] and Sreenivasan *et al.* [123], diagrams will be used to show the minimum forcing amplitude required for the natural instability of a given flow condition to be overtaken by external acoustic forcing. Second, the same diagrams will quantify the significance of the forced mode via the forced mode pixel intensity variance contribution Ψ as determined by eqn. 4.25. Two such diagrams will be presented, one with results for jets located at a PN and one for jets located at a PAN.

5.3.2.1 Jets Located at a Pressure Node

The first forcing susceptibility diagram is shown in Fig. 5.14, including 36 points for jets located at a PN. The x-axis is the nondimensional forcing frequency F determined using experimental values of f_F and f_{nat}. Three different values of the forcing frequency, $f_F = [1700, 2050, 2600]$ Hz, and two different values of the natural jet frequency $f_{nat} = [921, 970]$ Hz, are included, creating six different values of F shown in Fig. 5.14. Nondimensional forcing frequencies of 1.85, 2.23, and 2.82 correspond to $J = 2$, where the mean natural frequency is 921 Hz. Nondimensional forcing frequencies of 1.75, 2.11, and 2.68 correspond to $J = 6$, where the mean natural frequency is 970 Hz. Although it is desired to include cases where $F < 1$, F was maintained above unity due to facility constraints. The y-axis is the acoustic forcing amplitude represented by u' rather than the measured p'. This is done to describe amplitude with a variable which is more pertinent to a PN, where pressure amplitudes are approximately zero and the jet is instead perturbed by acoustic velocity fluctuations. The acoustic velocity perturbation is

estimated using

$$u' = \frac{p'_{max}}{\rho_c c}, \tag{5.4}$$

where p' is the average of the maximum pressure perturbation amplitudes at the adjacent PANs located at $y = \lambda/4$ and $y = -\lambda/4$. Equation 5.4 requires that acoustic waves are linear and one-dimensional, which is supported by experimental observation for the amplitudes employed in this study. After assuming that a perfectly sinusoidal wave takes shape in the transverse direction, p' at adjacent PANs were calculated by interpolation using pressure amplitude measurements at a point between a PN and a PAN, e.g. $y = \lambda/8$ and $y = -\lambda/8$. The ambient chamber density ρ_c and speed of sound are determined as functions of the measured chamber pressure and temperature following REFPROP fluid properties. Finally, the forcing susceptibility diagram utilizes different symbol sizes to illustrate the forced mode variance contribution Ψ. For example, a large, black-filled symbol represents a high value of Ψ, common in conditions with high levels of acoustic forcing. Conversely, low forcing amplitudes often result in small values of Ψ. In fact, conditions with low levels of forcing often cause the naturally occurring instability to remain dominant, and this type of result is represented by unfilled symbols and symbols filled with an $\times$.

First and foremost, Fig. 5.14 shows that an increase in u' increases the likelihood that the forced mode will overtake the natural jet instability as the most dominant mode. This should be expected, and will remain true for all results presented in this study. Next, as u' is increased beyond the point where the forced mode overtakes the natural mode, the variance contribution from the forced mode continues to increase, giving the forced mode greater and greater dominance over the natural behavior of the jet. There are exceptions to this relationship though. For $F = 2.68$ and $J = 6$, increasing the forcing amplitude beyond $u' = 0.3$ m/s did not result in a greater variance contribution from the forced mode.

Secondly, Fig. 5.14 reveals that the susceptibility of the jet to acoustic forcing at a PN is dependent on F. This is readily apparent for $J = 6$. For $J = 6$, the forced mode overtakes the natural mode at $u' \approx 0.1$ m/s for the lowest forcing frequency, but an equivalent amplitude at the highest frequency does not produce a jet response. In fact, the forced mode for the highest frequency was not detected within the twelve highest ranked POMs determined by POD analysis until the forcing amplitude was increased to $u' = 0.17$ m/s. An even greater amplitude was necessary for the forced mode to overtake the natural mode. This result corresponds directly to that of absolute instability lock-in experiments [118, 122, 123], whereby increasing F from unity causes greater resistivity to forcing. While this phenomenon alone does not allow one to conclude that absolute instability exists, it does indicate that naturally occurring instabilities are more difficult to overcome with forcing at higher frequencies, consistent with absolutely unstable behavior [25, 118].

If the natural jet instability is only convectively unstable though, a separate explanation for the results in Fig. 5.14 could possibly exist. Since the work of Buffum and Williams [27], it has been known that transverse acoustic forcing can induce sinusoidal whipping motions in a jet column. An instability of this type is not strictly a shear layer instability, but is instead a bulk column mode resulting from periodic changes in transverse momentum. This behavior is shown in the snapshot sequence in Fig. 5.15 for $J = 2$, and is also supported by the eigenvector images of the forced mode in Fig. 5.16. More recently, Carpentier *et al.* [26] and Baillot *et al.* [16] recognized that side-to-side or sinuous motions observed by Buffum and Williams are highly dependent on frequency, and that a short acoustic period will prevent a jet from gaining significant spanwise momentum prior to a reverse in the transverse acoustic velocity which occurs at a PN. Not only do the qualitative results of this study demonstrate antisymmetric, sinusoidal jet motions, but Fig. 5.14 supports the principle established by Carpentier *et al.*, stating that at a fixed amplitude, increasing f_F will decrease the amplitude of transverse jet

motions. A similar relationship with f_F was also observed in experiments by Graham *et al.* [104] and Rodriguez *et al.* [81], where a higher f_F caused a degraded sensitivity to transverse acoustic forcing. The observation of sinuous or antisymmetric shear-coaxial jet motion in the vicinity of a PN actually shares some similarities with the droplet combustion experiments described in Chapters 2 and 3 of this dissertation. For all fuels explored and for virtually all amplitudes of acoustic excitation, burning droplets situated precisely at a PN during excitation did not have stable, uni-directionally oriented flames. As described in section 3.2.2, the flames under these circumstances switched back and forth in time, and did not stabilize to an orientation to one direction or the other. This asymmetric, sinuous-like distortion of the flame may have similarities to the sinuous motions quantified for shear-coaxial jets situated at a PN.

Lastly, to show the effect of J, Fig. 5.17 shows a plot of Ψ versus u' for $J = 2$ and $J = 6$. For both momentum flux ratios, low values of u' result in negligible variance contribution from the forced mode as determined by the twelve highest ranked POMs. Although it is not clear that J influences the level of forcing necessary to overtake the natural mode, Fig. 5.17 shows that J influences receptivity to acoustic forcing by viewing the magnitudes of Ψ for each case, consistent with absolutely unstable behavior. The forced mode variance contribution values for $J = 6$ reach magnitudes which are generally larger than those for $J = 2$. For $J = 2$, it appears that a form of saturation has occurred when reaching $u' \approx 0.4$ m/s; higher forcing amplitudes do not excite a greater variance contribution from the forced mode. Conversely, $J = 6$ creates more receptive conditions and values of Ψ which are nearly twice as large as their $J = 2$ counterpart.

5.3.2.2 Jets Located at a Pressure Antinode

A second forcing susceptibility diagram is shown in Fig. 5.18, including 41 points for jets located at a PAN. The y-axis is the acoustic forcing amplitude represented by p' as

measured by the dynamic pressure transducer located directly behind the jet as viewed from the camera. This measurement, named $p_{dyn,2}$, is most important when the jet is located at a PAN. At this location, $u' \approx 0$, making p' the primary cause of acoustically induced jet dynamics.

As shown in Fig. 5.18, p' values of approximately 3.5 kPa are required in order to observe the forced mode in the jet dynamics. When viewing the twelve highest ranked POMs, acoustically forced cases with $p' < 3.5$ kPa did not produce any evidence of the forced mode. A further increase in p' produces a POM pair for the forced mode among the highest POMs, but an amplitude of $\sim$7 kPa is necessary for the forced mode to overtake the natural mode. This is true for both momentum flux ratios and all nondimensional frequencies shown in Fig. 5.18. For example, results for $J = 6$ and $F = 1.75$ show that a forcing amplitude of $p' = 6.27$ kPa asserts significant forced mode dynamics in the jet, but increasing the amplitude to $p' = 7.58$ kPa caused the forced mode to overtake the natural mode as the most dominant instability.

To best explain the influence of acoustic forcing frequency on jet dynamics, the jet's qualitative behaviors may first reveal the mechanism by which pressure fluctuations induce a forced mode instability. Jets located at a PN exhibit transverse side-to-side motion, while jets located at a PAN were observed to have axisymmetric vortex rings at the inner shear layer. This behavior is shown in the snapshot sequence in Fig. 5.19 for $J = 2$, and is also supported by the eigenvector images of the forced mode in Fig. 5.20. These vortex rings, or "puffs", are produced at the injector exit and become the most dominant mode for $p' \gtrsim 7$ kPa. Vortex rings have also been observed in previous experiments at AFRL [81, 104, 105]. Baillot *et al.* [16] observed similar axisymmetric instability for shear-coaxial jets at atmospheric pressure, and concluded that vortex rings result from outer jet gas pulsations. A momentary rise in chamber pressure at the beginning of an acoustic pressure cycle was said to impede the flow of the gas annulus,

followed by an increase in jet velocity due to the subsequent decline in pressure in the latter part of the acoustic cycle. Pulsations were not observed for the dense, liquid inner jet [16]. Using the following analytical derivation, the PAN jet pulsation phenomenon is shown to indeed be dependent on jet density as well as acoustic forcing frequency.

Consider Newton's Second Law when applied to the mass of fluid inside an injector. The downstream end of this mass of fluid is subject to a periodic force with an amplitude of F'_{PAN} at the injector exit, due to a pressure fluctuation p'. The mass of the body of fluid is equal to the product of density ρ and volume V, and the body of fluid has a periodic acceleration a which results from a periodic force applied at the exit of the injector. To obtain the streamwise u' resulting at the exit of an injector at a PAN location, Newton's second law is applied to one quarter of an acoustic cycle which yields

$$\begin{aligned} F_{PAN} &= ma \\ \int_0^{\frac{1}{4f_F}} F_{PAN}\mathrm{d}t &= \int_0^{\frac{1}{4f_F}} ma\mathrm{d}t \\ \int_0^{\frac{1}{4f_F}} F'_{PAN}\sin\left(2\pi f_F t\right)\mathrm{d}t &= \rho V \int_0^{\frac{1}{4f_F}} \frac{\mathrm{d}u}{\mathrm{d}t}\mathrm{d}t. \end{aligned} \tag{5.5}$$

Carrying out the integration of force and acceleration results in

$$\begin{aligned} F'_{PAN}\left[-\frac{1}{2\pi f_F}\cos\left(2\pi f_F t\right)\right]_0^{\frac{1}{4f_F}} &= m\left[u\right]_0^{\frac{1}{4f_F}} \\ F'_{PAN}\left[-\frac{1}{2\pi f_F}\left(\cos\frac{\pi}{2} - \cos 0\right)\right] &= m\left[0-(-u')\right] \\ \frac{F'_{PAN}}{2\pi f_F} &= mu', \end{aligned} \tag{5.6}$$

which can be simplified further by writing F'_{PAN} as the product of the injector exit area A and the pressure amplitude at the jet p' and by writing V as the product of A and the injector length l. These substitutions give a straightforward solution for the injector

fluid velocity fluctuations u' induced by the chamber pressure oscillations p' at a PAN,

$$u' = \frac{p'}{2\pi f_F \rho l} \tag{5.7}$$

This solution may be applied to the inner or outer jet by using ρ_{ij} and l_{ij} or ρ_{oj} and l_{oj}, respectively. If integration is performed over one-half an acoustic cycle rather than one-quarter of an acoustic cycle, then the same solution is reached. Eqn. 5.7 is a relation for injector-acoustic interactions occurring at a PAN, but should be treated as an approximate solution, as it does not account for the geometry of an injector plenum upstream of the constant area section l, nor does it account for potential acoustic resonance in the injector. Eqn. 5.7 also treats the fluid in the injector as a single body with constant mass, neglecting compressibility. Although, the assumptions made to reach this solution limit its applicability, the solution advocates that for a constant p' the pulsation velocity u' is inversely proportional to f_F and ρ.

Therefore, the derivation of the injector pulsation velocity and the results shown in Fig. 5.18 support the conclusions of Baillot *et al.* [16] by asserting an inverse relationship between both f_F and ρ and the amplitude of resulting outer jet pulsations. For the injector of interest here, l_{ij} and l_{oj} are of the same order of magnitude ($l_{ij} = 1.8 l_{oj}$), and differences in the pulsation amplitude u' are caused by a difference in ρ_{ij} and ρ_{oj}. Since $\rho_{ij} \approx 100 \rho_{oj}$, pulsations in the liquid nitrogen inner jet will be negligible in comparison to those in the gaseous helium outer jet. Therefore, one should expect the forced mode will influence the inner shear layer instability when the outer jet pulsations reach a significant velocity amplitude. Meanwhile, inner jet pulsations can be ignored. The inner jet may be indirectly effected by axisymmetric vortex rings which form at the exit of the outer jet and convect downstream, but will be less effected by chamber pressure fluctuations directly. As a result, the outer jet pulsation phenomenon will control the susceptibility of the jet to acoustic forcing. This concept is reenforced by two conclusions of this study. First, Fig. 5.18 shows that increasing the nondimensional forcing frequency F requires

an increase in p' in order for the forced mode to overtake the natural mode. Second, a critical PAN forcing amplitude will be shown to depend solely on outer jet conditions, because the forced mode is manifested specifically via the outer jet.

Concerning forcing frequency, comparing the minimum and maximum values of F for both $J = 2$ and $J = 6$ reveals the salient effect of F. Fig. 5.18 shows that for $J = 2$, at $F = 1.85$ a forcing amplitude of $p' = 6.00$ kPa caused the forced mode to overtake the natural mode, but at $F = 2.82$ an increased forcing amplitude of $p' = 7.93$ kPa was insufficient and the natural instability remained most dominant. For $J = 6$, at $F = 1.75$ a forcing amplitude of $p' = 4.55$ kPa and $p' = 6.27$ kPa caused the forced mode to appear within the twelve highest ranked POMs, an indication that the forced mode is nearly as significant as the natural mode in terms of pixel intensity variance. Further increasing the amplitude to $p' = 7.58$ kPa caused the forced mode to overtake the natural mode. Conversely, for $J = 6$ and $F = 2.68$, $p' = 0.95$ did not produce a significant forced mode, as the forced mode POM pair did not appear within the twelve highest ranked POMs.

Note that although the critical amplitude increases with F, one cannot estimate that this relationship holds for $F < 1$ or near $F = 1$. The current test matrix does not include the forcing frequencies necessary to make this conclusion. In a traditional lock-in diagram for absolute instability [122, 123] the minimum amplitude necessary for lock-in forms the well-known "V" shape, and requires an increase in the minimum amplitude as F is decreased below unity. The results in Fig. 5.18 do not precisely assert this type of behavior, but data at lower forcing frequencies are not available to study the phenomenon in detail. Nevertheless, the fact that there are forcing conditions that preclude lock-in does seem to suggest the appearance of absolutely unstable shear layers.

To understand the influence of J, Fig. 5.21 shows a plot of Ψ versus p' for $J = 2$ and $J = 6$ at a PAN. Similar to Fig. 5.17, low values of p' result in approximately zero

variance contribution from the forced mode as determined by the twelve highest ranked POMs. Significant forced mode variance occurs when p' is increased to a value between 3.5 kPa and 7.0 kPa, depending on J and F. Higher amplitudes cause increased values of Ψ, but this relationship is more pronounced for $J = 6$ than $J = 2$. Similar to a PN condition, forced mode variance contributions for $J = 6$ reach values nearly twice as large those for $J = 2$. Thus, holding all other variables approximately constant, $J = 6$ exhibits greater susceptibility to external acoustic forcing than $J = 2$ when the jet is located at a PAN.

Finally, to emphasize the importance of outer jet pulsations at a PAN, an effort is made to collapse the data in Fig. 5.21 using a nondimensional forcing amplitude on the x-axis rather than the measured quantity p'. If indeed the forced mode infiltrates the inner shear layer by manipulating the outer jet flow, then outer jet pulsations must rival natural turbulence levels which are introduced into the inner shear layer by the outer jet. These natural fluctuations in the outer jet will be proportional to the dynamic pressure of the outer jet $\frac{1}{2}\rho_{oj}u_{oj}^2$, while the forced pulsations at the outer injector exit are shown to be directly proportional to p' in eqn. 5.7. As a result, $p'/\frac{1}{2}\rho_{oj}u_{oj}^2$ was chosen as a nondimensional forcing amplitude and is the new x-axis in Fig. 5.22. When compared with the dimensional plot in Fig. 5.21, Fig. 5.22 shows a more meaningful distribution at $p'/\frac{1}{2}\rho_{oj}u_{oj}^2 = 1$, where both $J = 2$ and $J = 6$ result in positive values of the forced mode variance contribution Ψ. When $p' < \frac{1}{2}\rho_{oj}u_{oj}^2$ the acoustic forcing induces a negligible effect on the jet. In conclusion, when the liquid-gas coaxial jet was acoustically forced at a PAN condition, the forced mode began to influence the inner shear layer instability when the acoustic pressure perturbation p' was nearly equal to or greater than the outer jet dynamic pressure.

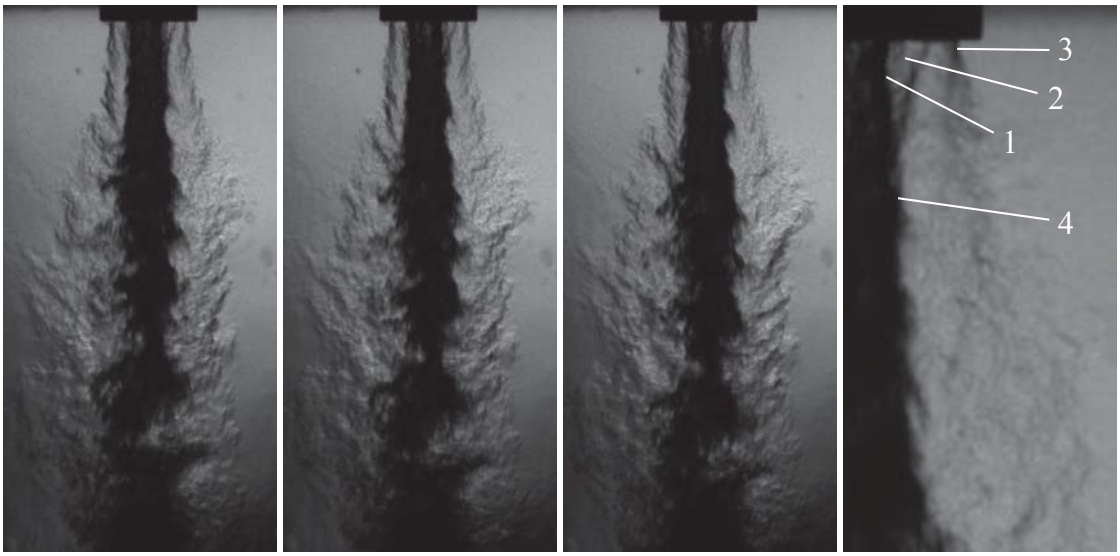

5.1: A sequence of unforced LN_2-GHe jet images acquired at a frame rate of 10 kHz, accompanied by a reduced field of view to show the (1) interface between the liquid nitrogen inner jet and the recirculation zone (2) recirculation zone (3) outer shear layer (4) inner shear layer forming at the downstream end of the recirculation zone.

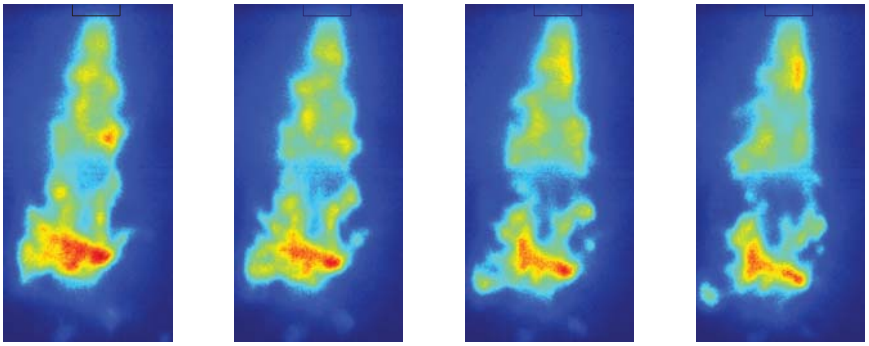

5.2: A consecutive sequence of unforced O_2-H_2 flame images acquired at a frame rate of 16 kHz. The intensifier gate duration, which is essentially the camera exposure time, is set to 61 s. Flame structures form near the injector exit and evolve as they travel downstream. $MR = 5.9$ ($\phi_{f/o} = 1.36$), $J = 2$, $p_c \approx 400$ psia $= 2.76$ MPa.

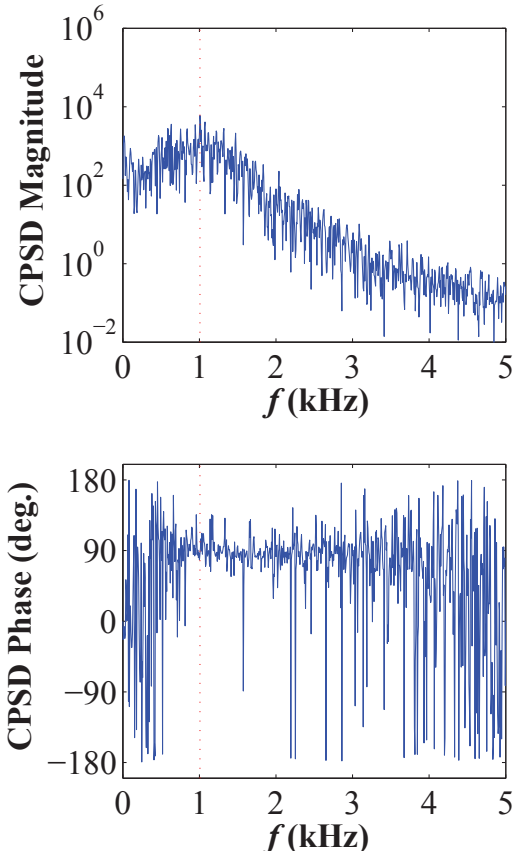

5.3: Cross power spectral density magnitude (top) and phase (bottom) for POD modes 3 and 4 for an unforced LN_2-GHe jet with $J = 6$. A vertical red line is located at $f = 945$ Hz represents the characteristic instability frequency for this particular case.

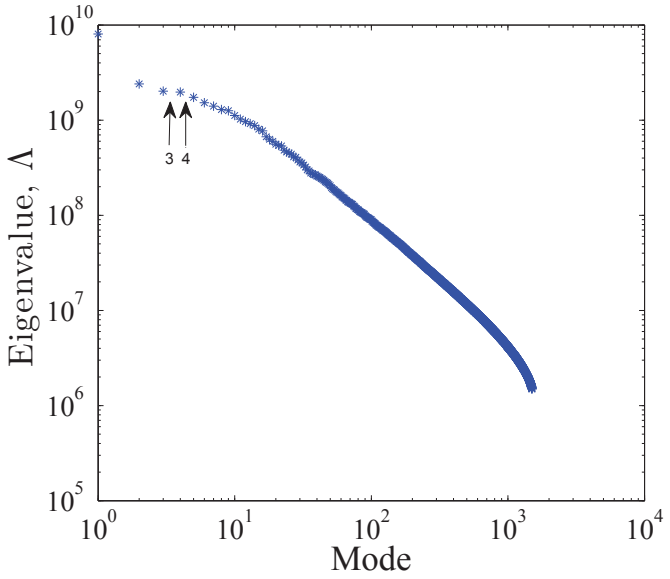

5.4: POD eigenvalues ranked according to magnitude show that although modes 3 and 4 have been chosen to assert the natural instability of the jet, the eigenvalues of modes 5-8 are nearly as high as the eigenvalues of 3 and 4. ($\Lambda = \sigma^2$)

5.5: POM images 1-12 are shown for an unforced LN_2-GHe jet at $J = 6$. Modes 3 and 4 are the highest ranked conjugate mode pair, together demonstrating a natural jet frequency of 945 Hz. The eigenvalues of modes 1 and 2 are greater than 3 and 4, but do not display coherent structures having a 90° phase difference.

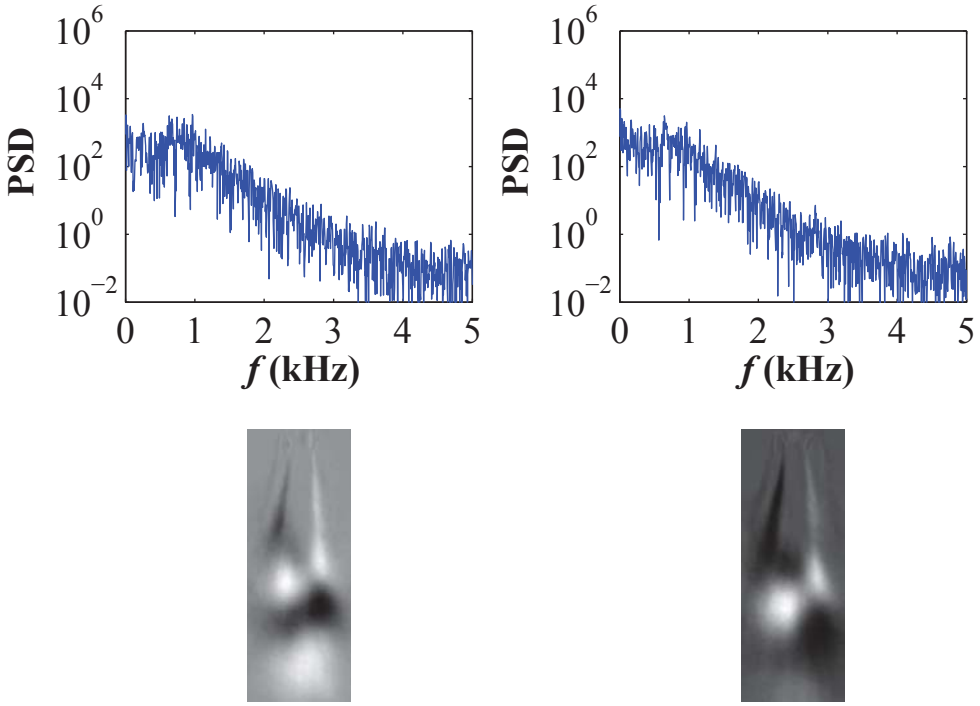

5.6: The naturally occurring mode for $J = 6$ is represented by the POM pair which consists of mode-3 (left) and mode-4 (right). Power spectral density plots are shown (top) with each corresponding eigenvector image (bottom). The natural mode is antisymmetric, and likely a helical instability. The eigenvector images of mode-3 and mode-4 appear to be 90° out-of-phase in the streamwise direction.

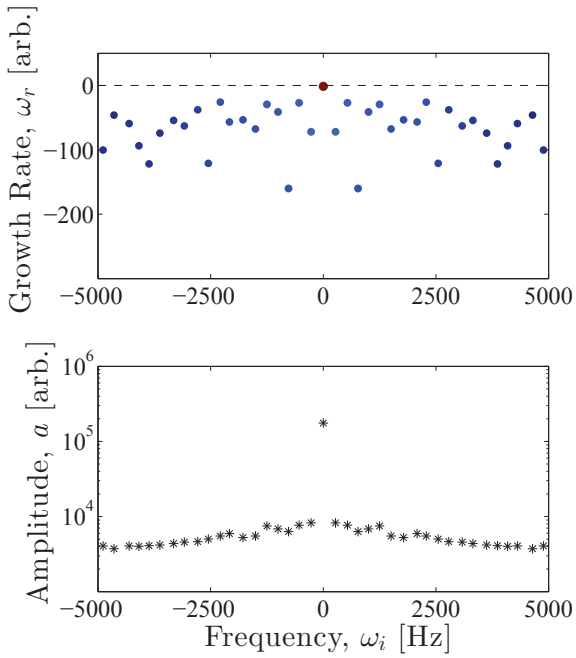

5.7: Top: Real eigenvalues ω_r (growth rate) and imaginary eigenvalues ω_i (frequency) plotted for DMD results computed for an unforced LN_2-GHe jet with $J = 6$. Each point represents a single mode identified by DMD, and the color and size of each point is scaled with the amplitude of each mode as calculated using eqn. 4.49. Bottom: Mode amplitudes plotted versus ω_i. A significant natural mode cannot be identified.

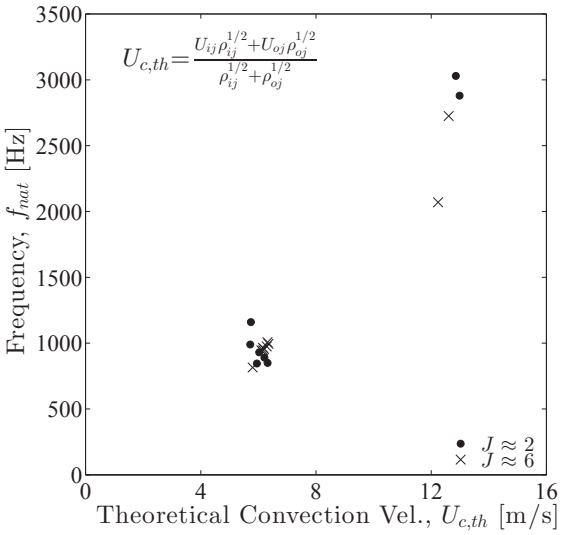

5.8: LN_2-GHe jet instability frequency, as measured by POD, plotted versus shear layer convective velocity. J is nominally maintained between 2 and 6. Each point corresponds to a point in Fig. 5.9 and exact values can be found in appendix A.

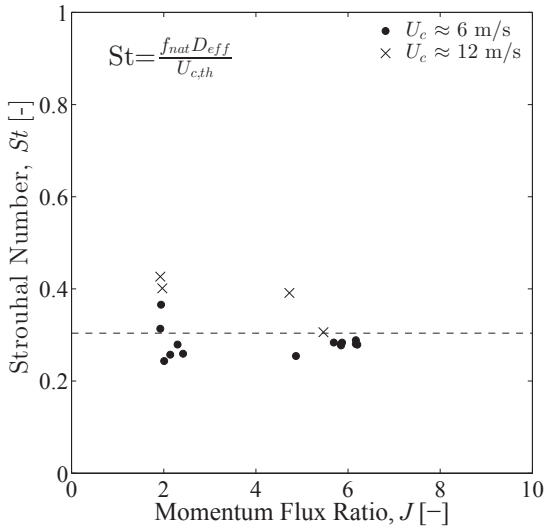

5.9: LN_2-GHe jet Strouhal number plotted versus J based on data in Fig. 5.8, using a theoretical shear layer convection velocity $U_{c,th}$.

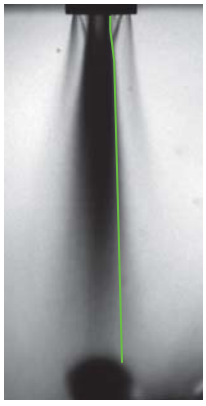

5.10: A time-averaged image of the LN_2-GHe shear-coaxial jet with the location of the inner shear layer curve s in green.

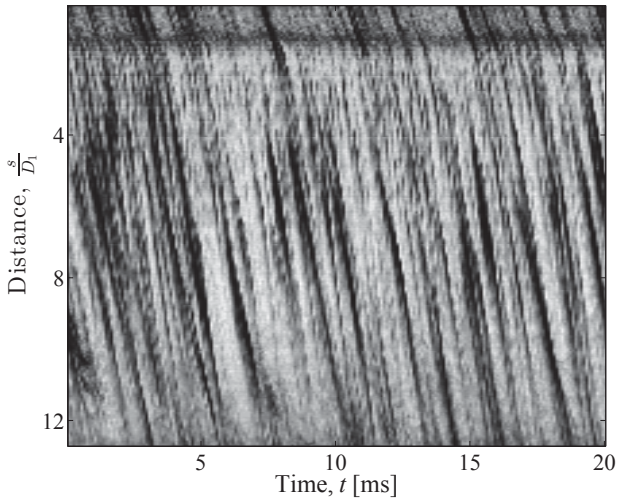

5.11: The pixels located on the shear layer curve s, defined in Fig. 5.10, shown for a period of time spanning 20 ms. Diagonal streaks are the convection of fluid structures of the inner shear layer, and the velocity of each structure is equal to the slope of each respective streak, $\Delta s/\Delta t$.

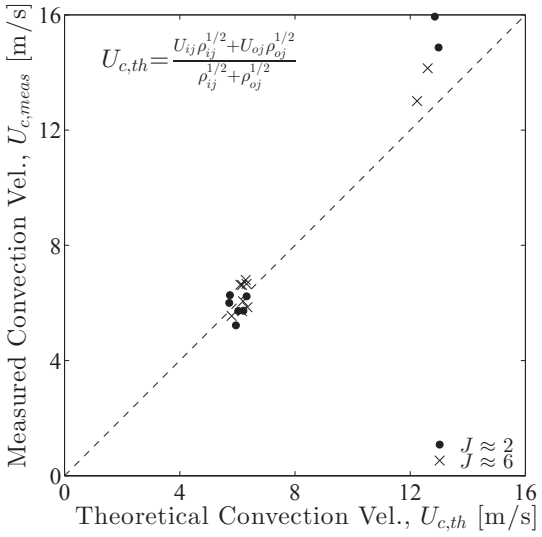

5.12: Measured shear layer convection velocities plotted versus theoretical values.

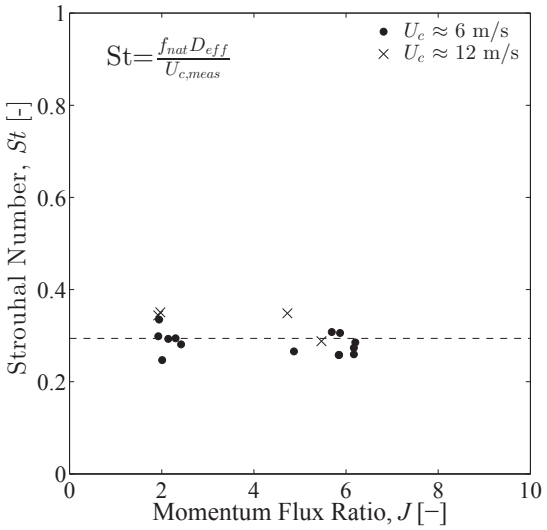

5.13: LN_2-GHe jet Strouhal number plotted versus J, using a measured shear layer convection velocity $U_{c,meas}$.

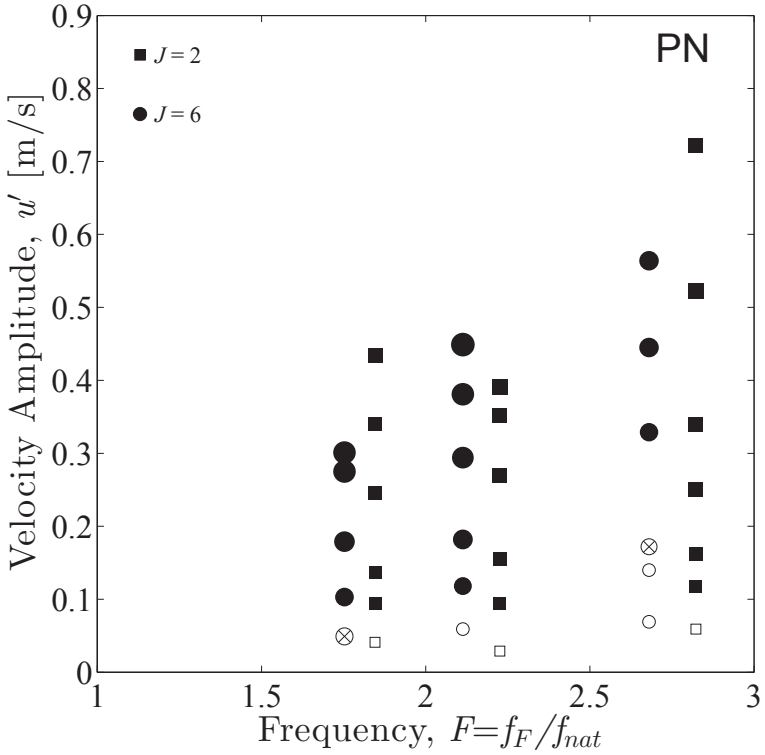

5.14: The acoustic forcing amplitude u' is plotted versus the nondimensional frequency for $J = 2$ and $J = 6$ for a jet located at a PN. Open symbols represent conditions in which the natural mode of the jet was most significant. Closed symbols represent conditions in which the natural mode was overtaken by the forced mode. The size of each symbol is scaled with the forced mode's variance contribution to the flow as determined by POD eigenvalues, e.g. large, filled symbols represent a condition where the forced mode has a large contribution to the total energy of the flow. Very small, open symbols represent a case in which the forced mode did not appear in the POD results. Symbols with an $\times$ represent cases in which the forced mode appeared in the POD results, but did not overtake the natural mode.

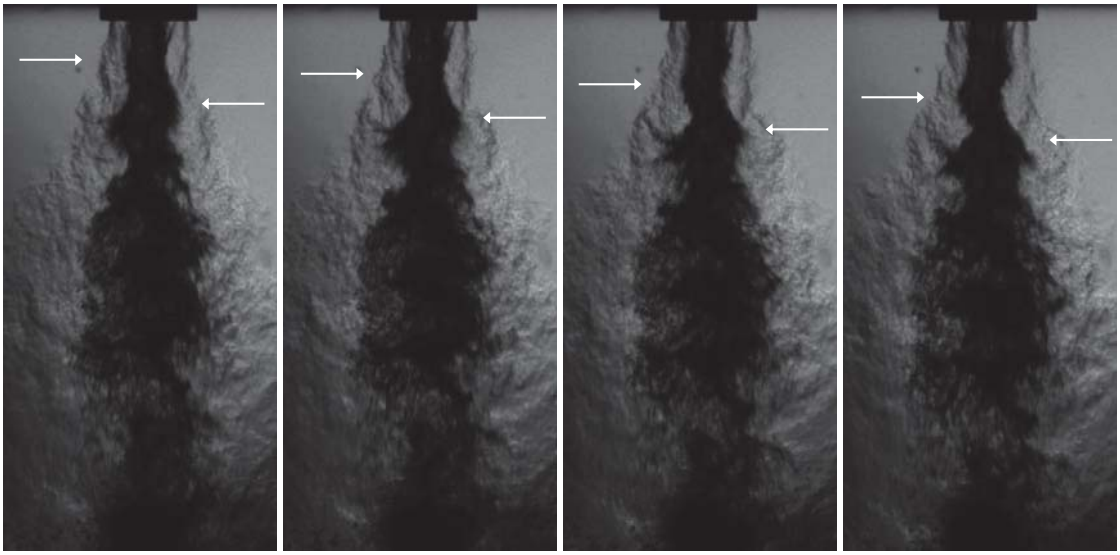

5.15: LN_2-GHe shear-coaxial jets exposed to external, transverse acoustic forcing at a pressure node. Four consecutive images are taken from a set of high-speed images acquired at 10 kHz. An antisymmetric instability forms as periodic spanwise motions caused by the acoustic velocity perturbation u'. $J = 2$, $p_c = 400$ psia $= 2.76$ MPa, $f_F = 1700$ Hz, $u' = 0.43$ m/s

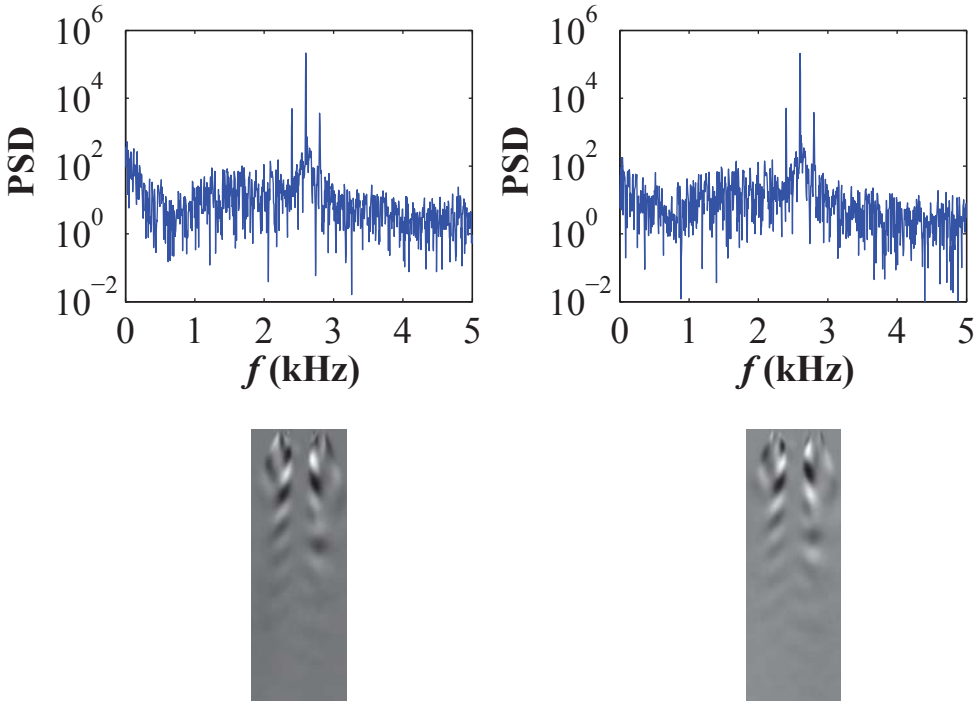

5.16: The forced mode for $J = 2$ at a PN is represented by the POM pair which consists of mode-2 (left) and mode-3 (right). Power spectral density plots are shown (top) with each corresponding eigenvector image (bottom). The forced mode occurring at a PN takes on an antisymmetric appearance. The eigenvector images of mode-2 and mode-3 appear to be 90° out-of-phase in the streamwise direction.

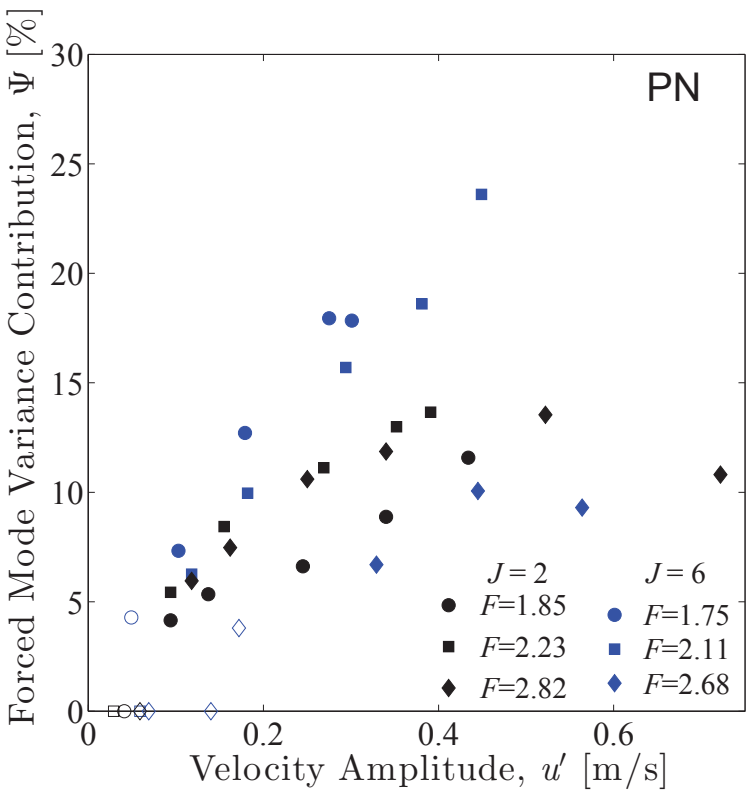

5.17: The forced mode variance contribution is plotted versus the acoustic velocity perturbation amplitude u' for $J = 2$ and $J = 6$ for a jet located at a PN. The nominal natural frequency for $J = 2$ and $J = 6$ is 921 Hz and 970 Hz, respectively. Open symbols represent conditions in which the natural mode of the jet was most significant. Closed symbols represent conditions in which the natural mode was overtaken by the forced mode.

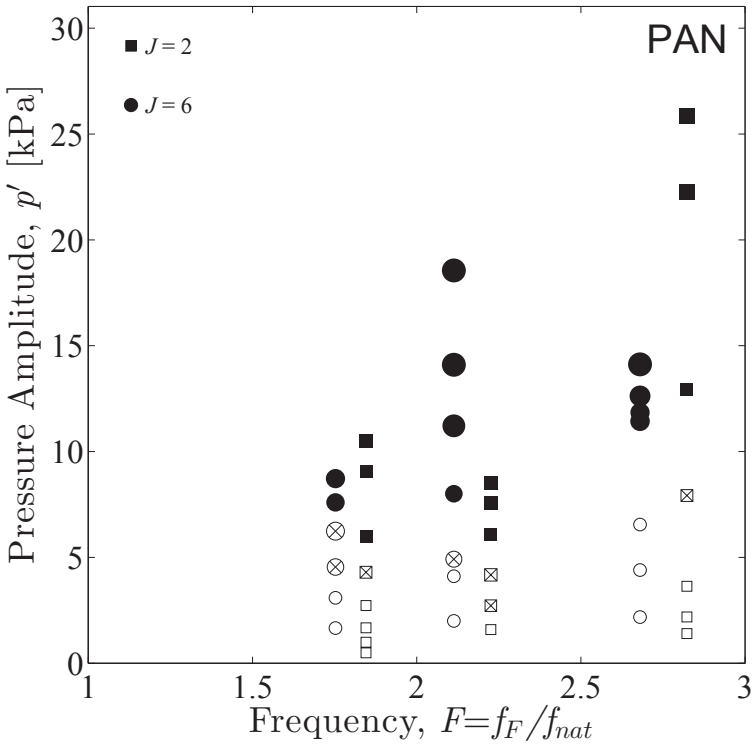

5.18: The acoustic forcing amplitude u' is plotted versus the nondimensional frequency for $J = 2$ and $J = 6$ for a jet located at a PAN. Open symbols represent conditions in which the natural mode of the jet was most significant. Closed symbols represent conditions in which the natural mode was overtaken by the forced mode. The size of each symbol is scaled with the forced mode's variance contribution to the flow as determined by POD eigenvalues, e.g. large, filled symbols represent a condition where the forced mode has a large contribution to the total energy of the flow. Very small, open symbols represent a case in which the forced mode was not exhibited in the POD results. Symbols with an $\times$ represent cases in which the forced mode appeared in the POD results, but did not overtake the natural mode.

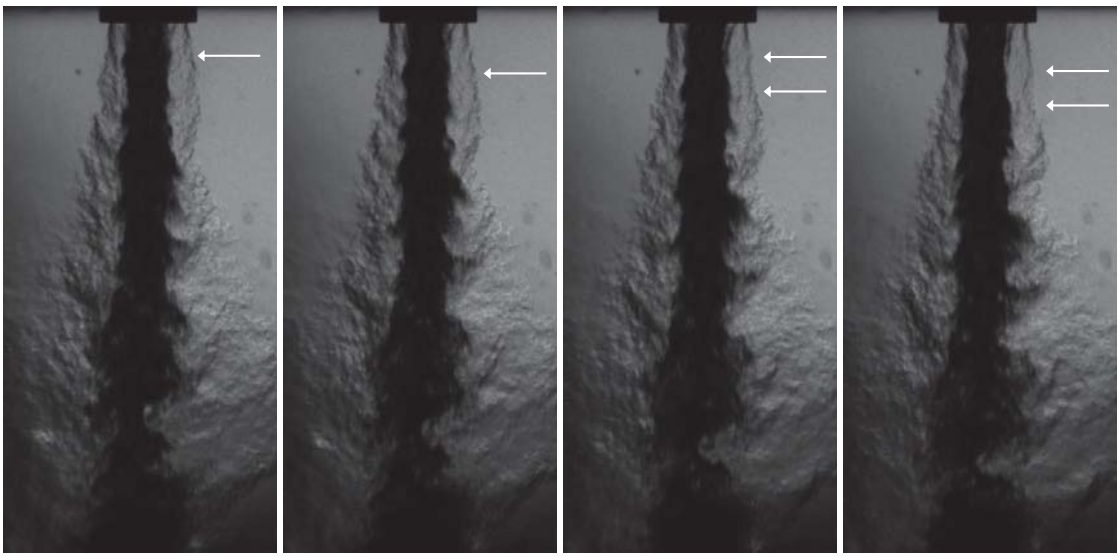

5.19: LN_2-GHe shear-coaxial jets exposed to acoustic forcing at a pressure antinode. Four consecutive images are taken from a set of high-speed images acquired at 10 kHz. An axisymmetric instability forms due to outer jet flow pulsations caused by the acoustic pressure perturbation p'. $J = 2$, $p_c = 400$ psia $= 2.76$ MPa, $f_F = 1700$ Hz, $p' = 1.53$ psi $= 10.55$ kPa

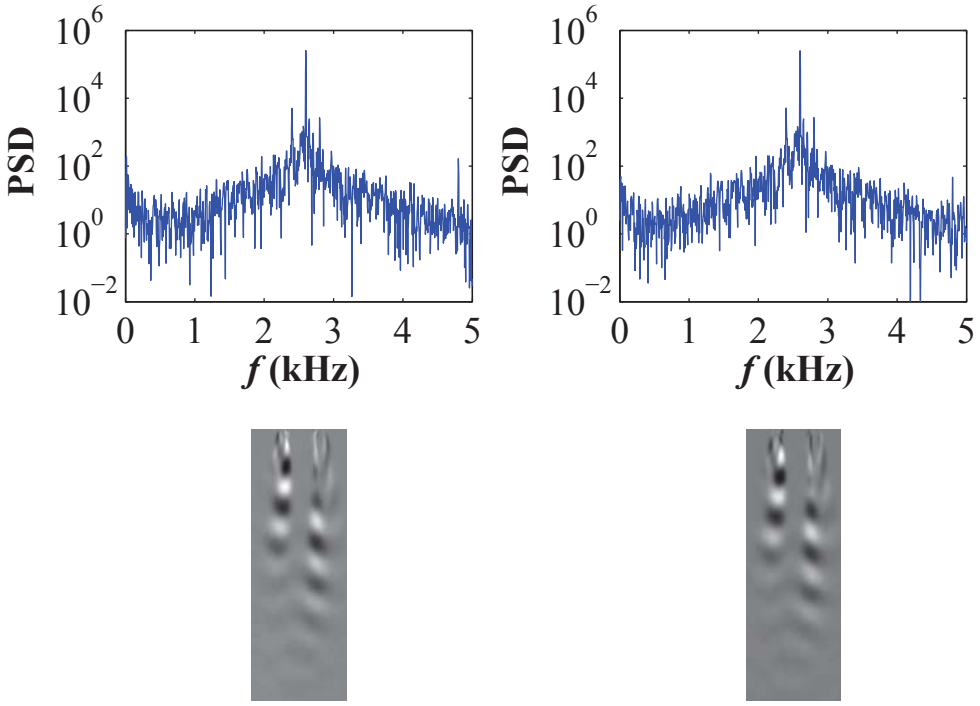

5.20: The forced mode for $J = 2$ at a PAN is represented by the POM pair which consists of mode-1 (left) and mode-2 (right). Power spectral density plots are shown (top) with each corresponding eigenvector image (bottom). The forced mode occurring at a PAN takes on an axisymmetric appearance. The eigenvector images of mode-1 and mode-2 appear to be 90° out-of-phase in the streamwise direction.

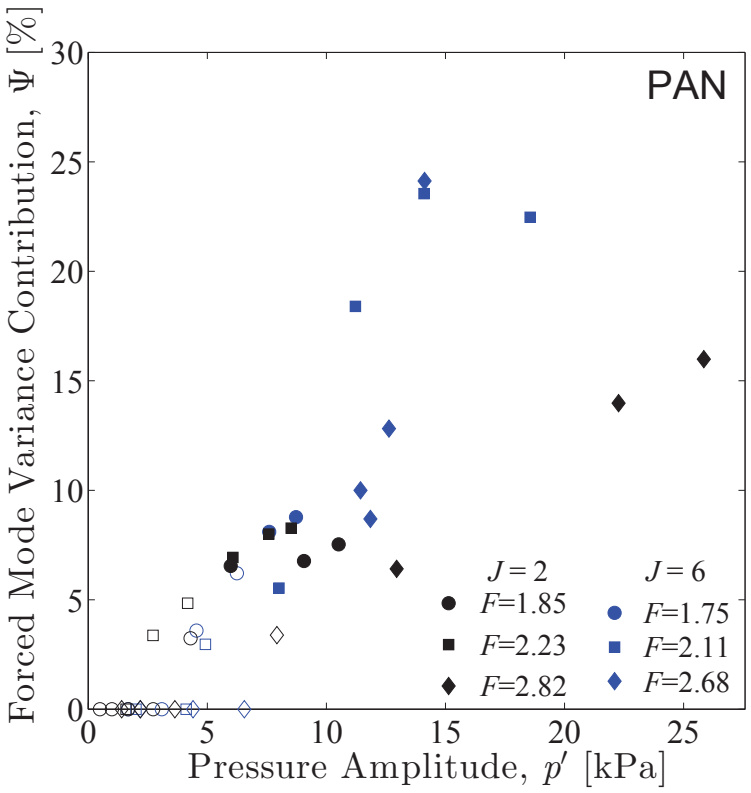

5.21: The forced mode variance contribution is plotted versus the acoustic pressure perturbation amplitude p' for $J = 2$ and $J = 6$ for a jet located at a PAN. The nominal natural frequency for $J = 2$ and $J = 6$ is 921 Hz and 970 Hz, respectively. Open symbols represent conditions in which the natural mode of the jet was most significant. Closed symbols represent conditions in which the natural mode was overtaken by the forced mode.

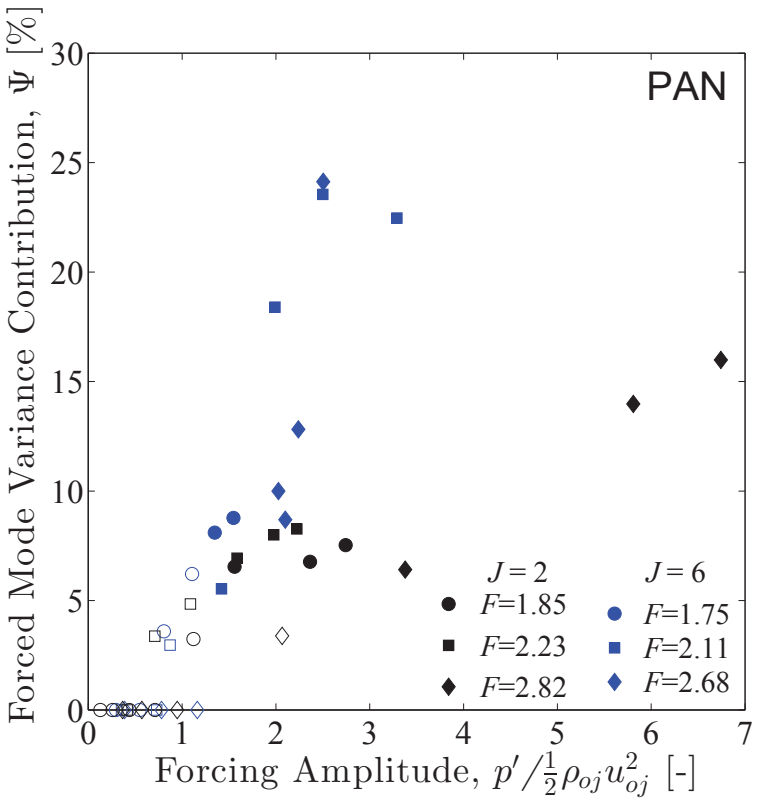

5.22: The forced mode variance contribution is plotted versus the acoustic pressure perturbation amplitude p' nondimensionalized by the outer jet dynamic pressure for $J = 2$ and $J = 6$, for a jet located at a PAN. The nominal natural frequency for $J = 2$ and $J = 6$ is 921 Hz and 970 Hz, respectively. Open symbols represent conditions in which the natural mode of the jet was most significant. Closed symbols represent conditions in which the natural mode was overtaken by the forced mode.

CHAPTER 6

Conclusions and Future Work

This dissertation has described extensive experiments relevant to acoustically-coupled combustion and transport processes. While both studies (on acoustically excited droplet combustion at UCLA and acoustically-coupled coaxial jets at AFRL) have helped to answer a number of fundamental scientific questions, there remain a number of issues on which future studies should focus.

6.1 Studies on Acoustically-coupled Droplet Combustion

The results in Chapter 3 on the fuel droplet combustion studies present strong evidence that the acoustic radiation force theory of Tanabe *et al.* [21, 73] does not properly account for the dynamic interactions between condensed phase combustion and acoustic excitation. Quantitatively, the amount of flame deformation and the locations of maximum flame deformation disagree with the prescribed theory. Qualitatively though, the location of flame switch is predicted fairly well, implying that acoustic radiation force theory plays a role in droplet combustion, but perhaps leaves essential combustion phenomena unaccounted for. Thermochemical relationships vital to condensed phase combustion may hold primary influences, rather than secondary influences, on the flame behaviors observed here.

To capture these effects, future work should explore the chemical kinetics frequency response in detail. First, the spatiotemporal relationship between flame standoff dis-

tance and acoustic phase could be enlightening. This relationship was not discussed in detail here, and could reveal a reaction phase delay which is frequency dependent. Any interdependency between chemical kinetics and frequency could contribute to the fact that Tanabe's theory is more accurate for higher frequencies than lower frequencies. Second, the well known Rayleigh criterion may predict different levels of instability for different acoustic flow conditions. The Rayleigh index, a transfer function calculated using the difference in phase between the pressure fluctuation p' and the heat release fluctuation q', can be found for each flow condition by synchronizing p' measurements with q' measurements, which can be inferred from global or local OH* chemiluminescence intensity. Should these studies provide illuminating results, a revised acoustic radiation force theory could provide a more comprehensive and accurate model of acoustic excitation coupled to condensed phase combustion, giving insight to the field of burning droplets as well as an array of other combustion instability problems.

6.2 Studies on Shear-coaxial Jets

To explore the susceptibility of shear-coaxial jets to external acoustic forcing, this study quantifies the amplitude at which the acoustically forced mode will overcome the naturally occurring mode as the most significant instability in the jet. It is evident that a critical forcing amplitude can indeed be identified, and its value will depend on the nondimensional forcing frequency F and jet flow conditions, such as the momentum flux ratio J. The critical forcing amplitude's dependence on F shares features with V-shaped lock-in diagrams common in absolute instability studies, where values of F which diverge from unity require increasingly large forcing amplitudes in order for the forced mode to overtake the natural mode. Indeed, a potential wake instability may produce absolute instability at the recirculation zone near the injector exit, but further theoretical work is required to determine the likelihood of absolute instability for the range of flow con-

ditions used here. An expanded test matrix to include $F < 1$ is also required to verify a V-shaped curve and confirm this relationship.

Alternatively, the results contain several indications that the natural mode of the jet instability is different from the typical absolutely unstable shear layer. The sinusoidal whipping of jets located at a PN and the streamwise pulsations of jets located at a PAN both are associated with periodic momentum fluctuations, whereby a long acoustic cycle encourages the production of a significant change in fluid momentum. As explained above, this mechanism will prohibit large amplitudes of momentum from being produced if the acoustic cycle is short, and thus an increase in f_F will cause an increase in the critical forcing amplitude for all F. Such a relationship has not been observed in prior studies of absolute instability, although in most studies of lock-in and associated phenomenon, a range of forcing frequencies can be studied without the requirement of creation of a standing wave. Again, an expanded test matrix can verify these relationships. The qualitative behavior of the jet after the acoustically forced mode overtakes the natural mode consistently revealed co-existing modes, whereby the forced mode became most dominant and the natural mode remained a significant mode within the mixing layer. While this is typically observed in absolutely unstable shear layers, there are some differences. The broadband nature of the natural instabilities observed have contrast to that of absolutely unstable flows, which are known to exhibit sharp peaks at a single frequency and higher harmonics. For the range of conditions explored in this study, it is believed that the naturally occurring jet instability is convectively unstable rather than absolutely unstable.

Reduced basis methods were successfully applied using a novel approach which compares the forced mode pixel intensity variance contribution Ψ from one case to another. In this way, quantitative measures of susceptibility to external forcing were obtained. Although qualitative conclusions were a valuable portion of this study, this quantita-

tive method shows great potential for future studies. Dynamic mode decomposition and proper orthogonal decomposition both showed advantages and disadvantages with regard to analyzing experimental images, and future work should continue to utilize and refine these algorithms where harsh environments make it difficult to use intrusive sensors alone. Although proper orthogonal decomposition was used for the majority of post-processing in this study, dynamic mode decomposition is recommended where specific frequencies must be extracted from dynamic flow structures.

The techniques noted above will prove to be powerful when applied to reactive combustion instability experiments, which is a paramount objective of this research campaign. To quantify the susceptibility of oxygen-hydrogen flames to acoustic forcing, reduced based methods will draw spectral information from high-speed images without requiring delicate instrumentation to be placed in a high pressure, high temperature combustion chamber. Ultimately, Strouhal number scaling laws will be refined for reactive conditions and forcing susceptibility diagrams will shine light on the inter-dependencies of the combustion instability feedback loop.

Appendix A

Shear-Coaxial Jet Experimental Methods Details

A.1 Acoustic Forcing System

The acoustic frequency sweeps conducted when characterizing the resonant freqencies of the acoustic system only approximately determined the frequency, amplitude, and phase difference of the sirens necessary to produce transverse standing waves. In order to achieve a more exact PN or PAN condition at the center of the inner chamber, a meticulous set of operations was carried out prior to each acoustically forced flow condition. Each of these operations is manual, and the complete procedure is itemized below.

- *Achieve a steady thermodynamic condition.* Prior to adjusting any acoustic parameters, the chamber speed of sound c must be nominally constant. This is done by setting p_c, $\dot{m}_{ij}$, $\dot{m}_{oj}$, T_{ij}, and T_{oj} according to a predetermined test matrix. The correct mean chamber pressure p_c is achieved by setting the chamber pressurization nitrogen flow accordingly. The mass flow rates $\dot{m}_{ij}$ and $\dot{m}_{oj}$ are set by adjusting needle valves in the supply lines, and as expected, T_{ij} and T_{oj} are adjusted separately using each heat exchanger.

- *Set the desired acoustic frequency f_F.* The signal generator, shown by the wiring diagram in Fig. A.3, is used to set f_F on output channels 1 and 2.

- *Set the desired siren phase difference* $\Delta\phi$. The phase difference $\Delta\phi_{SG}$ of signal generator channels 1 and 2 should be set to 0° and 180° to achieve PAN and PN conditions, respectively.

- *Set the pressure perturbation* p' *to a value approximately equal to the desired level.* The voltage output of signal generator output channels 1 and 2 are set independently.

- *Activate the acoustic sirens.* After activating channels 1 and 2, the sirens will produce an acoustic field which not a standing wave. Inner chamber pressure sensors located on the rear wall provide $p_{dyn,1}$, $p_{dyn,2}$, and $p_{dyn,3}$, which must be actively viewed on the graphical user interface of the data acquisition system. These sensors will reveal an asymmetric condition between the dynamic pressure left of the jet $p_{dyn,1}$ and the dynamic pressure right of the jet $p_{dyn,3}$. This asymmetric condition results from phase delays which are unique to each amplifier and are dependent on both frequency and amplitude.

- *Finalize the siren phase difference* $\Delta\phi$. This step requires the user to view the amplifier output monitor channels. Again, this is performed using the graphical user interface of the data acquisition system. The amplifier output monitor channels will reveal that $\Delta\phi_{AMP} \neq \Delta\phi_{SG}$. Then, $\Delta\phi_{SG}$ must be adjusted until $\Delta\phi_{AMP}$ has reached the desired value according to the data acquisition system. Following this step, the fluctuations observed with $p_{dyn,1}$ and $p_{dyn,3}$ will be nearly equal (symmetric), but output amplitude must often be adjusted to reach true symmetry.

- *Finalize the pressure perturbation* p' *to obtain symmetry.* Again, due to unequal amplifier frequency responses, equal signal generator output amplitudes may not result in equal amplifier output amplitudes. Thus, the signal generator output

amplitudes must be independently adjusted until the acoustic field of the chamber is symmetric, i.e. $p_{dyn,1} = p_{dyn,3}$. If acoustic drivers do not produce equal amplitudes, then standing waves are theoretically impossible. A successful procedure will result in a maximum p' at $p_{dyn,2}$ for a PAN condition, or will result in $p_{dyn,2} \approx 0$ for a PN condition.

A.2 Positive Semidefinite Proof

Where $\mathbf{R}$ is the covariance matrix of $\widetilde{\mathbf{A}}$ and $\mathbf{z}$ is any $m \times 1$ vector,

$$\mathbf{z}^T\mathbf{R}\mathbf{z} = \mathbf{z}^T\widetilde{\mathbf{A}}^T\widetilde{\mathbf{A}}\mathbf{z} = \left(\widetilde{\mathbf{A}}\mathbf{z}\right)^T\left(\widetilde{\mathbf{A}}\mathbf{z}\right) \equiv \mathbf{b}^T\mathbf{b} \geq 0. \tag{A.1}$$

Here, $\mathbf{b} \equiv \widetilde{\mathbf{A}}\mathbf{z}$, which makes $\mathbf{b}$ an $m \times 1$ vector with a magnitude equal to $\mathbf{b}^T\mathbf{b}$. Thus, $\mathbf{b}^T\mathbf{b}$ is non-negative and

$$\mathbf{z}^T\mathbf{R}\mathbf{z} \geq 0. \tag{A.2}$$

By definition, this makes the covariance matrix $\mathbf{R}$ *positive semidefinite*.

A.1: Data for unforced LN_2-GHe nonreactive experiments. Natural frequencies are determined using proper orthogonal decomposition. St_{th} is calculated using $U_{c,th}$. St_{meas} is calculated using $U_{c,meas}$.

J	R	S	T_c [K]	ρ_c [kg/m^3]	p_c [psia]	T_{oj} [K]	m_{oj} [g/s]	ρ_{oj} [kg/m^3]	U_{oj} [m/s]	Re_{oj} (x10^4)	T_{ij} [K]	m_{ij} [g/s]	ρ_{ij} [kg/m^3]	U_{ij} [m/s]	Re_{ij} (x10^4)	f_{nat} [Hz]	$U_{c,th}$ [m/s]	$U_{c,meas}$ [m/s]	St_{th}	St_{meas}
2.42	16.42	0.0090	287.9	32.7	402.7	274.8	0.55	4.8	43.67	0.92	120.0	2.43	534.5	2.66	1.81	890	6.21	5.73	0.259	0.281
2.30	16.18	0.0088	287.8	32.7	402.5	276.7	0.53	4.8	42.39	0.88	119.5	2.42	541.3	2.62	1.76	930	6.03	5.72	0.279	0.294
2.01	14.45	0.0096	287.7	32.7	402.6	274.6	0.52	4.8	41.46	0.87	121.9	2.44	497.8	2.87	2.09	850	6.32	6.23	0.243	0.247
2.14	15.54	0.0089	287.5	32.7	402.5	274.4	0.52	4.8	41.03	0.87	119.6	2.43	540.4	2.64	1.78	845	5.95	5.22	0.257	0.293
1.93	14.48	0.0092	269.7	36.7	421.4	277.0	0.50	5.0	37.98	0.83	119.7	2.42	541.8	2.62	1.76	990	5.72	6.00	0.313	0.299
1.94	14.57	0.0091	269.8	36.8	421.9	277.7	0.50	5.0	38.28	0.83	119.6	2.43	543.5	2.63	1.75	1160	5.74	6.27	0.366	0.335
4.87	23.40	0.0089	287.0	31.9	391.1	281.6	0.55	4.6	46.34	0.91	121.5	1.72	512.7	1.98	1.49	815	5.80	5.55	0.254	0.266
6.17	25.88	0.0092	286.8	32.6	399.3	274.0	0.64	4.8	51.24	1.08	120.8	1.75	518.8	1.98	1.38	975	6.29	6.80	0.281	0.259
5.84	25.11	0.0093	286.7	32.5	398.7	273.0	0.62	4.8	49.22	1.04	120.9	1.73	516.7	1.96	1.37	945	6.11	6.63	0.280	0.258
5.87	25.25	0.0092	286.7	32.5	398.5	275.4	0.62	4.7	49.74	1.03	121.1	1.72	512.5	1.97	1.39	965	6.16	5.71	0.283	0.306
5.85	25.11	0.0093	286.7	32.8	402.0	277.5	0.62	4.7	49.71	1.03	121.2	1.73	512.7	1.98	1.40	945	6.17	6.62	0.277	0.258
6.17	25.50	0.0095	288.6	32.7	402.6	277.3	0.64	4.8	50.75	1.06	121.7	1.70	502.5	1.99	1.44	1007	6.31	6.66	0.289	0.274
5.69	24.33	0.0096	288.4	32.7	403.9	274.0	0.64	4.8	50.11	1.06	121.7	1.76	501.4	2.06	1.48	995	6.35	5.85	0.284	0.308
6.20	25.43	0.0096	288.3	32.7	403.6	272.9	0.63	4.8	49.58	1.06	121.6	1.68	505.4	1.95	1.40	955	6.20	6.06	0.279	0.285
1.97	14.66	0.0092	272.2	34.9	404.3	274.3	1.10	4.8	86.78	1.84	120.5	5.30	525.4	5.92	4.09	2880	12.99	14.87	0.401	0.351
1.93	14.60	0.0090	271.5	35.0	404.2	275.6	1.08	4.8	86.07	1.81	120.2	5.34	531.2	5.90	4.04	3030	12.86	15.94	0.427	0.344
5.47	24.88	0.0088	270.3	35.4	407.3	275.0	1.27	4.8	99.79	2.12	119.0	3.75	548.8	4.01	2.65	2070	12.24	13.01	0.306	0.288
4.73	21.92	0.0098	269.8	37.1	425.8	275.5	1.27	5.1	95.69	2.12	121.5	3.82	513.7	4.37	3.07	2725	12.61	14.15	0.391	0.349

A.2: Data for acoustically forced LN_2-GHe nonreactive experiments. Data is presented for in units of psi (left) and kPa (right). For jets located at a PAN, the p' value is taken as the pressure perturbation at the jet. For jets located at a PN, the p' value is taken as the average of the pressure perturbations occurring at the PANs to the left and right of the jet. The velocity perturbation u' at a PN is calculated using eqn. 5.4, which relies on the p' values of the adjacent PANs.

J	f_F [Hz]	p' [psi]	
		PN	PAN
2	1700	0.05	0.07
		0.12	0.14
		0.17	0.24
		0.30	0.39
		0.42	0.62
		0.53	0.87
		-	1.31
		-	1.53
	2050	0.04	0.23
		0.13	0.39
		0.22	0.61
		0.38	0.88
		0.50	1.10
		0.55	1.24
	2600	0.10	0.20
		0.19	0.32
		0.26	0.53
		0.41	1.15
		0.55	1.88
		0.84	3.23
		1.17	3.75
6	1700	0.06	0.24
		0.12	0.45
		0.20	0.66
		0.31	0.91
		0.34	1.10
		-	1.27
	2050	0.08	0.29
		0.15	0.60
		0.24	0.71
		0.38	1.16
		0.50	1.63
		0.58	2.04
		-	2.69
	2600	0.10	0.32
		0.21	0.64
		0.26	0.95
		0.49	1.66
		0.67	1.72
		0.84	1.83
		-	2.05

J	f_F [Hz]	p' [kPa]	
		PN	PAN
2	1700	0.35	0.49
		0.80	0.99
		1.17	1.67
		2.08	2.72
		2.89	4.29
		3.69	5.98
		-	9.06
		-	10.52
	2050	0.28	1.59
		0.92	2.72
		1.51	4.17
		2.62	6.08
		3.43	7.58
		3.81	8.52
	2600	0.66	1.40
		1.31	2.18
		1.80	3.64
		2.79	7.92
		3.79	12.95
		5.82	22.27
		8.05	25.85
6	1700	0.38	1.66
		0.81	3.09
		1.40	4.55
		2.14	6.24
		2.34	7.60
		-	8.72
	2050	0.53	2.00
		1.05	4.11
		1.63	4.91
		2.64	8.00
		3.42	11.22
		4.03	14.10
		-	18.56
	2600	0.71	2.18
		1.45	4.40
		1.78	6.55
		3.40	11.43
		4.59	11.85
		5.82	12.62
		-	14.12

A.1: Piezoelectric acoustic siren, of aluminum construction.

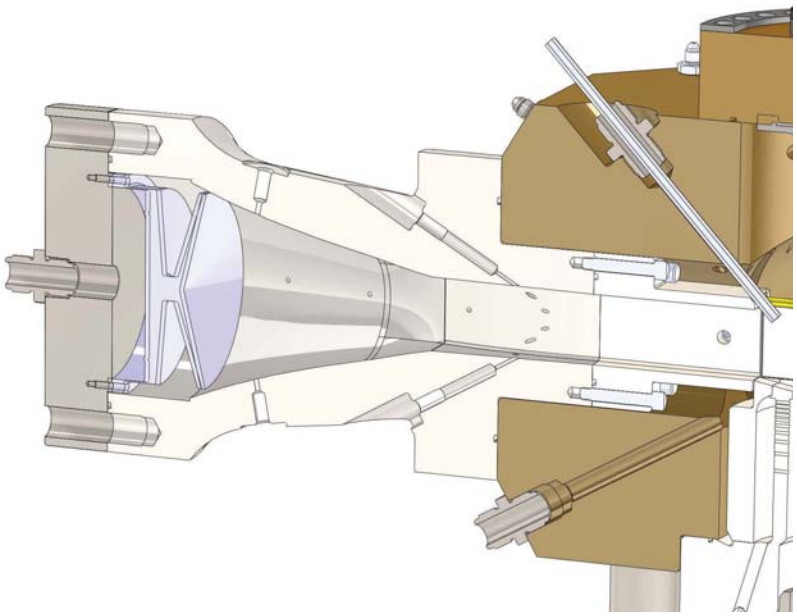

A.2: Cross sectional CAD rendering of the left waveguide.

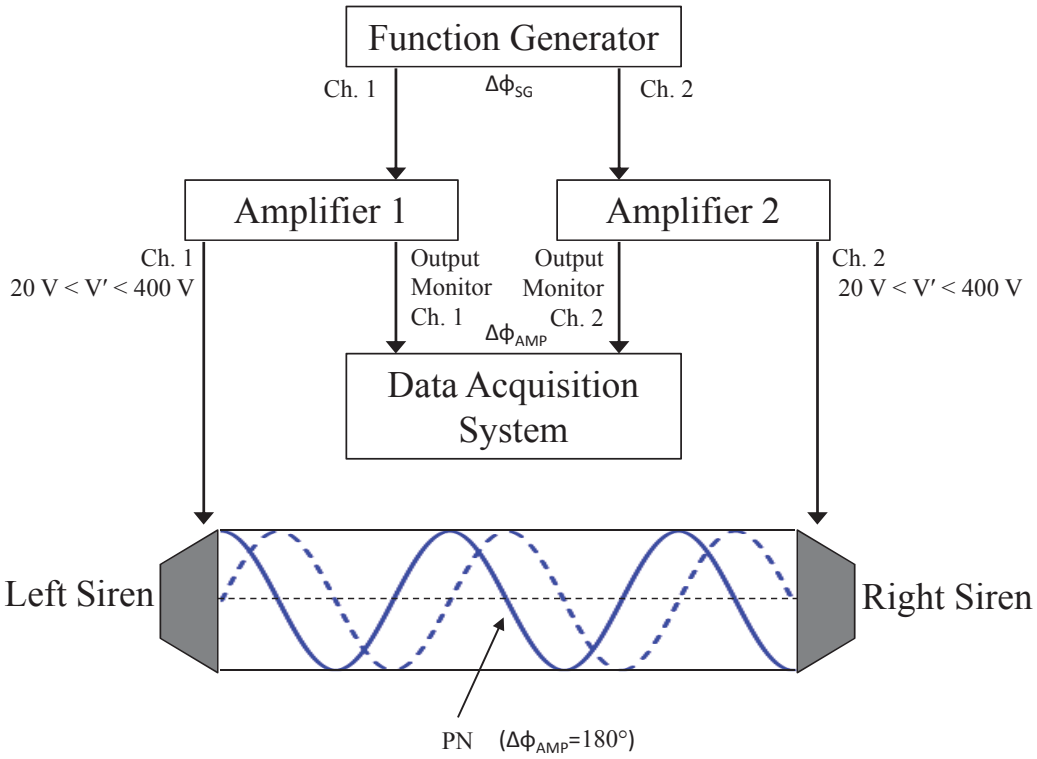

A.3: Acoustic wiring flow chart. The acoustic piezoelectric sirens are controlled using a dual-channel signal generator. Each of the two channels are controlled to have equal frequency, but unequal phase ϕ. Separate amplifiers produce high voltage signals for each siren, and the amplifiers also send an equivalent low voltage signal to the data acquisition system. The siren phase difference, then, is equal to $\Delta\phi_{AMP}$, which must be 0° to create a PAN at the center of the chamber and 180° to create a PN at the center. As a result of unique phase delays applied by each amplifier, the signal generator phase difference $\Delta\phi_{SG}$ must be dynamically adjusted for each acoustic condition in order to achieve a standing wave, i.e. for $\Delta\phi_{AMP} = 0°$ $\rightarrow$ $\Delta\phi_{SG}\neq 0°$, and for $\Delta\phi_{AMP} = 180°$ $\rightarrow$ $\Delta\phi_{SG}\neq 180°$

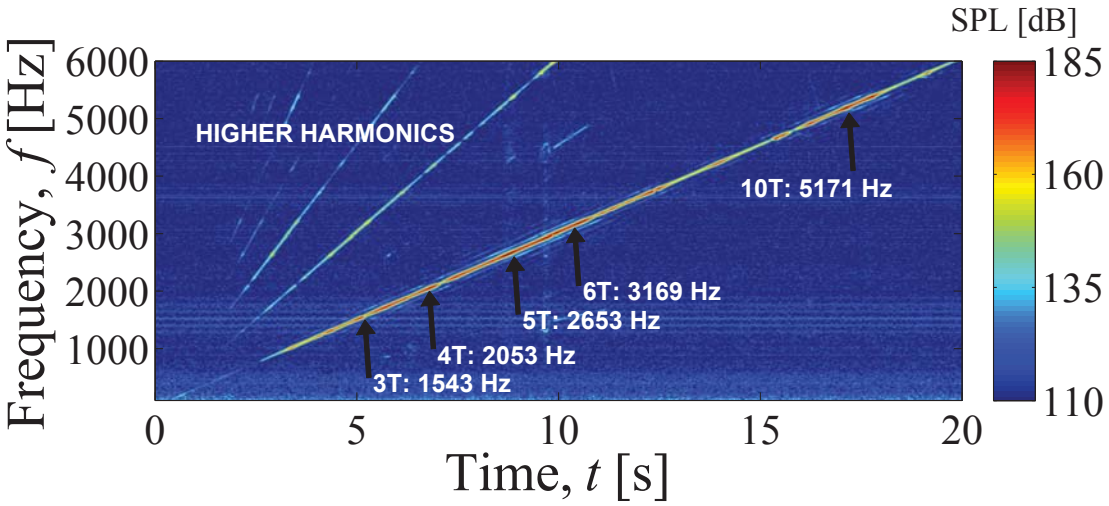

A.4: Acoustic pressure spectra results for a PAN condition measured using a pressure transducer in the center of the chamber. Magnitude is scaled with a sound pressure level (SPL) colormap, and key regions of transverse resonance are annotated. p_c=400 psia

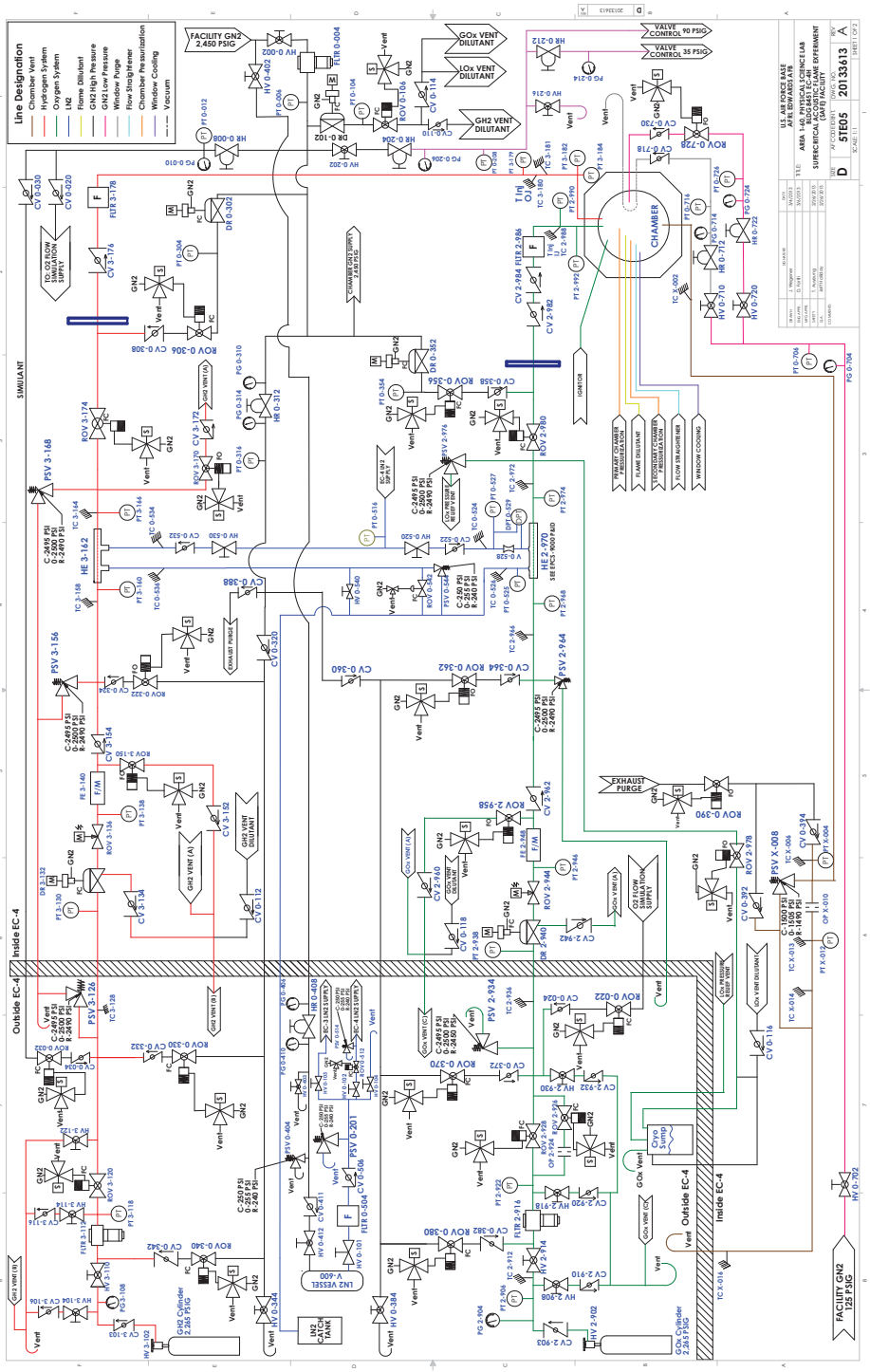

A.5: Facility PID page 1.

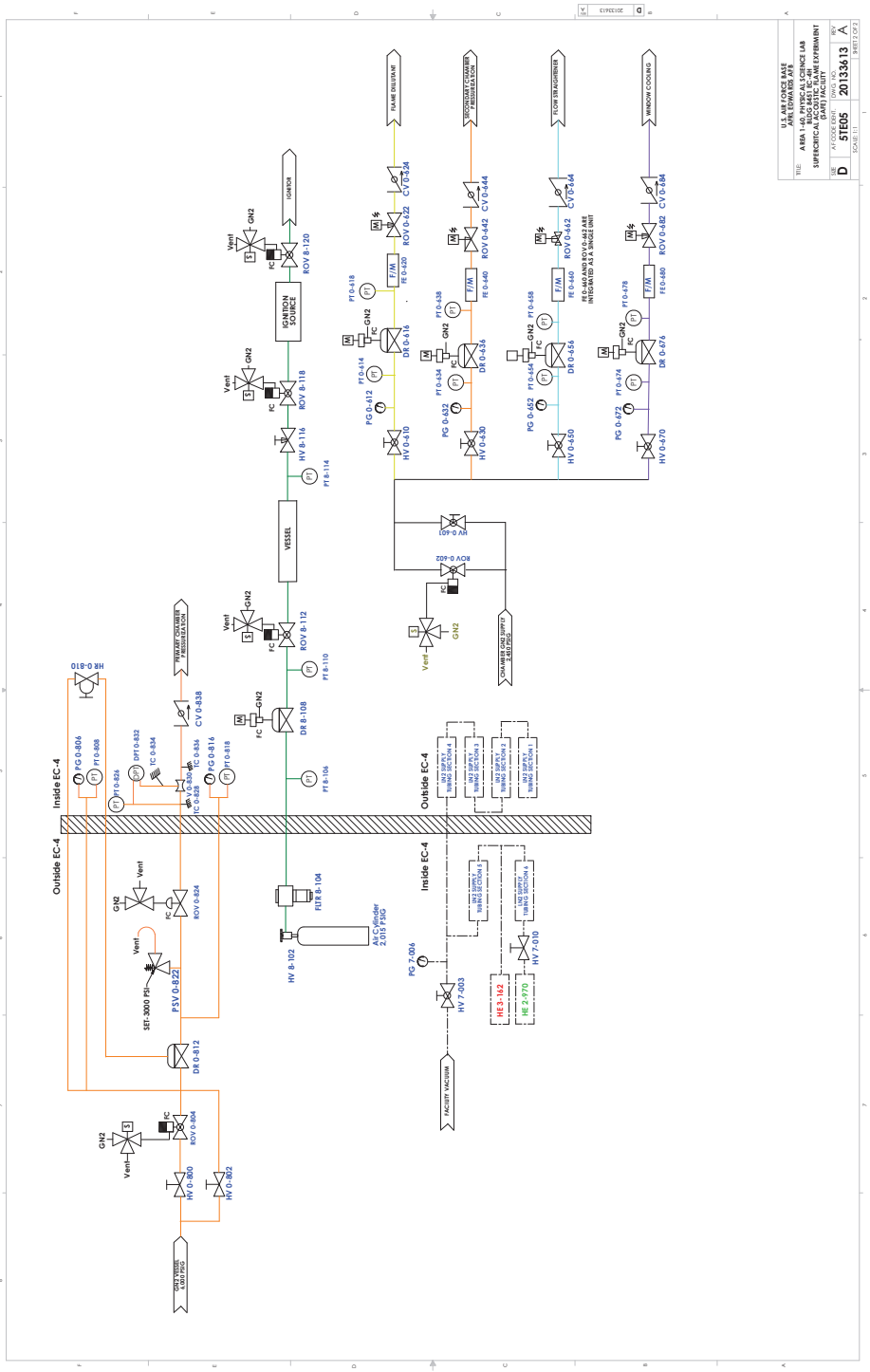

A.6: Facility PID page 2.

Bibliography

[1] T. C. Lieuwen and V. Yang. *Progress in Astronautics and Aeronautics: Combustion Instabilities in Gas Turbine Engines: Operational Experience, Fundamental Mechanisms, and Modeling*. AIAA, 2006.

[2] K. R. McManus, T. Poinsot, and S. M. Candel. A review of active control of combustion instabilities. *Progress in Energy and Combustion Science*, 19:1–29, 1993.

[3] F.E.C. Culick and V. Yang. Overview of combustion instabilities in liquid rocket engines. In V. Yang and W.E. Anderson, editors, *Progress in Astronautics and Aeronautics: Liquid Rocket Engine Combustion Instability*, pages 3–38. AIAA, 1995.

[4] A. M. Annaswamy and A. F. Ghoniem. Active control of combustion instability: Theory and practice. *Control Systems*, 22(6):37–54, 2002.

[5] Q. Diao. *Propellant injection strategy for suppressing acoustic combustion instability*. PhD thesis, University of Maryland, College Park, Mechanical and Engineering Department, June 2010.

[6] S. Candel. Combustion dynamics and control: progress and challenges. Number 29 in Proceedings of the Combustion Institute, pages 1–28, 2002.

[7] T. Lieuwen, H. Torres, C. Johnson, and B.T. Zinn. A mechanism for combustion instability in lean premixed gas turbine combustors. *J. of Engineering for Gas Turbines and Power*, 123:182–189, 2001.

[8] F. Richecoeur. *Experiments and numerical simulations of interactions between*

transverse acoustic modes and cryogenic flames. PhD thesis, Ecole Centrale Paris, November 2006.

[9] Y.C. Yu, S.M. Koeglmeier, J.C. Sisco, and W.E. Anderson. Combustion instability of gaseous fuels in a continuously variable resonance chamber (cvrc). 44th Joint Propulsion Conference and Exhibit, 2008. AIAA 2008-4657.

[10] P. Yecko, S. Zaleski, and J.-M. Fullana. Viscous modes in two-phase mixing layers. *Physics of Fluids*, 14(12):4115–4122, 2002.

[11] K.C. Kim and R.J. Adrian. Very large-scale motion in the outer layer. *Physics of Fluids*, 11(2):417–422, 1999.

[12] P. Givi, W.-H. Jou, and R.W. Metcalfe. Flame extinction in a temporally developing mixing layer. *Twenty-First Symposium (International) on Combustion*, pages 1251–1261, 1986.

[13] H.K. Chelliah, C.K. Law, T. Ueda, M.D. Smooke, and F.A. Williams. An experimental and theoretical investigation of the dilution, pressure and flow-field effects on the extinction condition of methane-air-nitrogen diffusion flames. *Twenty-Third Symposium (International) on Combustion*, pages 503–511, 1990.

[14] W.O.H. Mayer and J.J. Smith. Fundamentals of supercritical mixing and combustion of cryogenic propellants. In et al. Yang, V., editor, *Progress in Astronautics and Aeronautics: Liquid Rocket Engine Thrust Chambers*, page 339367. AIAA, 2004.

[15] Q. Diao, A. Ghosh, and K. H. Yu. Suppression of GO2/GH2 combustion instability using CH4 addition. Number AIAA-2008-1000 in 46th AIAA Aerospace Sciences Meeting, Reno, NV, January 2008.

[16] F. Baillot, J.-B. Blaisot, G. Boisdron, and C. Dumouchel. Behaviour of an air-assisted jet submitted to a transverse high-frequency acoustic field. *J. of Fluid Mechanics*, 640:305–342, 2009.

[17] J.C. Sisco, Y.C. Yu, V. Sankaran, and W.E. Anderson. Examination of mode shapes in an instable model combustor. *Journal of Sound and Vibration*, 330: 61–74, 2011.

[18] J.S. Hardi, M. Oschwald, and B. Dally. Acoustic characterisation of a rectangular rocket combustor with liquid oxygen and hydrogen propellants. *Proceedings of the Institution of Mechanical Engineers, Part G: Journal of Aerospace Engineering*, 227(3):436–446, 2013.

[19] Y. Mery, L. Hakim, P. Scouflaire, L. Vingart, S. Ducruix, and S. Candel. Experimental investigation of cryogenic flame dynamics under transverse acoustic modulations. *Comptes Rendus Mecanique*, 341:100–109, 2013.

[20] M. Tanabe, T. Morita, K. Aoki, K. Satoh, T. Fujimori, and J. Sato. Influence of standing sound waves on droplet combustion. *Proc. Comb. Inst.*, 28:1007–1013, 2000.

[21] M. Tanabe, T. Kuwahara, S. Kimiyoshi, T. Fujimori, J. Sato, and M. Kono. Droplet combustion in standing sound waves. *Proc. Comb. Inst.*, 30:1957–1964, 2005.

[22] S. Dattarajan, A. Lutomirski, R. Lobbia, O.I. Smith, and A.R. Karagozian. Acoustic excitation of droplet combustion in microgravity and normal gravity. *J. Combustion and Flame*, 144:299–317, 2006.

[23] S. Teshome. *Droplet Combustion and Non-Reactive Shear-Coaxial Jets with Trans-*

verse Acoustic Excitation. PhD thesis, University of California, Los Angeles, Department of Mechanical and Aerospace Engineering, March 2012.

[24] J. Hardi. *Experimental Investigation of High Frequency Combustion Instability in Cryogenic Oxygen-Hydrogen Rocket Engines*. PhD thesis, The University of Adelaide, School of Mechanical Engineering, June 2012.

[25] P. Huerre and P. A. Monkewitz. Local and global instabilities in spatially developing flows. *Annual Review of Fluid Mechanics*, 22:473–537, 1990.

[26] J.-B. Carpentier, F. Baillot, J.-B. Blaisot, and C. Dumouchel. Behavior of cylindrical liquid jets evolving in a transverse acoustic field. *Physics of Fluids*, 21(2): 1–15, 2009.

[27] F.G. Buffum and F.A. Williams. The response of a turbulent jet to transverse acoustic fields. Proceedings of the 1967 Heat Transfer and Fluid Mechanics Institute, pages 247–276, 1967.

[28] B. W. Davis and B. Chehroudi. The effects of pressure and acoustic field on a cryogenic coaxial jet. *42nd AIAA Aerospace Sciences Meeting & Exhibit*, 2004. Washington, D.C.

[29] I. A. Leyva, J. I. Rodriguez, B. W. Davis, and B. Chehroudi. Preliminary results on coaxial jet spread angles and the effects of variable phase transverse acoustic fields. *46nd AIAA Aerospace Sciences Meeting & Exhibit*, 2008. Reno, NV.

[30] S. Teshome, I.A. Leyva, and D.G. Talley. Proper orthogonal decomposition analysis of shear-coaxial injector flows with and without transverse acoustic forcing. *JANNAF Joint Subcommittee Meeting*, 2011. Huntsville, AL.

[31] J.W.S. Rayleigh. *The Theory of Sound*. vol. 2, New York: Dover, 1945.

[32] D.A. Smith and E.E. Zukoski. Combustion instability sustained by unsteady vortex combustion. *Twenty-first Joint Propulsion Conference*, AIAA-85-1248, 1985.

[33] K.H. Yu, A. Trouve, and J.W. Daily. Low-frequency pressure oscillations in a model ramjet combustor. *J. Fluid Mechanics*, 232:47–72, 1991.

[34] K.C. Schadow and E. Gutmark. Combustion stability related to vortex shedding in dump combustors and their passive control. *Progress in Energy and Combust. Sci.*, 18:117–132, 1992.

[35] H.C. Mongia, T.J. Held, G.C. Hsiao, and R.P. Pandalai. Incorporation of combustion instability issues into design process: General electric aeroderivative and aero engines experience. In *Progress in Astronautics and Aeronautics: Combustion Instabilities in Gas Turbine Engines: Operational Experience, Fundamental Mechanisms, and Modeling*, pages 89–107. AIAA, 2006.

[36] Standards of Performance for Stationary Gas Turbines Environmental Protection Agency, Standards of Performance for New Stationary Sources. Title 40. 2011. Sections 60.330-60.335, http://www.epa.gov/region7/air/nsps/nspsstandardcontacts.htm.

[37] C.T. Bowman. Control of combustion-generated nitrogen oxide emissions: Technology driven by regulation. volume 24 of *Twenty-Fourth Symposium on Combustion*, pages 859–878, 1992.

[38] K. O. Smith and J. Blust. Combustion instabilities in industrial gas turbines: Solar turbines' experience. In *Progress in Astronautics and Aeronautics: Combustion Instabilities in Gas Turbine Engines: Operational Experience, Fundamental Mechanisms, and Modeling*, pages 29–41. AIAA, 2006.

[39] T. Scarinci. Combustion instability and its passive control: Rolls-royce aeroderivative engine experience. In *Progress in Astronautics and Aeronautics: Combustion Instabilities in Gas Turbine Engines: Operational Experience, Fundamental Mechanisms, and Modeling*, pages 65–88. AIAA, 2006.

[40] B. Wassener. Airlines weigh the advantages of using more biofuel. 2011. The International Herald Tribune, October 10.

[41] G.P. Sutton and O. Biblarz. *Rocket propulsion elements*. John Wiley and Sons, 2001.

[42] NASA. J-2 engine fact sheet. *Saturn V News Reference*, December, 1968. retrieved by NASA 22 February 2012.

[43] D. Haeseler. Peenemuende roots and lessons. In *Liquid Propulsion History I: LOX/HC Propulsion I: Goddard - Peenemuende - Sputnik (8K71PS/8A91 R-7), Vanguard, Juno 1 to Titan, Atlas, Falcon and Beyond*. AIAA Joint Propulsion Conference Presentation Series, July 16, 2013.

[44] S. Bouley and B. Anderson. Rs-27, md-1, ma-5a-7, lr-89-105, h-1, f-1, s-3d, rs-84 (atlas, delta, thor, saturn 1b and v, jupiter. In *Liquid Propulsion History I: LOX/HC Propulsion I: Goddard - Peenemuende - Sputnik (8K71PS/8A91 R-7), Vanguard, Juno 1 to Titan, Atlas, Falcon and Beyond*. AIAA Joint Propulsion Conference Presentation Series, July 16, 2013.

[45] J. Hulka and J.J. Hutt. Instability phenomena in liquid oxygen/hydrogen propellant rocket engines. In V. Yang and W.E. Anderson, editors, *Progress in Astronautics and Aeronautics: Liquid Rocket Engine Combustion Instability*, pages 39–72. AIAA, 1995.

[46] F. E. C. Culick. Unsteady motions in combustion chambers for propulsion systems. 2006. AGARDograph, NATO/RDO-AG-AVT-039.

[47] J. C. Oefelein and V. Yang. Comprehensive review of liquid propellant combustion instabilities in F-1 engines. *Propulsion and Power*, 9(5):657–677, 1993.

[48] G. A. Dressler and J. M. Bauer. Trw pintle engine heritage and performance characteristics. Number AIAA-2000-3871 in 36th AIAA/ASME/SAE/ASEE Joint Propulsion Conference and Exhibit, July 2000.

[49] M. Habiballah, D. Lourme, and F. Pit. Numerical model for combustion stability studies applied to the ariane viking engine. *Propulsion and Power*, 7(3):322–329, 1991.

[50] H.E. Scott, H.E. Bloomer, and A.H. Mansour. M-1 engine subscale injector tests. *NASA Lewis Research Center*, TN D-4053, 1967.

[51] S.C. Fisher, F.E. Dodd, and R.J. Jensen. Scaling techniques for liquid rocket combustion stability testing. In V. Yang and W.E. Anderson, editors, *Progress in Astronautics and Aeronautics: Liquid Rocket Engine Combustion Instability*, pages 545–564. AIAA, 1995.

[52] A. R. Karagozian, W. J. A. Dahm, E. Glasgow, R. Howe, I. Kroo, R. Murray, and H. Shyu. Technology options for improved air vehicle fuel efficiency. 2006. Air Force Scientific Advisory Board Report, Technical Report SAB-TR-06-04.

[53] SrA Jason Hernandez. SECAF certifies synthetic fuel blends for B-52H. *Edwards Air Force Base, CA*, 2007. Edwards Air Force Base, CA. http://www.safie.hq.af.mil/news/story.asp?id=123064095.

[54] A. D. Sagar and S. Kartha. Bioenergy and sustainable development. *Annual Rev. of Environmental Resources*, 32:131–167, 2007.

[55] G. A. Mills and E. E. Ecklund. Alcohols as components of transportation fuels. *Annual Review of Energy*, 12(1):47–80, 1987.

[56] P. M. Morse, R. H. Boden, and H. Schecter. Acoustic vibrations and internal combustion engine performance, i. standing waves in the intake pipe system. *Applied Physics*, 9:16–23, 1938.

[57] D. E. Winterbone and R. J. Pearson. *Theory of Engine Manifold Design: Wave Action Methods for IC Engines*. Professional Engineering Publishing, London, 2000.

[58] F. Fischer. *The Conversion of Coal*. Ernst Benn, Ltd., 1925.

[59] 1st Lt Amanda Ferrell. Air force energy initiatives focus on fuel, beyond. *Edwards Air Force Base, CA*, 2007. http://www.af.mil/news/story.asp?id=123069617.

[60] G.A.E. Godsave. Burning of fuel droplets. Combustion and Flame, pages 818–830, 1953. Baltimore, MD. Williams and Wilkins.

[61] A. Williams. Combustion of droplets of liquid fuels - a review. *Combustion and Flame*, 21, 1973.

[62] C. K. Law and G. M. Faeth. Opportunities and challenges of combustion in microgravity. *Progress in Energy and Combustion Science*, 20, 1994.

[63] C. K. Law. Recent advances in droplet vaporization and combustion. *Progress in Energy and Combustion Science*, 8(3):171–201, 1982.

[64] S. R. Turns. *An Introduction to Combustion*. McGraw Hill, 2000.

[65] P. M. Struk, M. Ackerman, V. Nayagam, and D. L. Dietrich. On calculating burning rates during fibre supported droplet combustion. *Microgravity Science and Technology*, 11, 1998.

[66] A.J. Marchese, F.L. Dryer, V. Nayagam, and R.O. Colantino. Hydroxyl radical chemiluminescence imaging and the structure of microgravity droplet flames. Twenty-sixth Symposium (International) on Combustion, pages 1219–1226, 1996.

[67] A.J. Marchese, R.O. Colantino, F.L. Dryer, and V. Nayagam. Microgravity combustion of methanol and methanol/water droplets: Drop tower experiments and model predictions. Twenty-sixth Symposium (International) on Combustion, pages 1209–1217, 1996.

[68] S. Kumagai and H. Isoda. Combustion of fuel droplets in a vibrating air field. Fifth Symposium (International) on Combustion, 1955.

[69] J. Blaszczyk. Acoustically disturbed fuel droplet combustion. *Fuel*, 70(3):1023–1025, 1973.

[70] M. Saito, M. Sato, and I. Suzuki. Evaporation and combustion of a single fuel droplet in acoustic fields. *Fuel*, 73, 1994.

[71] M. Saito, M. Hoshikawa, and M. Sato. Enhacement of evaporation/combustion coefficient of a single fuel droplet by acoustic oscillation. *Fuel*, 75, 1996.

[72] K. Okai, O. Moriue, M. Araki, M. Tsue, M. Kono, J. Sato, and D. L. Dietrich. Combustion of single droplet and droplet pairs in a vibrating field under microgravity. *Proc. Comb. Inst.*, 28, 2000.

[73] M. Tanabe. Drop tower experiments and numerical modeling on the combustion-induced secondary flow in standing acoustic fields. *J. Microgravity Sci. Technol.*, 22:507–515, 2010.

[74] D.J. McKinney and D. Dunn-Rankin. Acoustically driven extinction in a droplet stream flame. *Combust. Sci. and Tech.*, 161:27–48, 2000.

[75] J.I. Rodriguez. *Acoustic Excitation of Liquid Fuel Droplets and Coaxial Jets.* PhD thesis, University of California, Los Angeles, Department of Mechanical and Aerospace Engineering, June 2009.

[76] M. Faraday. On a peculiar class of acoustical figures; and on certain forms assumed by groups of particles upon vibrating elastic surfaces. *Phil. Trans. R. Soc. Lond.*, 121:229, 1831.

[77] J.W.S. Rayleigh. On the pressure of vibrations. *Philos. Mag.*, 10:364–374, 1902.

[78] L.P. Gor'kov. On the forces acting on a small particle in an acoustical field in an ideal fluid. *Soviet Phys.-Doklady*, 6(9):773–775, 1962.

[79] W.L. Nyborg. Radiation pressure on a small rigid sphere. *J. Acoust. Soc. Am.*, 16 (1):947–952, 1967.

[80] C.P. Lee and T.G. Wang. Acoustic radiation pressure. *J. Acoust. Soc. Am.*, 94 (2):1099–1109, 1993.

[81] J.I. Rodriguez, S. Teshome, H.-S. Mao, A. Pezeshkian, O.I. Smith, and A.R. Karagozian. Acoustically driven droplet combustion with alternative liquid fuels. *46th AIAA Aerospace Sciences Meeting and Exhibit*, 2008.

[82] S. Teshome, A. Pezeshkian, O.I. Smith, and A.R. Karagozian. Influence of standing acoustic waves on combustion of alternative fuels. *Proc. Am. Phys. Soc.*, 2008.

[83] A.S.H. Kwan and N.W.M. Ko. Coherent structures in subsonic coaxial jets. *Journal of Sound and Vibration*, 48:203–219, 1976.

[84] W. Forstall and A.H. Shapiro. Momentum and mass transfer in coaxial gas jets. Massachusetts Institute of Technology, Guided Missiles Program, 1949.

[85] N.A. Chigier and J.M. Beer. The flow region near the nozzle in double concentric jets. *Journal of Basic Engineering*, 86:797–804, 1964.

[86] F.H. Champagne and I.J. Wygnanski. An experimental investigation of coaxial turbulent jets. *International Journal of Heat and Mass Transfer*, 14:1445–1464, 1971.

[87] N.W.M. Ko and A.S.H. Kwan. Experimental investigation of sub sonic coaxial jets. *Proceedings of the 5th Australian Conference on Hydraulics and Fluid Mechanics, University of Canterbury, New Zealand*, 1974.

[88] N.W.M. Ko and A.S.H. Kwan. The initial region of subsonic coaxial jets. *Journal of Fluid Mechanics*, 73:305–332, 1976.

[89] P.E. Dimotakis. Two-dimensional shear-layer entrainment. *AIAA Journal*, 24: 17911796, 1986.

[90] W.J.A. Dahm and P.E. Dimotakis. Mixing at large schmidt number in the self-similar far field of turbulent jets. *Journal of Fluid Mechanics*, 217:299–330, 1990.

[91] P.E. Dimotakis. *Turbulent free shear layer mixing and combustion*. AIAA, 1991.

[92] W.J.A. Dahm, C.E. Frieler, and G. Tryggvason. Vortex structure and dynamics in the near field of a coaxial jet. *Journal of Fluid Mechanics*, 241:371–402, 1992.

[93] J.-P. Matas, S. Marty, and A. Cartellier. Experimental and analytical study of the shear instability of a gas-liquid mixing layer. *Physics of Fluids*, 23:094112, 2011.

[94] N. Chigier and Z. Farago. Morphological classification of disintegration of round liquid jets in a coaxial air stream. *Atomization and Sprays*, 2:2, 1992.

[95] J.C. Lasheras and E.J. Hopfinger. Liquid jet instability and atomization in a coaxial gas stream. *Annual Review of Fluid Mechanics*, 32:275–308, 2000.

[96] J.A. Newman and T.A. Brzustowski. Behavior of a liquid jet near the thermodynamic critical region. *AIAA Journal*, 9:1595–1602, 1971.

[97] M. Oschwald, J. J. Smith, R. Branam, J. Hussong, A. Schik, B. Chehroudi, and D. Talley. Injection of fluids into supercritical environments. *Combustion Science and Technology*, 178, 2006.

[98] B. Chehroudi, D. Talley, and E. Coy. Visual characteristics and initial growth rates of round cryogenic jets at supercritical and supercritical pressures. *Physics of Fluids*, 14:850861, 2002.

[99] B. Chehroudi and D. Talley. Fractal geometry of a cryogenic nitrogen round jet injected into sub- and super-critical conditions. *Atomization and Sprays*, 14:81–91, 2004.

[100] J. Telaar, G. Schneider, and W. Mayer. Experimental investigation of breakup of turbulent liquid jets. *ILASS-Europe Conference*, 2000. Darmstadt, Germany.

[101] M. Oschwald, A. Schik, M. Klar, and W. Mayer. Investigation of coaxial ln2-gh2-injection at supercritical pressure by spontaneous raman scattering. *AIAA 99-2887, 35th Joint Propulsion Conference*, 1999. Los Angeles, CA.

[102] B. W. Davis and B. Chehroudi. Shear-coaxial jets from a rocket-like injector in a transverse acoustic field at high pressures. *44nd AIAA Aerospace Sciences Meeting & Exhibit*, 2006. Reno, NV.

[103] DW Davis. *On the Behavior of a Shear-Coaxial Jet Spanning Sub-to Supercritical Pressures With and Without an Externally Imposed Acoustic Field*. PhD thesis, PhD Thesis, Dept. of Mech. and Nuc. Eng., the Pennsylvania State University, 2006.

[104] J.J. Graham, I.A. Leyva, J.I. Rodriguez, and D. Talley. On the effect of a transverse acoustic field on a shear coaxial injector. *45th AIAA/ASME/SAE/ASEE Joint Propulsion Conference and Exhibit*, 2009-5142.

[105] I.A. Leyva, B. Chehroudi, and D. Talley. Dark core analysis of coaxial injectors at sub-, near-, and supercritical pressures in a transverse acoustic field. *43rd AIAA/ASME/SAE/ASEE Joint Propulsion Conference and Exhibit*, 5:275–282, 2007-5456.

[106] S.C. Crow and F.H. Champagne. Orderly structure in jet turbulence. *Journal of Fluid Mechanics*, 48:547–591, 1971.

[107] Anne-Laure Birbaud, Daniel Durox, Sébastien Ducruix, and S Candel. Dynamics of free jets submitted to upstream acoustic modulations. *Physics of Fluids*, 19: 013602, 2007.

[108] A. Talamelli and I. Gavarini. Linear instability characteristics of incompressible coaxial jets. *Flow Turbulence Combust*, 76:221–240, 2006.

[109] A. Segalini and A. Talamelli. Experimental analysis of dominant instabilities in coaxial jets. *Physics of Fluids*, 23:024103, 2011.

[110] J.-M. Chomaz. Global instabilities in spatially developing flows: Non-normality and nonlinearity. *Annual Review of Fluid Mechanics*, 37:357–392, 2005.

[111] P. A. Monkewitz, D. W. Bechert, B. Barsikow, and B. Lehmann. Self-excited oscillations and mixing in a heated round jet. *Journal of Fluid Mechanics*, 213: 611–639, 1990.

[112] D. M. Kyle and K. R. Sreenivasan. The instability and breakdown of a round variable-density jet. *Journal of Fluid Mechanics*, 249:619–664, 1993.

[113] P.J. Strykowski and D.L. Niccum. The stability of countercurrent mixing layers in circular jets. *Journal of Fluid Mechanics*, 227:309, 1991.

[114] P.J. Strykowski and D.L. Niccum. The influence of velocity and density ratio on the dynamics of spatially developing mixing layers. *Physics of Fluids*, 4:770, 1992.

[115] M. Provansal, C. Mathis, and L. Boyer. Benard-von karman instability: transient and forced regimes. *Journal of Fluid Mechanics*, 182:1–22, 1987.

[116] D. Hammond and L. Redekopp. Global dynamics of symmetric and asymmetric wakes. *Journal of Fluid Mechanics*, 331:231–260, 1997.

[117] S. Megerian, J. Davitian, L. S. de B. Alves, and A. R. Karagozian. Transverse jet shear-layer instabilities. part 1. experimental studies. *Journal of Fluid Mechanics*, 593:93–129, 2007.

[118] M.P. Juniper, L.K.B. Li, and J.W. Nichols. Forcing of self-excited round jet diffusion flames. *Proceedings of the Combustion Institute*, 32:1191–1198, 2009.

[119] M. P. Hallberg and P. J. Strykowski. Open-Loop Control of Fully Nonlinear Self-Excited Oscillations. *Physics of Fluids*, 20:041703, 2008.

[120] B. Pier. Open-Loop Control of Absolutely Unstable Domains. *Royal Society of London Proceedings Series A*, 459(2033):1105–1115, 2003.

[121] S. Jendoubi and P.J. Strykowski. Absolute and convective instability of axisymmetric jets with external flow. *Physics of Fluids*, 6:3000–3009, 1994.

[122] D.R. Getsinger, C. Hendrickson, and A.R. Karagozian. Shear layer instabilities in low-density transverse jets. *Exp Fluids*, 53:783–801, 2012.

[123] K.R. Sreenivasan, S. Raghu, and D. Kyle. Absolute instability in variable density round jets. *Exp Fluids*, 7:309–317, 1989.

[124] C.C. Miesse. The effect of ambient pressure oscillations on the disintegration and dispersion of a liquid jet. *Jet Propulsion*, 25:525–530, 1955.

[125] Ray Snyder, Gerald Herding, JUAN CARLOS ROLON, and Sébastien Candel. Analysis of flame patterns in cryogenic propellant combustion. *Combustion science and technology*, 124(1-6):331–370, 1997.

[126] S. Candel, G. Herding, R. Synder, P. Scouflaire, C. Rolon, D. Stepowski, A. Cessou, and P. Colin. Experimental investigation of shear coaxial cryogenic jet flames. *J. of Propulsion and Power*, 14(5):826–834, 1998.

[127] Louis Baker and Fred W Steffen. *Screaming Tendency of the Gaseous-hydrogen-Liquid-oxygen Propellant Combination*. National Advisory Committee for Aeronautics, 1958.

[128] Marcus F Heidmann. *Oscillatory combustion of a liquid-oxygen jet with gaseous hydrogen*. National Aeronautics and Space Administration, 1965.

[129] G. Singla, P. Scouflaire, C. Rolon, and S. Candel. Planar laser-induced fluorescence of oh in high-pressure cryogenic LOx/GH2 jet flames. *Combustion and Flame*, 144: 151–169, 2006.

[130] G. Singla, P. Scouflaire, C. Rolon, S. Candel, and L. Vingert. Oh planar laser-induced fluorescence and emission imaging in high-pressure LOx/Methane flames. *J. of Propulsion and Power*, 23(3):593–602, 2007.

[131] F. Richecoeur, S. Ducruix, P. Scouflaire, and S. Candel. Effect of temperature fluctuations on high frequency acoustic coupling. *Proc. of the Combustion Institute*, 32:1663–1670, 2009.

[132] Cédric Rey, Sébastien Ducruix, Franck Richecoeur, Philippe Scouflaire, Lucien

Vingert, and Sébastien Candel. High frequency combustion instabilities associated with collective interactions in liquid propulsion. *AIAA Paper*, 3518:11–14, 2004.

[133] S. Pavithran and L.G. Redekopp. The absolute-convective transition in subsonic mixing layers. *Physics of Fluids*, 1:1736, 1989.

[134] P.A. Monkewitz, D.W. Bechert, B. Barsikow, and B. Lehmann. Self-excited oscillations and mixing in a heated round jet. *Journal of Fluid Mechanics*, 213:611, 1990.

[135] J. Eldredge. Private communications. *UCLA*, 2009.

[136] K.T. Walsh, M.B. Long, M.A. Tanoff, and M.D. Smooke. Experimental and computational study of CH, CH*, and OH* in an axisymmetric laminar diffusion flame. Twenty-sixth Symposium (International) on Combustion, pages 615–623, 1998.

[137] H.N. Najm, P.H. Paul, C.J. Mueller, and P.S. Wyckoff. On the adequacy of certain experimental observables as measurements of flame burning rate. *Combustion and Flame*, 113:312–332, 1998.

[138] J. Kojima, Y. Ikeda, and T. Nakajima. Spatially resolved measurement of OH*, CH*, and C^*_2 chemiluminescence in the reactio zone of laminar methane/air premixed flames. *Proc. Comb. Inst.*, 28:1757–1764, 2000.

[139] A. F. Mills and B. H. Chang. Error analysis of experiments. *UCLA, Los Angeles, CA*, 2004.

[140] C. J. Dasch. One-dimensional tomography: a comparison of abel, onion-peeling, and filtered backprojection methods. *J. Applied Optics*, 31(8):1146–1152, 1992.

[141] L. Hoogterp-Decker and P. Schihl. The use of synthetic jp-8 fuels in military engines. 2009. RDECOM-TARDEC, Warren, MI.

[142] S. Teshome, O.I. Smith, and A.R. Karagozian. Droplet combustion in the presence of altered acceleration fields via acoustic excitation. *Western States Sections of the Combustion Institute*, 2009.

[143] W.L. Nyborg. Acoustic streaming due to attenuated plane waves. *J. Acoust. Soc. Am.*, 25(1):68–75, 1953.

[144] W.L. Nyborg. Acoustic streaming near a boundary. *J. Acoust. Soc. Am.*, 30(4): 329–339, 1958.

[145] A. L. Smith and C. C. Graves. Drop burning rates of hydrocarbon and nonhydrocarbon fuels. In *NACA RME 57*. F11, 1957.

[146] B. Vielle, C. Chauveau, X. Chesneau, A. Odeide, and I. Gokalp. High pressure droplet burning experiments in microgravity. *Proc. Combustion Inst.*, 26, 1996.

[147] B.R. Munson, A.P. Rothmayer, T.H. Okiishi, and W.W. Huebsch. *Fundamental Fluid Mechanics*. Wiley, 5th edition, 2005.

[148] Frank M White. *Viscous Fluid Flow 3e*. Tata McGraw-Hill Education, 1974.

[149] O.J. Haidn. Advanced rocket engines. In *Advances on Propulsion Technology for High-Speed Aircraft, Educational Notes RTO-EN-AVT-150*, pages 6–1 6–40. Neuilly-sur-Seine, France: RTO, 2008.

[150] A.G. Webster. Acoustical impedence, and the theory of horns and of the phonograph. *Proceedings of the National Academy of Sciences*, 5:275–282, 1919.

[151] A. D. Pierce. *Acoustics: An Introduction to Its Physical Principles and Applications*. Acoustical Society of America, 1991.

[152] P.J. Schmid. Dynamic mode decomposition of numerical and experimental data. *Journal of Fluid Mechanics*, 656:5–28, 2010.

[153] M. Arienti, M. Corn, G.S. Hagen, R.K. Madabhushi, and M.C. Soteriou. Proper orthogonal decomposition applied to liquid jet dynamics. *21st Annual ILASS-Americas Conference*, 2008. Orlando, FL.

[154] M. Arienti and M.C. Soteriou. Dynamics of free jets submitted to upstream acoustic modulations. *Physics of Fluids*, 21:112104, 2009.

[155] MR Jovanovic, PJ Schmid, and JW Nichols. Low-rank and sparse dynamic mode decomposition. pages 139–152, 2012.

[156] P.J. Schmid. Application of the dynamic mode decomposition to experimental data. *Experiments in Fluids*, 50:1123–1130, 2011.

[157] P.J. Schmid, L. Li, M.P. Juniper, and O. Pust. Applications of the dynamic mode decomposition. *Theor. Comput. Fluid Dyn.*, 25:249–259, 2011.

[158] National Institute of Standards and Technology. Thermophysical properties of fluid systems, 2011.

[159] R.D. Woodward, S. Pal, S. Farhangi, G.E. Jensen, and R.J. Santoro. LOx/GH2 shear coaxial injector atomization studies: effect of recess and non-concentricity. *45th AIAA Aerospace Sciences Meeting and Exhibit*, pages 1–22, 2007-571.

Forced and unforced shear coaxial mixing and combustion at subcritical and supercritical pressures

D. J. Forliti, Sierra Lobo, Inc., Edwards AFB, CA

I. A. Leyva and D. G. Talley, Air Force Research Lab, Edwards AFB, CA

J. I. Rodriguez, S. Teshome, and J. L. Wegener, ERC. Inc., Edwards AFB, CA

M. Roa, Sierra Lobo, Inc., Edwards AFB, CA

A. R. Karagozian, University of California, Los Angeles, CA

Abstract

Combustion instability remains one of the key technical challenges in the development of high-performance propulsion systems. The Air Force Research Lab at Edwards Air Force Base, over the past decade, has explored the mixing and combustion properties of coaxial jets and flames, which represents a model relevant to liquid rocket engines. These studies employed cryogenic fluids at both sub- and supercritical thermodynamic conditions, capturing many of the salient features associated with liquid rocket combustion chambers. The coaxial flows were investigated both under unforced and acoustically forced conditions, where the acoustic forcing was in the form of a transverse resonance. Mixing was characterized through the use of the dark core length, and generalized scaling correlations were developed. A variety of coaxial jet geometries were also investigated, and found to play a role in the coupling between the acoustics and the flow field. Forcing was found to couple to the flow field in a different manner depending on the coaxial jet geometry, flow parameters, and local acoustic conditions. The current state-of-the-art understanding of the coupling mechanisms will be described, and recent results under combustion conditions are presented. The results of this effort provide both the foundation for improved injector designs but also a framework for evaluating their robustness to acoustic disturbances.

Introduction

Combustion stability has been one of the pervasive issues with propulsion and energy systems. Combustion in a confined environment may exhibit a feedback loop phenomenon referred to as a thermoacoustic instability. Acoustic waves within the confined space can alter the mixing

process established by the injection system, resulting in a concomitant response in the heat release process. Unsteady heat release, when in proper phase with the acoustic field, can lead to amplification, closing the feedback loop. Although the description of such a feedback loop appears straightforward, the complexity is linked to the details in which the couplings occur between the acoustic field, propellant mixing, and combustion process.

There have been many studies on the physics of combustion instability, with each being motivated by a particular type of propulsion or energy system. Liquid rocket engines (LREs) are in particular impacted by combustion instability due to the extreme operating conditions of the combustion chamber and the severity of engine failure. The Air Force Research Lab (AFRL) at Edwards Air Force Base has sustained a focused effort to understand the mechanisms responsible for combustion instability in LREs. Both simulated and real propellants were employed, and characteristics relevant to LREs were incorporated including high-pressure operation and cryogenic propellants. Focus has been placed on the shear coaxial jet type propellant injector, the so-called coaxial jet, which is typical of hydrogen/oxygen LREs.

The Coaxial Jet

The coaxial jet has been the subject of study for several decades due to its relevance to propulsion and energy applications. As shown in Fig. 1(a), the coaxial jet is composed of two concentric jet flows that issue into an ambient environment. Ko and Kwan[1], a pioneer group of researchers in this area from the 70's, describe the coaxial jet into three spatial zones as shown in Fig. 1(a). The first zone downstream of the jet exit is referred to as the initial merging zone. In this region, both the inner and outer jets have potential cores bound by spatially-developing shear layers. The potential core is roughly defined as the region of the jet that has minimal vorticity. The downstream end of the initial mixing region is defined as the location where the two shear

layers begin to merge, which is also the location of the end of the outer jet potential core. This leads to the second zone, which is referred to as the intermediate merging zone. It is within this region that the inner and outer shear layers diffuse into one another and begin to spatially transform towards a single highly-disturbed shear layer. If the outer jet velocity is significantly higher than that of the inner jet (which is common for shear coaxial rocket injectors), a loci of maximums in the mean velocity distribution will emanate from the tip of the outer jet potential core. This local maximum velocity curve will move towards and eventually reach the jet centerline with increasing downstream distance. The location where the maximum mean velocity loci reaches the centerline is defined as the end of the intermediate merging zone and the beginning of the fully-merged zone. In this far field region, the coaxial jet flow field begins to exhibit the flow properties of a single round jet. Ko and coworkers explored this global flow field over a broad range of operating conditions where both jet flows are gases.[2-7]

In the context of combustion instability, the initial merging zone is of particular interest due to two factors. First, the presence of steep gradients and inflection points in the mean velocity field in this region can lead to hydrodynamic instabilities. Hence this region of the flow tends to be highly receptive to disturbances. Disturbances will tend to grow rapidly in this region in space and/or time. In a combustion scenario, these disturbances may directly lead to a *local* heat release fluctuation, or they may grow as they convect downstream and eventually lead to a more *global* heat release event. Second, the flame anchoring process occurs in the near field, often the flame attaches to the inner jet tube. Disturbances, both natural and external, can alter the flame stabilization mechanism, leading to axial or transverse flame motion, local quenching, and flame detachment. Dynamics of the flame stabilization process can play a role in a combustion

instability mechanism. Thus attention has been placed on natural instabilities in the coaxial jet near field, and the response of the flow to external forcing.

Figure 1(b) shows an illustration of the different near field hydrodynamic instabilities that are present in the coaxial jet. The region between the inner and outer flows is complicated by the presence of a finite thickness wall inner jet tube, which causes a wake region. Thus the layer between the inner and outer jet may exhibit an instability that is either of a shear layer, a wake mode, or a mixed mode. It is well known that there is a competition between the wake and shear layer instability mechanisms in this flow region.[8-14] In addition to the competition between the shear layer and wake instabilities downstream of the inner jet exit plane, the inner and outer shear layers can influence one another, leading to coupled dynamics.[11] Although the interaction between the two shear layers has been observed, a detailed understanding of the physics is still lacking, and the conditions under which strong synchronization occurs is not known.

The coaxial jet flow field is dependent on a variety of dimensionless groups based on the velocity and length scales as well as fluid properties. Regarding geometry, the coaxial jet has four characteristic diameters as shown in Fig. 1(b). The outer diameter of the outer jet tube, D_4, is expected to have negligible effect unless the coaxial jet is exposed to an external fluid that is moving. With this in mind, the geometry of the injector can be condensed into two parameters, the outer-to-inner jet area ratio, AR, and the dimensionless inner jet post thickness t/D_1. There is an additional geometrical parameter if the inner jet tube is recessed as shown in Fig. 2. There are two Reynolds numbers, one each for the inner and outer jet flows. Each shear layer is also known to be sensitive to the velocity and density ratio of the freestreams that bound the shear layer.[15] For coaxial jets, asymptotic analysis suggests that a key parameter is the outer-to-inner jet momentum flux ratio J,[16-18] which is defined as

$$J = \frac{\rho_2 U_2^2}{\rho_1 U_1^2}, \qquad \text{(Eq. 1)}$$

where the density ρ and velocity U are as represented in Fig. 1(b). The studies by Favre-Marinet et al.[19,20] on variable density coaxial gas jets supported the importance of momentum flux ratio, but also showed that density ratio has an additional separate effect. Although density ratio is acknowledged as a potentially important parameter, the leading parameter for the coaxial jet is considered to be the momentum flux ratio.

Figure 2 shows the more specific coaxial jet configuration of interest here, where the inner jet is liquid while the outer jet and ambient fluids are gases. Also shown in the figure is the presence of transverse acoustic waves, which impose pressure (p') and velocity (u') perturbations to the flow field. The presence of inner post recess is illustrated in the figure and represents an additional geometrical parameter. Having the inner jet tube recessed is expected have an impact on the mixing dynamics.[21] Injectors to be discussed in the current report have negligible recess. The presence of the liquid interface adds surface tension σ effects, which may be nondimensionalized to form the aerodynamic Weber number,

$$We = \frac{\rho_2 (U_2 - U_1)^2 D_1}{\sigma}. \qquad \text{(Eq. 2)}$$

For the case where the inner jet is liquid, the behavior of the multiphase flow of the coaxial jet can be broken into different regimes dependent on the liquid jet Reynolds number and the Weber number.[22] Visual results to be shown later will generally represent the fiber regime of atomization.

Figure 2 shows two additional key features of the two- phase coaxial jet. The first is the vortex pair anchored to the blunt trailing edge of the inner jet tube. These recirculation zones will be present with or without the wake instability (i.e. the recirculation zone may or may not be generating a vortex street), and this region is known to play a key role in flame stabilization in combustion applications.[23] The recirculation zone may also exhibit asymmetry depending on the velocity and density ratio between the two jet flows.[12,24] The location, size, and instability properties of these recirculation zones are likely to impact both the mixing dynamics and the response of the flow to external forcing. The second feature indicated on Fig. 2 is the dark core length, which is a measure of the length of the intact liquid column associated with the inner jet. The term dark is in reference to the fact that the liquid jet appears dark in backlit images. The dark core length is a global measure of the mixing process; a shorter dark core length indicates enhanced mixing between the inner and outer jets.

The last key bulk parameter of the two-phase coaxial jet is related to the operating pressure. As the ambient pressure is increased above the thermodynamic critical pressure of the inner jet fluid, the liquid surface tension disappears as does the sharp interface separating liquid from gas. The mixing of liquids and gases at supercritical pressure begins to behave like single phase mixing of fluids with extreme density differences.[25,26] Thus the reduced pressure is defined as

$$P_r = \frac{P}{P_{cr,1}}, \qquad \text{(Eq. 3)}$$

where P is the ambient pressure where mixing is occurring, and $P_{cr,1}$ is the critical point pressure of the inner jet fluid. When the fluids are all the same, e.g. nitrogen, the reduced pressure is a direct measure of sub/supercritical behavior. When different fluids are used, the characterization

of the operating regime is complicated by the fact that the critical point pressure is dependent on the mixture composition, thus it can be a quantity that varies in space and time.[27]

In addition to bulk parameters, the coaxial jet flow field is also sensitive to boundary conditions. The injectors used in these studies employed constant area tubes that are sufficient in length to establish fully-developed flow in the turbulent regime. Turbulence at the inner and outer jet exit is expected to play a role in disturbing the liquid interface in the near field, although results to be shown indicate that shear flow instabilities govern the formation of structures on the liquid surface.

Experimental Facilities and Instrumentation

Experimental Facilities

The experiments were conducted in the Combustion Stability Lab at the Air Force Research Laboratory located at Edwards Air Force Base, CA. Two facilities were used, one designed for nonreacting flows and the other for reacting flows. The nonreacting flow facility has been employed over the past several years to explore the dynamics of acoustically-forced cryogenic coaxial jets that simulate conditions representative of H2/O2 rocket engines.[28-30] The reacting flow facility, which was completed in 2014, has similar design and operation although has been designed to handle oxygen, hydrogen, and other hydrocarbons under combustion conditions. Pressurization for both facilities is achieved via high flow rate gaseous nitrogen. A choking orifice in the exhaust of the test section is used along with gaseous nitrogen flow in the outer chamber to set the chamber operating pressure. In addition, liquid nitrogen was used as the chilling fluid for achieving the desired inner and outer jet temperatures. The reacting flow

facility has a closed-loop temperature controlled heat exchanger that is safe for operation with oxygen.[31]

A schematic of the experimental test section concept used for both facilities is shown in Fig. 3(a). The design employ a "chamber within a chamber" approach, where the inner chamber creates an ideal environment for one-dimensional acoustic wave resonance, but is not sealed from the surrounding volume. This surrounding volume is the outer chamber, which has the structural integrity to withstand high pressure operation (13.8 MPa in the nonreacting flow facility, and 10.3 MPa in the reacting flow facility). As shown in Fig. 3, two acoustic sirens are located transversely offset relative to one another, allowing for the establishment of transverse acoustic resonance in the chamber. The circular piezoelectric sirens connect to the facility through carefully-designed waveguides. The sirens operate via resonance, and thus operate most effectively within narrow frequency bands. The nominal design resonant frequency for the sirens was 3 kHz, although a few additional resonant frequency bands are available.[31] The design of the chamber with waveguides was done to allow pure transverse modes to be generated near the natural frequencies of the acoustic sirens. Each siren is driven by a dedicated amplified sinuous waveform, with a relative phase shift between the two signals being used to establish different mode shapes within the chamber. For instance, in-phase driving signals can be used to establish a pressure antinode (PAN) at the middle of the chamber, while 180° out of phase driving signals result in a pressure node (PN) at this location. Figure 3(c) shows an image of the nonreacting flow test section while Fig. 3(b) and (d) show an engineering rendering and image of the reacting flow test section, respectively. More details of the facilities may be found in dissertations by Davis[28], Rodriguez[29], Teshome[30], and Wegener[31,32].

The nonreacting flow facility utilized high-pressure nitrogen supplies for the injector flows, while the reacting flow facility used a variety of fluids including nitrogen, oxygen, and helium. The injector flows are thermally conditioned using heat exchangers that employ liquid nitrogen. Motivated by relevant rocket operating conditions, for subcritical conditions, the inner jet was cooled to a sufficient condition to achieve a liquid state, while the outer jet was cooled but maintained as a gas.

Injector Design

A variety of shear coaxial injector configurations have been explored using the two facilities. Figure 4 provides a summary of the injector geometries including a schematic showing the relative scale of the various diameters (Fig. 4(a)). Injectors will be referred to as either I-V or using names using a combination of LAR or SAR and thin or thick, terms which are defined in Fig. 4. All injectors include a high length-to-diameter ratio to achieve fully-developed flow conditions. Figure 4(b) shows the two geometry parameters, area ratio AR and dimensionless post thickness t/D_1, for the five injectors. The designs sample the various combinations of thin and thick post thickness as well as high and low area ratio. It should be mentioned that the smallest normalized post thickness t/D_1 of ~ 0.1 studied here is still sufficiently large to expect a potential wake instability.[13] The larger post thickness configurations, injectors I and III, result in very large recirculation zones and a disruption/delay in the establishment of a shear layer-like between the inner and outer jet flows.

Figure 4(c) shows the operating conditions in terms of momentum flux ratio J and reduced pressure, $P/P_{cr,1}$. Injectors I through IV were explored at both sub- and supercritical conditions across a wide range of momentum flux ratios. The data shown reflects the conditions explored by Rodriguez[29], Teshome[30], and Wegener[31]. The main purpose of the studies by Rodriguez and

Teshome were to investigate both the nature of unforced injector flows and their response to high levels of acoustic forcing. The study by Wegener, using injector V, focused on two momentum flux ratios, approximately two and six, and investigated the sensitivity of injector behavior to variations in acoustic amplitude and frequency. The study by Wegener was limited to high subcritical operating conditions due to facility development timelines.

Instrumentation

Both facilities are fully instrumented with thermocouples and pressure transducers to characterize the condition of the working fluid at various points within the facility. Flow rates were measured using thermal mass flow meters. For the non-reacting facility, the injector exit temperatures were measured with a movable thermocouple that could measure near the exit plane of the injector. For the reacting facility, the injector exit conditions were based on temperatures measured near the inlet of the injector assembly. Mean exit velocities and momentum flux ratios were calculated using the measured mass flow rates, the temperatures at the inlets of the injector (for the reacting facility) or at the outlet of the injector (for the non-reacting facility), and the chamber pressure. The injector inlet temperature was used as an approximation to the injector outlet temperature for the reacting facility.

For the non-reacting facility there was a movable thermocouple and a Kulite pressure transducer that came up from the bottom of the chamber and allowed axial profiles of temperature and pressure to be obtained. Examples of such temperature profiles are shown in Fig. 5. These profiles are for the injector IV or LAR-thin. An accurate determination of the temperature at the exit of the injector increased the accuracy of parameters such as density and momentum flux ratios. Also, having detailed profiles of the temperature give a qualitative description of how much mixing between the inner and outer jets has occurred in this case by one D_1 downstream of

the exit plane. For example, in all the profiles in Fig. 5 there is hardly a flat temperature part for the inner jet, that is mixing has already occurred between the two jets at the measurement location. These profiles are also influenced by heat transfer between the inner and outer flows within the injector hardware.

Three Kulite differential pressure transducers were placed flush with the inside face of the back acrylic wall of the inner chamber to characterize the acoustic amplitude and mode. One pressure transducer was placed at the same transverse location as the injector while the other two were located equidistant on either side of the center. These transducers were used to optimize the acoustic sirens to achieve the desired acoustic environment.

The primary means of studying the coaxial jet flow dynamics was provided by backlit high-speed images. A Newport model 66986 variable power supply controlled a 300 W Xe lamp that emitted a collimated beam in the near ultraviolet spectrum and was used as the back-light source. Differences in the refractive index of the jets and the surrounding medium provided the necessary distinction between the fluids of interest. The inner jet, due to high fluid density, appeared as a dark column as viewed by the high-speed camera on the opposite side of the light source. The less dense outer jet was also in many cases distinguishable from the relatively warmer ambient gaseous nitrogen in the chamber.

Phantom v7.1 and v710 high-speed cameras (shown in Fig. 3(c) and 3(d)) were used to capture the rapid dynamical processes inherent to an unforced coaxial jet flow as well as those present during high-frequency acoustic forcing. An image frame rate of 20-30 kHz was used to avoid aliasing of up to the fourth harmonic of the forcing frequency. An external trigger was used to start recording of the image frames, which were synchronized to the Kulite dynamic pressure transducer recordings at the same sample rate of 20-30 kHz using an IRIG-B timecode. The

receptivity study of Wegener for injector V used a lower frame rate of 10 kHz to allow longer video records to be achieved to resolve potential low frequency phenomena.

Various image post-processing methods were applied to extract information from the data. Dark core lengths and shear layer spreading rates were measured through contrast-based algorithms.[29,30] Decomposition algorithms have become a critical tool in extracting organized behavior in the highly turbulent flow images. Proper orthogonal decomposition (POD)[33,34] and dynamic mode decomposition (DMD)[35-38] applied to the image sets have facilitated the identification of spatial and temporal behaviors intrinsic to the natural and forced flows. These techniques play a key role in isolating dynamics that are imbedded in noisy broadband data.

Results

Unforced nonreacting flow behavior

This section will give a brief account of the general observable behavior of the coaxial jets for the several injector configurations with varying momentum flux ratio at the different chamber pressures. Since the dense inner jet flow is best seen on the images, the discussion will be centered around the dark-core flow region and the identifiable flow structures on the periphery including the outer jet.

The effect of momentum flux ratio J on the mixing characteristics will first be explored for injector IV, a thin inner post and high area ratio design, at subcritical pressure operating conditions. It is to be noted that the inner jet tube for injector IV was not perfectly flush, but stuck out by about $0.2D_1$. This allowed for direct visual confirmation that the inner jet injector tube was not oscillating due to turbulent flow disturbances in the outer jet. This injector was operated with nitrogen for both the inner and outer jet, with the inner jet being condensed to a

liquid prior to reaching the injector. Figure 6(a) shows the unforced injector IV flows at various momentum flux ratios at a subcritical relative pressure Pr = 0.44. At J = 0.1, the presence of the very low momentum outer jet flow had minimal impact on the development of the liquid inner jet flow. The low aerodynamic Weber number of approximately 20[30] for this low J case enabled the inner jet to maintain integrity for over $20D_1$ downstream of the exit, which is about where the field of view in the image ends. Although small periodic surface wrinkles started forming about $10D_1$ downstream of the exit, they were not large enough to disrupt the continuity of the jet. As the outer jet flowrate was increased resulting in J = 0.5, the dark-core region stayed intact for over $20D_1$. However, surface instabilities were enhanced and occurred earlier than for the lower J case. The widening of the dense core is apparent as it mixes with the outer jet.

As J increased to a value higher than unity, the dark-core region could no longer remain intact within the field of view, and broke up into fine droplet spray. The presence of a higher shear force at the inner jet interface also aided in the formation of a fine mist of droplets on the periphery of the inner jet flow. Enhanced entrainment of the inner jet fluid into the outer flow was evident in the increased spread of the inner jet. Higher J values aided in the break-up and dispersion of the inner jet and enhanced mixing with the outer jet at closer distances to the injector exit. Accordingly the dark-core length became shorter with increasing J. For this injector, any influence of the inner jet post is limited to the very near field of the injector, and the mixing is governed by an apparent shear layer instability.

The mixing properties of injector III, a thick inner post design with a small area ratio, is shown in Fig. 6(b) as a function of J at subcritical pressure operating conditions. It should be noted that the inner jet diameter is nearly twice that of injector IV. At J = 0.1, just as with injector IV, the inner jet for injector III stayed intact and relatively undisturbed along the entire field of view of

which extends $13D_1$ in length. In contrast to the injector IV flow, the thick inner jet post of injector III causes the formation of an axisymmetric recirculation zone. For the low J case, the low momentum outer jet fluid predominates in the recirculation zone. The sense of the dominant rotation of the recirculating flow, evident from viewing sequential images, can change with operating conditions. For lower momentum flux ratios, the rotation direction was such that a local counterflow condition was established at the interface of the inner jet and the recirculation zone.

At J = 0.5, there was a significant presence of surface irregularities that formed ligaments just a few diameters D_1 downstream of the exit, and subsequently broke down and dispersed into droplets. Yet, the dark-core region still remained intact for the entire field of view. The recirculation zone also consisted of the outer jet fluid with small traces of droplets that came off the surface of the inner flow. The inner jet interface experienced reduced disturbances in the initial region where the recirculation zone is present. The merging of the outer jet flow to the inner jet interface, which occurs downstream of the recirculation zone, appears to match the location where the inner jet surface experiences enhanced diffusion.

When the momentum flux ratio increased to J = 2.1, the fluid inside the recirculation zone mainly consisted of the lower momentum inner jet fluid, and the predominant sense of rotation changed such that a counterflow existed at the inside boundary of the outer jet. As shown in Fig. 2, a pair of counter-rotating vortices is expected near the inner jet post exit plane. It is likely that the extreme density and velocity ratios across the post result in asymmetry in the vortex pair, and the imaging indicates a dominance of one of the vortices over the other.

The presence of the dense, dark fluid in the recirculation zone created a perception of "necking" in the dark-core flows. Further downstream, the dark-core could no longer maintain continuity and was fully dispersed into droplets. Small and larger scale surface disturbances are observed along the length of the inner jet core. As the momentum flux ratio increased to J = 5.7, the recirculation zone was completely obscured with inner jet fluid droplets. The remaining inner jet fluid experienced increased dispersion resulting in a shorter dark-core length. Increasing to J = 15 and J = 21 showed relatively small decreases in the dark-core length.

The subcritical mixing behavior presented in Fig. 6 is in general representative of other injectors designs tested in these facilities. Rodriguez[29] found that the transition of a droplet laden recirculation zone for injector I occurred at a momentum flux ratio above 2.6, while Teshome found the transition to occur near 2.1 for injector III. Wegener studied injector V up to a momentum flux ratio J = 6, and didn't observe significant droplet presence in the notably smaller recirculation zone (due to the small post thickness). It should be noted that Wegener employed helium in the outer jet, while Rodriquez and Teshome used nitrogen.

Injectors I-IV were also tested at supercritical pressure conditions (Pr = 1.05) to investigate the mixing process at conditions more representative of liquid rocket engines. Figure 7 shows the flow visualizations for injectors IV and III at different momentum flux ratios. These cases employ pure nitrogen in both the inner and outer jets and in the chamber, thus surface tension at the liquid interface is known to be eliminated. The mixing behavior with changing J is qualitatively similar to that observed at subcritical conditions. However, both injectors showed increased spread at supercritical conditions, especially at lower momentum flux ratio, as evident in the thicker inner flow region. This is a manifestation of no surface tension at supercritical

conditions. The dark-core regions were also shorter compared to the flows with similar J values at subcritical conditions.

As shown in Figs. 6(b) and 7(b), the recirculation zone has qualitatively similar behavior at supercritical conditions for injector III. The darkening of the recirculation zone, an indicator of higher presence of dense inner jet fluid, occurred at a lower momentum flux ratio of 0.5 at supercritical conditions, compared to the subcritical value of 2.1. Thus surface tension inhibits entrainment of inner jet fluid into the recirculation zone.

Dark-core Length

The length of the dark core can be defined and computed in many different ways. Therefore absolute values of this quantity are not as important as relative differences measured for different injectors for similar nominal conditions or different flow conditions for a given injector. In other words, relative increase or decrease of the dark core length as conditions change relative to a baseline value are more meaningful than comparing absolute values for the dark core lengths. Since the length of the inner jet is related to how rapidly mixing is occurring with the outer jet and the surrounding environment, shorter lengths denote faster mixing and vice versa. It is worth to point out that although qualitatively the dark core length is related to the potential core length, we did not measure the potential core in these studies.

For these studies, the dark core length was computed using a series of MATLAB® subroutines. First, the raw images from the camera are thresholded to a black and white (b&w) image. The length of the inner jet is determined by drawing a contour and measuring the axial length of the longest contour of the black portion of the image attached to the injector as shown in Fig. 8. This length is an axial length, in the sense that it does not take into account any curviness of the jet,

which is typically seen with acoustic forcing. In an attempt to investigate whether the transverse acoustic field does shorten the length of the jet or only curves it, the curved or total length was also measured. In this case, the same contour already used to measure the axial length is divided into a left and a right side (see Fig. 8(d)). The total length is defined as the average of the left and right sides. It turned out that for all the cases studied here the trends seen for the axial length were similar to the trends seen for the total curved length, so further studies only focused on the axial length.

When the technique to measure the dark core lengths was first developed, 50-60 images were randomly selected from each set of 2000 images for a given flow condition and the results given by MATLAB were manually compared with lengths selected using visual inspection. The technique was optimized until the results agreed well with those obtained manually by 2-3 researchers.

The most widely studied injector by this group was injector 1, LAR-thick. The data obtained by Davis[28] and Leyva, Chehroudi, and Talley[39] for LAR-thick, along with historical data for different injectors at a wide set of operating conditions, showed good separation into two branches, as shown in Fig. 9. The upper branch corresponds to two-phase subcritical cases and the lower branch corresponds to supercritical or single-phase data. It is clear that mixing of two-phase flows at subcritical pressures is slower than mixing for single-phase systems. The subcritical data has an approximate relation of $J^{-0.2}$ and the single-phase data has an approximate relation of $J^{-0.5}$. However, as research progressed at AFRL and different injectors were studied, the separation between the two branches seen in Fig. 9 was filled by data taken with injectors II-IV pointing to the importance of other parameters besides J to characterize mixing, as we will see below.

A very interesting feature that was observed for the data gathered at near critical pressures for LAR-thick is the effect of the density of the inner jet. As shown in Fig. 10(a), significant of scatter was observed on the dark core length data for a given value of J for similar chamber pressures. It was clear that the density of the inner jet varied significantly for the cases studied (ρ/ρ_{cr} varied from 0.5 to 1.8) and that even though the density ratio of the outer to the inner jet is taken into account in the definition of J, a different parameter was having an effect. Therefore, the data was normalized by the ratio of a reference density to the density of the jet being measured. The reference density was chosen to be 190.4 kg/m^3 corresponding to nitrogen at T = 129K and 3.55MPa, which are the average conditions of the data taken at ρ_{cr}=0.5-1. As can be seen in Fig. 10(b), the collapse is very good and all the data now more or less lie on the same curve. The same normalization was applied to data taken at ~5MPa and the collapse was also noticeable. This example is shown in this chapter to show the reader that there might be a direct effect of the inner jet density on mixing independent of other variables, and this effect could be explored further in new studies.

To understand the effects of geometry on mixing for a shear coaxial injector and whether they could be as strong as the effects of momentum flux ratio, four nominal geometries, injectors I-IV (Fig. 4), were studied. With these four geometries the effects of area ratio and inner jet post thickness could be studied. Injector V was nominally designed to be the same as injector II but due to manufacturing constraints it could not be reproduced identically.

The results obtained with injectors I through IV for subcritical pressure (Pr = 0.44) are shown in Fig. 11. All data are for nominally flush configurations except for SAR-thin (Graham et al.)[40] which has a $0.5D_1$ recess of the inner jet tube. Since each curve corresponding to a different geometry follows a different trend with J, it is shown that geometry plays a significant role in

mixing for the cases studied. The slowest mixing consistent across the range of J studied is for injector LAR-thin and the fastest mixing is for SAR-thick. However, comparing LAR-thin and LAR-thick, we see that for similar AR values, having a thick post with a pronounced recirculation zone helps mixing, which is intuitive, since the structures created in the recirculation zone are very efficient at mixing fluid from the outer and inner jets. The same general trend is true when comparing SAR-thin and SAR-thick, except that as set, the data for SAR injectors shows lower values for dark core length than the data for LAR injectors except for J > 10 when the values for LAR-thick and SAR-thin become about the same if one accounts for the errors bars. Observations from Champagne and Wygnanski[41] and Gladnick et al.[42] also point to longer potential core lengths with larger area ratio. This is somewhat intuitive since for LAR cases there is more volume of fluid to mix with in the outer jet.

The dark core length trends for the conditions near the critical pressure shown in Fig. 12 are not as clear as for subcritical cases. While the data for the recessed case for SAR-thin collapsed with the data for the same injector with no recess for subcritical pressures, this is not the case here. Therefore the data is included for completeness but the description below applies only to the flush injectors. It is still the case that the slowest and fastest mixing correspond respectively to LAR-thin and SAR-thick as for the subcritical case. However, the difference between LAR-thin and LAR-thick are much smaller. The dark core lengths for the SAR-thin injector are still consistently longer than those for SAR-thick as it was the case for subcritical pressures.

As a first attempt to capture the behavior and dependency of the dark core length with geometry and J, the data was fitted to a relation of the form:

$$\left(\frac{L}{D_1}\right) = c_1 J^{c2} \left(\frac{t}{D_1}\right)^{c3} \left(\frac{A_o}{A_i}\right)^{c4}. \qquad \text{(Eq. 4)}$$

The fit coefficients were determined using linear regression and the values for the exponents for the subcritical and near critical data are shown in Fig. 13(a-c). As can be seen from the exponents, for the subcritical data, the effects of area ratio and J are comparable but in the opposite direction. The effect of inner jet tube thickness is the smallest one. For the near-critical data, the effect of J is strongest and the effects of the two geometry parameters are comparable to each other though in opposite directions. In general, as already explained above directly from the plots, there is a negative dependence of the dark core length with normalized thickness of the inner jet and a positive dependence with area ratio.

Inner Shear Layer Convection Velocities

The evolution of structures on the inner jet boundary play an important role in the mixing process. Thus there is a need to understand the properties of these structures; their formation frequency, velocity, and growth rate. One of the key aspects of the coaxial jet is the frequency content associated with the mixing process. In terms of rocket combustion instability, one would ideally avoid matching natural frequencies in the flow field to the acoustic modes of the combustion chamber. Hence there is a need to establish frequency scaling laws for the coaxial jet. The Strouhal number, defined as

$$St = \frac{f_{nat} D}{U}, \qquad \text{(Eq. 5)}$$

where f_{nat} is the natural frequency of the flow field, D is the characteristic diameter, and U is the characteristic velocity. Independent of the type of flow being studied, the selection of characteristic scales is very important. For the velocity scale, the choice must either represent

the velocity of the instabilities, or at least be proportional to this velocity. For the variable density coaxial jet, it is unlikely that either the inner or outer jet velocity will be representative of the convection velocity of the instabilities over a broad range of conditions. Thus a definition for the characteristic velocity that was at the very least proportional to the convection velocity of the most prominent features in the coaxial jet was needed.

Dimotakis developed an analytical shear layer model for planar variable density shear layers. The convection velocity estimated by Dimotakis[43] in this model involved the velocity weighted by the square root of the density,

$$U_{c,th} = \frac{\rho_1^{1/2} U_1 + \rho_2^{1/2} U_2}{\rho_1^{1/2} + \rho_2^{1/2}} \qquad \text{(Eq. 6)}$$

where $U_{c,th}$ is this theoretical convection velocity. This convection velocity is derived by requiring the dynamic pressure of the two streams bounding the shear layer structure to be equal in the reference frame of the convecting structure. Equation 6 obviously neglects the effects of surface tension, thus the applicability is likely to depend on the Weber number.

To test the validity of Eq. 6, shear layer convection velocities were experimentally measured via image analysis. Consider an array of pixels as shown by the green curve in Fig. 14(a). A piecewise linear trajectory is manually selected along the edge of the inner jet shear layer as interpreted from the mean image. For a single pixel lying on this trajectory, the pixel intensity will oscillate in time from low (dark) to high (light) as dense fluid structures convect through the area. When the entire pixel trajectory is considered rather than a single point, the vortices will traverse through the array of pixels, creating areas of dark and light pixels which move in time. Figure 14(a) shows this streak pattern created over a sequence of images. On the y-axis the shear layer curve coordinate s is nondimensionalized by D_1, while the x-axis is time in milliseconds. A

diagonal streak represents the convection of a liquid structure which begin near the injector exit and travel downstream as time advances from one image to the next. Very close to the injector, $s/D_1 \approx 1$, a dark horizontal bar in the streak image represents the signature of the end of the recirculation zone. The convection velocity upstream of this dark horizontal feature, represented by the slope of the streaks, is less than the shear layer convection velocity downstream of the recirculation zone, where the much faster outer jet meets the inner jet. The streaks which appear at $s/D_1 > 1$ are of interest here. The slope of a single streak, $\Delta s/\Delta t$, is the velocity of the coherent structure represented by the streak. A collection of eight structures represented by dark diagonal lines in Fig. 14(a) were randomly chosen and their velocities were measured; the dashed line in the figure represents a streak from which one sample was determined. The average of this set of convection velocities was computed to represent the experimental convection velocity, $U_{c,meas}$, for each experimental condition.

Figure 14(b) shows predicted versus measured convection velocities for the two momentum flux ratios employed for injector V. Data was collected for nominal and a higher flow rate for both momentum flux ratios. The conditions for the two momentum flux ratios were selected to keep the convection velocity predicted using Eq. 6 fixed, hence the overlap of points for both momentum flux ratios. The agreement is quite good, indicating that the Dimotakis model may be employed for the current flow conditions. A deviation is observed at higher flow rates (high convection velocities) and is likely due to heat transfer within the injector. An error in temperature due to heat transfer within the injector leads to a direct error in the evaluated fluid density. The velocity is estimated using the calculated density and the measured flow rate, thus creating further error due to temperature uncertainty.

Proper Orthogonal Decomposition of Image Data

Proper orthogonal decomposition (POD), also known as principal component analysis (PCA), has proven to be a powerful means for extracting relevant qualitative and quantitative information from otherwise complicated and noise-ridden measurement data. Berkooz et al.[44] and Chatterjee[45] give an in-depth discussion on the fundamentals of POD. The POD algorithm was applied to injector visualization data using the singular value decomposition (SVD).[46] In this approach, the singular values represent the square root of the POD eigenvalues. The POD eigenvalue, in turn, represent the "energy" contribution of each mode to the overall signal energy. The mean image was subtracted from the data set prior to application of the SVD, thus the eigenvalues represent variance.

Figure 15 shows the POD results obtained for injector V operating at a momentum flux ratio of two. The POD spectrum, in terms of singular values, is shown in Fig. 15(a). The results shown in this figure are based on a POD of 2000 images, thus 2000 POD modes are generated. The POD spectrum indicates the broadband nature of the data, as the decay in singular value magnitude is relatively gradual. The horizontal lines on the figure indicate the levels where the variance contribution are $1/10^{th}$ and $1/100^{th}$ of the 1^{st} mode. For this case, the energy contribution drops to about $1/10^{th}$ the maximum at about mode twelve, and about $1/100^{th}$ at about mode 100. Although the higher modes (mode numbers > 100) when combined contribute significantly to the variance in the data set, these modes represent very small-scale behavior and noise, and each mode contributes very little to the overall signal. Most of the organized behavior is contained in the lower modes. Due to the spectrum shown in Fig. 15(a), attention was focused on the first 10-12 modes for each case.

Figure 15(b) shows the spatial mode shape of the first eight POD modes. These mode shapes represent spatial features that fluctuate in time to contribute to the mean subtracted data set. The

spatial mode for mode 1, showing negative and positive extended regions located symmetrically about the jet axis, appears to be representing an antisymmetric flapping behavior. Spectral analysis of the time dependent coefficient shows that this mode is very low frequency. Mode 2 shows a mixture of symmetric and antisymmetric features, thus appears to be capturing a "pulsing" of the jet width along with some flapping in the downstream half of the domain. Modes 3 through 8 have smaller positive and negative lobes that represent the structures along the liquid jet interface. There is a trend of decreasing structure size with increasing mode number, which is a common trend in POD of turbulent flows. It is within these lower modes (3 through 8) that the strongest hydrodynamic instabilities of the coaxial jet are captured. Although the flow is highly turbulent and contains a range of frequencies, there is a need to identify the characteristic frequency of the flow, i.e. the preferred mode.

The POD results isolate a number of modes that capture various phenomena ranging from global flapping, shear layer type instabilities, and random small-scale dynamics. Emphasis was placed on isolating hydrodynamic instabilities associated with convecting structures on the inner shear layer, as these features are likely drivers of combustion instabilities.[47-50] Arienti and Soteriou provide a criteria for identifying convective modes from POD data.[51] First the POD spectrum, meaning the eigenvalues as a function of mode number, is constructed and pairs of modes with similar eigenvalues are sought. Once a candidate mode pair is identified, the cross-power spectral density (CPSD) and phase difference is calculated between the temporal coefficients of the mode pair. Once this has been done, the mode pair can be determined to be representing a convecting mode if:

1. the peak in the CPSD is coincident with a region of ± 90° phase shift;

2. the spatial distribution of the POD eigenfunctions are similar with features that are shifted nominally half a wavelength in the convection direction.

If a mode pair satisfied these conditions, a convective dynamic mode has been identified and the frequency of the particular convective mode is associated with the peak in the CPSD. In this study, the preferred mode is associated with the convective mode having the most energetic POD mode pair (i.e. the mode pair with the highest eigenvalues). It is likely that multiple convective modes are present in the unforced cases due to the highly turbulent nature of the flow. Other convective modes with lower singular values are not considered as representing preferred modes.

As an example of this process, Fig. 16(a) shows an identified potential convective mode pair that have similar singular values (i.e. eigenvalues) and have spatial mode shapes that appear to have features that are shifted a half wavelength; the process of identifying potential mode pairs is subjective and many different combinations are evaluated. In this case, POD modes 3 and 4 appear to be potentially representing a convective process. The CPSD is calculated, and the amplitude and phase are calculated as shown in in Fig. 16(b). There is a spectral region where the phase angle is near 90°, and within this region, a peak in the amplitude is present near 1 kHz. Thus this represents the frequency of the preferred mode, since any other convective modes present in the POD decomposition will have lower energy, due to the energy ordering property of the POD technique.

The process described above to identify the preferred mode frequency of the coaxial jet was applied to a number of data sets for injector V for both momentum flux ratios of two and six, and nominal and high flow rates. The average of D_1 and D_2 was used as the characteristic diameter in the Strouhal number defined in Eq. 1. Figure 17 shows the dimensionless frequency as a function of momentum flux ratio for the two different convection velocities. The measured

convection velocity provides a slightly reduced level of scatter compared results using Eq. 6, in large part due to the deviation that occurs at higher convection velocities indicated on Fig. 14(b). The trend represents a nominally constant value for the Strouhal number of 0.3. Spectra near the potential core end for the free jet data of Ko and Davies[52] and coaxial jet data of Ko and Kwan[1], when recast in the form of Eqs. 4 and 5, fall within the scatter around 0.3.

Strongly Forced Coaxial Jets

Leyva, Rodriguez and Teshome investigated the response of injectors I-IV to high amplitude acoustic forcing at both sub- and supercritical pressure conditions. These research campaigns used the nonreacting flow facility, and employed near maximum siren amplitude at a frequency near 3 kHz. As mentioned in the experimental facilities section, the relative phase between the two piezoelectric sirens was varied to manipulate the acoustic environment. Rodriguez varied the relative phase angle in increments of 45° while Leyva and Teshome focused on 0° and 180° phase shift. A phase shift of zero will result in a pressure antinode (PAN) in the middle of the chamber, while a phase shift of 180° will generate a pressure node (PN) at this location.

Figure 18 shows the instantaneous backlit images for injector I operating at subcritical pressure conditions for a four different momentum flux ratios. For each momentum flux ratio, a variety of different phase angles are shown, with the first image in the upper left of each ensemble showing the unforced case for reference. For each image ensemble, the phase angle where maximum and minimum pressure fluctuation amplitude was achieved is labeled. Ideally these conditions would be zero and 180°, respectively, but spatial temperature and density variations as well as siren/electronics imperfections are likely responsible for the observed deviations.

Figure 18(a) corresponds to the low momentum flux ratio case where J = 0.17. The overall behavior of the jet does not change substantially with acoustic forcing, but a slight increase in mixing can be observed. For several phase angle cases, the inner jet experiences slightly enhanced spreading. In contrast, the 135° and the baseline conditions show very little spread and the core only starts to break up towards the bottom of the image.

The second set of subcritical images for injector I in Fig. 18(b) correspond to a momentum flux ratio of 2.6. The effects of the acoustics in this set of images are very clear. The inner jet dark core bends transversely for every phase angle reaching a minimum length at 180°, which corresponds the minimum pressure fluctuation amplitude but maximum velocity amplitude. For this case, mixing is enhanced significantly with large regions where the dark core structures have almost completely blended with their surroundings. The behavior at 315°, the phase angle associated with maximum pressure fluctuation amplitude, demonstrates the least transverse motion of the inner jet due to acoustic forcing.

The next set of images for the acoustically forced subcritical injector I configuration is shown in Fig. 18(c) and corresponds to a momentum flux ratio of 9.6. All the images feature a very thick dark core which differs substantially from the thin dark core regions observed in the previous two sets of images. This thickness is evidence that the high momentum flux of the outer jet is having a strong effect on the inner jet allowing it to expand very rapidly across the recirculation region at the exit of the injector as was shown in Fig. 6(b) for injector III. Transverse motion of the dark inner jet is observed, with no clear influence of the phase angle. In a sense, the dark core is too short to show any bending due to acoustic forcing. However, it is clear from all the acoustically forced images that downstream of the dark core breakup the ensuing mixing region is curved, widened and perturbed by the acoustic forcing.

Finally, the set of images for the forced subcritical injector I configuration corresponding to a momentum flux ratio of 23 appears in Fig. 18(d). The shape of the dark core does not seem to vary noticeably among the images and the only difference is the slight change in curvature towards the downstream end of the dark core for different acoustic conditions. However, just like in Fig. 15(d) the downstream region past the breakup of the dark core is curved, widened, and perturbed by the acoustics.

It should be mentioned that the results shown in Fig. 19 are for high levels of acoustic forcing, where the peak-to-peak pressure amplitude was in the 3-4% of the chamber mean pressure. In these tests, the momentum flux ratio was varied by holding the inner jet flow rate nominally constant while the outer jet flow rate was varied. Thus as the momentum flux ratio is varied, the dynamic pressures of the outer jet, both mean and fluctuating, change in the flow field. Thus the lower effect of the acoustic field on the coaxial jet mixing is likely contributed by the relative variation between acoustic and hydrodynamic pressure amplitudes.

Figure 19 shows the response of the coaxial jet to acoustic forcing at subcritical pressure for injector II. This injector has a relatively thin inner jet post thickness. The images shown in Fig. 19(a) correspond to a momentum flux ratio of 0.089. The upper left image in the ensemble shows the coaxial jet when no acoustics are present. The inner jet can be clearly distinguished from the outer jet and its surroundings. The thickness of the inner jet stays constant throughout the image. This injector has a dramatic response to acoustic forcing. For the phase angles from 0° to 90°, the inner jet bends noticeably and there is strong atomization taking place near the injector exit. The background flow of the chamber is difficult to notice and the dark core region is somewhat thicker and blurred. The next two phase angles show a perturbed, but straight, inner jet. The images corresponding to a phase difference between 225° and 315° show the liquid

stream from the inner jet shortened significantly, with large structures of liquid that have been separated from the inner jet. The acoustic response of injector II at low momentum flux ratio is dramatically different than that for injector I (Fig. 18(a)). While the percentage of the acoustic pressure to the chamber pressure was about the same as for injector I, the inner jet for injector II was operated at approximately half the velocity of injector I, thus the acoustics were operated at a much higher relative pressure compared to the dynamic pressure of the inner jet. This could be partly responsible for the enhanced influence of acoustics on the injector II case at low momentum flux ratio.

The set of images in Fig. 19(b) show injector II at a subcritical pressure and a momentum flux ratio of 2.0. There is a striking response of the coaxial jet to acoustic excitation in this case. The mixing is dramatically enhanced near phase angles of zero, which is associated with a pressure antinode. Large apparently coherent axisymmetric structures are formed near the injector exit. These structures become very large and facilitate rapid mixing and breakdown of the inner jet. A similar behavior has been observed for PAN forcing for injectors IV[30] and V[32]. It is apparent that this behavior is more prevalent when the inner jet post is thin. The acoustic response for phase angles around 180° shows a different behavior. There appears to be a lengthening and thinning effect on the inner jet. Although, not clear from this viewing angle, there might be a flattening effect that pressure node forcing can have on jets[53] and coaxial jets[54]. Views from the side of the jet would need to be taken to confirm this. The thinning of the inner jet happens some distance downstream of the exit plane. Note that immediately downstream of the exit plane the thickness of the inner jet is comparable to the baseline. The jet at a PN condition is clearly different than the sinuous motion generated for injector I (Fig. 18(b)). It is currently unclear why an injector flow responds so differently to PN excitation as highlighted by the differences

between Figs. 18(b) and 19(b). Lastly, the image taken at phase angle of 225 degrees, shows a very good example of the enhanced mixing between the inner and outer jets forming what appears to be coherent asymmetrical structures with mass from both jets.

Figures 19(c) and (d) show injector II at subcritical pressure at momentum flux ratios of 7.8 and 18, respectively. The results of these two momentum flux ratios are similar. The PAN forcing, which is associated with phase shifts near zero show the strongest impact of forcing. Apparent axisymmetric structures are formed on the inner jet surface, and mixing enhancement is observed. The effects of forcing near the PN condition do not manifest in any clear effects. The low effects of the acoustics present at J = 2.0 is not evident.

Acoustic forcing of injectors III and IV was conducted by Teshome.[30] Only two phase angles, pure PAN and PN forcing, were considered. Figure 20 shows injector IV at subcritical pressure under conditions of unforced, PAN forcing, and PN forcing at a variety of momentum flux ratios. Overall the behavior is similar to that observed by Rodriguez for injectors I and II. The PAN forcing results in the excitation of axisymmetric structures on the inner jet core. The wavelength of the instabilities, particularly in the lower momentum flux ratio range, increases with momentum flux ratio, which is partially caused by the manner in which the different momentum flux ratios were achieved. Forcing at PAN conditions enhanced mixing, with the effect degrading with increasing momentum flux ratio. As with the results of Rodriguez, the acoustic forcing amplitude was scaled to the mean chamber pressure.

The PN forcing for injector IV shown in Fig. 20(c) show an interesting trend with momentum flux ratio. The lowest momentum flux ratio case exhibits a modest wrinkling of the liquid surface with no jet deflection. As the momentum flux ratio is increased to 0.5, the response

changes to the sinuous behavior observed with injector I. The sinuous response continues at higher momentum flux ratios.

The subcritical pressure response of injector III to acoustic forcing is shown in Fig. 21. This injector is a thick post design like injector I, although it is significantly larger in size, allowing improved optical access to the near field. Here the PAN forcing is clearly seen to enhance liquid ligament formation, in particular at lower momentum flux ratios. At the two lowest values of J, the generation of coherent structures in the recirculation zone is clearly seen and their entrainment of outer jet mass. By the third value of J, the recirculation zone is much darker as mass from the inner jet is now more entrained and it is more difficult to identify coherent structures near the jet exit plane. In the three highest values of J, the recirculation zone is now all dark, giving the appearance of a much thicker inner jet core, and the coherent structures appear as features of the denser inner jet. These structures, as will be seen in later analysis are symmetric with respect to the jet axis, and the structures are likely axisymmetric.

The response of injector III to PN forcing as shown in Fig. 21(c) is different in nature. The lowest momentum flux ratio case appears to be experiencing some thinning in the near field near the center of the image, followed by enhancement of atomization. A similar observation was made by Baillot et al. when viewing PN forcing that caused the previously mentioned flattening effect.[54] The lowest momentum flux ratio in fact looks very similar to the PAN case in terms of the structures being generated in the recirculation zone but qualitatively the wavelength of each structure is smaller. The next image is also qualitatively similar to the corresponding one for PAN in the behavior of the recirculation zone but the outer jet seems to be less disturbed downstream. For the remaining three higher momentum flux ratios, the dark core is shorter than in the corresponding cases for PAN and there are less pronounced structures in the inner jet,

except for the very last case where structures are observed near the end of the core. However, no large-scale flapping occurred such as that observed for injector I (Fig. 18(b)). There are two substantial differences between injectors I and III. The first difference is the area ratio; injector I has a high area ratio and injector III has a low area ratio. The second difference is the scale of the injector (see Fig. 4). The inner jet for injector III is nearly three times larger than that for injector I. Noting that the forcing frequency was held constant near 3 kHz to maintain the highest acoustic amplitudes possible, but different scale injectors are likely to have different natural mode frequencies, thus the relative frequency may be substantially different.

The nonreacting flow facility was also used to explore the acoustically-forced flow response at supercritical pressure for injectors I-IV. Figure 2 shows injector I operated at supercritical pressure for three different momentum flux ratios. Once again, the relative phase between the two sirens was varied from zero to 360° in 45° increments. Maximum and minimum pressure fluctuation amplitude is indicated on each section of the figure, indicating the approximate PAN and PN conditions, respectively. The set of images shown in Fig. 22(a) corresponds to a momentum flux ratio J = 0.55. The unforced case shown in the upper left corner of the image ensemble illustrates an already perturbed behavior with structures forming naturally on the inner jet. Interestingly, this oscillating pattern is not enhanced by acoustic forcing as noticed in the various phase angle forcing images. Although the scale of the structures of the forced cases is smaller than that for the unforced case, there does appear to be enhanced mixing in the downstream region accompanied by a shortening of the dark-core length with acoustics.

The next set of images shown in Fig. 22(b) correspond to a momentum flux ratio of 4.9. In these images the effects of acoustics can be noticed on both the dark core length and its spreading behavior. The baseline image shows a thick jet as it exits the injector that eventually gets thinner

as it mixes with the surrounding fluid. This effect is not only enhanced for the dark core under acoustic forcing but it actually adds a curvature to the dark core region that was not present in the baseline case. The overall effect of this transversal motion of the jet is a shorter and slightly thinner dark core that shows noticeable bending which enhances mixing even further.

Figure 22(c) shows supercritical pressure injector I images at a momentum flux ratio of 9.3. The baseline case shows an extremely short dark core region that is completely entrained by the outer jet just a few diameters downstream the exit of the injector. The rest of the images with acoustic forcing are quite similar to the baseline case. They feature very short dark core regions and the spreading angle is almost non-existent. If there is an effect of acoustic forcing on the coaxial jet flow, it takes place after the two streams have completely mixed, and the behavior is not captured with the employed imaging method. Schmitt et al.[55] used large eddy simulation to simulate some of the results of Rodriguez[29], and found that the short dark core is driven by an axial recirculation zone that has been observed in single phase coaxial jets at high momentum flux ratios.[16,19]

Figure 23 shows the acoustic forcing response of injector IV at supercritical pressure across a range of momentum flux ratios. Only two momentum flux ratios were forced at PN conditions. Overall, the response of injector IV to acoustic forcing is qualitatively similar to that at subcritical conditions (Fig. 20). Forcing at the PAN condition results in symmetric structure formation on the inner/outer jets, although the structures are highly turbulent and noisy. The image for J = 1.9 is a good example of how the structures observed have mass from the inner and outer jets as the structures can be clearly observed as continuous between the two jets and the most downstream structures seem to have less dense fluid than the initial part of the inner jet as mixing has occurred. Increasing the momentum flux ratio in general leads to degraded impact of

acoustics, which in some part may be due to relative amplitude and frequency effects as stated earlier.

The results of injectors II and III forced at supercritical pressure show similar behavior, suggesting that operation at high pressure appears to be a secondary effect; see Rodriguez and Teshome for details.[29,30] For fixed momentum flux ratio and fluid temperatures, operating at different chamber pressure influences the density ratio between the two jet streams. This therefore causes a concomitant change in velocity ratio which can have an effect on the mixed recirculation zone/shear layer developed between the two jets.

Dark-core Length of Forced Injector Flows

The effects of acoustics on the dark core length for injector LAR-thick (injector I) for different pressures are shown in Fig. 24. This data set includes three chamber pressures: subcritical (1.45 - 1.51 MPa), nearcritical (3.55 - 3.58 MPa) and supercritical (4.95 - 4.97 MPa). This figure is a composite of dark core lengths for baseline conditions without acoustics (filled symbols) and conditions with the maximum acoustic pressure achieved (hollow symbols) with only one siren on one end of the chamber. There are a few features to note. First the acoustics have the most reduction on dark core length for a range of momentum flux ratio between 1 and 10 for subcritical conditions where the inner jet is liquid and the outer jet is a gas so mixing occurs between two fluids in different phases. The effect of acoustics are less for near and supercritical conditions. However, this is in part due to the fact that the amplitude of the acoustics was comparable for all conditions but as the chamber pressure increases the ratio of the acoustics to the chamber pressure was decreased. This data was taken with only one siren on one side of the chamber.

When a second siren was added to the chamber, the phase angle between the signals of the two sirens could be varied to explore the effect of acoustics on the injector by effectively placing the injector at different regions of the pressure field. For example, nominally when the phase angle between the two sirens is zero, a pressure antinode (velocity node) is created, while conditions with the phase angle near 180 degrees leads to a pressure node (velocity antinode) at the injector.

The results for the dark core length as a function of phase angle for injector LAR-thick are shown in Fig. 25. The results for subcritical pressures are shown in Fig. 25(a) and (d). It is easiest to see the effects of the phase angle in Fig. 25(d). Here we can see that the percentage change of dark core length is largest for the mid-range of J (here marked as MR since this is the early nomenclature this group used) from ~1 to 4.2, which is consistent with the results shown in Fig. 24. Also the shortest dark core lengths are achieved for the nominal condition of a pressure node corresponding roughly to 135 to 180 degrees. For the rest of the values of J studied, the dark core did not change significantly for any phase angle. Compared to the subcritical results, the data shown in Fig. 25(e) for near critical pressures shows a wider range of J with large reductions of dark core length. And finally the data obtained at supercritical pressures (Fig. 25(f)) shows about the same trend as for near critical pressure. However, notice that in all pressure ranges studied the maximum change in dark core length is about the same around 40% reduction. Interestingly, for the supercritical pressure data set there appears to be a few cases for the run at J = 9.9 where the dark core seems to grow instead of decreasing with the acoustics on. At high values of J the dark core lengths, even for baseline conditions, become shorter and it is harder to accurately measure changes in smaller dark cores.

Convective Modes in Forced Injector Flows

Teshome applied the POD technique for injectors III and IV to elucidate the properties of the strongest convective modes induced through acoustic forcing. Once again, the convective mode pair algorithm described earlier was used to identify the dominant mode. The CPSD of the dominant mode pair for both the forced and unforced cases were computed to show the temporal behavior of the flow.

Figure 26 shows the effects of PAN forcing in terms of the spatial and temporal properties of the dominant convective mode for injector IV at subcritical conditions at three different momentum flux ratios. At the low momentum flux ratio of 0.5 shown in Fig. 26(a), the unforced dominant convective mode shows weak structure in the near field, and graduate emergence of a mode that is antisymmetric towards the downstream region as lobes of different signs (black and white) appear in the left and right of the image at the same downstream distance from the exit plane. Forcing strongly at the PAN condition, the flow responds with a coherent symmetric structure formation as shown in the spatial mode shape. This apparent varicose mode is maintained over the full range of the image, with some distortion in the downstream region. The CPSD amplitude shown in the figure includes the spectrum for both the unforced and PAN forced dominant convective mode pairs. For the unforced case, the convective mode pair has a peak near 1.5 kHz. When forced near 3 kHz, a clear peak occurs at the forcing frequency and the first harmonic. Additionally, the broadband peak is seen to shift to center on the forcing frequency.

As shown by Fig. 26(b), a different forcing response is observed at a momentum flux ratio of 5.2. The unforced convective mode is seen to be once again antisymmetric with an enhanced spreading rate compared to the lower momentum flux ratio case. With the application of PAN forcing, the response is neither purely symmetric nor antisymmetric. The CPSD of the unforced and PAN forced case have strong overlap. It is apparent that the flow is being forced near the

peak frequency of the unforced case. The broadband spectra is nominally the same for both the PAN forced and unforced cases. The flow response to PAN forcing at this momentum flux ratio is limited to the forcing frequency, and no apparent harmonics are generated, at least within this spatial mode shape.

Figure 26(c) shows the PAN forcing behavior at a momentum flux ratio of 11. The unforced and PAN forced spatial mode shapes are similar, and the forced flow is predominantly antisymmetric. The CPSD is very similar for both cases, with a clear peak at the forcing frequency (with no harmonics) emerging with forcing. The preferred mode frequency of the unforced case appears to be approximately 4.5 kHz, which is higher than for the other two cases, thus the forcing at 3 kHz is effectively low frequency forcing. There appears to be some reorganization of spectral content from high to low frequency with the addition of acoustic forcing. There appears to be some broadband amplification with PAN forcing below 3 kHz.

The PN forcing response of injector IV at subcritical pressure is shown in Fig. 27. The PN forcing is seen to induce an antisymmetric response for all momentum flux ratios. At a low momentum flux ratio of 0.5, forcing at PN conditions has a dramatic impact on the dominant convective mode. The preferred mode frequency of the unforced case is approximately 1.5 kHz, thus forcing at 3 kHz is relatively high frequency forcing, however the peak of the broadband response changes to about 3 kHz when the jet is forced. This change in broadband peak is not always seen. The response includes a rapid formation of smaller scale structures as would be expected for high frequency forcing, as the wavelength is inversely proportional to frequency. The CPSD shows a similar trend as for PAN forcing; the broadband peak of the unforced case shifts to center on the forcing frequency. Two harmonics are also seen to be generated due to PN forcing. For the momentum flux ratio of 5.2 shown in Fig. 27(b), the emergence of structure

occurs upstream of the unforced case. The forcing frequency is again centered on the preferred mode frequency, and the CPSD experiences negligible changes other than the emergence of a peak at the forcing frequency. No harmonic peaks are apparent. Lastly, the low relative frequency forcing case of J = 11 is shown in Fig. 27(c). Both cases are antisymmetric, while the forcing case shows larger length scale structure as expected with low frequency forcing. The CPSD shows a clear peak at the forcing frequency, and a shifting of some high frequency energy into the low frequency range.

Injector III, which is a large post thickness injector, has a baseline behavior as well as a response to acoustics. Figure 28 shows the influence of PAN forcing of injector III at subcritical pressure for three different momentum flux ratios. As shown in Fig. 28(a), the PAN forcing at a momentum flux ratio of 2.1 shows negligible impact. The CPSD unforced case shows a relatively low frequency peak below 1 kHz, and forcing doesn't impact the distribution other than a minor peak at the forcing frequency. The spatial mode shape appears to show antisymmetric structure of similar characteristics for both unforced and PAN forcing. Forcing at higher momentum flux ratios of 5.7 and 15, shown in Figs. 28(b) and (c), respectively, shows more manifestation of forcing. Interestingly, the unforced spectrum shows no dramatic change in the CPSD, unlike the trend shown for injector IV. All cases involve relatively high frequency forcing, as the 3 kHz forcing frequency is higher than the peak frequency of the unforced cases for all momentum flux ratios. Peaks occur at the forcing frequency and two harmonics, and in general energy is shifted from lower frequency to higher frequency. The mode shapes of the forced cases show small scale structure that becomes highly symmetric at the maximum momentum flux ratio of 15. The limited impact of increasing momentum flux ratio on the

unforced spectra is likely caused by the reduced interaction of the inner and outer jet due to the large recirculation region.

The PN forcing of injector III at subcritical pressure is shown in Fig. 29. The general trend is similar to that for PN, in that forcing has a limited impact at low momentum flux ratio, and causes some redistribution from low to high frequency at higher momentum flux ratios. A single peak at the forcing frequency is observed without strong harmonics. The spatial mode shapes appear to indicate an antisymmetric response, which is clearer for the highest momentum flux ratio.

The characteristics of the convective modes at supercritical pressure conditions show a similar overall trend to that of subcritical conditions, and are thus not included here; see Teshome for further details on the convective modes at supercritical pressure.[30]

Receptivity Study

One of the key observations from the work of Teshome is the apparent sensitivity of the response which depended on whether the forcing frequency was above or below the frequency of the preferred mode of the unforced case. For instance, Fig. 26 shows that high relative frequency (achieved at low J) PAN forcing for injector IV leads to a symmetric response that shifts the entire broadband spectra peak. In contrast, forcing at low relative frequency (achieved at high J), the response is antisymmetric, and the impact on the overall spectrum of the convective mode is more limited. Thus the work of Teshome highlighted the potential importance of the ratio of the forcing to natural preferred mode frequencies.

Additionally, the amplitude of the forcing is known to be an important variable for acoustically-forced flows.[56] The studies by Rodriguez and Teshome were focused on strongly forced injector

flows in the context of combustion instability in rocket engines, hence maximizing the acoustics within the limits of the hardware was of interest. In contrast, Wegener conducted a study on the receptivity of injector V to acoustic forcing, where emphasis was placed on the manner in which acoustic forcing imposes changes on the flow as a function of amplitude. Acoustic fields impose both fluctuations in pressure and velocity. When the injector is placed at the PAN region, the pressure fluctuation p' is the dimensional measure of the acoustic amplitude, while for PN forcing, the transverse acoustic velocity fluctuation u' is maximized and is used to characterize the acoustic forcing amplitude. Wegener varied the acoustic amplitude with the injector located within the PAN and PN regions. Using the preferred mode frequency scaling law shown in Fig. 16, Wegener fixed the forcing to natural mode frequency ratio at three different values of 1.7, 2.0, and 2.6. These frequency ratios were enabled through use of the acoustic sirens at three different frequencies; see Wegener for further details.[57] Wegener also investigated the receptivity of injector V at two different momentum flux ratios, nominally two and six. As mentioned before the inner jet in this case is helium and the outer jet is nitrogen. Also injector V has a relatively thin post relative to the inner jet and a small area ratio, so the results obtained apply to cases where the effect of the recirculation zone are not as strong as for configurations such as injectors I and III.

Figure 30 shows images of injector V forced at a forcing to natural frequency of 2.6 at a PAN condition at different amplitudes. The momentum flux ratio was held near a value of two and the operating conditions are high subcritical pressure (see Fig. 4). The pressure amplitude was measured using a Kulite pressure transducer mounted in the inner chamber wall at the transverse location of the injector. The amplitude was nondimensionalized using the outer jet dynamic pressure. Three different regimes are highlighted on the figure. At low amplitude, there is no

measured influence of acoustic forcing on the flow field. This is referred to as no receptivity. However, qualitatively in the figures for 0.3, 0.44 and 0.73 one can observe enhancement on the mixing between the inner and outer jets through the generated structures. One can see longer ligaments of the inner jet protruding toward the outer jet in roll-up structures. At a particular forcing amplitude, a change may be detected through analysis of the POD of the data set. A new forced POD mode pair is observed, but the ordering of the forced mode is such that the natural mode is still the strongest convective mode. At higher amplitudes, the forced mode is dominant over the flow field, even though the natural mode is still detectable. Hence there are two transitions points. The first is the lowest amplitude at which detection of a forcing response is observed, and the second the amplitude at which the forced mode overtakes the naturally present mode. A qualitatively similar transition was observed for a momentum flux ratio of six.[57]

Figure 31 shows a more detailed illustration of the convective modes detected using POD on the data set shown in Fig. 30. Figure 31(a) shows the first eight POD modes for the zero amplitude PAN case. Modes three and four form a POD mode pair that represents a convecting hydrodynamic instability mode. There are other convective modes in the flow, although they contribute less to the image data as they are ordered later in the decomposition. The asymmetry noted in the spatial mode shapes is caused by slight misalignment of the inner jet tube with the outer jet. As the forcing amplitude is increased, eventually a new mode pair is detected in the lower mode range; here the lower twelve modes were analyzed. Figure 31(b) shows the detection of a new mode pair that was found to have the expected attributes of a convecting mode. Since this new mode pair is ordered after the natural mode pair, this is referred to as weak receptivity. Figure 31(c) shows the first eight POD modes for high amplitude forcing. A mode pair with strong similarities of the new mode pair found in Fig. 31(b) is observed to occur earlier

in the POD mode order, indicating that it is dominant over the natural mode. Although the natural mode immediately follows the forced mode, the eigenvalues are in general about an order of magnitude lower than the forced mode eigenvalues. Although not very clean due to the noted misalignment, the forced mode appears to represent a symmetric response.

Figure 32 shows images of injector V exposed to variable amplitude PN forcing. As for Fig. 31, the momentum flux ratio and frequency ratio are two and 2.6, respectively. The POD decomposition was again used to detect changes in the flow behavior. In this case, there were no cases involving weak receptivity; the lowest amplitude at which the forced mode was detected also has the forced mode ordered earlier in the POD representation related to the natural mode. The acoustic amplitude is presented as a dimensional estimate of the acoustic velocity using one-dimensional acoustic equations.[57] The highly forced case clearly shows an antisymmetric flapping of both the outer and inner jet.

The PAN receptivity study for injector V operated at subcritical pressure is summarized in Fig. 33. Three different frequency ratios and two momentum flux ratios were considered. The temperature of the propellants was held nominally constant.[57] The empty squares represent the highest forcing amplitude at which no forced mode was detected while the solid squares represent the lowest amplitude at which the forced mode dominates the natural mode. Thus the shaded area represents the range over which the forced mode emerges and takes over as the strongest mode. Both momentum flux ratios indicate that the flow field becomes less receptive to PAN forcing with increasing frequency ratio, although at the highest frequency, the momentum flux ratio of two appears to be more resistant to acoustics than the momentum ratio of six. It is interesting to note that the inception of receptivity occurs at a nominal dimensionless amplitude of unity. This is consistent with the arguments of Baillot et al.[54]

The PN forcing receptivity trends for injector V at subcritical pressure are shown in Fig. 34. The receptivity of the two momentum flux ratios is nominally the same except at the highest frequency ratio. A nearly tripling of the dimensional acoustic velocity is requires for the momentum flux ratio case of six to dominate the preferred mode at the highest forcing frequency. The lower momentum flux ratio case has limited dependence on the range of frequencies considered.

Physical Mechanisms

It is apparent that the nature in which acoustic disturbances influence coaxial jet flows is very complex, with multiple coupling mechanisms occurring depending on the operating conditions and acoustic environment. Within a liquid rocket engine experiencing a transverse acoustic resonance, the various injectors will experience different spatial regions of the acoustic mode shape based on their location. Injectors may be placed near a pressure antinode, pressure node, or in between these regions. Thus the coupling in these various regions must be fully understood to properly design an injector distribution on the injection face of the rocket engine.

The placement of the injector at a pressure antinode (PAN) exposes the flow field to an unsteady back pressure. The predominant mechanism, as proposed by Baillot et al.[54], appears to be related to an induced unsteady flow rate in the gaseous outer jet. The pulsing outer jet facilitates the generation of axisymmetric structures on the inner jet boundary, causing an enhancement of mixing. Baillot et al. found that this mechanism appears to become active when the acoustic pressure amplitude is larger than the outer jet dynamic pressure. A similar finding was found by Wegener and is presented in Fig. 33.[57] In support of this theory, Wegener developed a simple model of the unsteady flow within the injector exposed to a sinuous variation in back pressure, and found that the liquid inner jet experiences negligible unsteadiness due the inertia of the

liquid, while the gaseous flow experiences significant unsteadiness due to the lower fluid density. In further support of this mechanism, Carpentier et al. found that a single liquid jet (i.e. unassisted by a coflow of gas) does not response to high frequency forcing when placed at a PAN condition.[58]

Although the primary PAN coupling mechanism appears to be relatively well developed, the challenge of designing an injector that is non-receptive to discrete frequency forcing is complicated by the fact that the hydrodynamic stability properties of shear flows such as these are broadband. Forcing within the bandwidth of unstable frequencies will in general create a response, although the forced behavior will compete with the naturally growing most unstable mode. Overtaking the natural mode will require the forcing amplitude to exceed a critical value which would in general be governed by nonlinear effects. Factoring into this mechanism is the type of instability exhibited by the flow in terms of absolute or convective instability.[59] The wake region associated with the finite inner jet post thickness may be absolutely unstable.[9] Additionally, the two-phase coaxial jet at high momentum flux ratio can also transition to absolute instability.[60] Regions of absolute instability may lead to the development of a global instability that will in general render the flow less receptive to external disturbances.[61] Forcing globally unstable flows has been shown to generate a response referred to as “lock on”, where the qualitative behavior of the global mode is maintained but the frequency shifts to the forcing frequency.[62-64] The exploitation of global instability could be a promising strategy for interrupting the coupling between acoustic waves and injector flows, in particular within the PAN forcing environment.

The pressure node (PN) acoustic environment appears to have a more complicated effect on the coaxial jet. There are two effects that have been observed, the first being a flattening of the

liquid jet downstream of the exit plane and the second being a flapping of the jet. The mechanism that causes the flattening effect has received recent attention in the research community. Carpentier et al.[58], Baillot et al.[54], and Hoover et al.[65] all found that placement of a liquid jet or liquid/gas coaxial jet at a PN condition results in a flattening of the liquid jet in the plane perpendicular to the acoustic resonance. Cehroudi and Talley also observed the flattening effect using the nonreacting flow facility at AFRL for liquid jets.[53] Although flattening was not observed directly in the work of Leyva, Rodriguez[29] and Teshome[30], the thinning observed for PN forcing at low momentum flux ratio is indicative of this phenomenon. A recent set of simulations by Hakim et al. studied the unforced and PN forced coaxial jet flames at supercritical pressure.[66] The simulation at high relative frequency exhibited the same flattening of the inner jet. Thus the relative frequency appears to play a role in this mechanism.

The mechanism that leads to the deformation of the liquid into a flat sheet is current under debate. Baillot et al. provide arguments that the radiation pressure force caused by the acoustic field reflecting off the jet column is the cause for the flattening effect.[54] The azimuthal nonuniformity of the pressure distribution due to this force leads to the deformation into a sheet. The authors find that the acoustic field must reach a critical amplitude to overcome the stabilizing effects of surface tension. An alternative explanation to the flattening effect involves the hydrodynamic pressure field surrounding the jet exposed to an oscillating transverse flow. As the cross flow interacts with the jet column, a local low pressure region will be established on the sides of the jet, while a stagnation point and low pressure region will occur on the leading and trailing sides of the jet, respectively. If the transverse flow oscillates at high frequency, the jet will tend to have a mean low pressure on the sides where the transverse flow accelerates around the jet. The static pressure distribution will again lead to a flattening of the jet. If the

forcing frequency is sufficiently low, the jet column will experience significant displacement during the forcing cycle, resulting in the flapping of the jet which appears to interfere with the flattening effect. The simulations by Hakim et al. were analyzed in the context of these two possible explanations for the flattening effect. The authors concluded that the hydrodynamic interaction, as opposed to the acoustic radiation force, was most likely the cause for the flattening effect for their simulations. It should be noted that Baillot didn't observe the flattening effect at the PN condition when the injector flow was in the fibrous atomization regime, which is likely related to why flattening was not observed in the AFRL studies at moderate to high momentum flux ratio values.

As mentioned above, the PN forced coaxial jet can also exhibit a response in the form of a transversely distorted jet. An extreme example of this mode of response is shown in Fig. 18(b), while a subtler illustration is shown in Fig. 20(c). The arguments given by Hakim suggest that the interaction is essentially an unsteady crossflow effect. Buffum and Williams studied a high-speed liquid jet exposed to the PN region of a relatively low-frequency acoustic resonance, and found that the jet experienced sinusoidal transverse deflection.[67] They also conducted order of magnitude estimates of the various forces on the jet, and found that the drag force on the jet due to the acoustic velocity crossflow was the dominant external force. Using an empirical approach, they estimated the drag coefficient on the jet to be an order of magnitude larger than the steady state value on a cylinder, which is an approximation for the liquid jet column. They hypothesized that unsteady effects result in enhanced forces on the jet column. Thus the drag force on the jet appears to be much larger than would be expected based on steady state behavior of a jet in crossflow. This enhanced drag is also evident in the AFRL studies. Davis estimated the acoustic to jet momentum flux ratio and found that this ratio is much lower than unity.[28]

Based on steady state jet in cross flow studies, momentum flux ratios much lower than unity would not be expected to generate a jet deflection as observed by Buffum and Williams or the current study.[68-71]

Insight on the aerodynamic interactions between an unsteady low momentum crossflow and a jet can be provided by previous research on bluff bodies exposed to oscillating crossflow. Guided by literature on this topic, two additional dimensionless groups become relevant. The Keulegan-Carpenter number, defined as

$$KC = \frac{U_m}{fD}, \qquad \text{(Eq. 7)}$$

where U_m is the peak amplitude of the velocity oscillation, f is the frequency of the oscillation, and D is the jet diameter. The Keulegan-Carpenter number is essentially a ratio of oscillation to convective time scales. For the AFRL studies, KC << 1, thus the acoustic velocity oscillations are much faster than the time scale required to establish a quasi-steady flow behavior. The second parameter is the Stokes number, defined as

$$\beta = \frac{D^2 f}{\nu}, \qquad \text{(Eq. 8)}$$

where ν is the kinematic viscosity. The Stokes number is the ratio of viscous to velocity oscillation time scales, and for the AFRL studies is a very large number. Following Morison, Johnson, and Schaaf,[72] the effective transient drag coefficient on a bluff body exposed to oscillating cross flow is

$$C_{D,eff} = C_D \left|\cos(2\pi f)\right| \cos(2\pi f) - \frac{\pi^2}{KC} C_m \sin(2\pi f), \qquad \text{(Eq. 9)}$$

where C_D is the conventional drag coefficient and C_m is referred to as the inertial coefficient, and is essentially an added mass effect. The drag coefficient is a function of the Keulegan-Carpenter number and the Stokes number, while the inertial coefficient is primarily a function of the Stokes number.[73] As KC approaches zero, the inertial coefficient asymptotically approaches a value near two. The presence of KC in the denominator of the second term in Eq. 9 suggests an amplification of the inertial effect as KC approaches zero, causing a dramatic increase in the effective drag coefficient. It is worth noting that the inertial effect is also 90° out of phase with respect to the acoustic velocity. This transient drag phenomenon is likely the cause for the strong coupling observed in the present study even though the acoustic velocity amplitude (O~0.1 m/s) is much lower than the outer jet velocity (O~40 m/s). The dramatic increase in the effective drag coefficient amplifies the influence of the unsteady low momentum cross flow.

Lastly, placement of the injector in between PAN and PN locations adds complexity as a wide range of mechanisms become available, including acoustic radiation forces, unsteady backpressure fluctuations, and velocity coupling with the augmented drag effects due to unsteadiness. Baillot et al.[54] and Carpentier et al.[58] found that the acoustic radiation force causes a mean deflection of the jet towards the nearest pressure node. More work is required to investigate the role of the various available coupling mechanisms in regions between nodes and antinodes.

Reacting Flow Results

As mentioned earlier, the reacting flow facility was developed to facilitate the study of acoustically-forced rocket injector flames. Studies to date have focused on injector V employing liquid oxygen in the core and cooled gaseous hydrogen in the outer jet. The oxygen-to-hydrogen

mass flow ratio was nominally six, and the momentum flux ratio was 2.2. The chamber pressure was approximately 34 bar.

Figure 35 shows an instantaneous image of the nonreacting and reacting cases operating with liquid oxygen and gaseous hydrogen as described above. The nonreacting case is in general similar to the unforced cases shown for injector IV in Fig. 20. Under combustion conditions, a number of changes are observed. The dark core is substantially shortened by the presence of combustion. The darkening of the lower left region on the image was due to condensation of water vapor on the inner chamber window, an effect which has been subsequently mitigated. The surface of the liquid oxygen core is also less diffused with combustion, which is expected due to the enhanced evaporation associated with the temperature increase in the reacting zone. The combustion also results in a broadening of the jet boundary due to fluid expansion.

The flame is anchored at the inner jet post as has been verified by unfiltered chemiluminescence images, and is expected for cryogenic oxygen/hydrogen flames.[74] The presence of the flame in the inner jet post wake provides enhanced visual access in this region through evaporation of the liquid droplets. Due to this access, small liquid oxygen structures are seen to enter the recirculation zone and convect upstream to the post (as will be supported in Fig. 36). Hence the predominant rotational sense of the recirculation zone is such that counterflow is applied to the inner edge of the hydrogen flow.

Figure 36 shows inner shear layer streak imaging to capture the motion of liquid structures in both the reacting and nonreacting cases. For the nonreacting case, the shear layer structures are seen to emerge downstream of the recirculation zone and convect at a constant velocity; this velocity was shown earlier to be well approximated by the Dimotakis shear layer convection velocity model. Under reacting conditions, the shear layer structure velocity is not constant as

indicated by the curvature in the streaks; the structures start at low speed near the end of the recirculation zone and accelerate as they convect downstream. The presence of the flame inhibits the momentum transfer between the high-speed outer flow and the lower speed inner flow. The region within the recirculation zone shows evidence of structures moving upstream.

Localized spectral analysis of pixel intensities were used to provide insight on the effects of the flame on the times scales of the flow field. Figure 37 shows the time series and spectrum of pixel intensities for a location within the shear layer at two inner jet diameters downstream of the injector exit. The time signals are seen to be complex and contain a range of time scales. The spectra of the two cases do indicate that the presence of combustion tends to shift the intensity fluctuations into a lower frequency range. This is in general agreement with linear stability results which indicate that a flame in the shear region tends to have a stabilizing effect and a shift energy to lower frequencies (e.g. Mahalingam, Cantwell, and Ferziger[75]).

Instantaneous shadowgraph images of unforced and acoustically-forced cases under both nonreacting and reacting conditions are shown in Fig. 38. The forcing frequency was fixed near 3 kHz for all cases. The nonreacting forced cases show similar qualitative behavior as has been described earlier. Under reacting conditions, no local flame extinction was observed regardless of the acoustic forcing amplitude. Overall, the qualitative impact of acoustic excitation under combustion conditions is less dramatic. Forcing the flame at PAN conditions does result in the formation of small-scale coherent structure on the surface of the inner jet in the near field. This local response doesn't appear to generate a large alteration in the global mixing behavior. For the PN forced case, the dark core does not exhibit the large-scale flapping behavior demonstrated by the nonreacting case. The response of the flame is more subtle and requires more

sophisticated signal processing methods for detection. However, it is noticeable how the inner jet thins downstream as compared with the non-forced case.

Dynamic mode decomposition (DMD) was used to explore the spatial and temporal properties of the forced cases. Figure 39 shows the DMD spectrum for the maximum amplitude forcing condition with the injector placed at the PAN. It is evident from the DMD analysis that the flow has a sharp response at the forcing frequency for both nonreacting and reacting conditions. The reacting flow shows a strong peak at the forcing frequency as well as smaller peaks at two harmonics. The combustion case also shows higher amplitudes in the lower frequency range, which is consistent with the results shown in Fig. 37.

Figure 40 shows the real and imaginary DMD spatial modes at the forcing frequency. The real and imaginary components of the spatial modes capture a convective process in an analogous manner as the POD mode pairs used earlier. The DMD spatial mode illustrates a symmetric shear layer response, as indicated by the axially aligned intensity fluctuations in the DMD spatial mode shapes. This symmetry is expected as the mechanism that is associated with PAN forcing relates to azimuthally-coherent mass flow fluctuations in the outer jet as discussed earlier; the symmetry for the nonreacting case is somewhat degraded. The cold flow appears to have a response that is more global, while the flame has a more localized and coherent behavior near the inner jet post.

The DMD spectra for the maximum forcing amplitude PN cases are shown in Fig. 41. Similar to the PAN condition, a coupling of the shear layers at the forcing frequency was observed for the PN acoustic forcing. There is a reversal of the harmonics detected for the nonreacting and reacting conditions. For the nonreacting condition subjected to PN forcing, higher harmonics are

detected. The harmonics are not present for the reacting case, showing the opposite trend of the PAN forcing response.

Figure 42 shows the DMD spatial modes associated with the peak frequencies in Fig. 41. The antisymmetric nature of the response is similar to the structure observed for PN forcing for injector IV using POD. The presence of contrast in the outer shear layer for both cases represent a coupling between the inner and outer shear layers at the forcing frequency. There is particularly strong coupling between the inner and outer jet response for the reacting flow case. The broadening of the jet with combustion is also highlighted in the figure. The results of Figs. 39-42 highlight the utility using DMD for extracting temporal and spatial behavior at the forcing frequency and higher harmonics. In particular, detection of harmonics with unique spatial structure would be difficult using POD.

Future Research

The sustained effort at AFRL to understand the dynamics of cryogenic high-pressure coaxial jet flows, both natural and forced, has established a foundation for understanding important mechanisms responsible for combustion instability in LREs. Further inquiry should focus on a number of aspects that have not been sufficiently explored, including reacting flow with hydrocarbon fuels, different injector types, and multiple injectors as neighboring flames may have important interactions. The role of initial conditions at the injector exit should be investigated, as real RLEs are likely to have jet profiles that are not fully developed. Quantitative measures of unsteady heat release will also help explore how combustion feeds into the acoustic field. Such data will also help in the development and validation of engineering design tools. Although the study has shed insight on the mechanisms and parametric effects of injectors placed at pressure nodes and antinodes, further studies for injectors between these

locations will also be needed to have a more complete understanding of how combustion instabilities are generated and sustained in LREs.

References

1. Ko N, Kwan A. The initial region of subsonic coaxial jets. *J Fluid Mech.* 1976;73(02):305-332.

2. Kwan A, Ko N. Coherent structures in subsonic coaxial jets. *J Sound Vibrat*. 1976;48(2):203-219.

3. Kwan A, Ko N. The initial region of subsonic coaxial jets. part 2. *J Fluid Mech*. 1977;82(02):273-287.

4. Ko N, Au H. Coaxial jets of different mean velocity ratios. *J Sound Vibrat.* 1985;100(2):211-232.

5. Au H, Ko N. Coaxial jets of different mean velocity ratios, part 2. *J Sound Vibrat.* 1987;116(3):427-443.

6. Tang S, Ko N. Coherent structure interactions in an unexcited coaxial jet. *Exp Fluids*. 1994;17(3):147-157.

7. Tang S, Ko N. Experimental investigation of the structure interaction in an excited coaxial jet. *Exp Therm Fluid Sci*. 1994;8(3):214-229.

8. Bocanegra-Evans H, Allen JJ. Wake–shear layer interaction using a soap film tunnel. *Physics of Fluids (1994-present).* 2005;17(9):091112.

9. Wallace D, Redekopp L. Linear instability characteristics of wake-shear layers. *Physics of Fluids A: Fluid Dynamics (1989-1993).* 1992;4(1):189-191.

10. Boldman D, Brinich P, Goldstein M. Vortex shedding from a blunt trailing edge with equal and unequal external mean velocities. *J Fluid Mech*. 1976;75(04):721-735.

11. Dahm WJ, Frieler CE, Tryggvason G. Vortex structure and dynamics in the near field of a coaxial jet. *J Fluid Mech.* 1992;241:371-402.

12. Tian V, McKeon B, Leyva IA. Split stream flow past a blunt trailing edge with application to combustion instabilities. . 2012:3807.

13. Segalini A, Talamelli A. Experimental analysis of dominant instabilities in coaxial jets. *Phys Fluids*. 2011;23(2):024103.

14. Koochesfahani M, Frieler C. Instability of nonuniform density free shear layers with a wake profile. *AIAA J*. 1989;27(12):1735-1740.

15. Brown GL, Roshko A. On density effects and large structure in turbulent mixing layers. *J Fluid Mech*. 1974;64(04):775-816.

16. Villermaux E, Hopfinger E. Self-sustained oscillations of a confined jet: A case study for the non-linear delayed saturation model. *Physica D*. 1994;72(3):230-243.

17. Lasheras J, Villermaux E, Hopfinger E. Break-up and atomization of a round water jet by a high-speed annular air jet. *J Fluid Mech*. 1998;357:351-379.

18. Schumaker SA, Driscoll JF. Mixing properties of coaxial jets with large velocity ratios and large inverse density ratios. *Physics of Fluids (1994-present)*. 2012;24(5):055101.

19. Favre-Marinet M, Camano E, Sarboch J. Near-field of coaxial jets with large density differences. *Exp Fluids*. 1999;26(1-2):97-106.

20. Favre-Marinet M, Schettini EC. The density field of coaxial jets with large velocity ratio and large density differences. *Int J Heat Mass Transfer*. 2001;44(10):1913-1924.

21. Juniper MP, Candel SM. The stability of ducted compound flows and consequences for the geometry of coaxial injectors. *J Fluid Mech*. 2003;482:257-269.

22. Chigier N, Farago Z. Morphological classification of disintegration of round liquid jets in a coaxial air stream. *Atomization and Sprays*. 1992;2(2).

23. Singla G, Scouflaire P, Rolon J, Candel S. Flame stabilization in high pressure LO x/GH 2 and GCH 4 combustion. *Proceedings of the Combustion Institute*. 2007;31(2):2215-2222.

24. Oefelein JC. Thermophysical characteristics of shear-coaxial LOX–H 2 flames at supercritical pressure. *Proceedings of the Combustion Institute*. 2005;30(2):2929-2937.

25. Chehroudi B, Talley D, Coy E. Visual characteristics and initial growth rates of round cryogenic jets at subcritical and supercritical pressures. *Physics of Fluids (1994-present)*. 2002;14(2):850-861.

26. Chehroudi B. Recent experimental efforts on high-pressure supercritical injection for liquid rockets and their implications. *International Journal of Aerospace Engineering*. 2012;2012.

27. Oschwald M, Smith J, Branam R, et al. Injection of fluids into supercritical environments. *Combustion Sci Technol*. 2006;178(1-3):49-100.

28. Davis DW. *On the behavior of a shear-coaxial jet, spanning sub- to supercritical pressures, with and without an externally imposed transverse acoustic field.* Ph.D. thesis,The Pennsylvania State University; 2006.

29. Rodriguez JI. *Acoustic excitation of liquid fuel droplets and coaxial jets.* Ph.D. thesis, University of California, Los Angeles; 2009.

30. Teshome S. *Droplet combustion and non-reactive shear-coaxial jets with transverse acoustic excitation.* Ph.D. thesis, University of California, Los Angeles; 2012.

31. Wegener J, Leyva I, Forliti D, Talley D. Development of a facility for combustion stability experiments at supercritical pressure. 52nd AIAA Aerospace Sciences Meeting, National Harbor, MD, 2014.

32. Wegener JL. *Multi-phase combustion and transport processes under the influence of acoustic excitation.* [Ph.D.]. University of California, Los Angeles; 2014.

33. Berkooz G, Elezgaray J, Holmes P, Lumley J, Poje A. The proper orthogonal decomposition, wavelets and modal approaches to the dynamics of coherent structures. *Applied scientific research*. 1994;53(3-4):321-338.

34. Holmes P, Lumley JL, Berkooz G. *Turbulence, coherent structures, dynamical systems and symmetry.* Cambridge university press; 1998.

35. Schmid PJ, Li L, Juniper M, Pust O. Applications of the dynamic mode decomposition. *Theor Comput Fluid Dyn*. 2011;25(1-4):249-259.

36. Schmid PJ. Application of the dynamic mode decomposition to experimental data. *Exp Fluids*. 2011;50(4):1123-1130.

37. Alenius E. Mode switching in a thick orifice jet, an LES and dynamic mode decomposition approach. *Comput Fluids*. 2014;90:101-112.

38. Rowley CW, Mezić I, Bagheri S, Schlatter P, Henningson DS. Spectral analysis of nonlinear flows. *J Fluid Mech*. 2009;641:115-127.

39. Leyva IA, Chehroudi B, Talley D. Dark core analysis of coaxial injectors at sub-, near-, and supercritical pressures in a transverse acoustic field. . 2007:4342-4359.

40. Graham JJ, Leyva IA, Rodriguez JI, Talley D. On the effect of a transverse acoustic field on a flush shear coaxial injector. *AIAA Paper*. 2009;5142:2009.

41. Champagne F, Wygnanski IJ. An experimental investigation of coaxial turbulent jets. *Int J Heat Mass Transfer*. 1971;14(9):1445-1464.

42. Gladnick P, Enotiadis A, LaRue J, Samuelsen G. Near-field characteristics of a turbulent coflowing jet. *AIAA J*. 1990;28(8):1405-1414.

43. Dimotakis PE. Two-dimensional shear-layer entrainment. *AIAA J*. 1986;24(11):1791-1796.

44. Berkooz G, Holmes P, Lumley JL. The proper orthogonal decomposition in the analysis of turbulent flows. *Annu Rev Fluid Mech*. 1993;25(1):539-575.

45. Chatterjee A. An introduction to the proper orthogonal decomposition. *Curr Sci*. 2000;78(7):808-817.

46. Bjornsson H, Venegas S. A manual for EOF and SVD analyses of climatic data. *CCGCR Report*. 1997;97(1).

47. Smith SA, Zukoski EE. Combustion instability sustained by unsteady vortex combustion. 21st Joint AIAA/SAE/ASME/ASEE Propulsion Conference, Monterey, CA, 1985.

48. Poinsot TJ, Trouve AC, Veynante DP, Candel SM, Esposito EJ. Vortex-driven acoustically coupled combustion instabilities. *J Fluid Mech*. 1987;177:265-292.

49. Schadow K, Gutmark E. Combustion instability related to vortex shedding in dump combustors and their passive control. *Progress in Energy and Combustion Science*. 1992;18(2):117-132.

50. Ken HY, Trouve A, Daily JW. Low-frequency pressure oscillations in a model ramjet combustor. *J Fluid Mech*. 1991;232:47-72.

51. Arienti M, Soteriou MC. Time-resolved proper orthogonal decomposition of liquid jet dynamics. *Physics of Fluids (1994-present)*. 2009;21(11):112104.

52. Ko N, Davies P. The near field within the potential cone of subsonic cold jets. *J Fluid Mech*. 1971;50(01):49-78.

53. Chehroudi B, Talley D. Interaction of acoustic waves with a cryogenic nitrogen jet at sub-and supercritical pressures. 41st AIAA Aerospace Sciences Meeting & Exhibit, Reno, NV, 2002.

54. Baillot F, Blaisot J, Boisdron G, Dumouchel C. Behaviour of an air-assisted jet submitted to a transverse high-frequency acoustic field. *J Fluid Mech*. 2009;640:305-342.

55. Schmitt T, Rodriguez J, Leyva I, Candel S. Experiments and numerical simulation of mixing under supercritical conditions. *Physics of Fluids (1994-present)*. 2012;24(5):055104.

56. Crow SC, Champagne F. Orderly structure in jet turbulence. *J Fluid Mech*. 1971;48(3):547-591.

57. Wegener JL. *Multi-phase combustion and transport processes under the influence of acoustic excitation*. Ph.D. thesis, University of California, Los Angeles; 2014.

58. Carpentier J, Baillot F, Blaisot J, Dumouchel C. Behavior of cylindrical liquid jets evolving in a transverse acoustic field. *Physics of Fluids (1994-present)*. 2009;21(2):023601.

59. Huerre P, Monkewitz P. Absolute and convective instabilities in free shear layers. *J Fluid Mech*. 1985;159:151-168.

60. Otto T, Rossi M, Boeck T. Viscous instability of a sheared liquid-gas interface: Dependence on fluid properties and basic velocity profile. *Physics of Fluids (1994-present)*. 2013;25(3):032103.

61. Huerre P, Monkewitz PA. Local and global instabilities in spatially developing flows. *Annu Rev Fluid Mech*. 1990;22(1):473-537.

62. Sreenivasan K, Raghu S, Kyle D. Absolute instability in variable density round jets. *Exp Fluids*. 1989;7(5):309-317.

63. Olinger D, Sreenivasan K. Nonlinear dynamics of the wake of an oscillating cylinder. *Phys Rev Lett*. 1988;60(9):797.

64. Getsinger D. Shear layer instabilities and mixing in variable density transverse jet flows. Ph.D. thesis, The University of California, Los Angeles, CA, 2012.

65. Hoover D, Ryan H, Pal S, Merkle C, Jacobs H, Santoro R. Pressure oscillation effects on jet breakup. *ASME, Heat and Mass Transfer in Spray Systems HTD*. 1991;187:27-41.

66. Hakim L, Schmitt T, Ducruix S, Candel S. Dynamics of a transcritical coaxial flame under a high-frequency transverse acoustic forcing: Influence of the modulation frequency on the flame response. *Combust Flame*. 2015;162(10):3482-3502.

67. Buffum F, Williams F. The response of a turbulent liquid jet to transverse acoustic fields(behavior of high speed, coherent, turbulent liquid jet in planar, standing, transverse acoustic field). *Proceedings of the 1967 Heat Transfer and Fluid Mechanics Institute*, 1967:247-276.

68. Keffer J, Baines W. The round turbulent jet in a cross-wind. *J Fluid Mech*. 1963;15(04):481-496.

69. Fearn R, Weston RP. Vorticity associated with a jet in a cross flow. *AIAA J*. 1974;12(12):1666-1671.

70. Kamotani Y, Greber I. Experiments on a turbulent jet in a cross flow. *AIAA J*. 1972;10(11):1425-1429.

71. Karagozian AR. Transverse jets and their control. *Progress in Energy and Combustion Science*. 2010;36(5):531-553.

72. Morison J, Johnson J, Schaaf S. The force exerted by surface waves on piles. *J Pet Technol*. 1950;2(05):149-154.

73. Troesch AW, Kim S. Hydrodynamic forces acting on cylinders oscillating at small amplitudes. *J Fluids Struct*. 1991;5(1):113-126.

74. Forliti DJ, Badakhshan A, Wegener J, Leyva IA, Talley DG. The response of cryogenic H2/O2 coaxial jet flames to acoustic disturbances. 53rd AIAA Aerospace Sciences Meeting, 2015.

75. Mahalingam S, Cantwell B, Ferziger J. Stability of low-speed reacting flows. *Physics of Fluids A: Fluid Dynamics (1989-1993)*. 1991;3(6):1533-1543.

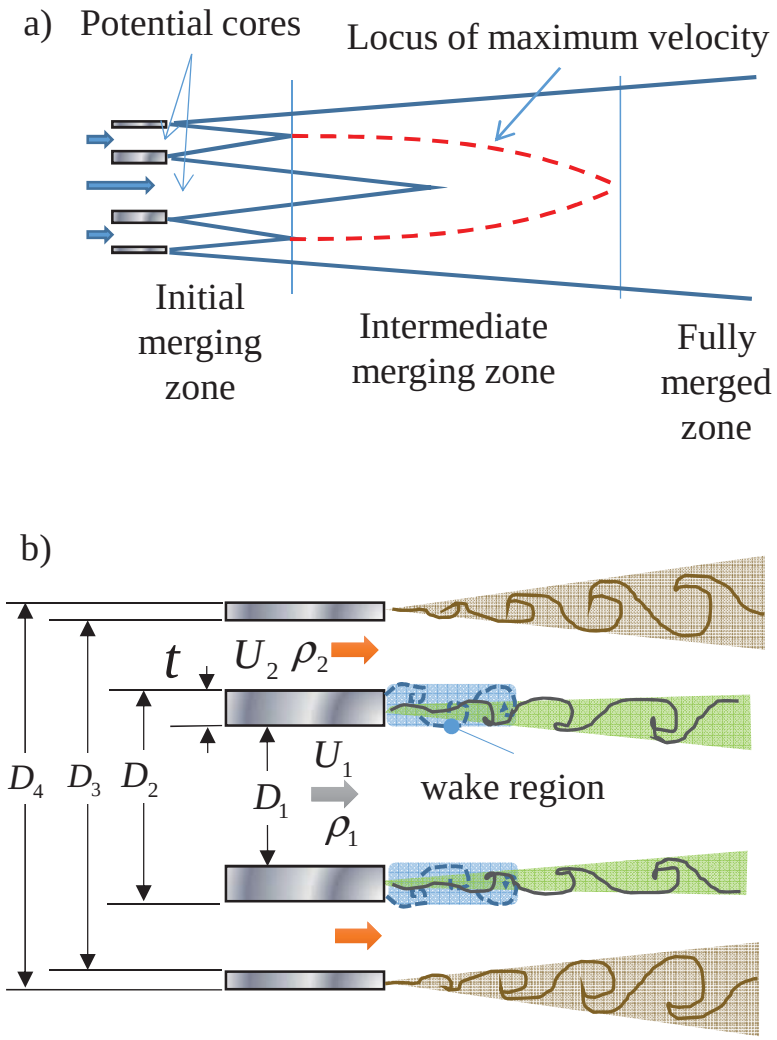

Figure 1: a) Overall flowfield and b) hydrodynamic instabilities of the coaxial jet.

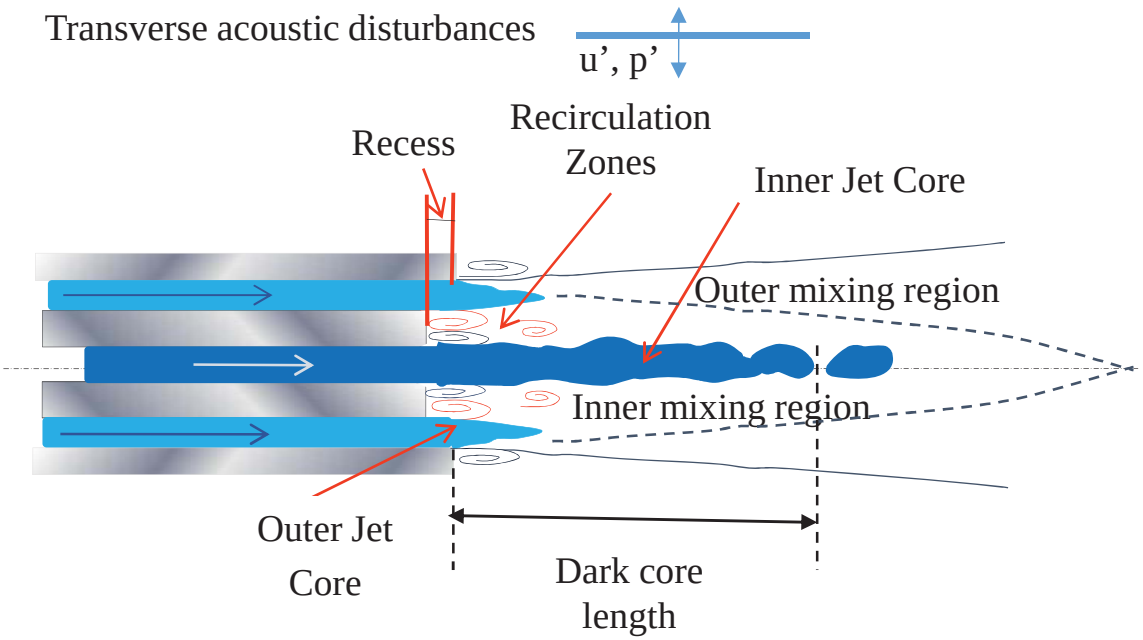

Figure 2: Structure of the acoustically-forced two-phase coaxial jet

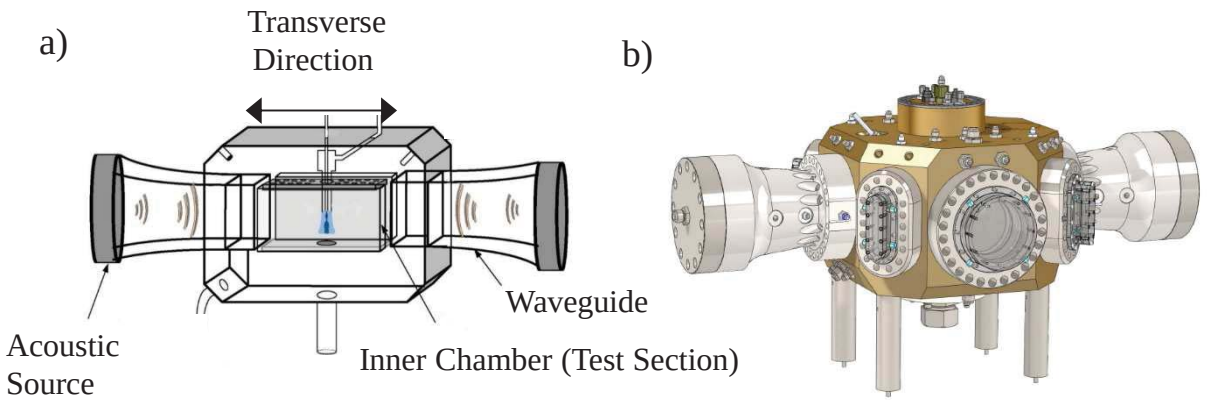

Figure 3: a) Conceptual experimental facility, b) CAD rendering of the reacting flow facility, c) image of the nonreacting flow facility, and d) image of the reacting flow facility.

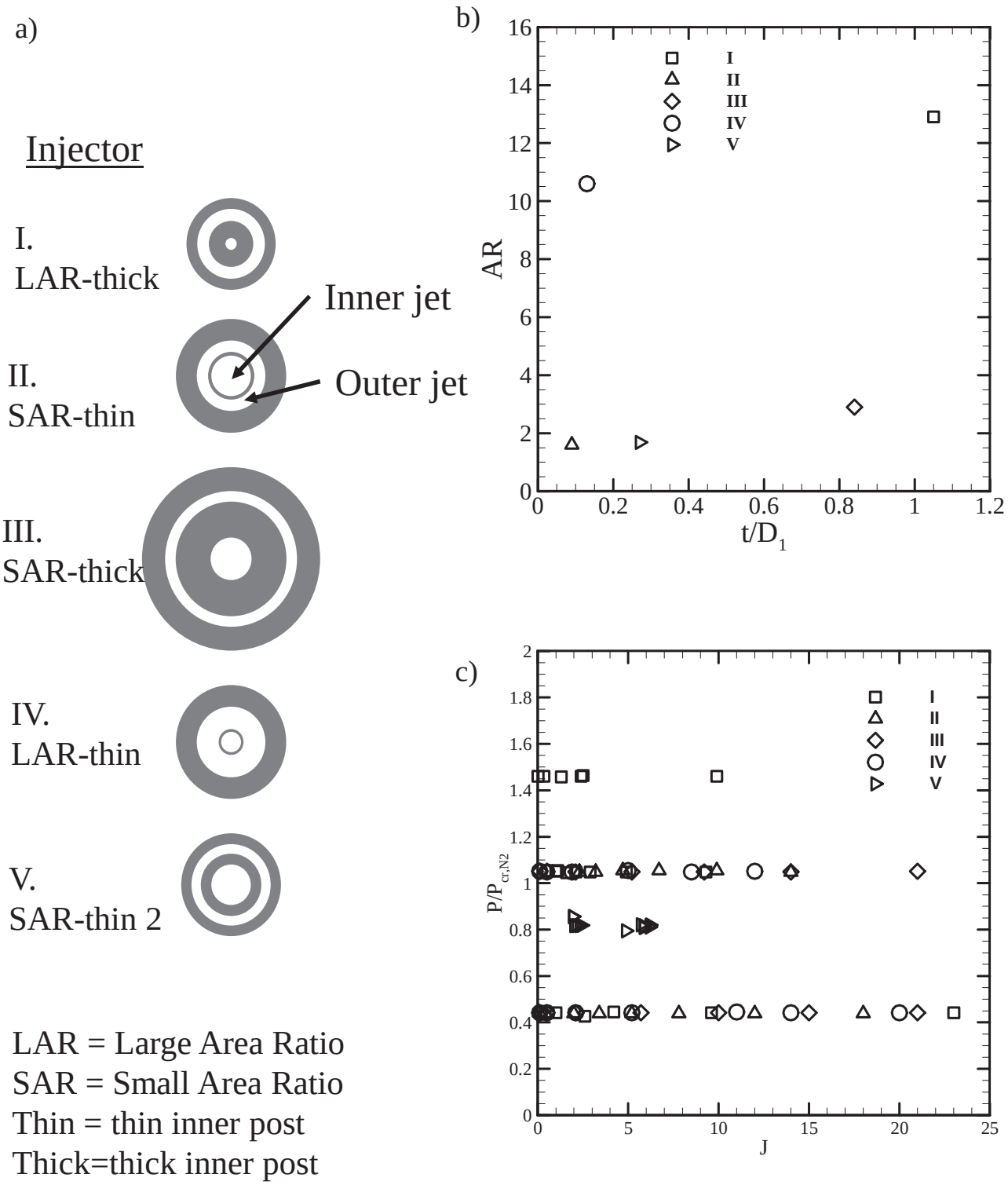

Figure 4: a) a schematic representation of the different injector exit geometries, b) injector area ratio AR as a function of dimensionless post thickness t/D_1, and c) reduced pressure and momentum flux ratio operation conditions.

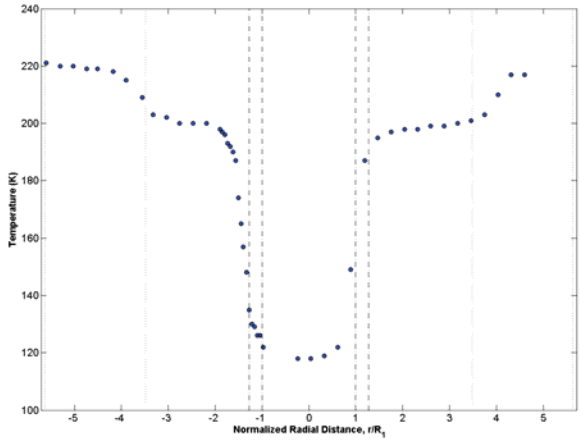

a)

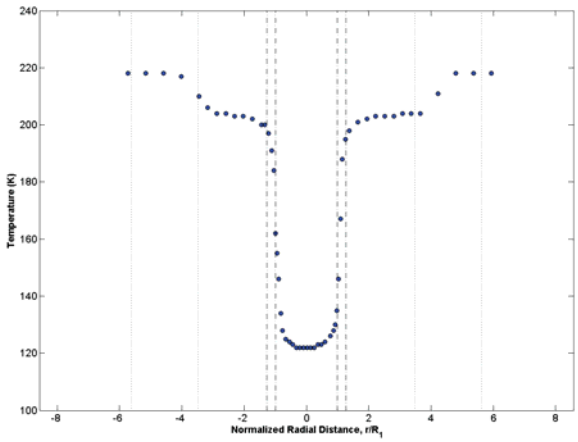

b)

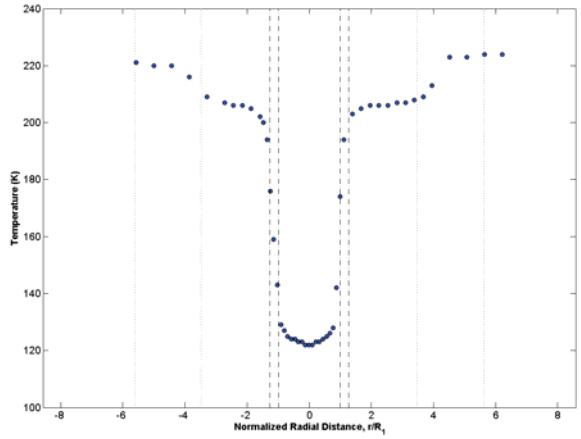

c)

Inner Jet Injector Boundary
Outer Jet Injector Boundary

	J	R	S	$T_{chamber}$ (K)	$\rho_{chamber}$ (kg/m³)	$P_{chamber}$ (MPa)	T_{outer} (K)	$\dot{m}_{outer}$ (mg/s)	ρ_{outer} (kg/m³)	u_{outer} (m/s)	Re_{outer} (10^4)	T_{inner} (K)	$\dot{m}_{inner}$ (mg/s)	ρ_{inner} (kg/m³)	u_{inner} (m/s)	Re_{inner} (10^4)
a)	1.9	4.1	0.11	221	57	3.56	200	3479	65	13.3	9.6	118	724	577	3.3	2.8
b)	5.0	6.5	0.12	223	57	3.58	203	4189	64	16.2	11	122	511	531	2.5	2.4
c)	8.5	8.5	0.12	225	56	3.56	208	5135	61	20.6	14	123	483	515	2.4	2.4

d)

Figure 5: Temperature profiles taken one D_1 downstream from the exit plane of injector IV (LAR-thin) for different J values. The running conditions for each profile are given in d).

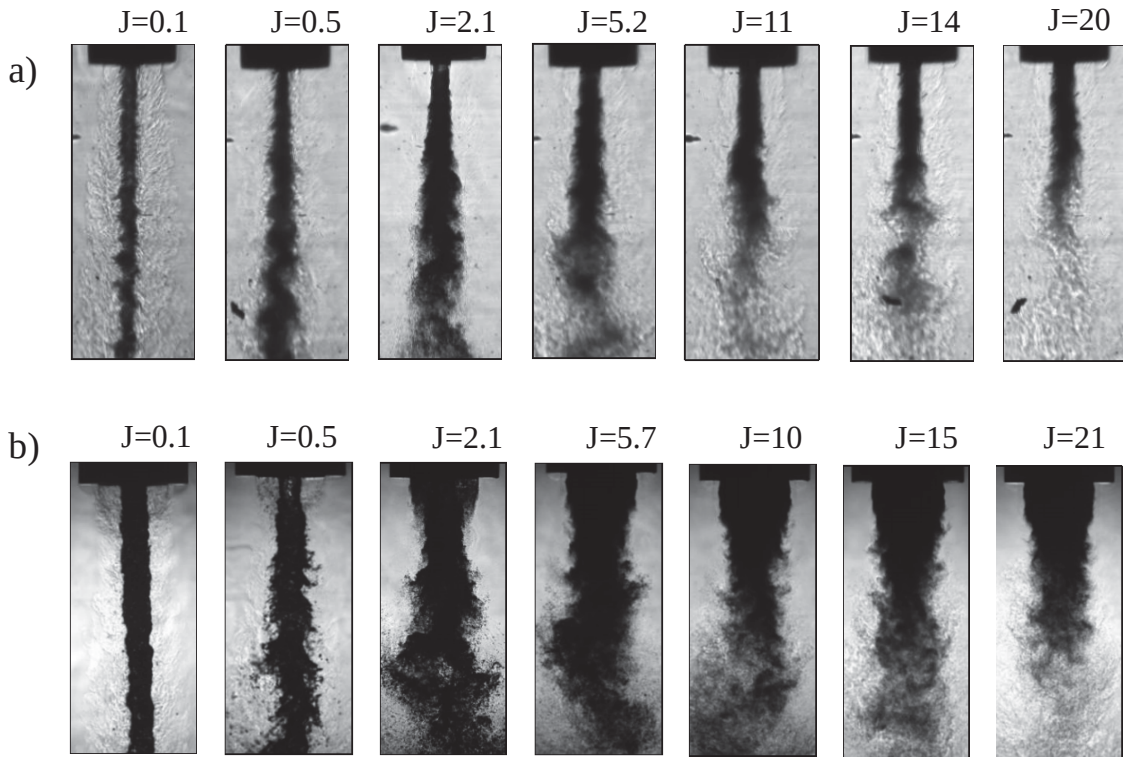

Figure 6: Instantaneous backlit shadowgraph images for injectors a) IV and b) III at various momentum flux ratios at subcritical conditions.

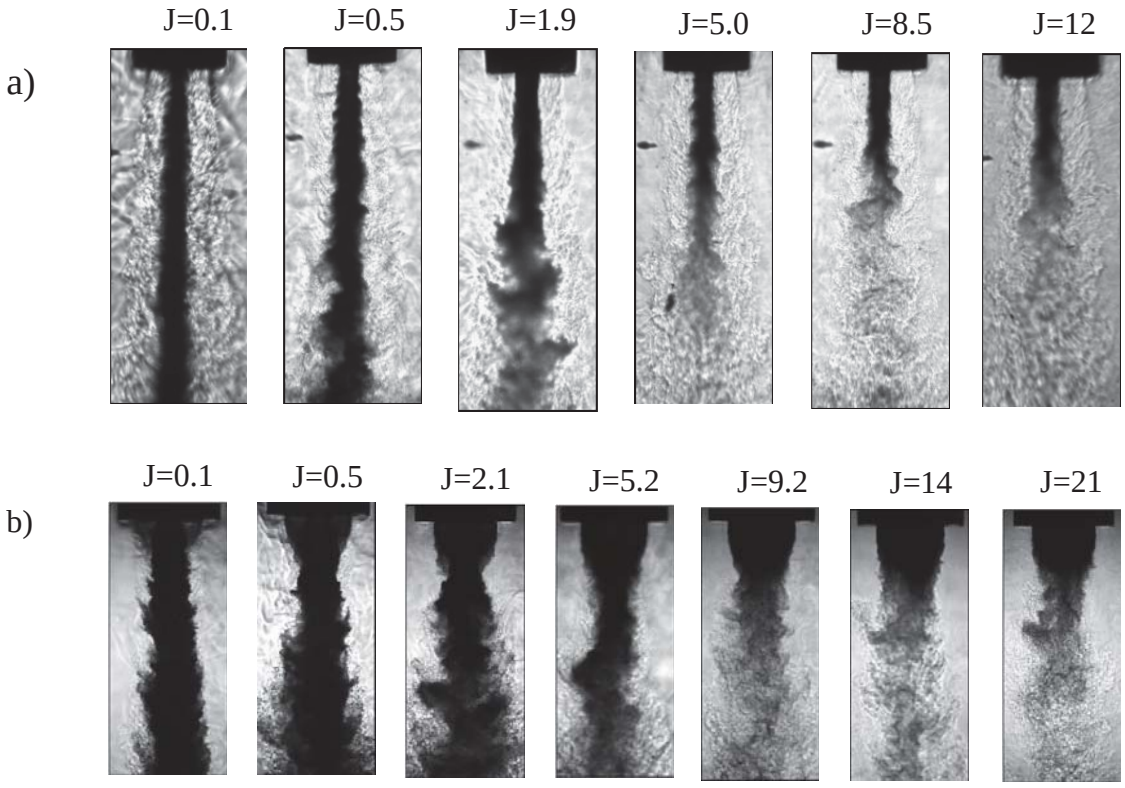

Figure 7: Instantaneous backlit shadowgraph images for injectors a) IV and b) III at various momentum flux ratios at supercritical conditions.

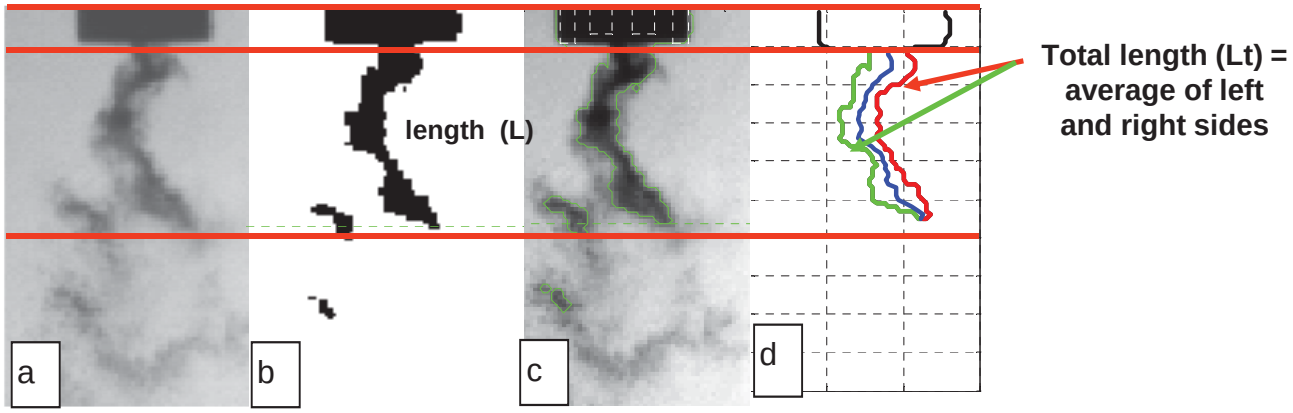

Figure 8: Measuring the dark-core length. a): original image. b): Black and white image after thresholding. c): Contour used to define axial length (L). d): Schematic of how the contour used to define the dark-core length.

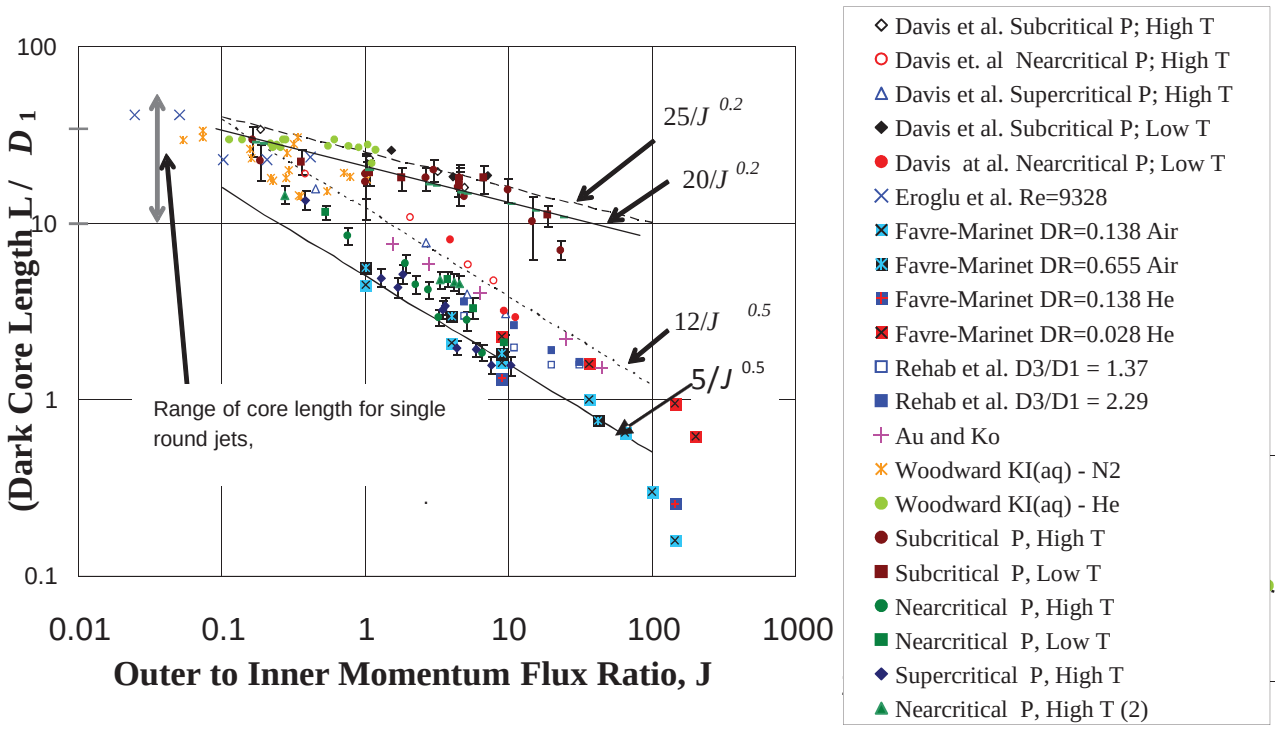

Figure 9: Comparison of data gathered at AFRL for LAR-thick with historical data.

.

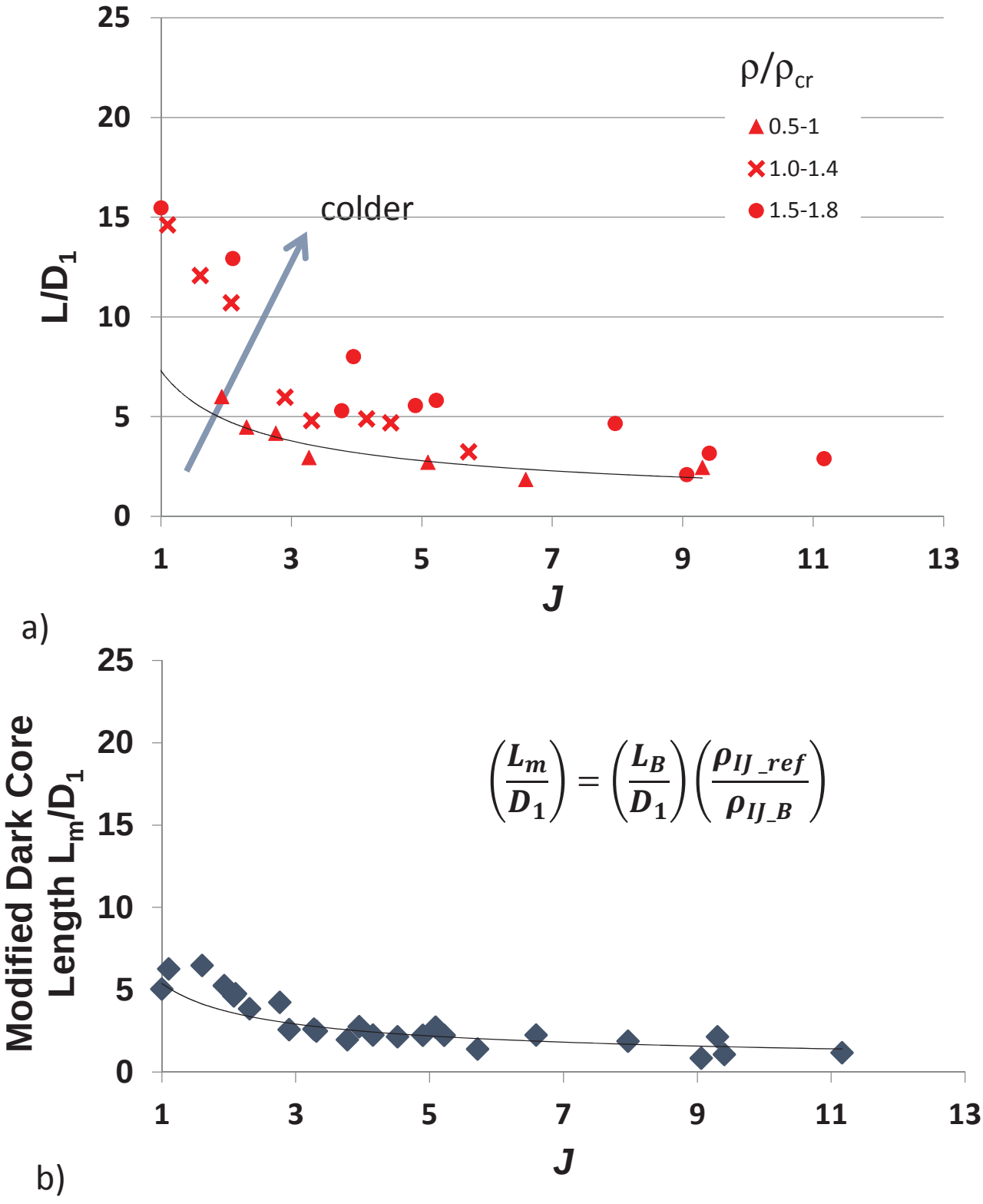

Figure 10: a) Compilation of dark core data taken for SAR-thick at 3.5-3.7MPa . b) Collapse of data in a) by normalizing by a reference density (@129K at 3.55MPa.

.

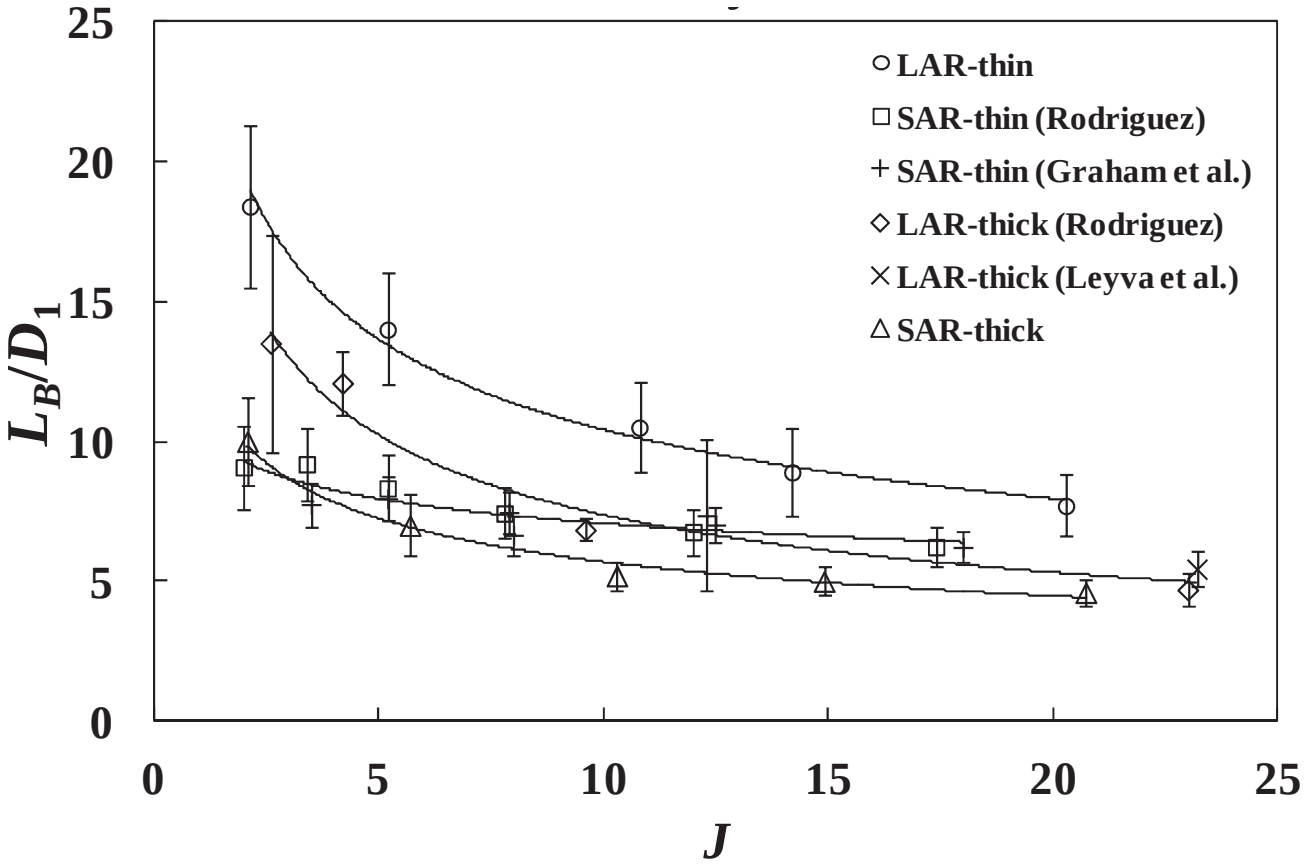

Figure 11: Baseline Normalized Dark Core Length, L_B/D_1 for $P_r = 0.44$. Four different injector geometries are included..

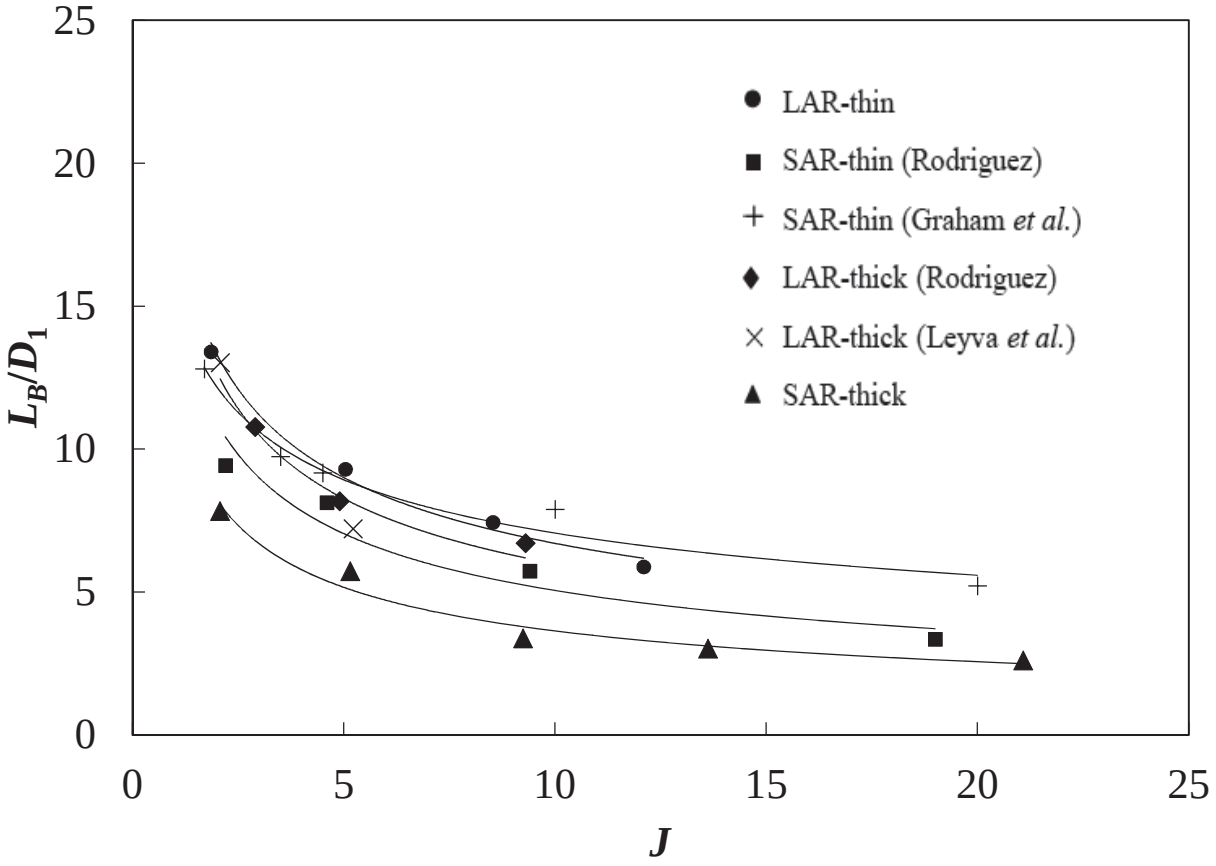

Figure 12: Baseline Normalized Dark Core Length, L_B/D_1 for $P_r = 1.05$. Four different injector geometries are included.

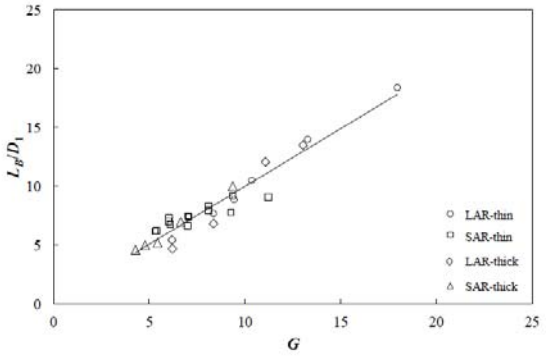

a)

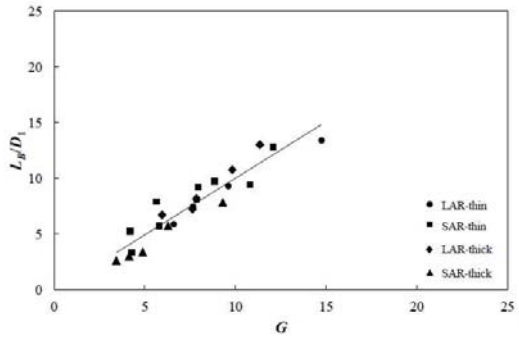

b)

$$G = c_1 J^{c_2} \left(\frac{t}{D_1}\right)^{c_3} \left(\frac{A_o}{A_i}\right)^{c_4}$$

Parameters for G				
P_r	c_1	c_2	c_3	c_4
0.44	9	-0.34	-0.15	0.30
1.05	11	-0.43	-0.12	0.15

c)

Figure 13: Measured dark core lengths for different injectors plotted versus G where the constants were obtained using non-linear regression. a) Pr=0.44, b) Pr=1.05 and c) values for the constants.

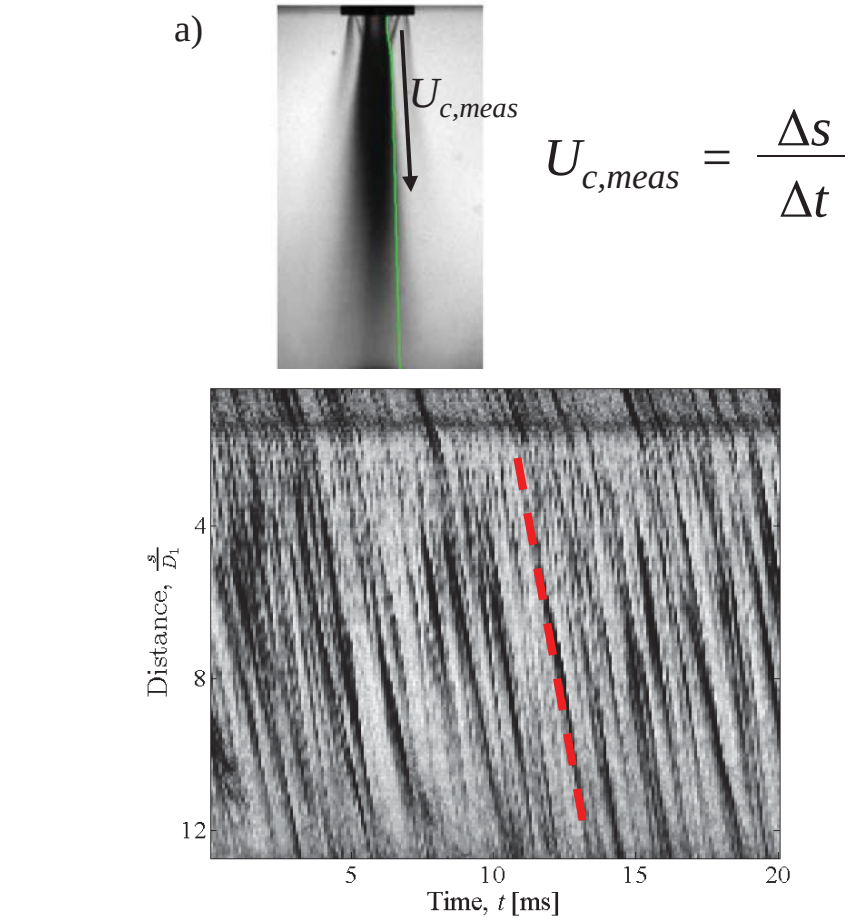

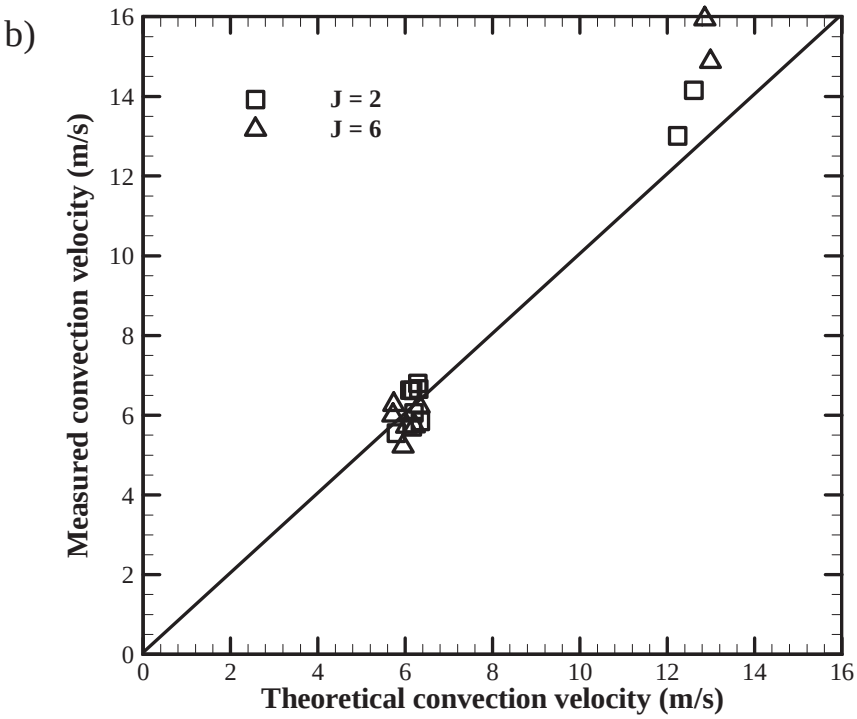

Figure 14: a) x-t pixel intensity history for use in estimating the convection velocity and b) the comparison of measured convection velocities to the Dimotakis estimate for variable density shear layers (injector V).

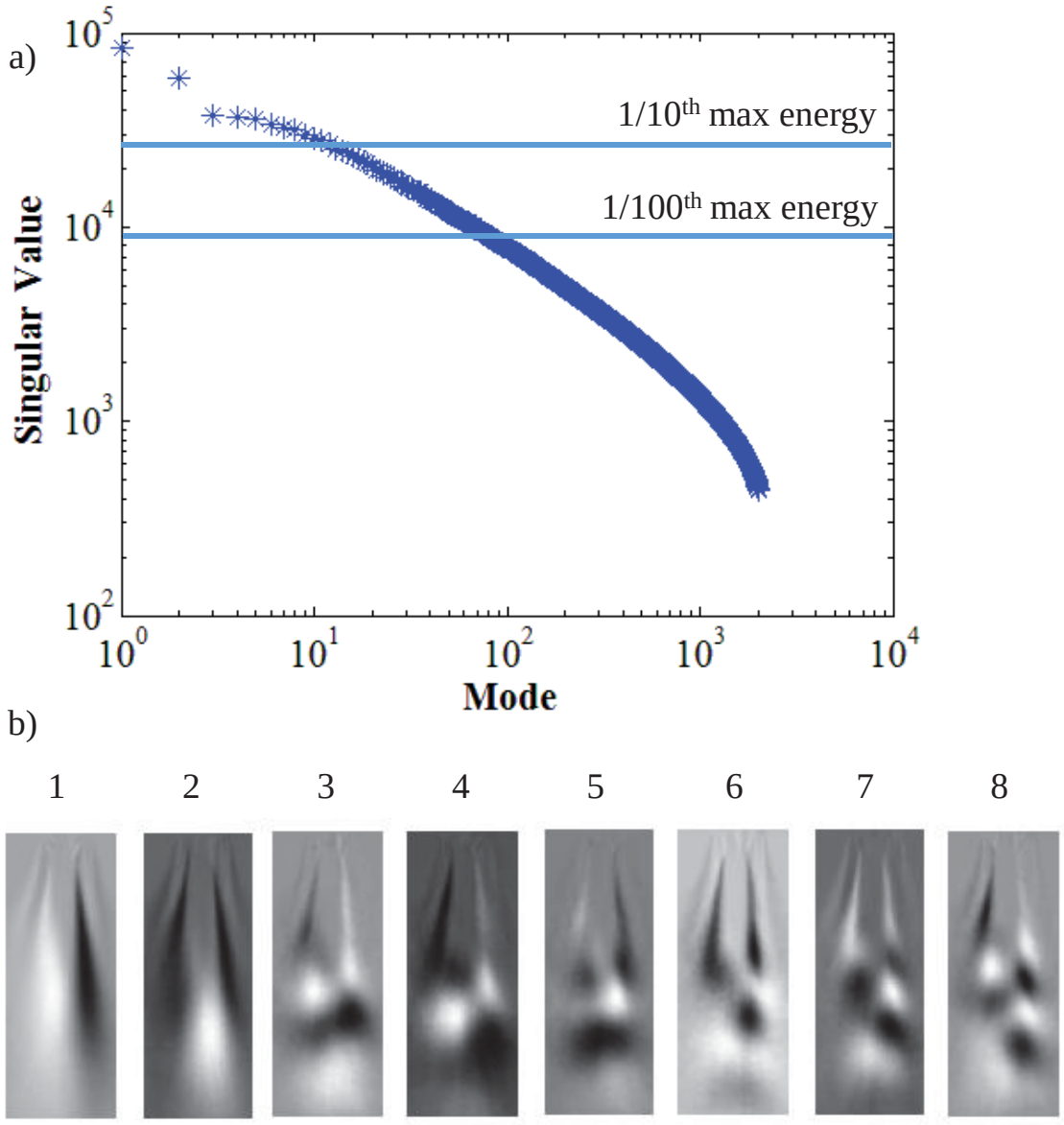

Figure 15: Proper orthogonal decomposition results: a) singular value distribution and b) spatial mode shapes for the first eight modes.

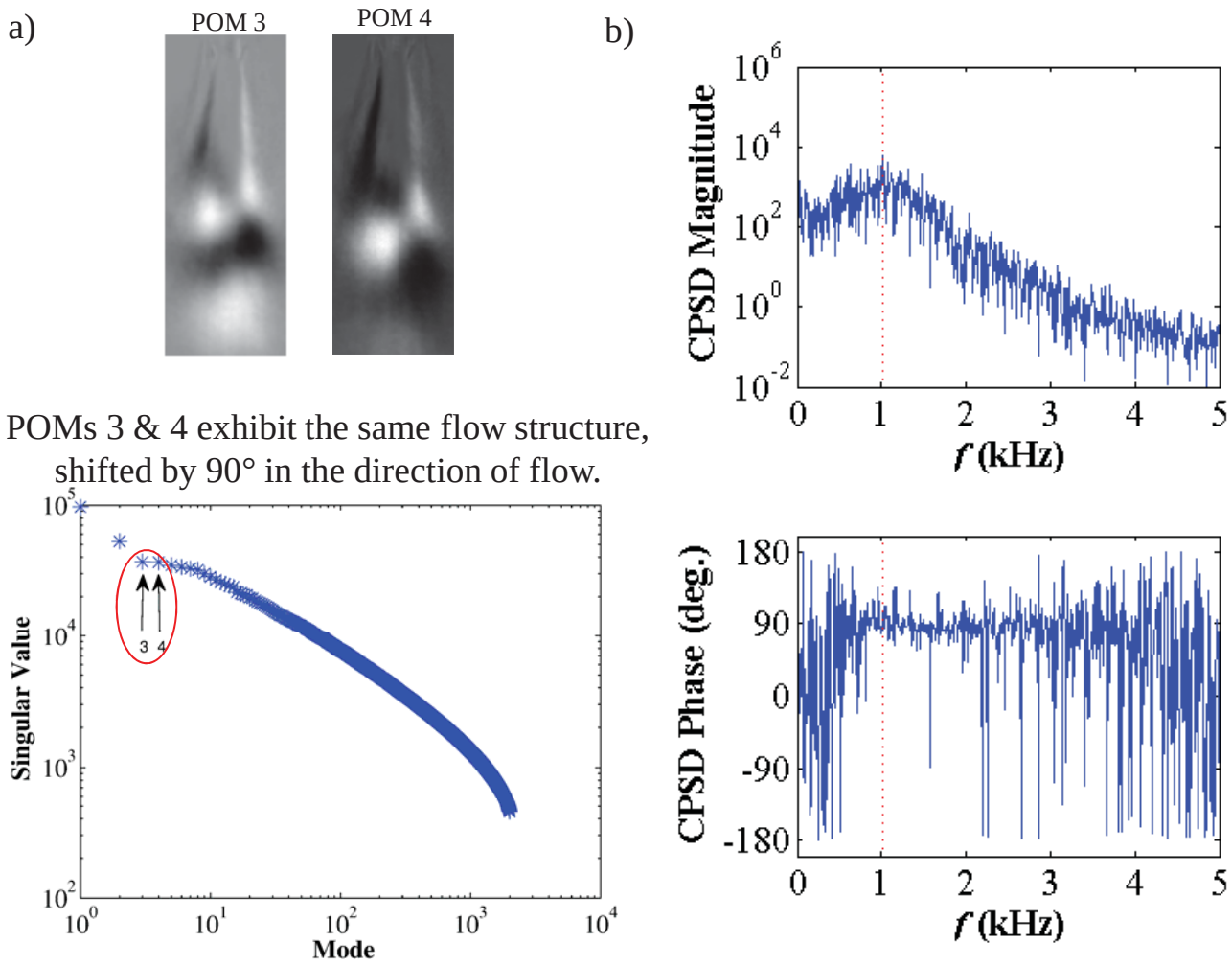

Figure 16: The detection of potential orthogonal mode pairs that represents a convective process involving a) spatial mode shapes and POD spectrum, and b) cross-power spectral density amplitude and phase between the modes.

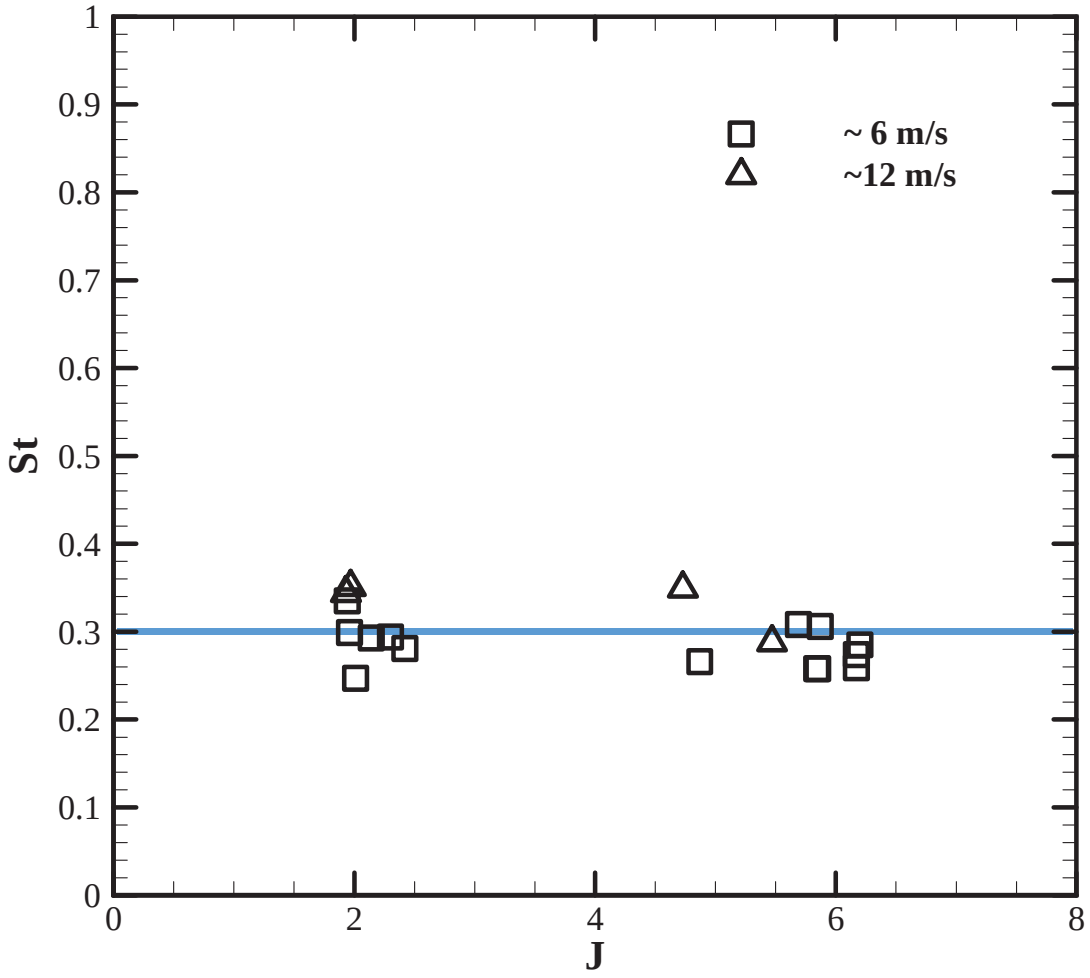

Figure 17: Strouhal number as a function of momentum flux ratio for subcritical conditions for injector V.

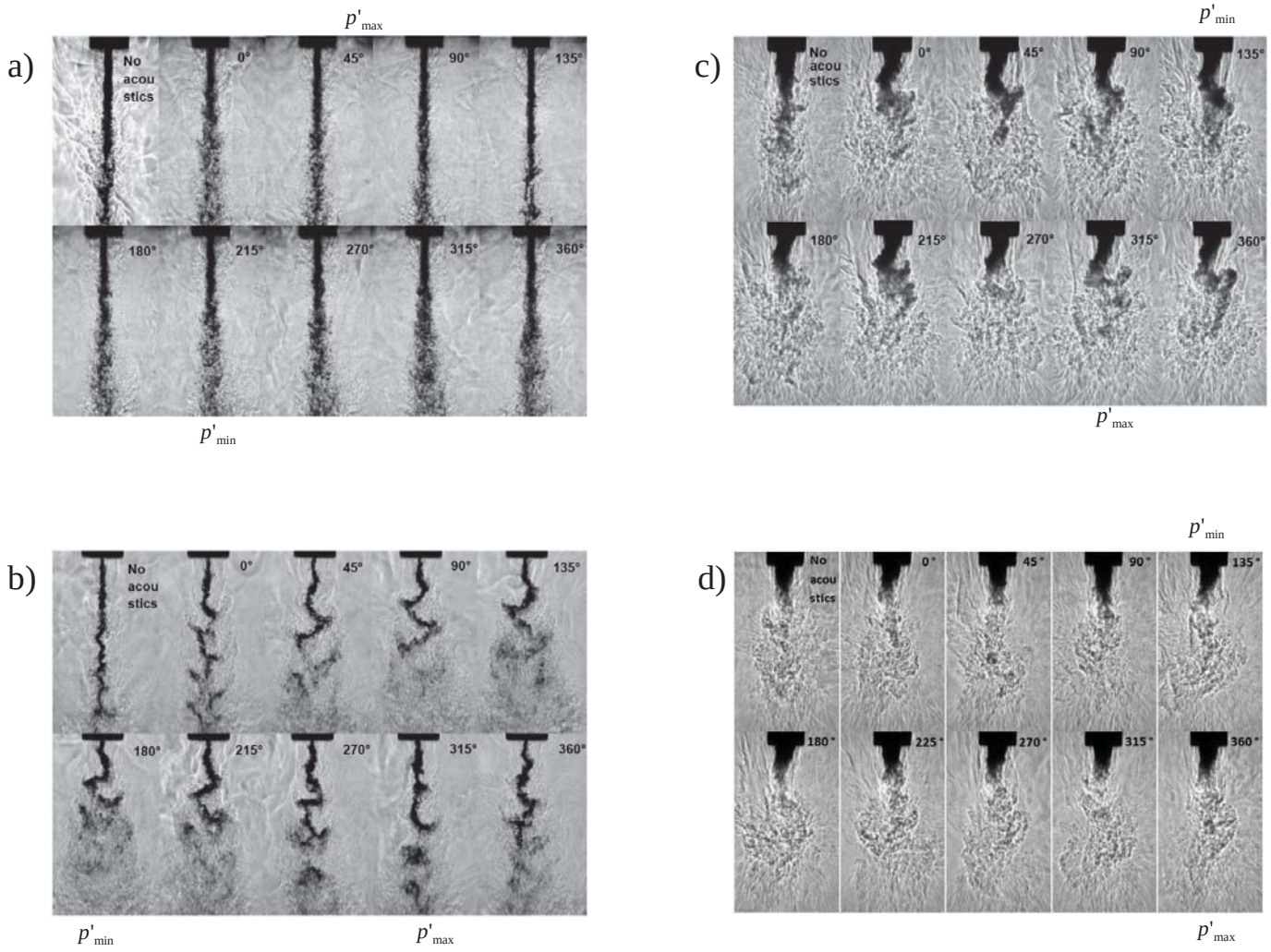

Figure 18: Visualizations of injector I under acoustic forcing conditions at subcritical pressure at momentum flux ratios J of a) 0.17, b) 2.6, c) 9.6, and d) 23.

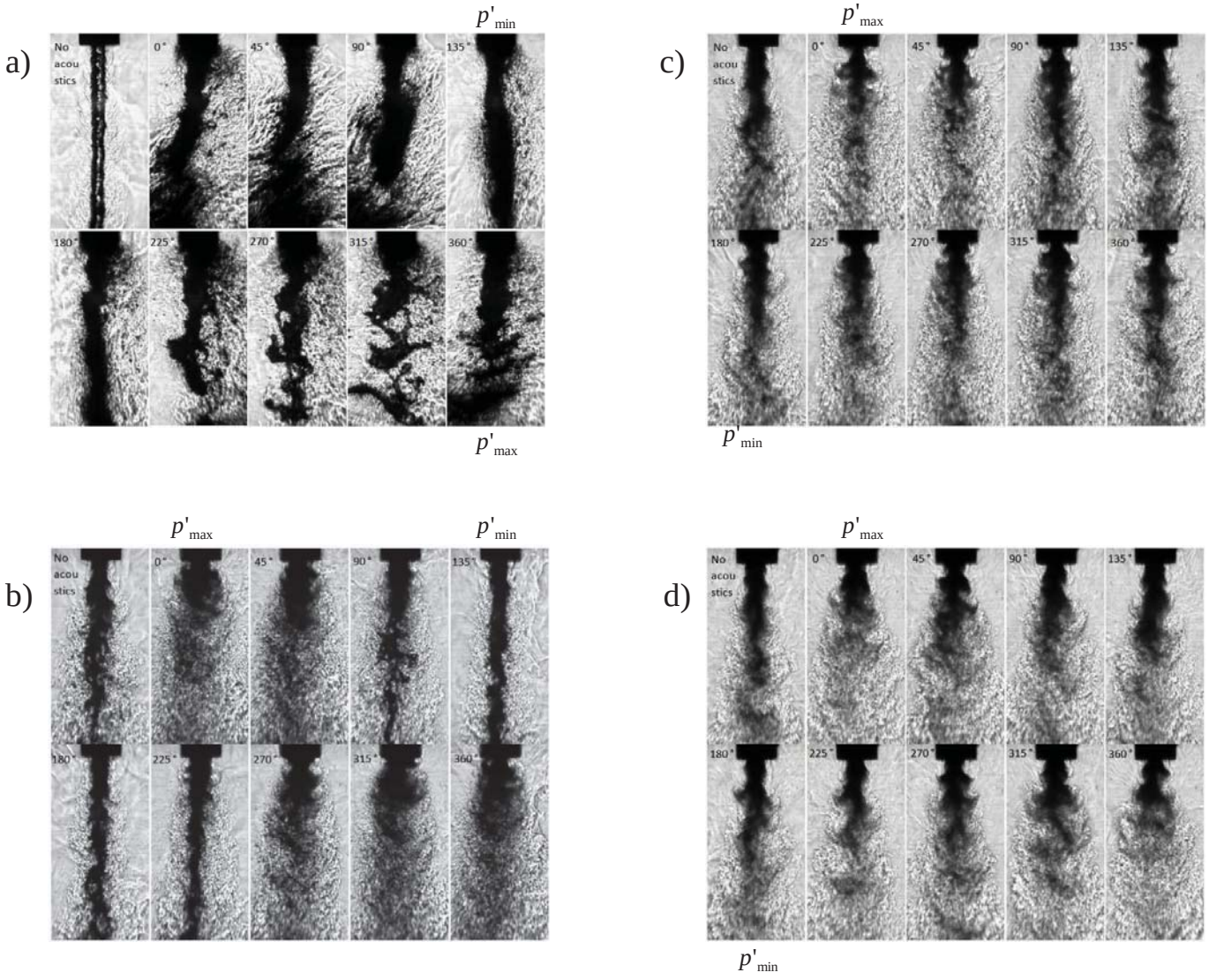

Figure 19: Visualizations of injector II under acoustic forcing conditions at subcritical pressure at momentum flux ratios J of a) 0.09, b) 2.0, c) 7.8, and d) 18.

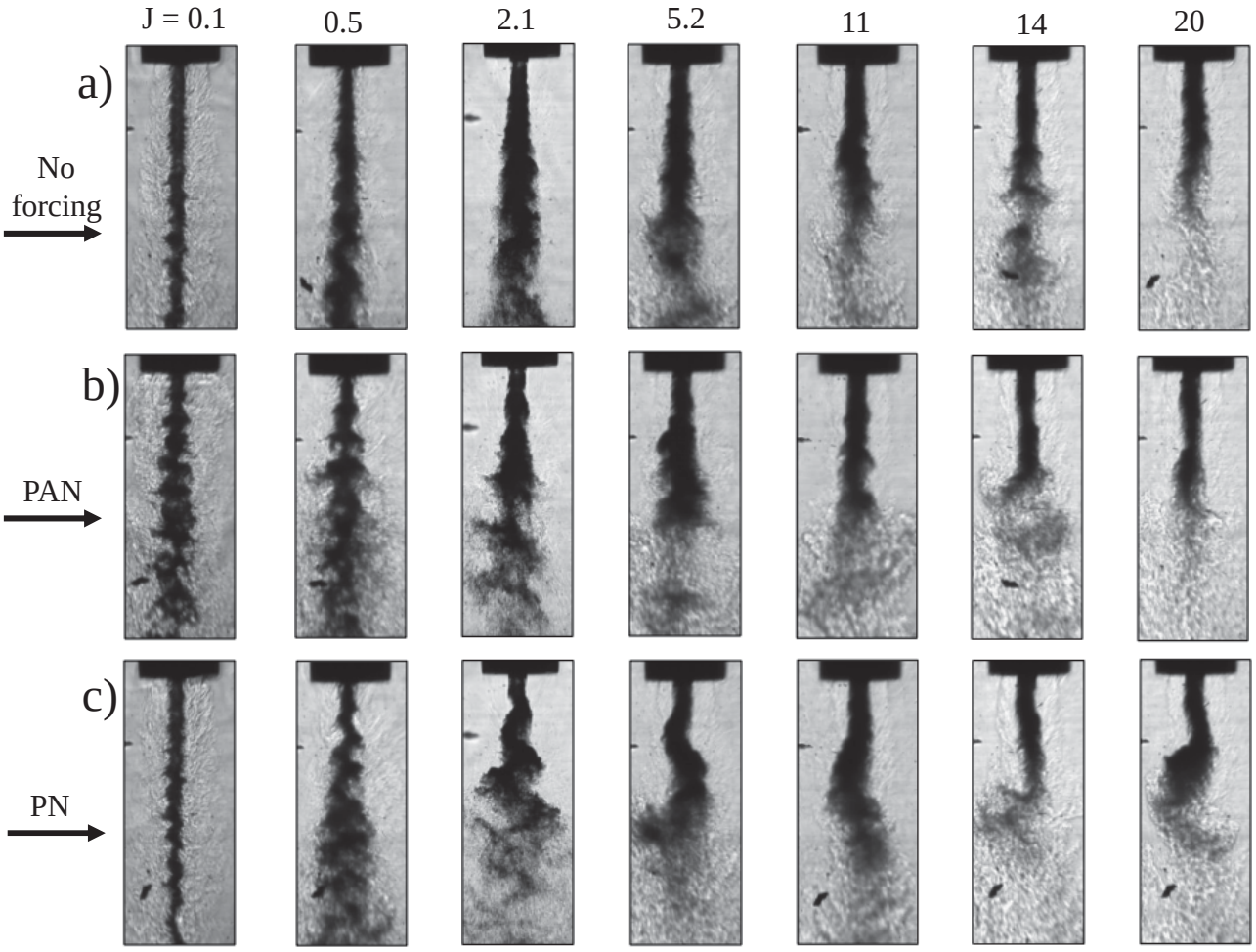

Figure 20: Visualizations of injector IV at subcritical pressure at momentum flux ratios of 0.1, 0.5, 2.1, 5.2, 11, 14, 20 under a) no acoustic forcing, b) pressure antinode forcing, and c) pressure node forcing.

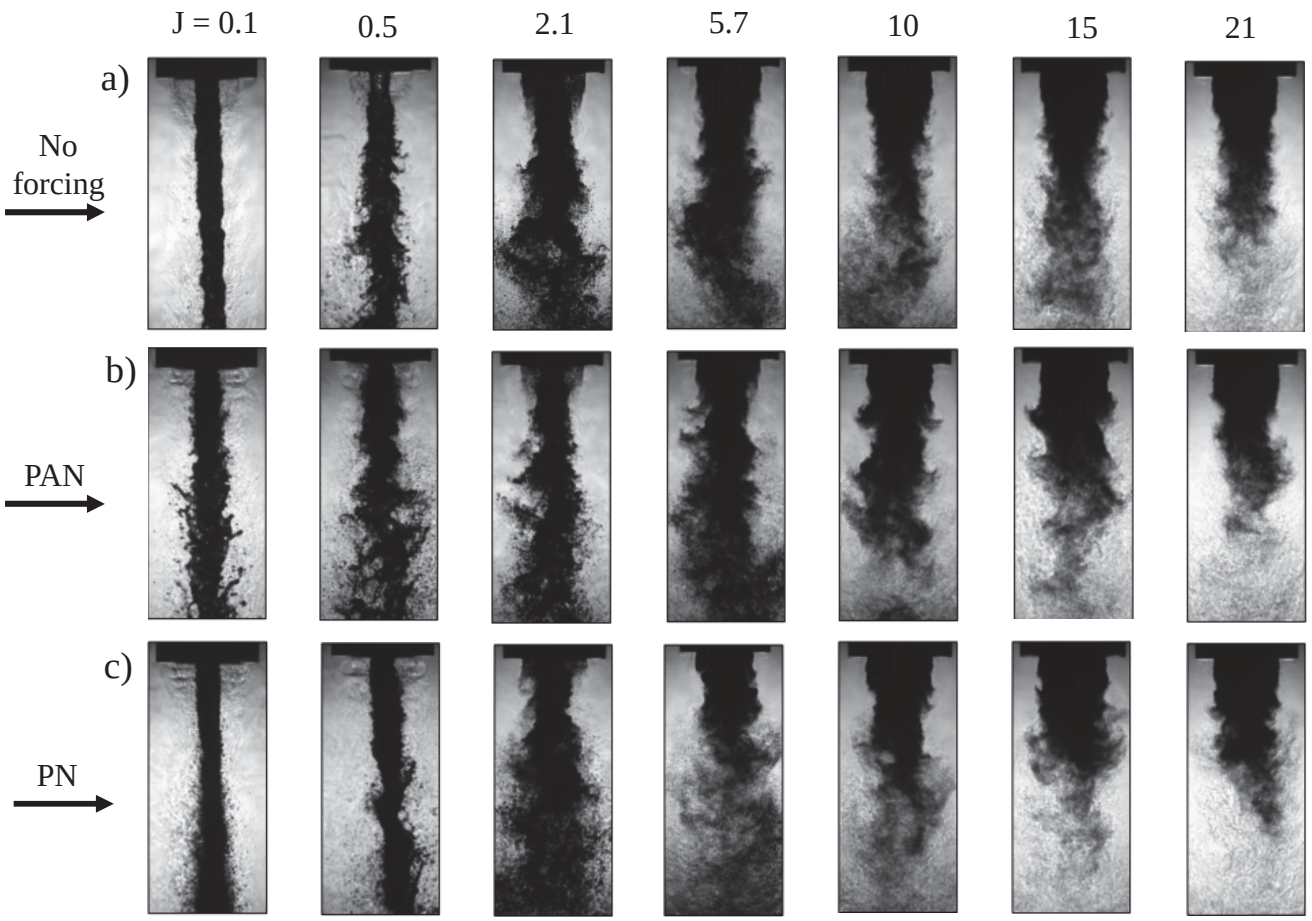

Figure 21: Visualizations of injector III at subcritical pressure at momentum flux ratios of 0.1, 0.5, 2.1, 5.7, 10, 15, 21 under a) no acoustic forcing, b) pressure antinode forcing, and c) pressure node forcing.

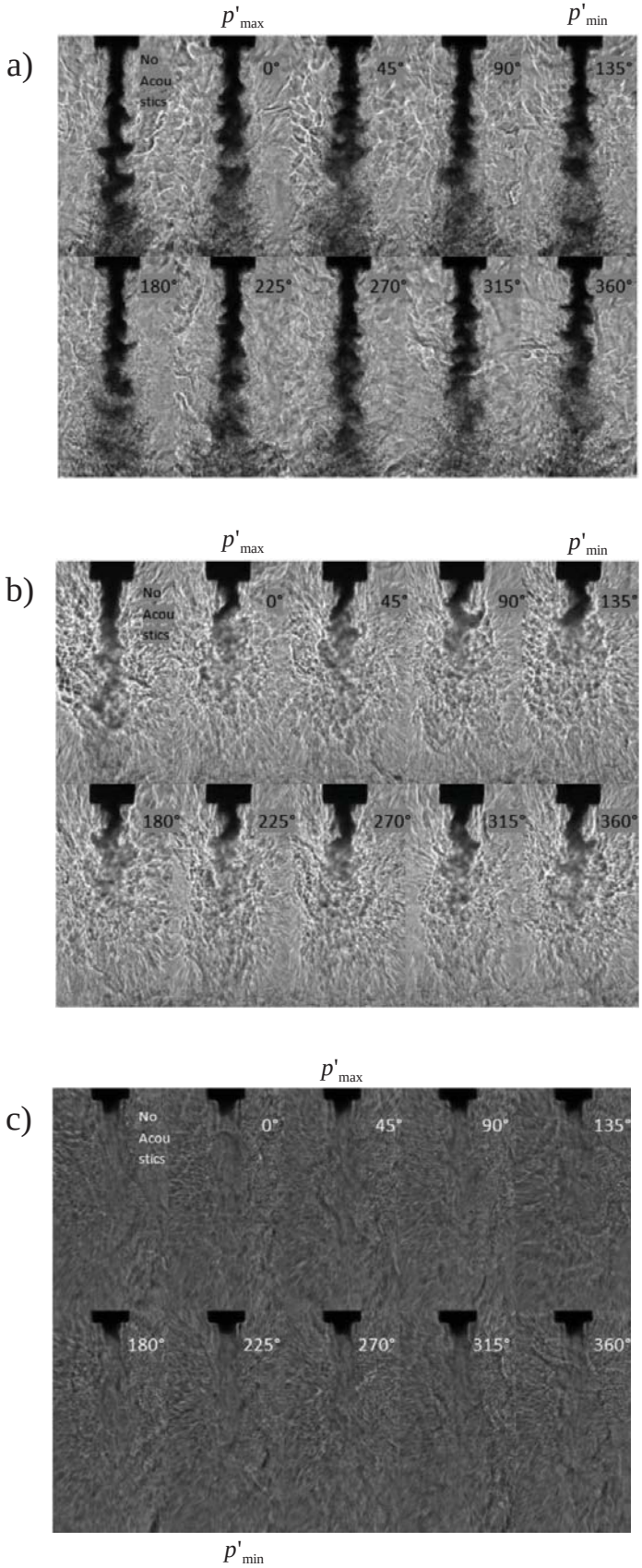

Figure 22: Visualizations of injector I under acoustic forcing conditions at supercritical pressure at momentum flux ratios J of a) 0.55, b) 4.9, and c) 9.3.

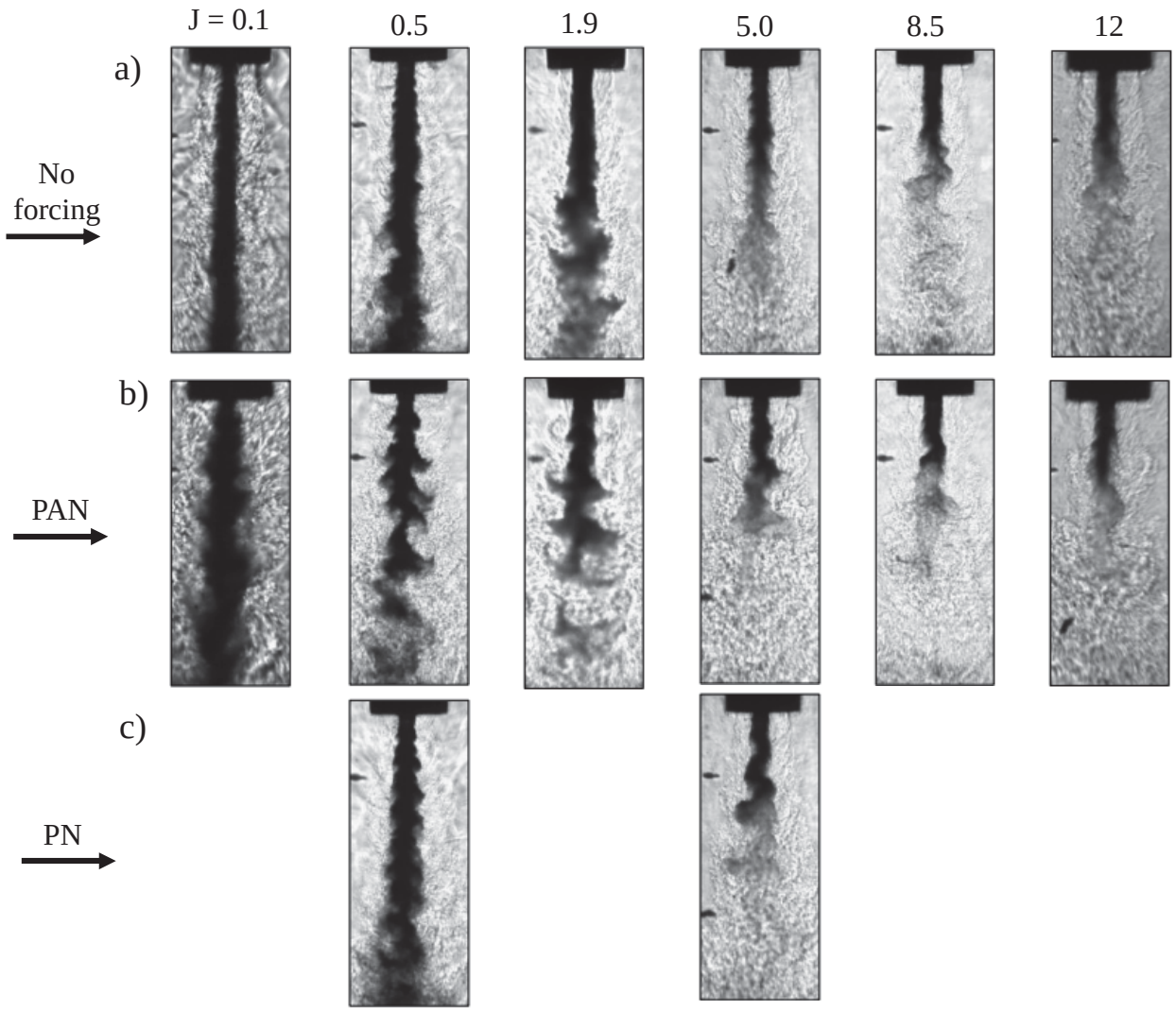

Figure 23: Visualizations of injector IV at supercritical pressure at momentum flux ratios of 0.1, 0.5, 1.9, 5.0, 8.5, and 12 under a) no acoustic forcing, b) pressure antinode forcing, and c) pressure node forcing.

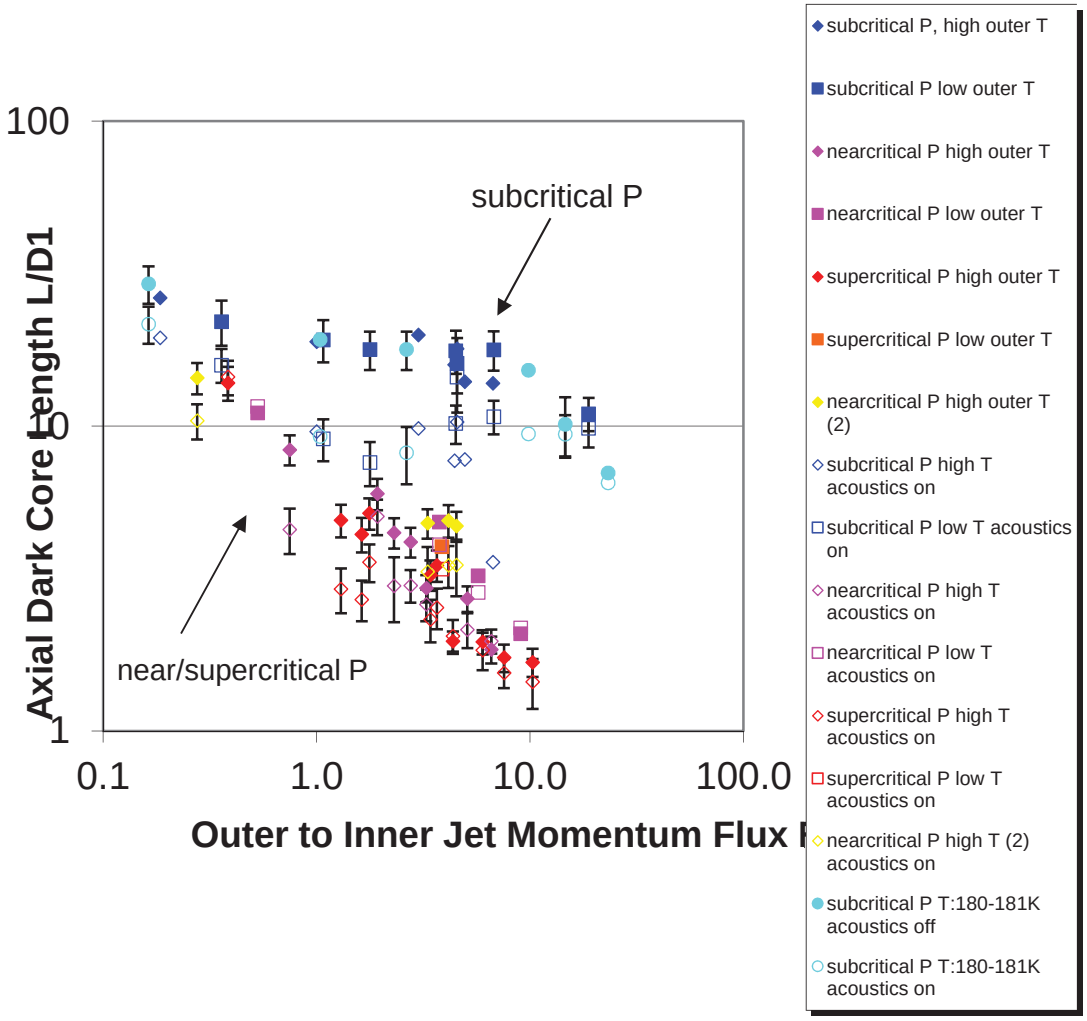

Figure 24: Axial Dark-Core Length, L vs J for sub-, near-, and supercritical conditions with acoustics on and off for injector LAR-thick.

.

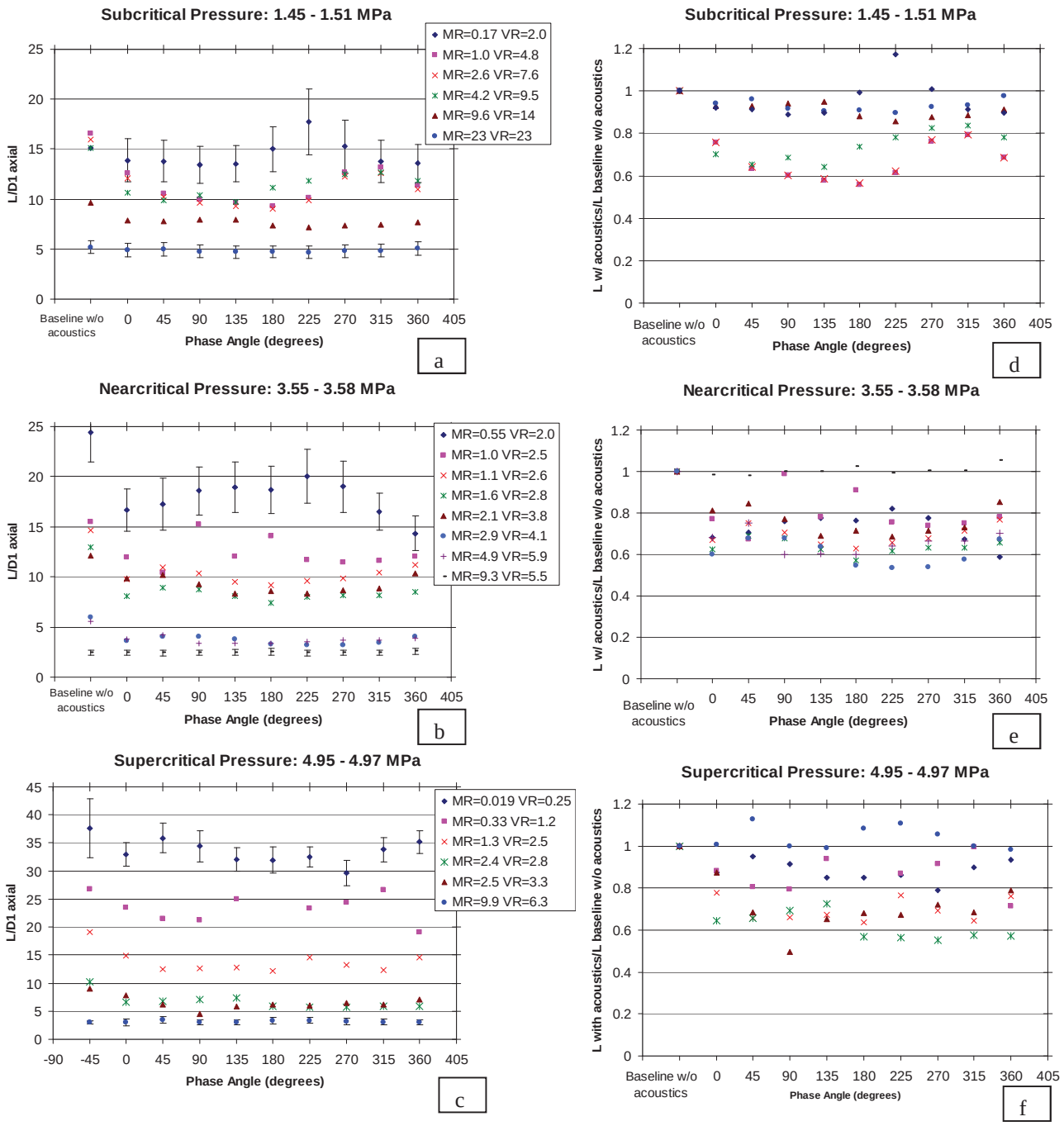

Figure 25: Dark core length for injector LAR-thick with no acoustics and as a function of the phase angle for a range of outer to inner momentum flux ratios (MR) for a) subcritical pressure, b) nearcritical pressure and c) supercritical pressure. Dark core length normalized by the baseline values with no acoustics as a function of the phase angle for d) subcritical pressure, e) nearcritical pressure and f) supercritical pressure.

.

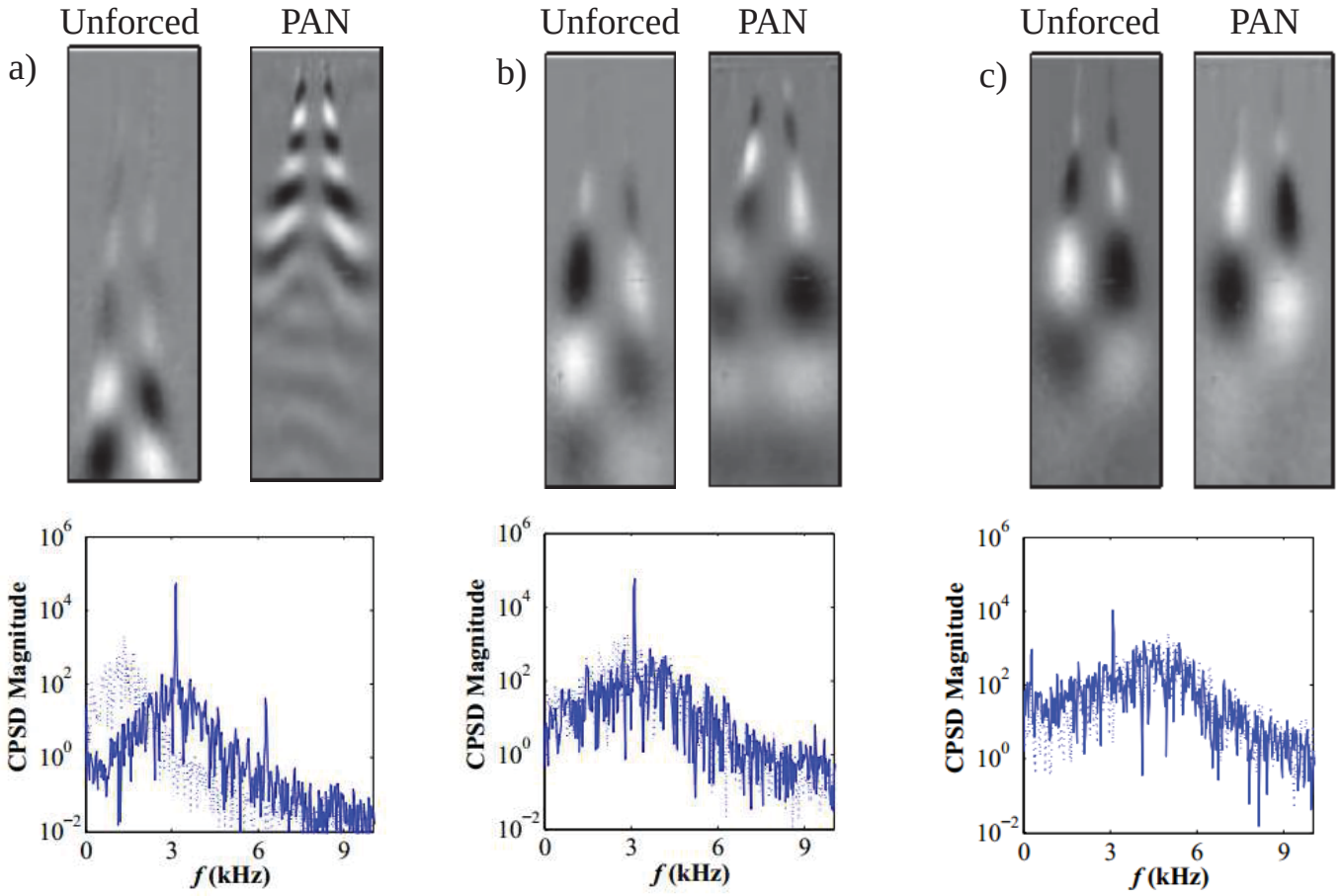

Figure 26: The unforced and PAN forced spatial mode of the dominant convective mode for injector IV at subcritical pressure at momentum flux ratio J of a) 0.5, b) 5.2, and c) 11.

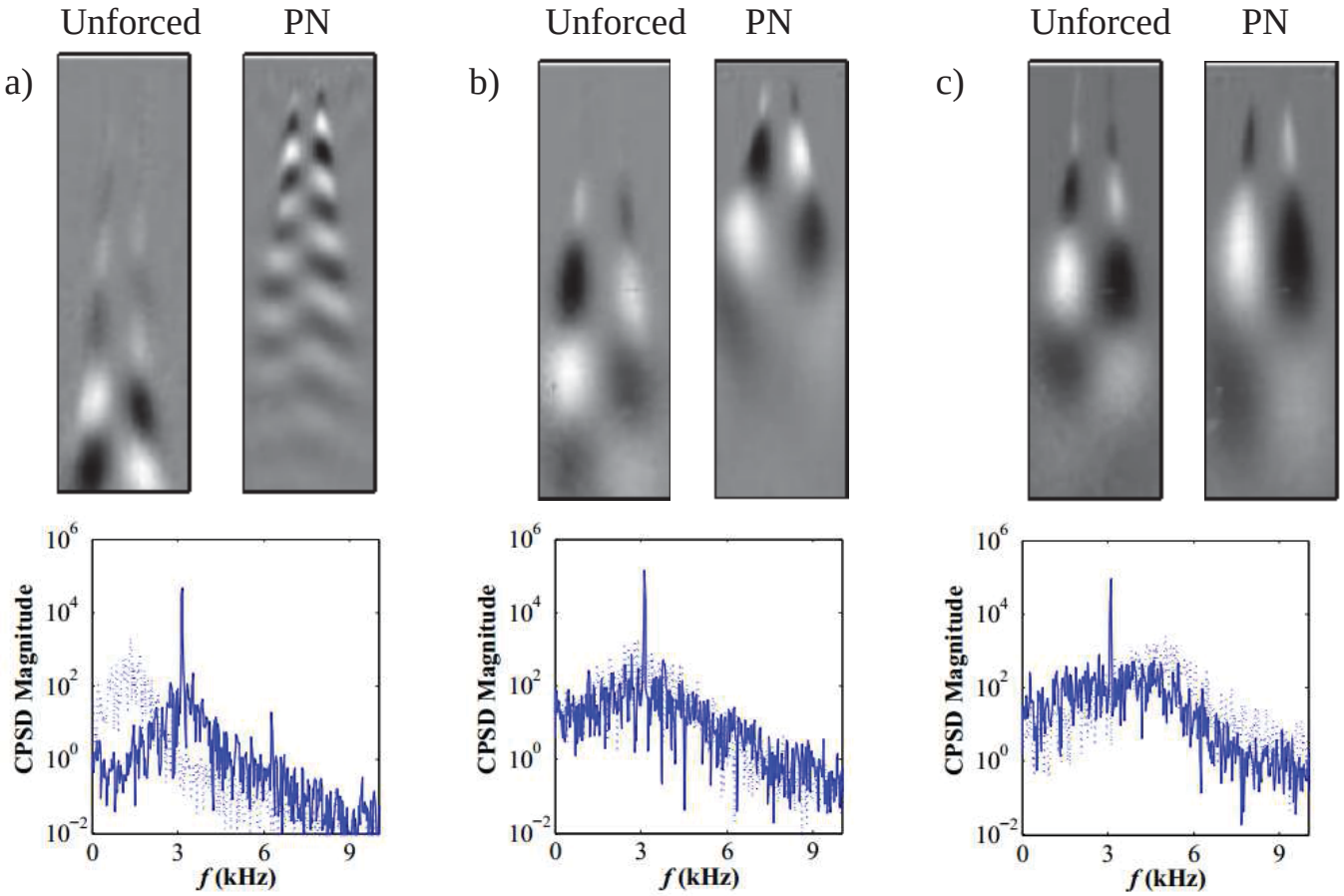

Figure 27: The unforced and PN forced spatial mode of the dominant convective mode for injector IV at subcritical pressure at momentum flux ratio J of a) 0.5, b) 5.2, and c) 11.

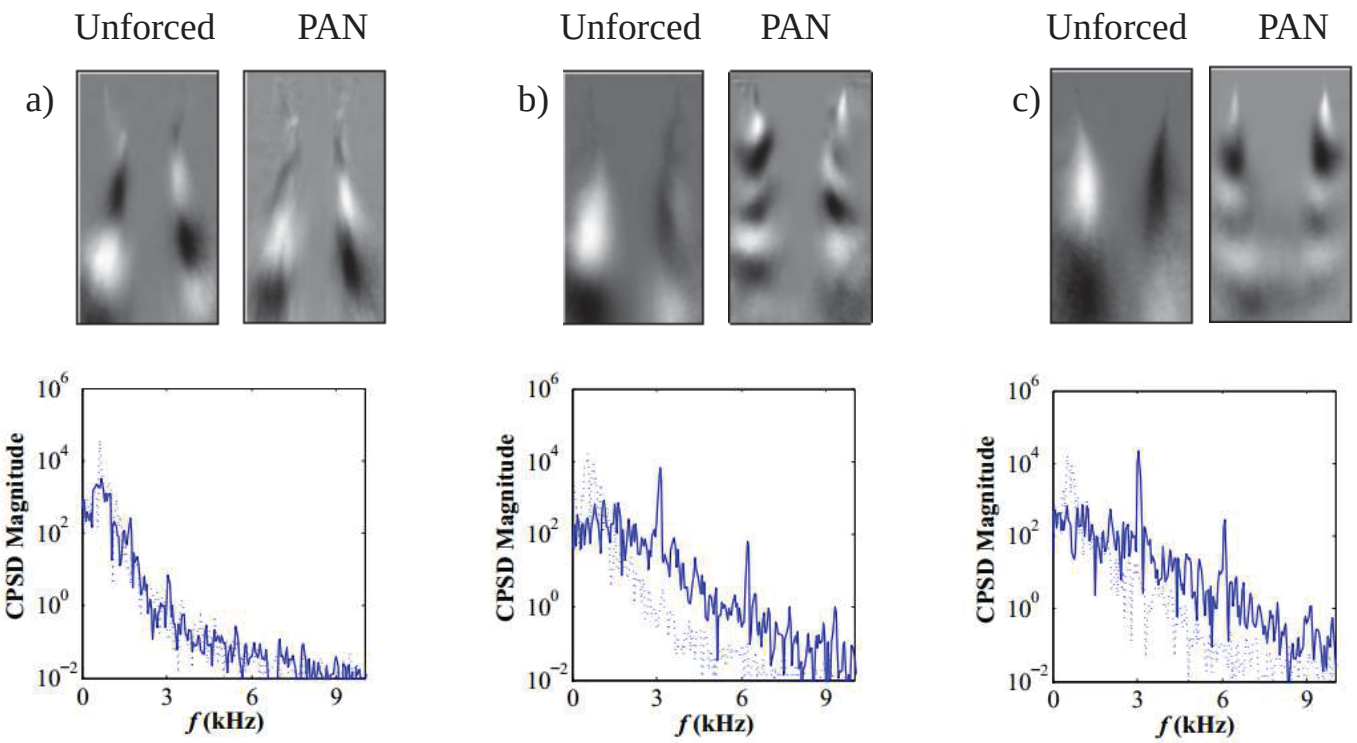

Figure 28: The unforced and PAN forced spatial mode of the dominant convective mode for injector III at subcritical pressure at momentum flux ratio J of a) 2.1, b) 5.7, and c) 15.

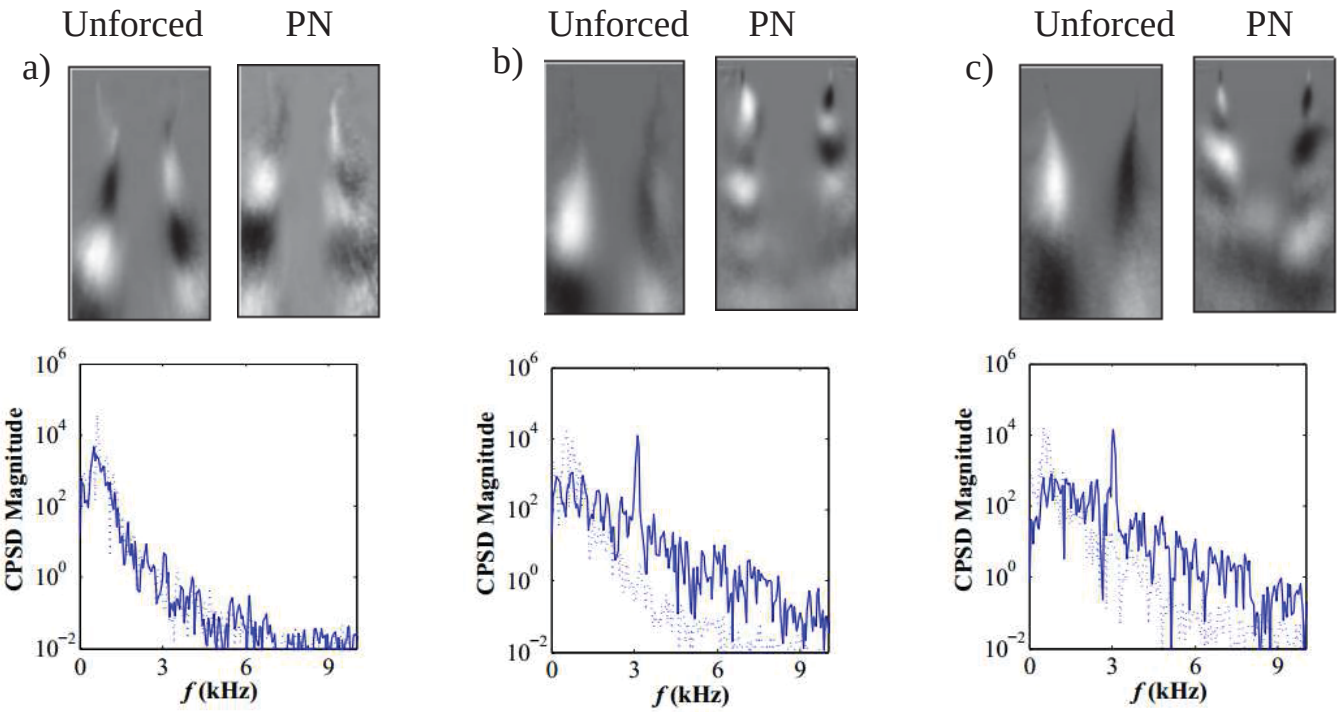

Figure 29: The unforced and PN forced spatial mode of the dominant convective mode for injector IV at subcritical pressure at momentum flux ratio J of a) 2.1, b) 5.7, and c) 15.

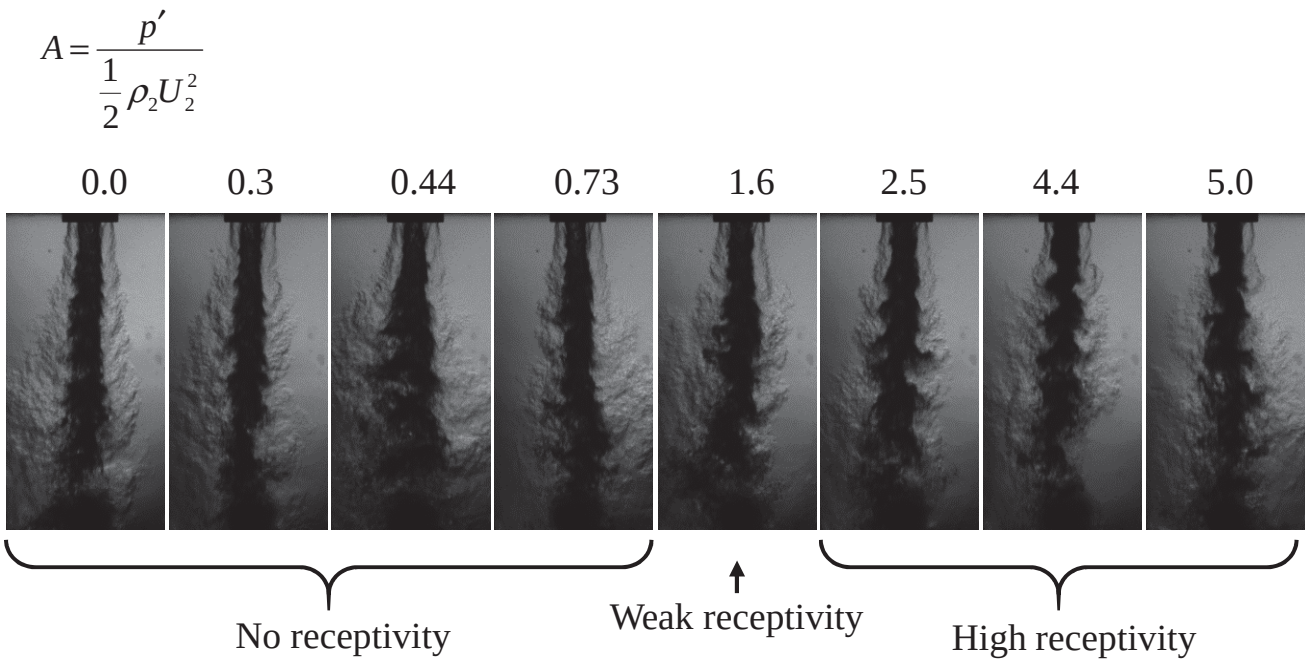

Figure 30: Pressure antinode (PAN) behavior for injector V at a momentum flux ratio of 2.0 as a function of acoustic forcing amplitude at a frequency ratio of 2.6.

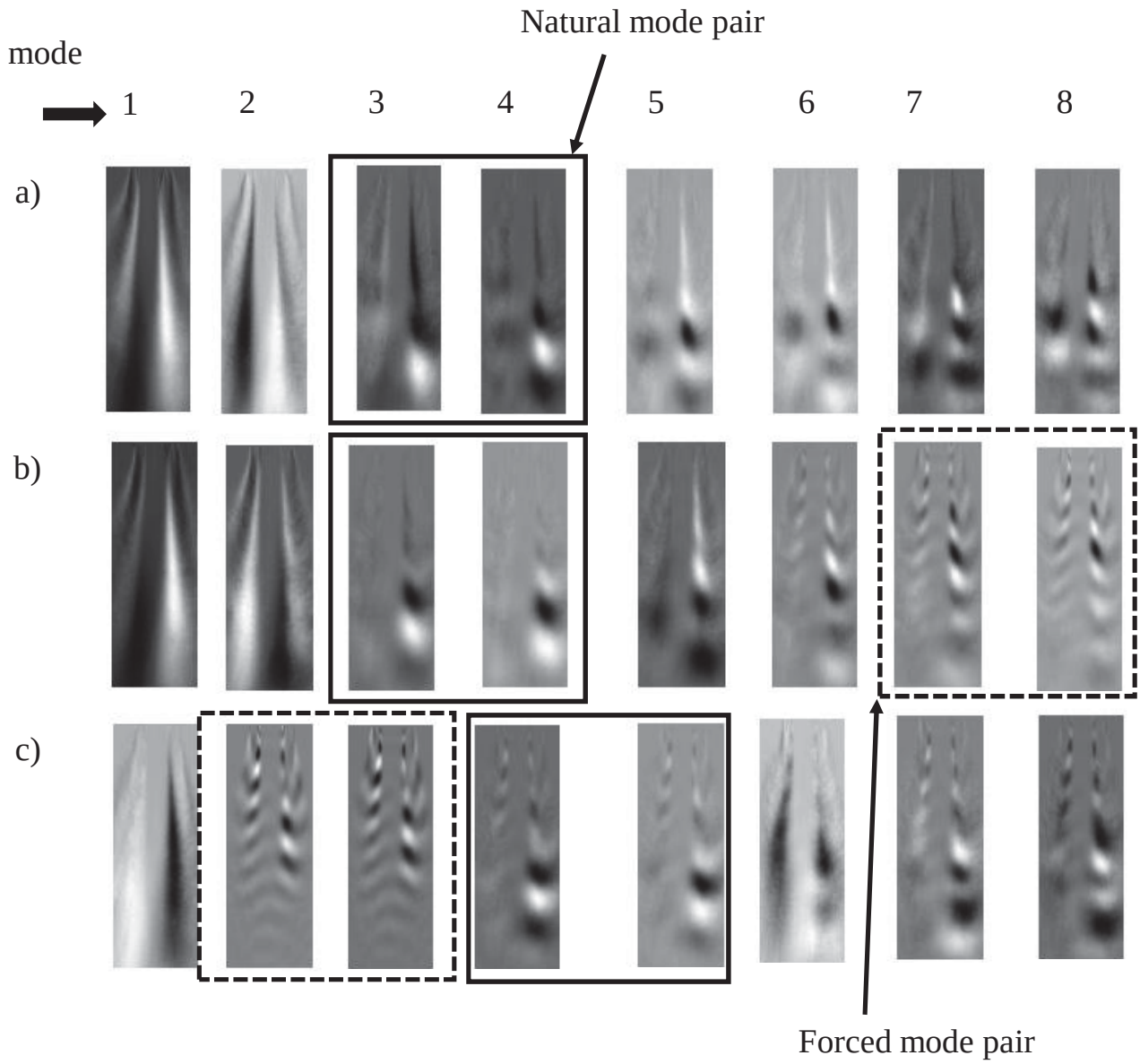

Figure 31: First eight POD modes for injector V for a) unforced case, b) a weakly forced case where a new mode is observed but of lower order than the natural mode, and c) a strongly forced case where the forced mode dominates the natural mode.

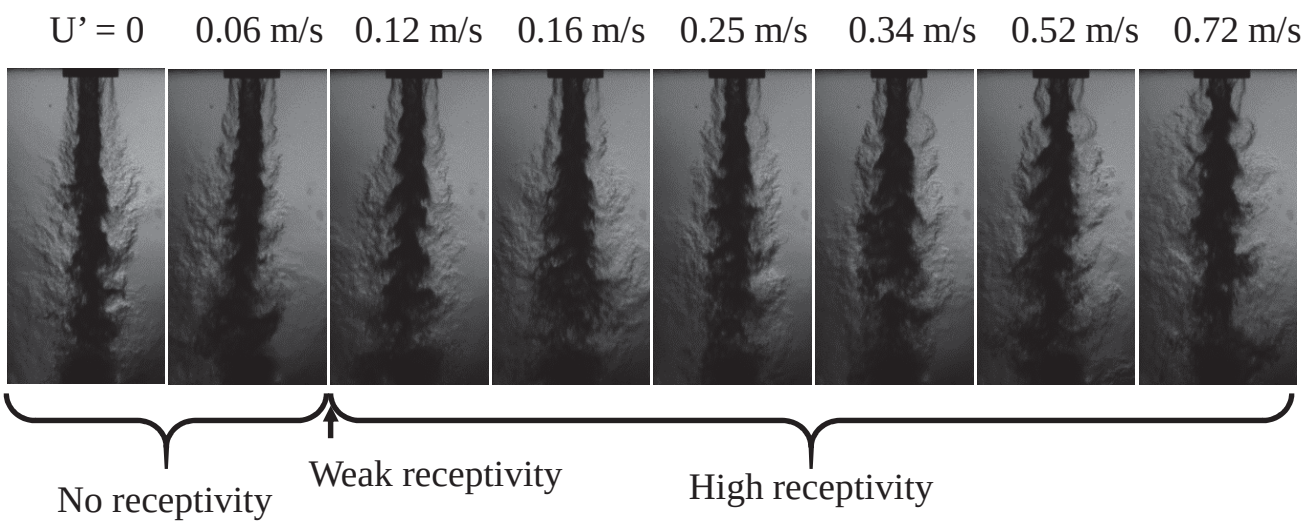

Figure 32: Pressure node (PN) behavior for injector V as a function of acoustic forcing amplitude at a frequency ratio of 2.6.

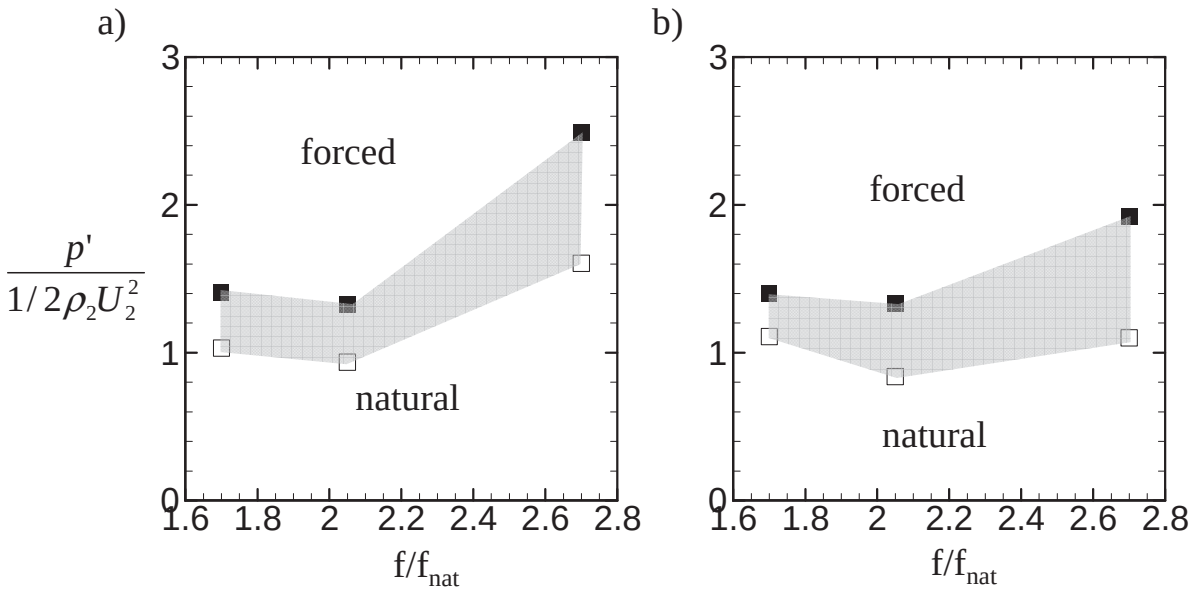

Figure 33: Pressure antinode (PAN) forcing receptivity diagram as a function of normalized frequency and normalized acoustic pressure amplitude for a) J = 2.0 and b) J = 5.9.

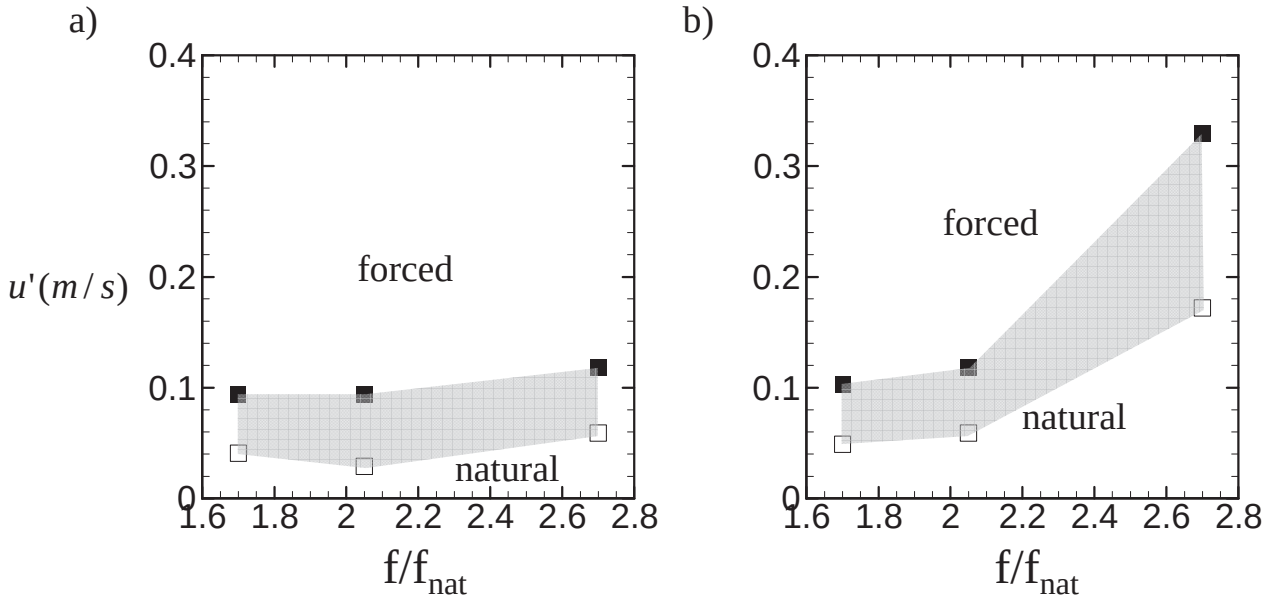

Figure 34: Pressure node (PN) forcing receptivity diagram as a function of normalized frequency and acoustic velocity amplitude for a) J = 2.0 and b) J = 5.9.

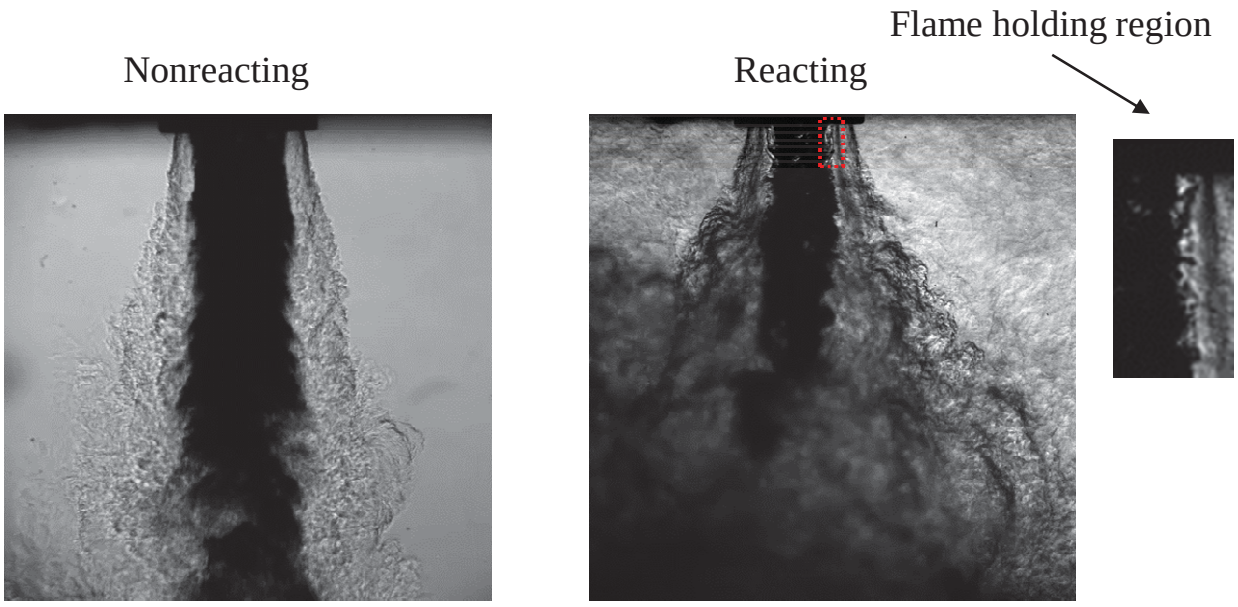

Figure 35: Backlit images of injector V operating with liquid oxygen and gaseous hydrogen for reacting and nonreacting conditions.

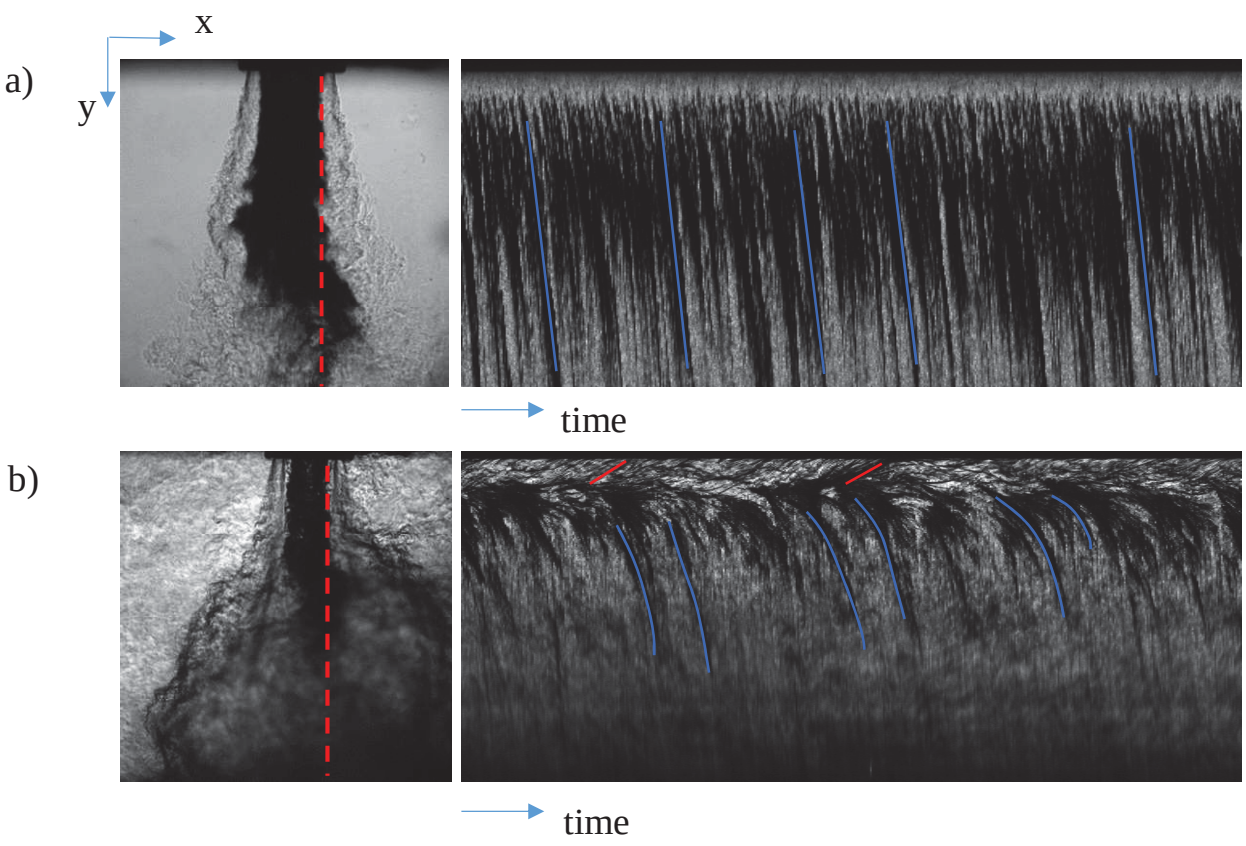

Figure 36: Pixel array y-t streak diagrams for a) nonreacting and b) reacting conditions.

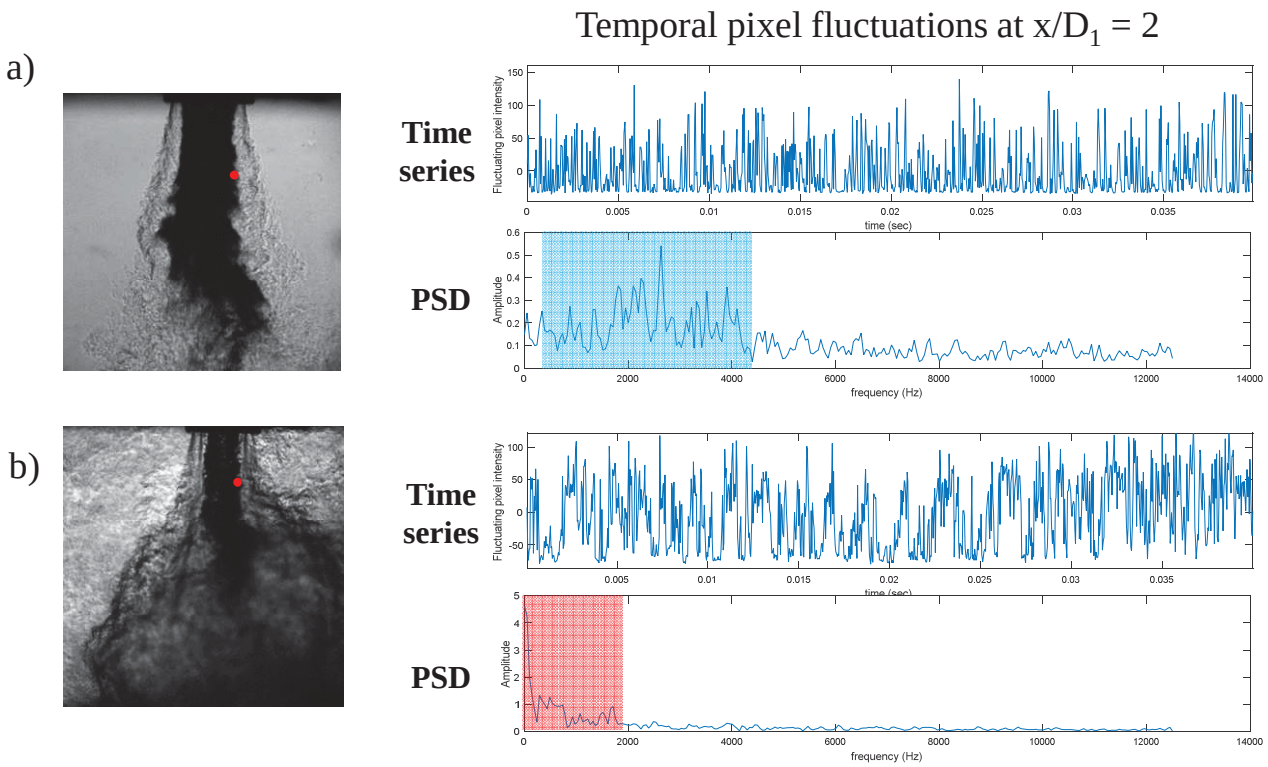

Figure 37: Temporal and spectral characteristics of pixel intensity fluctuations in the inner shear layer for a) nonreacting and b) reacting flow conditions.

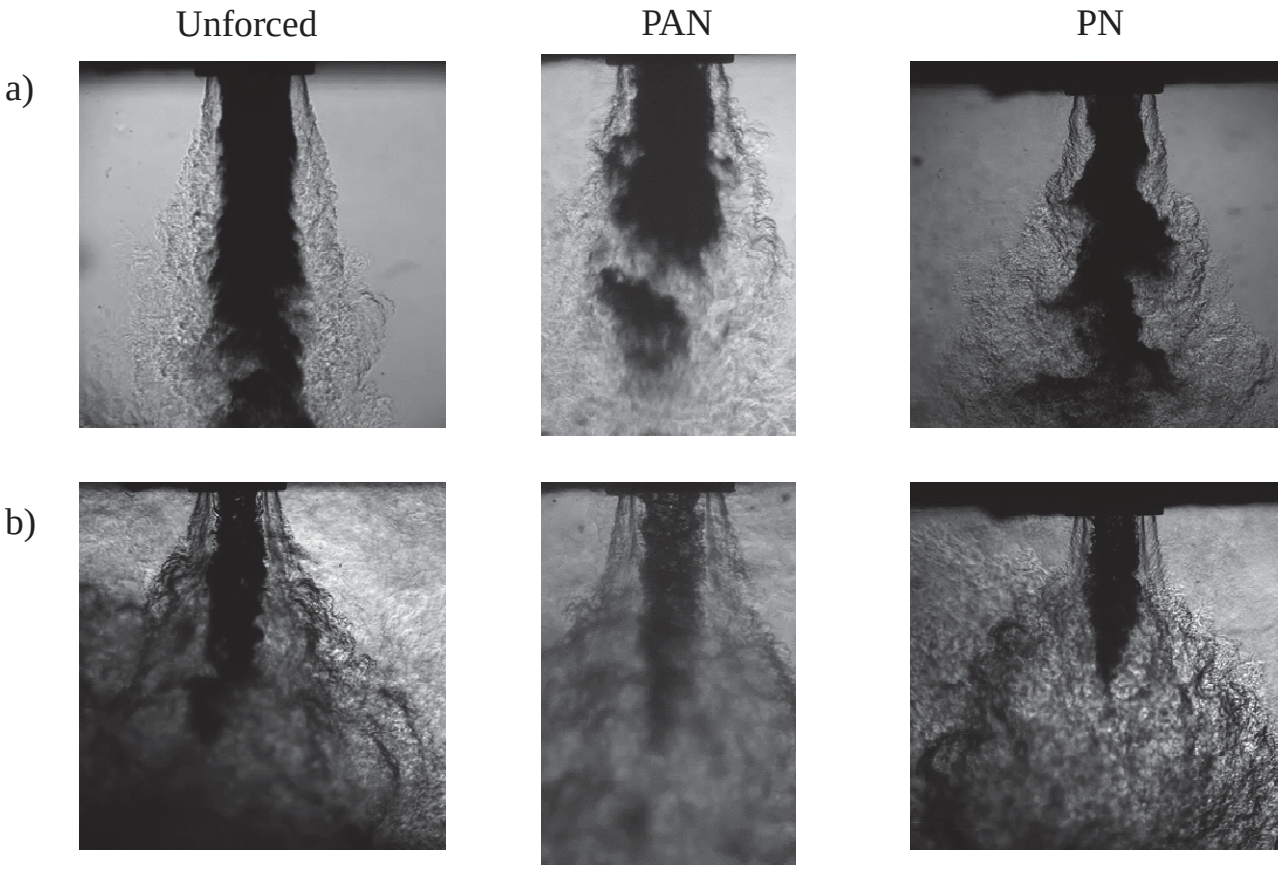

Figure 38: Backlit images of unforced, PAN forced, and PN forced cases for a) nonreacting and b) reacting flow conditions.

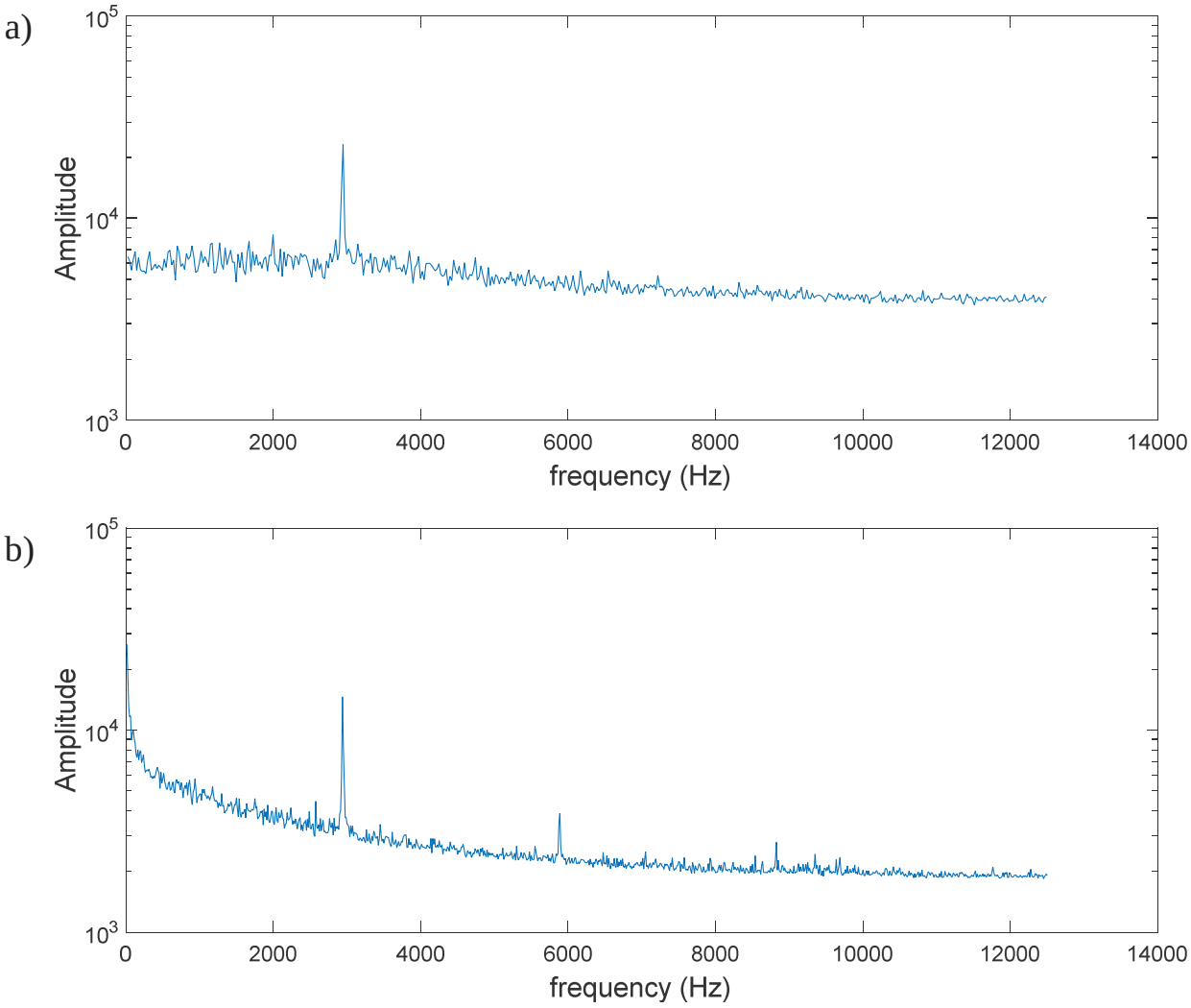

Figure 39: Dynamic mode decomposition spectrum for PAN forcing of the a) nonreacting and b) reacting cases.

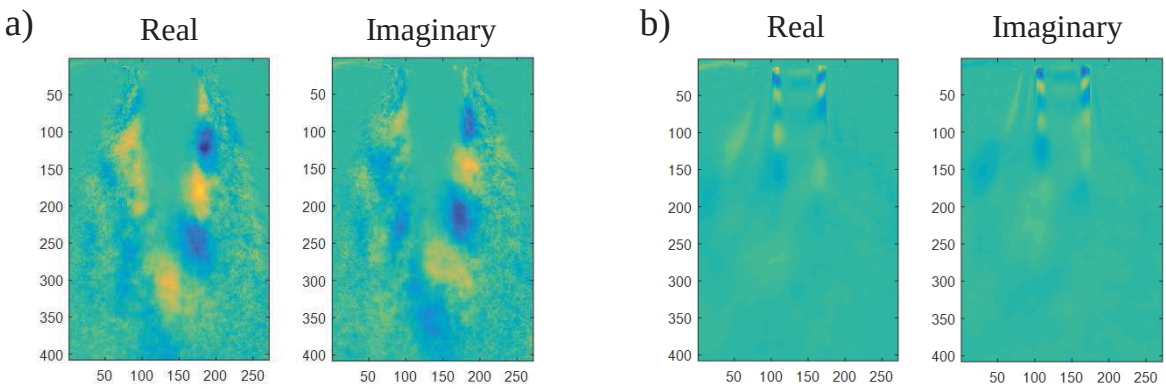

Figure 40: Real and imaginary spatial DMD modes for the PAN forced a) nonreacting and b) reacting cases.

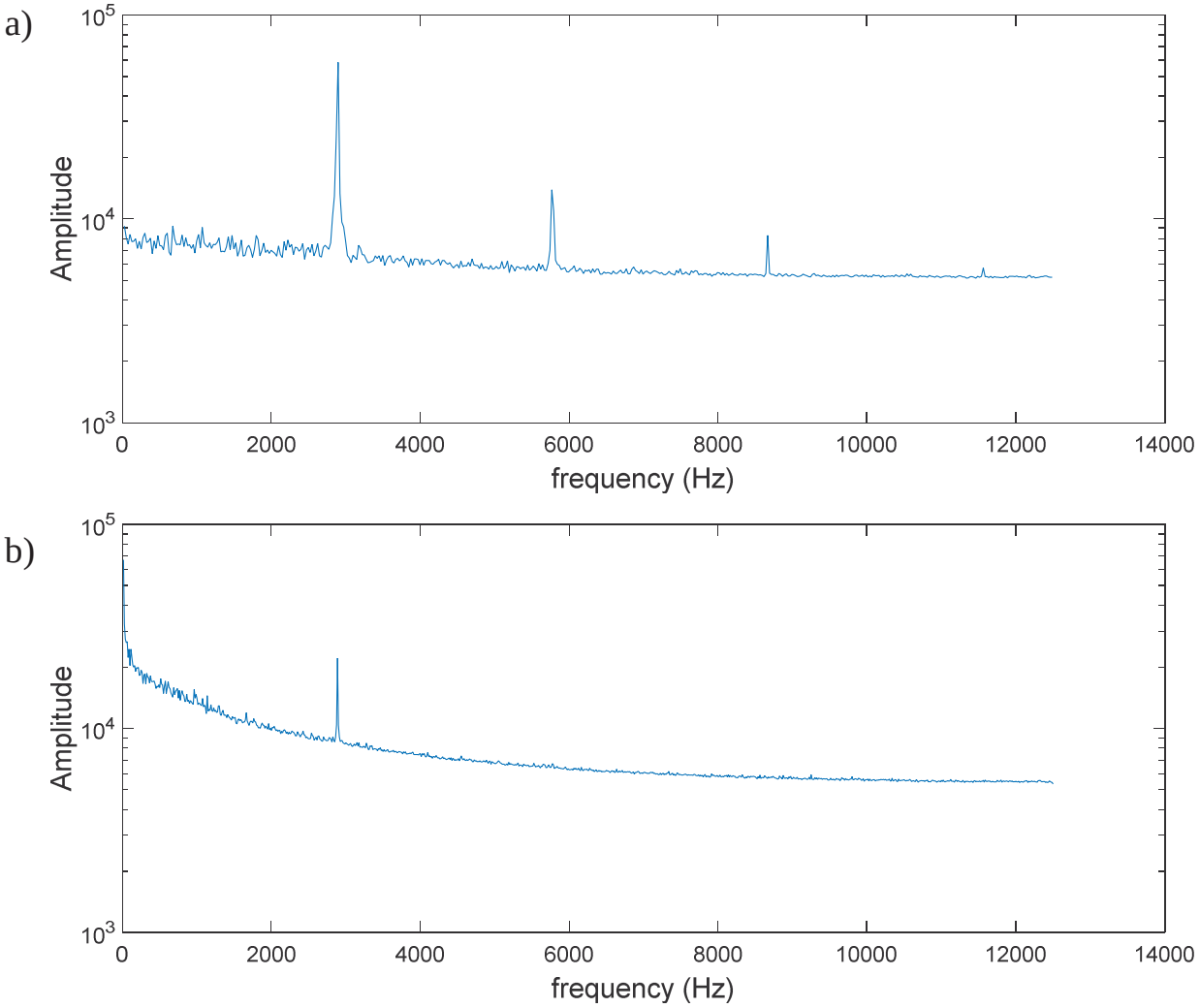

Figure 41: Dynamic mode decomposition spectrum for PN forcing of the a) nonreacting and b) reacting cases.

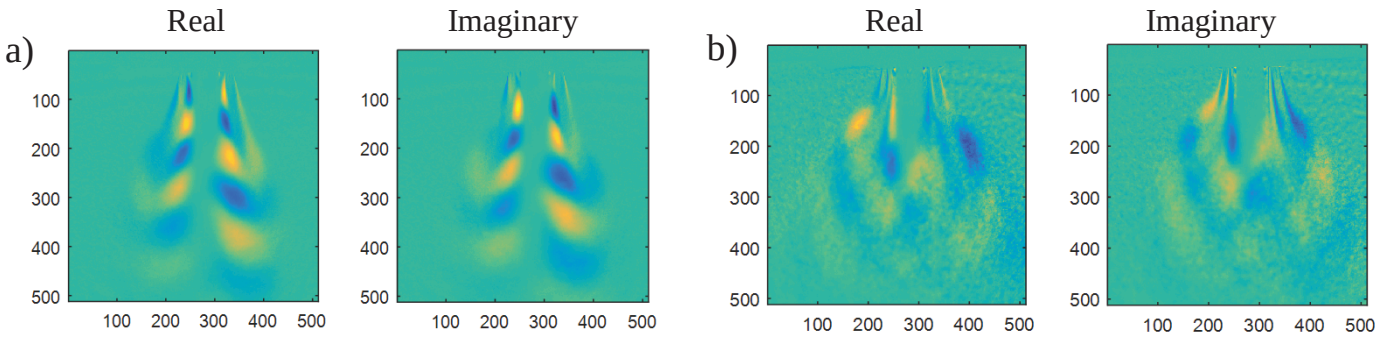

Figure 42: Real and imaginary spatial DMD modes for the PN forced a) nonreacting and b) reacting cases.

AFRL-RQ-ED-TR-2016-0023
Primary Distribution of this Report:

RQR
AFRL R&D Case Files
Completed Interim and Final Tech Reports Repository

AFRL/RQ Technical Library
6 Draco Drive
Edwards AFB, CA 93524-7130

Johns Hopkins University
Whiting School of Engineering
ATTN: Mary T. Gannaway/FSO
10630 Little Patuxent Pkwy, Suite 202
Columbia, MD 21044-3286

Defense Technical Information Center
(1 Electronic Submission via STINT)
Attn: DTIC-ACQS
8725 John J. Kingman Road, Suite 94
Ft. Belvoir, VA 22060-6218